Transactions of the ASME®

Journal of Heat Transfer

HEAT TRANSFER DIVISION
Chairman, **R. GREIF**
Secretary, **G. P. PETERSON**
Technical Editor, **R. VISKANTA (1995)**
Associate Technical Editors,
Y. BAYAZITOGLU (1995)
V. K. DHIR (1996)
A. FAGHRI (1996)
W. A. FIVELAND (1994)
L. S. FLETCHER (1994)
W. L. GROSSHANDLER (1995)
C. E. HICKOX, JR. (1995)
Y. JALURIA (1996)
J. R. LLOYD (1995)
M. F. MODEST (1996)
R. A. NELSON, JR. (1996)
T. W. SIMON (1995)
L. C. WITTE (1994)

BOARD ON COMMUNICATIONS
Chairman and Vice President
R. D. ROCKE

Members-at-Large
T. BARLOW, T. DEAR, L. KEER, J. KITTO,
W. MORGAN, E. M. PATTON, S. PATULSKI,
R. E. REDER, R. SHAH, A. VAN DER SLUYS,
F. M. WHITE, J. WHITEHEAD

OFFICERS OF THE ASME
President, **J. H. FERNANDES**
Executive Director,
D. L. BELDEN
Treasurer,
R. A. BENNETT

PUBLISHING STAFF
Mng. Dir., Publ.,
CHARLES W. BEARDSLEY
Managing Editor,
CORNELIA MONAHAN
Sr. Production Editor,
VALERIE WINTERS
Production Assistant,
MARISOL ANDINO

Transactions of the ASME, Journal of Heat Transfer (ISSN 0022-1481) is published quarterly (Feb., May, Aug., Nov.) for $165.00 per year by The American Society of Mechanical Engineers, 345 East 47th Street, New York, NY 10017. Second class *postage paid at New York, NY and additional* mailing offices. POSTMASTER: Send address changes to Transactions of the ASME, Journal of Heat Transfer, c/o THE AMERICAN SOCIETY OF MECHANICAL ENGINEERS, 22 Law Drive, Box 2300, Fairfield, NJ 07007-2300.
CHANGES OF ADDRESS must be received at Society headquarters seven weeks before they are to be *effective. Please send old label and new address.*
PRICES: To members, $40.00, annually: to nonmembers, $165.00.
Add $24.00 for postage to countries outside the United States and Canada.

STATEMENT from By-Laws. The Society shall not be responsible for statements or opinions advanced in papers or . . . printed in its publications (B7.1, para. 3).
COPYRIGHT © 1994 by The American Society of *Mechanical Engineers. Authorization to photocopy material* for internal or personal use under circumstances not falling within the fair use provisions of the Copyright Act is granted by ASME to libraries and other users registered with the Copyright Clearance Center (CCC) Transactional Reporting Service provided that the base fee of $3.00 per article is paid directly to CCC, 27 Congress St., Salem, MA 01970. Request for special permission or bulk copying should be addressed to Reprints/Permission Department.

INDEXED by Applied *Mechanics Reviews and Engineering Information, Inc.*
Canadian Goods & Services Tax Registration #126148048.

Published Quarterly by The American Society of Mechanical Engineers

VOLUME 116 • NUMBER 2 • MAY 1994

TECHNICAL PAPERS

1992 Max Jakob Memorial Award Lecture

Heat Conduction

Heat Conduction in Thin Films

Natural Convection

Multiphase Heat Transfer

Forced Convection in Porous Media

Downloaded 04 Feb 2011 to 194.85.80.107. Redistribution subject to ASME license or copyright; see http://www.asme.org/terms/Terms_Use.cfm

(Contents continued)

TECHNICAL NOTES

ANNOUNCEMENTS

The 1992 Max Jakob Memorial Award Lecture

Turbulent Prandtl Number—Where Are We?

William M. Kays
Professor Emeritus,
Stanford University,
Stanford, CA 94305

The objective of this paper is to examine critically the presently available experimental data on Turbulent Prandtl Number for the two-dimensional turbulent boundry layer, and for fully developed flow in a circular tube or a flat duct, and attempt to draw some conclusions as to where matters presently stand.

Introduction

The title is in the form of a question. Before attempting an answer we should perhaps address another question: Why is Turbulent Prandtl Number even relevant today? There are many who would argue, and quite convincingly, that recent advances in turbulent flow modeling make the concept of eddy diffusivity obsolete, and without an eddy diffusivity Turbulent Prandtl Number has no meaning. [See, for example, Launder (1989) or Nagano and Kim (1988).] If we are talking about three-dimensional flows or re-circulating flows, or in other words the completely general turbulent flow problem, then the concept of an eddy diffusivity certainly loses its usefulness and there is no argument. But if we restrict consideration to the two-dimensional turbulent boundary layer, or flow in a long pipe or duct, where in both cases the most important turbulent heat diffusion is only in a direction normal to the main flow direction, the use of higher level turbulence models for 98 percent of engineering calculations becomes absurdly complex. A very large number of experimentally determined constants becomes necessary, and even these have not all been satisfactorily determined. On the other hand an eddy diffusivity model, in which the eddy diffusivity for momentum is evaluated by either a mixing-length model or the k-ϵ model, and the eddy diffusivity for heat is evaluated using the Turbulent Prandtl Number concept, is extremely simple. It is capable of accurately predicting behavior in a great variety of situations—in fact in most engineering boundary layer problems that one is likely to encounter.

Were the Turbulent Prandtl Number a very complex function of a number of variables it would still not be very useful, but all the evidence suggests that it is a number near unity (which is essentially the classical Reynolds Analogy) and its departures from unity are not great except for very low Prandtl number fluids.

It should be noted that it must be possible to "back out" Turbulent Prandtl Number from any higher order turbulence model, so experimental data on Turbulent Prandtl Number provide a compact database, which must in any case be satisfied by such models.

The primary objective of this paper is then to examine critically the presently available experimental data on Turbulent Prandtl Number (which we will hereafter refer to as Pr-t) for the two-dimensional turbulent boundary layer and for fully developed flow in a circular pipe or a flat duct. We will examine data for favorable and adverse pressure gradients, flows with transpiration, and rough surfaces, but the primary emphasis will be on the simple flat plate boundary layer with no pressure gradient, and fully developed flow in a tube or duct. (For fully developed flow in a tube or duct there is of course a favorable pressure gradient.) We will emphasize constant fluid properties and velocities sufficiently low that viscous dissipation may be neglected. However, the properties of some of the *liquids* vary so markedly with temperature that we will be forced in that case to examine data where the properties [primarily viscosity and Prandtl number] do vary considerably.

Definition of Pr-t

For constant fluid properties and no viscous dissipation, the differential equations that must be satisfied in the boundary layer are (for flow in a circular tube the coordinate system need only be changed to cylindrical):

Continuity

$$\frac{\partial u}{\partial x}+\frac{\partial v}{\partial y}=0 \qquad (1)$$

Momentum

$$u\frac{\partial u}{\partial x}+v\frac{\partial u}{\partial y}+\left(\frac{1}{\rho}\right)\frac{dP}{dx}=\frac{\partial}{\partial y}\left(\nu\frac{\partial u}{\partial y}-\overline{u'v'}\right) \qquad (2)$$

Energy

$$u\frac{\partial t}{\partial x}+v\frac{\partial t}{\partial y}=\frac{\partial}{\partial y}\left(\alpha\frac{\partial t}{\partial y}-\overline{t'v'}\right) \qquad (3)$$

The eddy diffusivity concept introduces the following definitions:

$$\overline{u'v'}=-\epsilon_M\left(\frac{\partial u}{\partial y}\right) \qquad (4)$$

$$\overline{t'v'}=-\epsilon_H\left(\frac{\partial t}{\partial y}\right) \qquad (5)$$

and Eqs. (2) and (3) become:

$$u\frac{\partial u}{\partial x}+v\frac{\partial u}{\partial y}+\left(\frac{1}{\rho}\right)\frac{dP}{dx}=\frac{\partial}{\partial y}\left[(\nu+\epsilon_M)\frac{\partial u}{\partial y}\right] \qquad (6)$$

$$u\frac{\partial t}{\partial x}+v\frac{\partial t}{\partial y}=\frac{\partial}{\partial y}\left[(\alpha+\epsilon_H)\frac{\partial t}{\partial y}\right] \qquad (7)$$

Now let us define Turbulent Prandtl Number as:

$$\text{Pr-t}=\frac{\epsilon_M}{\epsilon_H} \qquad (8)$$

Contributed by the Heat Transfer Division and presented at the National Heat Transfer Conference, Atlanta, Georgia, August 8–11, 1993. Manuscript received by the Heat Transfer Division September 1993; revision received December 1993. Keywords: Forced Convection, Liquid Metals, Modeling and Scaling, Turbulence. Associate Technical Editor: R. Viskanta.

Substituting for ϵ_H in Eq. (7), and after slightly rearranging, the energy equation becomes:

$$u\frac{\partial t}{\partial x}+v\frac{\partial t}{\partial y}=\frac{\partial}{\partial y}\left\{\nu\left[\frac{1}{\text{Pr}}+\frac{\epsilon_M/\nu}{\text{Pr-t}}\right]\frac{\partial t}{\partial y}\right\} \tag{9}$$

It is now apparent that if a solution to the momentum Eq. (6) is available, u, v, and ϵ_M are known at all points in the boundary layer and all that is needed to solve the energy Eq. (9) for any temperature boundary conditions is Pr-t.

Evaluation of Pr-t

If we now substitute Eqs. (4) and (5) into (8) we obtain an equation that can be used to evaluate Pr-t from experimental data or from analytic solutions:

$$\text{Pr-t}=\frac{\overline{u'v'}\,\dfrac{\partial t}{\partial y}}{\overline{t'v'}\,\dfrac{\partial u}{\partial y}} \tag{10}$$

Thus to evaluate Pr-t at any point in the boundary layer from experimental data it is necessary to measure four quantities: the turbulent shear stress, the turbulent heat flux, the velocity gradient, and the temperature gradient. The difficulty of measuring all four of these quantities accurately at a single point in the boundary layer is the reason that direct measurements of Pr-t are relatively scarce, and the reason that the scatter of experimental data tends to be so large.

The Reynolds Analogy

The simplest possible model for turbulent heat transfer leads to the result:

$$\epsilon_H=\epsilon_M \tag{11}$$

Thus:

$$\text{Pr-t}=1.00 \tag{12}$$

This result is the Reynolds Analogy. The remarkable thing is that the Reynolds Analogy is very close to correct for most boundary layer flows, as we shall see. But it is not precisely correct and there are important departures from Pr-t = 1.00 that we will examine.

Evaluation of Pr-t From the "Log" Slope of Velocity and Temperature Profiles

The difficulty of accurately determining Pr-t from experimental data has been mentioned. However, there is one special case where it is not so difficult.

As is well known, the velocity profile over a substantial part of the simple turbulent boundary layer with no transpiration is logarithmic in form and can be expressed by the "law of the wall":

$$U^+=2.44\ln Y^+ + 5.00 \tag{13}$$

For moderate and high Prandtl number fluids for no transpiration the temperature profile over a substantial part of the boundary layer can be expressed by a similar equation:

$$T^+=C_1\ln Y^+ + C_2 \tag{14}$$

The reason for the limitation of Eq. (14) to fluids with moderate Prandtl numbers (and here we are referring to *molecular* Prandtl number, not *turbulent* Prandtl number) can be seen by examining the term in the inner brackets in Eq. (9):

$$\left[\frac{1}{\text{Pr}}+\frac{\epsilon_M/\nu}{\text{Pr-t}}\right]$$

The first term represents the contribution of molecular conduction, while the second is the turbulent conduction. For

Nomenclature

A^+ = Van Driest constant
c = specific heat at constant pressure
c_f = friction coefficient $= 2\tau_o/(\rho u_\infty^2)$, $2\tau_o/(\rho V^2)$
D = pipe diameter
EDR = eddy diffusivity ratio $= \epsilon_M/\nu$
h = heat transfer coefficient $= q_o''/(t_o - t_\infty)$, $q_o''/(t_o - t_m)$
k = molecular thermal conductivity
l = Prandtl mixing length
Nu = Nusselt number $= hD/k$
P = time-averaged pressure
Pe-t = turbulent Peclet number $= (\epsilon_M/\nu)\text{Pr}$
Pr = molecular Prandtl number $= \mu c/k$
Pr-eff = "effective" or "total" Prandtl number, see Eq. (16)
Pr-t = turbulent Prandtl number $= \epsilon_M/\epsilon_H$
q_o'' = heat flux at wall
Re = Reynolds number for flow in a pipe $= DV\rho/\mu$
Re-d = Reynolds number in a flat duct, based on hydraulic diameter (hydraulic diameter $= 2\times$ duct spacing)
Re-h = enthalpy thickness Reynolds number $= \Delta_2 u_\infty/\nu$
Re-m = momentum thickness Reynolds number $= \delta_2 u_\infty/\nu$
t = time-averaged temperature
t' = instantaneous fluctuating component of temperature
$\overline{t'v'}$ = turbulent "heat flux," time average of t', v' product
T^+ = temperature in "wall" coordinates $= (t - t_o)u_\tau \rho c/q''$
t_∞ = temperature at outer edge of boundary layer
t_m = mixed mean temperature in a pipe flow
t_o = temperature at wall surface
u = time-averaged velocity in x direction
u' = instantaneous fluctuating component of velocity in x direction
$\overline{u'v'}$ = turbulent "shear stress," time average of u', v' product
U^+ = mean velocity in "wall" coordinates $= u/u_\tau$
u_∞ = velocity at outer edge of boundary layer
u_τ = "shear" velocity $= \sqrt{(\tau_o/\rho)}$
V = mean velocity in a pipe
v = time-averaged velocity in y direction
v' = instantaneous fluctuating component of velocity in y direction
x = distance measured in direction of mean flow
y = distance measured in direction normal to mean flow
Y^+ = distance from wall in "wall coordinates" $= yu_\tau/\nu$
Δ_2 = enthalpy thickness of thermal boundary layer
δ_2 = momentum thickness of momentum boundary layer
ϵ_H = eddy diffusivity for heat, see Eq. (5)
ϵ_M = eddy diffusivity for momentum, see Eq. (4)
μ = dynamic viscosity coefficient
ν = kinematic viscosity coefficient $= \mu/\rho$
ρ = density
τ = shear stress
τ_o = shear stress at wall surface

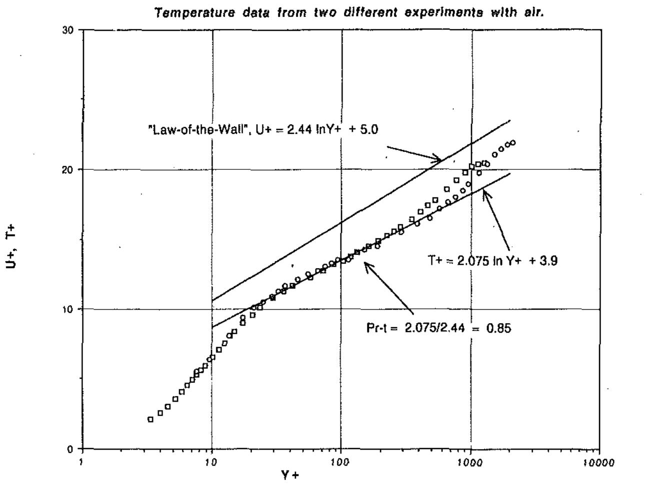

Fig. 1 Example of determination of turbulent Prandtl number from slope of T^+ curve in the "log" region, data of Blackwell et al. (1972)

Table 1 Turbulent Prandtl number from "log" region profile slopes

Pressure Gradient = 0.0

Experiment	Re-m	Re-h	Pr-t
Fluid: Air Pr≈ 0.7			
Reynolds (1958)	Various to	6400	0.73
Moffat (1967)	4419	4756	0.85
Thielbahr (1969)	1572	1684	0.85
Blackwell (1972)	2481	2648	0.85
	2609	3008	0.78
	2971	3180	0.79
Gibson (1984)	2750	3129	0.92
Simon (1980)	4445	1756	0.77
	6365	3746	0.78
	4957	4261	0.82
Pimenta (1979) (fully rough surface)	15142	15412	0.84
Fluid: Water Pr = 5.9			
Hollingsworth (1989)	1552	287	0.85
Fluid: Transformer oil, Pr = 64			
Zukauskas (1987)	1810	195	0.85

$Y^+ >$ about 30, $\epsilon_M/\nu = \kappa Y^+$ where $\kappa = 0.41$ for external boundary layers. As long as the molecular Prandtl number is near 1.00 or higher the molecular conductivity is negligible relative to the turbulent conductivity for $Y^+ > 30$. But at very low Prandtl number the molecular term can be as large or larger than the turbulent term even at very high values of Y^+ and is not negligible. Note that for the momentum equation, Eq. (6), the turbulent term is always much greater than the molecular term for $Y^+ > 30$ and thus the molecular term is always negligible. The logarithmic forms of Eqs. (13) and (14) are a direct result of the fact that molecular viscosity and conductivity are negligible in the region $Y^+ > 30$.

Referring now to Eq. (10), in the region from $Y^+ = 30$ to the start of the "wake" region (see below) the turbulent shear stress, $\overline{u'v'}$, and the turbulent heat flux, $\overline{t'v'}$, are close to constant, and are equal to the wall shear stress, τ_o, divided by ρ, and the wall heat flux, q_o'', divided by ρc, for the singular case where there is no axial pressure gradient, no transpiration, no axial surface curvature. Noting the definitions of U^+, Y^+, and T^+, we can now differentiate Eqs. (13) and (14) and substitute into Eq. (10) with the result:

$$\text{Pr-t} = C_1/2.44 \tag{15}$$

Thus for this unique but rather fundamental case Pr-t in the "log" region can be determined simply from the slope of the temperature profile plotted in semi-log coordinates. Note that this further implies Pr-t is a *constant* in this region, which apparently is the case. At very low Prandtl numbers (the liquid metal range, $\text{Pr} < 0.1$) the temperature profile is no longer logarithmic and Pr-t cannot be so easily deduced, nor is it a constant.

If there is an axial pressure gradient, Eq. (13) is still a good representation for the velocity profile and Eq. (14) can be used to represent the temperature profile. However, $\overline{u'v'}$ is no longer constant through the "log" region though $\overline{t'v'}$ may be so. So again Eq. (15) is not applicable. The same conclusion can be reached for flow over surfaces with axial curvature where $\overline{u'v'}$ varies markedly through the "log" region.

Figure 1 shows an example of Pr-t evaluated from the log slope of temperature profiles for airflow along a flat plate. In this case the result is Pr-t = 0.85, although it can be seen that there is some uncertainty in evaluation of the slope.

One of the problems is that there is a dearth of good temperature profile measurements at high Reynolds numbers and this means that the length of the "log" region tends to be short and thus its slope is sometimes difficult to measure accurately. Note the three distinct regions on this graph: the sublayer from $Y^+ = 0$ to about 30, the "log" region, and the "wake" region at the outer edge of the boundary layer. As Reynolds number is increased the "log" region extends to higher values of Y^+, while the "wake" retains its shape but moves to higher values of Y^+.

Table 1 shows the results of this method for determining Pr-t for a number of cases for air, water, and an oil. Although some variation in Pr-t is noted, it seems reasonable to conclude that Pr-t in the "log" region is essentially a constant at about 0.85 for all values of molecular Prandtl number from 0.7 to 64, and there is no reason to believe that it will differ at still higher values of Pr. The range of Reynolds numbers is somewhat limited, but note that the one case of a fully rough surface at Reynolds numbers considerably higher than the others still yields close to Pr-t = 0.85.

Turbulent Prandtl Number From Analytic Solutions

Before proceeding to an examination of the data for very low Prandtl number fluids it will be worthwhile to examine the results of two different attempts to determine turbulent Prandtl number analytically. Our purpose will be to attempt to establish the key variables upon which Pr-t depends so as to provide a rational scheme for representing the experimental data.

During the past 40 years dozens of solutions for Pr-t based on a variety of analytic models have appeared in the literature. Most of these have been inspired by the observation in the 1950s that the experimentally determined heat transfer coefficients for flow of liquid metals in pipes seemed to fall well below what would be predicted using models such as the Reynolds Analogy. It was first suggested by Jenkins (1951) that this was a result of the relatively high thermal conductivity of very low Prandtl number fluids, and Jenkins proposed a model based on the idea that a turbulent "eddy" could lose heat by simple conduction during its flight normal to the mean flow direction and thus the heat transferred by the turbulent exchange process would be lessened. Most of the other analyses are based on variations of the same idea, but virtually all contain free constants, which must be evaluated by comparison with the available experimental data.

More recently Yakhot et al. (1987) present an analytic solution based on what they call the "renormalization group

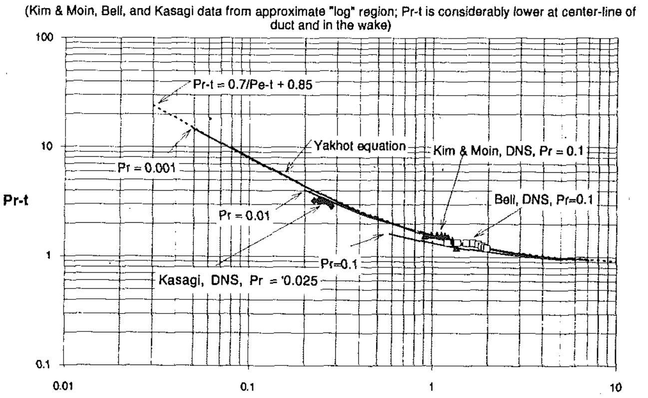

Fig. 2 Analytic solutions

method," and this result is apparently devoid of empirical input. The relatively simple equation given by Yakhot et al. is worth examining:

$$\left[\frac{\left(\frac{1}{\text{Pr-eff}}-1.1793\right)}{\left(\frac{1}{\text{Pr}}-1.1793\right)}\right]^{0.65}\left[\frac{\left(\frac{1}{\text{Pr-eff}}+2.1793\right)}{\left(\frac{1}{\text{Pr}}+2.1793\right)}\right]^{0.35}\cdot=\frac{1}{(1+\epsilon_M/\nu)}$$

where

$$\text{Pr-eff}=\frac{[1+\epsilon_M/\nu]}{\left[\frac{\epsilon_M/\nu}{\text{Pr-t}}+\frac{1}{\text{Pr}}\right]} \tag{16}$$

Equation (16) presumably covers all Prandtl numbers, and at high Pr and high values of ϵ_M/ν it converges on Pr-t = 0.85. It is not clear whether this result is expected to be valid over the entire boundary layer, or only in the "log" region, but we will use it in the "log" region only.

In this equation Pr-t appears as a function of Pr *and* ϵ_M/ν; however, on Fig. 2 Pr-t from Eq. (16) is plotted as a function of the product (ϵ_M/ν)Pr, which we will call the turbulent Peclet number, Pe-t. It is plotted for three values of Prandtl number, 0.1, 0.01, and 0.001. The important point is that the curves all collapse to close to a single function of Pe-t except at very low values of ϵ_M/ν, i.e., values encountered for $Y^+ < 100$. At high values of Pe-t the curve approaches 0.85, and for Pr near 1.00 and higher there is little variation with Pe-t, which is of course consistent with what was observed from the experimental data previously. At very low values of Pe-t the turbulent Prandtl number becomes very high, consistent with the observations for liquid metals in the "log region."

A simple empirical equation that fits the asymptotic curves very well is:

$$\text{Pr-t} = 0.7/\text{Pe-t} + 0.85 \tag{17}$$

This equation is similar in form to an equation suggested by Reynolds (1975), but in that case Pr-t is an effective average for the entire boundary layer and Pe-t is the product of the Prandtl number and the Reynolds number.

This result then suggests that Pr-t is close to a unique function of Pe-t. But whether this is only true in the "log" region, or over the entire boundary layer, remains a question.

The other analytic solutions that we need to consider are the results of the recent success of Direct Numerical Simulation (DNS) of both turbulent flow in ducts and the turbulent external boundary layer. DNS involves complete solution of the time-dependent Navier-Stokes and thermal energy equations for a turbulent flow. Supercomputers, an enormous finite-difference grid, and many hours of computation are necessary, but interesting results are beginning to appear. The results of three such calculations are shown in Fig. 3. The results of Kim and Moin (1989) are for fully developed flow in a flat duct at a Reynolds number, Re-d = 11,000, where the Reynolds number is based on the hydraulic diameter, which is 2 times the duct width. Three values of Prandtl number are considered, 0.1, 0.71, 2.0. Very similar results are reported by Lyons et al. (1991). Kasagi et al. (1991) carried out virtually the same calculations at a much lower Prandtl number, 0.025, and at a slightly lower Reynolds number. Finally the results of Bell et al. (1992) are for the simple turbulent boundary layer on a flat plate with no pressure gradient, at Pr = 0.1, 0.71, and 2.0. Here the momentum thickness Reynolds number, Re-m, is 669.

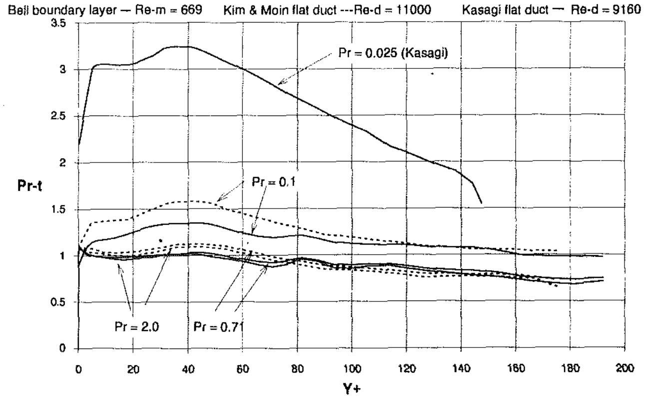

Fig. 3 Pr-t from DNS calculations

The only problem with the DNS calculations reported to date is that the Reynolds numbers are so low that it is difficult to distinguish the "log" region; the sublayer merges almost directly into the "wake." Be that as it may, a number of points from what appears to be the "log" region have been plotted on Fig. 2. Two conclusions are apparent: (1) Pe-t does appear to reasonably correlate these results; and (2) they coincide very closely with the Yakhot equation and with Eq. (17).

We will come back to the DNS calculations again when we examine the experimental data.

Experimental Measurements of Pr-t in the "Logarithmic" Region

In Fig. 4 there is plotted a large amount of data covering the entire Prandtl number range of available experiments. Some of the data are from experiments with fully developed flow in pipes, and others are from experiments on external flat-plate boundary layers with no pressure gradient. With two exceptions [Hollingsworth et al. (1989) and Zukauskas and Slanciauskas (1987)] these data are for "point" values of Pr-t evaluated using Eq. (10), and with two other exceptions are data taken from what is believed to be the "log" region, that is, excluding the sublayer region and the wake. The latter two exceptions are the data of Bremhorst and Krebs (1992), and of Sheriff and Kane (1981), both of which were obtained at or near a pipe centerline using a technique that involved injection of a small amount of hot fluid (sodium in this case) and measuring the diffusion of the temperature pulse.

The data in the central portion of the graph are primarily the results of experiments with air; the data at low values of Pe-t are largely for liquid metals; the data for Pe-t > 100 are for water and higher Prandtl number liquids. Note that there appears to be a continuum of states from the liquid metals to the high Prandtl number fluids, and that all of the data tend toward about Pr-t = 0.85 at high values of Pe-t.

But a difficulty is apparent in the liquid metal region. The Bremhorst and Krebs (1992) and the Sheriff and Kane (1981) data are included on this graph even though they were not obtained in the "log" region because they seem to correspond

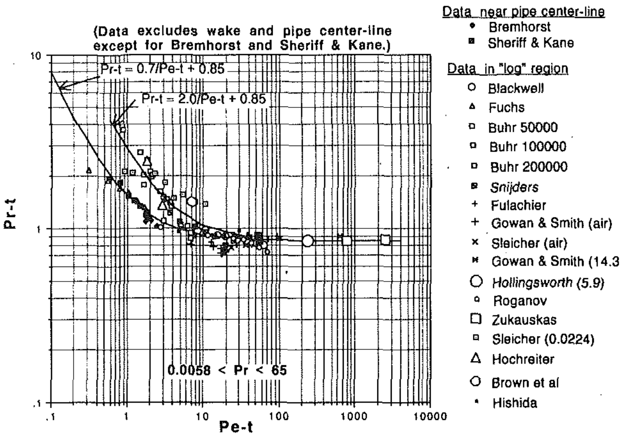

Fig. 4 Turbulent Prandtl number in the "logarithmic" region, $0.0058 < Pr < 65$

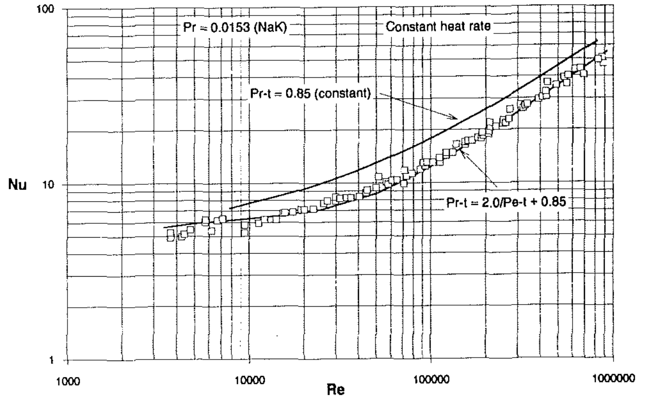

Fig. 5 Skupinski et al., experiments

very closely to Eq. (17), which, it will be recalled, closely approximates the Yakhot results and the various DNS results. A consistent picture would emerge were it not for the data of Fuchs (1973), which also correspond closely to Eq. (17). Unfortunately the Fuchs data are not in the open literature, but are reported by Bremhorst, and also by Lawn (1977), with the implication that they are data from the "log" region.

All of the other liquid metal data [Buhr et al. (1968), Sleicher et al. (1973), Hochreiter (1971), and Brown et al. (1957)] yield values of Pr-t that are considerably higher than Eq. (17), although the scatter of data is considerable. These results differ from the previously cited data in that they were all obtained from experiments in which Nusselt numbers as well as temperature profiles were measured.

It will now be instructive to compare measured Nusselt numbers with what would be predicted using Pr-t data from these experiments. The following equation is plotted on Fig. 4 as a reasonable approximation to these data:

$$\text{Pr-t} = 2.0/\text{Pe-t} + 0.85 \tag{18}$$

Figures 5, 6, and 7 show predicted Nusselt numbers for three sets of experiments, using Eq. (18), together with the relevant experimental data. All are for fully developed flow in a circular pipe; the first two are for fully developed *constant heat rate*, and the third is for fully developed *constant surface temperature*. The momentum and energy differential equations are ordinary differential equations for these cases and calculations were made using a relatively simple finite-difference procedure and a well-established mixing-length and eddy diffusivity model of turbulence. Equation 18) was used across the entire pipe, but the sublayer region [for very low Pr fluids] and the centerline region are rather insensitive to the value assigned to Pr-t.

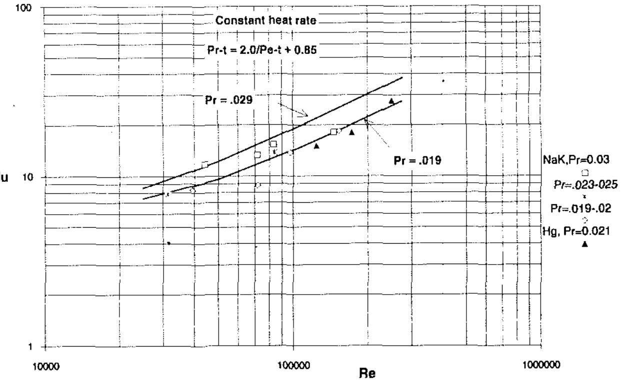

Fig. 6 Buhr et al., experiments

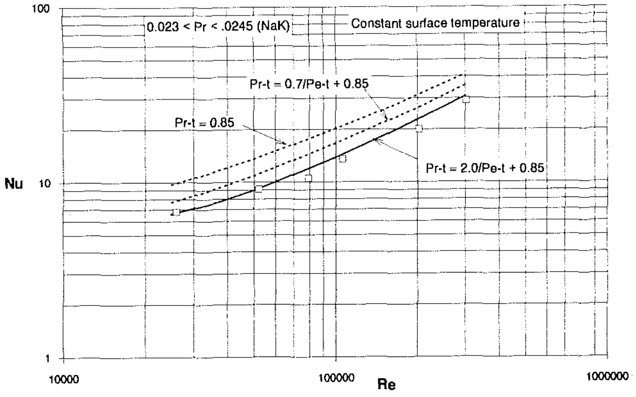

Fig. 7 Sleicher et al., experiments

Figure 5 shows the extensive data of Skupinski et al. (1965) for NaK, Pr = 0.0153. Calculations were also made using a constant value for Pr-t = 0.85 so that the influence of the higher Pr-t can be clearly seen. It is apparent that calculations using Eq. (18) fit the data as well as could be desired, and over the entire extensive Reynolds number range. The results of using Eq. (17) are not shown, but they would lie on a curve approximately halfway between the results using Eq. (18) and the results for Pr-t = 0.85. Note that the effect of the higher Pr-t is to decrease Nusselt number, and this is the effect that has been consistently observed. Skupinski et al. did not measure Pr-t, nor do they provide profiles from which Pr-t can be deduced, so it is only by this indirect procedure that Pr-t for their data can be determined.

Figure 6 shows the data of Buhr et al. (1968) and include data for both NaK and Hg. Since the Prandtl number of these various experiments varies from 0.019 to 0.029, two predicted curves using Eq. (18) are included, one for Pr = 0.019 and the other for Pr = 0.029. These data are not totally consistent with one another, but it appears that Eq. (18) provides a fair approximation for Pr-t. it can be seen on Fig. 4 that Eq. (18) does not actually fit the data of Buhr et al. precisely.

Figure 7 shows the constant surface temperature data of Sleicher et al. (1973) together with the predicted Nusselt numbers using Eq. (18). It will be seen here that at the higher Reynolds numbers still higher Pr-t than given by Eq. (18) is apparently implied. However, the same thing is seen on Fig. 4 where Sleicher's results are considerably higher than Eq. (18) at the higher values of Pe-t. In fact all of Sleicher's results on Fig. 4 vary with Pe-t in a way that seems inconsistent with the other data. If this is a result of the constant surface temperature rather than constant heat rate boundary condition, then this is unfortunate because it adds another complication to the problem. In fact, Youssef et al. (1992) suggest that there is such an influence.

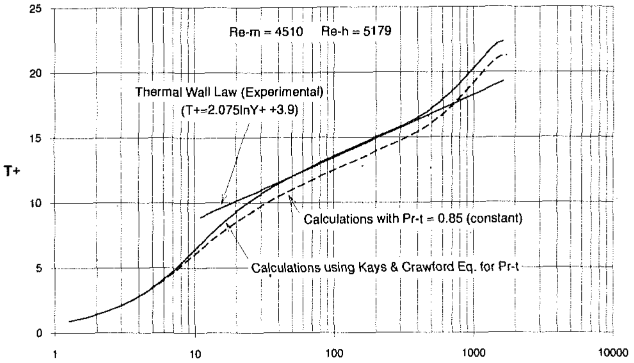

Fig. 8 Effect of Pr-t on air temperature profiles

So this is where the matter stands in the liquid metal region. There is a major discrepancy between the analytic solutions [and this is of particular concern with the DNS calculations] and the experiments where Nusselt numbers have actually been measured. Equation (18) is suggested as a reasonable basis for calculating actual heat transfer rates, but there remains an uneasy feeling that there could be some consistent error in liquid metal heat transfer experiments. One can only hope that this is not the case and that there is some other explanation for the discrepancy.

Referring again to Fig. 4, all of the data for Pe-t > 10 are quite consistent with a scatter of no more than about ±10 percent. Virtually all of the data for 10 < Pe-t < 100 have been obtained from experiments with *air*; above 100 the data are for *water*, *glycol*, and an *oil*. The results of the DNS calculations in Fig. 2 are very consistent with the experiments.

So far we have considered only data in the "logarithmic" region of the velocity profiles. The data for air and the higher Prandtl number fluids show nothing unusual in this region, but in the *sublayer* it is quite a different story. Let us now examine the available data for *air*, including the entire boundary layer.

Turbulent Prandtl Number for Air

Figure 8 shows a plot of nondimensional temperature, T^+, as a function of nondimensional distance from the wall Y^+, both in *wall coordinates*. The line labeled Thermal Wall Law is a plot of the following equation, which is simply a best fit to a very large amount of data from numerous experiments for air in the "log" region [see also Fig. 1] for the simple flat-plate turbulent boundary layer with no pressure gradient:

$$T^+ = 2.075 \ln Y^+ + 3.9 \tag{19}$$

[Slight variations of this equation will be found in the literature, but the differences are small.] Equation (19) then represents very closely the bulk of the experimental data for air in the "log" region.

The results of two sets of calculations are shown on Fig. 8. Both were made using a finite-difference procedure and a mixing-length model that reproduces the velocity profiles very well. The Van Driest equation was used for the sublayer and "log" regions, and a constant mixing length was assumed in the wake region. The Van Driest equation is:

$$l = \kappa y[1 - \exp(-Y^+/A^+)] \quad \text{where } A^+ = 25 \tag{20}$$

The dashed-line curve shows the result of using Pr-t = 0.85 constant throughout the boundary layer. As can be seen, in

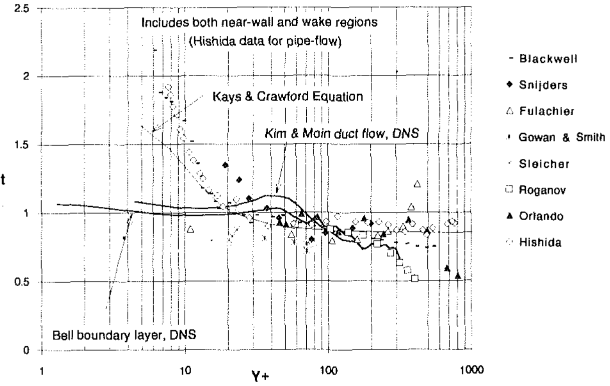

Fig. 9 Pr-t data for air

the "log" region the curve is parallel to Eq. (19) but lies about 10 percent below it. The only way a profile can be calculated that coincides with Eq. (19) in the "log" region is to introduce a higher value for Pr-t somewhere in the region $Y^+ < 30$, i.e., in the *sublayer* region. Later we will examine temperature profiles for water and for an oil that will illustrate this effect even more strongly.

The following equation for Pr-t, based on experimental data, is suggested by Kays and Crawford (1993). It provides a relatively high value of Pr-t near the wall, but approaches 0.85 as ϵ_M/ν, and thus Y^+, increases:

$$\text{Pr-t} = \frac{1}{\left\{0.5882 + 0.228(\epsilon_M/\nu) - 0.0441(\epsilon_M/\nu)^2\left[1 - \exp\left(\frac{-5.165}{(\epsilon_M/\nu)}\right)\right]\right\}} \tag{21}$$

The full-line curve on Fig. 8, calculated using Eq. (21), can be seen to fit Eq. (19) perfectly in the "log" region. This, then, is the basis for feeling the Pr-t must be greater than 0.85 somewhere near the wall. Note, however, that in the liquid metal region it makes little difference because the heat transfer by eddy conduction in the sublayer is virtually always very much smaller than that by molecular conduction [see Eq. (9)].

Figure 9 shows experimentally determined point values for Pr-t from Eq. (10) for air from eight different experiments, all plotted as a function of Y^+. All of these data, with the exception of those of Hishida et al. (1986), are for external flat plate boundary layers with no pressure gradient. The Hishida data are for flow in a pipe. In addition the DNS results of Kim and Moin (1989), and of Bell et al. (1992), are plotted as solid lines. Finally Eq. (21) is plotted as a thin line.

Between $Y^+ = 30$ and about 200 the experimental data are in fairly close agreement. The divergence of the data at higher values of Y^+ is partially caused by the difficulty of accurately measuring the four components of Eq. (10) [which is probably the cause for the high values reported by Fulachier (1972)], and partially the fact that in the "wake" region Pr-t seems to tend toward a value of about 0.5–0.7. Note that both of the DNS calculations have this characteristic, and are probably more accurate in this region than the experimental data. The presumption then is that experiments at higher Reynolds numbers would not show this drop from 0.85 until higher values of Y^+ are reached. As has been mentioned earlier, the limited Reynolds number range of the available experimental data is one of the difficulties in getting a clear picture of the behavior of Pr-t.

The more interesting region on Fig. 9 is at values of Y^+ below about 30. This is of course the viscous sublayer region. With the exception of one point by Fulachier (and this probably is a result of experimental uncertainty), the experiments that extend deeply into this region show a marked increase in Pr-t. The results of Hishida, and of Blackwell, are almost iden-

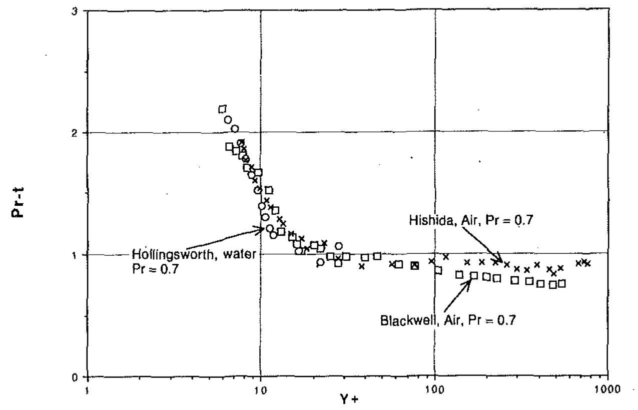

Fig. 10 Comparison of data for air and water

tical; Snijders et al. (1983) show a substantial rise although at a higher value of Y^+. But the disturbing fact is that neither of the DNS calculations show this behavior, although they do show a modest upward bulge in Pr-t in the range of $Y^+ = 40$–50. Furthermore, *none* of the experiments show an upward bulge in Pr-t in the 40–50 range despite the fact that this is a range in which there is substantial agreement between the experiments, and the range 30–200 is the range of Y^+ where experimental uncertainty in the least.

Figure 10 shows the experimental results of Hollingsworth et al. (1989) for *water*, together with the data of Hishida et al. (1986), and Blackwell et al. (1972), for *air*. The data for water are almost identical to those for air! It is worth noting further that we see here the results of three experiments, involving two different fluids, very different measuring techniques, two different laboratories, one in Japan and one in the US, and over a time span of about 17 years! Bell et al. (1992) attribute these differences to errors in the experiments, and further suggest that there are compensating errors in computations based on the experimental data. However, the experimental data on Pr-t involve nothing more than direct measurements of mean velocity and temperature.

So what can one conclude? The only real difference between the experiments and the DNS calculations is that the latter were carried out at very much lower Reynolds numbers. For example, the Bell calculations are at a momentum thickness Reynolds number of 669 while the Blackwell results are for about 3000, and the Hollingsworth results are for 1552. The Reynolds number difference *may* be the reason for the discrepancy, but this discrepancy must remain one of the unresolved problems with turbulent Prandtl number. Further difficulties in the sublayer region will appear when we examine heat transfer measurements at very much higher Prandtl numbers where most of the temperature profile is in the viscous sublayer.

Air, Effect of Pressure Gradient

Figure 11 shows the data of Blackwell et al. (1972) for two cases of an adverse pressure gradient in the flow direction, and the data of Roganov et al. (1984) for a strong favorable pressure gradient. The Blackwell data for no pressure gradient are shown in dark. Once more the Blackwell data show a steep rise in Pr-t in the sublayer.

From these results one could infer that there is indeed an effect of pressure gradient with an adverse pressure gradient causing a decrease in Pr-t and a favorable pressure gradient causing an increase. The data of Orlando et al. (1974), Fig. 12, are not so conclusive. The Orlando experiment involved a technique using a triple-wire, which allowed simultaneous measurement of all of the components of Eq. (10). However, the size of the probe made it impossible to make measurements in the sublayer, although the measurements in the "log" and "wake" regions may be among the most accurate ever made. Note that these results show a *decrease* of Pr-t in the wake as discussed earlier.

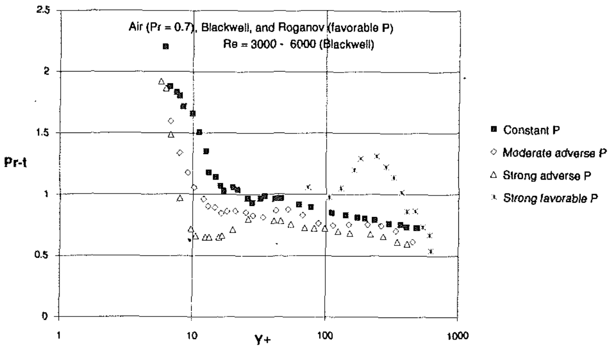

Fig. 11 Effects of pressure gradient

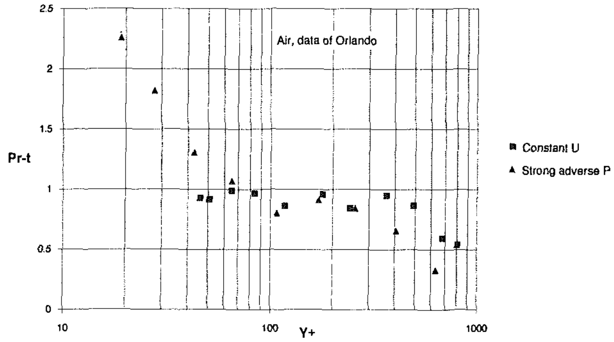

Fig. 12 Effect of adverse pressure gradient

The only conclusion that can be reached is that there *may* be an effect of pressure gradient as indicated, but that there are insufficient data to quantify this effect. However, the discrepancy between the two DNS calculations on Fig. 9 *may* be due to the favorable pressure gradient in a duct flow.

Air, Effect of Transpiration

Blackwell also made measurements for a boundary layer with both "blowing" and "suction," all with a moderate adverse pressure gradient. These are shown on Fig. 13 together with Blackwell's results for the same pressure gradient but with no transpiration. Again the tendency toward high Pr-t in the sublayer is seen, and it could be inferred that there is a small effect of transpiration. However, any such effect is pretty well masked by the probable experimental uncertainty and the only conclusion that can be drawn is that if there is such an effect it is small.

Air, Effect of Surface Roughness

On Fig. 14 are shown the data of Pimenta et al. (1979) for flow over an aerodynamically fully rough surface. Pimenta again used the technique developed by Orlando and was unable to make measurements close to the wall. However, for a fully rough surface one would not expect to find a viscous sublayer.

These results suggest that roughness has virtually no effect on Pr-t in the "log" region and in fact Eq. (18) would fit the data very well.

The Eddy-Diffusivity Ratio Very Close to the Wall

Before attempting to analyze the available data at high Prandtl number [which will include the data for *water* as well as those for much higher Prandtl numbers] it would be well to examine the behavior of the momentum eddy diffusivity at

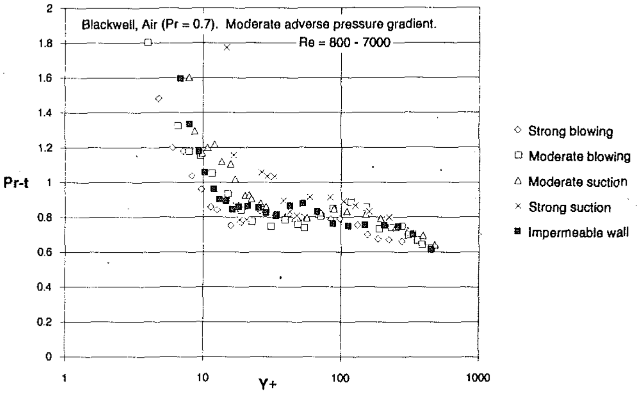

Fig. 13 Effects of blowing and suction

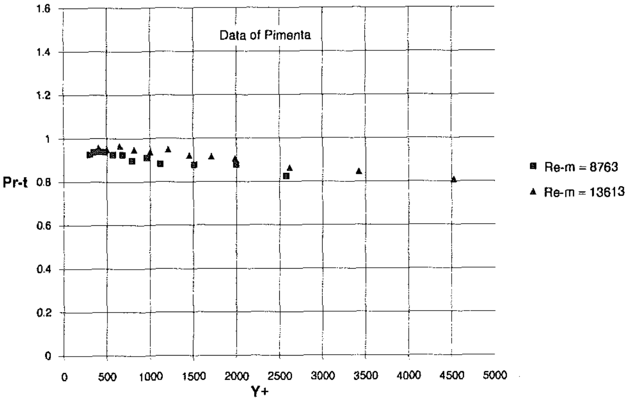

Fig. 14 Air flow over a fully rough surface

points very close to the wall, i.e., at values of $Y^+ < 5$. At high Prandtl number it is precisely in this region where much of the temperature profile resides. This can be seen by again examining the inner bracketed term in Eq. (9):

$$\left[\frac{1}{\mathrm{Pr}}+\frac{\epsilon_M/\nu}{\mathrm{Pr\text{-}t}}\right]$$

Even though the eddy diffusivity ratio, ϵ_M/ν, is very small in this region, the molecular conduction term, 1/Pr, can become the same order of magnitude or even smaller. Thus turbulent heat transport, and Pr-t, can be important even though turbulent momentum transport is negligible. [ϵ_M/ν will also be referred to as EDR in this paper.]

The reason for this concern with ϵ_M/ν near the wall is that it is virtually impossible to make experimental measurements in this region, so Pr-t will have to be inferred by indirect methods, i.e., by making complete boundary layer calculations using an eddy-diffusivity model, and this cannot be done without accurate data on ϵ_M/ν.

The Van Driest Eq. (20) provides a convenient way to evaluate ϵ_M/ν, and permits fairly accurate solution of the momentum equation, i.e., the velocity profile. In fact the suggested value for $A^+ = 25$ is determined so that it leads to the law-of-the-wall, Eq. (13) at values of Y^+ outside of the sublayer. However, solution to the momentum equation is totally insensitive to values of ϵ_M/ν for $Y^+ < 5$, quite unlike the situation for the energy equation at high Prandtl number. It is thus necessary to look more carefully at ϵ_M/ν in this region before trying to use the Van Driest equation for the energy equation at high Prandtl number.

The most likely source for accurate information on ϵ_M/ν in this region very close to the wall is the DNS calculations. On Fig. 15 there is plotted ϵ_M/ν as a function of Y^+ from the DNS calculations of Bell et al. (1992). Also plotted is ϵ_M/ν as calculated using the Van Driest equation. Although these results are very close for $Y^+ > 5$, there is a progressively larger discrepancy as Y^+ approaches 0.0. Further examination of the Van Driest results indicates that ϵ_M/ν varies as Y^{+4} as the wall is approached. It has been well established on theoretical grounds that ϵ_M/ν should vary as Y^{+3} near the wall. Assuming that this dependence would be valid to $Y^+ = 5$, the following equation is proposed:

$$\epsilon_M/\nu = 0.001\,Y^{+3} \tag{22}$$

Equation (22) fits the DNS results reasonably well down to $Y^+ = 0.1$, as can be seen, so it is proposed that in all subsequent calculation Eq. (22) be used for $Y^+ < 5$ and that the Van Driest equation be used for $Y^+ > 5$.

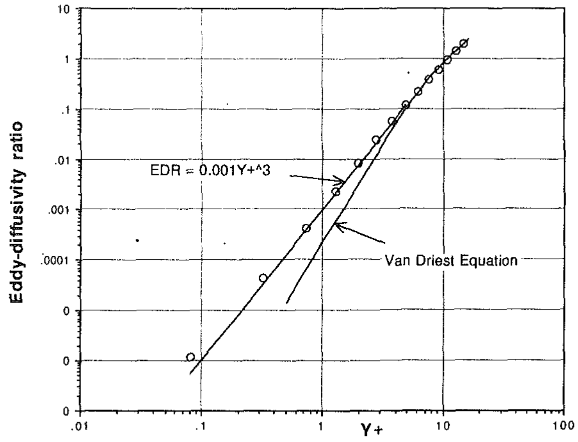

Fig. 15 Eddy-diffusivity ratio from DNS calculations

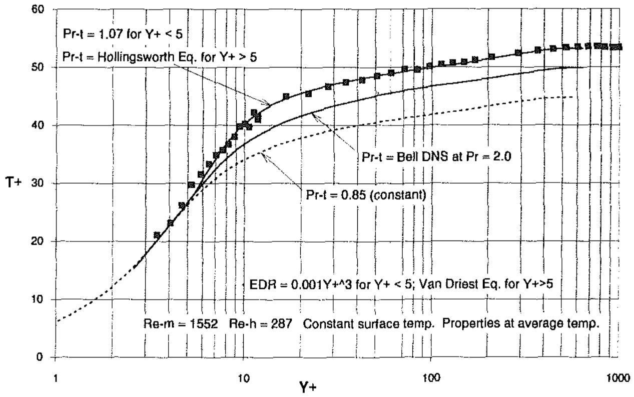

Fig. 16 Water, Pr = 5.63-6.19 (Hollingsworth)

Pr-t for Water

Figure 16 shows a temperature profile from the water data of Hollingsworth et al. (1989) plotted as T^+, a function of Y^+. Note first that a greater part of the temperature variation takes place in the sublayer as compared to air [see Fig. 1]. Hollingsworth's results for Pr-t are shown in Fig. 10. The following equation is proposed by Hollingsworth et al. (1989) as a reasonable fit to these data:

$$\mathrm{Pr\text{-}t} = 1 + 0.855 - \tanh\,[0.2(Y^+ - 7.5)] \tag{23}$$

It was previously noted that Pr-t = 0.85 can be deduced from the slope of Hollingsworth's temperature profile in the "log" region, and Eq. (23) does indeed approach 0.85 as Y^+ is increased.

As will be seen later when still higher Prandtl number data are examined, Pr-t cannot possibly reach the high values indicated by Eq. (23) in the region $Y^+ = 0$–5. It appears that Pr-t must be near 1.00 at and close to the wall, and the DNS

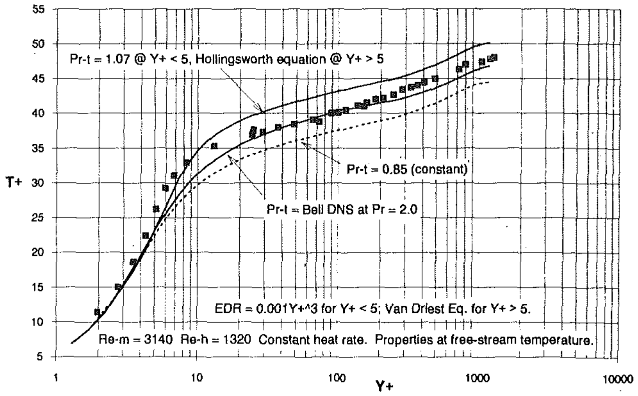

Fig. 17 Water, Pr = 4.53-5.38 (Zukauskas and Slanciauskas)

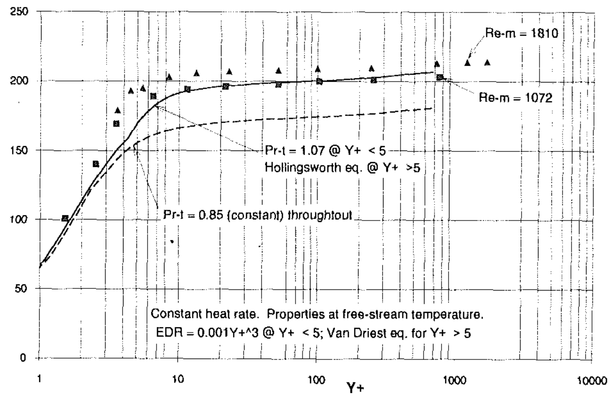

Fig. 18 Transformer oil, Pr = 48.6-64.3 (Zukauskas and Slanciauskas)

calculations of Kim and Moin, and Bell et al., indicate Pr-t just slightly above 1.00 at the wall. Therefore it appears that Pr-t must increase to high values in the neighborhood of $Y^+ = 10$, and then decrease to close to 1.00 at the wall. A tentative and rather crude suggestion is that Pr-t = 1.07 for $0 < Y^+ < 5$, and then Eq. (23) [or Eq. (21)] applies thereafter. The value 1.07 is based on the DNS results. Actually this behavior has little effect in the Prandtl number range of *water*, but it makes a substantial and progressively greater difference at higher Prandtl numbers.

Using this model, including Eq. (22) for ϵ_M/ν in the near-wall region and the Van Driest equation for $Y^+ > 5$, calculations were made using a finite-difference program for the Hollingsworth case. The resulting nondimensional temperature profile is shown on Fig. 16 where it passes through the data almost as well as could be desired. [It should be added that using Eq. (23) all the way to the wall, instead of Pr-t = 1.07, makes little difference in this result, but it makes a large difference when we examine higher Prandtl number data.]

Also included on this figure and shown as a dotted line is the temperature profile calculated using Pr-t = 0.85 constant. Not that in the "log" region this curve is parallel to the data but 15-20 percent below. As was the case for air, this is further evidence that a higher value for Pr-t is required in the near-wall region.

Further calculations were made using an empirical fit to the curve for Pr = 2 from the DNS results of Bell et al. (1992) from Fig. 3. As can be seen the DNS results begin to depart from the experimental data at about $Y^+ = 6$, and the difference is the result of the very high values of Pr-t indicated by the Hollingsworth equation, Eq. (23).

The Prandtl number of water, like most high Prandtl liquids varies markedly with temperature. Although the temperature difference across the boundary layer for the Hollingsworth experiment was small [≈3.9°C], note that the Prandtl number varied from 5.63 to 6.19. The calculations were carried out in a variable property mode using the actual properties of water as a function of temperature, but the variable property problem is still a vexing one when analyzing experimental data.

Before drawing any conclusions we should examine some additional data for water. The results of Zukauskas and Slanciauskas (1987) are available in very complete form and are plotted on Fig. 17. The same calculations were carried out as for the Hollingsworth data, but this time the Hollingsworth equation for Pr-t appears to be too high and the results from the Bell data are a little closer. The only clear conclusion is that Pr-t = 0.85 (constant) is too low in the near-wall region.

However, there are some peculiarities in the Zukauskas results. Close examination of Fig. 17 would suggest that Pr-t is indeed very high in the range of Y^+ from 5 to 9, and then dips to below 0.85 at $Y^+ = 20$, before becoming about 0.85 in the outer region. This kind of behavior does not seem likely.

The Prandtl number for the Zukauskas data varied through the boundary layer from 4.53 to 5.38, so there is greater variable-property effect than for the Hollingsworth data, but the method of calculation does take into consideration this effect. Another difference that may or may not be of importance is that the Hollingsworth experiment involved a rather large delayed heating length and thus a low enthalpy thickness Reynolds number, Re-h, whereas in the Zukauskas experiment the virtual origins of the momentum and energy boundary layers were apparently the same. The Zukauskas experiment was a *constant heat rate experiment* while the Hollingsworth experiment was a *constant surface temperature experiment*. It is still not clear whether or not wall temperature variation has a significant effect.

Pr-t for an Oil

Zukauskas and Slanciaukas (1987) present some fairly complete data for a flat plate boundary layer using a *transformer oil*. The Prandtl number varied through the boundary layer from 48.6 to 64.3, so there is a substantial variable property effect. The virtual origins of the two boundary layers were apparently the same. Again this was a *constant heat rate experiment*. The results for two temperature profiles are shown on Fig. 18. The solid curve shows the calculated results using the same models as for the previous two figures. Again the results using a constant Pr-t = 0.85 are shown as a dashed line for reference. Once more the necessity for a high value for Pr-t in the sublayer is evident.

These results strongly support the need for a high Pr-t in the region $Y^+ < 10$. In fact the data suggest that Pr-t has begun to rise as early as $Y^+ = 3$ or 4, although it is difficult to tell whether the steep rise in T^+ is not due simply to experimental uncertainty. Note that for $Y^+ > 30$, Pr-t = 0.85 is again quite reasonable. A bothersome result is that one of the two profiles is for Re-m = 1072, which is low and approaching the 669 of the Bell DNS results, and yet a much higher value for Pr-t is implied in the near-wall region than the DNS calculations yield. On the other hand this particular profile (Re-m = 1072) yields somewhat lower values of T^+ than does the profile for Re-m = 1810, consistent with lower values of Pr-t in the near-wall region.

On balance the results of Fig. 18 provide fairly strong support for the suggested Pr-t model.

Pr-t at Very High Prandtl Number

At *very* high Prandtl number the temperature profile moves closer and closer to the wall to the point where it is almost entirely inside of $Y^+ = 5$. But it is still very much governed by a *turbulent* exchange process because it has already been seen that the eddy diffusivity for heat, (ϵ_M/ν)/Pr-t, though small, is still very much greater than the molecular diffusivity for

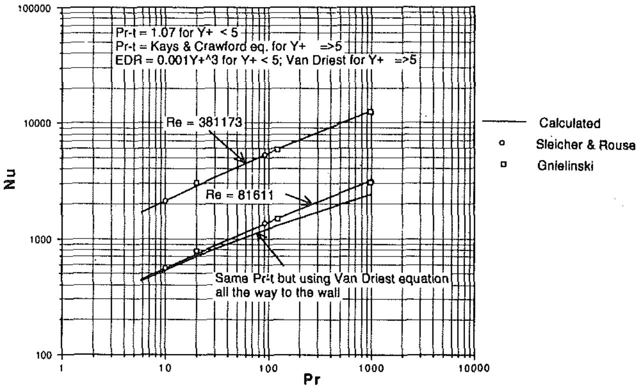

Fig. 19 Fully developed flow in a circular tube

heat, 1/Pr. Although it would be very difficult to make accurate experimental measurements in this region, and DNS calculations at high Pr are evidently not yet practicable, it is still possible to infer the behavior of Pr-t by indirect means. There is a considerable body of experimental data on heat transfer to high Prandtl number fluids for fully developed flow in a circular pipe, and there are a number of empirical correlations of these data. Two correlations for Nusselt number that yield very close to the same results, and that are now rather generally accepted as definitive, are those of Sleicher and Rouse (1975), and of Gnielinski (1976).

The Sleicher and Rouse equation is:

$$\mathrm{Nu} = 5 + 0.015\,\mathrm{Re}^{a}\,\mathrm{Pr}^{b} \tag{24}$$

where

$$a = 0.88 - 0.24/(4 + \mathrm{Pr}),$$

$$b = 0.333 + 0.5e^{-0.6\,\mathrm{Pr}}$$

The Gnielinski equation is:

$$\mathrm{Nu} = \frac{(\mathrm{Re} - 1000|)\,\mathrm{Pr}\,(c_f/2)}{[1.0 + 12.7(c_f/2)^{1/2}(\mathrm{Pr}^{2/3} - 1.0|)]} \tag{25}$$

Calculations can be carried out to solve the momentum and energy equations at various Reynolds and Prandtl numbers using the eddy diffusivity and turbulent Prandtl number models discussed above. This is a rather simple finite-difference calculation since the applicable equations are ordinary differential equations. Figure 19 shows the results of such calculations for two different Reynolds numbers and Prandtl numbers from 7 to 1000.

For these calculations Eq. (22) was used for Y^+ from 0 to 5, the Van Driest Eq. (20) was used for $Y^+ > 5$, and a constant eddy diffusivity was used in the pipe centerline region. The calculated friction coefficients were within a fraction of 1 percent of the well-known Karman-Nikuradse equation.

Pr-t = 1.07 was used for Y^+ from 0 to 5, and the Kays and Crawford Eq. (21) was used for $Y^+ > 5$. [Equation (21) and the Hollingsworth Eq. (23) give close to the same values for Nusselt number.]

These calculations are shown as solid lines on Fig. 19. It is apparent that the results are very close to both the Sleicher and Rouse equation and the Gnielinski equation over the entire Prandtl number range. At Pr = 1000 this becomes a particularly sensitive test of Pr-t in the region of Y^+ from 0 to 3, provided that the values of ϵ_M/ν used in this region are accurate, i.e., Eq. (22). All that can be said is that Eq. (22) is a very good fit to the DNS calculations. But it is also significant that a good fit to the empirical equations for Nusselt number is obtained over a very large range of Prandtl number, which is probably more than coincidental.

Had either Eq. (21), the Kays equation, or Eq. (23), the Hollingsworth equation, been used for Pr-t in the region $Y^+ < 5$, the calculated curves would lie considerably below those shown, especially at the higher values of Pr. So it seems that Pr-t must be near 1.00 very close to the wall [1.07 was used in this case], consistent with the DNS calculations. However, the data for air and water [and even the transformer oil] seem to indicate much higher values in the region of Y^+ from 5 to 30. Presumably Pr-t then approaches 0.85 at higher values of Y^+, although this would have little influence for Prandtl numbers greater than 100. This proposed model with a constant Pr-t near 1.00 close to the wall, and then an abrupt discontinuous rise to a much higher value at $Y^+ = 5$, is obviously not very elegant, but the dearth of reliable data in this region makes anything better rather difficult.

A further bothersome fact is that the data that support a high value for Pr-t in the sublayer are all from experiments on external constant pressure boundary layers, while the data that support a low value very near the wall are from experiments with fully developed flow in pipes where there is a favorable axial pressure gradient.

Note that a calculated curve is also included for the case where the Van Driest equation is used all the way to the wall. This provides a good measure of the sensitivity of the calculations to the accuracy of ϵ_M/ν in the region close to the wall.

Summary and Conclusions

1 In the "logarithmic" region, Pr-t appears to be primarily a function of a turbulent Peclet number, Pe-t = (ϵ_M/ν)Pr. At large values of Pe-t, Pr-t approaches a constant value of about 0.85. At small values of Pe-t, Pr-t increases indefinitely. For *gases* Pe-t is sufficiently large so that Pr-t tends to be close to constant in the "log" region; for higher Prandtl number liquids Pr-t is most definitely a constant. The region of Pe-t where Pr-t is high is almost exclusively in the Prandtl number range of the liquid metals.

2 Two different equations, Eqs. (17) and (18), are offered for the dependence of Pr-t on Pe-t. The primary difference between these equations is in the low Pe-t (and thus low Pr) region. Equation (17) is a good fit to the DNS calculations and the Yakhot analysis, and to experimental data obtained in the centerline region of a pipe. Equation (18), which yields higher values of Pr-t in the low Pe-t region, is an approximate and less good fit to the results of several liquid metal experiments in which temperature profiles and Nusselt numbers were measured directly. The reason for this discrepancy is not clear, but Eq. (18) is recommended if the experimental data on Nusselt number at low Pr are to be believed and it is desired to make calculations of Nusselt number consistent with these data.

3 In the "wake" region of an external turbulent boundary layer, and in the centerline region for fully developed turbulent flow in pipe, Pr-t apparently tends to decrease to values in the neighborhood of 0.5–0.7 for moderate and high Prandtl number fluids. These regions have not been extensively explored but fortunately the behavior of Pr-t in neither is of great importance in calculating heat transfer at a wall—in fact use of the "log" region Pr-t is usually sufficiently accurate.

4 There is compelling evidence that for air and water Pr-t in the sublayer region ($Y^+ < 30$) tends toward higher values than in the "logarithmic" region. But here there is a major discrepancy between the DNS calculations and the experiments. The DNS calculations show a peak value of Pr-t (about 1.10 for air) at about $Y^+ = 40$, whereas the experiments show no such peak at all but rather a sharp rise to much higher values in the region of Y^+ from 5 to about 15. This behavior is described by either of Eqs. (21) and (23). A difference between the DNS calculations and the experiments is that the DNS calculations have been carried out at very low Reynolds numbers, but whether this is the reason for the difference is not clear.

5 The DNS calculations indicate that Pr-t becomes lower

and approaches 1.00 as the wall is closely approached. The experimental data for very high Prandtl number fluids confirm this fact and indicate that Pr-t must be close to 1.00 in the region of Y^+ from 0 to 5. A model using Pr-t $= 1.07$ for Y^+ from 0 to 5 and then either Eq. (21) or (23) for $Y^+ > 5$ for calculations from Pr $= 7.0$ to 1000 produces results very close to the experimental data over this entire Prandtl number range. In the liquid metal Prandtl number range there are virtually no experimental data in the sublayer region, but molecular conduction is so dominant in this region that it is not necessary to know Pr-t accurately. The DNS calculations suggest that Pr-t approaches 1.00 at the wall just as at higher Prandtl numbers.

6 Experimental data for air suggest that there may be a pressure gradient effect on Pr-t with an adverse (positive) pressure gradient causing Pr-t to decrease, and a favorable (negative) pressure gradient causing Pr-t to increase. However, these results are far from conclusive.

7 Transpiration (blowing or suction) apparently has little effect upon Pr-t.

8 Surface roughness has little or no effect. For a fully rough surface there is virtually no sublayer region so the available data are all in the "logarithmic" region.

References

Note: This reference section includes publications containing explicit data on turbulent Prandtl number, publications containing data from which turbulent Prandtl number may be deduced, and publications related indirectly to the turbulent Prandtl number problem.

References

Antonia, R. A., Dahn, H. Q., and Prabhu, A., 1977, "Response of a Turbulent Boundary Layer to a Step Change in Surface Heat Flux," *Journal of Fluid Mechanics*, Vol. 80, pp. 153–178.

Antonia, R. A., 1980, "Behavior of the Turbulent Prandtl Number Near the Wall," *International Journal of Heat and Mass Transfer*, Vol. 23, pp. 906–908.

Antonia, R. A., and Browne, L. W. B., 1987, "Conventional and Conditional Prandtl Number in a Turbulent Plane Wake," *International Journal of Heat and Mass Transfer*, Vol. 30, No. 10, pp. 2023–2030.

Antonia, R. A., and Kim, J., 1991a, "Turbulent Prandtl Number in the Near-Wall Region of a Turbulent Channel Flow," *International Journal of Heat and Mass Transfer*," Vol. 34, No. 7, pp. 1905–1908.

Antonia, R. A., and Kim, J., 1991b, "Reynolds Shear Stress and Heat Flux Calculations in a Fully Developed Turbulent Duct Flow," *International Journal of Heat and Mass Transfer*, Vol. 34, No. 8, pp. 2013–2018.

Bagheri, X. X., et al., 1992, "Measurements of Turbulent Boundary Layer Prandtl Numbers and Space-Time Temperature Correlations," *AIAA Journal*, Vol. 30, No. 1, pp. 35–42.

Bell, D. M., Ferziger, J. H., and Spalart, P. R., 1992, "Direct Numerical Simulation of the Flat Plate Boundary Layer With Passive Scalars," submitted to the *Journal of Fluid Mechanics*,.

Blackwell, B. F., Kays, W. M., and Moffat, R. J., 1972, "The Turbulent Boundary Layer on a Porous Plate: An Experimental Study of the Heat Transfer Behavior With Adverse Pressure Gradients," Report No. HMT-16, Thermosciences Division, Dept. of Mechanical Engineering, Stanford Univ., Stanford, CA, Aug.

Blom, J., 1970, "Experimental Determination of the Turbulent Prandtl Number in a Developing Temperature Boundary Layer," 4th International Heat Transfer Conference, Paris, Versailles, Vol. II, FC 2.2, Aug.

Bremhorst, K., and Krebs, L., 1992, "Experimentally Determined Turbulent Prandtl Numbers in Liquid Sodium at Low Reynolds Numbers," *International Journal of Heat and Mass Transfer*, Vol. 35, No. 2, pp. 351–359.

Brown, H. E., Amstead, B. H., and Short, B. E., 1957, "Temperature and Velocity Distribution and Transfer of Heat in a Liquid Metal," *Trans. ASME*, Vol. 79, p. 279.

Buhr, H. O., Carr, A. D., and Balzhiser, R. E., 1968, "Temperature Profiles in Liquid Metals and the Effect of Superimposed Free Convection in Turbulent Flow," *International Journal of Heat and Mass Transfer*, Vol. 11, pp. 641–654.

Carr, A. D., and Balzhiser, R. E., 1967, "Temperature Profiles and Eddy Diffusivities in Liquid Metals," *Brit. Chem. Eng.*, Vol. 12, pp. 53–57.

Chambers, A. J., Antonia, R. A., and Fulachier, L., 1985, "Turbulent Prandtl Number and Spectral Characteristics of a Turbulent Mixing Layer," *International Journal of Heat and Mass Transfer*, Vol. 28, No. 8, pp. 1461–1468.

Chua, L. P., and Antonia, R. A., 1990, "Turbulent Prandtl Number in a Circular Jet," *International Journal of Heat and Mass Transfer*, Vol. 33, No. 2, p. 331.

Fuchs, H., 1973, "Heat Transfer to Flowing Sodium, "Thesis, Institut fur Reaktorforschung, Wurenlingen, Switzerland, EIR, Bericht, No. 241.

Fulachier, L., 1972, "Contribution a l'étude des analogies des champs dynamique et thermique dans une couche limité turbulente," These Docteur es Sciences, Université de Provence, France.

Fulachier, L., Verollet, E., and Dekeyser, I., 1977, "Experimental Results on a Turbulent Boundary Layer With Wall Suction and Heating," *International Journal of Heat and Mass Transfer*, Vol. 20, pp. 731–739.

Fulachier, L., and Antonia, R. A., 1984, "Spectral Analogy Between Temperature and Velocity Fluctuations in Several Turbulent Flows," *International Journal of Heat and Mass Transfer*, Vol. 27, No. 7, pp. 987–997.

Frueh. D. L., Schauer, J. J., Lung, F. Y., and Pan, J. C., 1988, "Experimental Determination of Turbulent Prandtl Number in Boundary Layers Under High Free Stream Turbulence," Conference Paper, Univ. of Dayton, OH.

Gibson, M. M., and Verriopoulos, C. A., 1984, *Experiments in Fluids*, Vol. 2, Springer-Verlag, New York, pp. 73–80.

Gnielinski, V., 1976, "New Equations for Heat and Mass Transfer in Turbulent Pipe and Channel Flow," *Int. Chem. Engng.*, Vol. 16, pp. 359–368.

Gowan, R. A., and Smith, J. W., 1967, "The Effect of Prandtl Number on Temperature Profiles for Heat Transfer in Turbulent Pipe Flow," *Chem. Engrg. Sci.*, Vol. 22, pp. 1701–1711.

Gowan, R. A., and Smith, J. W., 1968, "Turbulent Heat Transfer From Smooth and Rough Surfaces," *International Journal of Heat and Mass Transfer*, Vol. 11, pp. 1657–1673.

Hammond, X. X., 1985, "Turbulent Prandtl Number Within a Near-Wall Flow," *AIAA Journal*, Vol. 23, p. 1668.

Herrero, J., Grau, F. X., Grifoll, J., and Giralt, F., 1991, "A Near-Wall *k-e* Formulation for High Prandtl Number Heat Transfer," *International Journal of Heat and Mass Transfer*," Vol. 34, No. 3, pp. 711–721.

Hishida, M., Nagano, Y., and Tagawa, M., 1986, "Transport Process of Heat and Momentum in the Wall Region of a Turbulent Pipe Flow," *Proceedings of the 8th International Heat Transfer Conference*, Hemisphere Publishing Corp., Washington DC, Vol. 3, pp. 925–930.

Hochreiter, L. E., 1971, "Turbulent Structure of Isothermal and Nonisothermal Liquid Metal Pipe Flow," PhD Thesis, Purdue University, West Lafayette, IN.

Hollingsworth, D. K., Kays, W. M., and Moffat, R. J., 1989, Measurement and Prediction of the Turbulent Thermal Boundary Layer in Water on Flat and Concave Surfaces," Report No. HMT-41, Thermosciences Division, Dept. of Mech. Engr., Stanford Univ., Stanford, CA, Sept.

Jenkins, R., 1951, "Variation of the Eddy Conductivity With Prandtl Modulus and Its Use in Prediction of Turbulent Heat Transfer Coefficients," *Proceeding of the Heat Transfer and Fluid Mechanics Institute*, Stanford University Press, Stanford, CA.

Jischa, M., and Reike, H. B., 1979, "About the Prediction of Turbulent Prandtl and Schmidt Numbers," *International Journal of Heat and Mass Transfer*, Vol. 22, pp. 1547–1555.

Kader, B. A., and Yaglom, A. M., "Heat and Mass Transfer Laws for Fully Turbulent Wall Flows, *International Journal of Heat and Mass Transfer*, Vol. 15, pp. 2329–2351.

Kader, B. A., 1981, "Temperature and Concentration Profiles in Fully Turbulent Boundary Layers," *International Journal of Heat and Mass Transfer*, Vol. 24, No. 9, pp. 1541–1544.

Kasagi, N., Kuroda, A., and Hirata, M., 1989, "Numerical Investigation of Near-Wall Turbulent Heat Transfer Taking Into Account the Unsteady Heat Conduction in the Solid Wall," ASME Journal of Heat Transfer, Vol. 111, pp. 385–392.

Kasagi, N., Tomita, Y., Kuroda, A., 1992, "Direct Numerical Simulation of Passive Scalar Field in a Turbulent Channel Flow," ASME Journal of Heat Transfer, Vol. 114, No. 3, p. 598.

Kasagi, N., Ohtsubo, Y., and Tomita, Y., 1991, "Direct Numerical Simulation of the Low Prandtl Scalar Field in a Two-Dimensional Turbulent Channel Flow," *Eighth Symposium on Turbulent Shear Flows*, Tech. Univ. of Munich, II-11, Sept. 9–11.

Kays, W. M., and Crawford, M. E., 1993, Convective Heat and Mass Transfer, Third Edition, McGraw-Hill, New York.

Kim, J., and Moin, P., "Transport of Passive Scalars in a Turbulent Channel Flow," *Proceedings of Sixth International Symposium on Turbulent Shear Flows*, Toulouse, France, Sept. 7–9, 1987, Springer-Verlag, Berlin-Heidelberg, pp. 85–96.

Lai, Y. G., and So, R. M. C., 1990, "Near Wall Modeling of Turbulent Heat Fluxes," *International Journal of Heat and Mass Transfer*, Vol. 33, No. 7, p. 1429.

Launder, B., and Samaraweera, D., 1979, "Application of a Second Moment Turbulence Closure to Heat and Mass Transport in Thin Shear Flows—I. Two-Dimensional Transport," *International Journal of Heat and Mass Transfer*, Vol. 22, pp. 1631–1644.

Launder, B. E., 1989, "Second-Moment Closure Present—and Future?" *Int. J. Heat Fluid Flow*, Vol. 10, No. 14, pp. 282–300.

Lawn, C. J., 1977, "Turbulent Temperature Fluctuations in Liquid Metals," *International Journal of Heat and Mass Transfer*, Vol. 20, No. 10, pp. 1035–1044.

Lyons, S. L., Hanratty, T. J., and McLaughlin, J. B., 1991, "Direct Numerical Simulation of Passive Heat Transfer in a Turbulent Channel Flow," *International Journal of Heat and Mass Transfer*, Vol. 34, No. 4/5, pp. 1149–1161.

McEligot, D. M., Pickett, P. E., and Taylor, M. F., 1976, "Measurement of

Wall Region Turbulent Prandtl Numbers in Small Tubes," *International Journal of Heat and Mass Transfer*, Vol. 19, pp. 799–803.

Maekawa, H., Kawada, Y., Kobayashi, M., and Yamaguchi, H., 1991, "An Experimental Study on the Span-wise Eddy Diffusivity of Heat in a Flat-Plate Turbulent Boundary Layer," *International Journal of Heat and Mass Transfer*, Vol. 34, No. 8, pp. 1991–1998.

Malhotra, A., and Kang, S. S., 1984, "Turbulent Prandtl Number in Circular Pipes," *International Journal of Heat and Mass Transfer*, Vol. 27, pp. 2158–2161.

Moffat, R. J., and Kays, W. M., 1967, Report No. HMT-1, Thermosciences Div. Dept. of Mech. Engineering, Stanford Univ., Stanford, CA, Aug.

Nagano, Y., and Kim, C., 1988, "A Two-Equation Model for Heat Transport in Wall Turbulent Shear Flows," ASME Journal of Heat Transfer, Vol. 110, pp. 583–589.

Orlando, A. F., Moffat, R. J., and Kays, W. M., 1974, "Turbulent Transport of Heat and Momentum in a Boundary Layer Subject to Deceleration, Suction and Variable Wall Temperature," Report HMT-17, Thermosciences Division, Dept. of Mech. Engr., Stanford Univ., CA.

Patel, V. C., and Head, M. R., 1969, "Some Observations on Skin Friction and Velocity Profiles in Fully Developed Pipe and Channel Flows," *Journal of Fluid Mechanics*, Vol. 38, pp. 181–201.

Perry, A. E., and Hoffman, P. H., 1976, "An Experimental Study of Turbulent Convective Heat Transfer From a Flat Plate," *Journal of Fluid Mechanics*, Vol. 77, pp. 355–368.

Pimenta, M. M., Moffat, R. J., and Kays, W. M., 1979, "The Structure of a Boundary Layer on a Rough Wall With Blowing and Heat Transfer," ASME Journal of Heat Transfer, Vol. 101, pp. 193–198.

Quarmby, A., and Quirk, R., 1972, "Measurements of the Radial and Tangential Eddy Diffusivities of Heat and Mass Transfer in a Plane Tube," *International Journal of Heat and Mass Transfer*, Vol. 15, pp. 2309–2327.

Reynolds, A. J., 1975, "The Prediction of Turbulent Prandtl and Schmidt Numbers," *International Journal of Heat and Mass Transfer*, Vol. 18, pp. 1055–1069.

Reynolds, W. C., Kays, W. M., and Kline, S. J., 1958, NASA Memo 12-1-58W, Washington, DC.

Roganov, P. S., Zaboltsky, V. P., Shishov, E. V., and Leontiev, A. I., 1984, "Some Aspect of Turbulent Heat Transfer in Accelerated Flows on Permeable Surfaces," *International Journal of Heat and Mass Transfer*, Vol. 27, No. 8, pp. 1251–1259.

Sheriff, N., and Kane, D. T., 1981, "Sodium Eddy Diffusivity of Heat Measurements in a Circular Duct," *International Journal of Heat and Mass Transfer*, Vol. 24, pp. 205–211.

Simon, T. W., Moffat, R. J., Johnston, J. P., and Kays, W. M., 1980, Report No. HMT-32, Thermosciences Div. Dept. of Mech. Engineering, Stanford Univ., Stanford, CA, Nov.

Simpson, R. L., Whitten, D. G., and Moffat, R. J., "An Experimental Study of the Turbulent Prandtl Number of Air With Injection and Suction," *International Journal of Heat and Mass Transfer*, Vol. 13, pp. 125–143.

Skupinski, E., Tortel, J., and Vautrey, L., 1965; "Détermination de coefficients de convection d'un alliage sodium-potassium dans une tube circulaire," *International Journal of Heat and Mass Transfer*, Vol. 8, pp. 937–951.

Sleicher, C. A., 1958, "Experimental Velocity and Temperature Profiles for Air in Turbulent Pipe Flow," *Trans. ASME*, Vol. 80, pp. 693–704.

Sleicher, C. A., Awad, A. S., and Notter, K. H., 1973, "Temperature and Eddy Diffusivity Profiles in NaK," *International Journal of Heat and Mass Transfer*, Vol. 16, pp. 1565–1575.

Sleicher, C. A., and Rouse, M. W., 1975, "A Convenient Correlation for Heat Transfer to Constant and Variable Property Fluids in Turbulent Pipe Fow," *International Journal of Heat and Mass Transfer*, Vol. 18, pp. 677–683.

Smith, J. W., Gowan, R. A., and Wasmund, X. X., 1967, "Eddy Diffusivities and Temperature Profiles for Turbulent Heat Transfer to Water in Pipes," *Chem. Engrg. Prog. Symposium Ser. 63*, pp. 92–102.

Snijders, A. L., Koppius, A . M., Nieuwvelt, C., and deVries, D. A., 1978, "An Experimental Determination of the Turbulent Prandt Number in the Inner Boundary Layer for Air Flow Over a Flat Plate," *Sixth International Heat Transfer Conference*, Toronto, Vol. 2, pp. 519–523.

Snijders, A. L., Koppius, A. M., and Nieuwvelt, D., 1983, "An Experimental Determination of the Turbulent Prandtl Number in the Inner Boundary Layer for Air Flow Over a Flat Plate," *International Journal of Heat and Mass Transfer*, Vol. 26, No. 3, pp. 425–431.

Subramanian, C. S. and Antonia, R. A. "Effect of Reynolds Number on a Slightly Heated Turbulent Boundary Layer," *International Journal of Heat and Mass Transfer*, Vol. 24, No. 11, pp. 1833–1846.

Thielbahr, W. H., Kays, W. M., and Moffat, R. J., 1969, Report No. HMT-5, Thermosciences Div. Dept. of Mech. Engineering, Stanford Univ., Stanford, CA, Apr.

Wassel, A. T., and Catton, I., 1973, "Calculation of Turbulent Boundary Layers Over Flat Plates With Different Phenomenological Theories of Turbulence and Variable Turbulent Prandtl Number," *International Journal of Heat and Mass Transfer*, Vol. 16, pp. 1547–1563.

Yakhot, V., Orszag, S. A., and Yakhot, A., 1987, "Heat Transfer in Turbulent Fluids—1. Pipe Flow," *International Journal of Heat and Mass Transfer*, Vol. 30, No. 1, pp. 15–22.

Youssef M. S., Nagano, Y., and Tagawa, M., 1992, "A Two-Equation Heat Transfer Model for Predicting Turbulent Thermal Fields Under Arbitrary Wall Thermal Conditions," *International Journal of Heat and Mass Transfer*, Vol. 35, No. 11, pp. 3095–3104.

Zukauskas, A., and Slanciauskas, A., 1987, *Heat Transfer in Turbulent Fluid Flows*, Hemisphere Publishing Corp., Washington, DC.

S. Hingorani
Graduate Student.

C. J. Fahrner
Graduate Student.

D. W. Mackowski
Assistant Professor.

J. S. Gooding
Professor and Head.
Mem. ASME

Mechanical Engineering Department,
Auburn University,
Auburn, AL 36849-5341

R. C. Jaeger
Distinguished University Professor,
Electrical Engineering Department,
Auburn University,
Auburn, AL 36849-5341

Optimal Sizing of Planar Thermal Spreaders

Two-dimensional cylindrical and three-dimensional Cartesian thermal spreaders are studied. One of the surfaces is convectively coupled to a uniform environmental temperature while the opposite surface is subjected to a uniform heat flux distribution over a portion of its boundary. The problem is generalized through the introduction of appropriate dimensionless variables, and analytical solutions for the temperature field are presented for each coordinate system. The solutions depend on the usual geometric and heat transfer groups. It is found that, for a range of realistic Biot numbers and a given ratio of the spreader to heater dimensions, a dimensionless spreader thickness exists for which the temperature of the heater reaches a minimum value. Optimal thickness curves are presented for these ranges.

Introduction

There is a class of problems associated with satellite thermal design, solar collectors, channel plate heat exchangers, and computer chip cooling in which a planar thermal spreader is attached to a heat source for the purpose of increasing the surface area and thereby reducing the heater temperature. The geometry studied here is that of heated area placed on a flat thermal spreader and cooled by uniform convection on the underside as shown in Figs. 1(*a*) and 1(*b*).

The overall thermal resistance between the heated regime and its coolant is composed of conductive and convective components. Under some circumstances for fixed spreader dimensions, additional substrate material promotes lateral thermal spreading in the conductor, which results in an increase in the *effective* convective heat transfer area on the backside. As the spreader becomes thicker, the effective convective heat transfer area increases with a resultant decrease in convective thermal resistance. On the other hand, additional spreader material increases the conductive resistance. It would thus be expected that a critical thickness of the substrate exists that minimizes the overall heat transfer resistance. The concept here is analogous to the well-known critical insulation thickness for radial conduction/convection systems (Incropera and DeWitt, 1990).

With a different set of thermal boundary conditions, the problem identified in Fig. 1 has been examined by several previous investigators. Kennedy (1960) developed an analytical series solution for a problem involving uniform heat flux acting on a finite circular cylinder with isothermal and insulated boundary conditions at the cooled surface. Similarly, Wilcox (1963) used an analytical solution to study the temperature distribution for an infinite strip heat source (i.e., two-dimensional Cartesian coordinates) problem with an isothermal boundary condition at the cooled surface. Van Sant (1967) studied the variation of temperature on the convectively cooled surface for cases of spatially uniform heat flux and an isothermal condition at the heat surface. Schmitz (1970) evaluated the heat transfer through a slab maintained at constant temperature at the cooled surface and heated isothermally at the opposing surface. That author used a complete thermal analysis to present simplified expressions for heat losses under these conditions, which were offered in terms of slab thickness, heater size, and spacing under which the heat flux could be represented by his simple correlations.

Oliveira and Forslund (1974) were the first to identify the "thermal constriction resistance" (conductive resistance) of a slab with either a uniform heat flux or a convective condition on the heated surface, and convection on the opposing boundary. They found that for a given geometry, the constriction

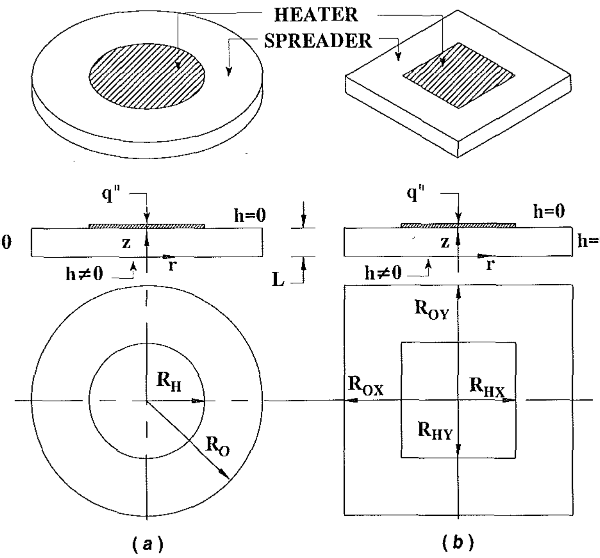

Fig. 1 Geometry of the heater and spreader: (*a*) cylindrical coordinates; (*b*) Cartesian coordinates

---

Contributed by the Heat Transfer Division for publication in the JOURNAL OF HEAT TRANSFER. Manuscript received by the Heat Transfer Division November 1992; revision received August 1993. Keywords: Augmentation and Enhancement, Conduction, Thermal Packaging. Associate Technical Editor: L. S. Fletcher.

resistance was less for a convective heat flux boundary condition that that for the uniform heat flux condition. Schneider et al. (1980) analyzed a Cartesian strip heater in two dimensions (x, z) with boundary conditions like those of Fig. 1(*b*). Schneider et al. (1980) also included cases of spatially varying heat flux from the surface heater. These authors presented their results only for the conductive thermal resistance associated with the spreading as the thickness and width of the spreader increased. In their conclusions, these same authors note that for small Biot number, an increase in dimensionless thickness leads to a decrease in the conductive or "nondimensional constriction" resistance. However, no minimization of the overall thermal resistance was noted. Venkataraman et al. (1982) extended the work of Schneider et al. (1980) to include the case of internal heat generation. The authors presented the thermal resistance as a function of the geometric parameters and Biot number for uniform and nonuniform internal generation cases. They concluded that the specific nature of the internal generation profile influenced significantly the behavior of the thermal resistance of the slab.

In a closely related paper to the one presented here, Kaddambi and Abuaf (1983) used a finite element code to study the overall thermal resistance of a slab in three-dimensional Cartesian and two-dimensional cylindrical coordinate systems with the boundary conditions shown in Fig. 1. The authors identified the effects of selected geometric and heat transfer parameters (aspect ratio, area ratio, eccentricity, the ratio of thickness to slab outer dimension, and the Biot number) on the accuracy of predicting the thermal resistance using a two-dimensional cylindrical coordinate system for a three-dimensional Cartesian coordinate problem. The authors also developed an approximate analytical solution for the two-dimensional cylindrical coordinate system using an integral method. In that work, all the nondimensional terms were based on either slab radius or thickness. Therefore no generalized criteria were presented for the optimal design of the planar thermal spreader.

Mehta and Bose (1983) developed an analytical solution to study the temperature distribution on an infinite circular plate heated with a centered disk source and an isothermal boundary condition at the cooled surface. Ellison (1984) performed an analysis comparable to that of Schneider et al. (1980) using a numerical code for slabs of finite thickness and checked his results against a known analytical solution for the shape factor in a semi-infinite space. Again, only the conductive thermal resistance term was studied. Hussein et al. (1990) studied the effect of a metallized layer on top of the substrate on the thermal performance of a single device and extended his work (Hussein et al., 1991) to determine the thermal interaction between two such devices. Krane (1991) found a series solution for two- and three-dimensional rectangular bodies with an *isothermal*-based boundary condition. Eades and Nelson (1991) modeled the rectangular case as an axisymmetric problem considering heat transfer from the bottom surface. The authors state that, when the dimensionless thickness, the spreader to heater ratio, and the Biot number "are all small, the results show a complex interaction between the heat flow paths in the substrate and the external resistance. A single correlating equation to express these results could not be found. Unfortunately, this is the region of most interest for high density powered hybrid microelectronics." They do not explore this phenomenon further. Nelson and Sayers (1992) compared the results of three-dimensional versus two-dimensional thermal analyses of the planar spreader using a finite difference method. These authors presented the conditions to approximate three-dimensional problems using two-dimensional models.

Forslund and Oliveira (1975) studied the constriction resistance in cylindrical annuli with axial heater strips (as in a channeled submarine hull heat exchanger design). These authors determined the correction factors that should be applied to known resistances in flat plate geometry in order to analyze cylindrical or spherical geometries. Schneider (1984) extended his previous work to include analysis of constriction resistances for cylindrical systems with axial channels for varying heat fluxes. This author used conformal mapping to represent the cylindrical problem in the same flat plate coordinates used in his previous paper (1980). He noted that the results obtained previously for flat plate geometry could be used for computation of constriction resistances in the cylindrical cases.

In summary, several investigators have noted that the conductive or constrictive resistance term decreases with additional supportive material under the heater, yet few have included explicit coupling of the two resistances (conductive or constrictive and convective) to show that increasing slab thickness can result in reaching a minimal value of the overall thermal resistance between the heater source and coolant. No previous

Nomenclature

R_{Hx} = heater half-dimension in the x direction
R_{Hy} = heater half-dimension in the y direction
R_{ox} = spreader half-dimension in the x direction
R_{oy} = spreader half-dimension in the y direction
R_H = for cylindrical coordinate: heater radius; for Cartesian coordinate: $(R_{Hx}+R_{Hy})/2$
R_o = for cylindrical coordinate: spreader radius; for Cartesian coordinate: $(R_{ox}+R_{oy})/2$
L = thickness of flat spreader material
L_c = critical thickness of flat spreader material
Bi = Biot number $\equiv hR_H/k$
h = heat transfer coefficient
k = thermal conductivity
q'' = heat flux
r = dimensionless coordinate $\equiv r^*/R_H$
x = dimensionless coordinate $\equiv x^*/R_H$
y = dimensionless coordinate $\equiv y^*/R_H$
z = dimensionless coordinate $\equiv z^*/R_H$
θ = dimensionless temperature $\equiv (T-T_\infty)/(q''R_H/k)$
θ_o = dimensionless temperature at $r=0$, $z=t$; $\equiv (T_{r=0,\,z=t}-T_\infty)/(q''R_H/k)$
t = dimensionless thickness ratio $\equiv L/R_H$
R = dimensionless outer radius of spreader $\equiv R_o/R_H$
T = temperature
T_∞ = ambient coolant temperature
r^*, z^* = cylindrical coordinate dimensions
x^*, y^*, z^* = Cartesian coordinate dimensions
λ_n, μ_m = eigenvalues of analytical solutions
A, B, C, G, Φ, s = functions used in Eqs. (1), (2), and (6), defined in text
AR_x, AR_y, AR_H, AR_o = geometric factors for Cartesian system defined in Eq. (6)

investigations have undertaken the problem in such a way as to result in a generalized optimal design of the planar thermal spreader.

Problem Statement

The problem here is simplified through the introduction of an appropriate set of dimensionless variables (R_o/R_H, L/R_H, hR_H/k, $(T-T_\infty)/(q''R_H/k)$). In most applications the heater dimensions are normally fixed. Accordingly, its *half-dimension* is taken to be the characteristic length so that optimal designs can be determined with respect to the two physical dimensions normally available for variation: the slab thickness and the outer dimension of the thermal spreader. As is done in the radial insulation case, the presence of contact resistance does not enter into the analysis here. The minimization results are independent of this constant additive term. Equivalent to minimization of overall thermal resistance is the minimization of the maximum characteristic temperature difference in the field (i.e., between the center of the heater and the coolant) with respect to the spreader thickness.

The dimensionless steady conduction equations ($\nabla^2\theta=0$) in both cylindrical and Cartesian coordinates with no internal generation and constant properties are solved subject to their respective dimensionless boundary conditions shown below.

Cylindrical coordinates	Cartesian coordinates
$\frac{\partial\theta}{\partial r}=0;\quad 0, z$	$\frac{\partial\theta}{\partial x}=0;\quad 0, y, z$
	$\frac{\partial\theta}{\partial y}=0;\quad x, 0, z$
$\frac{\partial\theta}{\partial r}=0;\quad R, z$	$\frac{\partial\theta}{\partial x}=0;\quad R, y, z$
	$\frac{\partial\theta}{\partial y}=0;\quad x, R, z$
$\frac{\partial\theta}{\partial z}=\mathrm{Bi}\theta;\quad r, 0$	$\frac{\partial\theta}{\partial z}=\mathrm{Bi}\theta;\quad x, y, 0$
$\frac{\partial\theta}{\partial z}=1;\quad r<1, t$	$\frac{\partial\theta}{\partial z}=1;\quad x<1, y<1, t$
$\frac{\partial\theta}{\partial z}=0;\quad r>1, t$	$\frac{\partial\theta}{\partial z}=0;\quad x>1, y>1, t$

Solutions in the Cylindrical System

For the cylindrical coordinate system, Laplace's equation for the dimensionless temperature is solved using the standard technique of separation of variables and superposition. This problem can be approached from two entirely different formulations. Both formulations of the problem yield infinite series solutions for the temperature distribution in the spreader. In the first approach, the spreader is taken to consist of two separate domains, corresponding to the region directly under the heater ($r<1$) and the region under the insulated top surface of the spreader ($r>1$). For this situation the choice of the separation constant is dictated by the inhomogeneous boundary conditions at the $r=1$ surface, which follows from the matching conditions of temperature and flux at the interface separating the two regions. The inner and outer solutions are represented by Eq. (1) for θ_{in} and Eq. (2) for θ_{out}, respectively:

$$\theta_{\text{in}}=\left(z+\frac{1}{\mathrm{Bi}}\right)+\sum_{n=1}^{\infty}A_nI_o(\lambda_n r)\left[\cos(\lambda_n z)+\frac{\mathrm{Bi}}{\lambda_n}\sin(\lambda_n z)\right] \tag{1}$$

$$\theta_{\text{out}}=\sum_{n=1}^{\infty}G_nI_o(\lambda_n r)[G_nI_o(\lambda_n r)+K_o(\lambda_n r)]B_n\left[\cos(\lambda_n z)+\frac{\mathrm{Bi}}{\lambda_n}\sin(\lambda_n z)\right] \tag{2}$$

Here the symbols I_x and K_x denote the modified Bessel functions of the first and second kind, respectively. The eigenvalues, λ_n, are found from

$$(\lambda_n t)\tan(\lambda_n t)=\mathrm{Bi}\ t \tag{3}$$

The constants of Eqs. (1) and (2) are

$$A_n=\lambda_nC_n[G_nI_1(\lambda_n)-K_1(\lambda_n)],\quad B_n=\frac{I_o(\lambda_n R)}{G_nI_o(\lambda_n)+K_o(\lambda_n)},$$

$$C_n=\frac{2\phi_n(\lambda_n t)}{t(\lambda_n^2+\mathrm{Bi}^2)+\mathrm{Bi}}$$

$$G_n=\frac{K_1(\lambda_n R)}{I_1(\lambda_n R)},\quad \phi_n=\cos(\lambda_n z)+\frac{\mathrm{Bi}}{\lambda_n}\sin(\lambda_n z)$$

In the second approach the spreader is treated as a single domain. Here, the choice of the separation constant is determined by the inhomogeneous boundary condition at the top ($z=t$) surface of the spreader—resulting from the uniform heat flux provided by the heater. An expression for the dimensionless temperature field is given by:

$$\theta=\frac{1}{R^2}\left(z+\frac{1}{\mathrm{Bi}}\right)+2\sum_{n=1}^{\infty}\frac{J_0(\lambda_n r)J_1(\lambda_n)}{\lambda_n^2R^2J_0^2(\lambda_n R)}\left[\frac{\lambda_n/\mathrm{Bi}+\tanh(\lambda_n z)}{1+(\lambda_n/\mathrm{Bi})\tanh(\lambda_n t)}\right]\frac{\cosh(\lambda_n t)}{\cosh(\lambda_n z)} \tag{4}$$

Here the symbol J_x denotes ordinary Bessel functions of the xth order and the eigenvalues are obtained from the transcendental equation

$$J_1(\lambda_n R)=0 \tag{5}$$

The solution to the problem is found in either set of Eqs. (1) and (2) or equivalently through Eq. (4); both yield identical numerical results. The first solution is expressed in terms of modified Bessel functions (I_x and K_x), which are exponential in nature and therefore quick to converge. Equation (4) is expressed in an ordinary Bessel function of the first kind (J_x), which is a slowly damped oscillatory nature and convergence here is relatively slow. The first solution thus offers a numerical advantage over that of the second. However, the second solution allows for an explicit expression for the derivative of the centerline heater temperature with respect to spreader thickness and thus provides an implicit equation for the critical thickness. Such a manipulation is not possible with the first formulation.

Solutions in the Cartesian System

The first technique involving inner and outer solutions matched at the common boundary becomes intractable for the three-dimensional Cartesian system as shown in Fig. 1(*b*). Using the second technique as described above, the dimensionless temperature field in a Cartesian system is given by:

$$\theta=\left[\left(\frac{AR_H}{AR_o}\right)\left(\frac{1}{AR_x}\right)^2\right]\left(z+\frac{1}{\mathrm{Bi}}\right)+\sum_{\substack{n=1\\m=0}}^{\infty}\times\left[\frac{\sin\left(\frac{2\lambda_n}{1+AR_H}\right)(AR_H)(1+AR_H)\cos(\lambda_n x)}{\lambda_n(AR_x)^2(AR_o)(s)}\right]\left[\frac{\tanh(sz)+\frac{s}{\mathrm{Bi}}}{1+\frac{s}{\mathrm{Bi}}\tanh(st)}\right]$$

$$\times \left(\frac{\cosh(sz)}{\cosh(st)}\right) + \sum_{\substack{n=1\\m=0}}^{\infty}\left[\sin\left(\frac{2\mu_m(AR_H)}{1+AR_H}\right)\frac{\cos(\mu_m y)(1+AR_H)}{\mu_m(AR_o)(AR_x)^2(s)}\right]$$

$$\times\left[\frac{\tanh(sz)+\dfrac{s}{\mathrm{Bi}}}{1+\dfrac{s}{\mathrm{Bi}}\tanh(st)}\right]\left(\frac{\cosh(sz)}{\cosh(st)}\right) + \sum_{m=1}^{\infty}\sum_{n=1}^{\infty}$$

$$\times\left[\frac{\sin\left(\dfrac{2\lambda_n}{1+AR_H}\right)\sin\left(\dfrac{2\mu_m(AR_H)}{1+AR_H}\right)\cos(\lambda_n x)\cos(\mu_m y)}{(\lambda_n)(\mu_m)(AR_o)\left(\dfrac{AR_x}{1+AR_H}\right)^2(s)}\right]$$

$$\times\left[\frac{\tanh(sz)+\dfrac{s}{\mathrm{Bi}}}{1+\dfrac{s}{\mathrm{Bi}}\tanh(st)}\right]\left(\frac{\cosh(sz)}{\cosh(st)}\right) \quad (6)$$

where

$$s=(\lambda_n^2+\mu_m^2)^{1/2}$$

$$AR_H=\frac{R_{HY}}{R_{HX}},\quad AR_o=\frac{R_{OY}}{R_{OX}},\quad AR_x=\frac{R_{OX}}{R_{HX}},\quad AR_y=\frac{R_{OY}}{R_{HY}}$$

The eigenvalues of Eq. (6) are

$$\lambda_n=\frac{n\pi(1+AR_H)}{2(AR_x)},\quad \mu_m=\frac{m\pi(1+AR_H)}{2(AR_y)(AR_o)} \quad (7)$$

Problems of this nature (satellite thermal design, solar collectors, channel plate heat exchangers, double-walled tubes, and computer chip thermal spreaders) are more realistically described in the Cartesian coordinate system of Fig. 1(*b*). However, in doing so, two more independent parameters are introduced; the aspect ratios of the heater and the substrate in the x and y directions. For the sake of simplicity, only that solution for a square heater centered on a square substrate is addressed here.

Kaddambi and Abuaf (1983) argue that numerical solutions of the two (cylindrical and Cartesian) problems should compare favorably when the heater areas are identical in size. This means the characteristic dimension (heater half-dimension) for the square case is a factor $\pi^{1/2}/2$ times that for the cylindrical case. For the cases presented here, when this value is factored into those dimensionless groups that contain a characteristic length (critical thickness and Biot number), it is found that results for the dimensionless temperatures as determined from Eqs. (4) and (6) differ by less than 1 percent for all ranges of Biot number and R_o/R_H. Results from previous numerical studies for aspect ratios other than unity have been presented by Kaddambi and Abuaf (1983) and Nelson and Sayers (1992). Further discussions herein are restricted to the cylindrical case only.

Both series expressed by Eqs. (4) and (6) converge slowly; the latter more so than the former. Results found from finite difference analyses for both coordinate systems were in agreement with those obtained from the analytical solutions.

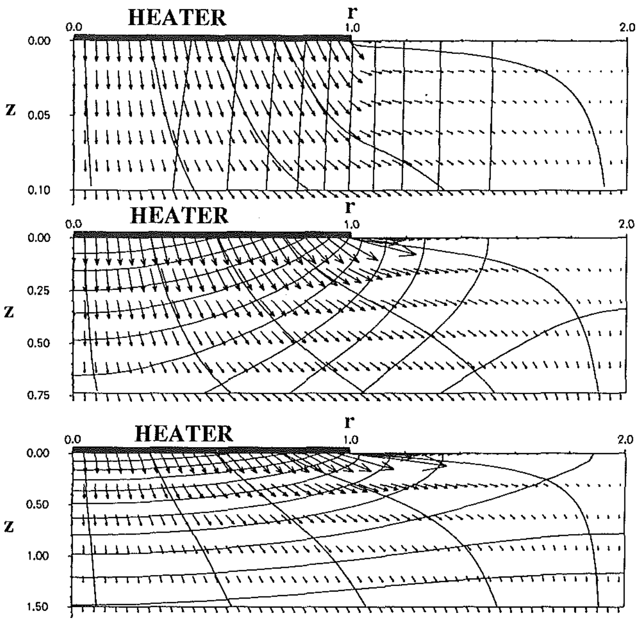

Fig. 2 Temperature and flux plots for the thermal spreader for: (*a*) dimensionless thickness of 0.1; (*b*) dimensionless thickness of 0.74; (*c*) dimensionless thickness of 1.5

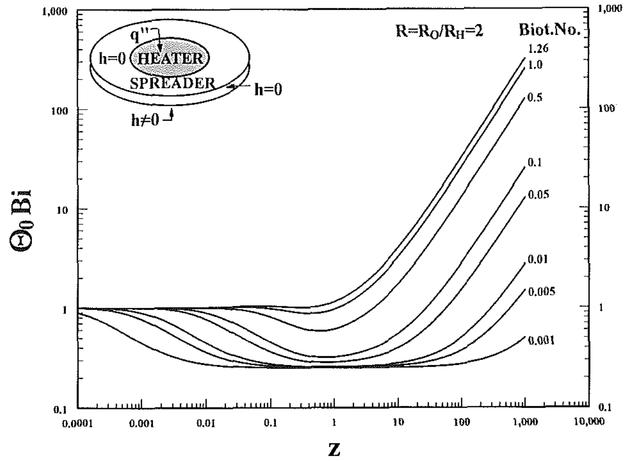

Fig. 3 Dimensionless temperature as a function of dimensionless spreader thickness for $R=2$

Minimum Temperature Difference

The hottest spot on the heated surface is located at the center of the heater at $z=t$ and $r=0$. For certain fixed values of

- heater and spreader radii
- heater flux
- ambient temperature
- heat transfer coefficient on the heat removal surface
- thermal conductivity of the thermal spreader

the addition of supportive material increases the radial thermal spreading and therefore increases the *effective* area over which the heat is removed from the back surface. Consequently the highest temperature on the heater surface will decrease. However, as more material is added, the axial conductive resistance increases to the point where additional material causes an increase in the temperature of the hottest point. This is illustrated in Fig. 2 wherein constant temperature lines, constant flux lines and flux vectors are plotted for $R_o/R_H=2$ and Biot number $=0.1$ at three different dimensionless spreader thicknesses. For a spreader whose dimensionless thickness ($t=0.1$) is less than critical ($t_c=0.74$ from Fig. 3 discussed below), Fig. 2(*a*) shows heat being shunted dominantly from heater directly to heat removal surface. At the critical thickness ($t_c=0.74$), Fig. 2(*b*) shows the flux on the heat removal surface to be nearly constant in magnitude across the entire radius. When the spreader thickness is greater than critical ($t=1.5$), all of the heat removal area has become effectively used. Additional thickness tends to increase overall thermal resistance resulting in an higher heater temperatures for a given flux.

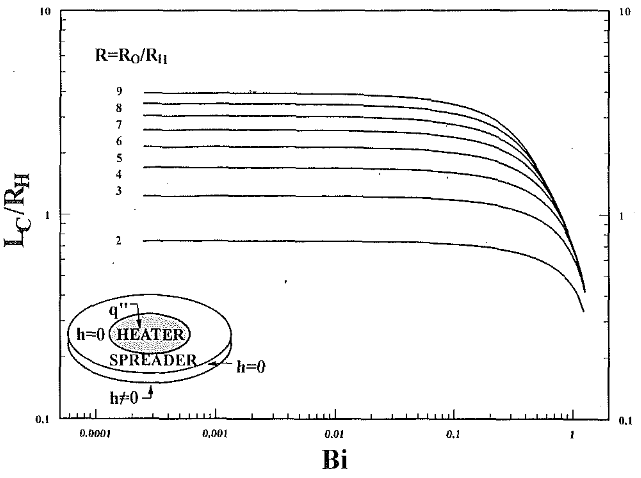

Fig. 4 Critical spreader thickness as a function of Biot number

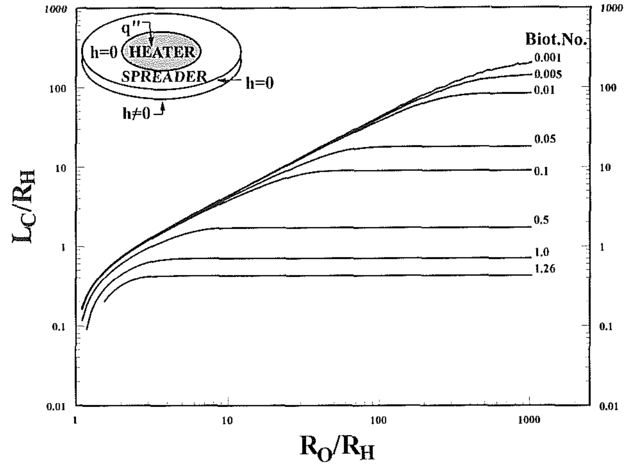

Fig. 5 Critical spreader thickness as a function of spreader to heater ratio

The highest dimensionless heater temperature is a function of the dimensionless thickness, the Biot number, and the ratio of spreader radius to heater radius:

$$\theta_o = \theta_{z=t,\ r=0} = f(t,\ \mathrm{Bi},\ R_o/R_h) \qquad (9)$$

When Eq. (4) is plotted as a function of t for fixed Bi and R_o/R_H, one finds that for low values of Biot number, θ_o reaches a minimum and then increases monotonically. The results are made common at the limit of zero substrate thickness by multiplying Eq. (4) by the Biot number. The parameter θ_o Bi is equivalent to $(T_{z=t,\ r=0} - T_\infty)/(q''/h)$, which can be interpreted as a dimensionless heater temperature for zero spreader thickness.

Figure 3 is a plot of θ_o Bi as a function of dimensionless substrate thickness for a substrate to heater radius (R_o/R_H) equal to 2 and a range of Biot numbers from 0.001 to 1.26. Examination of the results indicates that a critical thickness does not exist for Bi$>$1.26. As can be seen from this figure, the critical thickness for Bi$<$1.26 is nearly independent of Biot number and occurs at a value of about 0.7 ($t_c = 0.74$ for $R_o/R_H = 2$ and Biot No. $= 0.1$). For this range of Biot numbers, the addition of any material decreases the maximum temperature of the heater until t becomes approximately 0.7. This implies that a thermal spreader whose thickness is about equal to that of the heater radius will result in significant temperature reduction.

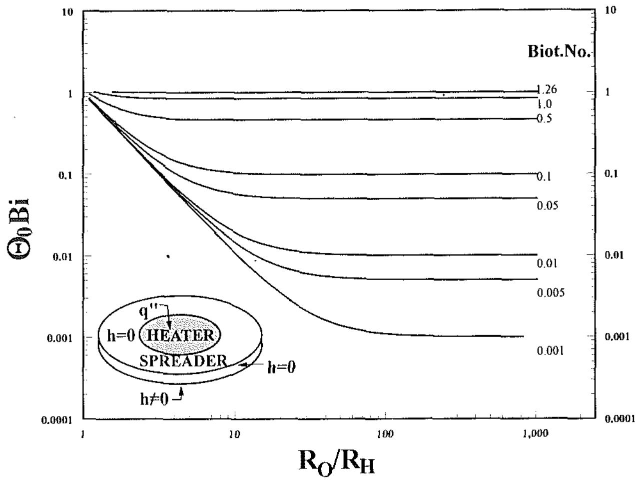

Fig. 6 Dimensionless temperature as a function of spreader to heater ratio

In the limit of Bi→0, θ_o Bi approaches 0.25 for $R = 2$. Low Biot numbers result from a large thermal conductivity of the spreader material or a small heat transfer coefficient. In either case, the temperature becomes uniform throughout the spreader material and the area over which heat is removed is quadrupled (2^2) over that without the spreader. Hence the addition of a spreader for Biot→0 reduces the temperature by a factor of four. The same physical arguments can be made for other values of R (θ_o Bi→1/9 for $R = 3$, etc.).

Figures 4 and 5 offer a tool for designing planar spreaders; both provide means of determining the thickness of spreader material required to minimize the highest temperature of the heater above ambient. The first is a plot of critical thickness as a function of Biot number over a range of R_o/R_H. For Bi$< \sim 0.1$, the critical thickness is nearly independent of Biot. As Biot approaches ~ 1.26, no minimum in θ_o Bi occurs for all values of R investigated. Figure 5 presents similar results with critical thickness as a function of an extended range of R but for the same range of Biot numbers. This figure shows that beyond a certain spreader radius, conduction in the axial direction is no longer influenced by additional material in the radial direction. Hence the critical thickness becomes constant with respect to R.

Finally, Fig. 6 shows the value of which the maximum heater temperature can be reduced with the addition of spreader material. The dimensionless temperature of the heater center, θ_o Bi, is plotted as a function of Bi and R at values of critical thickness. For all cases, increasing R_o causes a decrease in the maximum temperature or at least has no effect.

An example is offered as evidence that the addition of an optimized conductive thermal spreader can considerably reduce the heater center temperature. Consider the case of a 1 cm by 1 cm square heater centered on a square 2 cm by 2 cm spreader subjected to high-velocity multiple jet impingement air cooling (heat transfer coefficient of ~ 135 W/m^2-K) and with silicon as a spreader material ($k = 150$ W/m-K). In order for the areas of the two systems to be the same, the equivalent cylindrical heater and spreader radii must be 0.564 cm and 1.128 cm, respectively. [Each square half dimension is multiplied by $2/\pi^{1/2}$.] The resulting cylindrical Biot number becomes 0.005. From Fig. 3, the minimum value of θ_o Bi occurs at a value of L/R_H ($= t$) equal to 0.64. Thus the optimal spreader thickness is found to be 0.361 cm ($L = 0.64 * 0.564$). Use of this thickness results in a θ_o Bi value of 0.25. For zero thickness, the corresponding value is (by definition) equal to unity. Thus, by adding an optimally sized thermal spreader, the maximum heater temperature is reduced by a factor of four.

Conclusions

The problem of a heater placed on a conductive surface subject to uniform heat transfer coefficient from the surface opposite to that of the heater has been generalized and solved analytically for problems described in both cylindrical and Cartesian coordinate systems. For the cases of comparable heater areas (round and square) with other factors being the same, the two solutions yield nearly identical results. For Biot numbers less than 1.26, results indicate that for fixed spreader radius, a spreader thickness exists for which the heater temperature is minimized. Conversely, for fixed spreader thickness, there is a corresponding spreader radius that minimizes heater temperature. This aspect is important with regard to the optimum sizing of thermal spreaders.

Acknowledgments

This work was partially sponsored by the Alabama Microelectronics Science and Technology Center of Auburn University.

References

Eades, H. H., and Nelson, D. J., 1991, "Thermal Interaction of High-Density Heat Sources on Ceramic Substrates," *Proceedings of the Third ASME-JSME Thermal Engineering Joint Conference*, J. R. Lloyd and Y. Kurosaki, eds., Reno, NV, Mar. 17-22, Vol. 2, pp. 349-356.

Ellison, G. N., 1984, *Thermal Computations for Electronic Equipment*, Van Nostrand Reinhold Co., New York, pp. 112-116.

Forslund, R. P., and Oliveira, H. Q., 1975, "The Effect of Thermal Constriction Resistance in the Design of Channel Plate Heat Exchangers: Cylindrical Geometry," ASME JOURNAL OF HEAT TRANSFER, Vol. 97, pp. 619-621.

Hussein, M. M., Nelson, D. J., and Elshabini-Raid, A., 1990, "Thermal Management of Hybrids Circuits: Effect of Metallization Layer, Substrate Material and Thermal Environment," in: *Proceedings of the International Society for Hybrid Microelectronics*, ISHM, Chicago, IL, pp. 389-394.

Hussein, M. M., Nelson, D. J., and Elshabini-Raid, A., 1991, "Thermal Interaction of Semiconductor Devices on Copper-Clad Ceramics Substrates," *Proceedings of the Seventh Annual IEEE Semiconductor Thermal Measurement and Management Symposium* [*SEMI-THERM 1991*], pp. 117-121; obtainable from IEEE, New York, NY (Cat. No. 91CH2972-8), conference sponsored by IEEE/NIST, Phoenix, AZ, Feb. 12-14, 1991.

Incropera, F. P., and Dewitt, D. P., 1990, *Fundamentals of Heat and Mass Transfer*, Wiley, New York.

Kaddambi, V., and Abuaf, N., 1983, "Axisymmetric and Three-Dimensional Chip-Spreader Calculations," *Proceedings of the 1983 National Heat Transfer Conference*, AIChE Symposium Series No. 225, Vol. 79, pp. 130-139.

Kennedy, D. P., 1960, "Spreading Resistances in Cylindrical Semiconductor Devices," *Journal of Applied Physics*, Vol. 31, pp. 1490-1497.

Krane, M. J. M., 1991, "Constriction Resistance in Rectangular Bodies," ASME *Journal of Electronic Packaging*, Vol. 113, pp. 392-396.

Mehta, R. C., and Bose, T. K., 1983, "Temperature Distribution in a Large Circular Plate Heated by a Disk Heat Source," *International Journal of Heat and Mass Transfer*, Vol. 26, No. 7, pp. 1095-1098.

Nelson, D. J., and Sayers, W. A., 1992, "A Comparison of Two-Dimensional Planar and Three-Dimensional Spreading Resistances," *Proceedings of the Eighth IEEE SEMI-THERM Symposium*, pp. 62-68.

Oliveira, H. Q., and Forslund, R. P., 1974, "The Effect of Thermal Constriction Resistance in the Design of Channel Plate Heat Exchangers," ASME JOURNAL OF HEAT TRANSFER, Vol. 96, pp. 372-373.

Schmitz, R. A., 1970, "Heat Flux Through a Strip Heated Flat Plate," ASME JOURNAL OF HEAT TRANSFER, Vol. 92, pp. 201-202.

Schneider, G. E., Yovanovich, M. M., and Cane, R. L. D., 1980, "Thermal Resistance of a Convectively Cooled Plate With Nonuniform Applied Flux," *Journal of Spacecraft and Rockets*, Vol. 17, pp. 372-376.

Schneider, G. E., 1984, "Thermal Resistance of Circular Cylinder Cross Sections With Convective and Flux Prescribed Boundaries," *AIAA Journal*, Vol. 22, No. 6, pp. 857-860.

Van Sant, J. H., 1967, "Temperature Variations on the Surface Strip Heated Flat Plate," ASME JOURNAL OF HEAT TRANSFER, Vol. 89, pp. 372-373.

Venkataraman, N. S., Cardoso, H. P., and Filho, O. B. D. O., 1982, "Thermal Resistance of Convectively Cooled Plates With Applied Heat Flux and Internal Heat Generation," *Astronautica*, Vol. 9, No. 10, pp. 613-620.

Wilcox, W. R., 1963, "Heat Transfer in Power Transistors," *IEEE Transactions on Electron Devices*, Vol. ED-10, pp. 308-313.

A Thermal Barrier With Adaptive Heat Transfer Characteristics

P. Furmanski[1]

J. M. Floryan

Department of Mechanical Engineering,
The University of Western Ontario,
London, Ontario N6A5B9, Canada

A thermal barrier with adaptive heat transfer characteristics for applications in zero gravity environments is considered. The barrier consists of a mixture of fluid with a small volume fraction of arbitrarily oriented, randomly distributed particles of ellipsoidal shape. Heat flux control is obtained by changing the orientation of the particles. Heat flow may be increased up to several hundred times by rotating the particles from being parallel to the walls to being transverse to the walls and by increasing their aspect ratio, volume fraction, and relative thermal conductivity. An increase in the size of the particles results in the appearance of wall effects, which may substantially reduce heat flow as compared to the case of an infinite medium. Very large temperature variation is found to occur near the walls where an apparent "slip" of temperature occurs for barriers whose thickness is large compared to the particle size.

1 Introduction

In many technical processes there is a need for precise control of temperature. This can be achieved by switching on and off different thermal stabilization devices. The same goal can also be achieved by using a thermal barrier whose properties can be dynamically tuned. The barrier proposed in this paper consists of a layer of fluid mixed with nonspherical particles. Upon application of an electrical or magnetic field, the initial alignment of the particles may be changed, as shown in Figs. 1(*a*, *b*) resulting in a change of the effective thermal characteristics of the barrier. This process bears some resemblance to the behavior of electro-rheological fluids, which dramatically change their viscosity upon application of an external electrical field (Gandhi et al., 1989). The initial orientation of the particles can be restored by using the same external field. The proposed barrier can be utilized under conditions when sedimentation does not occur, such as in a zero gravity environment. Applications in a terrestrial environment are possible provided that the densities of the particles and the carrier fluid are matched. This may be achieved by, for example, coating the lightweight particles with a thin layer of ferromagnetic or ferro-electric substance, which would also increase the torque available for rotation of the particles.

Three modes of heat flow can be potentially involved in heat transport across the barrier. However, for a microgravity environment and nontransparent carrier fluid, thermal convection and radiation may be treated as negligible. Heat flow by conduction alone is influenced by many parameters, such as thermal conductivities of the particles and the carrier fluid, volume fraction, shape and orientation of the particles, and ratio of the barrier thickness to particle length. The purpose of this paper is to examine how the heat flow changes as a function of all these parameters. The main application of these results is in estimation of the possible range of heat flux control across the barrier. This analysis forms a part of the feasibility study of such barriers.

The problem as described above is most conveniently analyzed using methodologies developed in the analysis of transport phenomena in heterogeneous media. The most popular approach is to treat the multicomponent medium as a continuum with either constant or continuously varying effective properties (Buyevich and Shchelchkova, 1978). The latter approach has found applications in various multiphase problems such as heat and electrical conduction, electric and magnetic induction, sedimentation of small droplets or particles in fluids, filtration of fluid through a porous medium, elastic and viscoelastic behavior of composite materials, and the flow of suspensions. A common theoretical framework for all these problems was given by Batchelor (1974). Some new phenomena that have been studied recently included bubbly flows (Smereka and Milton, 1991), thermocapillary motion of bubbles and electrophoresis of colloidal particles (Acrivos et al., 1990), diffusion of chemical species (Koch et al., 1989) and determination of optical properties of inhomogeneous media (Landauer, 1977).

Most attention up to the present has been directed toward stationary, two-phase media with one phase being in the form of spherical inclusions (Jeffrey, 1973; Hinch, 1977; Herczynski and Pienkowska, 1980; Durlofsky and Brady, 1989). The available rigorous theory applies to very dilute suspensions with no particle interaction (Batchelor, 1974; Dutta and Mashelkar, 1987). The first possible extension of the results to higher particle volume fractions is based upon utilization of a virial expansion in growing powers of particle concentration (Jeffrey, 1973; Lu and Kim, 1990). The so-called "slender body" theory (Batchelor, 1974) permits analysis of slender, straight and parallel particles that are laterally close to each other (Phan-Thien, 1980). Another possibility is to presume that particles are dispersed according to a certain geometric pattern (Koch et al., 1989) or to assume that each particle is immersed in a fictitious medium whose properties depend on the location of the neighboring particles (Buyevich and Shchelchkova, 1978). One may also use variational principles to determine

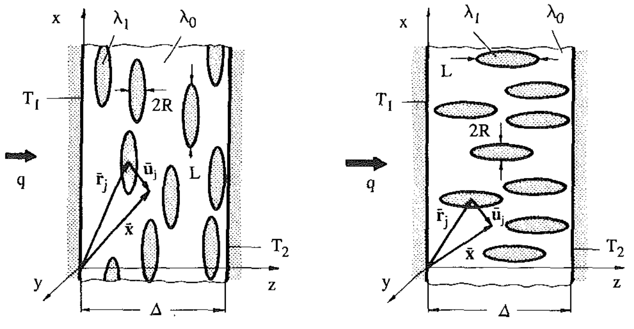

Fig. 1 Two extreme cases of particle orientation in the thermal barrier

---

[1] Visiting Professor; permanent address: Institute of Heat Engineering, Warsaw University of Technology, ul. Nowowiejska 25, 00-665 Warsaw, Poland.

Contributed by the Heat Transfer Division for publiction in the JOURNAL OF HEAT TRANSFER. Manuscript received by the Heat Transfer Division May 1992; revision received June 1993. Keywords: Conduction, Microgravity Heat Transfer, Thermophysical Properties. Associate Technical Editor: R. J. Simoneau.

bounds on the effective transport properties (Batchelor, 1974; Rubinstein and Torquato, 1989).

An important problem to be considered is the problem of wall effects. These effects may be significant, as discussed by Milliken et al. (1989) in the case of experimentally observable slip of suspension velocity, and by Melanson and Dixon (1985) in the case of temperature slip of a granular medium. The existing theoretical approaches are based on purely geometric considerations. For example, the flow of suspension is divided into a wall layer assumed to contain only pure carrier fluid and a core region containing suspension whose properties are not affected by the presence of the wall. The wall-layer thickness is then suitably adjusted to match the known experimental data (Maude, 1967). Description of single particle-wall interaction can be found, for example, in Tözeren and Skalak (1977).

In this paper, heat flow through a layer of suspension of a finite thickness is considered. The particles are assumed to have random distribution and to form a small volume fraction of the mixture. The effects of particle shape are studied by assuming them to be prolate ellipsoids and then changing their aspect ratio (particle length/diameter). This approach permits study of shapes varying from spheres to elongated fibers. Section 2 discusses a method of description of stationary heat conduction in heterogeneous media. In Section 3 this theory is applied to the analysis of heat flow through a suspension layer. Section 4 is devoted to a parametric study of the various factors affecting heat flow through the barrier. Finally, Section 5 provides a short summary of the main conclusions.

2 Effective Medium Theory

A method for averaging both the energy conservation equation and the Fourier constitutive relation must be found in order to obtain the effective medium formulation of equations describing heat conduction in heterogeneous media. Two procedures are usually applied: *volume averaging* over small physical regions representative of the structure of the medium (Koch et al., 1989; Pitchumani and Yao, 1991) or *ensemble averaging* over the ensemble of possible realizations of geometry of the medium (e.g., Hinch, 1977; Rubinstein and Torquato, 1989). Due to obvious advantages (commutability in space and time of differential operators, possibility for form averages in situations that lack spatial stationarity), ensemble averaging is considered more powerful than volume averaging; thus it is used in the following derivations.

The ensemble average of any arbitrary function $h(\bar{x}|\mathcal{A})$ is defined as

$$\{h(\bar{x})\} = \int h(\bar{x}|\mathcal{A})p(\mathcal{A})d\mathcal{A} \tag{1}$$

where integration is carried out over the whole ensemble of realizations (configurations $\mathcal{A}$) of the medium inner structure. In the above definition, $p(\mathcal{A})$ is the probability density function associated with configuration $\mathcal{A}$. The function is time independent due to assumed stationarity of structure of the medium. For a suspension of N spheroidal particles, it may be expressed as a function of a $3N$-dimensional phase space formed by vectors $\bar{r}_j$ (describing positions of centers of the particles), a $2N$-dimensional phase space of the unit vectors $\bar{\omega}$ (describing orientation of particle axes of symmetry), an N-dimensional phase space of aspect ratios ϵ of the particles (describing their particular shapes), and an N-dimensional phase space of radius R of the particles (describing their size).

An additional conditional average is used in the theory of suspensions:

$$\{h(\bar{x})\}^* = \int h(\bar{x}|\mathcal{A})p(\mathcal{A}|\bar{r}', \bar{\omega}, \epsilon, R)d(\mathcal{A}|\bar{r}', \bar{\omega}, \epsilon, R) \tag{2}$$

Nomenclature

$a = [(L/2)^2 - R^2]^{1/2}$
$\mathcal{A}$ = configuration of the particles
$A_j(A_r)$ = surface area of the jth particle (the reference particle)
$\bar{\bar{A}}$ = tensor defined in Eq. (23)
$\bar{\bar{B}}$ = tensor defined in Eq. (43)
$\bar{C}_0, \bar{\bar{C}}_1$ = coefficients (vector and tensor) in linear representation of $\bar{\varphi}_1$ in Eq. (31)
D_m = quantity defined in Eq. (54) and on Fig. 2
$\bar{f}, \bar{F}$ = vector functions defined in Eqs. (36), (37), and (41)
G = Green's function
G_∞ = Green's function for infinite medium
H = Heaviside step function
$\bar{\bar{K}}$ = tensor defined in Eq. (44)
L = particle length
$l(\mathcal{L})$ = micro (macro) length scale
$\bar{n}$ = unit vector normal to the surface pointing outward
n = number of particles per unit volume
$p(\mathcal{A})$ = probability density function associated with configuration $\mathcal{A}$
$p(\mathcal{A}|\bar{r}', \bar{\omega}, \epsilon, R)$ = conditional probability density function associated with configuration $\mathcal{A}$ for fixed position, orientation, shape, and dimension of a particle
$p(\bar{r}', \bar{\omega}, \epsilon, R)$ = one-particle probability distribution function
$\bar{\bar{P}}$ = shape tensor defined in Eqs. (34), (35)
P_1^m, Q_1^m = Legendre functions of the first and second kind
$\bar{q}$ = heat flux vector
q, q_0 = component of heat flux vector in the direction perpendicular to the walls for suspension and pure fluid, respectively
$\bar{r}_j$ = vector describing position of center of the jth particle
$\bar{r}' = (x', y', z')$ = vector describing position of the center of the reference particle
$\bar{r}_i^*$ = vector connecting the center of the ith image with the center of the reference particle (Fig. 2)
R = particle radius
$\mathcal{S}$ = area of cross section of the particle (Fig. 2), Eq. (55)
T = temperature
T_1, T_2 = temperatures of the walls
$\bar{u}_j, \bar{v}_j$ = position vectors with origin in the center of the jth particle
$\bar{u}, \bar{v}$ = position vectors with origin in the center of the reference particle $\bar{u} = (u_1, u_2, u_3)$; Fig. 2
$\bar{u}_i^*, \bar{v}_i^*$ = position vectors associated with the ith image of the reference particle

where $p(\mathcal{A}|\bar{r}', \bar{\omega}, \epsilon, R)$ is the conditional probability density function relevant to configuration $\mathcal{A}$ when the center of the reference particle $\bar{r}'$ as well as its orientation $\bar{\omega}$, shape ϵ, and size R are fixed. It emerges from the need to calculate a transfer process occurring in a chosen, reference (test) particle. More detailed discussion about the ensemble averaging was presented by Buyevich and Shchelchkova (1978) and Herczynski and Pienkowska (1980).

When averaged, the energy conservation equation for steady-state heat conduction without heat sources and the Fourier constitutive relation take the form

$$\overline{\nabla}\cdot\{\bar{q}(\bar{x})\}=0, \tag{3}$$

$$-\{\bar{q}(\bar{x})\}=\{\lambda(\bar{x})\overline{\nabla}T(\bar{x})\} \tag{4}$$

and the problem definition is completed by specifying the Dirichlet-type boundary conditions

$$T(0)=T_1,\ T(\Delta)=T_2. \tag{5}$$

Position-dependent thermal conductivity in Eq. (4) can be written with the help of a characteristic function θ as

$$\lambda(\bar{x}|\mathcal{A})=\lambda_1\theta(\bar{x}|\mathcal{A})+\lambda_0[1-\theta(\bar{x}|\mathcal{A})] \tag{6}$$

where λ_1 and λ_0 are particle and fluid thermal conductivities, respectively. The characteristic function θ assumes value 1 in the interior of the particles and value 0 in the fluid.

To derive an equation for distribution of the average temperature $\{T(\bar{x})\}$ in the medium, the average constitutive relation between $\{\bar{q}(\bar{x})\}$ and $\{T(\bar{x})\}$ must be found. This is a simple task if the dependence of $T(\bar{x}|\mathcal{A})$ on the average temperature $\{T(\bar{x})\}$ is known. In that case a simple substitution of $T(\bar{x}|\mathcal{A})$ into Eq. (4) leads to the desired constitutive equation. Since this dependence is not known, one begins by combining Eqs. (3) and (4) into

$$\lambda_0\overline{\nabla}\cdot\overline{\nabla}T(\bar{x}|\mathcal{A})+\overline{\nabla}\cdot[\lambda'(\bar{x}|\mathcal{A})\overline{\nabla}T(\bar{x}|\mathcal{A})=0 \tag{7}$$

where

$$\lambda'(\bar{x}|\mathcal{A})=\lambda(\bar{x}|\mathcal{A})-\lambda_0. \tag{8}$$

Afterward, the Green's function defined as

$$\lambda_0\overline{\nabla}\cdot\overline{\nabla}G(\bar{x},\bar{y})+\delta(\bar{x},\bar{y}) =0 \quad \text{in } \Omega, \quad G(\bar{x},\bar{y})=0 \quad \text{on } \partial\Omega, \tag{9}$$

is introduced, where $\delta(\bar{x},\bar{y})$ is the Dirac delta function and Ω and $\partial\Omega$ are volume and surface of the medium, respectively. The solution of Eq. (7) can be expressed in the form

$$T(\bar{x}|\mathcal{A})=-\int_\Omega \overline{\nabla}G(\bar{x},\bar{y})\cdot\lambda'(\bar{y}|\mathcal{A})\overline{\nabla}T(\bar{y}|\mathcal{A})d\Omega - \int_{\partial\Omega}\lambda_0\overline{\nabla}G(\bar{x},\bar{y})\cdot\bar{n}T(\bar{y}|\mathcal{A})d(\partial\Omega) \tag{10}$$

where $\bar{n}$ is the external unit vector perpendicular to $\partial\Omega$. After application of the ensemble-averaging procedure to both sides of Eq. (10) and subtraction of the result from Eq. (10), an expression for the local temperature takes the form

$$T(\bar{x}|\mathcal{A})=\{T(\bar{x})\}-\int_\Omega \overline{\nabla}G(\bar{x},\bar{y})\cdot[\lambda'(\bar{y}|\mathcal{A})\overline{\nabla}T(\bar{y}|\mathcal{A}) - \{\lambda'(\bar{y})\overline{\nabla}T(\bar{y})\}]d\Omega. \tag{11}$$

It is now assumed that the relation between the local and average temperatures can be written in form

$$T(\bar{x}|\mathcal{A})=\{T(\bar{x})\}+\int_\Omega \bar{\varphi}(\bar{x},\bar{y}|\mathcal{A})\cdot\overline{\nabla}\{T(\bar{y})\}d\Omega, \tag{12}$$

which allows explicit separation of the environmental temperature conditions from fluctuations caused by local variation

Nomenclature (cont.)

$\bar{x}, \bar{y}, \bar{z}$ = position vectors, $\bar{x}=(x, y, z)$, $\bar{y}(x, y, z)$, $\bar{z}(x, y, z)$
v = particle volume fraction $= n2\pi LR^2/3$
α, γ = angles describing orientation of the particle major axis (Fig. 2)
δ = Dirac delta function
Δ = thickness of the barrier
ϵ = particle aspect ratio $=L/2R$
ξ, ϑ', ϕ' or η, ϑ, ϕ = prolate spheroidal coordinate system associated with the center of the reference particle
η_R = value of the coordinate η in the prolate spheroidal system corresponding to surface of the reference particle
θ = characteristic function, Eq. (6)
Θ = nondimensional temperature $=(\{T\}-T_2)/(T_1-T_2)$
Θ_e = nondimensional temperature extrapolated to the wall (Fig. 3*b*)
λ = thermal conductivity, $\lambda'=\lambda-\lambda_0$
$\bar{\bar{\lambda}}_{ef}$ = effective thermal conductivity tensor
$\lambda_{ef}^{\perp}$ = component of $\bar{\bar{\lambda}}_{ef}$ in the direction perpendicular to the walls
$(\lambda_{ef}^{\perp})_\infty$ = component of $\bar{\bar{\lambda}}_{ef}$ in the same direction as $\lambda_{ef}^{\perp}$ for infinite domain
$\lambda_1(\lambda_0)$ = particle (fluid) thermal conductivity, $\lambda_1'=\lambda_1-\lambda_0$
$\sigma=\lambda_1/\lambda_0$ = relative thermal conductivity, $\sigma'=\sigma-1$
$\bar{\varphi}$ = microstructure function defined in Eq. (12)
$\bar{\varphi}_1, \bar{\bar{\varphi}}_2$ = functions defined in the expansion (16) for $\bar{\varphi}$
ψ = probability density function defined in Eq. (50)
$\bar{\omega}$ = vector describing orientation of the particle major axis
$\Omega, \partial\Omega$ = volume and surrounding surface of the medium
$\tilde{\Omega}$ = volume of suspension accessible to centers of the particles
$\{\ \}, \{\ \}^*$ = ensemble (conditional ensemble) averaged defined in Eqs. (1) and (2), respectively
$\overline{\nabla}$ = (vector) Nabla operator, in some equations $\overline{\nabla}=\partial/\partial\bar{x}$ or $\overline{\nabla}=\partial/\partial\bar{y}$ to make notation more explicit
$\bar{a}\cdot\bar{b}=d$ = scalar product of vectors $\bar{a}$ and $\bar{b}$
$\bar{\bar{a}}\cdot\bar{b}=\bar{c}$ = scalar product of second-order tensor $\bar{\bar{a}}$ and vector $\bar{b}$
$\bar{\bar{a}}\cdot\bar{\bar{b}}=\bar{\bar{c}}$ = scalar product of second-order tensors $\bar{\bar{a}}$ and $\bar{\bar{b}}$
$\bar{a}\,\bar{b}=\bar{\bar{c}}$ = affine product of vectors $\bar{a}$ and $\bar{b}$
$\bar{a}\cdot\bar{\bar{b}}\cdot\bar{a}=d$ = quadratic form (double product of vector $\bar{a}$ and second-order tensor $\bar{\bar{b}}$)
$\bar{\bar{1}}$ = unit tensor

of thermal properties of the inhomogeneous medium. Substitution of Eq. (12) into Eq. (11) leads to the expression

$$\bar{\varphi}(\bar{x}, \bar{z}|\mathfrak{A}) = -\int_{\Omega} \overline{\nabla} G(\bar{x}, \bar{y}) \cdot [\lambda'(\bar{y}|\mathfrak{A})\, (\delta(\bar{y}-\bar{z})\, \bar{\bar{1}} + \overline{\nabla}\bar{\varphi}(\bar{y}, \bar{z}|\mathfrak{A})) - \{\lambda'(\bar{y})(\delta(\bar{y}-\bar{z})\bar{\bar{1}} + \overline{\nabla}\bar{\varphi}(\bar{y}, \bar{z}))\}]d\bar{y} \quad (13)$$

for the vector function $\bar{\varphi}(\bar{x}, \bar{z}|\mathfrak{A})$ called subsequently *the microstructure function*. In the above, $\bar{\bar{1}}$ is the unit second-order tensor. The microstructure function depends on thermal conductivities of the components, structure of the medium, and the type of boundary conditions assumed on $\partial\Omega$, but not on the temperature distribution on the external surface of the medium.

When expression (12) is substituted into Eq. (4), the following form of the constitutive relation results:

$$-\{\bar{q}(\bar{x})\} = \int_{\Omega} \bar{\bar{\lambda}}_{ef}(\bar{x}, \bar{y}) \cdot \partial/\partial\bar{y}\{T(\bar{y})\}d\bar{y}, \quad (14)$$

with the effective thermal conductivity tensor defined as

$$\bar{\bar{\lambda}}_{ef}(\bar{x}\ \bar{y}) = \{\lambda(\bar{x})[\bar{\bar{1}}\delta(\bar{x}-\bar{y}) + \partial/\partial\bar{x}\ \bar{\varphi}(\bar{x}, \bar{y})]\}. \quad (15)$$

Equation (14) reveals a nonlocal character of the relation between the average heat flux and the temperature in the heterogeneous medium, as previously suggested by Dutta and Mashelkar (1987). This is to say that in the effective medium formulation, local heat flux at any point depends not only on the local temperature gradient but also on the temperature distribution in the whole medium.

The above equations can be simplified if the microstructure length scale ℓ (associated with variations in the thermal properties of the heterogeneous material) is much less than the smallest of the macroscopic length scales $\mathfrak{L}$ characterizing changes in the average temperature gradient of the medium. For the problem at hand the length scale ℓ is of the order of the particle length L. The length scale $\mathfrak{L}$ is of the order of barrier thickness ∇. If $\ell/\mathfrak{L} << 1$ then the following asymptotic expansion of multipole type may be introduced:

$$\bar{\varphi}(\bar{x}, \bar{y}|\mathfrak{A}) = [-\bar{x} + \bar{\varphi}_1(\bar{x}|\mathfrak{A})]\delta(\bar{y}-\bar{x}) - \ell\bar{\bar{\varphi}}_2(\bar{x}|\mathfrak{A}) \cdot \overline{\nabla}\delta(\bar{y}-\bar{x}) + 0(\ell^2). \quad (16)$$

The above expansion may be treated as an expansion in growing powers of the small parameter ($\ell/\mathfrak{L}$) with the first term describing (in effect) local transport properties, while the second one describes nonlocal effects. This expansion may not be valid if $\ell/\mathfrak{L} = 0(1)$, i.e., when the barrier thickness is of the particle length. It can be shown, however, that when a small volume fraction of the particles is considered ($v \to 0$), the ratio of the nonlocal and local effects is of the order of the volume fraction even when $\ell/\mathfrak{L} = 0(1)$ (Diener and Kaseberg, 1976; Furmanski, 1992; Jeffrey, 1981). Since the present analysis is focused on suspensions with small particle volume fraction, the nonlocal effects, i.e., the second term in the expansion (16), can be neglected regardless of the barrier thickness.

After substitution of the first term in the expansion (16) into Eqs. (14) and (15), the following form of the constitutive relation is obtained:

$$-\{\bar{q}(\bar{x})\} = \bar{\bar{\lambda}}_{ef}(\bar{x}) \cdot \overline{\nabla}\{T(\bar{x})\} \quad (17)$$

with

$$\bar{\bar{\lambda}}_{ef}(\bar{x}) = \{\lambda(\bar{x})\overline{\nabla}\bar{\varphi}_1(\bar{x})\}. \quad (18)$$

An expression for $\bar{\varphi}_1(\bar{x}|\mathfrak{A})$ can be derived by substituting Eq. (16) into Eq. (13)

$$\bar{\varphi}_1(\bar{x}|\mathfrak{A}) = \bar{x} - \int_{\Omega} \overline{\nabla} G(\bar{x}, \bar{y}) \cdot [\lambda'(\bar{y}|\mathfrak{A})\overline{\nabla}\bar{\varphi}_1(\bar{y}|\mathfrak{A}) - \{\lambda'(\bar{y})\overline{\nabla}\bar{\varphi}_1(\bar{y})\}]d\Omega. \quad (19)$$

The analytical expression for the characteristic function for a suspension containing spheroidal particles can be written as

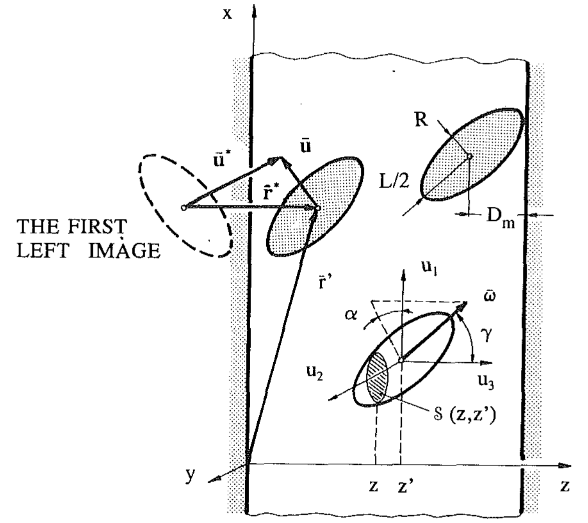

Fig. 2 Characteristic quantities used for estimation of the heat flow across the barrier

$$\theta(\bar{x}|\mathfrak{A}) = \sum_{j=1}^{N} \theta_j(\bar{x}|\mathfrak{A}) = \sum_{j=1}^{N} H(1 - \bar{u}_j \cdot \bar{\bar{A}} \cdot \bar{u}_j) \quad (20)$$

where H is the Heaviside function:

$$H(t) = \begin{cases} 0 \text{ for } t<0 \\ 1 \text{ for } t \geq 0 \end{cases} \quad (21)$$

and

$$\bar{u}_j = \bar{x} - \bar{r}_j. \quad (22)$$

The tensor $\bar{\bar{A}}$ accounts for the spheroidal shape of the particles and is defined as

$$\bar{\bar{A}} = R^{-2}\bar{\bar{1}} + R^{-2}(\epsilon^{-2} - 1)\bar{\omega}\,\bar{\omega} \quad (23)$$

where $\bar{\omega}$ is a vector describing the orientation of the particle, and R and ϵ are the radius and aspect ratio of the particle, respectively.

When Eq. (20), after taking into account Eqs. (6) and (8), is substituted into Eq. (19) and proper change from volume to surface integrals is made (utilizing Green's theorem and properties of function $\bar{\varphi}_1$; Furmanski, 1989) the following relation is obtained:

$$\bar{\varphi}_1(\bar{u}|\mathfrak{A}) + \lambda_1' \oint_{A_1=A_r} G(\bar{u}, \bar{v})\overline{\nabla}\bar{\varphi}_1(\bar{v}|\mathfrak{A}) \cdot \bar{n}dA_r + \lambda_1' \sum_{j=2}^{N} \oint_{A_j} G(\bar{u}_j, \bar{v}_j)\overline{\nabla}\bar{\varphi}_1(\bar{v}_j|\mathfrak{A}) \cdot \bar{n}dA_j = \bar{u} + \lambda_1' \int_{\partial\Omega} G(\bar{u}, \bar{v})\{\theta(\bar{v})\overline{\nabla}\bar{\varphi}_1(\bar{v})\} \cdot \bar{n}d(\partial\Omega) \quad (24)$$

where A_j is the surface of the jth particle. As particles are indistinguishable, the particle denoted by subscript 1 is considered to be a reference (or a test) particle with $\bar{u}_1 = \bar{u} = \bar{x} - \bar{r}'$. The relevant correction in the definition of $\bar{\varphi}_1$ due to shift of the origin of the coordinate axes (Fig. 2) has already been incorporated into Eq. (24). Equation (24) enables the microstructure function to be found for the assumed distribution of the particles.

3 Application of the Effective Medium Theory to Analysis of Heat Flow Across a Thermal Barrier

Let us assume that heat flows across a barrier made of a layer of suspension with known, constant temperatures T_1 and T_2 prescribed on its opposite sides ($T_1 > T_2$). The layer has a finite thickness but extends to infinity in the remaining two directions.

According to Eq. (18), distribution of the effective thermal conductivity may not be uniform in the suspension. Nevertheless, due to the assumed boundary conditions, heat flow through the barrier is, on average, one dimensional. So we can easily write a dimensionless expression for the steady heat flux in the direction transverse to the barrier as

$$q/q_0=\Delta/\int_0^{\Delta}[\lambda_{ef}^{\perp}(z)/\lambda_o]^{-1}dz \tag{25}$$

where Δ is the thickness of the barrier, $\lambda_{ef}^{\perp}(z)$ denotes the component of the effective thermal conductivity tensor in the direction of the bulk heat flow, q_0 stands for the heat flux through the layer of pure fluid and λ_0 denotes conductivity of the fluid. The main problem is calculation of $\lambda_{ef}^{\perp}(z)/\lambda_0$ for the barrier. The effective thermal conductivity may be estimated from definition (18) when the microstructure function $\overline{\varphi}_1$ is known. The latter may be obtained from solution of Eq. (24) if a proper Green's function is utilized. So let us first determine the required form of this function.

3.1 Form of Green's Function for a Suspension Layer. The Green's function is interpreted as the value of disturbance produced at point $\overline{x}$ when the source point is located at point $\overline{y}$. The explicit form of the Green's function satisfying boundary condition (9) can be found by application of the method of reflections (Jackson, 1975). When the method is used, two images of the source point are formed in the outer left and right-hand sides of the barrier, with the barrier walls treated as planes of mirror reflections. These two images are in turn treated as additional (though negative) source points and reflected in the left and right walls, respectively. In this way an infinite series of positive and negative images of the source point on the outer left and right-hand sides of the barrier is formed. If the Green's function G_∞ is expressed in the local coordinate system $(\overline{u}, \overline{v})$ associated with the center of the reference particle, then the Green's function for our problem may be cast in the form

$$\begin{aligned}G(\overline{u}, \overline{v})&=G_\infty(\overline{u}, \overline{v})-\sum_{i=0}^{\infty}G_\infty(\overline{u}_i^*, \overline{v}_i^*;\, 2i\Delta+2z')\\&+\sum_{i=1}^{\infty}G_\infty(\overline{u}_i^*, \overline{v}_i^*;\, 2i\Delta)-\sum_{i=0}^{\infty}G_\infty(\overline{u}_i^*, \overline{v}_i^*;\, 2(i+1)\Delta-2z')\\&+\sum_{i=0}^{\infty}G_\infty(\overline{u}_i^*, \overline{v}_i^*;\, 2(i+1)\Delta),\end{aligned} \tag{26}$$

where $G_\infty(\overline{u}_i^*, \overline{v}_i^*)$ are the Green's functions for the inifinite medium associated with the ith image; the values in the brackets after the semicolons describe distance between an image and the center of the reference particle. Positive and negative signs in the above expression arise from the requirement that the Green's function should satisfy Dirichlet type of boundary conditions, Eq. (9).

The Green's function for the infinite medium should account for the spheroidal shape of the particle and its arbitrary orientation in space. If we introduce a curvilinear, prolate spheroidal coordinate system (η, ϑ, ϕ) consistent with the particle shape and orientation, then the equation for the Green's function $G_\infty(\overline{u}, \overline{v})$ takes the following form:

$$\begin{aligned}&\frac{1}{(\sinh^2\eta+\sin^2\vartheta)}\left[\sinh^{-1}\eta\,\frac{\partial}{\partial\eta}\left(\sinh\,\eta\,\frac{\partial G_\infty}{\partial\eta}\right)\right.\\&\left.+\sin^{-1}\vartheta\,\frac{\partial}{\partial\vartheta}\left(\sin\,\vartheta\,\frac{\partial G_\infty}{\partial\vartheta}\right)\right]+\frac{1}{\sinh^2\eta\,\sin^2\vartheta}\,\frac{\partial^2G_\infty}{\partial\phi^2}\\&+\frac{\delta(\eta, \xi)\delta(\vartheta, \vartheta')\delta(\phi, \phi')}{\lambda_0a(\sinh^2\eta+\sin^2\vartheta)\sinh\,\eta\,\sin\vartheta}=0\end{aligned} \tag{27}$$

with G_∞ vanishing at infinity and $a=[(L/2)^2-R^2]^{1/2}=R(\epsilon^2-1)^{1/2}$.

The solution of the above equation may be sought in the form

$$G_\infty(\overline{u}, \overline{v})=\lambda_0^{-1}\sum_{l=0}^{\infty}\sum_{m=-1}^{m=1}\mathcal{R}(\xi, \eta)Y_{lm}(\vartheta, \phi)\tilde{Y}_{lm}(\vartheta', \phi') \tag{28}$$

where Y_{lm} are spherical harmonics (Moon and Spencer, 1961) and tilde denotės complex conjugate.

The function $\mathcal{R}(\xi, \eta)$ may be obtained in the manner described by Jackson (1975). The final expression for the infinite Green's function

$$\begin{aligned}G_\infty(\overline{u}, \overline{v})=\sum_{l=0}^{\infty}\sum_{m=-1}^{m=1}\frac{(-1)^m}{\lambda_0a}\,\frac{(l-m)!}{(l+m)!}\\\times[P_l^m(\cosh\,\xi)Q_l^m(\cosh\,\eta)H(\eta-\xi)\\+P_l^m(\cosh\,\eta)Q_l^m(\cosh\,\xi)H(\xi-\eta)]\,Y_{lm}(\vartheta, \phi)\tilde{Y}_{lm}(\vartheta', \phi')\end{aligned} \tag{29}$$

where $P_l^m$and $Q_l^m$are Legendre functions of the first and second type, respectively, and H denotes Heaviside function defined by Eq. (21). This form of the Green's function simplifies evaluations of the surface integrals in Eq. (24) for the microstructure function.

3.2 The Form of the Microstructure Function. The definition of the effective thermal conductivity, Eq. (18), may be cast into a different form when formula (6) is taken into account, i.e.,

$$\overline{\overline{\lambda}}_{ef}(\overline{x})=\lambda_0\overline{\overline{1}}+\lambda_1'\{\theta(\overline{x})\overline{\nabla}\overline{\varphi}_1(\overline{x})\}, \tag{30}$$

where $\{\overline{\nabla}\overline{\varphi}_1\}=\overline{\overline{1}}$. Because the characteristic function $\theta(\overline{x})$ is zero outside the particles, only the value of $\overline{\varphi}_1$ in the interior of the particles is of interest. The simplest acceptable form of $\overline{\varphi}_1$ is linear, i.e.,

$$\overline{\varphi}_1(\overline{x}\,|\,\mathcal{a})=\overline{C}_0(\mathcal{a})+\overline{\overline{C}}_1(\mathcal{a})\cdot\overline{u} \tag{31}$$

where vector $\overline{C}_0$ and second-order tensor $\overline{C}_1$ depend upon the configuration of the particles in the suspension. Substitution of the gradient of the above function into Eq. (24) results in an integral of the type

$$\oint_{A_j}G_\infty(\overline{u}_j, \overline{v}_j)\overline{n}dA_j$$

which is taken over the surface of each particle. The unit vector normal to the surface of any particle may be expressed in terms of a prolate spheroidal coordinate system as

$$\overline{n}=(\sinh^2\eta+\sin^2\vartheta)^{-1/2}\begin{bmatrix}\cosh\,\eta\,\sin\,\vartheta\,\cos\,\phi\\\cosh\,\eta\,\sin\,\vartheta\,\sin\,\phi\\\sinh\,\eta\,\cos\,\vartheta\end{bmatrix}. \tag{32}$$

After substitution of the proper form of the Green's function, the value of the above integral can be obtained through simple (although time-consuming) calculations. Details of the calculations are omitted. The final results are as follows:

$$\begin{aligned}&\int_{A_j}G_\infty(\overline{u}_j, \overline{v}_j)\overline{n}dA_j\\&=\lambda_0^{-1}\begin{cases}\overline{\overline{P}}\cdot\overline{u}_j & \text{for points } \overline{u}_j \text{ inside particle,}\\\overline{\overline{P}}\cdot\overline{f}(\overline{u}_j) & \text{for points } \overline{u}_j \text{ outside particle.}\end{cases}\end{aligned} \tag{33}$$

In Eq. (33), $\overline{\overline{P}}$ is a second-order tensor, whose principal values are given by the formulae:

$$P_{11}=P_{22}=-Q_1^1(\cosh\,\eta_R)\sinh\,\eta_R\,\cosh\,\eta_R/2, \tag{34}$$

$$P_{33}=Q_1^0(cosh\,\eta_R)\,sinh^2\eta_R, \tag{35}$$

and $\overline{f}(\overline{u}_j)$ is a vector function whose components are described by:

$$\begin{bmatrix} f_{11}(\bar{u}_j) \\ f_{22}(\bar{u}_j) \end{bmatrix} = \frac{P_1^1(\cosh \eta_R)}{Q_1^1(\cosh \eta_R)}\, aQ_1^1(\cosh \eta) \sin \vartheta \begin{bmatrix} \cos \phi \\ \sin \phi \end{bmatrix}, \tag{36}$$

$$f_{33}(\bar{u}_j) = \frac{P_1^0(\cosh \eta_R)}{Q_1^0(\cosh \eta_R)}\, aQ_1^0(\cosh \eta) \cos \phi, \tag{37}$$

where $\sinh \eta_R = (\epsilon^2 - 1)^{-1/2}$, $\cosh \eta_R = \epsilon(\epsilon^2 - 1)^{1/2}$. It should be noted that the tensor $\bar{\bar{P}}$ does not depend on the dimensions of the spheroid but solely on its shape.

Let us now consider again Eq. (24). Due to the assumption of small volume fraction of the particles, the direct influence of the neighboring particles on the microstructure function can be omitted except for their interaction through the effective field. Thus Eq. (24) may be rewritten as

$$\bar{\varphi}_1(\bar{u} \mid \mathcal{A}) + \lambda_1' \int_{A_r} G(\bar{u}, \bar{v}) \overline{\nabla} \bar{\varphi}_1(\bar{y} \mid \mathcal{A}) \bullet \bar{n}\, dA_r$$
$$= \bar{u} + \lambda_1' \int_\Omega \overline{\nabla} G(\bar{u}, \bar{v}) \bullet \{\theta(\bar{v}) \overline{\nabla} \bar{\varphi}_1(\bar{v})\}\, d\Omega. \tag{38}$$

If a position vector $\bar{u}$ corresponding to the interior of the particle is specified and the trial solution, Eq. (31), for the microstructure function is introduced, Eq. (38) is transformed into the following form:

$$\bar{C}_0(\mathcal{A}) + \bar{\bar{C}}_1(\mathcal{A}) \bullet \bar{u} + \sigma' (\bar{\bar{P}} \bullet [\bar{u} - \bar{F}(\bar{u})]) \bullet \bar{\bar{C}}_1(\mathcal{A})$$
$$= \bar{u} + \sigma' \{\theta(\bar{u}) (\bar{\bar{P}} \bullet [\bar{u} - \bar{F}(\bar{u})]) \bullet \bar{\bar{C}}_1\} \tag{39}$$

where

$$\sigma' = \lambda_1' / \lambda_0 \tag{40}$$

and

$$\bar{F}(\bar{u}) = \sum_{i=0}^{\infty} \bar{f}(\bar{u}_i^*;\, 2i\Delta + 2z') - \sum_{i=1}^{\infty} \bar{f}(\bar{u}_i^*;\, 2i\Delta)$$
$$+ \sum_{i=0}^{\infty} \bar{f}[\bar{u}_i^*;\, 2(i+1)\Delta - 2z'] - \sum_{i=0}^{\infty} \bar{f}[\bar{u}_i^*;\, 2(i+1)\Delta]. \tag{41}$$

In order to obtain explicit, analytical expressions for the constants $\bar{C}_0$ and $\bar{\bar{C}}_1$, linearization of functions $\bar{f}(\bar{u}_i^*)$ must be carried out. These functions are expanded into series of Legendre functions of variable $\bar{u}$ (Fig. 2) and expansions are truncated after two terms ($\bar{u}$ is considered small), i.e,

$$\bar{f}(\bar{u}_i^*) = \bar{f}(\bar{r}_i^* + \bar{u}) = \bar{f}(\bar{r}_i^*) + \overline{\nabla} \bar{f}(\bar{r}_i^*) \bullet \bar{u} + \ldots \tag{42}$$

In the above, $\bar{r}_i^*$ is a vector connecting the center of the ith image with the center of the reference particle.

After substitution of the above expansion into Eq. (39) and matching terms of the same order in $\bar{u}$, we obtain a system of two equations for the unknowns $\bar{C}_0$, $\bar{\bar{C}}_1$. As the latter constant is of special interest in determination of $\bar{\bar{\lambda}}_{ef}$, the equation for $\bar{\bar{C}}_1$ is presented below:

$$[\bar{\bar{1}} + \sigma' \bar{\bar{P}} \bullet (\bar{\bar{1}} - \bar{\bar{K}})] \bullet \bar{\bar{C}}_1(\mathcal{A}) = \bar{\bar{1}} + \sigma' \{\theta [\bar{\bar{P}} \bullet (\bar{\bar{1}} - \bar{\bar{K}})] \bullet \bar{\bar{C}}_1\} = \bar{\bar{B}} \tag{43}$$

where

$$\bar{\bar{K}} = \sum_{i=0}^{\infty} \overline{\nabla} \bar{f}(\bar{r}_i^*;\, 2i\Delta + 2z') - \sum_{i=1}^{\infty} \overline{\nabla} \bar{f}(\bar{r}_i^*;\, 2i\Delta)$$
$$+ \sum_{i=0}^{\infty} \overline{\nabla} \bar{f}[\bar{r}_i^*;\, 2(i+1)\Delta - 2z'] - \sum_{i=1}^{\infty} \overline{\nabla} \bar{f}[\bar{r}_i^*;\, 2(i+1)\Delta]. \tag{44}$$

Equation (43) has a stochastic character; however, its solution can be easily found because its right-hand side is independent of any particular distribution of the particles in the suspension. The left-hand side of Eq. (43) can be solved for $\bar{\bar{C}}_1$

$$\bar{\bar{C}}_1(\mathcal{A}) = [\bar{\bar{1}} + \sigma' \bar{\bar{P}} \bullet (\bar{\bar{1}} - \bar{\bar{K}})]^{-1} \bullet \bar{\bar{B}}. \tag{45}$$

where $\bar{\bar{B}}$ denotes the right-hand side of Eq. (43). The above expression may then be introduced into the right-hand side of Eq. (43) to obtain equation for the unknown value of constant $\bar{\bar{B}}$

$$\bar{\bar{B}} = \bar{\bar{1}} + \sigma' \{\theta [\bar{\bar{P}} \bullet (\bar{\bar{1}} - \bar{\bar{K}})] \bullet [\bar{\bar{1}} + \sigma' \bar{\bar{P}} \bullet (\bar{\bar{1}} - \bar{\bar{K}})]^{-1}\} \bullet \bar{\bar{B}}. \tag{46}$$

With $\bar{\bar{B}}$ known, $\bar{\bar{C}}_1$ is determined by Eq. (45). The relevant expression for $\bar{C}_0$ may be derived in the same manner.

3.3 The Effective Thermal Conductivity of the Medium. Let us now calculate the effective conductivity from definition (30). Substitution of Eq. (31) into Eq. (30) results in

$$\bar{\bar{\lambda}}_{ef}(\bar{x} = \lambda_0 \bar{\bar{1}} + \lambda_1' \{\theta(\bar{x}) \bar{\bar{C}}_1\}. \tag{47}$$

Substitution of $\bar{\bar{C}}_1(\mathcal{A})$ from Eq. (45) leads to an expression for $\bar{\bar{\lambda}}_{ef}/\lambda_0$:

$$\bar{\bar{\lambda}}_{ef}(\bar{x})/\lambda_0 = \bar{\bar{1}} + \sigma' \{\theta [\bar{\bar{1}} + \sigma' \bar{\bar{P}} \bullet (\bar{\bar{1}} - \bar{\bar{K}})]^{-1}\}$$
$$\bullet [\bar{\bar{1}} - \sigma' \{\theta [\bar{\bar{P}} \bullet (\bar{\bar{1}} - \bar{\bar{K}})] \bullet [\bar{\bar{1}} + \sigma' \bar{\bar{P}} \bullet (\bar{\bar{1}} - \bar{\bar{K}})]^{-1}\}]^{-1}. \tag{48}$$

One of the main factors influencing heat flow through the layer is orientation of the particles. It is defined in terms of the unit vector $\bar{\omega}$, directed along the particle major axis. Orientation of this vector is described by two inclination angles (α, γ) with respect to the coordinate system (u_1, u_2, u_3) (Fig. 2). In general, directions of the principal axes of tensor $\bar{\bar{K}}$ are different from those of tensor $\bar{\bar{P}}$, which complicates determination of the effective thermal conductivity in the direction perpendicular to the boundary walls. Equation (48) is simplified considerably in two special cases, when particle major axes are either perpendicular ($\gamma = 0$) or parallel ($\gamma = \pi/2$) to the walls. It can be shown that in these two cases α does not effect $\lambda_{ef}^{\perp}$. Effective use of Eq. (48) requires evaluation of statistical averages of the type $\{\theta(\mathbf{x}) h(\mathbf{x})\}$, which is discussed in the next subsection.

3.4 Evaluation of the Ensemble Averages. In order to calculate the ensemble average containing the characteristic function $\theta(\mathbf{x})$ and an arbitrary function $h(\bar{x} \mid \mathcal{A})$, it is convenient to express the average in the form

$$\{\theta(\bar{x}) h(\bar{x})\} =$$
$$\iiiint \{\theta(\bar{x} \mid \bar{r}', \bar{\omega}, \epsilon, R) h(\bar{x} \mid \bar{r}', \bar{\omega}, \epsilon\ R)\}^*$$
$$\times p(\bar{r}', \bar{\omega}, \epsilon, R)\, d\bar{r}'\, d\bar{\omega}\, d\epsilon\, dR \tag{49}$$

by making use of the conditional ensemble average defined in Eq. (2) and the obvious relation

$$p(\mathcal{A}) = p(\bar{r}', \bar{\omega}, \epsilon, R)\, p(\mathcal{A} \mid \bar{r}', \bar{\omega}, \epsilon, R).$$

In Eq. (49) $p(\bar{r}', \bar{\omega}, \epsilon, R)$ is understood to be the probability density function for a single (reference) particle centered at $\bar{r}'$. This particle has fixed orientation $\bar{\omega}$, shape ϵ, and dimension R. The function $p(\bar{r}', \bar{\omega}, \epsilon, R)$ is often referred to as the "one-particle distribution function" and its determination forms a separate problem in statistical physics. For the present case, it is assumed that the particle positions $\bar{r}'$ are totally random away from the walls, and are strongly influenced by the presence of the walls in the immediate vicinity of the walls (due to geometric constraints). The thickness of such a "wall layer" can be assumed to be equal to the half-length of the particle major axis $L/2$ in order to permit free particle rotation. The one-particle distribution function may be approximated by the formula

$$p(\bar{\mathbf{r}}', \bar{\omega}, \epsilon, R) = \tilde{\Omega}^{-1} \psi(\bar{\omega}, \epsilon, R)(H[z' - L/2]$$
$$- H[z' - (\Delta - L/2)]) \tag{50}$$

where $\tilde{\Omega}$ is the volume of the suspension accessible to the centers of the particles, H denotes the Heaviside function defined in Eq. (21), and $\psi(\bar{\omega}, \epsilon, R)$ is the probability density function for the reference particle having orientation $\bar{\omega}$, aspect ratio ϵ, and minor axis R.

In the analysis that follows we will limit ourselves to a suspension of monodimensional particles of a definite value of ϵ and R. If expressions (20) and (50) are introduced into definition (49) and allowance is made for the fact that the particles are indistinguishable, the expression for the ensemble average may be written as

$$\{\theta(\bar{x})h(\bar{x})\} = n\,\frac{\Delta}{(\Delta-L)}\int_{\Omega}\int_{4\pi}\{h(\bar{x}|\bar{r}',\,\bar{\omega})H[1-(\bar{x}-\bar{r}')\bullet\bar{\bar{A}}\bullet(\bar{x}-\bar{r}')]\}^{*}(H[z'-L/2]-H[z'-(\Delta-L/2)])\psi(\bar{\omega})d\bar{\omega}d\bar{r}' \tag{51}$$

where n is the particle number concentration (i.e., number of particles per unit volume).

The averages appearing in the expression for the effective conductivity, Eq. (48), do not depend on the coordinates x', y' of the center $\bar{r}'$ of the reference particle; nor do they depend on the distribution of the neighboring particles. Equation (51) may, therefore, be simplified to a form

$$\{\theta(\bar{x})h(\bar{x})\} = n\,\frac{\Delta}{(\Delta-L)}\int_0^{\Delta}\left\{h(\bar{x}|z')\mathcal{S}(z,\,z',\,\epsilon,\,R)\times H\left[1-\frac{|z-z'|}{D_m}\right]\right\}_{\omega}(H[z'-L/2]-H[z'-(\Delta-L/2)])dz' \tag{52}$$

where

$$\{g\}_{\omega} = \int_{4\pi} g(\bar{\omega})\psi(\bar{\omega})d\bar{\omega}, \tag{53}$$

denotes averaging over the orientation $\bar{\omega}$,

$$D_m = R[(\epsilon^2-1)\cos^2\gamma+1]^{1/2}, \tag{54}$$

and

$$\mathcal{S}(z,\,z',\,\bar{\omega},\,\epsilon,\,R) = \pi\epsilon R^3[D_m^2-(z-z')^2]/D_m^3 \tag{55}$$

is an area of the cross section of the particle by a plane parallel to the wall and located at a distance z away from the wall (Fig. 2). In the present case the probability density function $\psi(\bar{\omega})$ is chosen as

$$\psi(\bar{\omega}) = \delta(\tilde{\gamma}-\gamma)/2$$

where $\tilde{\gamma}\epsilon\langle 0,\,\pi\rangle$.

It may be noticed that the right-hand side of the formula (52) depends on the distance z from the wall due to the form of the functions appearing in Eq. (48). Integration in Eq. (52) is carried out over z' for all nonzero values of the integrand with the coordinate z kept constant.

4 Discussion of Results

In order to estimate the heat flow across the barrier from Eq. (25) it is necessary to calculate the effective thermal conductivity of the suspension. First, $\bar{\bar{K}}$ was found by truncating the series in Eq. (44) and then summing them up. The number of terms retained was determined automatically in the calculations by specifying the desired accuracy. Following that all ensemble-averaged quantities appearing in formula (48) were calculated according to expression (52). A typical plot of the effective thermal conductivity, in the direction perpendicular to the walls, is presented in Fig. 3(*a*). The local value of $\lambda_{ef}^{\perp}$ changes across the barrier. Near the boundaries it is smaller than the corresponding value $(\lambda_{ef}^{\perp})_{\infty}$ for the unbounded domain (i.e., domain with $\Delta \Rightarrow \infty$). It attains the limiting value equal to the thermal conductivity λ_0 of the carrier fluid at the boundaries. In the middle of the barrier the effective thermal conductivity is greater than $(\lambda_{ef}^{\perp})_{\infty}$. This is caused by an increase of the volume fraction of the particles in this part of the barrier with respect to its average value in the whole barrier. When the thickness of the barrier increases as compared to the length of the particles (Δ/L increases) then $\lambda_{ef}^{\perp}$ quickly approaches the limiting value of $(\lambda_{ef}^{\perp})_{\infty}$ in the middle of the barrier. The region where the effective thermal conductivity remains constant is broadened for growing values of Δ/L leaving only a thin "wall layer" near the wall where $\lambda_{ef}^{\perp}$ abruptly changes.

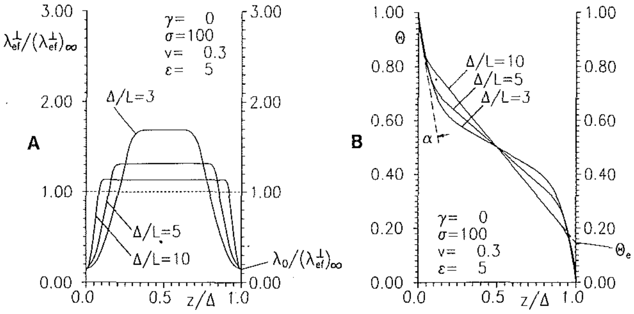

Fig. 3 Distribution of (A) effective thermal conductivity $\lambda_{ef}^{\perp}/(\lambda_{ef}^{\perp})_{\infty}$ and (B) temperature $\Theta = (\{T\} - T_2)/(T_1 - T_2)$: $\lambda_{ef}^{\perp}$ = local effective thermal conductivity, $(\lambda_{ef}^{\perp})_{\infty}$ = effective thermal conductivity for infinite medium, $\alpha = \cot\,[(\lambda_{ef}^{\perp})_{\infty}/\lambda_0]$, Θ_e = temperature at the wall extrapolated from temperature gradient inside the barrier

The ensemble-averaged temperature $\{T(z)\}$ at any location within the barrier may be obtained from the expression

$$\{T(z)\} = T_2 + q\int_0^z [\lambda_{ef}^{\perp}(z)]^{-1}dz$$

after noting that the heat flux is constant across the barrier. Variation of the effective thermal conductivity across the barrier leads to a distortion in the temperature distribution (Fig. 3*b*). For very high values of the barrier thickness as compared to the particle length, the dimensionless temperature gradient at the wall approaches the limiting value of $(\lambda_{ef}^{\perp})_{\infty}/\lambda_0$. For high, though not extreme, values of Δ/L the linear temperature distribution inside the barrier can be extrapolated to the wall, leading to the prediction of a temperature slip Θ_e at the wall (Fig. 3*b*). This prediction is consistent with experimental measurements of temperature distributions in granular media (e.g., Melanson and Dixon, 1985).

The heat flow through the barrier depends on the internal structure of the barrier and on the transport properties of the barrier components. The first factor of interest is the effect of rotation of the particles. Figure 4 demonstrates that rotation of the particles by 90 deg (from being parallel to the wall, $\gamma = \pi/2$, to being perpendicular to the wall, $\gamma = 0$) significantly increases the heat flux. The functional dependence of the heat flux on the orientation angle γ shows that this increase is not very sensitive to the small misalignment of the particles that might occur around both extremal positions (Fig. 4).

Effects of rotation are more pronounced for particles of high aspect ratio (Fig. 5*a*). This is mainly due to the fact that heat flux increases significantly for growing values of ϵ when particles are perpendicular to the wall ($\gamma = 0$). When particles are parallel to the walls, heat flux slightly decreases with increasing values of ϵ (Fig. 5*a*).

The influence of the thickness Δ of the barrier as compared to the particle length L is of interest due to formation of the "wall layers." It can be seen (Figs. 4-6) that the presence of the walls substantially reduces the heat flow as compared to the case of infinite medium, especially for $\Delta/L < 10$ and $\epsilon \geq 10$. As Δ/L increases, q/q_0 tends to the asymptotic values corresponding to infinite domains (Furmanski, 1982; Hatta and Taya, 1986) (Figs. 4-6).

Layers of suspensions are often used in experimental determination of their effective properties. The present results show that the apparent thermal conductivity of the suspension obtained in such measurements will be smaller than the actual $(\lambda_{ef}^{\perp})_{\infty}$ unless the ratio of the layer thickness to particle diameter

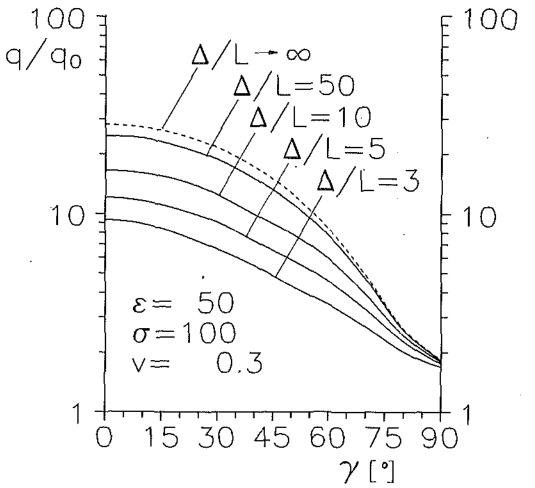

Fig. 4 Variation of heat flux q/q_0 as a function of particle orientation angle γ. Particles axes are assumed to be parallel to each other.

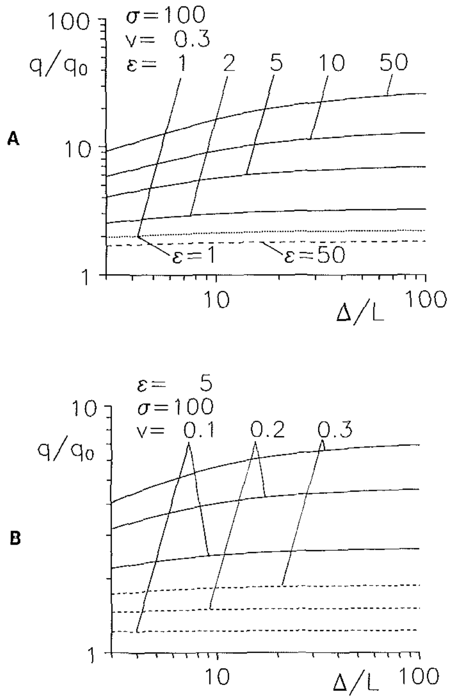

Fig. 5 Variation of heat flux q/q_0 as a function of Δ/L for (A) various particle aspect ratios ϵ and (B) various particle volume fractions v: —— $-\gamma=0$, - - - - $-\gamma=\pi/2$, ····· $-\epsilon=1$. Note that q/q_0 for $\epsilon=1$ is the same for both $\gamma=0$ and $\gamma=\pi/2$.

is sufficiently large. By analogy, this conclusion also applies to the effective viscosity of suspensions, and in fact, such an effect has been found experimentally (Milliken et al., 1989).

Heat flow is greater when the average particle volume fraction v ($v = n2\pi LR^2/3$) increases (Fig. 5b). This is to be expected when thermal conductivity of the particles is larger than the thermal conductivity of the fluid ($\sigma > 1$). When $\sigma < 1$, and opposite effect is observed (Fig. 6). Calculations were carried out only for v up to 0.3 in order not to violate the small volume fraction assumption made in the analysis. Previous calculations made for the periodic system of spheres (e.g., McPherdan and McKenzie, 1978) indicate that interaction between the particles can be neglected in estimation of the bulk heat flow when $v < 0.3$.

The last factor studied was the effect of the relative conductivity of the particles $\sigma = \lambda_1/\lambda_0$. Figure 6 shows that the

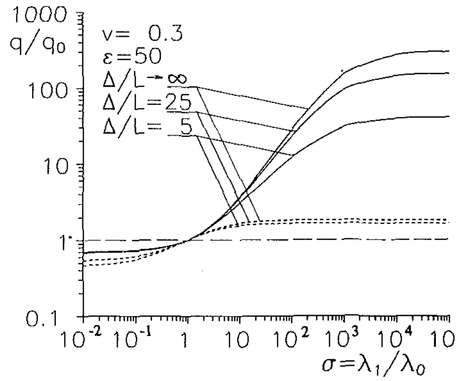

Fig. 6 Variation of heat flux q/q_0 as a function of the particle relative conductivity σ: —— $-\gamma=0$, - - - - - $\gamma=\pi/2$

largest changes in heat transfer due to rotation of the particles occur when the particles have conductivity higher than the carrier fluid. There is an upper limit on the possible increase of the heat flux and this limit is practically reached for $\sigma \geq 1000$.

Finally, one should note that conclusions discussed above are valid only for the particle shapes considered here, i.e., prolate ellipsoids. Change in the shape of the particles may invalidate some of the above predictions.

5 Summary

Results of calculations indicate that a thermal barrier made of a small volume fraction suspension of nonspherical particles is very effective in controlling heat flux. Change of the effective thermal characteristics of the barrier is obtained by externally induced change in the orientation of the particles. Rotation of the particles by 90 deg, from being parallel to the wall to being perpendicular to the wall, can increase heat flux up to several hundred times. This increase is not sensitive to a small misalignment of the particles. An increase in the range of heat flux control is obtained by using longer particles, increasing their thermal conductivity (above that of the carrier fluid) and by increasing their volume fraction. It has been found that wall effects tend to decrease heat flow (as compared to the case of infinite medium) especially for large particles.

Acknowledgments

The authors would like to acknowledge support for this work received from the NSERC of Canada and from the KBN of Poland (Grant No. 3-1003-91-01).

References

Acrivos, A., Jeffrey, D. J., and Saville, D. A., 1990, "Particle Migration in Suspensions by Thermocapillary or Electrophoretic Motion," *J. Fluid Mechanics*, Vol. 212, pp. 95–110.

Batchelor, G. K., 1974, "Transport Properties of Two-Phase Materials With Random Structure," *Annual Review of Fluid Mechanics*, Vol. 6, pp. 227–255.

Buyevich, Yu., and Shchelchkova, I. N., 1978, "Flow of Dense Suspensions," *Progress in Aerospace Science*, Vol. 18, pp. 121–150.

Diener, G., and Kaseberg, F., 1976, "Effective Linear Response in Strongly Heterogeneous Media. Self-Consistent Approach," *Int. J. Solids & Structures*, Vol. 12, pp. 173–184.

Durlofsky, L. J., and Brady, J. F., 1989, "Dynamic Simulation of Bounded Suspensions of Hydrodynamically Interacting Particles," *J. Fluid Mechanics*, Vol. 200, pp. 39–67.

Dutta, A., and Mashelkar, R. A., 1987, "Thermal Conductivity of Structured Liquids," *Advances in Heat Transfer*, Vol. 18, pp. 161–239.

Furmanski, P., 1982, "Determination of Effective Thermal Conductivity of Composites With Inclusions of Various Shape," *Archives of Thermodynamics*, Vol. 3, No. 3-4, pp. 223–235 [in Polish].

Furmanski, P., 1989, "Generalized Method for Description of Heat Conduction Process in Heterogeneous Media," *Mechanika*, Warsaw University of Technology Publications, No. 120 [in Polish].

Furmanski, P., 1992, "Effective Macroscopic Description for Heat Conduction in Heterogeneous Materials," *Int. J. Heat Mass Transfer*, Vol. 35, pp. 3047–3058.

Ganani, E., and Powell, R. L., 1985, "Suspensions of Rod-like Particles: Literature Review and Data Correlations," *J. Composite Materials*, Vol. 19, pp. 194–215.

Gandhi, M. V., Thompson, B. S., and Choi, S. B., 1989, "A New Generation of Innovative Ultra-advanced Intelligent Composite Materials Featuring Electro-Rheological Fluids: An Experimental Investigation," *J. Composite Materials*, Vol. 23, Dec. pp. 1232–1255.

Hatta, H., and Taya, M., 1986, "Equivalent Inclusion Method for Steady State Heat Conduction in Composites," *Int. J. Engineering Science*, Vol. 24, No. 7, pp. 1159–1172.

Herczynski, R., and Pienkowska, I., 1980, "Toward a Statistical Theory of Suspension," *Ann. Rev. Fluid Mechanics*, Vol. 12, pp. 237–269.

Hinch, E. J., 1977, "An Averaged-Equation Approach to Particle Interactions in a Fluid Suspension," *J. Fluid Mechanics*, Vol. 83, Part 4, pp. 695–720.

Jackson, J. D., 1975, *Classical Electrodynamics*, Wiley, N.Y.

Jeffrey, D. J., 1973, "Conduction Through a Random Suspension of Spheres," *Proc. R. Soc. London*, Vol. A 335, No. 1602.

Jeffrey, D. J., 1981, "A Point Source of Heat in a Composite Material," in: *Continuum Models of Discrete Systems 4*, O. Brulin and R. K. T. Hsieh, eds., North Holland Publishing Company.

Koch, D. L., Cox, R. G., Brenner, H., and Brady, J. F., 1989, "The Effect of Order on Dispersion in Porous Media," *J. Fluid Mechanics*, Vol. 200, pp. 173–188.

Landauer. R., 1977, "Electrical Conductivity in Inhomogeneous Media," *Electrical, Transport and Optical Properties of Inhomogeneous Media*, AIP Conference No. 40, Ohio State University.

Lu, S-Y., and Kim, S., 1990, "Effective Thermal Conductivity of Composites Containing Spheroidal Inclusions," *AIChE Journal*, Vol. 36, No. 6, pp. 927–938.

Maude, A. D., 1967, "Theory of Wall Effect in the Viscometry of Suspensions," *British J. Applied Physics*, Vol. 18, pp. 1193–1197.

McPherdan, R. C., and McKenzie, D. R., 1978, "The Conductivity of Lattices of Spheres. I. The Simple Cubic Lattice," *Proc. R. Soc. London*, Vol. A. 359, pp. 45–63.

Melanson, M. M., and Dixon, A. G., 1985, "Solid Conduction in Low d_t/d_p Beds, Spheres, Pellets and Rings," *Int. J. Heat Mass Transfer*, Vol. 28, No. 2, pp. 383–394.

Milliken, W. J., Gottlieb, M., Graham, D. L., Mondy, L. A., and Powell, R. L., 1989, "The Viscosity-Volume Fraction Relation for Suspensions of Rod-Like Particles by Falling-Ball Rheometry," *J. Fluid Mechanics*, Vol. 202, pp. 217–232.

Moon, P., and Spencer, D. E., 1961, *Field Theory Handbook*, Springer-Verlag, Berlin–Göttingen–Heidelberg.

Phan-Thien, N., 1980, "On the Thermal and Mechanical Properties of Slender-Fibre Reinforced Materials at Non-dilute Concentration," *Int. J. Engineering Science*, Vol. 18, pp. 1319–1323.

Pitchumani, R., and Yao, S. C., 1991, "Correlation of Thermal Conductivities of Unidirectional Fibrous Composites Using Local Fractal Techniques," ASME JOURNAL OF HEAT TRANSFER, Vol. 113, pp. 788–796.

Rubinstein, J., and Torquato, S., 1989, "Flow in Random Porous Media: Mathematical Formulation, Variational Principles, and Rigorous Bounds," *J. Fluid Mechanics*, Vol. 206, pp. 25–46.

Smereka, P., and Milton, G. W., 1991, "Bubbly Flow and Its Relation to Conduction in Composites," *J. Fluid Mechanics*, Vol. 223, pp. 65–81.

Tözeren, A., and Skalak, R., 1977, "Stress in a Suspension Near Rigid Boundaries," *J. Fluid Mechanics*, Vol. 82, Part 2, pp. 289–307.

G. Chen
Assistant Professor,
Department of Mechanical Engineering
and Materials Science,
Duke University,
Durham, NC 27708
Assoc. Mem. ASME

C. L. Tien
A. Martin Berlin Professor,
Department of Mechanical Engineering,
University of California,
Berkeley, CA 94720
Honorary Mem. ASME

Thermally Induced Optical Nonlinearity During Transient Heating of Thin Films

This work studies the temperature field and the optical response of weakly absorbing thin films with thermally induced optical nonlinearity during picosecond to nanosecond pulsed-laser heating. A one-dimensional model is presented that examines the effects of the temperature dependent optical constants and the nonuniform absorption caused by interference. The energy equation is solved numerically, coupled with the matrix method in optical multilayer theory. Both cadmium sulfide (CdS) thin films and a zinc selenide (ZnSe) interference filter are considered. The computational results compare favorably with available experimental data on the ZnSe interference filter. This study shows that the transient temperature distributions in the films are highly nonuniform. Such nonuniformity yields Airy's formulae for calculating the thin-film reflectance and transmittance inapplicable. Applications of the work include optical bistability, localized change of the film structure, and measurement of the thermal diffusivity of thin films.

Introduction

Transient heating of weakly absorbing thin films is important in many applications. Examples include pulse laser annealing of semiconductor thin films (Liu et al., 1982), damage of optical coatings (Wood, 1986), and optical recording (Terao et al., 1989). Depending on the wavelength of the heating laser pulse, the optical constants of thin films are often temperature dependent: a phenomenon known as thermally induced optical nonlinearity (or optothermal nonlinearity). Such nonlinearity provides a feedback to the propagation of light through absorption and subsequent heating of the optical media. It gives rise to the optical bistability phenomenon, where two stable states of reflection and transmission from a thin film system exist at the same incident radiant flux. Thermally induced optical bistability has attracted much attention because of its potential use in optical logic and computation (Jäger, 1989).

Some work has been done on the heat transfer in thin films subjected to laser heating. Bloom and Costich (1975) considered interference effects on the temperature distribution and stress in optical coatings. Burgener and Reedy (1982) derived the Green's function solution for heat conduction in a two-layer structure by considering the heat source at the surface. Calder and Sue (1982) studied steady-state heat conduction in multilayer structures. They approximated the absorption in the film by an exponentially decaying source and developed integral expressions for the temperature distribution for two and three layers. Abraham and Halley (1987) calculated temperature profiles in an absorbing film deposited on a nonabsorbing substrate, assuming uniform volumetric absorption in the film. The same group (Abraham and Ogilvy, 1987) also presented a linear steady-state heat conduction theory in an interference filter with an absorbing spacer. Baufay et al. (1987) investigated interference effects during laser-induced oxidation of copper. Bloisi and Vicari (1988) presented an analytical solution for the steady-state temperature field generated by the weak absorption of a Gaussian beam in an optically and thermally thin film bounded by two transparent plates. Flik et al. (1990) employed thin film optics in their simulation of the bolometric response of high-temperature superconducting thin films but neglected the temperature dependence of optical constants. Park et al. (1992) used matrix formulation in optical multilayer theory (Knittl, 1976) to model the probe laser response during a nanosecond pulse laser heating of amorphous silicon thin films. The films, however, were opaque to the pump pulse such that it was not necessary to consider the interference effects on temperature distributions.

Most of the previous work has assumed either surface absorption, an exponentially decaying source, or uniform absorption for the heat source distribution in the film. In fact, the absorption in a weakly absorbing thin film is highly nonuniform due to interference (Knittl, 1976). The uniform-volumetric-absorption assumption is justified when the laser pulse duration is much longer than the characteristic heat diffusion time. The exponentially decaying and the surface absorption assumptions are valid for highly absorbing films so that interference can be neglected. For the nanosecond and picosecond dynamic heating of weakly absorbing thin films, the effects of the localized absorption caused by interference need to be investigated. Also unexplored is how the thermally induced optical nonlinearity affects the transient temperature distribution and the optical response of thin films. Chen and Tien (1993a) studied internal reflection effects on transient photothermal reflectance and showed that the Fresnel formula is no longer applicable during picosecond to nanosecond heating processes. The applicability of Airy's formulae for the reflectance and transmittance of thin films during the dynamic heating process remains unanswered.

This work studies the temperature distribution and optical response of weakly absorbing thin films with thermally induced optical nonlinearity subjected to short-pulse laser heating. A transient one-dimensional model is built to examine the effects of the temperature-dependent optical constants and the nonuniform absorption in a thin film. The energy equation is discretized by the control volume method. The discretization also conveniently divides the film into an optical multilayer system, to which the matrix method in optical multilayer theory is applied to obtain the absorption in each layer. Sample calculations are performed for cadmium sulfide (CdS) thin films and a zinc selenide (ZnSe) interference filter. Both configurations are often used in optical bistability studies (Kazukauskas et al., 1990; Wherrett et al., 1990).

Contributed by the Heat Transfer Division and presented at the 28th National Heat Transfer Conference, San Diego, California, August 9–12, 1992. Manuscript received by the Heat Transfer Division January 1993; revision received June 1993. Keywords: Conduction, Conjugate Heat Transfer, Radiation Interactions. Associate Technical Editor: M. F. Modest.

Analysis

The thermal diffusivities of CdS and ZnSe are $\sim 1.0 \times 10^{-5}$ m^{2}s^{-1}. For a nanosecond pulse, the characteristic thermal diffusion length is ~ 0.1 μm. Since laser beam diameters are generally larger than 10 μm, the lateral heat conduction can be neglected during picosecond and nanosecond pulse heating processes. Along the laser beam, however, the characteristic length of the heat source distribution is one half of the *inside-the-film* wavelength due to interference (Knittl, 1976), which is about 0.1 μm for an argon laser. Apparently, heat diffusion can not be neglected in this direction. A one-dimensional analysis is thus appropriate. The one-dimensional heat conduction equation is

$$C\frac{\partial T}{\partial t}=k\frac{\partial^2 T}{\partial x^2}+I(t)S(t,x) \tag{1}$$

Here constant thermophysical properties are assumed. This assumption is based on the following considerations: (1) The temperature dependence of those properties of the studied materials are not available in the literature; (2) a best estimation based on similar materials shows that thermal diffusivity might decrease by 50 percent. This variation, if included, does not significantly affect the optical phenomena discussed in this work. The initial and boundary conditions for Eq. (1) are

$$t=0:\quad T(x,0)=T_o$$
$$x=0:\quad dT/dx=0;\quad x=h:\quad dT/dx=0 \tag{2}$$

An estimation of the energy loss due to radiation and convection to the ambient for a temperature rise of 100 K during one nanosecond is 10^{-9} J/cm^2, which is at least 5 orders of magnitude smaller than the energy absorbed in the films considered. This justifies the adiabatic boundary conditions given above. Later in this work, a ZnSe interference filter on a glass substrate will also be examined. The corresponding boundary conditions are the continuity of the temperature and heat flux at the film—substrate interface, and the constant ambient temperature deep inside the substrate.

The pump laser pulse usually has a Gaussian profile:

$$I(t)=2I_o \exp\left[-(t/t_p)^2\right]/\sqrt{\pi}t_p \tag{3}$$

where I_o is the total energy intensity in the pulse, and t_p is half the pulse width at e^{-1} peak intensity.

Because this work considers short laser pulses (30 ps for the ZnSe interference filter) and thin films, it is legitimate to ask whether the Fourier heat conduction equation is still valid. Possible mechanisms that may invalidate the Fourier heat conduction equation include (Özisik and Tzou, 1992; Tien and Chen, 1992): (1) the wave or hyperbolic heat conduction effects, (2) the nonequilibrium states of heat carriers, (3) the nonlocal energy transport in the case of a large temperature gradient. The clues to assess their importance are the heat-carrier mean free path and relaxation time. For heat conduction in CdS and ZnSe, the major heat carriers are phonons. The phonon mean free path, Λ, can be estimated from thermal diffusivity and sound velocity, $\Lambda \sim 3a/v$. The mean free path for ZnSe and CdS thus estimated is ~ 70 Å. The heat carrier scattering time τ $(=\Lambda/v)$ is 1.5 ps, which is an order of magnitude smaller than the laser pulse duration. Tzou gave a general criteria for the importance of wave behavior over diffusion (Özisik and Tzou, 1992),

$$\frac{\partial T}{\partial t} >> \frac{T_o C^2}{2a}\exp\left(\frac{C^2 t}{a}\right) \tag{4}$$

For the 30 ps heating of the ZnSe interference filter, $\partial T/\partial t \sim 10^{13}$ K s^{-1}. The right-hand side of the above expression at $t = 1$ ps is $\sim 10^{16}$ K s^{-1}. This suggests that wave effects can be neglected. During laser heating of ZnSe and CdS, electron and hole pairs are excited and heat is released during their recombination. If the recombination process takes longer than the laser pulse duration, these electrons and holes contribute to the energy transport and refractive index change. Bolger et al. (1992) performed picosecond pump-and-probe experiments on a ZnSe interference filter and observed that the thermal effects become dominant within 2 ~ 6 ps. They attributed the ultrafast recombination to the grain boundaries in the thermally evaporated ZnSe thin film. Based on this observation, the electronic contribution is not included in the current study. The comparison of the current simulation with experimental data in the subsequent study will show that such treatment may incur certain error during the initial heating stage. Another possible mechanism that may invalidate the Fourier heat conduction equation is the nonlocal energy transport (Mahan and Claro, 1988). Characterizing this phenomenon is the temperature penetration depth defined as $T_c/(dT/dx)$ (Tien and Chen, 1992), where the characteristic temperature T_c is taken as the maximum temperature difference in the film. For the ZnSe interference filter to be studied, this length is on the order of 500 Å, which is seven times longer that the heat carrier mean free path and thus suggests that the nonlocal energy transport effect can be neglected. It is noted, however, that this neglect may cause some error because the phonon mean free path is a value averaged over the whole phonon spectrum. The spectral phonon

Nomenclature

a = thermal diffusivity, m^{2}s^{-1}
A = nondimensional absorption distribution
c = speed of light, m s^{-1}
C = volumetric heat capacity, J m^{-3}K^{-1}
$\mathfrak{D}$ = nondimensional parameter
E = electric field, N C^{-1}
h = film thickness, μm
H = magnetic field, C m^{-1} s^{-1}
I = pump pulse intensity, W m^{-2}
j = $\sqrt{-1}$
k = thermal conductivity, W m^{-1} K^{-1}
m = matrix element
M = interference matrix
n = real part of optical constants (refractive index)
N = optical constant = $n + i\kappa$
r = complex reflection coefficient
R = reflectance at air-film interface
$\mathfrak{R}$ = reflectance of a homogeneous film
S = normalized heat source distribution, m^{-1}
t = time, s
T = temperature, K
$\mathfrak{T}$ = transmittance of a homogeneous film
x = coordinate perpendicular to film
y = admittance
α = absorption coefficient = $4\pi\kappa/\lambda$, cm^{-1}
δ = round trip phase delay = $4\pi nh/\lambda$
δ_o = phase change due to reflection
Δ = nondimensional parameter = $2\pi h/\lambda$
θ = nondimensional temperature
κ = imaginary part of optical constants
λ = wavelength in vacuum, μm
Λ = heat carrier mean free path
μ = free space permeability
ξ = nondimensional distance
τ = nondimensional time
ϕ = angle of incidence

Subscripts

k = kth optical layer
n = at film-substrate interface
o = initial state, at air-film interface
p = laser pulse

Superscript

$*$ = complex conjugate

mean free path can be much longer than 70 Å, as is indicated in the study of gallium arsenide crystals (Chen and Tien, 1993b).

Equation (1) is nondimensionalized for ease of data presentation,

$$\frac{\partial\theta}{\partial\tau}=\mathfrak{D}\frac{\partial^2\theta}{\partial^2\xi}+S_o \exp(-\tau^2)A(\tau, \xi) \tag{5}$$

with the initial and boundary conditions

$$\tau=0: \quad \theta=0$$

$$\xi=0: \quad d\theta/d\xi=0; \quad \xi=1: \quad d\theta/d\xi=0 \tag{6}$$

where the nondimensional parameters used in Eq. (5) are defined as

$$\begin{gathered}\theta=(T-T_o)/T_o, \quad \xi=x/h, \quad \tau=t/t_p, \quad \mathfrak{D}=t_p a/h^2, \\ A(\tau, \xi)=S(\tau, \xi)h/(1-\mathfrak{R}_o-\mathfrak{I}_o), \\ S_o=2(1-\mathfrak{R}_o-\mathfrak{I}_o)I_o/(\sqrt{\pi}CT_o h)\end{gathered} \tag{7}$$

and the subscript o denotes quantity at the initial film temperature. The initial reflectance and transmittance are given by Airy's formulae (Knittl, 1976). For an isolated film, they can be written as

$$\mathfrak{R}_o=\frac{R[(e^{-\alpha h/2}-e^{\alpha h/2})^2+4\sin^2(\delta/2)]}{(e^{\alpha h/2}-Re^{-\alpha h/2})^2+4R\sin^2(\delta_o+\delta/2)} \tag{8}$$

$$\mathfrak{I}_o=\frac{(1-R)^2}{(e^{\alpha h/2}-\mathrm{Re}^{-\alpha h/2})^2+4R\sin^2(\delta_o+\delta/2)} \tag{9}$$

where the reflectance at the air-film interface, R, can be obtained from the Fresnel formula.

The difficulty in the solution of Eq. (5) lies in how to determine the heat source distribution. For an optically homogeneous film, the electromagnetic field inside the film can be solved and the energy absorption at each location is then obtained by differentiating the Poynting vector (Knittl, 1976). For a nonlinear medium, however, the temperature field generates a nonuniform distribution of optical constants. In this case, the applicability of Airy's formulae, which are derived for films of uniform optical constants, is subject to question. Since analytical solutions for the electromagnetic field inside the film appear not feasible, numerical solutions are sought instead.

To find numerical solutions of the energy equation and the heat source distributions, the control volume method (Patankar, 1980) is advantageous because it can be easily incorporated with the matrix method in optical multilayer theory (Knittl, 1976). The discretization is shown in Fig. 1, where the dots locate the temperature nodes and the lines define the boundaries of each control volume. The lines also become the interfaces between two adjacent optical layers. The relation between the total electric field, E, and the total magnetic field, H, at the left-hand sides of the two interfaces of the kth layer is

$$\begin{pmatrix}E_{k-1}\\H_{k-1}\end{pmatrix}=M_k\begin{pmatrix}E_k\\H_k\end{pmatrix} \tag{10}$$

The interference matrix M_k is given by

$$M_k=\begin{pmatrix}\cos(\Delta N_k\xi_k\cos\phi_k) & j\sin(\Delta N_k\xi_k\cos\phi_k)/y_k\\ jy_k\sin(\Delta N_k\xi_k\cos\phi_k) & \cos(\Delta N_k\xi_k\cos\phi_k)\end{pmatrix} \tag{11}$$

where ξ_k is nondimensional thickness. The admittance at the kth interface, y_k, is defined as

$$y_k=H_k/E_k=\begin{cases}-N_k\cos\phi_k/(\mu c) & \text{for TE}\\ N_k/(\cos\phi_k\mu c) & \text{for TM}\end{cases} \tag{12}$$

The above matrix formulation assumes a continuous incident wave so that there are an infinite number of reflections inside the film. The distance that light travels inside the film during 1 ps is of the order of 0.1 mm. For a 10 ps pulse and a film 20 μm thick, there are about 25 reflections inside the film, large enough for the matrix formulation to be valid.

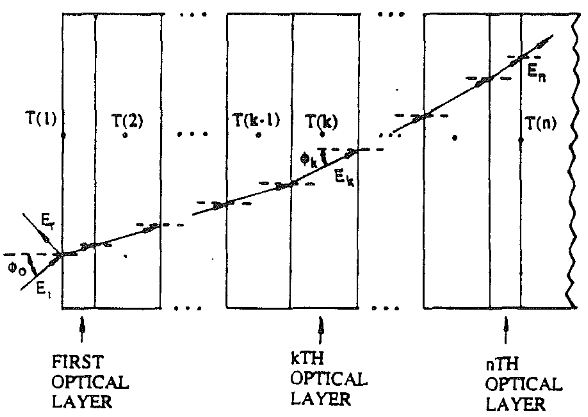

Fig. 1 Discretization and the optical multilayer system

From Eqs. (10)–(12), the complex reflection coefficient of the multilayer system can be obtained,

$$r=\frac{m_{11}-y_o^{-1}y_n m_{22}+y_n m_{12}-y_o^{-1}m_{21}}{m_{11}+y_o^{-1}y_n m_{22}+y_n m_{12}+y_o^{-1}m_{21}} \tag{13}$$

where m_{ij} are the matrix elements of the products of the interference matrices $M = \Pi M_k$.

With r known, E_o and H_o can be determined, and E_k and H_k are then obtained by inverting Eq. (10), beginning from the first layer. The absorbed energy in the kth layer is given by

$$S_k=[\mathrm{Re}(E_{k-1}H_{k-1}^*-E_kH_k^*)]/[\mathrm{Re}(E_iH_i^*)h\Delta\xi_k] \tag{14}$$

The discretization proceeds by integrating Eq. (5) for each control volume and time interval. A fully implicit scheme is employed to ensure numerical stability. The algebraic equations are solved iteratively with the temperature-dependent source distribution. Smaller control volume sizes are used near the two interfaces. The computation starts at $t = 2 \sim 3t_p$ before the arrival of the pulse center. The temporal increment is taken as $\Delta\tau \sim 10^{-2}$–10^{-4}. The total number of control volumes is about 1000–2000, and converging criteria of 10^{-6}–10^{-7} °C are used for the maximum absolute temperature difference between two successive iterations. No increase of accuracy is observed by further decreasing of control volume sizes and time steps. The numerical accuracy of the scheme is tested by studying the case of a semi-infinite medium with constant optical properties subjected to a step radiation heating. The analytical solution for such a problem is given by Carslaw and Jaeger (1959). The relative accuracy between the numerical and the analytical results is 0.005 percent.

Results and Discussion

Calculations are performed for CdS thin films and a ZnSe interference filter. Both materials are widely used in thermally originated optical bistability studies.

CdS Thin Films. The incident laser wavelength is taken as 514 nm, corresponding to an argon laser. Lambsdorff et al. (1986) measured the temperature dependence of the absorption coefficient for the optical bistability experiments at the argon wavelength. The calculation terminates when temperature rises above 400 K since temperature-dependent optical constant data are available only below it. The thermal diffusivity and specific heat are taken to be 10^{-5} m^{2}s^{-1} (Thoma et al., 1991) and 347.1 Jkg^{-1}K^{-1} (Touloukian, 1970), respectively. The temperature dependence of the real part of the optical constants is taken as

$$n=2.62+2.5\times10^{-4}(T-300) \tag{15}$$

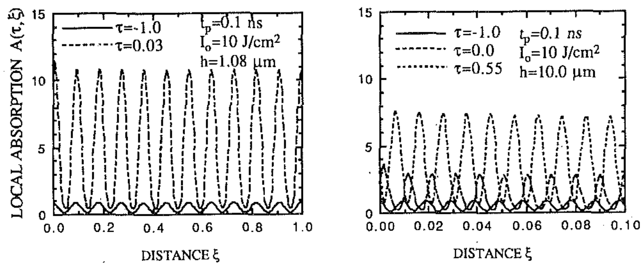

(a) (b)

Fig. 2 Absorption distributions in two isolated CdS thin films

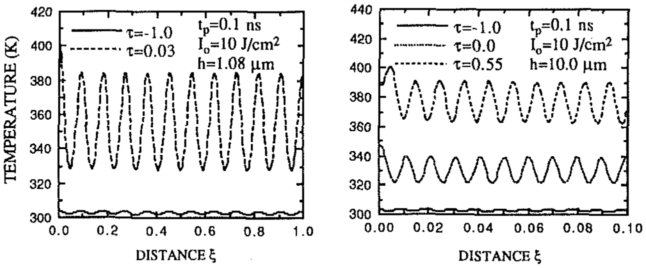

(a) (b)

Fig. 3 Temperature distributions in two isolated CdS thin films

where 2.62 is derived from the requirement that the normal reflectance at the air–CdS interface is 0.2 (Gutowski et al., 1989). It is close to the interpolated value of 2.72 (Palik, 1991). The temperature coefficient of 2.5×10^{-4} was used by Thoma et al. (1991). The temperature dependence of the imaginary part of the optical constants, for which no simple relation can be found, is matched with the measurement of Lambsdorff et al. (1986) using polynomials (with a 5 percent relative error) for the ease of numerical implement. The initial temperature is set at 300 K. Normal incidence is considered for all the CdS thin films.

Figures 2(*a* and *b*) show the local heat source distribution $A(\tau, \xi)$ in isolated CdS films of different thickness at various incidence intensity and pulse duration. Since the film is weakly absorbing, the heat source distribution inside the film is almost a periodic function of location due to interference effect, with the period equaling one half of the *inside-the-film* wavelength. The distance between the absorption peak and the valley is then one quarter of the wavelength, which is 0.049 μm at room temperature. If the optical constants are temperature independent, the heat source distribution should be time independent. Because of the temperature dependence of optical constants, the absorption increases with time. The increment, however, is not uniform along the film but centered at locations where constructive interference occurs. For a film with thickness around 1 μm (Fig. 2*a*), the absorption peaks are relatively fixed to their original positions. As the films become thicker, the change of the real part of the optical constants introduces an appreciable phase shift so that the absorption peaks also change their positions with time, as seen in Fig. 2(*b*).

The temperature distributions in Figs. 3(*a* and *b*) are readily explainable based on the understanding of the internal absorption distributions. When the films are thin, as in Fig. 3(*a*), heat conduction reduces the sharpness of the absorption pictures. Yet large local temperature differences are still generated in the film. Such a large temperature difference offers the potential for localized structure change of the film, through either melting or nonmelting processes. For the 10 μm film (Fig. 3(*b*), since the absorption peaks are constantly moving, the local temperature difference is smeared out. Notice that in Figs. 3(*a* and *b*), the peak temperature near the front surface rises higher than other peaks. This is a combined effect of the temperature dependence of refractive index and the adiabatic boundary conditions. The temperature dependence of refractive index changes the optical path length and shifts the absorption peak at the front surface into the media. Heat generated between this peak and the front surface cannot transfer to its adjacent absorption valley because of the energy barrier at the peak, nor can it be dissipated to the ambient due to the adiabatic boundary condition. This phenomenon is not raised at the back of the films because heat generated near the boundary can diffuse to its adjacent valley.

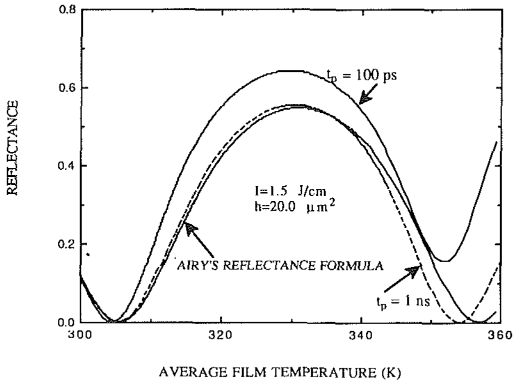

Fig. 4 Reflectance as a function of average film temperature for a CdS film

Figure 4 illustrates the validity of Airy's formulae for the fast heating processes. To use Airy's formulae, the optical constants are taken at the average film temperature. It is clear from the figure that Airy's formulae are no longer applicable for sub-nanosecond pulses. The real peak reflectance is higher than that obtained from Airy's reflectance formula [Eq. (8)]. This can be explained by the optical multilayer theory. It is a common practice in optics to use high-and-low refractive index quarter-wavelength film stacks to obtain high reflectance (Knittl, 1976), as will be seen in the following treatment for interference filter. In the current case, the temperature peak and valley span just a quarter wavelength. The temperature-induced change of the optical constants effectively generates a high-and-low quarter-wavelength stack, thus yielding a higher reflectance than calculated using homogeneous-medium-based Airy's reflectance formula. Furthermore, the response is asymmetric during fast heating. Several factors are responsible for this: First, for films as thick as 20 μm, the absorption-caused decay of the field intensity becomes appreciable, so that the forward and the backward fields at the front surface do not completely cancel each other; second, the temperature peak near the surface is different from other locations due to the adiabatic condition, which causes an asymmetry of the optical constant distribution. For the 1 ns pulse, the peak reflectance does not differ from that obtained from Airy's formula because the temperature variation in the film is not large for a 20 μm film. This slight variation, however, changes the optical path length such that the average film temperature corresponding to the minimum reflectance is lower compared with a film of uniform temperature.

Although many optical bistability experiments were performed on isolated films, a more common arrangement is the film on a substrate. The substrate influences the temperature distribution in a film in two ways. One way is to change the total absorbed energy level and the local absorption distribution. Since the reflectance at the film–substrate interface is different from that at the film–air interface, complete destructive interference does not occur in the film. The other way is to reduce the film temperature by conducting heat away from the film. Calculations were performed for the CdS films on a sapphire substrate. The results agree with the general discussions above. Because of the substrate, the absorption is slightly more uniform and the temperature variation is not as sharp

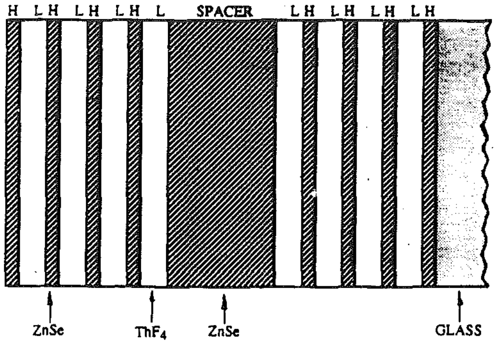

Fig. 5 The ZnSe interference filter

as that in an isolated film. During the heating period, however, only the temperature spike adjacent to the substrate is affected, while the other spikes barely feel the existence of the substrate. This means that the presence of the substrate will not have significant effects in the short heating period if the film contains several quarter wavelengths. More substrate effects will be seen in the following discussion of the ZnSe interference filter.

ZnSe Interference Filter. The ZnSe interference filter is similar to that used by Wherrett et al. (1990) in the optical bistability studies. Figure 5 shows the structure of the interference filter. It consists of a ZnSe spacer layer surrounded by four high-and-low refractive-index layer pairs on each side. The high refractive index material is again ZnSe and the low index ThF$_4$. The filter is on a glass substrate. Table 1 lists the structural and physical properties used in the following simulation. The thermal physical properties of ZnSe and ThF$_4$ are taken to be the same based on an estimation of Bloom and Costich (1975). The light source is a frequency-doubled Nd-YAG pulse laser at 532 nm wavelength. At this wavelength, the filter has a transmission peak at an incidence angle of 39.2 deg. The temperature coefficient of the refractive index is taken as 1.0×10^{-4} instead of 1.5×10^{-4} as recommended by Wherrett et al. (1990), with the purpose of matching the experimentally measured transmittance change. The fundamental argument for the use of this lower value is that at the initial heating stage, light-generated electrons will cause a change in refractive index opposite in sign to the change brought about by the temperature rise. The absorption coefficient increases by a factor of 2 during the heating due to two-photon and free carrier absorption (Wherrett et al., 1990). This increase is not included in the current treatment because no detailed data are available. Kummrow and Eichler (1989) measured the absorption coefficient of ZnSe$_{1.36}$ as a function of temperature at 514 nm and showed that it obeys a generalized Urbach rule. Their results, however, are not applicable to the current calculation because of different Se composition. A function relating the absorption coefficient and temperature, similar to that used by Kummrow and Eichler (1989), was first employed in the calculation, but further calculation showed that it does not change the basic features in the calculated optical response. This is because the filter has a high finesse and is very sensitive to the change in the refractive index when the transmission is close to the peak. Based on these considerations, the results presented below used a constant absorption coefficient of 1000 cm^{-1} (Wherrett et al., 1990). The incident angle was set at 39.2 deg.

Table 1 Parameters for the ZnSe interference filter

	ZnSe	ThF$_4$	Glass
Thickness (nm)	509 (Spacer) 69 (High)	101.5	~ 10^6
Refractive Index	2.55	1.55	1.52
Absorption Coefficient·(cm^{-1})	1000	0	0
Thermal Diffusivity (ms^{-2})	$5.7\text{x}10^{-6}$	$5.7\text{x}10^{-6}$	$7.8\text{x}10^{-7}$
Thermal Conductivity (W m^{-1}K^{-1})	19.0	19.0	1.3
Temperature Coefficient of Refractive Index (K^{-1})	$1.0\text{x}10^{-4}$	0	0

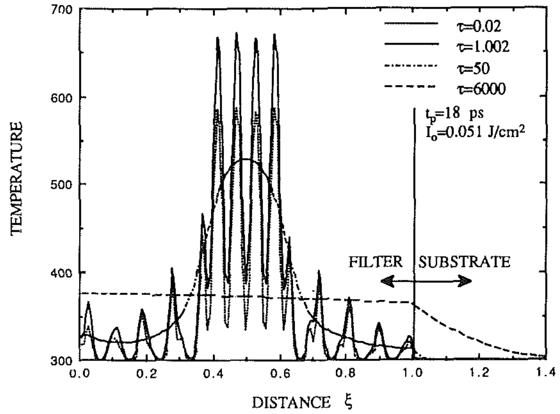

Fig. 6 Temperature distributions in the ZnSe interference filter

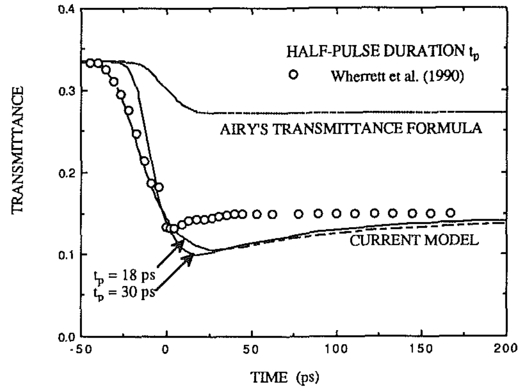

Fig. 7 Comparison of the Airy formula and the current model with experiment

The temperature distributions in the filter during the heating and relaxation periods are shown in Fig. 6. During the heating period, they are very similar to those in the single CdS film except that for a ZnSe filter the absorption is centered in the spacer layer and is much weaker in the stack layers. With time advancement, the thermal diffusion smears out the temperature spikes in the filter, but the temperature is still nonuniformly distributed. The relaxation to a nearly uniform temperature distribution takes a much longer time (90 ns). Wherrett et al. (1990) estimated that the average film temperature raises about 200 K. From the figure, it can be seen that the local temperature rise can be as high as 400 K even though the average temperature rise agrees with their estimation.

Figure 7 compares the transmittance of the filter calculated from the current model and the Airy formula with the experimental data of Wherrett et al. (1990). Results for two pulse durations are presented. The half pulse duration, $t_p = 18$ ps, is indicated by Wherrett et al. in their experiment, while it is found that $t_p = 30$ ps matches better with experimental data at the initial heating stage. The curve marked by the Airy formula is calculated for $t_p = 18$ ps and it differs from the $t_p = 30$ ps case slightly at the initial heating stage. Clearly, the current model compares favorably with the experiment while the Airy formula cannot predict the measurement. This figure also shows that the transient switching contrast in a bistable filter (the ratio of transmittance before and after the pulse) can be much larger than that predicted by the Airy transmittance formula. The dip observed in both the current model and the experiment is caused by the temperature-spike-generated high-and-low refractive index stack in the spacer region. The temporal span of this dip is a measure of the time taken for the temperature spikes to diffuse into a smoother temperature distribution in Fig. 6. The calculated relaxation time is ~ 90 ps while the experimentally measured one is ~ 50 ps. The electronic effects, which induce a refractive index change opposite in sign to thermal effects, may be the reason for the faster relaxation. The calculated transmittance after 90 ps gradually increases and approaches the value given by Airy's formula. Besides the electronic effects, other factors that may contribute to the discrepancy between the model and the experiments are: (1) Exact structure of the filter is not known, (2) the optical absorption as a function of temperature is not available, (3) thermophysical properties of thin films may differ from their corresponding bulk values, and (4) nonlocal energy transport may affect the temperature distribution. These effects will be studied in further investigations.

The relaxation process of the uneven temperature distribution inside the thin films offers a potential of measuring the thermal diffusivity of weakly absorbing thermally induced optical nonlinear thin films. It is known that the thermal conductivities of thin films can be 1 ~ 2 orders of magnitude lower than their corresponding bulk values. Paddock and Eesley (1986) used a picosecond pulse laser to measure thermal diffusivity of metallic thin film, but the method has not been used for dielectric thin films. The current results show that even though the absorption is volumetric, the temperature distributions are highly nonuniform during the heating period. Such nonuniformity causes a deviation of the reflectance or the transmittance signal from Airy's formulae. Thermal diffusivity of the film is thus detectable by measuring the temporal change of the optical signal. The optical properties of the films, however, must be precisely known before the thermal physical properties can be derived.

Conclusions

This work presents a study of the temperature and optical response of weakly absorbing thin films with thermally induced optical nonlinearity during picosecond to nanosecond pulsed laser heating. Both CdS thin films and a ZnSe interference filter are considered. The computational results reveal that the transient temperature distribution can be highly nonuniform within the films, which yields the Airy formulae inapplicable for calculating their reflectance and transmittance. Results from the model compare favorably with available experimental data.

The current work suggests that the thermal diffusivity of weakly absorbing thin films can be measured from its optical response. Also, the highly nonuniform temperature distribution inside a micron-thick film may allow for local structure change inside the film, through either a melting or nonmelting process. The optical response demonstrates the importance of considering the local temperature field in modeling transient thermally induced optically bistable processes.

Acknowledgments

The authors thank Professor B. S. Wherrett of Heriot-Watt University, United Kingdom, for kindly providing the details of his experiments and a preprint of his paper. They also gratefully acknowledge the financial support from the U.S. Department of Energy, and the K. C. Wong Education Foundation in Hong Kong.

References

Abraham, E., and Halley, J. M., 1987, "Some Calculations of Temperature Profiles in Thin Films With Laser Heating," *Applied Physics A*, Vol. 42, pp. 279–285.

Abraham, E., and Ogilvy, I. J. M., 1987, "Heat Flow in Interference Filters," *Applied Physics B*, Vol. 42, pp. 31–34.

Baufay, L., Houle, F. A., and Wilson, R. J., 1987, "Optical Self-Regulation During Laser-Induced Oxidation of Copper," *Journal of Applied Physics*, Vol. 61, pp. 4640–4651.

Bloisi, F., and Vicari, L., 1988, "Laser Induced Thermal Profiles in Thermally and Optically Thin Films," *Applied Physics B*, Vol. 47, pp. 67–69.

Bloom, A. L., and Costich, V. R., 1975, "5.5 Design for High Power Resistance," in: NBS Special Publication, Vol. 435, pp. 248–253.

Bolger, J., Kar, A. K., and Wherrett, B. S., 1992, "Refractive Optical Nonlinearities in a Thin Film ZnSe Interference Filter," *Journal of Optical Materials*, Vol. 1, pp. 71–74.

Burgener, M. L., and Reedy, R. E., 1982, "Temperature Distributions Produced in a Two-Layer Structure by a Scanning cw Laser or Electron Beam," *Journal of Applied Physics*, Vol. 53, pp. 4357–4363.

Calder, I. D., and Sue, R., 1982, "Modeling of cw Laser Annealing of Multilayer Structures," *Journal of Applied Physics*, Vol. 53, pp. 7545–7550.

Carslaw, H. S., and Jaeger, J. C., 1959, *Conduction of Heat in Solids*, 2nd ed., Oxford, UK.

Chen, G., and Tien, C. L., 1993a, "Internal Reflection Effects on Transient Photothermal Reflectance," *Journal of Applied Physics*, Vol. 73, pp. 3461–3466.

Chen, G., and Tien, C. L., 1993b, "Thermal Conductivity of Quantum Well Structures," AIAA *Journal of Thermophysics and Heat Transfer*, Vol. 7, pp. 311–318.

Flik, M. I., Phelan, P. E., and Tien, C. L., 1990, "Thermal Model for the Bolometric Response of High T_c Superconducting Films to Optical Pulses," *Cryogenics*, Vol. 30, pp. 1118–1128.

Gutowski, J., Hollandt, J., and Broser, I., 1989, "Thin CdS Platelets—A Model Case for the Study and Optimization of Thermally Induced Absorptive and Dispersive Optical Bistability," *Zeitschrift für Physik B*, Vol. 76, pp. 547–557.

Jäger, D., 1989, "Optical Bistability: Semiconductor Devices for Digital Optical Signal Processing," SPIE Vol. 1127, *Nonlinear Optical Materials II*.

Kazukauskas, V., Grohs, J., Klingshirn, C., Wingen, G., and Jäger, D., 1990, "Dynamics of Optical and Electrooptical Switching in Photo-thermal Bistable CdS Crystals," *Zeitschrift für Physik B*, Vol. 79, pp. 149–157.

Knittl, Z., 1976, *Optics of Thin Films*, Wiley, London, United Kingdom.

Kummrow, A., and Eichler, H. J., 1989, "Absorptive Bistability in Evaporated ZnSe$_x$ Thin Films," *Applied Physics B*, Vol. 49, pp. 497–502.

Lambsdorff, M., Dörnfeld, C., and Klingshirn, C., 1986, "Optical Bistability in Semiconductors Induced by Thermal Effects," *Zeitschrift für Physik B*, Vol. 64, pp. 409–416.

Liu, J. M., Kurz, H., and Bloembergen, N., 1982, "Picosecond Time-Resolved Plasma and Temperature-Induced Change of Reflectivity in Silicon," *Applied Physics Letters*, Vol. 41, pp. 643–646.

Mahan, G. D., and Claro, F., 1988, "Nonlocal Theory of Thermal Conductivity," *Physical Review B*, Vol. 38, pp. 1963–1969.

Özisik, M. N., and Tzou, D. Y., 1992, "On the Wave Theory in Heat Conduction," ASME HTD-Vol. 227, pp. 13–27.

Paddock, C. A., and Eesley, G., 1986, "Transient Thermoreflectance From Thin Metal Films," *Journal of Applied Physics*, Vol. 60, pp. 285–290.

Palik, E. D., ed., 1991, *Handbook of Optical Constants of Solids II*, Academic Press, Boston, MA.

Park, H. K., Xu, X., Grigoropoulos, C. P., Do, N., Klees, L., Leung, P. T., and Tam, A. C., 1992, "Temporal Profile of Optical Transmission Probe for Pulsed-Laser Heating of Amorphous Silicon Films," *Applied Physics Letters*, Vol. 61, pp. 749–751.

Patankar, S. V., 1980, *Numerical Heat Transfer and Fluid Flow*, Hemisphere, Washington, DC.

Terao, M., Miyauchi, Y., Andoo, K., Yasuoka, H., and Tamura, R., 1989, "Progress of Phase-Change Single-Beam Overwrite Technology," SPIE Vol. 1078, *Optical Data Storage Topical Meeting*, pp. 2–10.

Thoma, M. L., Weber, C., and Klingshrin, C., 1991, "Spatial-Temporal Structure Formation and Self-Diffraction in CdS Using Laser-Induced Thermal Grating," *Applied Physics A*, Vol. 53, pp. 255–260.

Tien, C. L., and Chen, G., 1992, "Challenges in Microscale Radiative and Conductive Heat Transfer," ASME HTD—Vol. 227, pp. 1–12.

Touloukian, Y. S., Powell, R. W., Ho, C. Y., and Klemens, P. G., eds., 1970, *Thermal Physical Properties of Matter*, Vol. 5, pp. 650–652, IFI/Plenum.

Wherrett, B. S., Darzi, A. K., Chow, Y. T., McGuckin, B. T., and Van Stryland, E. W., 1990, "Ultrafast Thermal Refractive Nonlinearity in Bistable Interference Filters," *Journal of Optical Society of America B*, Vol. 7, pp. 215–219.

Wood, R. M., 1986, *Laser Damage in Optical Materials*, IOP Publishing Ltd., Adam Hilger.

K. E. Goodson[1]

M. I. Flik

Department of Mechanical Engineering.

L. T. Su

D. A. Antoniadis

Department of Electrical Engineering and
Computer Science.

Massachusetts Institute of Technology,
Cambridge, MA 02139

Prediction and Measurement of the Thermal Conductivity of Amorphous Dielectric Layers

Thermal conduction in amorphous dielectric layers affects the performance and reliability of electronic circuits. This work analyzes the influence of boundary scattering on the effective thermal conductivity for conduction normal to amorphous silicon dioxide layers, $k_{n,eff}$. At 10 K, the predictions agree well with previously reported data for deposited layers, which show a strong reduction of $k_{n,eff}$ compared to the bulk conductivity, k_{bulk}. A steady-state technique measures $k_{n,eff}$ near room temperature of silicon dioxide layers fabricated using oxygen-ion implantation (SIMOX). The predictions and the SIMOX data, which agree closely with k_{bulk}, show that boundary scattering is not important at room temperature. Lower than bulk conductivities of silicon dioxide layers measured elsewhere near room temperature must be caused by interfacial layers or differences in microstructure or stoichiometry.

1 Introduction

The performance of transistors and the reliability of interconnects are affected by temperature fields in electronic circuits. Layers of amorphous dielectric materials electrically insulate circuit components and protect them from corrosion. These layers have very low thermal conductivities, near 1 $\mathrm{Wm^{-1}K^{-1}}$ at room temperature. Conduction normal to the layers can be an important obstacle to the cooling of devices and interconnects. Energy dissipated in aluminum interconnects in conventional integrated circuits, for example, must travel through an amorphous silicon dioxide layer between 0.5 and 1 μm thick to reach the substrate heat sink. In silicon-on-insulator (SOI) circuits, devices are separated from the substrate by a silicon dioxide layer from 0.3 to 1.0 μm thick (Goodson and Flik, 1992; Goodson et al., 1993b). To predict the mean time to failure of an interconnect or the drain current of a SOI field-effect transistor, both of which depend on temperature, a circuit designer needs to know the thermal resistance for conduction normal to amorphous dielectric layers. Most experimental techniques cannot separate the internal thermal resistance for conduction normal to a layer from the thermal resistances of its boundaries. They measure the effective thermal conductivity normal to a layer, $k_{n,\mathrm{eff}}$, which is defined as the layer thickness divided by the total thermal resistance of the layer *and its boundaries*.

Data for the thermal conductivity of bulk amorphous dielectrics, k_{bulk}, vary little among different samples of the same material (Berman, 1976). In contrast, data for $k_{n,\mathrm{eff}}$ of amorphous dielectric layers vary substantially and can be an order of magnitude less than k_{bulk}. Figure 1 compares the data of Lambropoulos et al. (1989), Brotzen et al. (1992), and Schafft et al. (1989) for $k_{n,\mathrm{eff}}$ of silicon dioxide layers fabricated using several techniques. The layers of Schafft et al. (1989) contained 4 mass percent of phosphorus, whose influence on the conductivity has not been assessed. Although different experimental techniques were used, often yielding unknown or very large uncertainties, the data indicate that the effective conductivity decreases with decreasing layer thickness and depends on the fabrication technique. This is consistent with earlier data for amorphous dielectric layers (Guenther and McIver, 1988).

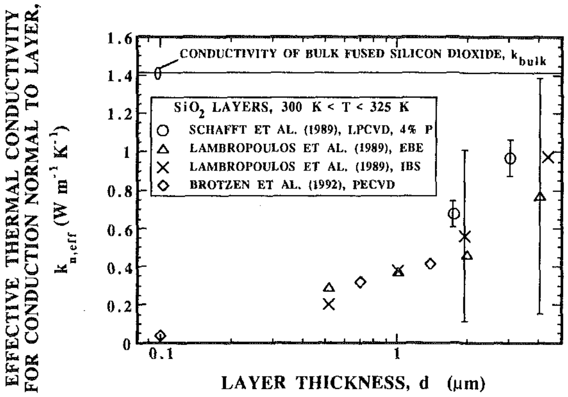

Fig. 1 Previous data for the effective thermal conductivity for conduction normal to silicon dioxide layers, $k_{n,\mathrm{eff}}$. LPCVD = low-pressure chemical-vapor deposition. EBE = electron-beam evaporation. IBS = ion-beam sputtering. PECVD = plasma-enhanced chemical-vapor deposition. The layers of Schafft et al. (1989) contained 4 mass percent of phosphorus atoms. The bulk conductivity k_{bulk} was measured by Sugawara (1969).

The difference between $k_{n,\mathrm{eff}}$ and k_{bulk} has been attributed to three phenomena: (*a*) Schafft et al. (1989) indicated that the boundary scattering of phonons is responsible. (*b*) A microstructure or stoichiometry in the layers different than in the bulk could make $k_{n,\mathrm{eff}}$ smaller than k_{bulk}. The conductivity $k_{n,\mathrm{eff}}$ would be thickness dependent if the microstructure or stoichiometry changed near the layer boundaries. (*c*) A thermal boundary resistance would cause $k_{n,\mathrm{eff}}$ to decrease with decreasing layer thickness. This would be indistinguishable from the highly resistive interfacial layers proposed by Brotzen et al. (1992). The present work makes progress toward resolving this puzzle by predicting the effective conductivity normal to amorphous silicon dioxide layers considering (*a*) phonon-boundary scattering, and by measuring the effective conductivity of layers with varying thicknesses with a known accuracy. The data and predictions yield conclusions about the importance of (*b*) and (*c*).

Thermal conduction in bulk amorphous solids was reviewed by Zaitlin and Anderson (1975), Berman (1976), and Freeman and Anderson (1986b). Figure 2 shows the difference between the periodic structure of a crystal and the random network of atoms in an amorphous material. Phonons of wavelength small compared to the lattice constant of the material in crystalline

---

[1] Present address: Daimler Benz AG, Forschung und Technik (F1W/FF), 89013 Ulm, Federal Republic of Germany.

Contributed by the Heat Transfer Division for publication in the JOURNAL OF HEAT TRANSFER. Manuscript received by the Heat Transfer Division January 1993; revision received July 1993. Keywords: Conduction, Electronic Equipment, Measurement Techniques. Associate Technical Editor: R. Viskanta.

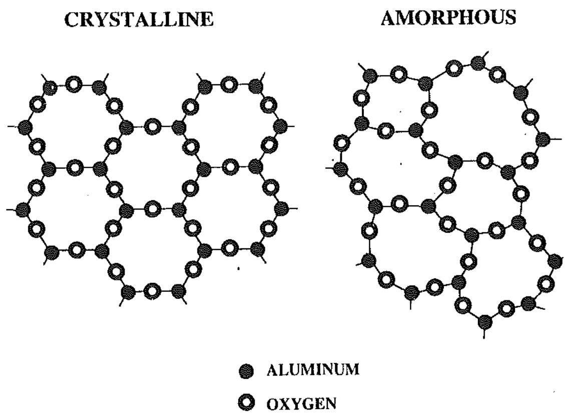

Fig. 2 Spatial configurations of atoms in two-dimensional analogs of crystalline and amorphous Al_2O_3 *(after Zachariasen, 1932)*

form are scattered strongly by the disorder and have mean free paths of a few angstroms (Kittel, 1949, 1986). Phonons of wavelength large compared to this lengthscale have mean free paths that increase rapidly with the wavelength. This is analogous to the Rayleigh scattering of radiation on particles small compared to the radiation wavelength, where the photon mean free path is proportional to the fourth power of the wavelength (Bohren and Huffman, 1983). The scattering of the long-wavelength phonons on the boundaries of a layer can strongly reduce $k_{n,\mathrm{eff}}$ at cryogenic temperatures, where these phonons carry much of the thermal energy.

Many studies of phonon-boundary scattering in amorphous materials were for low temperatures. The analysis and data of Matsumoto et al. (1977) showed that the boundary scattering of long-wavelength phonons strongly reduces the effective thermal conductivity normal to epoxy layers with thicknesses between 1 and 10 μm below 10 K. But Zaitlin et al. (1975) observed no effect of boundary scattering on the thermal conductivity along 2.9 to 71 μm thick mylar and glass layers below 10 K. This was attributed to the specular reflection of phonons at the layer boundaries, which reduces conduction normal to a layer but does not affect conduction along the layer. Zhu and Anderson (1990) measured the thermal conductivities of epoxies filled with epoxy particles below 9 K, and concluded that phonons had an increased rate of scattering near the particle boundaries, analogous to hypothesis (*c*) given here. Love and Anderson (1990) developed a function for the dependence of the phonon mean free path on the phonon frequency. They predicted that phonons with mean free paths longer than about 10 Å contribute significantly to thermal conduction only at temperatures below 50 K. While they did not consider conduction in layers, their calculations indicate that phonon-boundary scattering is unimportant in silicon dioxide layers above 50 K. This cannot be confirmed by the room-temperature data shown in Fig. 1, which all show a strong reduction of $k_{n,\mathrm{eff}}$ with respect to k_{bulk}.

The present work predicts the influence of boundary scattering on the effective conductivity normal to silicon-dioxide layers above 10 K using a frequency dependence of the phonon mean free path similar to that of Love and Anderson (1990). The effective conductivity considering boundary scattering is calculated using the approximate relations of Matsumoto et al. (1977) and Chen and Tien (1992). The technique of Swartz and Pohl (1987) is adapted to measure $k_{n,\mathrm{eff}}$ near room temperature in silicon dioxide layers fabricated using oxygen-ion implantation (SIMOX), and a general expression for the uncertainty of the technique is developed.

2 Effective Conductivity Considering Boundary Scattering

The kinetic formula for the conductivity of dielectrics is (Ziman, 1960),

$$k=\frac{1}{3}C_s v_s \Lambda_s \tag{1}$$

where C_s is the phonon specific heat per unit volume and v_s is the speed of sound. Equation (1) defines the phonon mean free path Λ_s accounting for phonons *of all frequencies*. The *frequency-dependent* phonon mean free path, Λ_ω, is the mean distance phonons of a given frequency, or energy, travel between collisions. The use of the phonon mean free path Λ_s neglects the energy dependence of the carrier free paths. This approximation has been used with reasonable success to analyze electron-boundary scattering (Tien et al., 1969; Flik and Tien, 1990; Kumar and Vradis, 1991), since electrons contributing to net transport all possess nearly the same energy. But in dielectrics, where phonons of energies varying by several orders of magnitude contribute to conduction, Λ_s must be used with care. This was demonstrated by Savvides and Goldsmid (1972), who observed boundary-scattering effects on the phonon conductivity in silicon crystals of dimensions orders of magnitude larger than Λ_s. The crystals had been irradiated

Nomenclature

a = dimension of scattering site, m
B = boundary-scattering parameter, Eqs. (4) and (5)
C_s = *phonon specific heat at* constant volume per unit volume, $\mathrm{Jm^{-3}K^{-1}}$
$C_s(x, T)$ = Debye specific heat function, defined by Eq. (3), $\mathrm{Jm^{-3}K^{-1}}$
d = layer thickness, m
d_{sub} = substrate thickness, m
E_0 = fitting parameter for Λ_{SR}, J
h_P = Planck's constant divided by $2\pi = 1.05\times10^{-34}$Js
I = current, A
i = integer in summations, Eqs. (12) and (13)
k_B = Boltzmann constant $=1.38\times10^{-23}\mathrm{JK^{-1}}$
k_{bulk} = thermal conductivity measured in bulk samples, $\mathrm{Wm^{-1}K^{-1}}$
$k_{n,\mathrm{eff}}$ = effective thermal conductivity for conduction normal to layer, $\mathrm{Wm^{-1}K^{-1}}$
k_{sub} = substrate thermal conductivity, $\mathrm{Wm^{-1}K^{-1}}$
L = length, m
N_a = atomic number density, $\mathrm{m^{-3}}$
N_D = number density of scattering sites, $\mathrm{m^{-3}}$
Q = heat flow, W
q = argument of relative uncertainty function $=U(q)$
R_T = thermal resistance, $\mathrm{m^2KW^{-1}}$
S_D = fitting parameter for Λ_D, $\mathrm{m\,rad^4s^{-4}}$
S_{SR} = fitting parameter for Λ_{SR}
T = temperature, K
ΔT = temperature difference, K
T^* = k_BT/E_0 = dimensionless temperature
T_B = average substrate temperature below bridge A, K
T_0 = substrate or chuck temperature, K
$U(q)$ = relative uncertainty in parameter q
V = voltage difference along bridge, V
v_s = average speed of sound, $\mathrm{ms^{-1}}$
W = half width of substrate, m
w = width, m
x = dimension along substrate, m

with neutrons, introducing point defects that cause the Rayleigh scattering of phonons.

Equation (1) can be written as an integral over all phonon angular frequencies ω using the Debye model for phonons (Berman, 1976)

$$k=\frac{1}{3}v_s\int_0^{\theta/T}C_s[x_\omega,\ T]\Lambda_\omega[x_\omega,\ T]dx_\omega \qquad (2)$$

where the Debye specific heat function is

$$C_s[x_\omega,\ T]=9N_ak_B\left(\frac{T}{\theta}\right)^3\frac{(x_\omega)^4\exp(x_\omega)}{[\exp(x_\omega)-1]^2} \qquad (3)$$

The dimensionless phonon frequency is $\chi_\omega=h_p\omega/k_\beta T$. The Debye model constants for amorphous silicon dioxide are $\theta=492$ K, $v_s=4100$ ms^{-1}, and $N_a=6.62\times10^{28}$ m^{-3} (Stephens, 1973). The Debye angular frequency is $\omega_D=k_B\theta/h_P=6.441\times10^{13}$ rads^{-1}.

If the material is bulk, i.e., has no boundaries, then Λ_ω is the bulk mean free path, $\Lambda_{\omega,\text{bulk}}$. Callaway (1959) and Holland (1963) accounted for boundary scattering using a frequency-independent mean free bath for boundary scattering, $\Lambda_{s,b}=Bd$, where B is a dimensionless constant not too far from unity and d is the smallest specimen dimension, e.g., the layer thickness. Matthiessen's rule (Ziman, 1960) yields

$$\frac{1}{\Lambda_\omega}=\frac{1}{\Lambda_{\omega,\text{bulk}}}+\frac{1}{\Lambda_{s,b}}=\frac{1}{\Lambda_{\omega,\text{bulk}}}+\frac{1}{Bd} \qquad (4)$$

Matsumoto et al. (1977) used Eqs. (2)–(4) to calculate $k_{n,\text{eff}}$ for epoxy layers below 10 K. They assumed a frequency and temperature dependence for $\Lambda_{\omega,\text{bulk}}$ and fitted bulk epoxy thermal conductivity data using $d=\infty$, i.e., $\Lambda_\omega=\Lambda_{\omega,\text{bulk}}$. The predicted temperature dependence of $k_{n,\text{eff}}$ agreed with the data for layers when B was used as an adjustable parameter.

The nature of phonon reflection and transmission at the boundaries depends on the ratio of the phonon wavelength to the standard deviation of the boundary profile (Ziman, 1960). When this ratio is near or smaller than unity, the phonons are reflected and transmitted diffusely. At room temperature, phonons with wavelengths from a few angstroms to a few tens of nanometers contribute to energy transport. The shortest wavelength phonons, which carry most of the energy, are diffusely reflected by any practical interface. The longest wavelength phonons may not scatter diffusely on the boundaries of many interfaces. Swartz and Pohl (1989) derived the approximate diffuse mismatch model for the diffuse transmission and reflection of phonons at an interface, and showed that the boundary resistance predicted by this model agrees well with data for metal–dielectric interfaces and differs little from that predicted by the theory of Little (1959) for an ideal smooth interface. The diffuse mismatch model is used here for the transmission coefficients of phonons of all wavelengths. The error due to the non-diffuse transmission and specular reflection of long wavelength phonons at the boundaries is expected to be small, but has not been quantified.

The diffuse mismatch model assumes complete contact between the layer and the bounding media, and accounts neither for changes in microstructure near the interface, nor for interfacial layers. High-resolution transmission electron micrographs of interfaces of deposited (Schroder, 1987) and SIMOX (Celler and White, 1992) amorphous silicon dioxide layers with silicon show no evidence of incomplete contact on length scales down to a few angstroms, nor of a different microstructure in the silicon near the boundary. These micrographs show only that the microstructures of the layers were not periodic up to the interface with the silicon. Two of the hypotheses discussed in Section 1, (*b*) a thickness-dependent microstructure or stoichiometry, and (*c*) thermal boundary resistances or interfacial layers, are not excluded.

When the diffuse mismatch model is employed at both boundaries, one-dimensional phonon conduction normal to a layer is analogous to radiation between diffuse gray walls in an absorbing medium. This problem has been solved for grey media, i.e., when the photon mean free path is independent of the photon frequency (e.g., Siegel and Howell, 1981). To estimate the energy transport for nongrey media, the solution for grey media can be integrated over all frequencies to yield Eqs. (2)–(4) with (Chen and Tien, 1993)

$$B=\frac{3}{4\left(\dfrac{1}{\alpha_0}+\dfrac{1}{\alpha_1}-1\right)} \qquad (5)$$

This approximation assumes that phonon modes of different frequencies are independent, i.e., that they do not exchange energy. This approach provides a good estimate of *energy* transport in nongrey media, and is the best available.

3 Bulk Phonon Mean Free Path

Walton (1974), Matsumoto et al. (1977), and Love and Anderson (1990) each used three regimes for the frequency dependence of $\Lambda_{\omega,\text{bulk}}$ in amorphous silicon dioxide. The pre-

Nomenclature (cont.)

x_ω = dimensionless phonon frequency $=h_P\omega/(k_BT)$
y = dimension normal to substrate, m
$\alpha_{0,1}$ = phonon transmission coefficients from layer
Γ = gamma function
θ = Debye temperature, K
Λ_G = phonon mean free path limited by geometric scattering, m
Λ_s = phonon mean free path, m
$\Lambda_{s,b}$ = Bd = phonon mean free path limited by boundary scattering, m
Λ_ω = frequency-dependent phonon mean free path, m
$\Lambda_{\omega,\text{bulk}}$ = bulk frequency-dependent phonon mean free path, m
$\Lambda_{\omega,D}$ = frequency-dependent phonon mean free path limited by Rayleigh scattering, m
$\Lambda_{\omega,SR}$ = frequency-dependent phonon mean free path limited by scattering on structural relaxation, m
Λ_0 = frequency-independent phonon mean free path of Kittel (1949), m
λ_i = parameter, Eqs. (12) and (13), m^{-1}
λ_s = $2\pi v_s/\omega$ = phonon wavelength, m
ρ = mass density, kgm^{-3}
$\delta\rho$ = deviation in mass density, kgm^{-3}
ρ_e = electrical resistivity, Ωm
τ_0 = fitting parameter for Λ_{SR}, s
ω = phonon angular frequency, rads^{-1}
ω^* = $\omega\tau_0$ = dimensionless phonon frequency
ω_D = Debye angular frequency, rads^{-1}

Subscripts

A = property or parameter of bridge A
C = property or parameter of bridge C
D = property or parameter of bridge D

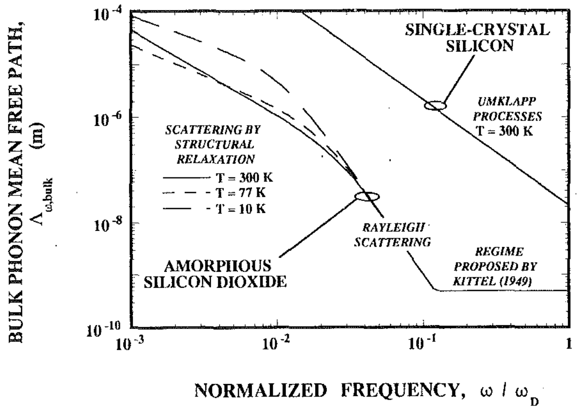

Fig. 3 The phonon mean free path in bulk amorphous silicon dioxide, $\Lambda_{\omega,\mathrm{bulk}}$, showing the three regimes of its frequency dependence. Also shown is the mean free path in crystalline silicon limited by Umklapp scattering (Holland, 1963).

sent work uses the frequency dependence shown in Fig. 3, which combines expressions that are successful in each regime. For the *high-frequency regime*, $\omega > \sim 0.1\ \omega_D$, the frequency-independent phonon mean free path of Kittel (1949, 1986) is used, Λ_0. It is Λ_s in Eq. (1), calculated using thermal-conductivity and specific-heat data above 300 K (Sugawara, 1969; Touloukian and Buyco, 1970) where Λ_s varies little with temperature and phonons in the high-frequency regime dominate conduction. The average value between 300 and 500 K is used, $\Lambda_0 = 4.94$ Å.

In the *intermediate frequency regime*, $0.01\ \omega_D < \omega < 0.1\ \omega_D$, the mechanism responsible for phonon scattering is unknown. Freeman and Anderson (1986a) closely fitted the temperature dependence of the thermal conductivity of many amorphous solids, including silicon dioxide, using Eq. (2) and

$$\Lambda_{\omega,D} = \frac{S_D}{\omega^4}, \quad S_D = 1.76 \times 10^{42}\ \mathrm{m\ rad^4 s^{-4}} \tag{6}$$

This frequency dependence is analogous to the Rayleigh scattering of phonons on regions with different elastic properties and dimensions small compared to the wavelength (Ziman, 1960). For a region with a deviation in mass density $\delta\rho$ compared to the surrounding medium of density ρ, the phonon mean free path is given approximately by Eq. (6) and

$$S_D = \frac{144 v_s^4}{\pi N_D a^6} \left(\frac{\delta\rho}{\rho}\right)^{-2} \tag{7}$$

where N_D is the number density and a the typical dimension of the scattering sites. The opposing limit to Rayleigh scattering is geometric scattering for high-frequency phonons, which yields the frequency-independent mean free path $\Lambda_G = (N_D \pi a^2/4)^{-1}$. If this expression and Eq. (7) are solved for a and N_D using $\Lambda_G = \Lambda_0$ and $\delta\rho = \rho$, the volume of scattering sites exceeds the material volume. This indicates that if Rayleigh scattering occurs, Λ_0 is smaller than the corresponding geometrical-scattering limit.

The mean free paths of phonons in the *low-frequency regime*, $\omega < 0.01\ \omega_D$, are limited by *structural relaxation* and can be measured through the attenuation of sound waves (Hunklinger and Arnold, 1976). Structural relaxation is the rearrangement of atoms in the amorphous material due to elastic waves. The structural relaxation can occur out of phase with the long-wavelength phonons and absorb their energy. The theory for this phenomenon is similar to the Debye relaxation model, which determines the influence of electric dipoles in liquids on the photon mean free path (Bohren and Huffman, 1983). Gilroy and Phillips (1981) developed the *asymmetric double-well potential model* to describe phonon absorption by structural relaxation. Bonnet (1991) approximated their integrals, yielding

$$\frac{1}{\Lambda_{\omega,SR}} = \frac{\pi S_{SR}\omega}{2v_s}\left[\sqrt{\pi}\,\frac{\Gamma\left(\frac{T^*}{2}+1\right)}{\Gamma\left(\frac{T^*}{2}+\frac{3}{2}\right)}\,\frac{T^*}{\cos\left(\frac{\pi}{2}T^*\right)}\,(\omega^*)^{T^*} - \frac{T^*}{1-T^*}\,\omega^*\right] \tag{8}$$

where $\Lambda_{\omega,SR}$ is the phonon mean free path limited by structural relaxation, $\omega^* = \omega\tau_0$, $T^* = k_B T/E_0$, and Γ is the gamma function. Bonnet (1991) closely fitted the data of Vacher et al. (1981) for amorphous silicon dioxide from 10 to 300 K using $\tau_0 = 2.5 \times 10^{-13}$, $E_0 = 5.02 \times 10^{-21}$ J, and $S_{SR} = 1.89 \times 10^{-3}$. These values and Eq. (8) are used here. Equation (6) models Rayleigh scattering in the intermediate frequency regime. The transition between the low and intermediate frequency regimes is modeled using Matthiessen's rule,

$$\frac{1}{\Lambda_{\omega,\mathrm{bulk}}} = \frac{1}{\Lambda_{\omega,D}} + \frac{1}{\Lambda_{\omega,SR}} \tag{9}$$

The mean free path $\Lambda_{\omega,\mathrm{bulk}}$ used here agrees well with the data of Vacher et al. (1981) at 3.5×10^{10} Hz and with the data of Jones et al. (1964) near 5×10^8 Hz at temperatures between 10 and 300 K. The mean free path also agrees with data presented by Love and Anderson (1990) near 3×10^{10} and 2×10^{11} Hz at 90 and 300 K. The only significant disagreement occurs at 2×10^{11} Hz at 90 K, where one measurement indicates a smaller mean free path than that shown in Fig. 3. But the value of $\Lambda_{\omega,\mathrm{bulk}}$ at this frequency in Fig. 3 was obtained by fitting Eq. (2) to low-temperature thermal conductivity data, which are also relevant to the present work. The mean free path used here is very similar to that of Love and Anderson (1990). These authors used a slightly different model for scattering on structural relaxation than that developed by Gilroy and Phillips (1981), called the *symmetric double-well potential model.* It is not known which model is most appropriate for amorphous materials.

Figure 3 shows the phonon mean free path in silicon at room temperature limited by Umklapp scattering (Holland, 1963). The room-temperature thermal conductivity of silicon is about two orders of magnitude larger than that of silicon dioxide, which is due almost entirely to the much larger mean free path of phonons. In silicon dioxide, phonons experiencing Rayleigh scattering are responsible for more of the specific heat at 77 K than at 300 K. Since these phonons have longer mean free paths than the high-frequency phonons, boundary scattering is more important at 77 K than at room temperature.

The effective conductivity of silicon dioxide layers is calculated using Eqs. (2)–(6), (8), and (9). From 10 to 300 K, the conductivity predicted using $d = \infty$ differs by up to 20 percent from bulk data. This is due to the approximate Debye model for the phonon density of states. In this work, the Debye model is assumed only to predict the *relative contributions* of phonons of different frequencies to the total conductivity. This allows the calculated $k_{n,\mathrm{eff}}$ to be normalized by the k_{bulk} calculated using $d = \infty$. The final prediction for $k_{n,\mathrm{eff}}$ is

$$k_{n,\mathrm{eff}} = [k_{\mathrm{bulk}}]_{\mathrm{measured}} \times \left[\frac{k_{n,\mathrm{eff}}}{k_{\mathrm{bulk}}}\right]_{\mathrm{calculated}} \tag{10}$$

4 Experimental Technique

4.1 Apparatus. Figure 4 is a cross section of the test structure. It is based on that used by Swartz and Pohl (1987) for thermal boundary resistance measurements. The width of bridge A is $w = 5\ \mu$m, yielding nearly one-dimensional conduction normal to the sample layer. The width of the nonheating bridges is near 1 μm. Section 4.2 analyzes thermal

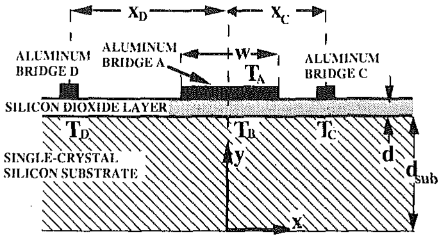

Fig. 4 Cross section of test structure used here to measure $k_{n,\mathrm{eff}}$

conduction in the substrate, whose contribution to the uncertainty is estimated using a second nonheating bridge D. The center-to-center bridge separations are $x_C = 5.5$ μm and $x_D = 14.5$ μm. The temperature change that occurs when the heater bridge A is switched on, i.e., when it suddenly carries a large current, is ΔT. The temperature change ΔT_A is measured by bridge A, and ΔT_B is obtained from ΔT_C by modeling the heat conduction in the substrate. The conductivity $k_{n,\mathrm{eff}}$ is calculated from the heater power Q and length L using

$$R_T = \frac{d}{k_{n,\mathrm{eff}}} = \frac{\Delta T_A - \Delta T_B}{Q/(wL)} \tag{11}$$

The wafer is secured to a Temptronic Model TP38B temperature-control chuck, a copper disk with 88.9 mm diameter and thickness 19.1 mm, by means of suction through holes on the surface of the chuck. A thermocouple with one junction soldered to the chuck surface measures the test-structure temperature. The error due to this arrangement is determined using a second thermocouple attached to a wafer. The calibration of each bridge consists of determining the temperature derivative of its electrical resistance, which is affected by an error in the measured temperature *change* of the test structure. The relative uncertainty in the resistance thermometer calibration is found to be $U(\partial R_i/\partial T_i) = 0.04$ for all temperature changes between 273 and 423 K, where $U(q)$ is the relative uncertainty in the parameter q.

The bridge cross section is isothermal due to the low values of the thermal resistances for conduction normal to the bridge and across its cross section compared to the thermal resistance of the silicon dioxide layer. As a result, w in Eq. (11) is the width of the aluminum-silicon dioxide contact. Scanning electron microscopy yields the relative dimensions of the cross section of the bridge, from which w is calculated using the measured electrical resistivity of the bridge material and the length and electrical resistance of the bridge.

4.2 Substrate Thermal Conduction Analysis.

The temperature change ΔT_B is calculated from the measured ΔT_C by solving the heat diffusion equation, $\nabla^2 T = 0$, in the substrate. Except for the thinnest layers, the difference between ΔT_B and ΔT_C is much less than ΔT_A, and approximations in this analysis have a small effect on the measurement. The model uses the two-dimensional coordinate system in Fig. 4 and the following approximations:

1 The effect of bridges C and D on conduction in the substrate is neglected. This results in a plane of symmetry and an adiabatic boundary condition at $x = 0$.

2 Substrate conduction is assumed to be two dimensional in the x-y plane. The ratio of the bridge length to the substrate thickness is approximately 4.2.

3 The wafer is assumed to possess a uniform temperature T_0 at $y = 0$.

4 The energy flux from bridge A, of width near 5 μm, is uniform in x and travels directly through the silicon dioxide layer, resulting in a heat-flux boundary condition at $y = d_{\mathrm{sub}}$ of $-Q/(wL)$ for $0 < x < w/2$. This neglects the influence of spreading in the silicon dioxide on ΔT_B, but is estimated to yield a relative error of less than 1 percent in $k_{n,\mathrm{eff}}$.

5 Conduction out of the substrate through the silicon dioxide to the air on top is neglected, yielding an adiabatic boundary condition at $y = d_{\mathrm{sub}}$ for $x > w/2$.

6 The substrate side boundaries are assumed to be far from the heater compared to d_{sub}. The boundary condition there has no effect on the temperature near the heater. The boundary condition $T = T_0$ at $x = W$ and the requirement $W/d_{\mathrm{sub}} \gg 1$ are used.

Separation of variables yields ΔT_C and ΔT_D,

$$\Delta T_{C,D} = \frac{2Q}{LwWk_{\mathrm{sub}}} \sum_{i=0}^{\infty} \tanh(\lambda_i d_{\mathrm{sub}}) \frac{\sin(\lambda_i w/2)\cos(\lambda_i x_{C,D})}{(\lambda_i)^2},$$
$$\lambda_i = \frac{\pi}{W}\left(\frac{2i+1}{2}\right), \quad W \gg d_{\mathrm{sub}} \tag{12}$$

The average temperature at the interface of the silicon and the silicon-dioxide underneath the heater bridge is the average value of Eq. (12) for $0 < x < w/2$,

$$\Delta T_B = \frac{4Q}{Lw^2 Wk} \sum_{i=0}^{\infty} \tanh(\lambda_i d_{\mathrm{sub}}) \frac{\sin^2(\lambda_i w/2)}{(\lambda_i)^3} \tag{13}$$

The temperature difference ΔT_B for Eq. (11) is

$$[\Delta T_B]_{\mathrm{experiment}} = [\Delta T_C]_{\mathrm{experiment}} + [\Delta T_B - \Delta T_C]_{\mathrm{analysis}} \tag{14}$$

The normalized uncertainty due to the approximate thermal-conduction analysis is estimated from the difference between the predicted and measured temperatures of bridges C and D,

$$U([\Delta T_B - \Delta T_C]_{\mathrm{analysis}}) = \frac{[\Delta T_C - \Delta T_D]_{\mathrm{experiment}} - [\Delta T_C - \Delta T_D]_{\mathrm{analysis}}}{[\Delta T_C - \Delta T_D]_{\mathrm{experiment}}} \tag{15}$$

4.3 Uncertainty Analysis.

The thermal resistance determined in these experiments is related to the measured quantities by

$$R_T = \frac{[\Delta T_A]_{\mathrm{experiment}} - [\Delta T_C]_{\mathrm{experiment}} - [\Delta T_B - \Delta T_C]_{\mathrm{analysis}}}{Q/(wL)}$$
$$= \frac{\left[\Delta\left(\frac{V_A}{I_A}\right)\left(\frac{dR_A}{dT_A}\right)^{-1} - \frac{\Delta V_C}{I_C}\left(\frac{dR_C}{dT_C}\right)^{-1} - [\Delta T_B - \Delta T_C]_{\mathrm{analysis}}\right]}{I_A V_A/(wL)} \tag{16}$$

where V_A, I_A, V_C, and I_C are the voltage drops and currents measured for bridges A and C. The quantities $\Delta(V_A/I_A)$ and $\Delta(V_C/I_C)$ are the changes of the resistances of bridges A and C, which occur when the heater bridge turns on. The current I_C is very stable, but I_A, V_A, and V_C experience small fluctuations in time, which are used for their uncertainties here. The uncertainty in the bridge length L is negligible. For simplicity, the uncertainties in $\Delta(V_A/I_A)$ and ΔV_A are treated as independent. The total uncertainty in the thermal resistance is calculated using Eq. (16) and the sum-of-squares technique (Holman, 1984),

$$[U(R_T)]^2 = \left[U\left(\frac{dR_A}{dT_A}\right)\right]^2 \left[\frac{\Delta T_A}{\Delta T_A - \Delta T_B}\right]^2 + \left[U\left(\Delta\left(\frac{V_A}{I_A}\right)\right)\right]^2 \left[\frac{\Delta T_A}{\Delta T_A - \Delta T_B}\right]^2$$
$$+ \left[U\left(\frac{dR_C}{dT_C}\right)\right]^2 \left[\frac{\Delta T_C}{\Delta T_A - \Delta T_B}\right]^2 + [U(\Delta V_C)]^2 \left[\frac{\Delta T_C}{\Delta T_A - \Delta T_B}\right]^2$$
$$+ [U([\Delta T_B - \Delta T_C]_{\mathrm{analysis}})]^2 \left[\frac{\Delta T_B - \Delta T_C}{\Delta T_A - \Delta T_B}\right]^2$$
$$+ [U(V_A)]^2 + [U(I_A)]^2 + [U(w)]^2 \tag{17}$$

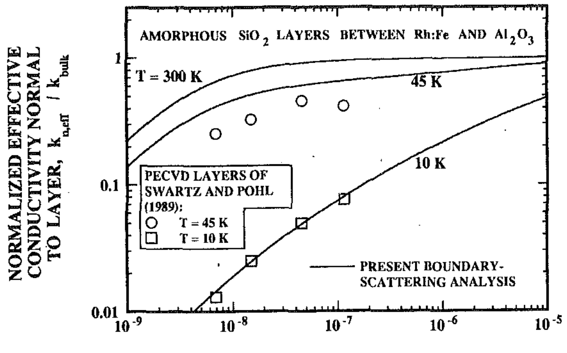

Fig. 5 Predictions of the thermal conductivity ratio $k_{n,eff}/k_{bulk}$ considering phonon-boundary scattering, compared with data for PECVD silicon-dioxide layers

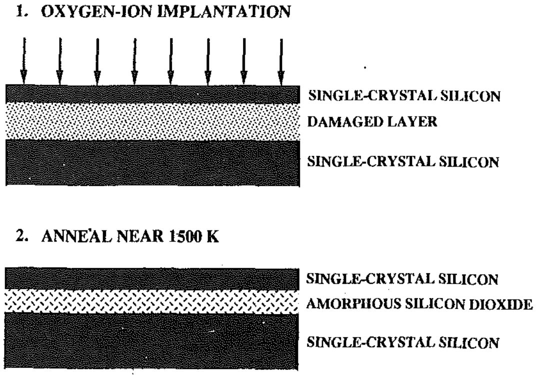

Fig. 6 Separation by implantation with oxygen (SIMOX) fabrication process (e.g., Celler and White, 1992)

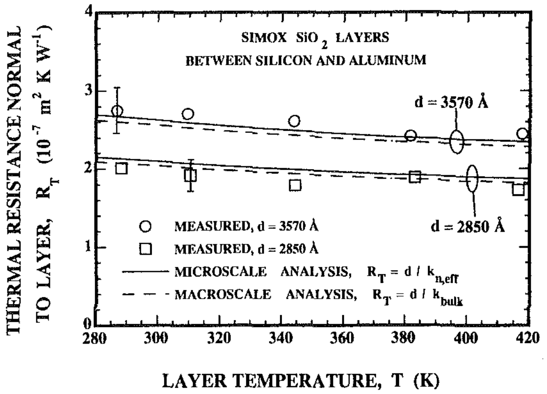

Fig. 7 Comparison of boundary-scattering (microscale) analysis with data for SIMOX silicon-dioxide layers

In the present work, this technique is applied to layers near 0.3 μm thick. For these layers, the approximate largest values of the terms on the right of Eq. (17) are $(0.056)^2$, $(0.034)^2$, $(0.032)^2$, $(0.032)^2$, $(0.028)^2$, $(0.01)^2$, $(0.01)^2$, and $(0.063)^2$, yielding $U(R_T)=0.106$. The uncertainty is dominated by the uncertainties of the width of bridge A and the calibration of bridge A. For much thinner layers, where $\Delta T_B - \Delta T_C$ can be comparable to $\Delta T_A - \Delta T_B$, the uncertainty due to the thermal analysis is significant (Goodson et al., 1993a). The present experimental technique is similar to those of Schafft et al. (1989) and Brotzen et al. (1992), because it uses a thin-layer bridge to heat the sample layer. But both sets of authors determined ΔT_B using the measured temperature at the *bottom* of the substrate. This temperature difference is always much larger than $\Delta T_B - \Delta T_C$, so that the approximations in the thermal-conduction analysis are much more important than those used here. It is important to minimize this component of the uncertainty when measuring very thin layers, i.e., $d \leq 0.1$ μm. While this uncertainty was negligible in the measurements of Schafft et al. (1989) for layers thicker than 1 μm, its impact on the data of Brotzen et al. (1992) for layers as thin as 0.1 μm needs to be assessed.

5 Results and Discussion

Figure 5 compares the predictions of the phonon-boundary scattering analysis with the low-temperature data of Swartz and Pohl (1989) for PECVD silicon dioxide layers bounded by Rh:Fe, which is rhodium with a small fraction of iron, and sapphire. The data are represented in this plot using the k_{bulk} data of Zeller and Pohl (1971). Boundary scattering is more important at low temperatures where low-frequency phonons, which have long mean free paths, account for more of the conductivity. The agreement is excellent at 10 K for a range of thicknesses, which supports the use of Eqs. (2)-(5). This agreement relies heavily on the transmission coefficients calculated using the diffuse mismatch model of Swartz and Pohl (1989), because at this temperature many phonons travel ballistically between the boundaries without scattering internally. At 45 K, the ratio $k_{n,eff}/k_{bulk}$ is overpredicted by the present analysis. This would be consistent with the *agreement* at 10 K if the phonon mean free paths in the layers were the same as in Fig. 3 in the low and intermediate-frequency regimes, which are most important at low temperatures, but were less than those given in Fig. 3 in the high-frequency regime, which becomes important above about 10 K. But Fig. 3 may still be correct for bulk fused silicon dioxide, since this material may have a different microstructure than the PECVD layers. The poor agreement at 45 K may also be due to a failure of the diffuse mismatch model above 30 K. This failure was observed for many interfaces by Swartz and Pohl (1989), who argued that highly resistive interfacial layers at the interfaces could be responsible. Figure 5 shows that $k_{n,eff}/k_{bulk}$ is approximately unity at room temperature for layers thicker than a few hundred angstroms, i.e., phonon-boundary scattering is not important. This is also the case if the calculation is performed using the *transmission coefficients from silicon dioxide into aluminum* and silicon, which were the bounding materials for the layers whose conductivities are given in Fig. 1. But the data in Fig. 1 yield ratios $k_{n,eff}/k_{bulk}$ that are much smaller than unity, indicating that the problem at 45 K in Fig. 5 becomes more important at higher temperatures.

The data for the silicon dioxide layers fabricated using oxygen-ion implantation (SIMOX) are compared with the predictions of the boundary-scattering analysis. The test structures were made from SOI wafers provided by Ibis Corporation in Danvers, MA, using the SIMOX process, which is depicted in Fig. 6. Oxygen atoms are implanted into a lightly doped single-crystal silicon substrate, forming a damaged sublayer. After an anneal near 1500 K, a silicon-dioxide layer forms beneath a single-crystal silicon overlayer of thickness near 0.22 μm. Devices are usually fabricated from the silicon overlayer. In this work, the silicon overlayers are etched away and the test structures are deposited onto the exposed silicon-dioxide layers. Figure 7 compares the near-room-temperature data for the SIMOX layers with the predictions of the phonon-boundary scattering analysis. *Microscale* analysis considers phonon-boundary scattering, while *macroscale* analysis yields the volume resistance of a layer from the bulk conductivity. The microscale and macroscale predictions are within 3 percent of each other, i.e., boundary scattering is not important. The SIMOX data are consistent with the boundary-scattering analysis. But the 11 percent relative uncertainty of these data makes it impossible for them to confirm or refute the predictions.

The data show that the SIMOX fabrication technique results in layers that are far different than those fabricated using other techniques. The conductivities $k_{n,eff}$ of SIMOX layers agree very well with k_{bulk}, which is a first for amorphous silicon dioxide layers and is in stark contrast to the data shown in Fig. 1. The dramatic difference between the conductivities reported here for SIMOX layers and those reported previously for deposited layers indicates that the microstructure of the SIMOX layers is different than those of the deposited layers. This may result from a difference in porosity between the deposited and the SIMOX layers. Deposition techniques can yield a porosity in layers, which can reduce their thermal conductivities (e.g., Lambropoulos et al., 1991), but it is unlikely that pores form in the SIMOX layers. Another possibility is that the high-temperature anneal of the SIMOX layers causes an atomic-scale reordering (e.g., Nagasima, 1972), which improves the conductivity. Goodson et al. (1993a) showed that annealing improved the thermal conductivity of LPCVD silicon dioxide layers by up to 23 percent.

The agreement of the SIMOX data with k_{bulk} provides evidence that both the microstructure and stoichiometry of the SIMOX layers closely resemble those in bulk samples. The absence of a thickness-dependent conductivity in these layers indicates that neither thermal boundary resistances nor highly resistive interfacial layers are present. These findings are important for the designers of SOI circuits, because they make it appropriate to use $k_{n,\text{eff}} = k_{\text{bulk}}$ rather than the much smaller values of $k_{n,\text{eff}}$ in Fig. 1. Based on the SIMOX data in Fig. 7, Goodson et al. (1993b) used $k_{n,\text{eff}} = k_{\text{bulk}}$ when modeling thermal conduction in the SIMOX silicon dioxide layers in SOI circuits. Since the temperature field in SOI circuits is very sensitive to the conductivity of the SIMOX layer, the close agreement of their predictions with their data for transistor channel temperatures is a confirmation of the thermal conductivity values reported here.

6 Conclusions and Recommendations

Phonon-boundary scattering is of little practical importance in silicon dioxide layers above room temperature. As a result, the low conductivities in Fig. 1 measured elsewhere must be attributed to a thickness-dependent microstructure or stoichiometry in the layers, to distinct, highly resistive interfacial layers, or to measurement uncertainties. The interfacial layer hypothesis is questionable. For an interfacial layer to contribute significantly to the total thermal resistance, it would need a thermal conductivity much smaller than the remainder of the amorphous silicon dioxide, which has a thermal conductivity among the lowest of any nonporous solid. A more plausible explanation is an increased porosity near the boundaries of the layer, which would also account for the thickness dependence of the effective thermal conductivity.

This work adapts the technique of Swartz and Pohl (1987) for room-temperature measurements of the thermal conductivity normal to layers with a relative uncertainty of ± 11 percent. The large or unknown uncertainties of existing techniques for this measurement show that there is a need for standardized techniques with well-known limitations, such as exist for bulk solids. The technique used here is recommended as a standard.

It is important to measure the conductivity of layers fabricated in the same way as those in the circuit for which the effective thermal conductivity is needed. An SOI circuit designer employing data from Fig. 1 rather than from Fig. 7 would overpredict the temperature of devices and interconnects, which might result in a circuit of lower performance because it was overdesigned for interconnect reliability.

Acknowledgments

The SOI wafers used in this study were provided by IBIS Corp. D. A. A. and L. T. S. acknowledge the support of the Semiconductor Research Corporation (SRC) under contracts 91-SP-080 and 92-SP-309. K. E. G. and L. T. S. were supported by academic fellowships from the Office of Naval Research and AT&T Bell Labs, respectively.

References

Berman, R., 1976, *Thermal Conduction in Solids*, Oxford University Press, Oxford, United Kingdom, Chap. 9, p. 23.

Bohren, C. F., and Huffman, D. R., 1983, *Absorption and Scattering of Light by Small Particles*, Wiley, New York, pp. 130-136, 259-265.

Bonnet, J. P., 1991, "On the Thermally Activated Structural Relaxation in Glasses," *J. Non-crystalline Solids*, Vol. 127, pp. 227-331.

Brotzen, F. R., Loos, P. J., and Brady, D. P., 1992, "Thermal Conductivity of Thin SiO$_2$ Films," *Thin Solid Films*, Vol. 207, pp. 197-201.

Callaway, J., 1959, "Model for Lattice Thermal Conductivity at Low Temperatures," *Phys. Rev.*, Vol. 113, pp. 1046-1051.

Celler, G. K., and White, A. E., 1992, "Buried Oxide and Silicide Formation by High-Dose Implantation in Silicon," *MRS Bulletin*, Vol. 17, June, pp. 40-46.

Chen, G., and Tien, C. L., 1993, "Thermal Conductivity of Quantum Well Structures," *J. Thermophysics and Heat Transfer*, Vol. 7, pp. 311-318.

Flik, M. I., and Tien, C. L., 1990, "Size Effect of the Thermal Conductivity of High-T_c Thin-Film Superconductors," ASME JOURNAL OF HEAT TRANSFER, Vol. 112, pp. 872-881.

Freeman, J. J., and Anderson, A. C., 1986a, "Normalized Thermal Conductivity of Amorphous Solids," in: *Phonon Scattering in Condensed Matter*, A. C. Anderson and J. P. Wolfe, eds., Vol. 5, pp. 32-34.

Freeman, J. J., and Anderson, A. C., 1986b, "Thermal Conductivity of Amorphous Solids," *Phys. Rev. B*, Vol. 34, pp. 5684-5690.

Goodson, K. E., and Flik, M. I., 1992, "Effect of Microscale Thermal Conduction on the Packing Limit of Silicon-on-Insulator Electronic Devices," *IEEE Trans. Components, Hybrids, and Manufacturing Technology*, Vol. 15, pp. 715-722.

Goodson, K. E., Flik, M. I., Su, L. T., and Antoniadis, D. A., 1993a, "Annealing-Temperature Dependence of the Thermal Conductivity of LPCVD Silicon-Dioxide Layers," *IEEE Electron Device Letters*, Vol. 14, pp. 490-492.

Goodson, K. E., Flik, M. I., Su, L. T., and Antoniadis, D. A., 1993b, "Prediction and Measurement of Temperature Fields in Silicon-on-Insulator Electronic Circuits," *Solutions to CFD Benchmark Problems in Electronic Packaging*, ASME HTD-Vol. 255, D. Agonafer, ed., pp. 11-19; submitted to ASME JOURNAL OF HEAT TRANSFER.

Gilroy, K. S., and Phillips, W. A., 1981, "An Asymmetric Double-Well Potential Model for Structural Relaxation Processes in Amorphous Materials," *Philos. Mag.*, Vol. B42, pp. 735-746.

Guenther, A. H., and McIver, J. K., 1988, "The Role of Thermal Conductivity in the Pulsed Laser Damage Sensitivity of Optical Thin Films," *Thin Solid Films*, Vol. 163, pp. 203-214.

Holland, M. G., 1963, "Analysis of Lattice Thermal Conductivity," *Phys. Rev.*, Vol. 132, pp. 2461-2471.

Holman, J. P., 1984, *Experimental Methods for Engineers*, McGraw-Hill, New York, pp. 50-57.

Hunklinger, S., Arnold, W., 1976, "Ultrasonic Measurements in Amorphous Solids," in: *Physical Acoustics*, W. P. Mason and R. N. Thurston, eds., Vol. 12, pp. 155-209.

Jones, C. K., Klemens, P. G., and Rayne, J. A., 1964, "Temperature Dependence of Ultrasonic Attenuation in Fused Quartz up to 1 kMc/s," *Phys. Lett.*, Vol. 8, pp. 31-32.

Kittel, C., 1949, "Interpretation of the Thermal Conductivity of Glasses," *Phys. Rev.*, Vol. 75, pp. 972-974.

Kittel, C., 1986, *Introduction to Solid State Physics*, Wiley, New York, Chap. 17.

Kumar, S., and Vradis, G. C., 1991, "Thermal Conduction by Electrons Along Thin Films: Effects of Thickness According to Boltzmann Transport Theory," in: *Micromechanical Sensors, Actuators, and Systems*, D. Cho et al., eds., ASME DSC-Vol. 32, pp. 89-101.

Lambropoulos, J. C., Jolly, M. R., Amsden, C. A., Gilman, S. E., Sinicropi, M. J., Diakomihalis, D., and Jacobs, S. D., 1989, "Thermal Conductivity of Dielectric Thin Films," *J. Appl. Phys.*, Vol. 66, pp. 4230-4242.

Lambropoulos, J. C., Jacobs, S. D., Burns, S. J., Shaw-Klein, L., and Hwang, S. S., 1991, "Thermal Conductivity of Thin Films: Measurement and Microstructural Effects," in: *Thin Film Heat Transfer—Properties and Processing*, M. K. Alam et al., eds., ASME HTD-Vol. 184, pp. 21-32.

Little, W. A., 1959, "The Transport of Heat Between Dissimilar Solids at Low Temperatures," *Can. J. Phys.*, Vol. 37, pp. 334-349.

Love, M. S., and Anderson, A. C., 1990, "Estimate of Phonon Thermal Transport in Amorphous Materials Above 50 K," *Phys. Rev. B*, Vol. 42, pp. 1845-1847.

Matsumoto, D. S., Reynolds, C. L., and Anderson, A. C., 1977, "Thermal Boundary Resistance at Metal-Epoxy Interfaces," *Phys. Rev. B*, Vol. 16, pp. 3303-3307.

Nagasima, N., 1972, "Structure Analysis of Silicon Dioxide Films Formed by Oxidation of Silane," *J. Appl. Phys.*, Vol. 43, pp. 3378-3386.

Savvides, N., and Goldsmid, H. J., 1972, "Boundary Scattering of Phonons in Silicon Crystals at Room Temperature," *Phys. Lett.*, Vol. A41, pp. 193-194.

Schafft, H. A., Suehle, J. S., and Mirel, P. G. A., 1989, "Thermal Conductivity Measurements of Thin-Film Silicon Dioxide," *Proc. IEEE Int. Conf. on Microelectronic Test Structures*, Vol. 2, pp. 121-124.

Schroder, D. K., 1987, *Advanced MOS Devices*, Addison-Wesley, Reading, MA, pp. 204-206.

Siegel, R., and Howell, J. R., 1981, *Thermal Radiation Heat Transfer*, Hemisphere, New York, pp. 476-481.

Stephens, R. B., 1973, "Low-Temperature Specific Heat and Thermal Conductivity of Noncrystalline Solids," *Phys. Rev. B*, Vol. 8, pp. 2896-2905.

Sugawara, A., 1969, "Precise Determination of Thermal Conductivity of High Purity Fused Quartz from 0° to 650°C," *Physica*, Vol. 41, pp. 515-520.

Swartz, E. T., and Pohl, R. O., 1987, "Thermal Resistance at Interfaces," *Appl. Phys. Lett.*, Vol. 51, pp. 2200-2202.

Swartz, E. T., and Pohl, R. O., 1989, "Thermal Boundary Resistance," *Rev. Mod. Phys.*, Vol. 61, pp. 605-668.

Tien, C. L., Armaly, B. F., and Jagannathan, P. S., 1969, "Thermal Conductivity of Thin Metallic Films and Wires at Cryogenic Temperatures," *Proc. Eighth Conference on Thermal Conductivity,* C. Y. Ho and R. E. Taylor, eds., Plenum Press, New York, pp. 13-19.

Touloukian, Y. S., and Buyco, E. H., 1970, "Specific Heat: Nonmetallic Solids," *Thermophysical Properties of Matter*, Vol. 5, IFI/Plenum, New York.

Vacher, R., Pelous, J., Plicque, F., and Zarembowitch, A., 1981, "Ultrasonic and Brillouin Scattering Study of the Elastic Properties of Vitreous Silica Between 10 and 300 K," *J. Non-crystalline Solids*, Vol. 45, pp. 397-410.

Walton, D., 1974, "Random-Network Model, Density Fluctuation, and Thermal Conductivity of Glasses," *Solid State Comm.*, Vol. 14, pp. 335-339.

Zachariasen, W. H., 1932, "The Atomic Arrangement in Glass," *J. American Chemical Society*, Vol. 54, pp. 3841-3851.

Zaitlin, M. P., and Anderson, A. C., 1975, "Phonon Thermal Transport in Noncrystalline Materials," *Phys. Rev. B*, Vol. 12, pp. 4475-4486.

Zaitlin, M. P., Scherr, L. M., and Anderson, A. C., 1975, "Boundary Scattering of Phonons in Noncrystalline Materials," *Phys. Rev. B*, Vol. 12, pp. 4487-4492.

Zeller, R. C., and Pohl, R. O., 1971, "Thermal Conductivity and Specific Heat of Noncrystalline Solids," *Phys. Rev. B*, Vol. 4, pp. 2029-2041.

Zhu, D. M., and Anderson, A. C., 1990, "Low-Temperature Thermal Conductivity of a Glassy Epoxy-Epoxy Composite," *J. Low Temp. Phys.*, Vol. 80, pp. 153-160.

Ziman, J. M., 1960, *Electrons and Phonons*, Oxford University Press, Oxford, United Kingdom, pp. 221-223, 357-370, and 456-460.

ERRATA

To the paper "Correlations for Laminar Mixed Convection Flows on Vertical, Inclined, and Horizontal Flat Plates" by T. S. Chen, B. F. Armaly, and N. Ramachandran, published in the ASME JOURNAL OF HEAT TRANSFER, Vol. 108, November 1986, pp. 835–840.

In Eq. (4), p. 836, the expression for F_1 (Pr) should read

$$F_1(\mathrm{Pr}) = 0.339\ \mathrm{Pr}^{1/3}[1 + (0.0468/\mathrm{Pr})^{2/3}]^{-1/4}$$

The constant 0.339 was printed as 0.399 in the original paper. We regret the typographical error, which we failed to catch.

G. Chen
Department of Mechanical Engineering
and Materials Science,
Duke University,
Durham, NC 27708
Assoc. Mem. ASME

C. L. Tien
A. Martin Berlin Professor,
Department of Mechanical Engineering.
Fellow ASME

X. Wu[1]

J. S. Smith

Department of Electrical Engineering and
Computer Science.

University of California,
Berkeley, CA 94720

Thermal Diffusivity Measurement of GaAs/AlGaAs Thin-Film Structures

This work develops a new measurement technique that determines the thermal diffusivity of thin films in both parallel and perpendicular directions, and presents experimental results on the thermal diffusivity of GaAs/AlGaAs-based thin-film structures. In the experiment, a modulated laser source heats up the sample and a fast-response temperature sensor patterned directly on the sample picks up the thermal response. From the phase delay between the heating source and the temperature sensor, the thermal diffusivity in either the parallel or perpendicular direction is obtained depending on the experimental configuration. The experiment is performed on a molecular-beam-epitaxy grown vertical-cavity surface-emitting laser (VCSEL) structure. The substrates of the samples are etched away to eliminate the effects of the interface between the film and the substrate. The results show that the thermal diffusivity of the VCSEL structure is 5–7 times smaller than that of its corresponding bulk media. The experiments also provide evidence on the anisotropy of thermal diffusivity caused solely by the effects of interfaces and boundaries of thin films.

Introduction

Thermophysical properties of thin films generally differ from the values of their corresponding bulk materials due to the effects of microstructures, boundaries, and interfaces. A variety of techniques has been developed to measure the thermal conductivity or diffusivity of thin films (Cahill et al., 1988; Hatta, 1990; Lambropoulos et al., 1992). A detailed examination of these methods and measurements reveals several drawbacks (Tien and Chen, 1992). First, most of these techniques can characterize thermophysical properties of thin films in only one direction, i.e., either parallel or perpendicular to the film plane. The prediction of an anisotropic thermal conductivity caused solely by size effects (Chen and Tien, 1993a; Flik and Tien, 1990) has never been proven experimentally. Second, most of the experiments were performed on polycrystalline or amorphous thin films on a substrate. These measurements do not give an unambiguous answer to the question whether the reduction of thermal conductivity occurs due to effects of the interface between the film and the substrate, the boundaries, or the microstructures in the film. Experimental techniques and measurements that can overcome these drawbacks will enhance the understanding of fundamental physical processes of thermal energy transport in thin film structures.

Heating represents a major problem in gallium arsenide (GaAs) based vertical-cavity surface-emitting lasers (VCSELs) (Osinski, 1991) and the facet damage of edge-emitting lasers (Chen and Tien, 1993b). The investigation of the thermal characteristics of semiconductor lasers requires an accurate knowledge of their thermophysical properties. Chen and Tien (1993a) and Ren and Dow (1982) predicted a reduction in the thermal conductivity of GaAs/AlGaAs-based quantum well structures and superlattices compared to their corresponding bulk value. Using an AC calorimetric method developed by Hatta et al. (1985), Yao (1987) measured the thermal diffusivity of GaAs/AlGaAs superlattice materials in the direction parallel to the film and observed a reduction. The thermal diffusivity in the perpendicular direction of such structures remains unknown.

This work describes a new experimental technique, which determines the thermal diffusivity of thin film structures in both parallel and perpendicular directions to the film, and utilizes this method to measure the thermal diffusivity of GaAs/AlGaAs-based VCSEL structures. In the experiments, a modulated argon laser heats up a free-standing thin-film sample, and a temperature sensor measures the thermal response. The thermal diffusivity of the sample is obtained from the phase difference between the sensor and the heating signal. In the parallel direction, the method is similar to the AC calorimetric method (Hatta et al., 1985). The thermal diffusivity in the perpendicular direction is measured by the direct patterning of a fast-response gold temperature sensor. This appears to be the first experiment that provides evidence on the anisotropy of thermophysical properties of thin films caused solely by the interfaces and boundaries of the films.

Principles of Measurement

Figures 1(*a*) and 1(*b*) show the principles of the thermal diffusivity measurement in the directions parallel and perpendicular to the film. A modulated laser light heats up the sample, and a temperature sensor picks up the thermal response of the sample. Different configurations are used for the measurement in the parallel and perpendicular directions.

Thermal Diffusivity Parallel to the Film. The measurement in the parallel direction evolves from the AC calorimetric method developed by Hatta et al. (1985). In this method, part of the sample is shielded from the modulated radiation by using a mask [Fig. 1(*a*)]. When the modulation frequency of the heating source is sufficiently low, the temperature is uniform in the direction perpendicular to the film. The AC temperature rise of the sample is (Hatta et al., 1985).

$$T(x) = [Q/4\pi f\rho ch] \exp[-mx - i(mx + \pi/2)] \qquad (1)$$

where $m = (\pi f/a_\parallel)^{1/2}$. Here $a_\parallel$ is the thermal diffusivity of the

---

[1] Current Address: Senior Device Engineer, Xilinx, 2100 Logic Drive, San Jose, CA 95124.

Contributed by the Heat Transfer Division and presented at the ASME Winter Annual Meeting, New Orleans, Louisiana, November 28–December 3, 1993. Manuscript received by the Heat Transfer Division April 1993; revision received August 1993. Keywords: Conduction, Measurement Techniques, Thermophysical Properties. Associate Technical Editor: R. Viskanta.

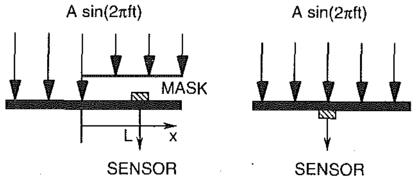

(a) (b)

Fig. 1 **Schematic sketches of the principles of the measurement: (*a*) parallel direction and (*b*) perpendicular direction**

film in the parallel direction, c the specific heat, f is the modulation frequency, h the film thickness, Q the absorbed heat flux, and ρ the density of the film. Hatta et al. (1985) used a thermocouple to measure the AC temperature rise at the sensor. By moving the mask along the film, the distance, L, between the edge of the mask and the temperature sensor can be varied. The relation between the amplitude of the temperature signal and distance L is

$$\ln T(L) = \ln (Q/4\pi f\rho ch) - mL \tag{2}$$

The thermal diffusivity of the film can be obtained from the slope of the $\ln T(L) - L$ relation.

The current measurement utilizes the relation between the phase delay and the distance L:

$$\varphi(L) = -mL - \pi/2 \tag{3}$$

The temperature response of the sample is picked up by a temperature sensor that is directly patterned on the sample. A lock-in amplifier detects the phase delay between the heating source and the temperature sensor. Since it is difficult to determine exactly when $L=0$ in the experiment, the phase difference relative to a reference point is used in the processing of the experimental data,

$$\varphi(L) - \varphi_0(L_o) = -m(L - L_o) \tag{4}$$

This treatment also eliminates the necessity of calibrating the phase of the lock-in amplifier because its initial phase is fixed for a specific modulation frequency. The thermal diffusivity is obtained from the slope of the phase delay:

$$a_{\parallel} = \frac{\pi f}{(d\varphi/dL)^2} \tag{5}$$

Themal Diffusivity Perpendicular to the Film. The thermal diffusivity perpendicular to the film is more difficult to measure due to the short heat diffusion time across the film ($1 \sim 10$ μs for a 10-μm-thick sample). Fast modulation is necessary for the measurement. Using a thermocouple measuring the temperature response of such a film is not feasible because the diameter of a thermocouple junction is usually larger than the film thickness. To overcome this difficulty, a thin-film resistive temperature sensor is directly patterned onto the sample. The sensor is made of a gold film with a thickness ranging between 1000 Å and 6000 Å. The heat diffusion time across such a film is on the order of 10^{-9} s, much shorter than the time needed for heat diffusion across a sample 10 μm thick. Figure 1(*b*) shows the configuration for the measurement in the perpendicular direction. The solution of the one-dimensional heat conduction equation perpendicular to the film yields the AC temperature response at the back surface of the film as [see Yang et al. (1991) for a slightly different solution]

$$T(h) = \frac{2Q}{nk} \frac{e^{-nh}}{(1+\alpha/nk)^2 - (1-\alpha/nk)^2 e^{-2nh}} \tag{6}$$

where $n = (\pi f/a_{\perp})^{1/2}\,(1+i)$, α is the effective heat transfer coefficient to the ambient due to natural convection and thermal radiation, and k the thermal conductivity of the film. For the measurement in the perpendicular direction, nk is on the order of 10^6 W/m^{2}K, much larger than α. Equation (6) can be simplified to

$$T(h) = \frac{2Q}{nk} \frac{e^{-nh}}{1 - e^{-2nh}} \tag{7}$$

The phase difference between the heating source and the temperature at the back of the film is

$$\varphi = \frac{\pi}{4} + \frac{1}{2} y + \arctan \left\{ \frac{e^{-y} \sin(y)}{1 - e^{-y} \cos(y)} \right\} \tag{8}$$

where $y = 2(\pi f/a_{\perp})^{1/2} h$.

Since it is difficult to match the constant $\pi/4$ in Eq. (8) due to the initial phase uncertainty of the optical setup and the electronic system, the relative phase difference between the modulation frequency and a reference frequency is used in matching the thermal diffusivity in the perpendicular direction,

$$\varphi(f) - \varphi(f_o) = \frac{1}{2}(y - y_o) + \arctan \left\{ \frac{e^{-y} \sin(y)}{1 - e^{-y} \cos(y)} \right\} - \arctan \left\{ \frac{e^{-y_o} \sin(y_o)}{1 - e^{-y_o} \cos(y_o)} \right\} \tag{9}$$

The thermal diffusivity is obtained by matching the measured phase delay as a function of modulation frequency according to the equation above. To obtain an accurate measurement, a calibration of the phase accuracy of the lock-in amplifier is necessary because it depends on the modulation frequency due to cable capacitance and signal drift (Meade, 1983). In this experiment, calibration is achieved by sending the output from a function generator to the reference channel of the lock-in amplifier and the sensor simultaneously. The voltage drop at the sensor is sent back to the lock-in amplifier. The phase difference between the signal and the reference channels is recorded and subtracted from the phase delay measured when the experiment is performed in the perpendicular configuration.

Effective Thermal Diffusivity of Layered Materials. The derivations above assume a homogeneous film with well-de-

Nomenclature

a = thermal diffusivity, m^2/s
c = specific heat, J/kgK
f = modulation frequency, Hz
g = function defined by Eq. (20)
h = film thickness, m
i = $(-1)^{1/2}$
k = thermal conductivity, W/mK
L = distance between the edge of the mask and the temperature sensor, m
m = parameter, m^{-1}
n = parameter, m^{-1}
Q = absorbed heat flux, W/m^2
R = thermal boundary resistance, m^{2}K/W
T = temperature, K
t = time, s
x = coordinate, m
y = parameter $= 2(\pi/a)^{1/2} h$
α = effective heat transfer coefficient, W/m^{2}K
β = coefficient
γ = coefficient
ρ = density, kg/m^3
φ = phase

Subscripts

i = ith layer
o = reference
s = sensor
$\parallel$ = parallel to the film
$\perp$ = perpendicular to the film

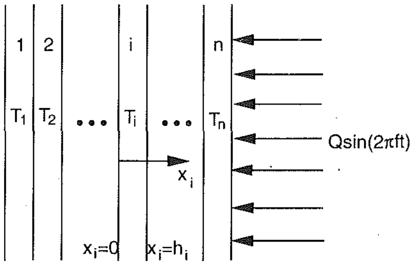

Fig. 2 A multilayer thin film under periodic heating

fined thermophysical properties. The thin-film samples used in this study consist of multilayers of thin films. Thermal diffusivities derived from the experiments represent effective values of the whole structure. For a heat wave propagating in the parallel direction, the effective thermal diffusivity can be calculated from the properties of each individual layer,

$$a_{/\!/} = \sum_{i=1}^{n} k_i h_i \Big/ \sum_{i=1}^{n} \rho_i c_i h_i \tag{10}$$

The relation above is readily obtained by applying energy balance to a differential element of the film assuming a uniform temperature across the film thickness. Albin et al. (1989) gave a vigorous proof for the two-layer case. One premise of Eq. (10) is that each constituent layer has well-defined properties. This premise may break down in the microscale heat transfer regimes due to the long-range interaction of heat carriers between different layers (Tien and Chen, 1992). In this study, Eq. (10) serves the purpose of comparing the current measurement results with the ideal case when the bulk data are still valid for each layer.

In the perpendicular direction, a simple relation like Eq. (10) no longer exists. Taylor (1983) pointed out that the concept of diffusivity is subject to question due to the discontinuous nature of thermal conductivity. There are, however, several reasons to examine if a value of effective thermal diffusivity can represent the thermal response of a multilayer structure. First, this value facilitates a comparison with the experimental results in the parallel direction. Second, the superlattice sample studied here consists of several hundreds extremely thin layers. The long range heat carrier (phonon) interaction between different layers may well invalidate the concept of thermophysical property for each individual layer and require the whole structure to be treated as one identity (Ren and Dow, 1982). Third, even if each layer has well-defined thermophysical properties (if it is relatively thick), the mathematical treatment of a composite film made of hundreds of layers is very involved.

Consider a composite film made of n layers (Fig. 2). The periodic steady-state temperature variation in the ith layer is

$$T_i(x_i, t) = \beta_i \left[\cosh(n_i x_i) + \gamma_i \sinh(n_i x_i)\right] \exp(i2\pi f t) \tag{11}$$

where β_i and γ_i are undetermined coefficients and $n_i = (\pi f / a_i)^{1/2}(1+i)$. The continuity of temperature and heat flux at the interface of the $(i-1)$th and ith layer yields the following recursive relations:

$$\gamma_i = \frac{k_{i-1} n_{i-1}}{k_i n_i} \frac{\gamma_{i-1} + \tanh(n_{i-1} h_{i-1})}{1 + \gamma_{i-1} \tanh(n_{i-1} h_{i-1})} \tag{12}$$

$$\beta_i = \beta_{i-1} \left[\cosh(n_{i-1} h_{i-1}) + \gamma_{i-1} \sinh(n_{i-1} h_{i-1})\right] \tag{13}$$

The adiabatic boundary condition at $x_1 = 0$ gives (a more general boundary condition can be assumed but is not necessary based on the discussion in the previous section):

$$\gamma_1 = 0 \tag{14}$$

The heat flux boundary condition at $x_n = h_n$ yields

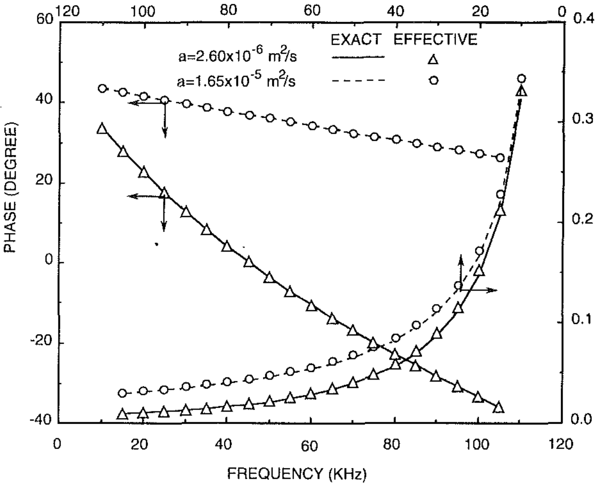

Fig. 3 Comparison of the temperature response of a multilayer thin film calculated from the effective thermal diffusivity with exact solutions

$$\beta_n = -\frac{Q}{k_n n_n \left[\sinh(n_n h_n) + \gamma_n \cosh(n_n h_n)\right]} \tag{15}$$

Sample calculations were carried out for a structure similar to the tested superlattice sample. The effective thermal conductivity of the composite layer required by Eq. (7) was calculated according to standard thermal resistance networks method. Figure 3 illustrates the temperature response at the un-irradiated surface of the composite film assuming $Q = 10^6$ W/m^2. The effective thermal diffusivity, 1.65×10^{-5} m^2/s, is derived by matching the phase calculated from Eq. (7) and the exact solution given by Eqs. (11)–(15) assuming bulk value of thermal diffusivity for each layer. The figure clearly shows that the effective thermal diffusivity represents well the response of the film in both amplitude and phase. This effective thermal diffusivity, however, cannot be calculated from dividing the effective thermal conductivity by the effective heat capacity (which gives 3.0×10^{-5} m^2/s). In the following experiments, the measured effective thermal diffusivity is much smaller than that calculated from assuming bulk thermophysical property data for each individual layer. The question then is whether this reduction is caused by an equal, smaller, or larger reduction in the thermal diffusivity of each individual layer. This situation is illustrated by the results for $a = 2.6 \times 10^{-6}$ m^2/s in Fig. 3. In this case, it is assumed that thermal conductivity (and diffusivity) of each individual layer is reduced uniformly by a factor of 6.4. The resultant effective thermal diffusivity is correspondingly 6.4 times smaller than $a = 1.65 \times 10^{-5}$ m^2/s. This implies that an anisotropy in thermophysical properties exists if the ratios of the measured thermal diffusivity to that calculated from bulk value are different in different directions.

The analysis above shows that an effective thermal diffusivity can be defined for a composite structure under the considered situations. This effective thermal diffusivity provides a basis for comparing the experimental results in two directions. The exact solution also provides a way of matching the thermal diffusivity of an individual layer once properties of all other layers are known.

Sample Preparation and Experimental Setup

Sample Preparation. Two different samples were used in this experiment, both of which were grown on single crystalline GaAs substrate using the molecular-beam-epitaxy (MBE) facility of the Quantum Electronics Laboratory of University of California at Berkeley. The first sample is a GaAs film about 10 μm thick (MBE635). Between the GaAs film and the sub-

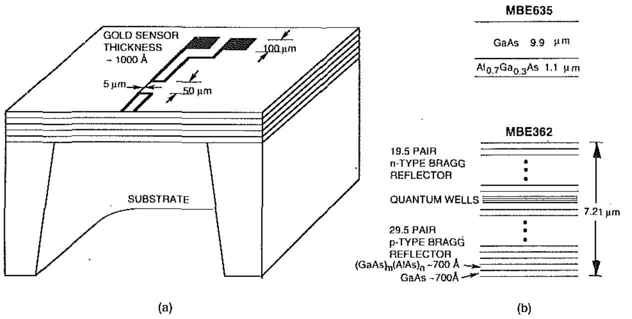

Fig. 4 Schematic sketches of (*a*) patterned sample and (*b*) film structures

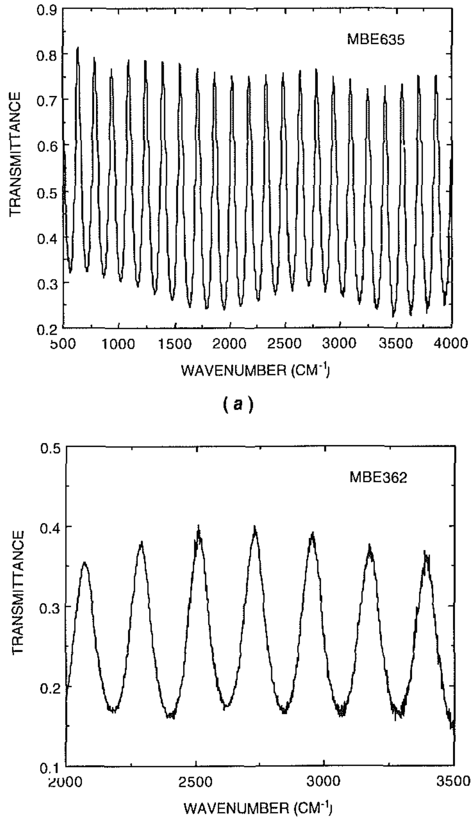

Fig. 5 Transmittance of the etched samples: (*a*) MBE635 and (*b*) MBE362

strate is a 1-μm-thick etch-stop layer of $Al_{0.7}Ga_{0.3}As$. The growth of the film was monitored by reflection high-energy electron diffraction (RHEED) patterns and indicated good single-crystal quality. The second sample is a VCSEL structure (MBE362). It consists of a 29.5-pair *n*-type GaAs/AlGa As Bragg reflector, a one-wavelength-long (0.31 μm) active region with three InGaAs quantum wells, a 19.5-pair *p*-type GaAs/AlGaAs Bragg reflector, and a *p*-type phase-matching layer. The Bragg reflector consists of quarter wavelength layers (~ 700 Å) of $Al_{0.67}Ga_{0.33}As$ and GaAs, where the AlGaAs alloy is actually approximated by short-period superlattices. A detailed description of the growth and structure of this sample was given by Walker et al. (1991). Figure 4 shows schematic sketches of the samples and film structures.

After the films were grown, samples about 5×5 mm^2 were cleaved from the wafer. For sample MBE635, a resistive gold sensor was patterned onto the film by a lift-off technique. The thickness of the gold film was measured by a crystal monitor during the evaporation process to be 1000 Å. A thin layer of chromium film about 100 Å thick was deposited between the sample and the gold film to ensure adhesion of the gold sensor. The total thickness of the sensor was confirmed by measuring the line height on an Alphastep 200 profiler. For sample MBE362, the pattern was obtained by etching the gold film that was already grown on it. A measurement of the etched line height on the Alphastep 200 profiler shows that the thickness of the sensor is about 6000 Å.

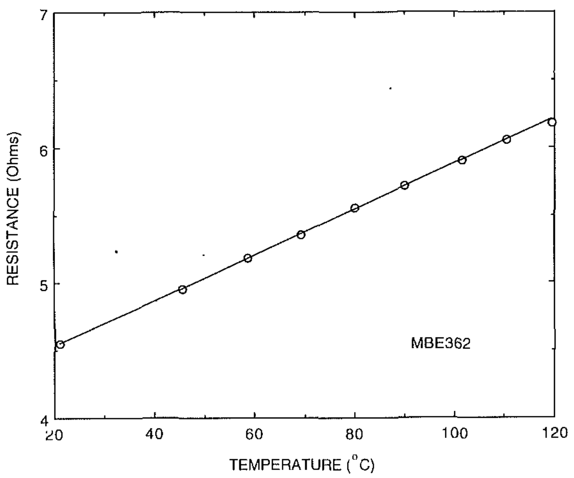

Fig. 6 Calibration of the temperature sensor

After the sensor was pattern onto the film, the substrate was removed by a selective etching technique (LePore, 1980). The etchant is a mixture of 30 percent hydrogen peroxide (H_2O_2) and 30 percent ammonium hydroxide (NH_4OH) with a volume ratio of 80:1. Etching a 400 μm substrate took about 2.7 hours. The etched area is about 3×3 mm^2, and is smooth and shiny. Examination by the Alphastep 200 profiler of a broken piece shows that the surface roughness is below 100 Å.

To determine the final thickness of the etched samples, the transmittance of the thin-film samples was measured in a Fourier Transform Infrared Spectrometer (FTIR) (Richter et al., 1993). The thickness of each sample was determined from the spacing of the interference peaks in the transmission pattern using tabulated values of optical constants for GaAs and AlGaAs (Palik, 1991). Figures 5(*a*) and 5(*b*) show the transmittance for samples MBE635 and MBE362 respectively. For MBE635, there are two periodicities: one is due to the GaAs film of 9.9 μm, the other is due to the AlGaAs etch-stop layer of 1.1 μm. For sample MBE362, the whole film could be treated as an effective medium and the film thickness was determined to be 7.21 μm. It should be noted, however, that these transmission curves are not supposed to be an absolute measurement of the transmittance because the temperature sensor will diffract part of the transmitted light.

After etching and cleaning, the sample was glued onto a 24-pin ceramic package by silver paste. A hole about 2mm in diameter was drilled in the ceramic holder before packaging and the sensor was carefully aligned as close as possible to the center of the hole. The sensor electrodes were subsequently bonded onto the package with an ultrasonic bonder.

The resistance of the sensor as a function of temperature was calibrated even though an absolute calibration is not necessary for the current method. Such a calibration served to monitor the average and transient temperature rise of the sample during experiments. A copper-constantant thermocouple was placed close to the sample and an infrared lamp was used as a heating source. The resistance of the sensor was measured by a HP4145A Semiconductor Parameter Analyzer. Figure 6 shows a calibration curve for sample MBE362.

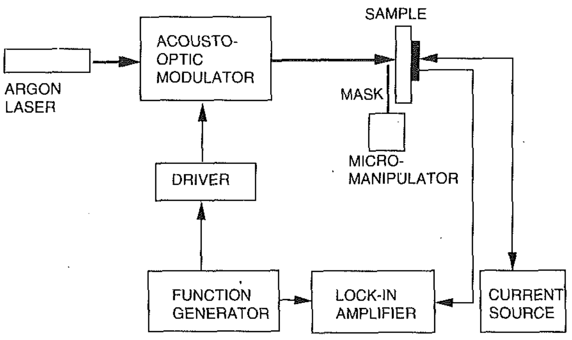

Fig. 7 Experimental setup

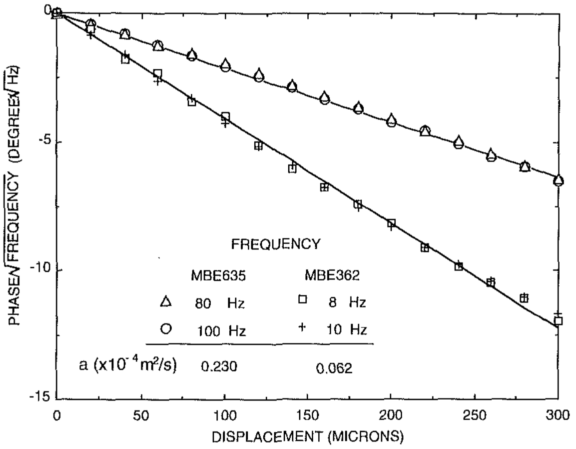

Fig. 8 Experimental results in the parallel direction

Experimental Setup. Figure 7 illustrates the experimental setup. An argon laser is used as the heating source. Its output is modulated by either a mechanical chopper or an acousto-optical modulator for low and high-frequency modulation, respectively. Because the argon laser emits photons of 2.41 eV, much larger than the band gap of GaAs (1.42 eV) and AlAs (2.163 eV), the photon energy is absorbed within a very thin layer of the sample (~ 0.1 μm). For measurement in the parallel direction, a mask is installed on a micromanipulator. The laser spot is large enough to cover the whole sample. For measurement in the perpendicular direction, the laser spot is about 2 mm. The output from the sample is sent to a lock-in amplifier and compared with the phase of the modulator.

Results and Discussion

The average temperature rise of the sample was less than 10 K during all the experiments. In the parallel direction, the modulation frequency was less than 200 Hz. In the perpendicular direction, the modulation frequency ranged from 20 kHz to 90 kHz.

Parallel Direction. The phase delay in the parallel direction as a function of the displacement of the mask edge relative to a reference point is shown in Fig. 8. From Eq. (4), the phase delay normalized by the square root of the modulation frequency should fall into a straight line independent of the modulation frequency. The slope of this line determines the thermal diffusivity of the sample. The measurement follows this prediction very well. Higher frequencies are used for sample MBE635 because its thermal diffusivity is larger and the effects of the finite size of the sample sets in at lower modulation frequencies (Hatta et al., 1987). The measured thermal diffusivities of samples MBE635 and MBE362 are 0.23×10^{-4} m^2/s and 0.068×10^{-4} m^2/s, respectively. Since both samples consist of multilayers of thin films, the measured values are compared with the effective thermal diffusivity calculated from Eq. (10). For sample MBE635, thermal conductivities of GaAs and $Al_{0.7}Ga_{0.3}$ As are 44 W/mK and 12 W/mK, respectively (Casey and Panish, 1978). The specific heat of GaAs is 330 J/kgK and the specific heat of $Al_{0.7}Ga_{0.3}As$ is estimated to be 410 J/kgK. The calculated effective thermal diffusivity of MBE635 is 0.24×10^{-4} m^2/s, which agrees with the measured value. This agreement is expected because the calculation (Chen and Tien, 1993a) shows that the thermal conductivity of a 10 μm GaAs film in the parallel direction should agree with the bulk value of GaAs. The size effect on the thermal conductivity of the 1.1 μm AlGaAs compound is not expected to be large because it has a much larger internal scattering rate, which causes its bulk thermal conductivity to be 4 and 8 times smaller than that of GaAs and AlAs, respectively. For MBE362 sample, the calculated bulk thermal diffusivity is 0.33×10^{-4} m^2/s, which is 4.85 times larger than the measured value. There are three possible reasons for the reduction of thermal diffusivity of this sample. The first is due to the doping of the top and bottom Bragg reflectors, the second is due to the interface scattering of phonons (Chen and Tien, 1993a), and the third is due to the phonon spectra change in the superlattice (Ren and Dow, 1982). The third is a quantum mechanical result of phonon scattering at the interfaces of a superlattice. Amith et al. (1965) measured thermal conductivity of GaAs at different doping concentrations and observed only a reduction of 20 percent for doping concentrations up to 6.4×10^{19} cm^{-3}. This indicates that the large reduction of the thermal diffusivity originates mainly from the interface scattering of phonons.

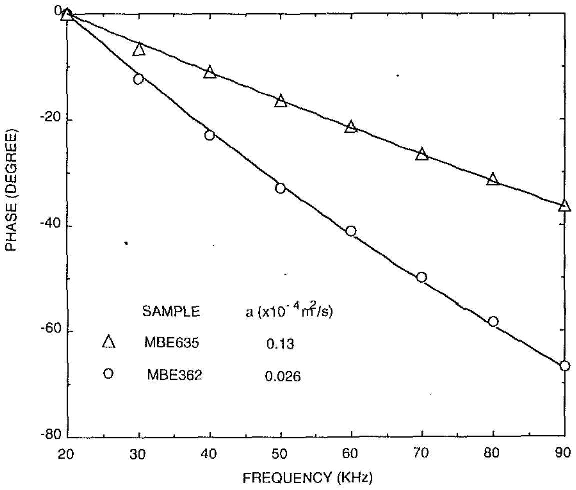

Fig. 9 Experimental results in the perpendicular direction

Perpendicular Direction. Figure 9 shows the results of the measurement in the perpendicular direction. The effective thermal diffusivities of samples MBE635 and MBE362 are 0.13×10^{-4} m^2/s and 0.026×10^{-4} m^2/s, respectively. To compare the measurement with bulk values, the effective thermal diffusivities of both samples were simulated according to the method described previously. For sample MBE635, the calculated effective thermal diffusivity is $0.121 \times 10^{-4} m^2/s$, which agrees with the measured value. The effective thermal diffusivity of sample MBE362 cannot be determined exactly because the $Al_{0.67}Ga_{0.3}As$ layer is approximated by complicated short period GaAs/AlAs superlattices (Walker et al., 1991). Instead, two possible extreme cases were considered. The lower limit is to assume that the thermal diffusivity of this layer approaches that of $Al_{0.67}Ga_{0.3}As$ compound. Experiments of Yao (1987) showed that thermal diffusivities of AlGaAs superlattices in the parallel direction are larger than those of their corresponding AlGaAs compounds. The effective thermal diffusivity calculated for this case is 0.126×10^{-4} m^2/s. The upper limit is to assume that thermal diffusivity of this AlGaAs layer in the perpendicular direction equals that calculated for the parallel direction (0.433×10^{-4}m^2/s). The effective thermal diffusivity thus calculated is 0.175×10^{-4} m^2/s. The measured thermal diffusivity of sample MBE362 is 4.85 times and 6.73 times smaller than the effective thermal diffusivity calculated from the bulk value for the worst and the best situations, respectively. Compared to the 4.85 times reduction in the parallel direction and based on the discussion following Eq. (15), the experimental data in the perpendicular direction suggest the reduction of thermal diffusivity in this direction is more severe than in the parallel direction. This anisotropy of thermal diffusivity is caused by the interface and boundary scattering of heat carriers. Furthermore, the discussion above is based on the assumption that thermophysical properties of each individual layer are well defined even though they are reduced. As pointed out, the long-range phonon interaction in the superlattice structure may well obscure the identity of each individual layer and require the whole superlattice structure be treated as one identity. In this case, the thermal diffusivity in the perpendicular direction is only 38 percent as large as the value in the parallel direction.

Error Analysis. From Eq. (5), the error of the measurement in the parallel direction can be estimated:

$$\left|\frac{\Delta a_{/\!/}}{a_{/\!/}}\right| = \left|\frac{\Delta f}{f}\right| + 2\left|\frac{d\Delta\varphi/dL}{d\varphi/dL}\right| \tag{16}$$

where $\Delta f/f$ is determined by the Q factor of the lock-in amplifier, which was 0.05 for most measurements. The value of the second term on the right-hand side of Eq. (17) is 0.28. The total relative error for the measurement in the parallel direction is 33 percent.

One concern in explaining the experimental results in the perpendicular direction is how sensitively the results depend on the thermal boundary resistance between the sensor and the sample. To answer this question, consider a composite film consisting of two layers: the sample and the sensor [Fig. 1 (b)]. Since the sensor is much thinner than the film, a lumped analysis for the sensor layer is justified. Solving the one-dimensional heat conduction equation yields the temperature rise of the sensor as

$$T_s = \frac{T_o/R}{1/R + i2\pi f\rho_s c_s h_s} \tag{17}$$

where R is the thermal boundary resistance between the film and the sensor, T_o the temperature at the film side of the film-sensor interface, and the subscript s represents properties of the sensor. The equation above implies that the importance of the thermal boundary resistance depends on its relative magnitude to the heat capacity of the film and the modulation frequency. For the gold sensor used in the experiment, the maximum value of $2\pi f\rho_s c_s h_s$ is 10^5 W/m^{2}K. There are, however, no experimental data on the thermal boundary resistance between the materials used in the experiments. A relatively close set of data is the thermal boundary resistance between Rh: FE and sapphire (Swartz and Pohl, 1987). At room temperature, the value of $1/R$ is in the range of $10^7 \sim 10^8$ W/Km^2, much larger than $2\pi f\rho_s c_s h_s$ in the denominator. Neglecting the latter leads to $T_s = T_0$, which means that the thermal boundary resistance between the film and the temperature sensor does not have significant effects on the results.

To estimate the experimental error in the perpendicular direction, Eq. (9) is first differentiated with respect to the grouped variable y, and then to the individual variables in y using the chain rule, which yields

Table 1 Summary of the experimental results

Sample	$a_{/\!/}(\times10^{-4}\text{m}^2/\text{s})$		$a_{\perp}(\times10^{-4}\text{m}^2/\text{s})$	
	Bulk	Measured	Bulk	Measured
MBE635	0.238	0.23 ± 0.075	0.121	0.13 ± 0.02
MBE362	0.330	0.062 ± 0.022	0.126 − 0.175	0.026 ± 0.003

$$\left|\frac{\Delta a_{\perp}}{a_{\perp}}\right| = 2\left|\frac{\Delta\varphi}{yg(y)}\right| + \left|\frac{\Delta f}{f}\right| + 2\left|\frac{\Delta h}{h}\right| \tag{18}$$

where $g(y)$ is the derivative of the right hand side of Eq. (9) with respect to y,

$$g(y) = \frac{1 - e^{-y}\sin(y) - e^{-2y}}{2[1 - 2e^{-y}\cos(y) + e^{-2y}]} \tag{19}$$

The maximum values of the first term on the right-hand side of Eq. (18) for samples MBE362 and MBE635 are 0.02 and 0.04, respectively. The relative error is 0.05 in frequency and 0.03 in thickness. The total relative uncertainties for samples MBE362 and MBE635 are 13 and 15 percent, respectively.

Table 1 summarizes the results of the measurement. Also given in the table are values of the corresponding bulk data for these samples. It clearly shows a large reduction in thermal diffusivity for the VCSEL structure and suggests an anisotropy in the thermal diffusivity, which are caused by the scattering of heat carriers at the interfaces and boundaries of the samples.

Conclusions

This work describes a new experimental method that can characterize the thermal diffusivity of thin films in both parallel and perpendicular directions and presents the experimental results on molecular-beam-grown single-crystal GaAs/AlGaAs thin-film structures. The results show that the thermal diffusivity of the vertical-cavity surface-emitting-laser structure is 5-7 times smaller than its corresponding bulk value. The experimental data also suggest an anisotropy of thermal diffusivity. This appears to be the first experiment that provides evidence on the anisotropy of thermophysical properties in single-crystal films without the influence of the substrate.

Acknowledgments

The authors would like to thank Dr. J. Walker for supplying sample MBE362 and Mr. T. Ha for lending them the jet etcher. They also gratefully acknowledge the assistance of their colleagues in the Quantum Electronics laboratory and staff in the Berkeley Microfabrication Laboratory. This project is financially supported by the Department of Energy.

References

Albin, S., Winfree, W. P., and Crews, B. S., 1989, "Thermal Diffusivity of Diamond Films," *SPIE*, Vol. 1146, pp. 85-94.

Amith, A., Kudman, I., and Steigmier, E. F., 1965, "Electron and Phonon Scattering in GaAs at High Temperatures," *Physical Review*, Vol. 138, pp. A1270-A1276.

Cahill, D. G., Fischer, H. E., Klitsner, T., Swartz, E. T., and Pohl, R. O., 1988, "Thermal Conductivity of Thin Films: Measurements and Understanding," *Journal of Vacuum Science and Technology A*, Vol. 7, pp. 1259-1266.

Casey, H. C., Jr., and Panish, M. B., 1978, *Heterostructure Lasers, Part B: Materials and Operating Characteristics*, Academic Press, New York, pp. 12, 232.

Chen, G., and Tien, C. L., 1993a, "Thermal Conductivity of Quantum Well Structures," AIAA *Journal of Thermophysics and Heat Transfer*, Vol. 7, pp. 311-318.

Chen, G., and Tien, C. L., 1993b, "Facet Heating of QW Lasers," *Journal of Applied Physics*, Vol. 74, pp. 2167-2174.

Flik, M. I., and Tien, C. L., 1990, "Size Effects on the Thermal Conductivities of High-T_c Thin-Film Superconductors," ASME JOURNAL OF HEAT TRANSFER, Vol. 112, pp. 872-881.

Hatta, I., Sasuga, Y., Kato, R., and Maesono, A., 1985, "Thermal Diffusivity Measurement of Thin Films by Means of an ac Calorimetric Method," *Review of Scientific Instruments*, Vol. 56, pp. 1643-1647.

Hatta, I., Kato, R., and Maesono, A., 1987, "Development of ac Calorimetric

Method for Thermal Diffusivity Measurement, *Japanese Journal of Applied Physics*, Vol. 26, pp. 475–478.

Hatta, I., 1990, "Thermal Diffusivity Measurement of Thin Films and Multilayered Composites," *International Journal of Thermophysics*, Vol. 11, pp. 293–303.

Lambropoulos, J. C., Jacobs, S. D., Burns, S. J. and Shaw-Klein, L., 1992, "Effects of Anisotropy, Interfacial Thermal Resistance, Microstructures, and Film Thickness on the Thermal Conductivity of Dielectric Thin Films," ASME HTD-Vol. 227, pp. 37–49.

LePore, J. J., 1980, "An Improved Technique for Selective Etching of GaAs and $Ga_{1-x}Al_xAs$," *Journal of Applied Physics*, Vol. 51, pp. 6441–6442.

Meade, M. L., 1983, *Lock-in Amplifiers: Principles and Applications*, Peter Peregrinus Ltd., London, UK.

Osinski, M., 1991, "Vertical-Cavity Surface-Emitting Semiconductor Lasers: Present Status and Future Prospects," *SPIE*, Vol. 1418, pp. 1–24.

Palik, E. D., ed., 1991, *Handbook of Optical Constants of Solids II*, Academic Press, Boston.

Ren, S. Y., and Dow, J. D., 1982, "Thermal Conductivity of Superlattice," *Physical Review B.*, Vol. 25, pp. 3750–3755.

Richter, K., Chen, G., and Tien, C. L., 1992, "Partial Coherence Theory of Multilayer Thin-Film Optical Properties," *Optical Engineering*, Vol. 32, pp. 1897–1903.

Swartz, E. T., and Pohl, R. O., 1987, "Thermal Resistance at Interfaces," *Applied Physics Letters*, Vol. 51, pp. 2200–2222.

Taylor, R., 1983, "Thermal Diffusivity of Composites," *High Temperature—High Pressure*, Vol. 15, pp. 299–309.

Tien, C. L., and Chen, G., 1992, "Challenges in Microscale Radiative and Conductive Heat Transfer," ASME HTD-Vol. 227, pp. 1–10.

Walker, J. D., Kuchta, D. M., and Smith., J. S., 1991, "Vertical-Cavity Surface-Emitting Laser Diodes Fabricated by Phase-Locked Epitaxy," *Applied Physics Letters*, Vol. 59, pp. 2079–2081.

Yang, G., Migone, A. D., and Johnson, K. W., 1991, "Automated Apparatus for the Determination of the Specific Heat and the Thermal Diffusivity of Nonconducting Solids Using ac Technique," *Review of Scientific Instruments*, Vol. 62, pp. 1836–1839.

Yao, T., 1987, "Thermal Properties of AlAs/GaAs Superlattices," *Applied Physics Letters*, Vol. 51, pp. 1798–1800.

Experimental Study on Convective Heat Transfer for Turbulent Flow in a Square Duct With a Ribbed Rough Wall (Characteristics of Mean Temperature Field)

M. Hirota
Assistant Professor,
Department of Mechanical Engineering.

H. Fujita
Professor,
Department of Mechanical Engineering.

H. Yokosawa
Professor,
School of Informatics and Sciences.

Nagoya University,
Furocho, Chikusa-ku,
Nagoya 464-01, Japan

This paper presents experimental results concerning a time-mean temperature field obtained in forced convection heat transfer for a turbulent flow through a square duct with a ribbed rough bottom wall. The secondary flow pattern in the duct is reflected in the distribution of the local Nusselt number, the values of which on the smooth walls of the rough duct are 1.71 ~ 1.97 times those of the smooth duct. In the upper half cross section near the upper smooth wall opposite the bottom ribbed rough wall, the profile of the mean temperature distribution is similar to that of the primary flow velocity distribution, and the validity of the temperature inner law was confirmed. However, in the lower half cross section near the bottom ribbed rough wall, the dissimilarity between the mean velocity and the mean temperature fields becomes pronounced, and the inner law is not valid for mean temperature distributions. The mechanism of the heat transfer near the ribbed rough wall was examined based on the transport equations of turbulent shear stress and turbulent heat flux.

Introduction

The application of ribs for roughening the inner surfaces of noncircular ducts is one of several typical ways of heat transfer improvement, and a number of research works by Sparrow and Tao (1983, 1984), Han (1984, 1988), Han et al. (1985), Metzger et al. (1990), and Liou and Hwang (1992) have dealt with related issues. In ducts with a noncircular cross section, the anisotropic turbulent stress field generates a secondary flow of the second kind (e.g., Melling and Whitelaw, 1976; Humphrey and Whitelaw, 1980). The present authors have directed their attention to changes in the turbulence structure in rectangular ducts due to the rough surfaces and the resulting secondary flow. They have previously reported that the secondary flows observed in various rectangular ducts with rough walls have different patterns from those observed in the corresponding smooth ducts (Fujita et al., 1989a, 1990a, 1990b; Yokosawa et al., 1989).

As for a smooth-walled square duct, it has been proven experimentally and documented numerically that characteristics of heat transfer as well as turbulence structure are under the influence of the secondary flow of the second kind (Brundrett and Burroughs, 1967; Launder and Ying, 1973; Emery et al., 1980). Therefore, it is expected that, combined with the effects of rough walls on heat transfer augmentation inherent in the rough wall, the secondary flow makes for a highly complicated mechanism of forced convection heat transfer in rough ducts (Fujita et al., 1988). Until now most published papers reporting heat transfer augmentation in rough ducts have focused only on the high heat transfer rate on the rough wall. However, one should also examine the mechanism of heat transfer improvement in rough ducts, not only the rough wall heat transfer coefficient but the characteristics of the entire temperature field in the ducts, with attention to the secondary flow effects as well. To the best of our knowledge, very few papers have pursued this to date (Metzger et al., 1990).

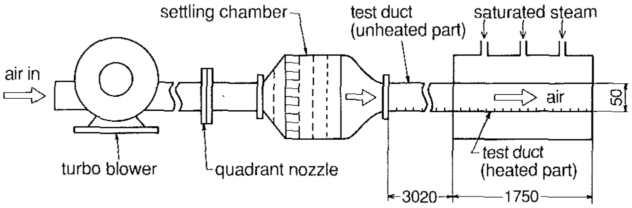

Fig. 1 Schematic diagram of experimental apparatus

The purpose of this study is to help understand the heat transfer augmentation mechanism in ducts with a single rough wall and to grasp experimentally the characteristics of the time-mean temperature field. The results of mean temperature measurements in a square duct with a ribbed bottom wall are compared with those obtained in a smooth square duct. On the basis of the transport equations of turbulent shear stress and turbulent heat flux, the mechanism of heat transfer enhancement by the rough wall is discussed.

Recently, with the progress in turbulence models, numerical analyses on turbulent heat transfer in a smooth square duct have been conducted (e.g., Myong, 1991). The present experimental results could be used to examine the results of these numerical analyses and to check the validity of existing and future turbulence models.

Experiment

Figure 1 shows a diagram of the experimental apparatus. Air at room temperature is introduced into the straight test duct after flowing through a quadrant flow nozzle and a settling chamber. The square test duct is $D = 50$ mm wide and 4770 mm (= 95.4 D) in length. The duct includes a heating part

---

Contributed by the Heat Transfer Division and presented at the 29th National Heat Transfer Conference, Atlanta, Georgia, August 8-11, 1993. Manuscript received by the Heat Transfer Division October 1992; revision received July 1993. Keywords: Forced Convection, Turbulence. Associate Technical Editor: T. W. Simon.

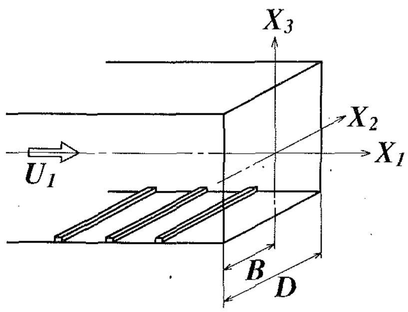

Fig. 2(*a*) Definition of coordinate system and geometric parameters

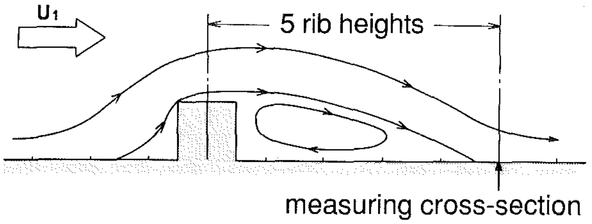

Fig. 2(*b*) Location of the measuring cross section relative to rib and schema of the streamlines

Fig. 2 Coordinate system and location of the measuring cross section

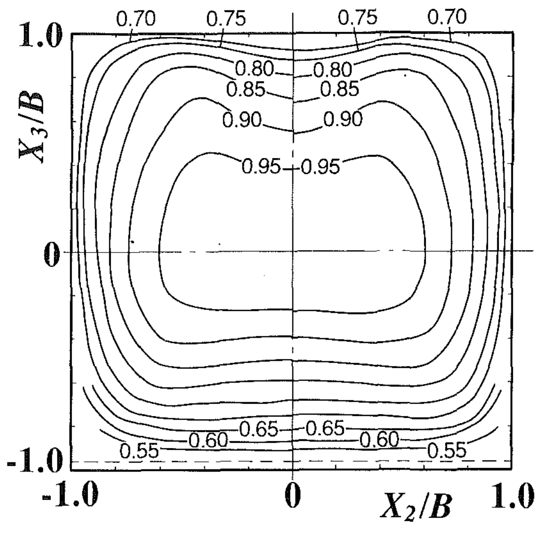

(a) Isothermal **(b) Heated**

Fig. 3 Comparison of U_1/U_s in (*a*) isothermal condition and (*b*) heated condition (broken line at the bottom of the figure corresponds to the roughness height)

that has a double-duct structure and is between the duct exit and 1750 mm (=35 *D*) upstream from the exit. From the preliminary measurements of the primary flow velocity in the smooth walled duct, it was ascertained that the fully developed velocity profiles are attained about 50 *D* downstream from the duct entrance. Therefore, the flow is fully developed when it reaches the heating part. The inner duct of the heating part, which is the test duct of D = 50 mm, is made of 10-mm-thick aluminum plate. Saturated steam at atmospheric pressure flows through the passage between the inner and outer ducts of the heating part, and condenses on the outer surface of the inner duct to maintain the whole wall of the inner duct isothermally at a temperature of about 373 K. No active methods were used to remove condensed steam from the inner-duct walls. In order to verify that the isothermal heating condition was satisfied, 52 thermocouples were inserted in the inner-duct walls along the wall bisectors at a pitch of 260 mm between 1.6 *D* to 22.4 *D* downstream of the heating part entrance and around the circumference of the inner duct at locations of 27.6 *D* and 33 *D* downstream of the entrance. The scattering of the measured wall temperatures was less than 0.3°C and the uniformity of the wall temperature distribution is considered to be excellent. Note that the condition of the isothermal wall for a temperature field corresponds to the wall boundary condition of "nonslip" for a flow field.

Figure 2(*a*) shows the coordinate system. The origin of the X_1 axis is located at the entrance of the test duct. The bottom wall of the duct is the rough wall and is perpendicular to the X_3 axis. The rough wall with two-dimensional ribs of 1 mm × 1 mm cross section was produced by machining from an aluminum plate. The rib roughness elements are arranged perpendicularly to the X_1 axis at a pitch of 10 mm over the total length of the test duct (477 ribs from X_1 = 5 mm to X_1 = 4765 mm) and are maintained at practically the same temperature as their base. Measurements were made at the cross section 100 mm (=2 *D*) upstream from the duct exit, i.e., at a location of X_1/D = 93.4, where both velocity and temperature fields can be considered to be fully developed (Hishida

Nomenclature

B = $D/2$
C_p = specific heat of fluid under constant pressure
D = hydraulic diameter of duct = side length of duct cross section
k = thermal conductivity of fluid
Nu = local Nusselt number = $q_w \cdot D/\{k \cdot (T_w - T_b)\}$
$\overline{Nu}$ = average Nusselt number
Pr_t = turbulent Prandtl number
q_w = local wall heat flux
Re = Reynolds number = $U_b \cdot D/\nu$
T = time-mean temperature of fluid
t = fluctuating temperature of fluid
T_w = wall temperature
T^+ = dimensionless time-mean temperature of fluid = $(T_w - T)/T^*$
T^* = friction temperature = $q_w/(\rho \cdot C_p \cdot U^*)$
t^+ = dimensionless fluctuating temperature of fluid = $\sqrt{\overline{t^2}}/T^*$
U_b = fluid velocity averaged over a duct cross section
U_1, U_2, U_3 = time-mean velocity components in the X_1, X_2, and X_3 directions
U^+ = dimensionless time-mean velocity = U_1/U^*
U^* = friction velocity = $\sqrt{\tau_w/\rho}$
u_1, u_2, u_3 = fluctuating velocity components in the X_1, X_2, and X_3 directions
X_1, X_2, X_3 = coordinate system defined in Fig. 2
Y = wall distance
Y^+ = dimensionless wall distance = $U^* \cdot Y/\nu$
Θ = difference between wall temperature T_w and fluid temperature = $(T_w - T)$
ν = kinematic viscosity of fluid
ρ = density of fluid
τ_w = local wall shear stress

Subscripts

b = values averaged over a duct cross section
s = values at the center of a duct cross section

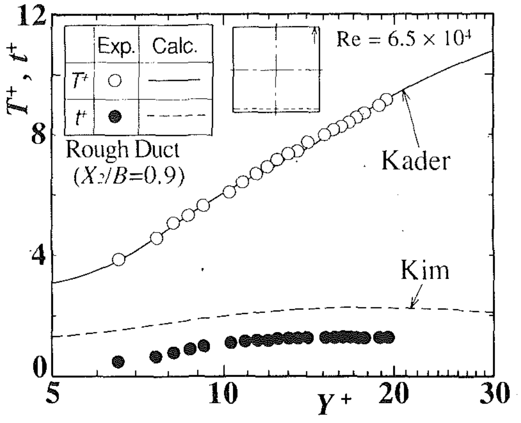

Fig. 4 Mean and fluctuating temperature distributions immediately near the upper smooth wall

and Nagano, 1979). In the rough duct, a midway point between successive roughness elements was selected to set a measuring cross section. Figure 2(*b*) shows the location of the present measuring cross section relative to the rib roughness and a schema of the streamlines near the rough wall (Hirota et al., 1992). The present measuring cross section (5 rib heights downstream of the upstream rib) is set in the immediate vicinity of the flow reattachment point, which is estimated to be located about 4.5 rib heights downstream of the rib (Hijikata et al., 1987). In the preceding experiments, the authors have made clear that the distribution profiles of the turbulence stresses do not change depending on the locations of the measuring cross section relative to the rib, despite considerably large differences in the streamwise distributions of the production rates of those stresses (Hirota et al., 1992). It is therefore expected that the experimental results obtained in the present cross section can be applied to other locations such as cross sections nearer the rib.

Measurements of the temperature and the velocity distributions in the duct cross section were made with a single Reynolds number of 6.5 × 10^4 based on the air properties at the entrance of the heating part. The range of the air temperature entering the heating part was from 15.0°C to 18.8°C. The conditions of the present experiment, according to the classification of Metais and Eckert (1964), demonstrate a phenomenon that can be regarded as turbulent forced convection with negligible effects of natural convection. In Fig. 3, contour maps of the primary flow velocities in the rough duct with and without heating are shown for comparison. Conformation of the experimental results in the two conditions confirms that there is a negligible influence of natural convection.

An average Nusselt number, $\overline{Nu}$, obtained in the present rough duct was expressed for the Reynolds numbers $2.0 \times 10^4 < Re < 8 \times 10^4$ as $\overline{Nu} = 0.0266 \times Re^{0.824}$, where $\overline{Nu}$ was obtained by circumferential and flow directional integration between the entrance and the exit of the heating part of the test duct. For the smooth duct, $\overline{Nu}$ was expressed as $\overline{Nu} = 0.0221 \times Re^{0.8}$ (Fujita et al., 1989b). The values of $\overline{Nu}$ calculated by this empirical formula are smaller by 6.7 percent than those given by Sieder-Tate equation (Kays and Perkins, 1985) developed for smooth walled circular pipes.

Air temperature was measured by a resistance thermometer with a tungsten-wire temperature sensor of length 1.0 mm and diameter 5 μm. Because of the low cut-off frequency (~400 Hz), quantitative discussion on fluctuation temperature is omitted here. The maximum uncertainties involved in measured values were estimated as follows (JSME, 1987): U_1: ±1.4 percent, U_3 ±6.0 percent, $\overline{u_1^2}$: ±2.4 percent, $\overline{u_3^2}$: ±8.6 percent, $\overline{u_1 u_3}$: ±4.9 percent, T: ±2.3 percent, q_w: ±14.1 percent.

Since the results of measurements at the cross section were extremely symmetric with respect to the axis of geometric symmetry of the duct cross section (X_3 axis), only the results in half the cross section are presented in the rest of this paper.

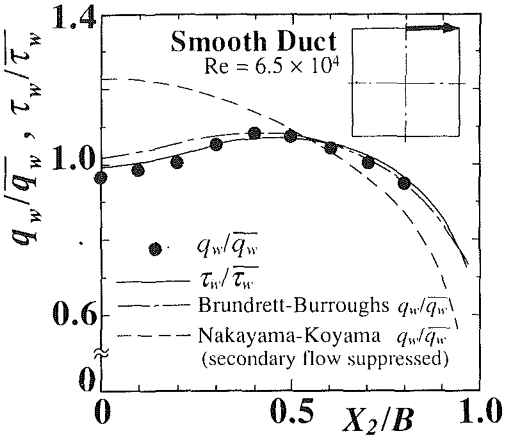

Fig. 5 Distributions of local wall heat flux q_w and local wall shear stress τ_w in the smooth duct

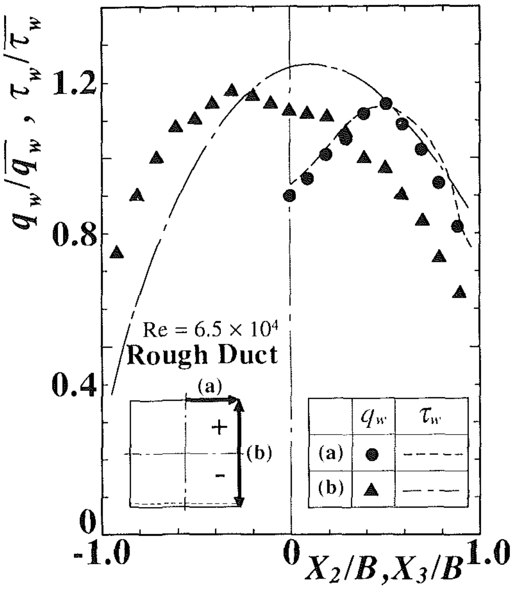

Fig. 6 Distributions of local wall heat flux q_w and local wall shear stress τ_w in the rough duct

Experimental Results

Local Wall Heat Flux. In general, it is very difficult to measure a local wall heat flux, q_w, on an isothermally heated wall. In the present experiment, q_w was calculated using equation $q_w = -k(dT/dY)_w$. To obtain the mean temperature gradient at the wall surface $(dT/dY)_w$, air temperatures at $Y <$ 0.3 mm were measured at 10 μm intervals, where Y denotes the vertical distance from the wall. Temperature measurement was limited to the area above the smooth walls. Since the diameter of the tungsten-wire temperature sensors was extremely small, the measurement error in the reading of the mean temperature T, which might be caused by the temperature gradient dT/dY, was negligibly small, and no calibrations were made in the data of $(dT/dY)_w$. The uncertainties involved in $(dT/dY)_w$ were estimated to be rather larger (~ ±14 percent) than those involved in other quantities measured in the present experiment.

Figure 4 is an example of the distributions of the dimensionless mean temperature T^+ and fluctuating temperature t^+, which was obtained near the upper corners of the rough duct where $X_2/B = 0.9$. In the figure the solid line shows Kader's

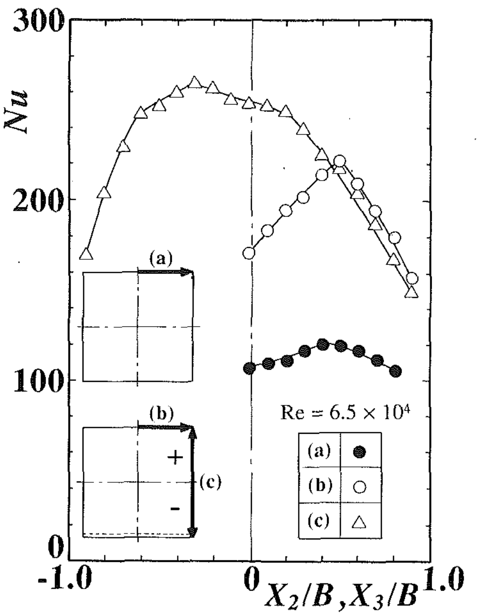

Fig. 7 Distributions of local Nusselt numbers

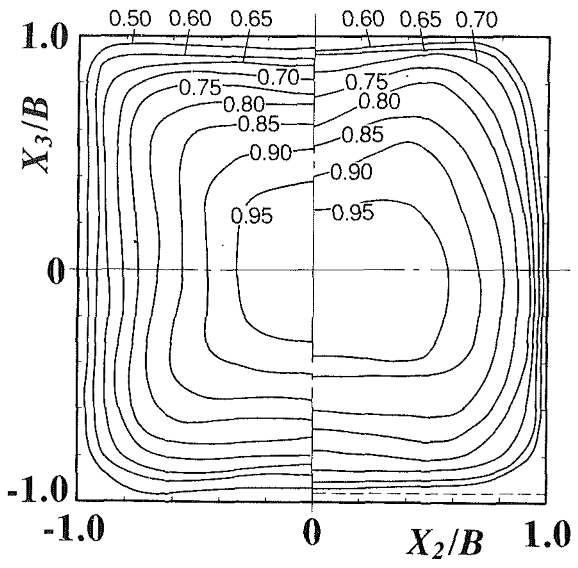

(a) Smooth Duct (b) Rough Duct

Fig. 8 Contour map of mean temperature Θ/Θ_s

(1981) theoretical results for a mean temperature distribution while the broken line indicates a fluctuation temperature distribution obtained by Kim (1987) by means of DNS (Direct Numerical Simulation). These two lines are for turbulent flows in a two-dimensional passage with smooth walls. The results of mean temperature T^+ are in very good accordance with Kader's results. This shows that immediately near the upper smooth wall ($Y^+ < 20$) the distributions of T^+ agree well with those obtained in the two-dimensional passage and the influences of the neighboring wall do not appear prominently in the T^+ distributions. Moreover, the distributions of T^+ immediately near the side smooth wall of the rough duct were also in accordance with Kader's theory.

As for t^+, the measured value increases with the increase in Y^+ immediately near the wall and varies little in $Y^+ > 15$. The qualitative tendency is in accordance with that of the results of DNS, though there is a considerable quantitative difference between the two. It is thought that the values smaller than DNS obtained are caused by deterioration in the response of the resistance thermometer to high frequencies in fluctuating temperature due to the finite heat capacity of the tungsten sensor. From a quantitative viewpoint, the present experimental results of t^+ may be less reliable than those of T^+.

Figures 5 and 6 show the distributions of local wall heat flux q_w obtained in the smooth duct and on the smooth walls of the rough duct, respectively, with local wall stress τ_w measured for an isothermal flow in the corresponding ducts (Fujita et al., 1990b). q_w and τ_w were normalized by $\overline{q_w}$ and $\overline{\tau_w}$, respectively, both obtained by circumferential integration on each smooth wall. In the smooth duct, as shown in Fig. 5, the distribution of q_w obtained in the present experiment is in strong accordance with the values of q_w measured by Brundrett and Burroughs (1967) represented by a dot-dashed line. q_w has the local minimum value at the midpoint of a wall ($X_2/B = 0$) and increases with X_2/B to attain the maximum at $X_2/B = 0.5$, then decreases toward the corners of the duct. This distribution of q_w agrees well with that of τ_w. Nakayama and Koyama (1986) obtained q_w numerically for the turbulent flow in a smooth-walled square duct with suppression of the secondary flow of the second kind. This result is represented by the broken line in Fig. 5. The differences between the experimental values and this numerical result show that the secondary flow brings about circumferentially uniform distribution of q_w.

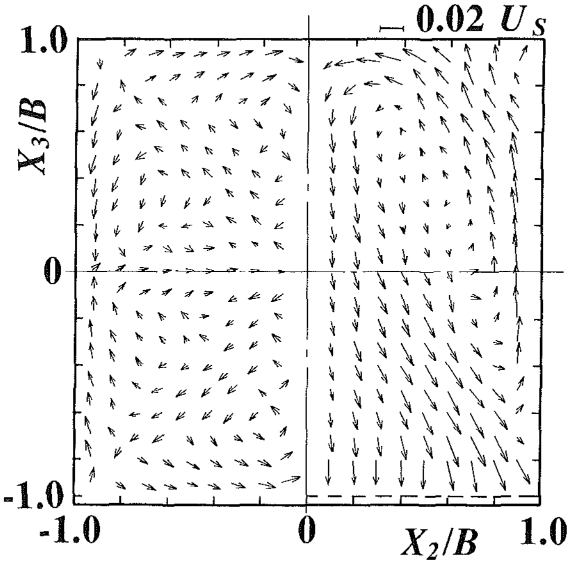

(a) Smooth Duct (b) Rough Duct

Fig. 9 Secondary flow vector diagrams

In the rough duct, shown in Fig. 6, q_w on the upper smooth wall shows qualitatively a similar tendency as in the smooth duct, although the difference between the maximum value at $X_2/B = 0.5$ and the local minimum at $X_2/B = 0$ is considerably larger than that in the smooth duct. As for the side smooth walls of the duct, there is no local minimum in the distribution. The maximum value is found at $X_3/B = -0.3$, close to the bottom rough wall. On the upper smooth wall, the distribution of τ_w agrees very well with that of q_w, as observed in the smooth duct. On the other hand, on the side wall the distribution of τ_w differs from that of q_w. Dissimilarity in the distributions of q_w and τ_w is especially prominent on the lower half (nearer the rough wall) of the side wall. It is thought that this dissimilarity in q_w and τ_w distributions reflects the dissimilarity in the distributions of the primary flow velocity and the mean temperature, which will be described in detail in the following sections.

Figure 7 shows the distributions of the local Nusselt number

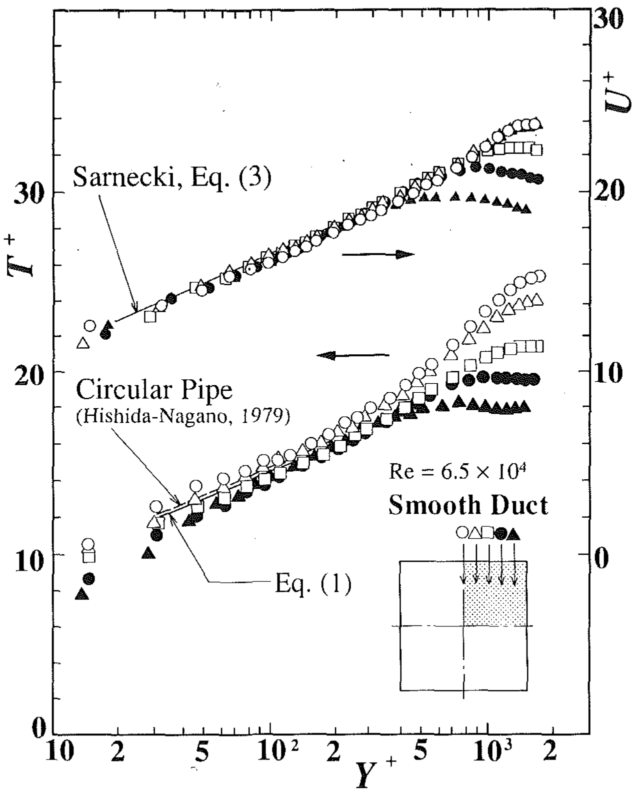

Fig. 10 Distributions of mean temperature and velocity in wall coordinates in the smooth duct

$\mathrm{Nu} = q_w \cdot D/\{k \cdot (T_w - T_b)\}$ on the smooth walls in the rough and smooth ducts, where T_b denotes the bulk temperature of air obtained at $X_1/D = 93.4$. The averaged value of local Nusselt number on the upper smooth wall of the rough duct is about 188, which is 1.71 times the averaged value of the smooth duct at about 110. In the cases of the side smooth walls, the averaged value of Nu is 217, or 1.97 times that of the smooth duct. These ratios of Nu averaged on each smooth wall of the rough duct to the corresponding value of the smooth walled duct are in good agreement with the results reported by Metzger et al. (1990), who obtained the ratios of 1.47 at $\mathrm{Re} = 2.5 \times 10^4$ and 1.68 at $\mathrm{Re} = 5.7 \times 10^4$ in a square duct with two ribbed rough walls on opposite sides. These data indicate that heat transfer coefficients increase not only on the rough wall but also on the smooth walls in the rough duct. This heat transfer enhancement observed on the smooth walls of the rough duct is attributed to the secondary flow intensified by the presence of the rough wall (see Fig. 9).

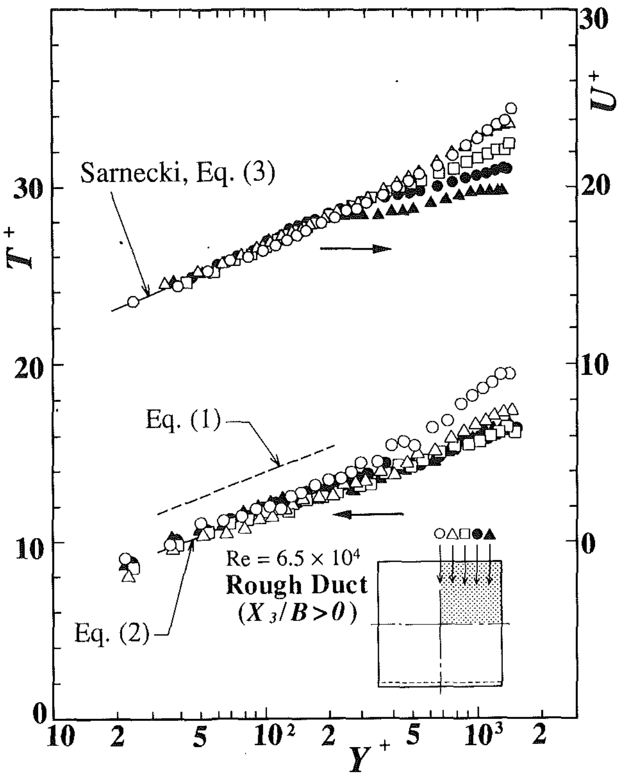

Fig. 11(*a*) Upper half ($X_3/B>0$)

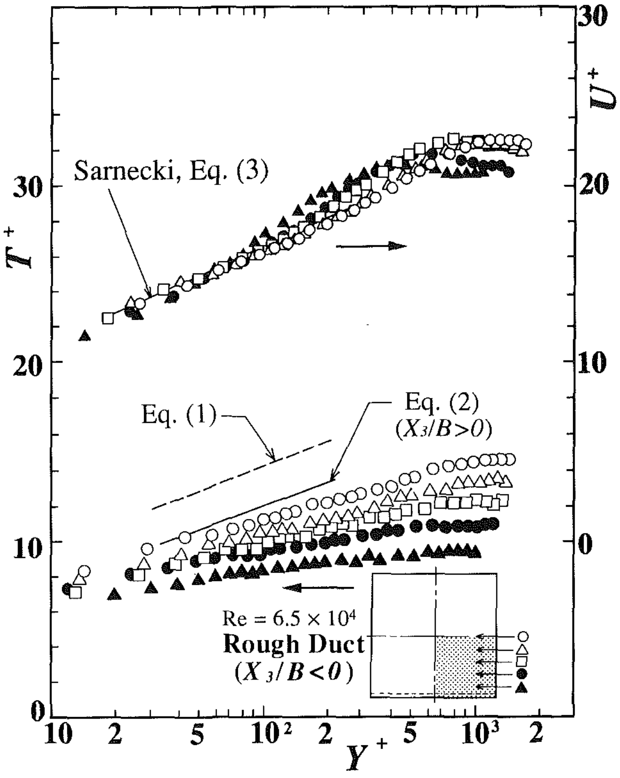

Fig. 11(*b*) Lower half ($X_3/B<0$)

Fig. 11 Distributions of mean temperature and velocity in wall coordinates in the rough duct

Mean Temperature Distributions. Figure 8 shows contour maps of the mean temperature Θ/Θ_s for the smooth and rough ducts. Contours for the smooth duct have bulges toward corners along corner bisectors. They bear a close resemblance to those of the mean primary flow velocities seen elsewhere (e.g., Melling and Whitelaw, 1976). In the rough duct shown in Fig. 8(*b*), the contours have depressions near the upper smooth wall and bulges near the side walls. These characteristics qualitatively resemble those of the mean primary flow velocity shown in Fig. 3. The distortion observed in the contour map of Fig. 8 is illustrated by the secondary flow vector diagram shown in Fig. 9 (Fujita et al., 1989a). In the smooth duct, the bulge of contours shows that the secondary flow transports low-temperature fluid from the core to the corners of the duct. In the rough duct, downward secondary flows near the X_3 axis cause the depression in the temperature contours near the upper smooth wall. Consequently, the mean temperature gradient in the X_3 direction, dT/dX_3, on the upper smooth wall is small at $X_2/B = 0$ and is larger at $X_2/B = 0.5$, which reflects the location of the local minimum and the maximum in the q_w distribution shown in Fig. 6.

Figure 10 shows the universal temperature distributions and the universal velocity distributions for the smooth duct. The broken line shows the distribution of T^+ for a turbulent flow

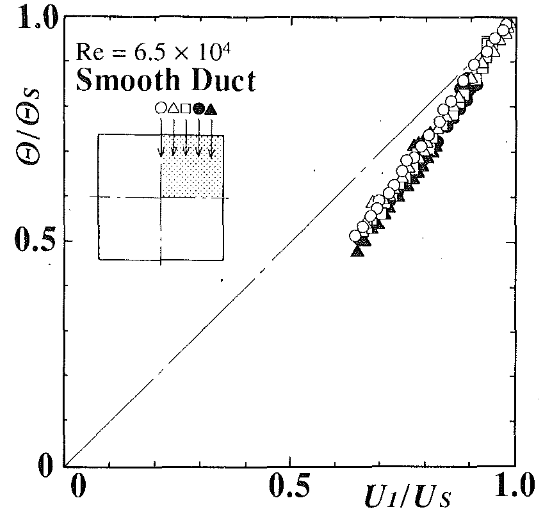

Fig. 12 Correlation between U_1/U_s and Θ/Θ_s in the smooth duct

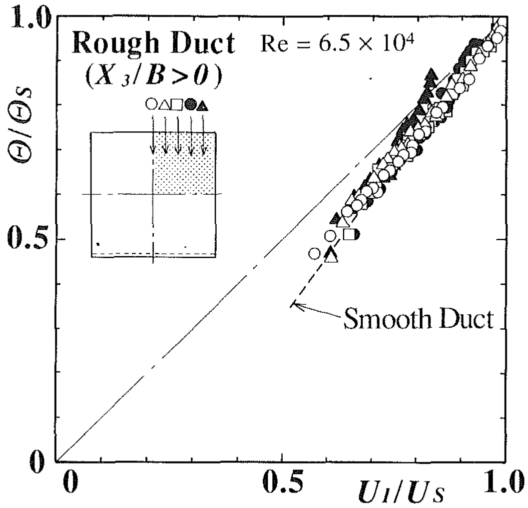

Fig. 13(*a*) Upper half ($X_3/B > 0$)

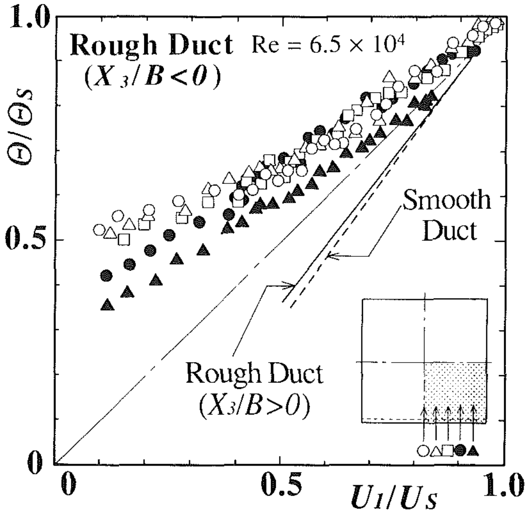

Fig. 13(*b*) Lower half ($X_3/B < 0$)

Fig. 13 Correlation between U_1/U_s and Θ/Θ_s in the rough duct

in a circular pipe obtained by Hishida and Nagano (1979). The results of T^+ obtained along each constant value of X_3/B fall on a line in the turbulent part of the wall region $30 < Y^+ < 200$ where an inner law is generally valid (Hishida and Nagano, 1979). This indicates that the inner law expressed by the logarithmic formulation is valid for the mean temperature distribution in the smooth duct. The following logarithmic law was obtained for a relation between T^+ and Y^+, and is shown by the solid line in Fig. 10.

$$T^+ = 4.98 \log Y^+ + 4.48 \tag{1}$$

The distribution of Eq. (1) is similar to that obtained by Brundrett and Burroughs (1967) in a smooth square duct.

Figure 11(*a*) shows the universal temperature and velocity distributions for the rough duct obtained along the lines perpendicular to the upper smooth wall in the upper half of the cross section ($X_3/B > 0$). On this wall, the distribution of q_w was similar to that of τ_w as shown in Fig. 6. A relation between T^+ and Y^+ is expressed at $30 < Y^+ < 200$ even near the corner as:

$$T^+ = 4.32 \log Y^+ + 3.14 \tag{2}$$

This shows that the temperature inner law holds near the upper wall. Equation (2) was also applied for the distribution of T^+ near the side walls in the upper half of the rough duct. But in the lower half nearer the rough wall ($X_3/B < 0$), where the dissimilarity was found between q_w and τ_w distributions, the profiles of T^+ differ from each other depending on the values of X_3/B as shown in Fig. 11(*b*). The inner law is therefore not valid for the mean temperature profile in the lower half of the rough duct.

As shown in Figs. 10 and 11, in the turbulent part of the wall region ($30 < Y^+ < 200$), the mean velocity profiles measured along lines perpendicular to the smooth walls of both the smooth and rough ducts are in good agreement with the logarithmic law velocity profile proposed by Sarnecki, which is expressed by the following equation (Patel, 1965):

$$U^+ = 5.5 \log Y^+ 5.4 \tag{3}$$

The turbulent Prandtl number Pr_t in the turbulent part of the wall region is calculated as (Hishida et al., 1986):

$$\mathrm{Pr}_t = \kappa_m/\kappa_t = \frac{\partial T^+/\partial Y^+}{\partial U^+/\partial Y^+} \tag{4}$$

where κ_m and κ_t denote the Karman constants of the velocity and temperature fields, respectively. The values of the Karman constants for the smooth duct are determined from Eqs. (1) and (3) as $\kappa_t = 0.462$ and $\kappa_m = 0.419$, respectively. Those for the upper half of the rough duct are $\kappa_t = 0.533$ and $\kappa_m = 0.419$. Therefore, Eq. (4) leads to the estimation of $\mathrm{Pr}_t = 0.91$ for the smooth duct, and $\mathrm{Pr}_t = 0.79$ for the upper half of the rough duct. In the lower half of the duct, however, Pr_t is expressed as a function of the location in the cross section and does not have a constant value. These results lead to the conclusion that the assumption of a constant turbulent Prandtl number everywhere in a cross section as generally used in numerical analysis of temperature field (e.g., Myong, 1991) is valid only for the smooth duct and completely inapplicable to the rough duct. Improved models of turbulent heat transfer that do not include the turbulent Prandtl number must be used for the numerical prediction of heat transfer in rough ducts.

Comparison of Mean Temperature and Velocity Profiles. To examine the similarity between the temperature and the velocity fields, the correlation between the mean temperature Θ/Θ_s and the mean velocity U_1/U_s, both of which have been measured between $X_2/B = 0$ to $X_2/B = 0.8$ at a pitch of $0.2\,B$ in the cross section of $X_1/D = 93.4$, is shown in Figs. 12 and 13 for the smooth and rough ducts, respectively. When the temperature profile is in perfect agreement with that of velocity, Θ/Θ_s is equal to U_1/U_s everywhere, and the correlation follows the straight line shown by a dot-dashed line in the figure (Subramanian and Antonia, 1981). Accordingly it is plausible that the more the temperature Θ/Θ_s correlates with

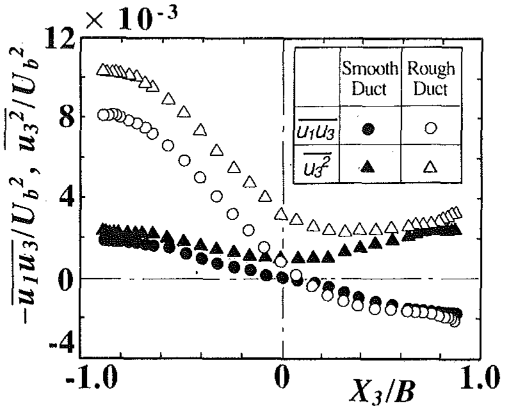

Fig. 14 Distributions of $-\overline{u_1u_3}$ and $\overline{u_3^2}$ on the X_3 axis

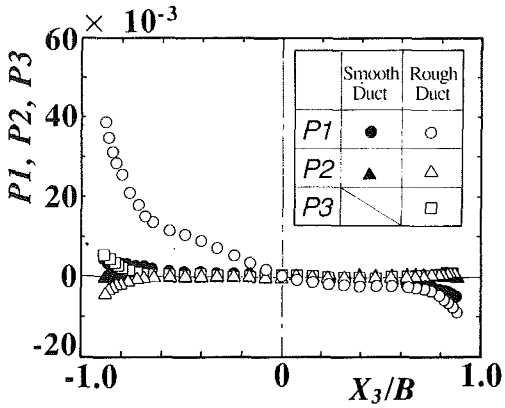

Fig. 15 Distributions of the production term for $-\overline{u_1u_3}$

the velocity U_1/U_s, the more complete is the similarity between the temperature and the velocity fields.

In the smooth duct, as shown in Fig. 12, the results fall on a straight line. This demonstrates that Θ/Θ_s correlates highly with U_1/U_s and suggests the similarity between the temperature and the velocity fields. The values of Θ/Θ_s are smaller than those of U_1/U_s for $\Theta/\Theta_s < 0.9$. Similar results are also found in the relationship between Θ/Θ_s and U_1/U_s obtained in a circular pipe by Hishida and Nagano (1979).

Figure 13(*a*) shows the results for the upper half ($X_3/B > 0$, nearer the upper smooth wall) of the rough duct. The dashed line in the figure was obtained from the results in the smooth duct by the least-squares method. Comparing Fig. 13(*a*) with Fig. 12, the correlation between Θ/Θ_s and U_1/U_s in the upper half of the rough duct is similar to the results in the smooth duct.

As for the lower half ($X_3/B < 0$, nearer the rough wall) of the rough duct shown in Fig. 13(*b*), however, the results deviate prominently from the dot-dashed line, and the differences due to trace lines of the sensor probes are pronounced. There is little correlation between $\Theta/\Theta_s$and U_1/U_s in the lower half of the rough duct. It follows that the dissimilarity between the temperature and the velocity fields is very pronounced in the lower half of the rough duct. In addition, at almost all measuring points in the lower half, the values of Θ/Θ_s are larger than those of U_1/U_s. In a fictitious duct in which the transport process of heat due to turbulence is assumed to be exactly analogous to that of momentum, the values of Θ/Θ_s should agree with those of U_1/U_s everywhere in the duct cross section. The larger values of Θ/Θ_s observed in Fig. 13(*b*), i.e., lower values of mean fluid temperature T than expected in this fictitious duct, suggest that the turbulence transport of heat in the present rough duct is smaller than that in the fictitious duct. This leads to the conclusion that, in the area near the rough wall of the present rough duct, heat transfer due to turbulence is inferior to momentum transfer.

Discussion

In the preceding study on turbulence kinetic energy in the rough duct (Hirota et al., 1992), it was reported that the reattachment of flow downstream of the rib may restrain the heat transfer enhancemnt by the rough wall through the negative production of the fluctuation velocity normal to the rough wall. For our discussion on the mechanism of momentum and heat transfer enhancement in the turbulent flow through the present rough duct, we must estimate the characteristics of the turbulent shear stress and the turbulent heat flux normal to the rough wall ($-\overline{u_1u_3}$ and $\overline{u_3t}$, respectively). Hence, attention to the production of $-\overline{u_1u_3}$ and $\overline{u_3t}$ on the X_3 axis ($X_2/B = 0$) must be made when discussing the characteristics of the temperature field in the rough duct.

Table 1 Relation between the sign of the production term and its contribution

	sign	contribution
$X_3/B > 0$	+	loss
	−	gain
$X_3/B < 0$	+	gain
	−	loss

Turbulent Stresses. A comparison of fluctuation velocity $\overline{u_3^2}$ and of turbulent shear stress $-\overline{u_1u_3}$ on the X_3 axis of the smooth and rough ducts is shown in Fig. 14. Near the rough wall ($X_3/B = -1.0$) both the values of $\overline{u_3^2}$ and $-\overline{u_1u_3}$ are about four times greater than those obtained in the smooth duct, suggesting that the momentum exchange is very active near the rough wall.

Production of Turbulent Shear Stress $-\overline{u_1u_3}$. The production term in the transport equation for turbulent stress $-\overline{u_iu_j}$ can be expressed as (Launder, 1989):

$$P_{ij} = \overline{u_iu_k}\frac{\partial U_j}{\partial X_k} + \overline{u_ju_k}\frac{\partial U_i}{\partial X_k} \tag{5}$$

This equation, taking the symmetry of the flow about the X_3 axis into consideration, is simplified in relating to $-\overline{u_1u_3}$ as

$$P_{13} = \overline{u_3^2}\frac{\partial U_1}{\partial X_3} + \overline{u_1u_3}\frac{\partial U_3}{\partial X_3} + \overline{u_1u_3}\frac{\partial U_1}{\partial X_1} + \overline{u_1^2}\frac{\partial U_3}{\partial X_1} \tag{6}$$

Every term in Eq. (6) is normalized as follows and evaluated separately:

$$P1 = \overline{u_3^2}\frac{\partial U_1}{\partial X_3}\frac{D}{U_b^3}, \quad P2 = \overline{u_1u_3}\frac{\partial U_3}{\partial X_3}\frac{D}{U_b^3}$$

$$P3 = \overline{u_1u_3}\frac{\partial U_1}{\partial X_1}\frac{D}{U_b^3}, \quad P4 = \overline{u_1^2}\frac{\partial U_3}{\partial X_1}\frac{D}{U_b^3} \tag{7}$$

The distributions of $P1$, $P2$, and $P3$ are shown in Fig. 15. The effect of $P4$ was not evaluated in the present analysis, because the velocity gradient $\partial U_3/\partial X_1$ could not be evaluated from the present experimental data. According to the experimental results obtained by Hijikata et al. (1984) in a two-dimensional channel with larger ribs, U_3 changes greatly in the X_1 direction immediately after the separation of flow and has nearly a constant value near the point of reattachment. The present measurement was carried out in the cross section close to the point of flow reattachment. Therefore, the values of $\partial U_3/\partial X_1$ can be estimated to be very small and the contribution

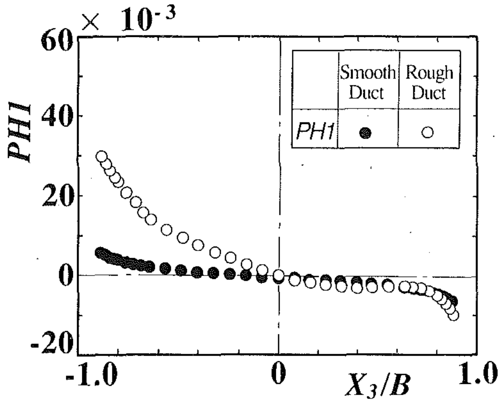

Fig. 16 Distributions of the production term for $\overline{u_3t}$

of $P4$ can be estimated to be negligibly small compared to other terms. In addition, since $P3$ is peculiar to a rough wall with ribs, it takes zero value for a fully developed flow in the smooth duct. At $X_3/B>0$, $-\overline{u_1u_3}$ is negative; and at $X_3/B<0$, it is positive. The relations between the sign of each production term and its gain or loss are shown in Table 1.

In the smooth and rough ducts, $P1$ is larger than the other terms and exhibits a gain near the walls. In addition, the values of $P1$ near the rough wall ($X_3/B = -1.0$) are much larger than those in the smooth duct as shown in Fig. 15. The increase in $P1$ near the rough wall is based mainly on the increase in $\overline{u_3^2}$, as could be predicted from Fig. 14. The values of $P2$ and $P3$ are smaller than $P1$ in the smooth duct and the contributions of $P2$ and $P3$ are negligible. The same is true near the upper smooth wall ($X_3/B=1.0$) in the rough duct, where an increase in U_3,the secondary flow velocity normal to the rough wall, was observed as shown in Fig. 9. Nevertheless, the stress production $P2$ caused by the U_3 gradient is very small. Accordingly, near the upper smooth wall, it is plausible that the effects of U_3 on the production of $-\overline{u_1u_3}$ appear indirectly in $\partial U_1/\partial X_3$ included in $P1$ through the convective transport of the primary flow by U_3.

On the other hand, near the rough wall, absolute values of $P2$ and $P3$, caused by the reattachment of separated flow, are fairly large and attain more than 10 percent of $P1$, respectively. From the condition of continuity, the sum of both terms is expressed as

$$P2+P3=-\overline{u_1u_3}\frac{\partial U_2}{\partial X_2}\frac{D}{U_b^3} \tag{8}$$

As the values of U_2 near the rough wall are nearly zero in the wide extent of X_2/B under the influence of the two-dimensional ribs, the values of Eq. (8) are very small. Accordingly, the loss in $P2$, caused by the reattachment of the flow separated at the ribs, is made up almost perfectly by the gain in $P3$. This fact shows that, as has been observed in the smooth duct, only $P1$ in fact contributes to the generation of $-\overline{u_1u_3}$.

Production of Turbulent Heat Flux $\overline{u_3t}$. The production of $\overline{u_3t}$ on the X_3 axis PH reads (Launder, 1989):

$$PH=-\left(\overline{u_3^2}\frac{\partial T}{\partial X_3}+\overline{u_3t}\frac{\partial U_3}{\partial X_3}+\overline{u_1u_3}\frac{\partial T}{\partial X_1}+\overline{u_1t}\frac{\partial U_3}{\partial X_1}\right) \tag{9}$$

Since the mechanisms of the production of $\overline{u_3t}$ and $-\overline{u_1u_3}$ are considered to be similar, each term of Eq. (7) corresponds to each term of Eq. (9) as follows:

$$P1\cdots PH1=\overline{u_3^2}\frac{\partial \Theta}{\partial X_3}\frac{D}{U_b^2\Theta_b},\quad P2\cdots PH2=-\overline{u_3t}\frac{\partial U_3}{\partial X_3}\frac{D}{U_b^2\Theta_b}$$

$$P3\cdots PH3=\overline{u_1u_3}\frac{\partial \Theta}{\partial X_1}\frac{D}{U_b^2\Theta_b},\quad P4\cdots PH4=-\overline{u_1t}\frac{\partial U_3}{\partial X_1}\frac{D}{U_b^2\Theta_b} \tag{10}$$

Among these terms, the distributions of $PH1$ are shown in Fig. 16; the contribution of $PH1$ to the production of $\overline{u_3t}$ is expected to be the largest from the analogy of $-\overline{u_1u_3}$. The relations between the signs of $PH1$ and the gain and loss are the same as shown in Table 1. $PH1$ has qualitatively a similar distribution to $P1$ shown in Fig. 15. The active production of $\overline{u_3t}$ near the rough wall ($X_3/B=-1.0$) shows the augmentation of heat transfer caused by the rough wall.

Next, we estimate the contributions of the other terms of PH to the production of $\overline{u_3t}$ in the rough duct. Based on the analogy between $\overline{u_3t}$ and $-\overline{u_1u_3}$, the contribution of $PH2$ seems almost of the same level as that of $P2$. $PH2$ is expectedly very small near the upper smooth wall and changes to loss near the rough wall. The contribution of $PH4$ cna be estimated to be negligibly small because the values of $\partial U_3/\partial X_1$ are small, as stated above. Details on $PH3$ distribution are unknown, because $\partial\Theta/\partial X_1$ could not be estimated quantitatively from the present experiment. However, it is expected that $\partial\Theta/\partial X_1$ near the rough wall is smaller than $\partial U_1/\partial X_1$ because U_1 is negative in the recirculating region formed immediately downstream of the rib and changes to positive downstream of this region, while Θ is positive at any location. According to the numerical analysis by Fodemski and Collins (1988), in fact, the change of local Nusselt numbers in the X_1 direction between two successive ribs is less than that of the local wall shear stress. Furthermore, the isothermal lines run almost parallel to the wall immediately downstream of the ribs. Based on these data, it can be expected that near the rough wall $\partial\Theta/\partial X_1$ is smaller than $\partial U_1/\partial X_1$ and the gain in the production of $\overline{u_3t}$, $PH3$, is smaller than the gain in the production of $-\overline{u_1u_3}$, $P3$. As shown in Fig. 15, in the production of $-\overline{u_1u_3}$ near the rough wall, the gain in $P3$ compensated the loss in $P2$. As for the production of $\overline{u_3t}$, however, the gain in $PH3$ cannot compensate for the loss in $PH2$. Consequently, the total production of $\overline{u_3t}$ is smaller than that of $-\overline{u_1u_3}$.

If the above $PH3$ estimation is valid, the dissimilarity between the temperature and velocity fields in the lower half of the rough duct (nearer the rough wall) shown in Fig. 13(*b*) would be brought about by the fact that the production of $\overline{u_3t}$, which controls heat transfer, is inferior to the production of $-\overline{u_1u_3}$, which controls momentum transfer. A detailed experimental examination of $\overline{u_3t}$ is required to prove the hypothesis mentioned above.

Conclusion

1 In the smooth duct, local wall heat flux q_w shows a local minimum on the wall bisector, and attains the maximum value midway between the wall bisector and the adjacent wall. This distribution is similar to that of τ_w. The bulges in the contour lines of mean temperature near the duct corners show the similarity between the temperature and velocity distributions in the smooth duct. The mean temperature profile is expressed by the logarithmic inner law at $30<Y^+<200$.

2 The peripherally averaged local Nusselt numbers on smooth walls of the rough duct are 1.71 ~ 1.97 times larger than those of the smooth duct. The distribution of q_w on the upper smooth wall opposite the rough wall is similar to that of τ_w influenced by the behavior of the secondary flow. However, the dissimilarity between the distributions of q_w and τ_w is more pronounced at the lower half (nearer the rough wall) of a side smooth wall adjacent to the rough wall.

3 Contour lines of mean temperature in the upper half of the rough duct (nearer the upper smooth wall) become depressed under the influence of the secondary flow. This peculiarity in the contour map is similar to that observed in contours of the mean velocity. The mean temperature profile in this region is expressed by a logarithmic inner law.

4 In contrast to the statement in (3), the mean temperature is not expressed by the inner law in the lower half of the rough

duct (nearer the rough wall). The profile of mean temperature is dissimilar to that of mean velocity in this region, indicating that the turbulent transport of heat is inferior to that of momentum.

5 The production of the turbulent heat flux $\overline{u_3t}$ is large near the rough wall, which corresponds to the heat transfer augmentation by the rough wall. The dissimilarity between the velocity and temperature fields near the rough wall is explained by the differences between $P3$ and $PH3$, both of which are a component of the production terms for turbulent shear stress $-\overline{u_1u_3}$ and turbulent heat flux $\overline{u_3t}$, respectively.

Acknowledgments

The authors express their thanks to Mr. Naoyasu Shiraki, a research engineer of Nagoya University, for his cooperation in producing the experimental apparatus. They also thank Messrs. Shinsuke Kagami and Toshimitsu Murofushi for their assistance in conducting the experiment. A part of the present experiment was supported by a grant-in-aid from General Petroleum Inc.

References

Brundrett, E., and Burroughs, P. R., 1967, "The Temperature Inner-Law and Heat Transfer for Turbulent Flow in a Vertical Square Duct," *Int. J. Heat Mass Transfer*, Vol. 10, pp.1133-1142.

Emery, A. F., Neighbors, P. K., and Gessner, F. B., 1980, "The Numerical Prediction of Developing Turbulent Flow and Heat Transfer in a Square Duct," ASME JOURNAL OF HEAT TRANSFER, Vol. 102, pp. 51-57.

Fodemski, T. R., and Collins, M. W., 1988, "Flow and Heat Transfer Simulation for Two- and Three-Dimensional Smooth and Ribbed Channels," *Proc. Second UK National Conference on Heat Transfer*, Vol. 1, pp. 845-860.

Fujita, H., Yokosawa, H., Hirota, M., and Nagata, C., 1988, "Fully Developed Turbulent Flow and Heat Transfer in a Square Duct With Two Roughened Facing Walls," *Chemical Engineering Communications*, Vol. 74, pp. 95-110.

Fujita, H., Yokosawa, H., and Hirota, M., 1989a, "Secondary Flow of the Second Kind in Rectangular Ducts With One Rough Wall," *Experimental Thermal and Fluid Science*, Vol. 2, pp. 72-80.

Fujita, H., Hirota, M., and Yokosawa, H., 1989b, "Forced Convection Heat Transfer in a Turbulent Flow Through a Square Duct," *Memoirs of the Faculty of Engineering*, Nagoya University, Vol. 40, No. 2, pp. 327-336.

Fujita, H., Hirota, M., Yokosawa, H., Hasegawa, M., and Gotoh, I., 1990a, "Fully Developed Turbulent Flows Through Rectangular Ducts With One Roughened Wall," JSME *International Journal*, Series II, Vol. 33, No. 4, pp. 692-701.

Fujita, H., Hirota, M., and Yokosawa, H., 1990b, "Experiments on Turbulent Flow in a Square Duct With a Rough Wall," *Memoirs of the Faculty of Engineering*, Nagoya University, Vol. 41, No. 2, pp. 280-294.

Han, J. C., 1984, "Heat Transfer and Friction in Channels With Two Opposite Rib-Roughened Walls," ASME JOURNAL OF HEAT TRANSFER, Vol. 106, pp. 774-781.

Han, J. C., Park, J. S., and Lei, C. K., 1985, "Heat Transfer Enhancement in Channels With Turbulence Promoters," ASME *Journal of Engineering for Gas Turbines and Power*, Vol. 107, pp. 628-635.

Han, J. C., 1988, "Heat Transfer and Friction Characteristics in Rectangular Channels With Rib Turbulators," ASME JOURNAL OF HEAT TRANSFER, Vol. 110, pp. 321-328.

Hijikata, K., Mori, Y., and Ishiguro, H., 1984, "Turbulent Structure and Heat Transfer of Pipe Flow With Cascade Smooth Turbulence Surface Promoters," *Trans. JSME*, Vol. 50, No. 458, pp. 2555-2562 [in Japanese].

Hijikata, K., Ishiguro, H., and Mori, Y., 1987, "Heat Transfer Augmentation in a Pipe Flow With Smooth Cascade Turbulence Promoters and Its Application to Energy Conversion," in: *Heat Transfer in High Technology and Power Engineering*, W. J. Yang and Y. Mori, eds., Hemisphere, Washington, DC, pp. 368-379.

Hirota, M., Yokosawa, H., and Fujita, H., 1992, "Turbulence Kinetic Energy in Turbulent Flows Through Square Ducts With Rib-Roughened Walls," *Int. J. Heat Fluid Flow*, Vol. 13, No. 1, pp. 22-29.

Hishida, M., and Nagano, Y., 1979, "Structure of Turbulent Velocity and Temperature Fluctuations in Fully Developed Pipe Flow," ASME JOURNAL OF HEAT TRANSFER, Vol. 101, pp. 15-22.

Hishida, M., Nagano, Y., and Tagawa, M., 1986, "Transport Processes of Heat and Momentum in the Wall Region of Turbulent Pipe Flow," *Proc. 8th Int. Heat Transfer Conf.*, C. L. Tien et al., eds., Vol. 3, Hemisphere, Washington, DC, pp. 925-930.

Humphrey, J. A. C., and Whitelaw, J. H., 1980, "Turbulent Flow in a Duct With Roughness," *Turbulent Shear Flows*, J. S. Bradbury et al., eds., Vol. 2, Springer-Verlag, Berlin, pp. 174-188.

JSME, 1987, *Measurement Uncertainty* (translated from ASME Performance Test Codes, Supplement on Instruments and Apparatus, Part 1), Maruzen, Tokyo, Japan.

Kader, B. A., 1981, "Temperature and Concentration Profiles in Fully Turbulent Boundary Layers," *Int. J. Heat Mass Transfer*, Vol. 24, No. 9, pp. 1541-1544.

Kays, W. M., and Perkins, H. C., 1985, "Forced Convection, Internal Flow in Duct," *Handbook of Heat Transfer Fundamentals*, 2nd ed., W. M. Rohsenow et al., eds., McGraw-Hill, New York, Chap. 7, pp. 7-30.

Kim, J., 1987, "Investigation of Heat and Momentum Transport in Turbulent Flows Via Numerical Simulations," *Proc. 2nd Int. Symp. Transport Phenomena in Turbulent Flows*, pp. 707-721.

Launder, B. E., 1989, "On the Computation of Convective Heat Transfer in Complex Turbulent Flows," ASME JOURNAL OF HEAT TRANSFER, Vol. 110, pp. 1112-1128.

Launder, B. E., and Ying, W. M., 1973, "Prediction of Flow and Heat Transfer in Ducts of Square Cross-Section," *Proc. Instn. Mech. Engrs.*, Vol. 187, pp. 455-461.

Liou, T. M., and Hwang, J. J., 1992, "Turbulent Heat Transfer Augmentation and Friction in Periodic Fully Developed Channel Flows," ASME JOURNAL OF HEAT TRANSFER, Vol. 114, pp. 56-64.

Melling, A., and Whitelaw, J. H., 1976, "Turbulent Flow in a Rectangular Duct," *J. Fluid Mechanics*, Vol. 78, pp. 289-315.

Metais, B., and Eckert, E. R. G., 1964, "Forced, Mixed, and Free Convection Regime," ASME JOURNAL OF HEAT TRANSFER, Vol. 86, pp. 295-296.

Metzger, D. E., Fan, C. S., and Yu, Y., 1990, "Effects of Rib Angle and Orientation on Local Heat Transfer in Square Channels With Angled Roughness Ribs," in: *Compact Heat Exchangers, A Festschrift for A. L. London*, Hemisphere Publishing Corporation, New York, pp. 151-167.

Myong, H. K., 1991, "Numerical Investigation of Fully Developed Turbulent Fluid Flow and Heat Transfer in a Square Duct," *Int. J. Heat Fluid Flow*, Vol. 12, No. 4, pp. 344-352.

Nakayama, A., and Koyama, H., 1986, "Numerical Prediction of Turbulent Flow and Heat Transfer Within Ducts of Cross-Shaped Cross Section," ASME JOURNAL OF HEAT TRANSFER, Vol. 108, pp. 841-847.

Patel, V. C., 1965, "Calibration of the Preston Tube and Limitations on Its Use in Pressure Gradients," *J. Fluid Mechanics*, Vol. 23, Part 1, pp. 185-208.

Sparrow, E. M., and Tao, W. Q., 1983, "Enhanced Heat Transfer in a Flat Rectangular Duct With Streamwise-Periodic Disturbances at One Principal Wall," ASME JOURNAL OF HEAT TRANSFER, Vol. 105, pp. 851-861.

Sparrow, E. M., and Tao, W. Q., 1984, "Symmetric vs Asymmetric Periodic Disturbances at the Walls of a Heated Flow Passage," *Int. J. Heat Mass Transfer*, Vol. 27, No. 11, pp. 2133-2144.

Subramanian, C. S., and Antonia, R. A., 1981, "Effect of Reynolds Number on a Slightly Heated Turbulent Boundary Layer," *Int. J. Heat Mass Transfer*, Vol. 24, No. 11, pp. 1833-1846.

Yokosawa, H., Fujita, H., Hirota, M., and Iwata, S., 1989, "Measurement of Turbulent Flow in a Square Duct With Roughened Walls on Two Opposite Sides," *Int. J. Heat Fluid Flow*, Vol. 10, No. 2, pp. 125-130.

Film-Cooling From Holes With Compound Angle Orientations: Part 1—Results Downstream of Two Staggered Rows of Holes With 3d Spanwise Spacing

P. M. Ligrani
Associate Professor,
University of Utah,
Salt Lake City, UT 84112
Mem. ASME

J. M. Wigle
Graduate Student.

S. Ciriello
Graduate Student.

S. M. Jackson
Graduate Student.

Department of Mechanical Engineering,
Naval Postgraduate School,
Monterey, CA 93943

Experimental results are presented that describe the development and structure of flow downstream of two staggered rows of film-cooling holes with compound angle orientations. With this configuration, holes are spaced 3d apart in the spanwise direction, inclined at 35 deg with respect to the test surface when projected into the streamwise/normal plane, and inclined at 30 deg with respect to the test surface when projected into the spanwise/normal plane. Results are presented for an injectant to free-stream density ratio near 1.0, and injection blowing ratios from 0.5 to 1.50. Comparisons are made with measurements from two other configurations to determine: (1) the effects of hole angle orientation for constant spanwise hole spacing, and (2) the effects of spanwise hole spacing when the hole angle orientation is maintained constant. Results from the first comparison show that the compound angle injection configuration provides significantly improved film-cooling protection compared to a simple angle configuration for the same spanwise hole spacing, normalized streamwise location x/d, and blowing ratio m, for $x/d<60$. At $x/d>60$, spanwise-averaged adiabatic effectiveness data downstream of the two configurations generally cover about the same range. Results from the second comparison show that spanwise-averaged effectiveness values are 25 to 40 percent higher when 3d spanwise hole spacing is employed compared to 3.9d spanwise hole spacing for the same m and x/d, for $x/d<40$. At $x/d>40$, differences between the two configurations range from 12 to 30 percent. Results from all configurations studied show that spanwise-averaged iso-energetic Stanton number ratios cover approximately the same range of values and show roughly the same trends, ranging between 1.0 and 1.25. In particular, St_f/St_o values increase with m at each x/d, and show little variation with x/d for each value of m tested.

Introduction

In recent years, film-cooling holes with compound angle orientations have been employed on a number of components within gas turbines, including turbine blades, turbine endwalls, combustion chamber linings, and afterburner linings. Film holes with compound angle orientations are inclined to the test surface such that the injectant is issued with a spanwise velocity component relative to the mainstream flow when viewed in the streamwise/spanwise plane. Simple angle holes inject cooling air at an angle with respect to the test surface when viewed in the streamwise/normal plane, but approximately in the direction of the mainstream flow when viewed in the streamwise/spanwise plane.

Compound angle orientations are used because they are believed to produce injectant distributions over surfaces that give better protection and higher film effectiveness values than injectant from holes with simple angle orientations. Improved thermal protection from the film is needed to increase engine efficiency and engine operating lifetimes. Effective film cooling schemes are a necessity considering the large stress magnitudes on component materials, especially on the blades of the first turbine stage that result from exposure to temperatures approaching 2000 K in an environment with high rotational speeds. The problem with current design approaches employing compound angle holes is that only a few sets of data are available in the archival literature, in spite of widespread use of these holes.

Of these, Mayle and Camarata (1975) studied the effects of hole spacing and blowing ratio on heat transfer and film effectiveness for a staggered-hole array. The holes were angled 30 deg to the plate surface in planes oriented 45 deg from the flow direction. Spanwise spacings between holes were 8*d*, 10*d*, and 14*d*. Higher values of effectiveness were measured downstream of the holes with the smaller spacings. Kim et al. (1978) investigated heat transfer to a full-coverage, film-cooled surface with holes having the same angles as employed by Mayle and Camarata (1975). For one injection temperature and one blowing ratio, Kim et al. (1978) concluded that heat transfer coefficients downstream of the compound angle configuration were half as high as ones measured downstream of simple angle holes slanted 30 deg from the test surface. In a study of turbine vane leading edge heat transfer, Mehendale and Han (1992) employed compound angle holes angled 30 deg to the surface in planes oriented 90 deg from the flow direction. However, like the other two studies mentioned, this study did not undertake any sort of systematic comparison between results obtained downstream of simple and compound angle holes. The present study is aimed at remedying this deficiency by providing new information on the differences in protection

---

Contributed by the Heat Transfer Division for publication in the JOURNAL OF HEAT TRANSFER. Manuscript received by the Heat Transfer Division November 1992; revision received July 1993. Keywords: Forced Convection, Turbines. Associate Technical Editor: T. W. Simon.

that result downstream of injection holes with compound angle orientations as compared to measurements downstream of injection holes with simple angle orientations.

To accomplish this, the present experiment is designed to match a number of operating parameters existing in the first turbine stages of gas turbine engines. These include (range of values are indicated in parentheses): (1) compound angle injection geometry including centerline to centerline spacing of injection holes (3.0) as well as spanwise spacing of holes along the test surface (6.0) and elliptical coverage of the film holes in the plane of the test surface, (2) x/d range (6.8–98.7), (3) blowing ratio range (0.5–1.50), (4) momentum flux ratio range (0.25–2.25), (5) injection hole Reynolds number range (3200–26,000), (6) Reynolds number range based on length along the test surface (7.4×10^5–12.8×10^5), (7) ratio of boundary layer thickness to injection hole diameter (1.03), and (8) nondimensional injection temperature range ($\theta=0.0$–3.0). Other effects present in operating high-temperature engines (i.e., curvature, high free-stream turbulence, variable properties, stator/blade wake interactions, shock waves, compressibility, rotation, viscous dissipation, injectant to free-stream density ratio) are left out of our experiment since these may obscure and complicate the interaction of interest.

The experiment employs two staggered rows of holes, with individual holes inclined at 35 deg with respect to the test surface when projected into the streamwise/normal plane, and 30 deg with respect to the test surface when projected into the spanwise/normal plane. Within each row, holes are spaced 6.0d apart, where d is the hole diameter, which gives 3.0d spacing between adjacent holes in the two staggered rows. Results presented include distributions of surface Stanton numbers, adiabatic film cooling effectiveness and iso-energetic Stanton number ratios deduced from Stanton number ratios using superposition, and injectant distributions. Also presented are plots showing the streamwise development of distributions of mean streamwise velocity. Of particular interest are comparisons of these results to ones obtained downstream of film cooling holes with simple angle orientations. With this simple angle arrangement, the holes are inclined 35 deg with respect to the test surface in the streamwise/normal plane with the same spanwise hole spacing as the compound angle arrangement. Comparisons are also made with results measured downstream of another compound angle arrangement with the same hole angles with respect to the test surface but different spanwise hole spacing (3.9d).

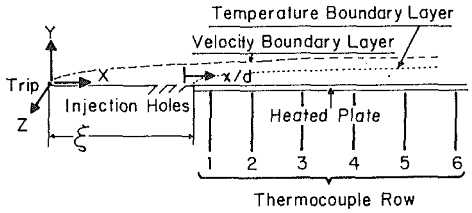

Fig. 1 **Coordinate system and schematic of wind tunnel test section**

Experimental Apparatus and Procedures

Wind Tunnel and Coordinate System. The wind tunnel is the same one used in the experiments of Ligrani et al. (1992). The facility is open-circuit and subsonic. A centrifugal blower is located at the upstream end, followed by a diffuser, a header containing a honeycomb and three screens, and then a 16 to 1 contraction ratio nozzle. The nozzle leads to the test section, which is a rectangular duct 3.05 m long, 0.61 m wide, and 0.203 m high at its entrance with a top wall having adjustable height to permit a zero pressure gradient to be set along the length of the test section (without the film-cooling) to within 0.01 in. of water differential pressure. The free-stream velocity is 10 m/s and the free-stream turbulence intensity is approximately 0.13 percent based on the same velocity. The boundary layer is tripped using a 2-mm-high spanwise uniform strip of tape near the nozzle exit 1.072 m upstream of the constant heat flux transfer surface for the compound angle injection system. Profiles of mean velocity and longitudinal turbulence intensity are presented by Ligrani et al. (1992), which illustrate normal turbulent boundary layer behavior with a high degree of regularity across the span of the wind tunnel test surface.

A schematic showing the test section and coordinate system is presented in Fig. 1. Locations of the boundary layer trip, film cooling holes, heat transfer test surface, and thermocouple rows along this test surface are evident. Dimensional values

Nomenclature

A = heat transfer surface area
c = specific heat
d = injection hole diameter
h = heat transfer coefficient with film injection
h_o = baseline heat transfer coefficient, no film injection
h_f = iso-energetic heat transfer coefficient with film injection
I = momentum flux ratio = $\rho_c U_c^2/\rho_\infty U_\infty^2$
k = thermal conductivity
m = blowing ratio = $\rho_c U_c/\rho_\infty U_\infty$
q = wall heat flux
Re_d = injection Reynolds number = dU_c/ν
Re_x = Reynolds number based on streamwise distance = XU_∞/ν
St = Stanton number with film injection
St_o = baseline Stanton number, no film injection
St_f = iso-energetic Stanton number with film injection
$\overline{\mathrm{St}_f}$ = spanwise-averaged iso-energetic Stanton number with film injection
T = static temperature
U = streamwise mean (time-averaged) velocity
X, x = streamwise distance
Y, y = distance normal to the surface
Z, z = spanwise distance from test surface centerline
α = thermal diffusivity = $k/\rho c$
β = injection hole angle with respect to the test surface as projected into the spanwise/normal plane
η = adiabatic film cooling effectiveness = $(T_{aw}-T_{r,\infty})/(T_{r,c}-T_{r,\infty})$
$\bar{\eta}$ = spanwise-averaged adiabatic film cooling effectiveness
θ = nondimensional injection temperature = $(T_{r,c}-T_{r,\infty})/(T_w-T_{r,\infty})$
ν = kinematic viscosity
ξ = unheated starting length
ρ = density
Ω = injection hole angle with respect to the test surface as projected into the streamwise/normal plane

Subscripts

aw = adiabatic wall
c = injectant at exits of injection holes
cond = conduction heat transfer
o = stagnation condition or baseline data
r = recovery condition
rad = radiation heat transfer
w = wall
∞ = free-stream

Superscripts

$\overline{}$ = spanwise average

Table 1 Test section geometry characteristics for injection configurations 1, 2, and 3

	Compound angle configuration 1		
	X (m)	x/d	x (m)
Downstream edge of injection holes	1.059	0.00	0.000
Unheated starting length, ξ	1.072	1.38	0.013
Row 1*	1.122	6.67	0.063
Row 2*	1.222	17.25	0.163
Row 3*	1.372	33.12	0.313
Row 4*	1.572	54.29	0.513
Row 5*	1.772	75.45	0.713
Row 6*	1.972	96.61	0.913
	Simple angle configuration 2		
	X (m)	x/d	x (m)
Downstream edge of injection holes	1.083	0.00	0.000
Unheated starting length, ξ	1.097	1.48	0.014
Row 1*	1.147	6.77	0.064
Row 2*	1.247	17.35	0.164
Row 3*	1.397	33.23	0.314
Row 4*	1.597	54.39	0.514
Row 5*	1.797	75.56	0.714
Row 6*	1.997	96.72	0.914
	Compound angle configuration 3		
	X (m)	x/d	x (m)
Downstream edge of injection holes	1.059	0.00	0.000
Unheated starting length, ξ	1.072	1.41	0.013
Row 1*	1.122	6.81	0.063
Row 2*	1.222	17.62	0.163
Row 3*	1.372	33.83	0.313
Row 4*	1.572	55.46	0.513
Row 5*	1.772	77.08	0.713
Row 6*	1.972	98.70	0.913

*Refers to thermocouple row locations.

of distances labeled in Fig. 1 are given in Table 1 for all three film hole arrangements investigated (configurations 1, 2, and 3). In all cases, an unheated starting length exists when the heat transfer surface is at elevated temperature, and the direction of heat transfer is from the wall to the gas. In regard to the coordinate system, Z is the spanwise coordinate measured from the test section spanwise centerline, X is measured from the upstream edge of the boundary layer trip, and Y is measured normal to the test surface. x is measured from the downstream edge of the injection holes and generally presented as x/d. The total boundary layer thickness just downstream of the injection holes ($x/d = 2.75$) is 0.973 cm, giving a thickness to hole diameter ratio of 1.03. The ratios of momentum thickness to hole diameter and displacement thickness to hole diameter at this location are then 0.13 and 0.22, respectively.

Injection System. The injection system is described by Ligrani et al. (1992). Air for the injection system originates in two 1.5 hp DR513 Rotron Blowers capable of producing 30 cfm at 2.5 psig. From the blowers, air flows through a regulating valve, a Fisher and Porter rotometer, a diffuser, and finally into the injection heat exchanger and plenum chamber. The exchanger provides means to heat the injectant above ambient temperature. With this system and test plate heating, the nondimensional injection temperature parameter θ is maintained at values ranging from 0.0 to 3.0, which includes values within the range of gas turbine component operation. The ratio of injectant to free-stream density ρ_c/ρ_∞ is from 0.94 to 1.00. The upper surface of the plenum chamber is connected to the injection tubes of the different injection configurations, where each tube is about 7.6 cm long, giving a length to diameter ratio of about 8. Additional details on injection system performance, and procedures to measure discharge coefficients and blowing ratios are presented by Ligrani et al. (1989, 1992).

Streamwise Mean Velocity Measurements. The streamwise mean velocity is measured using a five-hole pressure probe with a conical tip manufactured by United Sensors Corporation. Celesco transducers and Carrier Demodulators are used to sense pressures when connected to probe output ports. The same automated traverse used for injectant surveys is used to obtain these surveys. With this device, the pressure probe is traversed over 10.2 cm by 20.3 cm spanwise/normal planes at 800 locations spaced 0.51 cm apart in each direction. At each location, 50 samples of the output from each of the five pressure ports are acquisitioned for later processing. These devices, measurement procedures employed, as well as data acquisition equipment and procedures used are further detailed by Ligrani et al. (1989, 1992), Bishop (1990), and Ciriello (1991).

Stanton Number Measurements. The heat transfer surface is also described by Ligrani et al. (1989, 1992). Briefly, it is designed to provide a constant heat flux over its area using a surface next to the air stream, which is stainless steel foil painted flat black. Immediately beneath this is a liner containing 126 thermocouples, which is just above an Electrofilm Corp. etched foil heater rated at 120 V and 1500 W. Located below the heater are several layers of insulating materials including Lexan sheets, foam insulation, Styrofoam, and balsa wood. Surface temperature levels and convective heat transfer rates are controlled by adjusting power into the heater using a Standard Electric Co. Variac, type 3000B. To determine the heat loss by conduction, an energy balance is performed. Radiation losses from the top of the test surface are analytically estimated. The thermal contact resistance between thermocouples and the foil top surface is based on a correlation dependent on heat flux through the foil, thermocouple readings, and measurements from calibrated liquid crystals on the surface of the foil. Corrections to account for streamwise and spanwise conduction along the test surface are also employed using procedures developed and described by Ciriello (1991).

Mean Temperature Measurements. Copper-constantan thermocouples are used to measure temperatures along the surface of the test plate, the free-stream temperature, as well as temperature distributions, which are correlated to injection distributions. For the distributions, a thermocouple is traversed over spanwise/normal planes (800 probe locations) using an automated two-dimensional traversing system, which may be placed at different streamwise locations. Voltages from thermocouples and the Carrier Demodulators (used for the mean velocity measurements) are digitally sampled and read using a Hewlett-Packard 3497A Data Acquisition Control Unit with a 3498A Extender. These units are controlled by a Hewlett-Packard Series 9000 Model 310 computer.

Adiabatic Film-Cooling Effectiveness Measurements. Adiabatic film-cooling effectiveness values are determined using linear superposition theory applied to Stanton number ratios measured at different injection temperatures. The details of this approach are described by Ligrani et al. (1992), including a test to check the procedure using a direct η measurement with a near-adiabatic condition on the test plate. η differences from the two techniques were always less than experimental uncertainties, ranging from 7 to 15 percent (Ligrani et al., 1992).

Briefly, the superposition technique employed to determine effectiveness values is based on the equation given by

$$\mathrm{St}/\mathrm{St}_o = \mathrm{St}_f/\mathrm{St}_o\,(1-\theta\eta) \qquad (1)$$

where $\theta = (T_{r,c} - T_{r,\infty})/(T_w - T_{r,\infty})$ and $\eta = (T_{aw} - T_{r,\infty})/(T_{r,c} - T_{r,\infty})$. To obtain η and $\mathrm{St}_f/\mathrm{St}_o$ values, $\mathrm{St}/\mathrm{St}_o$ are measured at different θ, where θ is varied by changing the injection temperature. The plot of the $\mathrm{St}/\mathrm{St}_o$ versus θ data then gives a straight line with a vertical axis intercept of $\mathrm{St}_f/\mathrm{St}_o$, and a horizontal axis intercept of $1/\eta$. In most cases, no extrapolation is needed to determine St_f/St_o because St/St_o is measured directly at $\theta = 0$ ($T_{r,c} = T_{r,\infty}$).

Equation (1) is based on the equality of two equations for q, the heat flux with film cooling. The first one is given by

$$q = h_f(T_w - T_{aw}) \tag{2}$$

where T_{aw} is the adiabatic wall temperature, and h_f is the iso-energetic heat transfer coefficient. The second equation provides a definition for the heat transfer coefficient h, and is expressed in the form

$$q = h(T_w - T_{r,\infty}) \tag{3}$$

This approach applies only so long as temperature variations are small enough that fluid properties are reasonably invariant as θ is changed, and as long as fluid properties are reasonably invariant with respect to all three coordinate directions (Ligrani and Camci, 1985; Ligrani, 1990; Ligrani et al., 1992). In addition, the three-dimensional energy equation that describes the flow field must be linear and homogeneous in its dependent variable, temperature. To meet these conditions, near-constant property conditions are maintained throughout the boundary layer by employing low subsonic speeds and temperature differences less than 30°C.

Baseline Data Checks. Repeated measurements of spanwise-averaged Stanton numbers show good agreement (maximum deviation is 4 percent) with the correlation from Kays and Crawford (1993) for turbulent heat transfer to a flat plate with unheated starting length and constant heat flux boundary condition. Ciriello (1991) and Bishop (1990) provide additional details.

Experimental Uncertainties. Uncertainty estimates are based upon 95 percent confidence levels, and determined following procedures described by Kline and McClintock (1953) and Moffat (1982). Typical nominal values of free-stream recovery temperature and wall temperature are 18.0 and 40.0°C, with respective uncertainties of 0.13 and 0.21°C. The free-stream density, free-stream velocity, and specific heat uncertainties are 0.009 kg/m^3 (1.23 kg/m^3), 0.15 m/s (10.0 m/s), and 1 J/kgK (1006 J/kgK), where typical nominal values are given in parentheses. For convective heat transfer, heat transfer coefficient, and heat transfer area, 10.5 W (270 W), 1.03 W/m^{2}K (24.2 W/m^{2}K), and 0.0065 m^2 (0.558 m^2) are typical uncertainties. The uncertainties of St, St/St_o, m, and x/d are 0.000086 (0.00196), 0.058 (1.05), 0.025 (0.50), and 0.36 (41.9). Uncertainties of $\bar{\eta}$ and St_f/St_o are dependent upon the linear superposition technique employed. The uncertainty of St_f/St_o is the same as for St/St_o. The uncertainty of $\bar{\eta}$ varies between 0.02 and 0.04 effectiveness units where higher values in this range apply when $\bar{\eta}$ is less than about 0.15.

Injection Configurations

Schematic drawings showing the film hole geometries employed (configurations 1-3) are presented in Figs. 2-4. Each figure shows the hole arrangement along the test surface (X-Z plane) as seen in the negative Y direction. In each case, holes are placed in two rows such that the holes are staggered with respect to each other. Each row contains five injection cooling holes arranged so that the centerline of the middle hole in the downstream row is located on the spanwise centerline ($Z = 0.0$ cm) of the test surface.

For configuration 1, which is shown in Fig. 2, the spanwise spacings between adjacent holes is $3.9d$, and centerlines of holes in separate rows are separated by $5.2d$ in the streamwise direction. Hole diameter d is 0.945 cm. Compound angle holes are employed with $\Omega = 35$ deg and $\beta = 30$ deg, where Ω is the angle of the injection holes with respect to the test surface as projected into the streamwise/normal plane, and β is the angle of the injection holes with respect to the test surface as projected into the spanwise/normal plane. Thus, holes are oriented so that the spanwise components of injectant velocity are directed in the negative Z direction. The plane of each injection hole is angled at 50.5 deg from the streamwise/normal (X-Y) plane, and, within the plane of each hole, hole centerlines are oriented at angles of 24 deg from the plane of the test surface (X-Z).

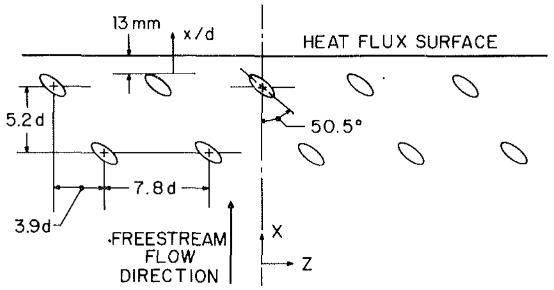

Fig. 2 Test surface injection geometry for film cooling holes arranged with configuration 1 compound angle holes

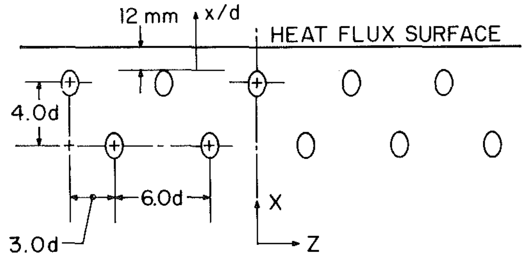

Fig. 3 Test surface injection geometry for film cooling holes arranged with configuration 2 simple angle holes

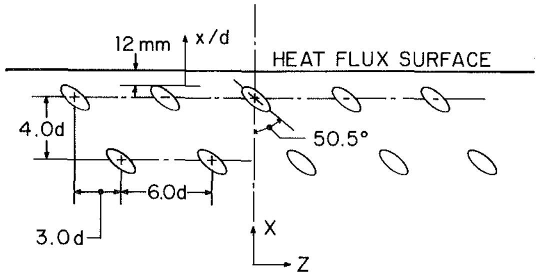

Fig. 4 Test surface injection geometry for film cooling holes arranged with configuration 3 compound angle holes

For configuration 2, which is shown in Fig. 3, the spanwise spacing between adjacent holes is $3.0d$, and centerlines of holes in separate rows are separated by $4.0d$ in the streamwise direction. Hole diameter is 0.945 cm. In this case, the holes are oriented with simple angles such that $\Omega = 35$ deg and $\beta = 90$ deg. Thus, holes are located in streamwise/normal (X-Y) planes, and oriented so that the injectant has no spanwise component of velocity as it exits the holes. Within the plane of each hole, individual hole centerlines are then oriented at angles of 35 deg from the plane of the test surface.

Configuration 3, which is shown in Fig. 4, has the same spanwise hole spacing as configuration 2 and the same hole angles with respect to the test surface as configuration 1. Thus, spanwise hole spacing is $3.0d$, $\Omega = 35$ deg, and $\beta = 30$ deg. The nominal hole diameter for configuration 3 is 0.925 cm. Thus, by comparing results from configurations 1 and 3, the influences of spanwise hole spacing ($3.0d$ compared to $3.9d$) on compound angle film cooling are apparent. A comparison of results from configurations 2 and 3 then provides information on the effects of compound angle orientation ($\Omega = 35$ deg, $\beta = 30$ deg) relative to simple angle orientation ($\Omega = 35$ deg, $\beta = 90$ deg) with the same spanwise hole spacing ($3d$). The geometry of the simple angle holes exactly matches the pro-

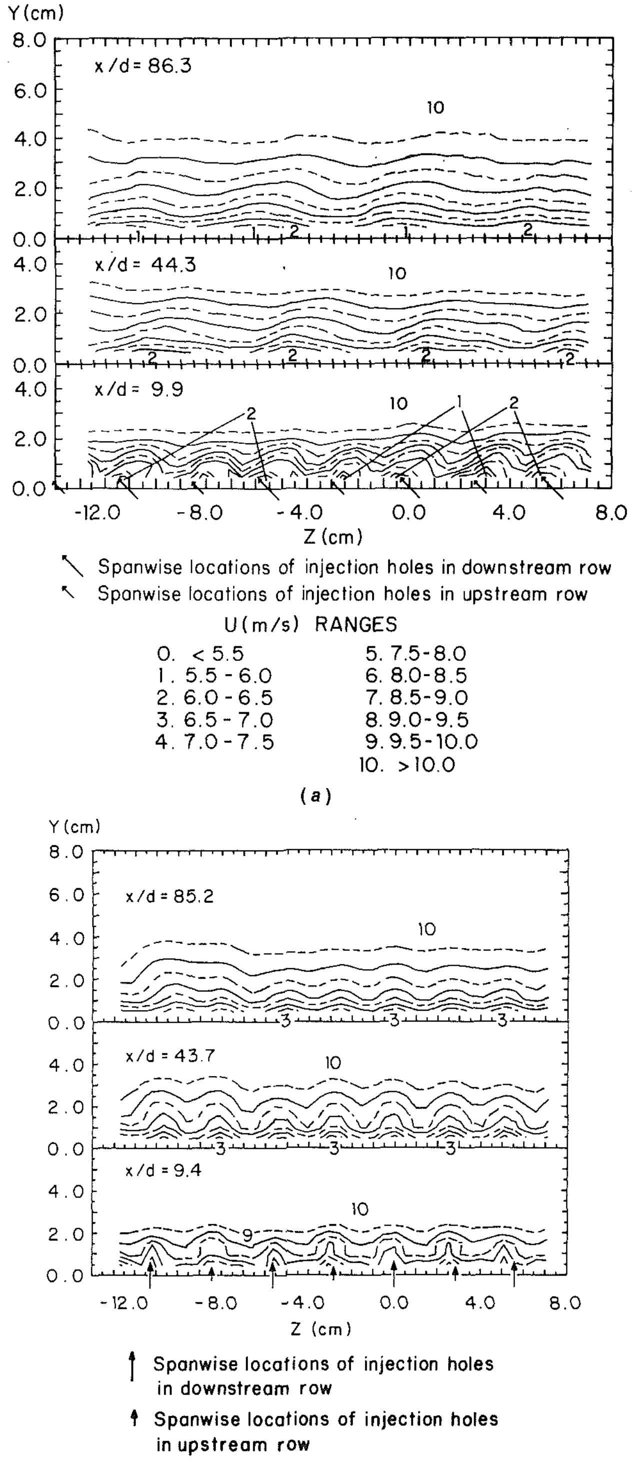

Fig. 5 Streamwise mean velocity development with streamwise distance, as measured downstream of two rows of holes with $m = 1.0$: (*a*) compound angle configuration 3; (*b*) simple angle configuration 2

jection of the compound angle holes into the streamwise/normal plane to provide a systematic basis for this comparison. This systematic basis for comparison is also maintained because many experimental approach details, flow parameters, and additional injection geometry characteristics are held constant as the comparisons are made.

Thus, the present test program is designed to provide answers to two principal questions by maintaining all parameters constant except those pertaining directly to these questions. First, which injection hole orientation (simple angle or compound angle) produces the highest effectiveness values and the best film-cooling protection? Second, for injection from holes with compound angle orientations, which spanwise hole spacing ($3d$ or $3.9d$) produces the highest effectiveness values and the best film-cooling protection? To answer these questions, most attention is given to results obtained using compound angle configuration 3, and to comparisons between configuration 3 and configurations 1 and 2. Comparisons between configuration 1 and configuration 2 are also important, however, these are discussed in detail elsewhere by Ligrani et al. (1992).

Mean Velocity Surveys

Surveys of mean velocity measured downstream of configuration 3 compound angle holes are presented in Fig. 5(*a*), and results measured downstream of configuration 2 simple angle holes are presented in Fig. 5(*b*). In both cases, the blowing ratio is 1.0. Locations of film holes are denoted by arrows on the abscissa of each plot, where large arrows denote holes in the downstream row and small arrows denote holes in the upstream row.

At $x/d = 9.9$, velocity deficits in Fig. 5(*a*) are skewed and flattened with the largest velocity gradients at Y ranging from 0.5 cm to 2.5 cm, which appear to be largest in the direction that film is ejected from the surface. Because of the negative spanwise components of velocity at the exits of the film holes, deficits are also displaced about -2.5 cm by the time they reach $x/d = 9.9$. Here, adjacent deficits appear to be quite similar even though they result from injectant that issues from staggered holes in two different rows. However, as the film-cooled boundary layer convects downstream, deficits resulting from injection from the downstream row of holes persist, whereas injectant deficits from the upstream row of holes become less apparent. This occurs because injectant from upstream holes eventually merges and coalesces with injectant that originated from holes in the downstream row. Consequently, half as many velocity deficits are eventually present across the measurement plane in Fig. 5(*a*) at x/d of 44.3 and 86.3 compared to results at the $x/d = 9.9$ location.

The simple angle results in Fig. 5(*b*) show considerably different qualitative and quantitative behavior. The $x/d = 9.9$ results in Fig. 5(*a*) show velocity deficits that are skewed and flattened with nonsymmetric velocity gradients. The $x/d = 9.4$ simple angle results in Fig. 5(*b*) show periodic velocity deficits across the span of the measurement plane. Because the injectant emerges from the holes in the streamwise direction with no spanwise velocity component, these deficits are at the same spanwise locations as the injection holes. In addition, the qualitative and quantitative characteristics of the different deficits are very similar even though adjacent film injection holes are staggered at different streamwise locations. As the film-cooled boundary layer then develops downstream, results at $x/d = 43.7$ and $x/d = 85.2$ show velocity deficits that continue to be spanwise periodic at the same spanwise locations as the results at $x/d = 9.4$. Adjacent deficits are spanwise similar at these far downstream locations, except for outer boundary layer regions at Z values less than -7.0 cm. Here, some spanwise nonuniformity is evident, especially for $x/d = 85.2$, because these locations are in close proximity to the spanwise edge of the injectant distribution.

Local Adiabatic Effectiveness, Injectant, and Stanton Number Ratio Distributions

Measurements downstream of configuration 3 compound angle holes are discussed in this section. These include distributions of adiabatic film cooling effectiveness, iso-energetic Stanton number ratio, and Stanton number ratio for $\theta = 1.72$. Also presented are surveys of injectant distributions as well as

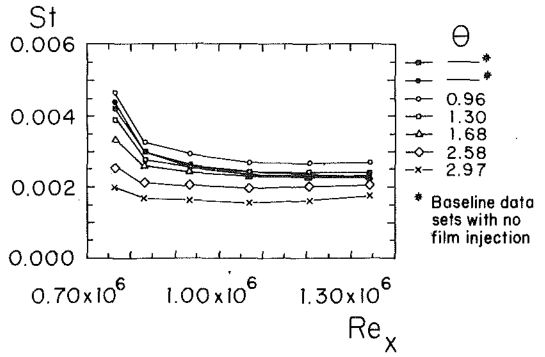

Fig. 6 Stanton number distributions with Reynolds number illustrating variations for different nondimensional temperatures θ, as measured downstream of two staggered rows of configuration 3 compound angle holes with $m = 1.0$

a plot showing the dependence of spanwise-averaged Stanton number on streamwise Reynolds number at different θ.

Streamwise Development of Adiabatic Effectiveness and Stanton Number Ratio Distributions. As mentioned earlier, local adiabatic film effectiveness values are determined from measurements of local St/St_o at different magnitudes of the nondimensional injection temperature, θ. Examples of spanwise-averaged St measured at different θ are presented in Fig. 6 as dependent upon Reynolds number based on streamwise distance X. Also included on this plot are two baseline data sets measured with no film injection. From these results, it is evident that significant Stanton number variations occur as the nondimensional injectant temperature is altered. At a given Re_x, St decreases as θ increases, which indicates nonzero values of spanwise-averaged adiabatic film effectiveness as well as improved protection as the difference between the wall temperature and injectant temperature increases. At a given value of θ, St distributions generally decrease as the Reynolds number increases.

Spanwise distributions of the adiabatic film cooling effectiveness η for $m = 1.0$ are presented in Fig. 7(*a*) at x/d of 6.8, 17.6, 33.8, 55.5, 77.1, and 98.7. With the exception of larger Z/d locations at x/d ranging from 33.8 to 98.7, η variations are spanwise periodic with Z/d at each streamwise location. At the larger Z/d at larger x/d, no spanwise periodicity is present and local effectiveness magnitudes decrease relative to ones at smaller Z/d. This is because the edge of the injectant distribution convects in the negative Z direction as x/d increases, leaving little injectant and little protection at larger Z/d when $x/d > 33.8$. Within the spanwise periodic variations, higher values of η correspond to locations where injectant is plentiful. Spanwise periodicity is more pronounced at smaller x/d of 6.8 and 17.6 because of accumulations of injectant such as the ones shown for $x/d = 9.9$ in Fig. 8(*a*). At larger x/d, the small amplitude spanwise periodicity is also affected by injectant accumulations; however, perturbations to the velocity boundary layer such as the ones for $x/d = 86.3$ in Fig. 5(*a*) also play a role.

Local St_f/St_o data, and St/St_o data (measured directly) for $\theta = 1.72$ in Figs. 7(*b*) and 7(*c*), also show spanwise periodicity; however, this periodicity is somewhat out of phase with the η distributions. Here, higher values correspond to regions of higher mixing, which occur just to the left of injectant accumulations (at smaller Z/d), especially for St_f/St_o. These local maxima also correspond to high-velocity regions that exist near the wall between the streamwise velocity deficits evident in Fig. 5(*a*). The local maxima are particularly evident at larger x/d from 33.8 to 98.7. Here, the spanwise periodicity of the St_f/St_o and St/St_o variations are much more significant across the span of the test surface than the η spanwise periodicity in Fig. 7(*a*). At locations where injectant distributions are relatively scarce (larger Z/d at x/d ranging from 33.8 to 98.7), local magnitudes of St_f/St_o and St/St_o are higher than magnitudes where injectant is more plentiful.

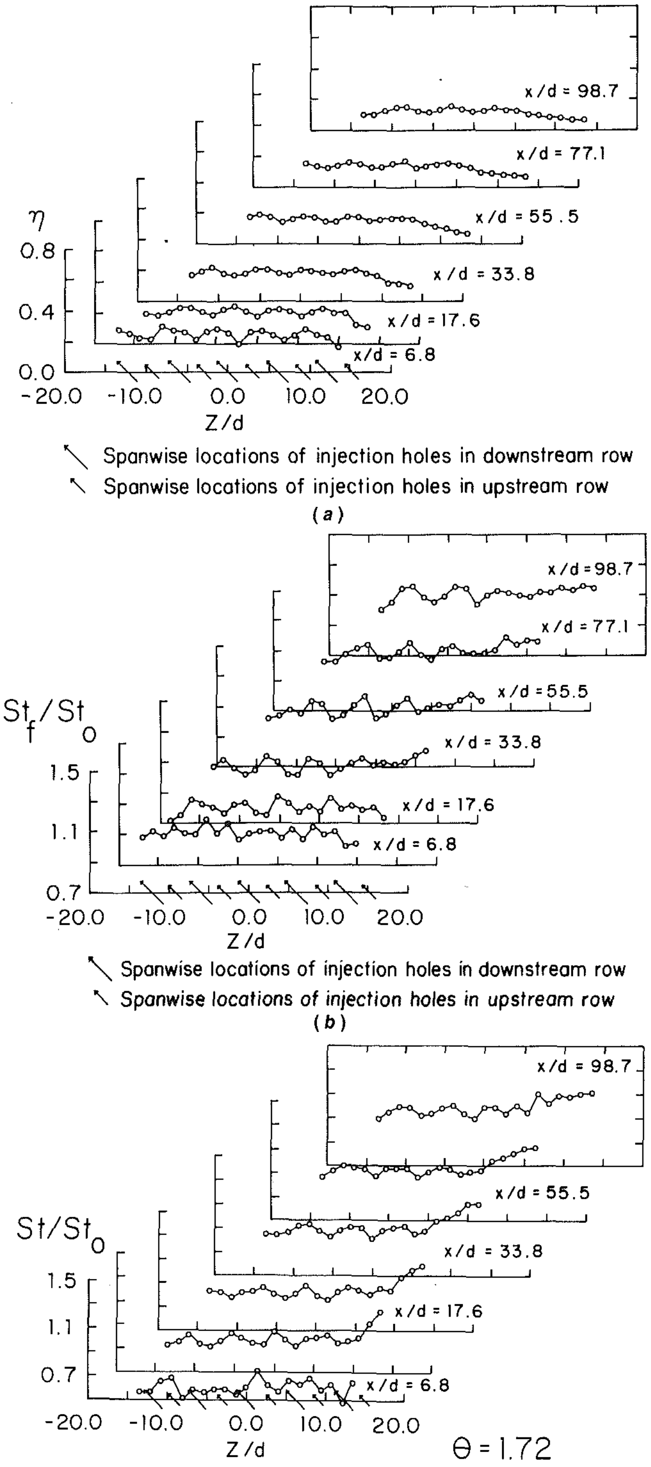

Fig. 7 Streamwise development of: (*a*) local adiabatic film cooling effectiveness, (*b*) local iso-energetic Stanton number ratios, and (*c*) local Stanton number ratios for $\theta = 1.72$, downstream of two rows of compound angle configuration 3 film cooling holes with $m = 1.0$

Streamwise Development of Injectant Distributions. Injection distribution surveys measured downstream of configuration 3 compound angle injection holes and downstream

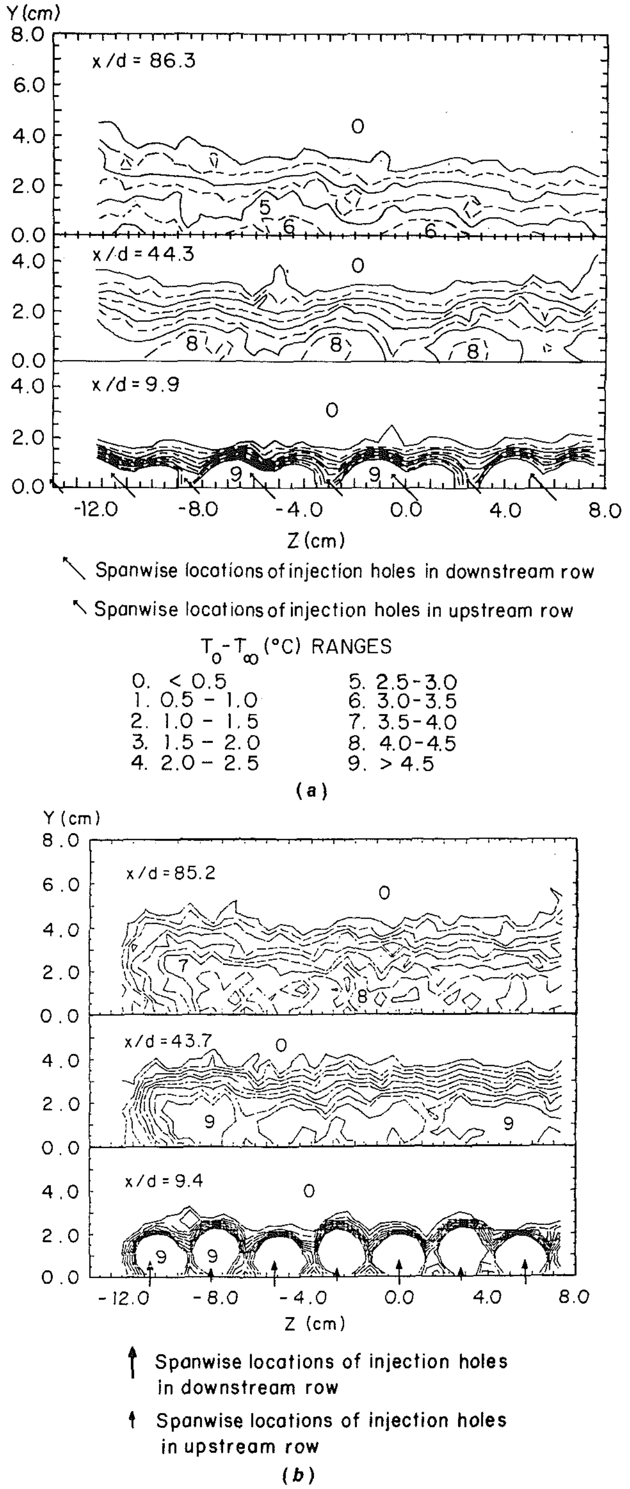

Fig. 8 Mean temperature fields showing distributions of film injectant downstream of two rows of film cooling holes with $m = 1.0$: (a) compound angle configuration 3; (b) simple angle configuration 2

of configuration 2 simple angle injection holes are presented in Figs. 8(*a*) and 8(*b*), respectively. In both cases, results are presented for a blowing ratio m of 1.0. These distributions are obtained using procedures described by Ligrani et al. (1989) in which the injectant is heated without providing any heat to the test plate. With this approach, the injectant is the only source of thermal energy relative to the free-stream flow. Distributions of $(T_o - T_\infty)$ such as the ones in Figs. 8(*a*) and 8(*b*) thus show how injectant accumulates and is rearranged in the boundary layer, mostly as a result of convective processes including the influences of any secondary flow that may be present. The temperature field is thus employed to show injectant distributions in spanwise/normal planes at different streamwise locations.

As for the velocity surveys, large and small arrows along the abscissae of Figs. 8(*a*) and 8(*b*) indicate film hole locations in downstream and upstream rows, respectively. In Fig. 8(*a*), skewed and lopsided injectant concentrations are evident in the spanwise/normal plane at $x/d = 9.9$ where accumulations from the downstream row of holes cover larger portions of the measurement plane than accumulations from the upstream row of holes. Each accumulation from an individual hole in the downstream row of holes is also in close proximity with the accumulation from the nearest hole in the upstream row. This is evidenced for $x/d = 9.9$ in Fig. 8(*a*) by a connected region of injectant concentration in the spanwise/normal plane for each pair of holes. Between these concentrations, well-defined deficits of injectant are evident that closely correspond with η minima at $x/d = 6.8$ in Fig. 7(*a*) (accounting for the slight change of spanwise location between $x/d = 6.8$ and $x/d = 9.9$). With streamwise convection to x/d of 44.3 and 86.3, injectant accumulations become more diffuse and dissipated. In addition, the injectant concentrations from the upstream row of holes completely merge with the concentrations from the downstream row of holes resulting in half as many accumulations across the span of the measurement plane at x/d of 44.3 and 86.3 compared to $x/d = 9.9$. This behavior is consistent with the velocity survey of Fig. 5(*a*), since injectant accumulations for all three x/d show close correspondence to streamwise velocity deficits. One injectant accumulation is present for each velocity deficit such that accumulations lie just to the right (at larger Z) of streamwise velocity deficits. Injectant accumulations at x/d of 44.3 and 86.3 also show close correspondence to local η maxima in Fig. 7(*a*), and approximate correspondence to locally lower $\mathrm{St}_f/\mathrm{St}_o$ in Fig. 7(*b*).

The distributions in Fig. 8(*a*) are significantly different from the ones in Fig. 8(*b*) measured downstream of two staggered rows of simple angle configuration 2 holes with the same spanwise hole spacing and blowing ratio m. Injectant distributions in the bottom portion of this latter figure represent large circular concentrations of injectant in the spanwise/normal plane at $x/d = 9.4$. Every other accumulation is qualitatively similar and adjacent distributions are different since injectant from the downstream row of holes is located slightly closer to the wall than injectant from the upstream row of holes. However, in spite of this spanwise periodicity, η, $\mathrm{St}/\mathrm{St}_o$, and $\mathrm{St}_f/\mathrm{St}_o$ data measured downstream of the simple angle holes show little spanwise variations at slightly lower (6.7) and slightly higher (17.2) values of x/d (Ligrani et al., 1992). Farther downstream, at x/d of 43.7 and 85.2, injectant accumulations from neighboring holes become more spread out to eventually merge together to form a uniform layer across the span of the test surface. The results measured downstream of the compound angle holes near the same x/d (Fig. 8*a*) are significantly different since they continue to evidence spanwise periodic concentrations of injectant. This spanwise periodicity continues to Z values less than -12 cm as a result of convection of the injectant in the negative Z direction. In contrast, injectant accumulations downstream of the simple angle holes (Fig. 8*b*) discontinue for Z values less than about -12 cm because spanwise convection of injectant is minimal and because no simple angle injection holes are located at $Z < -11.3$ cm.

Effects of Blowing Ratio on Local Adiabatic Film-Cooling Effectiveness and Injectant Distributions. Results showing the influences of blowing ratio on local adiabatic effectiveness distributions and on local injectant distributions are presented in Figs. 9 and 10, respectively. These data, which were obtained downstream of the compound angle holes, are presented for blowing ratios of 0.5, 1.0, and 1.5, which are equivalent to

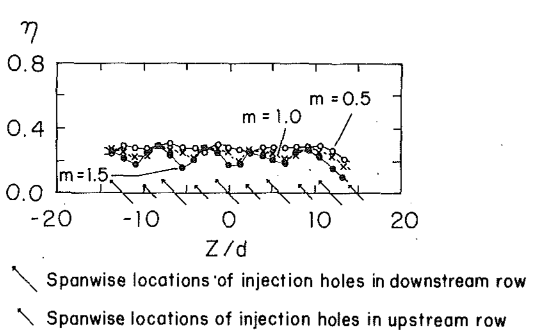

Fig. 9 Spanwise variations of adiabatic film cooling effectiveness downstream of two rows of compound angle configuration 3 film cooling holes at $x/d = 6.8$ for $m = 0.5$, 1.0, and 1.5

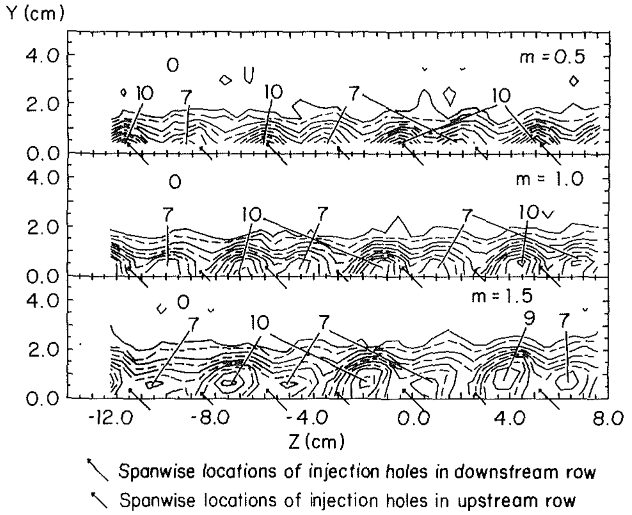

$T_0 - T_\infty$ (°C) RANGES

0.	< 0.5	6.	5.0 - 6.0
1.	0.5 - 1.0	7.	6.0 - 7.0
2.	1.0 - 2.0	8.	7.0 - 8.0
3.	2.0 - 3.0	9.	8.0 - 9.0
4.	3.0 - 4.0	10.	>9.0
5.	4.0 - 5.0		

Fig. 10 Mean temperature fields showing distributions of film injectant downstream of two rows of compound angle configuration 3 film-cooling holes at $x/d = 9.9$ for $m = 0.5$, $m = 1.0$ and $m = 1.5$

momentum flux ratios of 0.25, 1.0, and 2.25. In each figure, large arrows along the abscissa indicate the spanwise locations of injection holes in the downstream row, and small arrows indicate the spanwise locations of injection holes in the upstream row. The effectiveness results are determined from measurements at $x/d = 6.8$, whereas the injectant surveys are given for $x/d = 9.9$.

Figure 9 shows that the highest η magnitudes across the span of the measurement plane occur at a blowing ratio of 0.5. Of the three effectiveness distributions, this distribution also shows the greatest spanwise uniformity and the least spanwise periodicity. The only exception occurs for $Z/d > 10$, where all three distributions decrease because they are measured at locations slightly away from the spanwise edge of the injectant. At $Z/d < 10$, the spanwise periodicity of the η distributions increases with blowing ratio such that higher η values correspond to locations where abundant amounts of injectant are spread along the test surface, and lower values correspond to locations where the injectant coverage is more sparse. The nearly spanwise uniform η distribution for $m = 0.5$ thus evidences a more uniform distribution of injectant than is present for $m = 1.0$ and 1.5. Local η minima become lower with blowing ratio, and thus, the $m = 1.5$ distribution evidences periodic injectant concentrations and deficits across the span of the test surface.

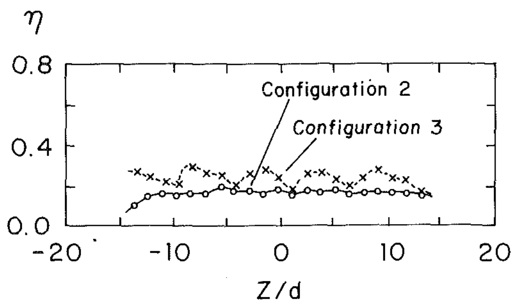

Fig. 11 Spanwise variations of adiabatic film cooling effectiveness for $m = 1.0$ downstream of two rows of compound angle configuration 3 film-cooling holes at $x/d = 6.8$ and downstream of two rows of simple angle configuration 2 film-cooling holes at $x/d = 6.8$.

Additional explanation of the trends seen in Fig. 9 is obtained from an examination of Fig. 10. Injectant distributions in this figure are spanwise periodic for all three blowing ratios, as expected. Adjacent accumulations are dissimilar, and every other accumulation is qualitatively similar since they originate from the same row of injection holes (either upstream or downstream). Of these, the most significant originate in the downstream row of holes. The results for $m = 0.5$ are different from the ones at $m = 1.0$ and $m = 1.5$ in several respects. First, the spanwise spacing between individual injectant accumulations for $m = 0.5$ is more uniform for $Y > 0.5$ cm; second, the injectant is spread more uniformly along the wall for $Y < 0.5$ cm; and third, the accumulations are convected away from the injection holes a smaller distance in the spanwise direction. In addition, the results for $m = 0.5$ are different from the ones at $m = 1.0$ (Fig. 8*a*) since they show greater spanwise uniformity at $x/d = 44.3$ and $x/d = 86.3$ (Wigle, 1991).

As the blowing ratio increases to 1.0 to 1.5, Fig. 10 shows injectant concentrations for $x/d = 9.9$ that are located farther and farther from the test plate. Such lift-off behavior is consistent with Ligrani et al. (1992), and probably initiated by lift-off of injectant from individual holes in the upstream row. The injectant from an individual hole in the upstream row is then convected downstream away from the wall until it coalesces with injectant from the closest hole in the downstream row. This produces localized regions where less injectant covers the test surface, resulting in regions of lower protection. For $m = 1.5$, these are located at Z of -10 cm, -4.5 cm, 1.5 cm, and 6.5 cm in Fig. 10, and at the locations of η minima in Fig. 9 at Z/d of -11, -5, 1.5, and 7. Thus, both spanwise-averaged $\overline{\eta}$, and local η minima decrease in magnitude as the blowing ratio increases because of decreased local protection, which results as increasing amounts of injectant are lifted off the test surface.

Comparison of Local Adiabatic Film Cooling Effectiveness Distributions From Configurations 2 and 3. Local adiabatic film cooling effectiveness distributions for $x/d = 6.8$ and $m = 1.0$ from configurations 2 and 3 are presented in Fig. 11. These results provide a comparison of the local η produced by the simple angle and compound angle hole arrangements with the same spanwise hole spacing.

η values for compound angle configuration 3 are higher and show significantly greater spanwise periodicity than the ones for simple angle configuration 2. The spanwise periodicity results from periodic regions of lower protection across the span of the test surface. As illustrated by Figs. 8(*a*) and 10, these develop as injectant from the upstream row of holes lifts off the test surface and then coalesces with the injectant from the downstream row of holes. Injectant trajectories from simple angle configuration 2 (Fig. 8*b*) tend to produce spanwise uniform η; however, because of the way in which they are distributed along the surface, the spanwise-averaged effectiveness at $x/d = 6.8$, $\overline{\eta}$, is lower than for the compound angle configuration 3. More injectant remains in close proximity to the wall downstream of individual compound angle holes (Fig. 8*a*). Consequently, the wall is exposed to a wider range of temperatures across the span of the test surface. For simple angle holes, Fig. 8(*b*) shows that the largest concentrations of injectant barely touch the surface, which results in a nearly constant distribution of η with Z/d.

The η distribution for configuration 2 should be ignored for $Z/d < -10$, and the η distribution for configuration 3 should be ignored for $Z/d > 10$ because these locations lie away from the regions of injectant coverage along the test surface.

Spanwise-Averaged Adiabatic Film-Cooling Effectiveness Values and Stanton Number Ratios

The discussion that follows is presented in three parts. First, the effect of hole orientation (compound angle or simple angle) with constant spanwise hole spacing is discussed. This is followed by discussion of the effects of spanwise hole spacing on film cooling from holes with compound angle orientations. Finally, some of the present results are compared to ones from other studies. Spanwise-averaged magnitudes of effectiveness and Stanton number are determined from local measurements of these quantities for each thermocouple row (Fig. 1) by averaging the first 13 data points from each row over a Z/d range from -13.7 to 2.7.

Effects of Hole Orientation (Compound Angle or Simple Angle) With Constant Spanwise Hole Spacing. Spanwise-averaged values of the adiabatic film cooling effectiveness measured downstream of configuration 3 compound angle holes as well as downstream of configuration 2 simple angle holes are presented in Fig. 12(*a*). These two injection configurations have the same spanwise hole spacing and the two sets of data are obtained using similar experimental conditions so that the changes to film protection resulting from the use of compound angle holes instead of simple angle holes are illustrated.

Referring first to the compound angle (configuration 3) data in Fig. 12(*a*), data at x/d less than 20 decrease with blowing ratio because of the lift-off of injectant from the test surface discussed earlier in reference to Figs. 9-11. However, as the boundary layers convect farther downstream, $\overline{\eta}$ values for $m = 0.5$ are lower than values for $m = 1.0$ and 1.5 since a smaller amount of film is spread along the test surface. These differences also result partially because of the different ways in which the injectant spreads along the test surface. When $m = 0.5$, the injectant is fairly uniform along the test surface, especially for $x/d > 40$. However, at the higher blowing ratios greater than or equal to 1.0, injectant from the upstream row of holes coalesces with injectant from the downstream row of holes (Figs. 8*a* and 10), resulting in distributions that are spatially nonuniform across the test surface span at x/d even as large as 98.7. This is probably one reason why spanwise-averaged effectiveness values for $m = 1.0$ and $m = 1.5$ are so close together for $x/d > 20$.

The trends of the present simple angle (configuration 2) data in Fig. 12(*a*) are fairly complex for $x/d < 40$. Complicated lift-off behavior is evidenced by $\overline{\eta}$ values, which decrease with m at $x/d = 6.8$ but change from this trend at $x/d = 17.4$ and $x/d = 33.2$. The qualitative trends shown by these data for $m = 0.5$ and $m = 1.0$ are similar to trends measured by Goldstein and Yoshida (1982) downstream of a single row of simple angle holes (turbulent injection, turbulent free-stream, $3d$ spacing, $\Omega = 30$ deg. and $\beta = 90$ deg) with the same m. At larger x/d (>50-60) simple angle $\overline{\eta}$ values in Fig. 12(*a*) increase with blowing ratio, which is consistent with the fact that more injectant is present along the test surface to provide better heat sink characteristics and improved thermal protection. In addition, effectiveness, Stanton number ratios, and injectant distributions for the same x/d indicate that this injectant is spread fairly uniformly over the test surface for all three m tested (Wigle, 1991; Ligrani et al., 1992).

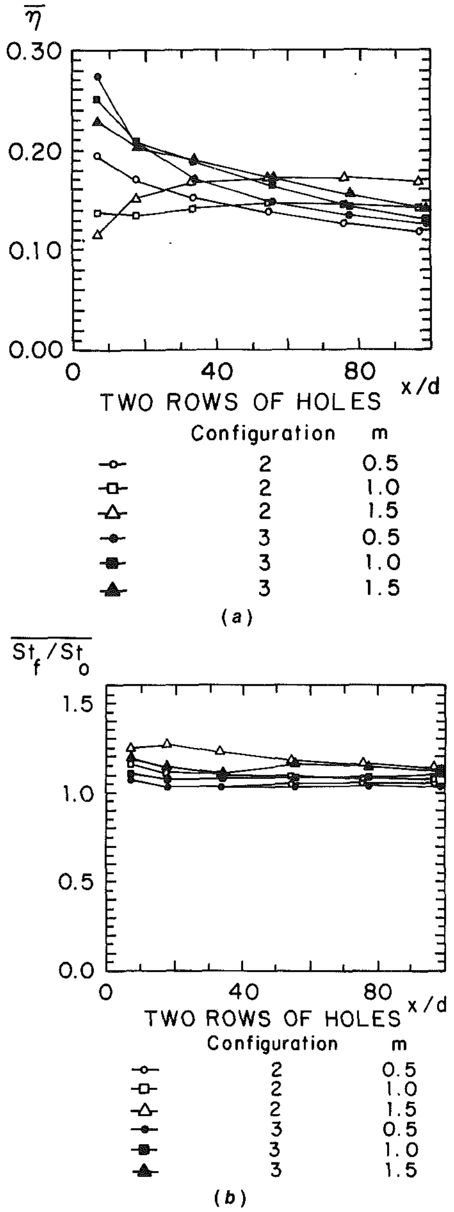

Fig. 12 Spanwise-averaged magnitudes of adiabatic film cooling effectiveness and iso-energetic Stanton number ratio, shown as dependent upon normalized streamwise distance downstream of two rows of compound angle configuration 3 film cooling holes. Results are compared to ones measured downstream of two rows of simple angle configuration 2 film-cooling holes.

Comparing effectiveness values for configurations 2 and 3 in Fig. 12(*a*), it is evident that the simple angle data lie below the compound angle data, especially for $x/d < 60$. Thus, at smaller x/d, the compound angle data indicate significantly improved protection for the same spanwise hole spacing x/d and blowing ratio m. For $m = 1.5$, the change in effectiveness at $x/d = 6.8$ is from 0.115 to 0.229, which amounts to an increase of 99 percent. For $m = 0.5$, the change in effectiveness at $x/d = 6.8$ is from 0.195 to 0.273, which amounts to an increase of 40 percent. At x/d larger than 60, the compound angle data generally cover about the same range as the simple angle data. This is particularly evident if the data at individual blowing ratios are examined, and believed to occur because equivalent amounts of injectant from each of the two configurations cover the downstream portion of the test surface.

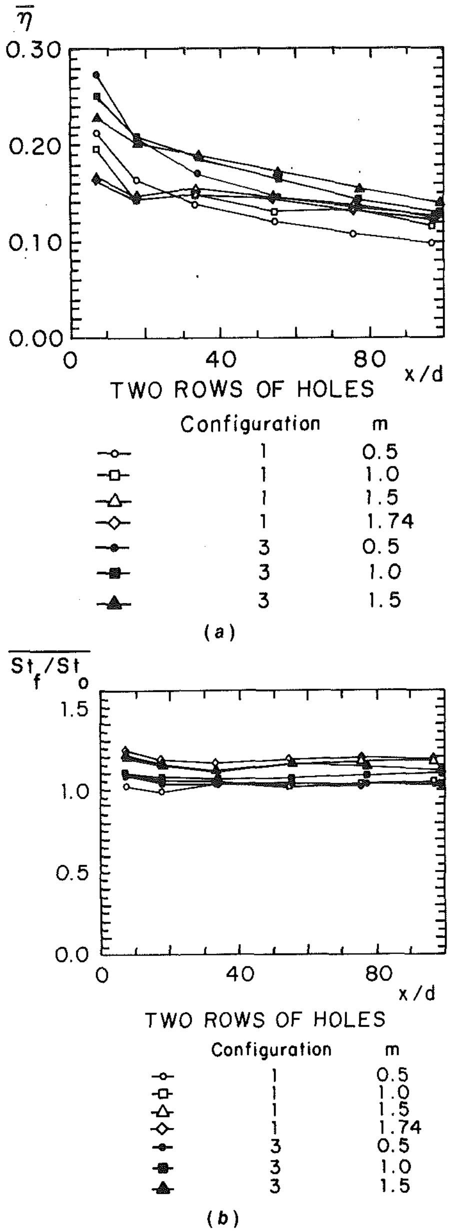

Fig. 13 Spanwise-averaged magnitudes of adiabatic film cooling effectiveness and iso-energetic Stanton number ratio, shown as dependent upon normalized streamwise distance downstream of two rows of compound angle configuration 3 film-cooling holes. Results are compared to ones measured downstream of two rows of compound angle configuration 1 film-cooling holes.

According to Ligrani et al. (1992), lift-off of the injectant from two rows of compound angle holes (with 3.9*d* spanwise spacing) is probably occurring at momentum flux ratios between 1.0 and 2.0. The present data for 3.0*d* spanwise spacing show similar behavior. In contrast, the simple angle configuration show significant decreases of effectiveness as momentum flux increases from 0.25 to 1.0, indicating lift-off at a lower value of momentum flux. These differences result, first of all, because the lateral component of momentum of the injectant from the compound angle holes causes the injectant to spread out much more in the lateral direction as it is convected downstream and penetrates into the mainstream. Second, the hole angles with respect to the test surface are 24 deg for the compound angle arrangement compared to 35 deg for the simple angle arrangement.

Spanwise-averaged iso-energetic Stanton number ratios in Fig. 12(*b*) for compound angle configuration 3 and for simple angle configuration 2 show a number of interesting trends.

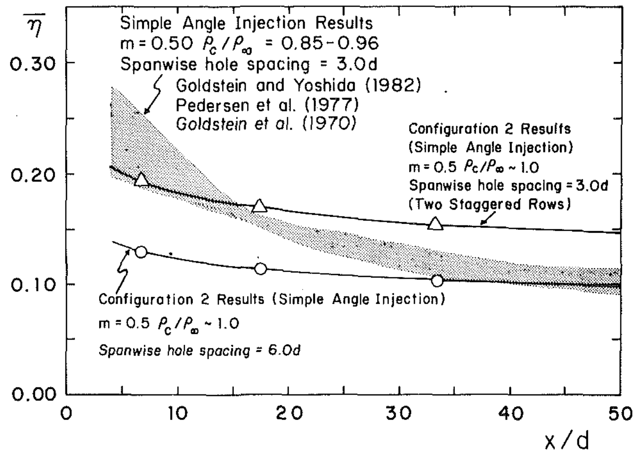

Fig. 14 Spanwise-averaged magnitudes of adiabatic film cooling effectiveness as dependent upon normalized streamwise distance. The present results measured downstream of one and two rows of configuration 2 simple angle holes are compared to ones from Goldstein and Yoshida (1982), Pedersen et al. (1977), and Goldstein et al. (1970) for equivalent experimental conditions.

First, little St_f/St_o variation with x/d is evident for each value of m. Second, compound angle data cover approximately the same range of values as the simple angle data, especially when the two sets of results are compared at the same blowing ratio. Third, for each x/d, St_f/St_o values generally increase with m (Ligrani et al., 1994).

Effects of Spanwise Spacing of Compound Angle Injection Holes. Results measured downstream of compound angle configurations 1 and 3 are compared in Figs. 13(*a*) and 13(*b*). The two configurations are similar in that both have the same injection hole angles with respect to the test surface such that $\Omega = 35$ deg and $\beta = 30$ deg. The two configurations are different since the spanwise hole spacing of configuration 1 is 3.9*d*, whereas the spanwise hole spacing of configuration 3 is 3.0*d*.

Figure 13*a* shows that spanwise-averaged effectiveness values are higher when smaller hole spacing is employed provided data are compared at the same m and x/d. At x/d less than 40, $\overline{\eta}$ values downstream of configuration 3 are 25 to 40 percent higher than the ones measured downstream of configuration 1. These differences increase as x/d becomes smaller. For example, for $x/d = 6.7$–6.8 and $m = 1.5$, $\overline{\eta}$ equals 0.229 downstream of configuration 3, which is 37 percent higher than 0.167, the value measured downstream of configuration 1. At x/d greater than 40, the complicated interactions that occur just downstream of the holes are not present, and spanwise averaged effectiveness values are mostly dependent upon the density of the injectant distribution along the test surface and hence, the spanwise hole spacing. Here, differences between the two configurations range from 12 to 30 percent.

Spanwise-averaged magnitudes of the iso-energetic Stanton number ratio are presented in Fig. 13(*b*). Close examination reveals trends that are very similar to the ones evident in Fig. 12(*b*). Ligrani et al. (1992) provide additional information, especially pertaining to results measured downstream of configuration 1.

Comparison With Other Studies. Figure 14 presents a comparison of spanwise-averaged effectiveness results from the present study measured downstream of simple angle configuration 2, and the results of Goldstein and Yoshida (1992), Pedersen et al. (1977), and Goldstein et al. (1970) (these three references are hereafter referred to collectively as GYPG). The GYPG results are used for comparison with ones from the present study because their injection geometry and flow conditions provide the closest match of the data available in the archival literature.

GYPG employ a single row of holes with individual holes spaced $3d$ apart in the spanwise direction, and inclined at angles of 30 deg. from the test surface ($\Omega = 30$ deg and $\beta = 90$ deg). The injection geometry of configuration 2 is similar since it also employs simple angle holes with $3d$ spanwise spacing. The geometry is slightly different because holes are inclined 35 deg from the test surface ($\Omega = 35$ deg and $\beta = 90$ deg), and arranged in two staggered rows (Fig. 3). The GYPG data are presented for a blowing ratio m of 0.5, and density ratio ρ_c/ρ_∞ ranging from 0.85 to 0.96. Our blowing ratio is also 0.5; however, our density ratio is slightly higher at approximately 1.0. Both the injectant and the boundary layer are fully turbulent in GYPG and the present investigation. In addition, both employ thermal test surfaces, which begin just downstream of injection holes (producing an unheated starting length in the present study), as well as constant heat flux boundary conditions along test surfaces. The thermal boundary conditions are different in that GYPG employ a zero heat flux to produce an adiabatic boundary whereas a finite magnitude of flux is employed in the present study.

Figure 14 shows that the present results for $3d$ spanwise hole spacing fall well within the range of the GYPG data for $x/d < 20$. At higher x/d, the present results are higher than the GYPG data, and thus, the present results show a smaller variation with x/d compared to GYPG. However, when experimental uncertainties are considered, the uppermost portions of the GYPG data lie at the lower edge of the uncertainty band of the present data for $3d$ spanwise spacing (0.030 to 0.035 effectiveness units) for the entire range of x/d shown in Fig. 14. In addition, the GYPG data for $x/d > 20$ are bracketed by the present results for $3d$ spanwise hole spacing and the present results for $6d$ spanwise hole spacing. This is evident since the present results for $6d$ spanwise spacing lie near the lower bound of the GYPG data range for $x/d > 40$. Jabbari and Goldstein (1978) also measured the adiabatic film-cooling effectiveness downstream of two staggered rows of simple angle holes having geometries similar to the configuration 2 holes used in the present study. However, because their spanwise hole spacings are half as much ($1.5d$), their $\bar{\eta}$ data are 60–80 percent higher when compared at $m = 0.5$.

Some of the differences between the present results for $3d$ spanwise spacing and GYPG are due to the small differences in injection geometry and flow conditions mentioned above (one row versus two staggered rows, slightly different Ω, slightly different ρ_c/ρ_∞, and different magnitudes of test surface heat flux). However, the different variations with streamwise development, which are evidenced by $\bar{\eta}$ from the present study, which are higher for $x/d > 20$, are probably mostly due to different ratios of boundary layer displacement thickness to injection hole diameter at the location of the injection holes. Because of this, different percentages of the injectant are contained in the boundary layers as they are convected downstream. The ratio of boundary layer displacement thickness to injection hole diameter is 0.14 for Goldstein and Yoshida (1982), 0.162 for Pedersen et al. (1977), and 0.124 for Goldstein et al. (1970) (giving an average GYPG value of 0.142) compared to 0.22 in the present study. The average ratio of total boundary layer thickness to injection hole diameter for GYPG is then approximately 0.66 compared to 1.03 for the present study. This means that most of the injectant in the present study is spread throughout the boundary layer as it is convected downstream, whereas a significant portion of the injectant in the GYPG studies may be spread *outside* of the boundary layer as well as within the boundary layer. Consequently, higher concentrations of injectant are contained near the wall in the present study just downstream of the injection holes as well as at streamwise locations farther downstream. Higher concentrations of injectant near the wall produce better thermal protection and higher film effectiveness values. For these reasons, the present $\bar{\eta}$ results for $3d$ spanwise hole spacing in Fig. 14 decrease less rapidly with x/d, and are as much as 0.029 effectiveness units higher than ones from GYPG at x/d from 20 to 50.

Summary and Conclusions

Experimental results are presented that describe the development and structure of flow downstream of two staggered rows of film-cooling holes with compound angle orientations. With this configuration, which is denoted number 3, holes are spaced $3d$ apart in the spanwise direction, inclined at 35 deg with respect to the test surface when projected into the streamwise/normal plane, and inclined at 30 deg with respect to the test surface when projected into the spanwise/normal plane. Results are presented for an injectant to free-stream density ratio near 1.0, x/d ranging from 6.8 to 98.7, injection blowing ratios from 0.5 to 1.50, and momentum flux ratios from 0.25 to 2.25. These results are compared to ones from configuration 2 to determine the effects of hole angle orientations for constant spanwise hole spacing, and with results from configuration 1 to determine the effects of spanwise hole spacing when the hole angle orientation is maintained constant.

The most important conclusion from the present study comes from a comparison of spanwise-averaged adiabatic effectiveness values measured downstream of injection hole configurations 2 and 3. From this, it is evident that the compound angle injection configuration 3 provides significantly improved protection compared to simple angle configuration 2 for the same spanwise hole spacing, normalized streamwise location x/d, and blowing ratio m, for $x/d < 60$. At $x/d = 6.8$ just downstream of the holes, the data measured downstream of injection hole configuration 3 lie 40 to 99 percent higher than data measured downstream of configuration 2, depending upon the blowing ratio. Local adiabatic effectiveness values at $x/d = 6.8$ downstream of the configuration 3 holes also show greater spanwise periodicity than ones downstream of configuration 2. This is because of spanwise periodic regions of lower protection, which develop as injectant from the upstream row of configuration 3 holes lifts off the surface and then coalesces with injectant from the downstream row of holes. At x/d larger than 60, spanwise-averaged adiabatic effectiveness data downstream of configuration 3 generally cover about the same range as the data measured downstream of the configuration 2 injection holes.

A comparison of results measured downstream of compound angle configurations 1 and 3 shows that spanwise-averaged effectiveness values are 25 to 40 percent higher when smaller hole spacing is employed provided data are compared at the same m and x/d, for $x/d < 40$. At x/d greater than 40, the complicated interactions that occur just downstream of the holes are not present, and spanwise-averaged effectiveness values are mostly dependent upon the density of the injectant distribution along the test surface and hence, the spanwise hole spacing. Here, differences between the two configurations range from 12 to 30 percent.

Spanwise-averaged values of the adiabatic film cooling effectiveness measured downstream of configuration 3 are highest with a blowing ratio of 0.5, and decrease with blowing ratio because of injection jet lift-off effects for $x/d < 20$. Lift-off at $m = 1.5$ is confirmed by injection distribution surveys, which show that injectant from an individual hole in the upstream row coalesces with the injectant from the closest hole in the downstream row. This produces spanwise periodic concentrations of injectant and local protection. However, as the boundary layers convect farther downstream to $x/d > 20$, $\bar{\eta}$ values for $m = 0.5$ are lower than values for m of 1.0 and 1.5 since a smaller amount of film is spread along the test surface. Velocity and injectant surveys at these higher m show half as many velocity deficits and injectant accumulations across spanwise/normal planes at x/d of 86.3 and 44.3 compared to $x/d = 9.9$. In contrast, the injectant with $m = 0.5$ is fairly uniform along the span of the test surface, especially for x/d greater than or equal to 44.3.

Spanwise-averaged iso-energetic Stanton number ratios range between 1.0 and 1.25. Data measured downstream of compound angle configuration 3 cover approximately the same range of values and show roughly the same trends as values measured downstream of configurations 1 and 2, particularly when results are compared for the same blowing ratio. In addition, St_f/St_o values measured downstream of all three configurations increase with m at each x/d, and show little variation with x/d for each value of m tested.

Acknowledgments

This study was supported by: (1) the Naval Sea Systems Command, Job Order Numbers N622711-RGPLG and N622712-RTBPL (Dr. Dan Groghan and Dr. Sam Shepard were program monitors), and (2) the Aero-Propulsion Laboratory of Wright Patterson Air Force Base, MIPR Numbers FY 1455-89-N0670 and FY 1455-92-N0641 (Dr. Bill Troha was program monitor). Of the different portions of the study, the NSSC supported the portions of the investigation pertaining to configuration 3, and WPAFB supported the portions of the investigation pertaining to configurations 1 and 2.

References

Bishop, D. T., 1990, "Heat Transfer, Adiabatic Effectiveness and Injectant Distributions Downstream of Single and Double Rows of Film-Cooling Holes With Compound Angles," M. S. Thesis, Department of Mechanical Engineering, Naval Postgraduate School, Monterey, CA.

Ciriello, S., 1991, "Heat Transfer, Adiabatic Effectiveness and Injectant Distributions Downstream of Single and Double Rows of Film-Cooling Holes With Simple and Compound Angles," M. S. Thesis, Department of Mechanical Engineering, Naval Postgraduate School, Monterey, CA.

Goldstein, R. J., Eckert, E. R. G., Eriksen, V. L., and Ramsey, J. W., 1970, "Film Cooling Following Injection Through Inclined Circular Tubes," *Israel Journal of Technology*, Vol. 8, pp. 145-154.

Goldstein, R. J., and Yoshida, T., 1982, "The Influence of a Laminar Boundary Layer and Laminar Injection on Film Cooling Performance," ASME JOURNAL OF HEAT TRANSFER, Vol. 104, No. 2, pp. 355-362.

Jabbari, M. Y., and Goldstein, R. J., 1978, "Adiabatic Wall Temperature and Heat Transfer Downstream of Injection Through Two Rows of Holes," ASME *Journal of Engineering for Power*, Vol. 100, pp. 303-307.

Kays, W. M., and Crawford, M. E., 1993, *Convective Heat and Mass Transfer*, 3rd ed., McGraw-Hill, New York.

Kim, H. K., Moffat, R. J., and Kays, W. M., 1978, "Heat Transfer to a Full-Coverage, Film-Cooled Surface With Compound-Angle (30° and 45°) Hole Injection," Report No. HMT-28, Thermosciences Division, Department of Mechanical Engineering, Stanford University, Stanford, CA.

Kline, S. J., and McClintock, F. A., 1953, "Describing Uncertainties in Single-Sample Experiments," *Mechanical Engineering*, Jan., pp. 3-8.

Ligrani, P. M., and Camci, C., 1985, "Adiabatic Film Cooling Effectiveness From Heat Transfer Measurements in Compressible, Variable Property Flow," ASME JOURNAL OF HEAT TRANSFER, Vol. 107, pp. 313-320.

Ligrani, P. M., Ortiz, A., Joseph, S. L., and Evans, D. L., 1989, "Effects of Embedded Vortices on Film-Cooled Turbulent Boundary Layers," ASME *Journal of Turbomachinery*, Vol. 111, pp. 71-77.

Ligrani, P. M., 1990, "Comment on 'Behavior of a Coolant Film With Two Rows of Holes Along the Pressure Side of a High Pressure Nozzle Guide Vane'," ASME *Journal of Turbomachinery*, Vol. 112, pp. 520-521.

Ligrani, P. M., Ciriello, S., and Bishop, D. T., 1992, "Heat Transfer, Adiabatic Effectiveness, and Injectant Distributions Downstream of a Single Row and Two Staggered Rows of Compound Angle Film-Cooling Holes," ASME *Journal of Turbomachinery*, Vol. 114, pp. 687-700.

Ligrani, P. M., Wigle, J. M., and Jackson, S. W., 1994, "Film-Cooling From Holes With Compound Angle Orientations: Part 2—Results Downstream of a Single Row of Holes With 6*d* Spanwise Spacing," ASME JOURNAL OF HEAT TRANSFER, Vol. 116, this issue, pp. 353-362.

Mayle, R. E., and Camarata, F. J., 1975, "Multihole Cooling Film Effectiveness and Heat Transfer," ASME JOURNAL OF HEAT TRANSFER, Vol. 97, pp. 534-538.

Mehendale, A. B., and Han, J. C., 1992, "Influence of High Mainstream Turbulence on Leading Edge Film Cooling Heat Transfer," ASME *Journal of Turbomachinery*, Vol. 114, pp. 707-715.

Moffat, R. J., 1982, "Contributions to the Theory of Single-Sample Uncertainty Analysis," ASME *Journal of Fluids Engineering*, Vol. 104, pp. 250-260.

Pedersen, D. R., Eckert, E. R. G., and Goldstein, R. J., 1977, "Film Cooling With Large Density Differences Between the Mainstream and the Secondary Fluid Measured by the Heat-Mass Transfer Analogy," ASME JOURNAL OF HEAT TRANSFER, Vol. 99, pp. 620-627.

Wigle, J. M., 1991, "Heat Transfer, Adiabatic Effectiveness and Injectant Distributions Downstream of Single and Double Rows of Film-Cooling Holes With Compound Angles," M. S. Thesis, Department of Mechanical Engineering, Naval Postgraduate School, Monterey, CA.

Film-Cooling From Holes With Compound Angle Orientations: Part 2—Results Downstream of a Single Row of Holes With 6d Spanwise Spacing

P. M. Ligrani
Associate Professor,
Department of Mechanical Engineering,
University of Utah,
Salt Lake City, UT 84112
Mem. ASME

J. M. Wigle
Graduate Student.

S. W. Jackson
Graduate Student.

Department of Mechanical Engineering,
Naval Postgraduate School,
Monterey, CA 93943

Experimental results are presented that describe the development and structure of flow downstream of a single row of film-cooling holes with compound angle orientations. With this configuration, holes are spaced 6d apart in the spanwise direction, inclined at 35 deg with respect to the test surface when projected into the streamwise/normal plane, and inclined at 30 deg with respect to the test surface when projected into the spanwise/normal plane. Results are presented for an injectant to free-stream density ratio near 1.0, and injection blowing ratios from 0.5 to 1.50. Comparisons are made with measurements from two other configurations to determine: (1) the effects of hole angle orientation for constant spanwise hole spacing, and (2) the effects of spanwise hole spacing when the hole angle orientation is maintained constant. Results from the first comparison show that the compound angle injection configuration provides significantly improved film-cooling protection compared to a simple angle configuration for the same spanwise hole spacing, normalized streamwise location x/d*, and blowing ratio* m*, for* $x/d<30$ *when* $m=0.50$ *and for* $x/d<60$ *when* $m=1.0$ *and 1.5. At* $x/d>60$*, spanwise-averaged adiabatic effectiveness data downstream of the two configurations generally cover about the same range. Results from the second comparison show that spanwise-averaged effectiveness values are 20 to 39 percent higher when 6d spanwise hole spacing is employed compared to 7.8d spanwise hole spacing for the same* m *and* x/d*, for* $x/d<60$*. When plotted in* $\bar{\eta}/m$ *versus* Xl/s *coordinates, spanwise-averaged film effectiveness data measured downstream of one and two rows of holes from all injection configurations tested show a reasonable collapse. For* m *values between 1 and 3, spanwise-averaged iso-energetic Stanton number ratios measured just downstream of one row of holes are lower than results measured just downstream of two rows of holes, which evidences greater mixing and higher turbulence levels when the injectant emerges from two rows of holes.*

Introduction

The objective of this investigation is to provide new data that illustrate the behavior of film cooling from holes with compound angle orientations. Of particular interest are the differences in protection that result downstream of injection holes with compound angle orientations as compared to regions downstream of injection holes with the same spanwise hole spacing but with simple angle orientations. Also of interest are the changes in protection that occur as the spanwise spacing between holes with compound angle orientations is changed. As such, the study is important because almost no data are available in the archival literature on heat transfer and boundary layer behavior downstream of film cooling holes with compound angle orientations, in spite of widespread use of these holes.

The present study is thus aimed at remedying this deficiency by providing information on a film produced by a single row of injection holes with 6d spanwise spacing, where d is the injection hole diameter. The present paper presents results from Part 2 of the study that are complementary to ones from Part 1 (Ligrani et al., 1994) in which film-cooling from two staggered rows of holes with 3d spanwise spacing is discussed. The present results measured downstream of the single row of holes are important because they provide important information for designers. They also provide insight into the behavior and influences of injectant trajectories from individual holes. This is because the relatively large hole spacing results in minimal coalescence and interactions between injectant fluid from adjacent holes at small x/d.

A number of operating parameters existing in the first turbine stages of gas turbine engines are matched in the experiment. These are discussed in Part 1 of this investigation (Ligrani et al., 1994), along with effects present in operating high-temperature engines that are not matched in the study. The holes employed are inclined at 35 deg with respect to the test surface when projected into the streamwise/normal plane, and 30 deg with respect to the test surface when projected into the spanwise/normal plane. Results include distributions of surface Stanton numbers, adiabatic film cooling effectiveness and iso-energetic Stanton number ratios deduced from Stanton number ratios using superposition, and injectant distributions. Also presented are plots showing the streamwise development of distributions of mean streamwise velocity. The simple angle arrangement used for comparison has holes that are inclined 35 deg with respect to the test surface in the streamwise/normal plane with the same spanwise hole spacing as the compound angle arrangement. Comparisons are also made with results

---

Contributed by the Heat Transfer Division for publication in the JOURNAL OF HEAT TRANSFER. Manuscript received by the Heat Transfer Division November 1992; revision received July 1993. Keywords: Forced Convection, Turbines. Associate Technical Editor: T. W. Simon.

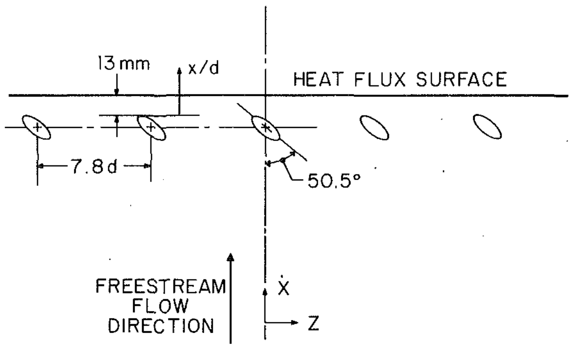

Fig. 1 Test surface injection geometry for film-cooling holes arranged with configuration 1 compound angle holes

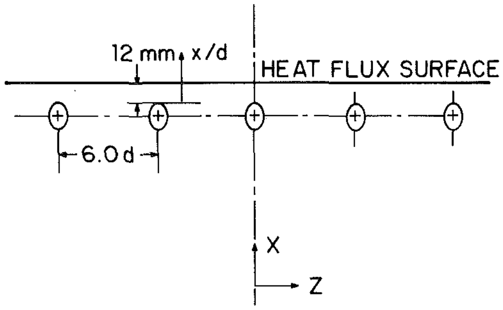

Fig. 2 Test surface injection geometry for film-cooling holes arranged with configuration 2 simple angle holes

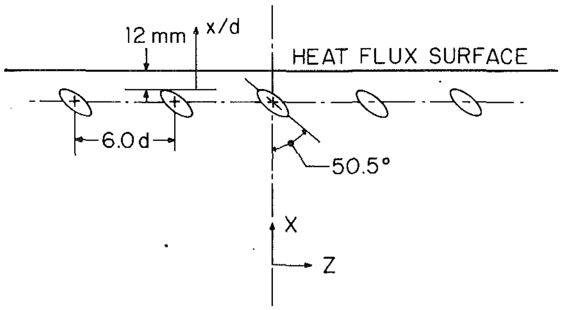

Fig. 3 Test surface injection geometry for film-cooling holes arranged with configuration 3 compound angle holes

measured downstream of another compound angle arrangement with the same hole angles with respect to the test surface but different spanwise hole spacing (7.8d).

Experimental Apparatus and Procedures

The experimental apparatus and procedures are described in Part 1 of this investigation (Ligrani et al., 1994). Included in that paper is information on the open-circuit, subsonic wind tunnel, the test section and coordinate system, and the injection system for film cooling. The paper also describes the procedures employed to measure streamwise mean velocity distributions, mean temperatures, injectant distributions, Stanton numbers, adiabatic film effectiveness values, and iso-energetic Stanton numbers. A number of baseline data checks are also described by Ligrani et al. (1994). These authors also present a table with dimensional values of distances to thermocouple rows along the test surface.

The present coordinate system is the same as the one employed in Part 1. With this system, Z, is the spanwise coordinate measured from the test section spanwise centerline, X is measured from the upstream edge of the boundary layer trip, and Y is measured normal to the test surface. x is measured from the downstream edge of the injection holes and generally presented as x/d.

Uncertainty estimates are also presented in Part 1 (Ligrani et al., 1994).

Injection Configurations

Schematic drawings showing the film hole geometries employed (configurations 1-3) are presented in Figs. 1-3. Each figure shows the hole arrangement along the test surface (X-Z plane) as seen in the negative Y direction. In each case, holes are placed in a single row with five injection cooling holes arranged so that the centerline of the middle hole is located on the spanwise centerline ($Z = 0.0$ cm) of the test surface.

For configuration 1, which is shown in Fig. 1, the spanwise spacing between adjacent holes is 3.9d, and hole diameter d is 0.945 cm. Compound angle holes are employed with $\Omega = 35$ deg and $\beta = 30$ deg, where Ω is the angle of the injection holes with respect to the test surface as projected into the streamwise/normal plane, and β is the angle of the injection holes with respect to the test surface as projected into the spanwise/normal plane. Thus, holes are oriented so that the spanwise components of injectant velocity are directed in the negative

Nomenclature

d = injection hole diameter
h = heat transfer coefficient with film injection
h_o = baseline heat transfer coefficient, no film injection
h_f = iso-energetic heat transfer coefficient with film injection
I = momentum flux ratio = $\rho_c U_c^2/\rho_\infty U_\infty^2$
m = blowing ratio = $\rho_c U_c/\rho_\infty U_\infty$
Re_d = injectant Reynolds number based on hole diameter = dU_c/ν
Re_x = Reynolds number based on streamwise distance $= XU_\infty/\nu$
s = equivalent slot width
St = Stanton number with film injection
St_o = baseline Stanton number, no film injection
St_f = iso-energetic Stanton number with film injection
$\overline{\mathrm{St}_f}$ = spanwise-averaged iso-energetic Stanton number with film injection
T = static temperature
U = mean (time-averaged) velocity
X, x = streamwise distance
Y = distance normal to the surface
Z = spanwise distance from test surface centerline
β = injection hole angle with respect to the test surface as projected into the spanwise/normal plane
η = adiabatic film cooling effectiveness = $(T_{aw} - T_{r,\infty})/(T_{r,c} - T_{r,\infty})$
$\bar{\eta}$ = spanwise-averaged adiabatic film cooling effectiveness
θ = nondimensional injection temperature = $(T_{r,c} - T_{r,\infty})/(T_w - T_{r,\infty})$
ν = kinematic viscosity
ξ = $(x/ms)(\mathrm{Re}_d)^{-0.25}$
ρ = density
Ω = injection hole angle with respect to the test surface as projected into the streamwise/normal plane

Subscripts

aw = adiabatic wall
c = injectant at exits of injection holes
o = stagnation
r = recovery condition
w = wall
∞ = free-stream

Superscripts

$\overline{}$ = time-averaged

Z direction. The plane of each injection hole is angled at 50.5 deg from the streamwise/normal (*X*–*Y*) plane, and, within the plane of each hole, hole centerlines are oriented at angles of 24 deg from the plane of the test surface (*X*–*Z*).

For configuration 2, which is shown in Fig. 2, the spanwise spacing between adjacent holes is 3.0*d*, and hole diameter is 0.945 cm. In this case, the holes are oriented with simple angles such that $\Omega = 35$ deg and $\beta = 90$ deg. Thus, holes are located in streamwise/normal (*X*/*Y*) planes, and oriented so that the injectant has no spanwise component of velocity as it exits the holes. Within the plane of each hole, individual hole centerlines are then oriented at angles of 35 deg from the plane of the test surface.

Configuration 3, which is shown in Fig. 3, has the same spanwise hole spacing as configuration 2 and the same hole angles with respect to the test surface as configuration 1. Thus, spanwise hole spacing is 3.0*d*, $\Omega = 35$ deg, and $\beta = 30$ deg. The nominal hole diameter for configuration 3 is 0.925 cm. Thus, by comparing results from configurations 1 and 3, the influences of spanwise hole spacing (3.0*d* compared to 3.9*d*) on compound angle film cooling are apparent. A comparison of results from configurations 2 and 3 then provides information on the effects of compound angle orientation ($\Omega = 35$ deg, $\beta = 30$ deg) relative to simple angle orientation ($\Omega = 35$ deg, $\beta = 90$ deg) with the same spanwise hole spacing (3*d*). The geometry of the simple angle holes exactly matches the projection of the compound angle holes into the streamwise/normal plane to provide a systematic basis for this comparison. This systematic basis for comparison is also maintained by holding many experimental approach details, flow parameters, and additional injection geometry characteristics constant (which may not be held constant or the same in other investigations) as the comparisons are made (Ligrani et al., 1994).

Thus, the present test program is designed to provide answers to two principal questions by maintaining all parameters constant except those pertaining directly to these questions. First, which injection hole orientation (simple angle or compound angle) produces the highest effectiveness values and the best film-cooling protection? Second, for injection from holes with compound angle orientations, which spanwise hole spacing (6*d* or 7.8*d*) produces the highest effectiveness values and the best film-cooling protection? To answer these questions, most attention is given to results obtained using compound angle configuration 3, and to comparisons between configuration 3 and configurations 1 and 2. Comparisons between configuration 1 and configuration 2 are also important; however, these are discussed in detail elsewhere by Ligrani et al. (1992).

Mean Velocity Surveys

Surveys of mean velocity measured downstream of configuration 3 compound angle holes are presented in Fig. 4(*a*), and results measured downstream of configuration 2 simple angle holes are presented in Fig. 4(*b*). In both cases, the blowing ratio is 1.0 and the spanwise hole spacing is 6.0*d*. Spanwise locations of film holes are denoted by arrows on the abscissa of each plot.

At $x/d = 9.9$, Fig. 4(*a*) shows that velocity deficits produced by the injectant from different holes are quite similar. Each one is skewed and flattened with the largest gradients in the direction that film is ejected from the surface at *Y* ranging from 0.5 cm to 2.0 cm. Because of the negative spanwise components of velocity at the exits of the film holes, deficits are also displaced about -1.5 to -2.0 cm by the time they reach $x/d = 9.9$. As the film-cooled boundary layer convects downstream to x/d of 44.3 and 86.3, the deficits are convected to even smaller *Z* locations. Velocity surveys downstream of two staggered rows of holes (Ligrani et al., 1994) show greater spanwise uniformity because the spacings between adjacent holes are half as much.

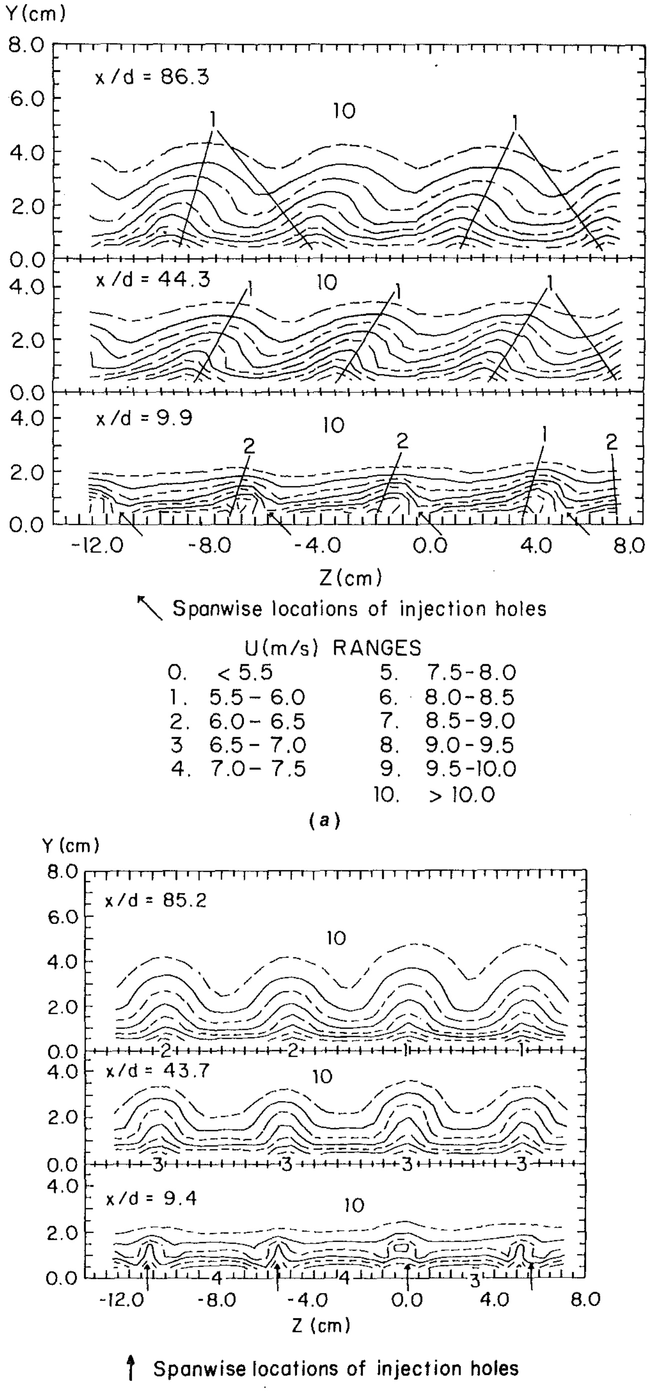

(*b*)

Fig. 4 Streamwise mean velocity development with streamwise distance, as measured downstream of one row of holes with $m = 1.0$: (*a*) compound angle configuration 3; (*b*) simple angle configuration 2

Mean velocity surveys measured downstream of holes with simple angle orientations (configuration 2) also producing injectant at a blowing ratio of 1.0 are given in Fig. 4(*b*). At $x/d = 9.4$, high-velocity regions are present on either sides of velocity deficits. Similar distributions near injection holes are presented by Subramanian et al. (1992), who measured streamwise velocities downstream of a single simple angle injection hole ($\Omega = 30$ deg and $\beta = 90$ deg) with $m = 1.5$. Mean vorticity distributions indicate that variations such as the ones shown at $x/d = 9.4$ in Fig. 4(*b*) are due to vortexlike structures, which form around the injectant as it leaves the holes. After comparing these results to the ones in the previous figure, it is apparent that velocity deficits are symmetric about streamwise/

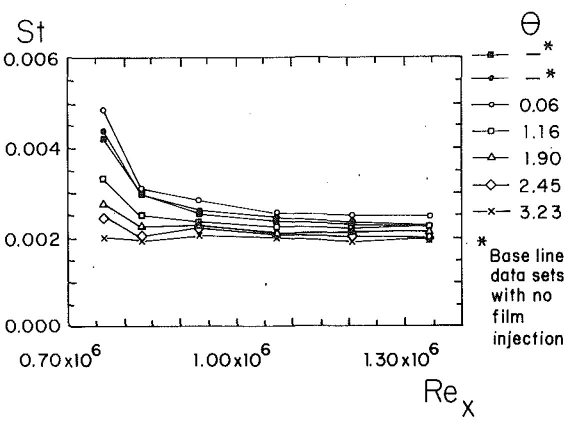

Fig. 5 Stanton number distributions with Reynolds number illustrating variations for different nondimensional temperatures θ, as measured downstream of one row of configuration 3 compound angle holes with $m = 1.0$

normal planes, and not skewed and flattened. Because the injectant emerges from the holes in the streamwise direction with no spanwise velocity component, the deficits in Fig. 4(*b*) are at the same spanwise locations as the injection holes that the film-cooled boundary layer convects downstream to x/d of 43.7 and 85.2.

Local Adiabatic Effectiveness, Injectant, and Stanton Number Ratio Distributions

Measurements downstream of configuration 3 compound angle holes are discussed in this section. These include distributions of adiabatic film cooling effectiveness, iso-energetic Stanton number ratio, and Stanton number ratio for $\theta = 1.16$. Also presented are surveys of injectant distributions as well as a plot showing the dependence of spanwise-averaged Stanton number on streamwise Reynolds number at different θ.

Streamwise Development of Adiabatic Effectiveness and Stanton Number Ratio Distributions. As mentioned earlier, local adiabatic film effectiveness values are determined from measurements of local $\mathrm{St}/\mathrm{St}_o$ at different magnitudes of the nondimensional injection temperature, θ. Examples of spanwise-averaged St measured at different θ are presented in Fig. 5 as dependent upon Reynolds number based on streamwise distance X. Also included on this plot are two baseline data sets measured with no film injection. From these results, it is evident that significant Stanton number variations occur as the nondimensional injectant temperature is altered. At a given Re_x, St decrease as θ increases, which indicates nonzero values of spanwise-averaged adiabatic film effectiveness as well as improved protection as the differences between the wall temperature and injectant temperature increases. At a given value of θ, St distributions generally decrease as the Reynolds number increases.

Spanwise distributions of the adiabatic film cooling effectiveness η are presented in Fig. 6(*a*) at x/d of 6.8, 17.6, 33.8, 55.5, 77.1, and 98.7 for $m = 1.0$. At each streamwise location, η variations are spanwise periodic with Z/d, where higher values correspond to locations where injectant is plentiful. The spanwise periodicity is more pronounced at smaller x/d near 6.8 because of accumulations of injectant such as the ones shown in Fig. 7(*a*) for $x/d = 9.9$.

Local $\mathrm{St}_f/\mathrm{St}_o$ data, and $\mathrm{St}/\mathrm{St}_o$ data for $\theta = 1.16$ in Figs. 6(*b*) and 6(*c*), also show spanwise periodicity; however, this periodicity is somewhat out of phase with the η distributions. Here, higher values correspond to regions of higher mixing, which occur just to the left of injectant accumulations (at smaller Z/d), especially for $\mathrm{St}_f/\mathrm{St}_o$. These local maxima also correspond to high-velocity regions that exist near the wall between the streamwise velocity deficits evident in Fig. 4(*a*). Distributions in all three Figs. 6(*a*), 6(*b*), and 6(*c*) should be ignored for $Z/d > 10$ since almost no injectant coverage is present over this region.

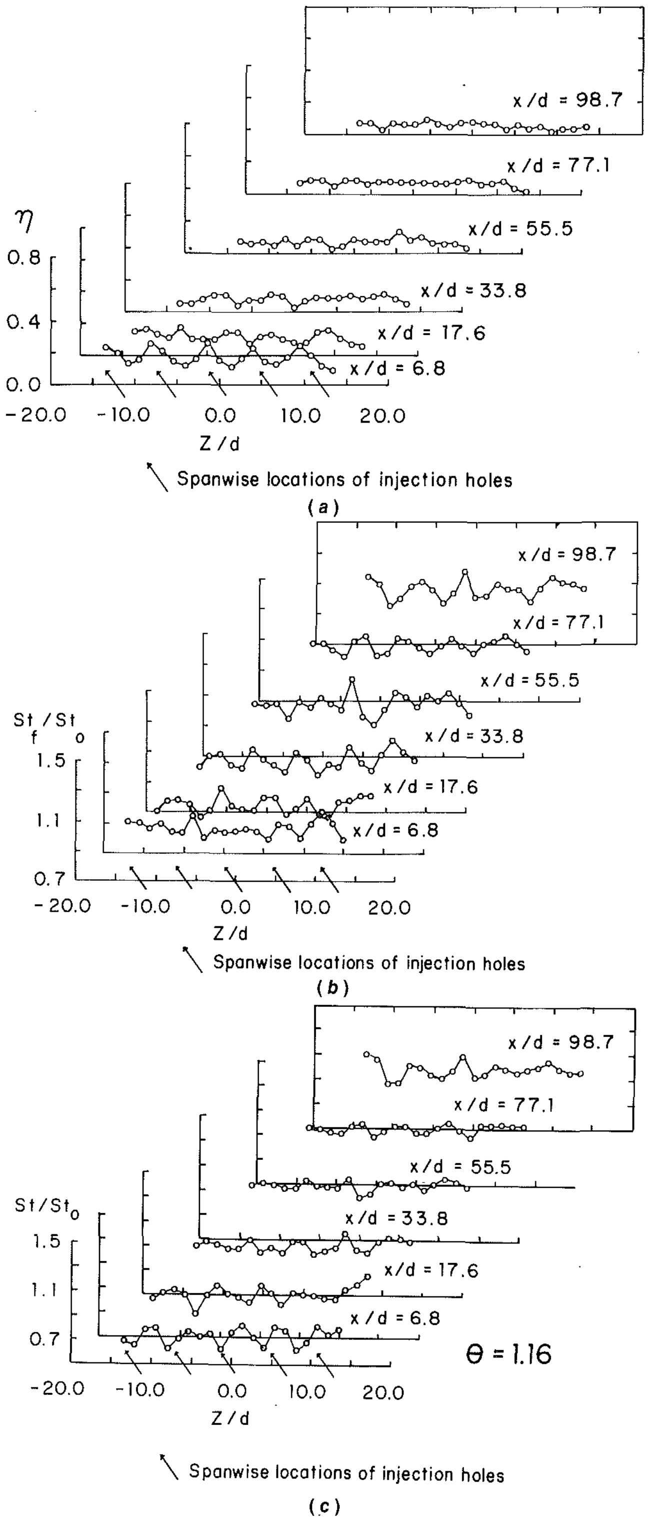

Fig. 6 Streamwise development of: (*a*) local adiabatic film cooling effectiveness, (*b*) local iso-energetic Stanton number ratios, and (*c*) local Stanton number ratios for $\theta = 1.16$, downstream of one row of compound angle configuration 3 film-cooling holes with $m = 1.0$

Streamwise Development of Injectant Distributions. Injectant distribution surveys measured downstream of one row of configuration 3 compound angle injection holes with $m = 1.0$ are given in Fig. 7(*a*). These distributions are obtained using the same procedures employed by Ligrani et al. (1994)

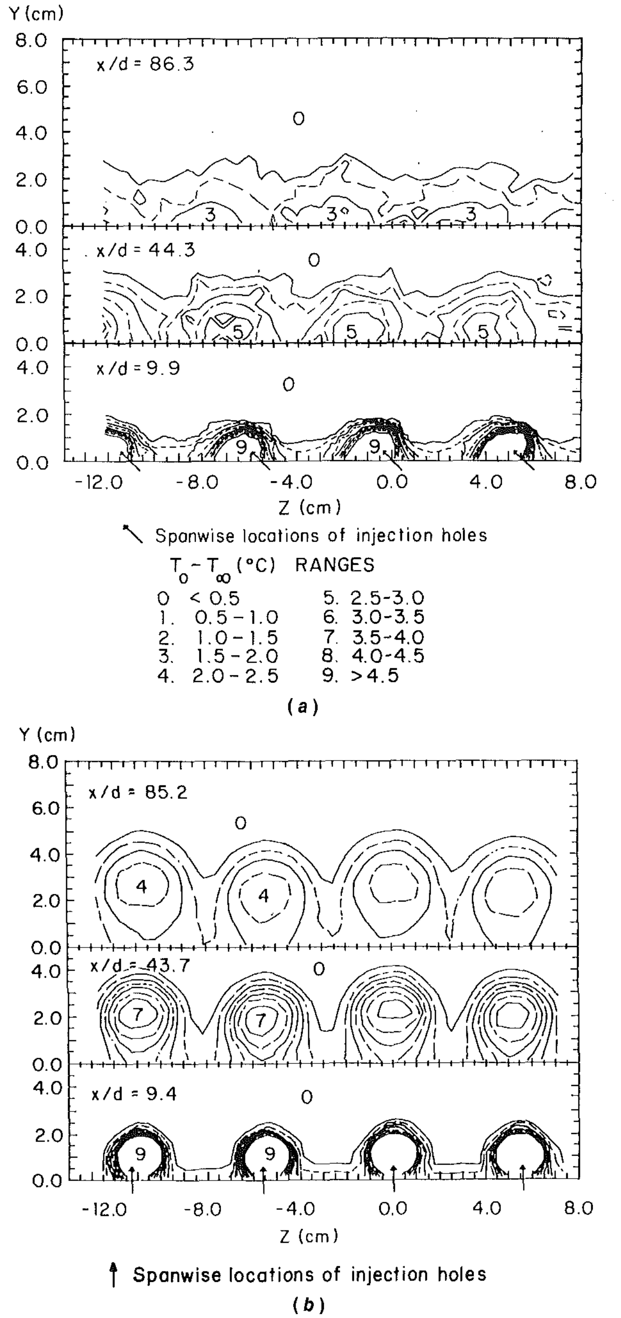

Fig. 7 Mean temperature fields showing distributions of film injectant downstream of one row of film-cooling holes with $m = 1.0$: (a) compound angle configuration 3; (b) simple angle configuration 2

in which the injectant is heated and then detected, as the test plate remains unheated and near ambient temperature. As for the velocity surveys, arrows along the abscissa in Fig. 7(a) indicate film hole locations. Skewed and lopsided injectant concentrations are evident in the spanwise/normal plane at $x/d = 9.9$ between regions where injectant is almost nonexistent. With streamwise convection to x/d of 44.3 and 86.3, these accumulations become more diffuse and dissipated. Injectant accumulations for all three x/d show close correspondence to streamwise velocity deficits in Fig. 4(a) and to local η maxima in Fig. 6(a), and approximate correspondence to locally lower St_f/St_o in fig. 6(b). The distributions in Fig. 7(a) are significantly different from the ones in Fig. 7(b) measured at the same m downstream of one row of simple angle configuration 2 holes. For all three x/d values, injectant distributions in this latter figure represent circular or oval concentrations of injectant in spanwise/normal planes.

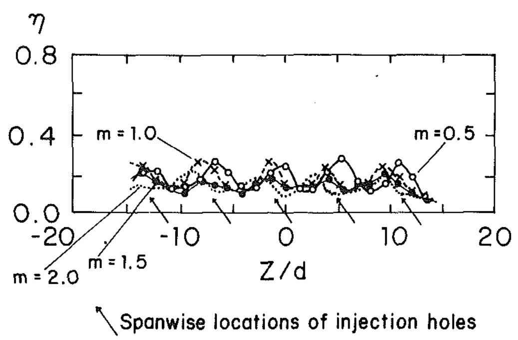

Fig. 8 Spanwise variations of adiabatic film-cooling effectiveness downstream of one row of compound angle configuration 3 film-cooling holes at $x/d = 6.8$ for $m = 0.5$, 1.0, 1.5, and 2.0

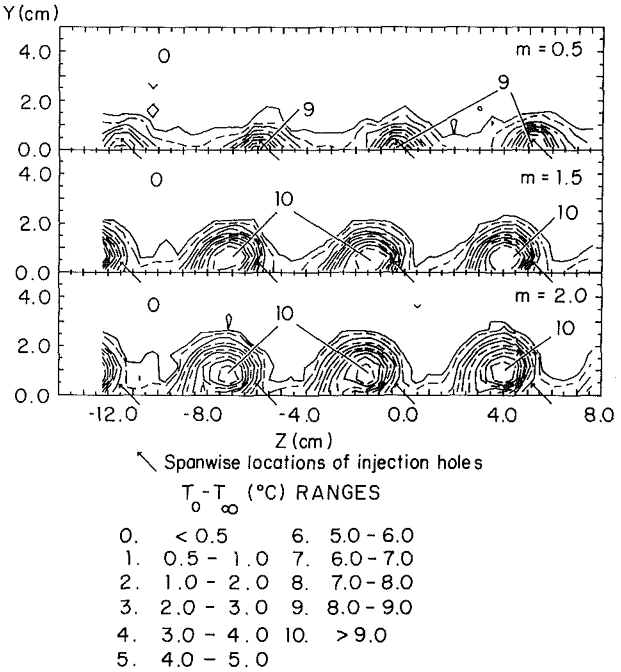

Fig. 9 Mean temperature fields showing distributions of film injectant downstream of one row of compound angle configuration 3 film-cooling holes at $x/d = 9.9$ for $m = 0.5$, $m = 1.5$, and $m = 2.0$

Effects of Blowing Ratio on Local Adiabatic Film Cooling Effectiveness and Injectant Distributions. Results showing the influences of blowing ratio on local adiabatic effectiveness distributions and on local injectant distributions are presented in Figs. 8 and 9, respectively. These data, which were obtained downstream of the compound angle holes, are presented for blowing ratios of 0.5, 1.0, 1.5, and 2.0, which are equivalent to momentum flux ratios of 0.25, 1.0, 2.25, and 4.0. In each figure, arrows along the abscissa indicate the spanwise locations of injection holes. The effectiveness results are determined from measurements at $x/d = 6.8$, whereas the injectant surveys are given for $x/d = 9.9$.

The results in Fig. 8 show spanwise periodic variations of η for all four m, where the highest local maxima exist at the lowest blowing ratio because jet lift-off is more pronounced at the higher m. These local maxima shift to smaller Z/d as m increases because of injectant momentum, which causes injectant to move in the negative spanwise direction as it is convected downstream. The only exception occurs for $Z/d > 10$–12, where all four distributions decrease because they are measured at locations slightly away from the spanwise edge of the injectant. At $Z/d < 10$, the spanwise periodicity of the η distributions decreases with blowing ratio such that higher η values correspond to locations where abundant amounts of

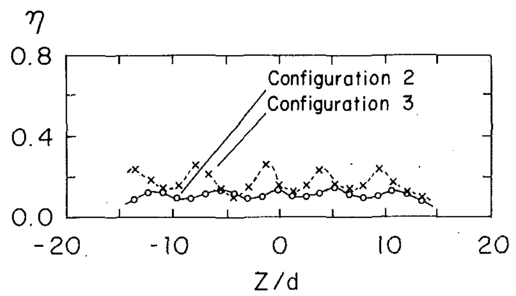

Fig. 10 Spanwise variations of adiabatic film-cooling effectiveness for $m = 1.0$ downstream of one row of compound angle configuration 3 film-cooling holes at $x/d = 6.8$ and downstream of one row of simple angle configuration 2 film-cooling holes at $x/d = 6.8$

injectant are spread along the test surface, and lower values correspond to locations where the injectant coverage is more sparse.

Additional explanation of the trends seen in Fig. 8 is obtained from an examination of Fig. 9, which shows injectant distributions at $x/d = 9.9$ for m of 0.5, 1.5, and 2.0. For each m, injectant distributions in this figure are spanwise periodic such that individual distributions are similar to each other, as expected. For $m = 0.5$, injectant accumulations are most significant just downstream of the spanwise centerlines of the injection holes. For $m = 1.5$ and 2.0, injectant accumulations at $x/d = 9.9$ are most significant just to the left of the spanwise centerlines of the injection holes (i.e., at smaller Z). The results for $m = 0.5$ are thus different from the ones at $m = 1.5$ and $m = 2.0$ because accumulations are convected away from the injection holes a smaller distance in the spanwise direction. This spanwise shift with streamwise convection is consistent with the results in Fig. 8.

As the blowing ratio increases from 0.5 to 1.5 and 2.0, Fig. 9 also shows injectant concentrations for $x/d = 9.9$ that are located farther and farther from the test plate (i.e., farther from $Y = 0$ cm). Such lift-off behavior is consistent with results in Fig. 8 as well as with results presented by Ligrani et al. (1992, 1994). In those studies as well as in the present one, both spanwise-averaged $\bar{\eta}$ and local η minima decrease in magnitude as the blowing ratio increases because of decreased local protection, which results as increasing amounts of injectant are lifted off the test surface.

Comparison of Local Adiabatic Film Cooling Effectiveness Distributions From Configurations 2 and 3. Local adiabatic film cooling effectiveness distributions for $x/d = 6.8$ and $m = 1.0$ from configurations 2 and 3 are presented in Fig. 10. These results provide a comparison of the local η produced by the simple angle and compound angle hole arrangements with the same spanwise hole spacing.

η values for compound angle configuration 3 are higher and show significantly greater spanwise periodicity than the ones for simple angle configuration 2. The spanwise periodicity results from periodic regions of lower and higher protection across the span of the test surface. As illustrated by Figs. 7(*a*) and 9, these develop because the injectant is concentrated at spanwise periodic intervals across the span of the test surface. Local η maxima are higher for configuration 3 at $x/d = 6.8$ because concentrations of injectant along the test surface just downstream of individual compound angle holes are significantly greater than with configuration 2. This is because the compound angle holes are oriented at smaller angles with respect to the test surface compared to the simple angle holes (within the plane of each injection hole). In addition, injectant spanwise velocity components at the hole exits produce initial injectant distributions, which are subsequently swept along the test surface by the mainstream flow just downstream of the compound angle holes. This sweeping action then keeps injectant concentrations closer to the test surface. The η distribution for configurations 2 and 3 should be ignored for $Z/d > 10$ because these locations lie away from the regions of injectant coverage along the test surface.

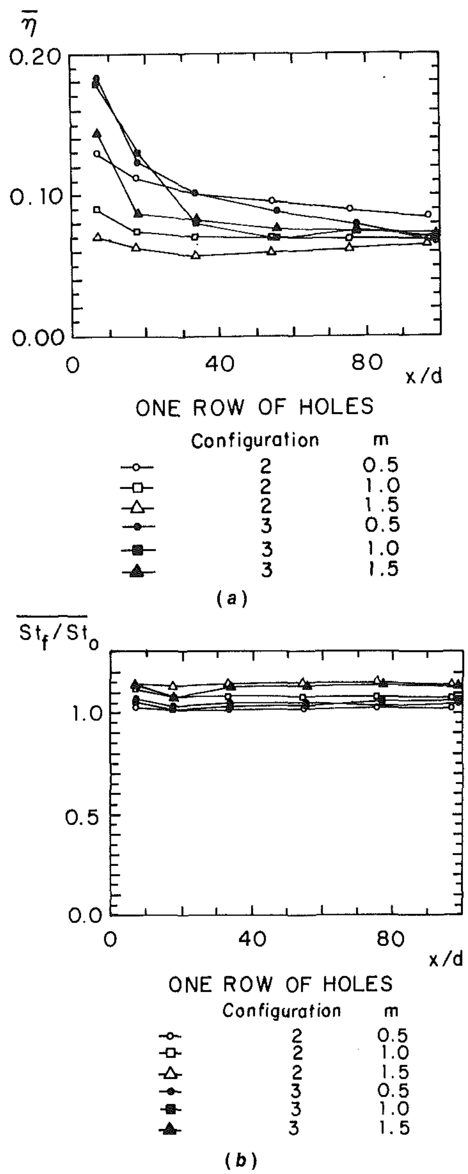

Fig. 11 Spanwise-averaged magnitudes of adiabatic film-cooling effectiveness and iso-energetic Stanton number ratio, shown as dependent upon normalized streamwise distance downstream of one row of compound angle configuration 3 film-cooling holes. Results are compared to ones measured downstream of one row of simple angle configuration 2 film-cooling holes.

Spanwise-Averaged Adiabatic Film-Cooling Effectiveness Values and Iso-Energetic Stanton Number Ratios

The discussion that follows is presented in two parts. First, the effect of hole orientation (compound angle or simple angle) with constant spanwise hole spacing is discussed. This is followed by a discussion of the effects of spanwise hole spacing on film cooling from holes with compound angle orientations. Spanwise-averaged magnitudes of effectiveness and Stanton number are determined by averaging local measurements of these quantities such as the ones presented in Figs. 6(*a*) and 6(*b*). For each x/d, the average is computed using the 13 data points corresponding to Z/d locations from -13.7 to 2.7.

Effects of Hole Orientation (Compound Angle or Simple Angle) With Constant Spanwise Hole Spacing. Spanwise-averaged values of the adiabatic film cooling effectiveness measured downstream of configuration 3 compound angle holes as well as downstream of configuration 2 simple angle holes are presented in Fig. 11(*a*). These two injection configurations have the same spanwise hole spacing (6*d*) and the two sets of data are obtained using similar experimental conditions so that the changes to film protection resulting from the use of compound angle holes instead of simple angle holes are illustrated.

Referring first to the compound angle (configuration 3) data in Fig. 11(*a*), $\overline{\eta}$ generally decreases with x/d for each blowing ratio as injectant is diffused and convected downstream. For each x/d less than 10, $\overline{\eta}$ values decrease with blowing ratio because of the lift-off of injectant from the test surface discussed earlier in reference to Figs. 7–9. Lift-off becomes more severe as injectant momentum increases, and results in accumulation of free-stream and boundary layer fluid between the film and the surface. This diminishes the insulating characteristics of the film as well as the accompanying thermal protection ordinarily provided by it at lower m. With the exception of the $m = 1.0$ data, the trend of decreasing $\overline{\eta}$ with m at each x/d continues downstream to $x/d = 77.1$. The $\overline{\eta}$ data for $m = 1.0$ show behavior different from this trend because they are in close proximity to the $m = 0.5$ data at x/d of 6.8 and 17.6. This is because a minimal amount of lift-off occurs as the injectant issues from the holes at $m = 1.0$ (Fig. 9), which results in spanwise variations of η at $x/d = 6.8$ similar to ones measured with $m = 0.5$ (Fig. 8). At larger x/d from 33.8 to 98.7, Fig. 11(*a*) shows that the $\overline{\eta}$ data for $m = 1.0$ are in close proximity to data obtained with $m = 1.5$. This is because of convection and diffusion of the $m = 1.0$ injectant in the spanwise direction as it is convected farther downstream, behavior evidenced by the $x/d = 6.8$ η data in Fig. 8. Here, local effectiveness maxima for $m = 1.0$ are located at smaller Z/d than the $m = 0.5$ data, and at about the same Z/d as the $m = 1.5$ data. As x/d then becomes greater than 30–40, the $m = 1.0$ injectant becomes increasingly diffuse and spread out (Fig. 7*a*) resulting in lower η and $\overline{\eta}$ values (Figs. 6*a* and 11*a*) relative to results obtained with $m = 0.5$.

The $\overline{\eta}$ data measured downstream of the configuration 2 simple angle holes in Fig. 11(*a*) show trends with some similarities and some differences compared to the ones measured downstream of the configuration 3 holes. Like the configuration 3 results, the ones from configuration 2 generally decrease with x/d for each blowing ratio. $\overline{\eta}$ values downstream of configuration 2 are different from the ones measured downstream of configuration 3 because they decrease with blowing ratio at individual x/d for all x/d tested from 6.8 to 96.7.

Comparing effectiveness values for configurations 2 and 3 in Fig. 11(*a*), it is evident that the simple angle data lie below the compound angle data, especially for $x/d < 30$ when $m = 0.5$, and for $x/d < 60$ when m equals 1.0 and 1.5. Thus, at smaller x/d, the compound angle data indicate significantly improved protection for the same spanwise hole spacing x/d and blowing ratio m. At x/d larger than 60, the compound angle data generally cover about the same range as the simple angle data. This is particularly evident if the data at individual blowing ratios are examined, and believed to occur because equivalent amounts of injectant from each of the two configurations cover the downstream portion of the test surface. The differences at small x/d result mostly because the injectant from the compound angle holes is less likely to lift off of the test surface than the injectant from the simple angle holes. These differences results, first of all, because the lateral component of momentum of the injectant from the compound angle holes causes the injectant to spread out much more in the lateral direction as it is convected downstream and penetrates into the mainstream. Second, the hole angles with respect to the test surface are 24 deg for the compound angle arrangement compared to 35 deg for the simple angle arrangement.

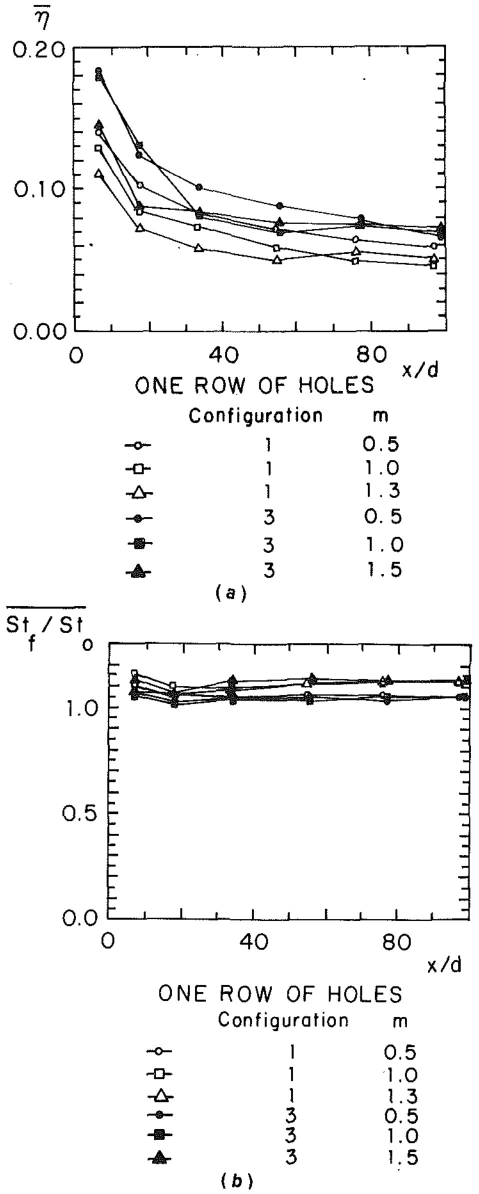

Fig. 12 Spanwise-averaged magnitudes of adiabatic film-cooling effectiveness and iso-energetic Stanton number ratio, shown as dependent upon normalized streamwise distance downstream of one row of compound angle configuration 3 film-cooling holes. Results are compared to ones measured downstream of one row of compound angle configuration 1 film-cooling holes.

Compared to results measured downstream of two staggered rows of configuration 3 holes (with 3*d* spanwise spacing) (Ligrani et al., 1992), spanwise-averaged effectiveness values measured downstream of one row of holes (with 6*d* spanwise spacing) are significantly lower. Differences range from 41 to 98 percent, and are due to different concentrations and distributions of injectant near the test surface with the two arrangements.

Spanwise-averaged iso-energetic Stanton number ratios in Fig. 11(*b*) for compound angle configuration 3 and for simple angle configuration 2 show a number of interesting trends. First, little St_f/St_o variation with x/d is evident for each value of m. Second, compound angle data cover approximately the same range of values as the simple angle data, especially when the two sets of results are compared at the same blowing ratio. Third, for each x/d, St_f/St_o values generally increase with m.

Effects of Spanwise Spacing of Compound Angle Injection Holes. Results measured downstream of compound angle configurations 1 and 3 are compared in Figs. 12(*a*) and 12(*b*). The two configurations are similar in that both have the same injection hole angles with respect to the test surface such that $\Omega = 35$ deg and $\beta = 30$ deg. The two configurations are different since the spanwise hole spacing of configuration 1 is $7.8d$, whereas the spanwise hole spacing of configuration 3 is $6.0d$.

Figure 12(a) shows that spanwise-averaged effectiveness values are higher when smaller hole spacing is employed provided data are compared at the same m and x/d. At x/d less than 60, $\overline{\eta}$ values downstream of configuration 3 are 20 to 39 percent higher than the ones measured downstream of configuration 1. These differences generally increase as x/d becomes smaller. For example, for $x/d = 6.7$–6.8 and $m = 1.0$, $\overline{\eta}$ equals 0.179 downstream of configuration 3, which is 39 percent higher than 0.129, the value measured downstream of configuration 1. At x/d greater than 60, differences between the two configurations range from 13 to 62 percent.

Spanwise averaged magnitudes of the iso-energetic Stanton number ratio are presented in Fig. 12(b). Close examination reveals trends that are very similar to the ones evident in Fig. 11(b). Ligrani et al. (1992) provide additional information, especially pertaining to results measured downstream of configuration 1.

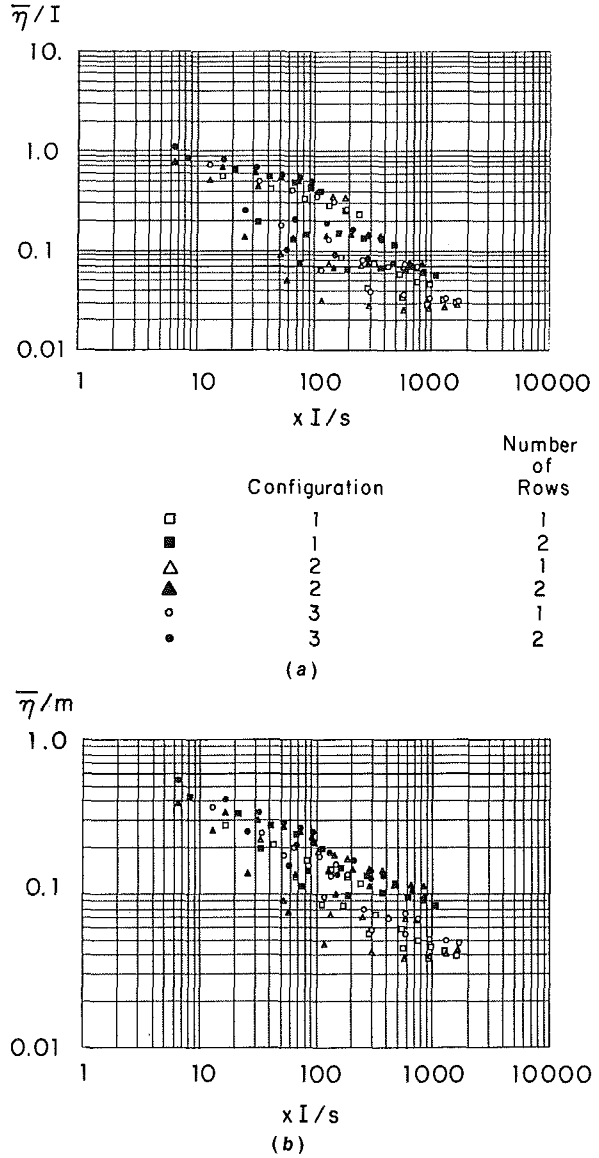

Fig. 13 Spanwise-averaged adiabatic film-cooling effectiveness variations measured downstream of one and two rows of holes with configuration 1, 2, and 3 orientations: (a) $\overline{\eta}/I$ versus xI/s coordinates; (b) $\overline{\eta}/m$ versus xI/s coordinates

Comparison and Correlation of Spanwise-Averaged Adiabatic Film-Cooling Effectiveness Values

Spanwise-averaged film effectiveness values are plotted in Figs. 13(a) and 13(b) using $\overline{\eta}/I$ versus XI/s coordinates and $\overline{\eta}/m$ versus XI/s coordinates, respectively. In both figures, data measured downstream of all three configurations of film injection holes (1, 2, and 3) are included. The data are distinguished by closed or open symbols depending whether two staggered rows (Ligrani et al., 1992), or a single row of film injection holes is employed.

In Fig. 13(a), the $\overline{\eta}/I$ data collect into groupings according to the blowing ratio and number of rows of film cooling holes. Each data grouping is spread into a distribution across the plot that is approximately horizontal. Data measured downstream of two rows of holes with the lowest blowing ratio tested, 0.5, are at the top of the distribution and farthest to the left. These results are just above data measured downstream of one row of holes with a blowing ratio of 0.5. At the bottom of the distribution, data are presented for a blowing ratio of 1.5 from one row of injection holes. The $\overline{\eta}/m$ data in Fig. 13(b) are distributed in a similar manner except they are compacted into a smaller portion of the plot. Here, the results measured downstream of one row of holes are collected together in a distribution that generally lies below the data measured downstream of two rows of holes.

The results across the top of the two row data in Fig. 13(b) collect into a region that evidences film cooling that is approximately two dimensional, similar to that which would emanate from a slot or a porous strip. The behavior of such a film is described by Pedersen et al. (1977), who used coordinates similar to the ones employed in Fig. 13(b) ($\overline{\eta}/m$ versus I) to collapse data with different injectant to free-stream density ratios together for particular values of x/d. Two dimensional slot like behavior is best illustrated when $\overline{\eta}$ data are plotted versus $\xi = (x/ms)(\mathrm{Re}_d)^{-0.25}$. When plotted in this way, the present results show more scatter than the plots in Figs. 13(a) and 13(b). Configuration 2 data in these coordinates decrease with m at smaller ξ because of injectant lift-off. Configuration 3 data do not follow two dimensional slot behavior exactly, but they are closer than the configuration 2 data and show less tendency to lift-off. With spanwise hole spacing smaller than $3d$, the compound angle configuration will probably produce behavior that is nearly two dimensional.

Influences of Blowing Ratio and Momentum Flux Ratio on Spanwise-Averaged Iso-Energetic Stanton Number Ratios

Influences of blowing ratio and momentum flux ratio are discussed in reference to $\overline{\mathrm{St}_f/\mathrm{St}_o}$ data measured at $x/d = 6.7$–6.8 in Figs. 14(a) and 14(b). Higher levels of $\overline{\mathrm{St}_f/\mathrm{St}_o}$ are generally believed to result from higher levels of mixing and turbulence, and higher streamwise velocity magnitudes near the test surface. This is evidenced by the local $\mathrm{St}_f/\mathrm{St}_o$ distributions in Fig. 6(b) as they are compared to the streamwise velocity surveys in Fig. 4(a), as well as by results from Ligrani et al. (1992, 1994). The results of Jabbari and Goldstein (1978) are also consistent since they attribute increases of $\overline{\mathrm{St}_f/\mathrm{St}_o}$ for $m > 0.5$ to "agitation of flow due to the injection at higher velocities." Jabbari and Goldstein observed h_f/h_o increases with m downstream of two staggered rows of simple angle holes. For $m < 1.6$, their $x/d = 6.11$ data are occasionally slightly higher but generally in reasonable agreement with the results measured downstream of 2 rows of holes in Fig. 14(a).

In Fig. 14(a), $\overline{\mathrm{St}_f/\mathrm{St}_o}$ data from the present study measured downstream of two rows of holes increase with m for $m < 2$–2.5. The results measured downstream of one row of holes increase with m for m up to 2.5–3.5. These differences and the fact that the data measured downstream of one row of

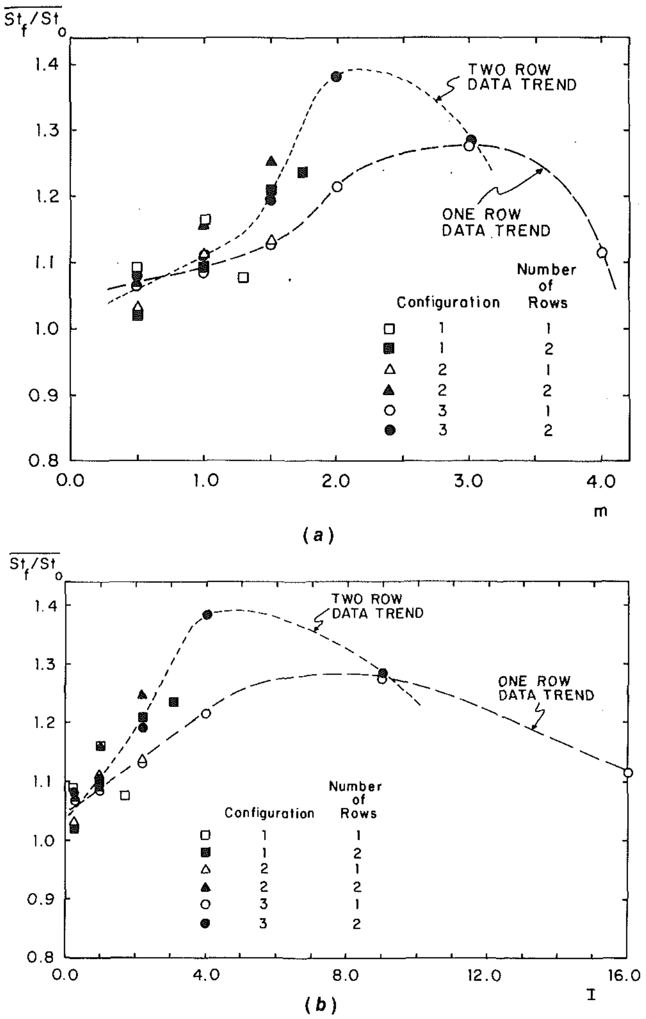

Fig. 14 Spanwise-averaged iso-energetic Stanton number ratio variations measured downstream of one and two rows of holes with configuration 1, 2, and 3 orientations: (*a*) dependence on blowing ratio, *m*; (*b*) dependence on momentum flux ratio, *I*

holes are lower than the two row results (for blowing ratios from 1 to 3) evidence greater mixing and higher turbulence levels when the injectant emerges from two rows of holes. The decreases of St_f/St_o with m that occur for $m>2.5$–3.5 may result because the boundary layer turbulence and mixing augmentations produced by the injectant are becoming less significant. High injectant velocities probably cause the injectant to be jetted away from the holes and test surface, and then into the free-stream flow outside of the boundary layer. The result is minimal film protection, low effectiveness values, and $\overline{St_f/St_o}$, which approach 1 (Wigle, 1991).

The same $\overline{St_f/St_o}$ data in Fig. 14(*a*) for $x/d=6.7$–6.8 are presented as a function of momentum flux ratio I in Fig. 14(*b*). Like the data in Fig. 14(*a*), the data measured downstream of one row of holes show a trend that is different from the data measured downstream of two rows of holes, where the two row trend is illustrated by lines with short dashes, and the one row trend is illustrated by lines with long dashes. Thus, the relative magnitudes of individual data points in Fig. 14(*b*) at particular values of I are the same as the relative magnitudes observed at particular m in Fig. 14(*a*). The most important differences are related to the locations of St_f/St_o maxima. In Fig. 14(*b*), these occur at I from 4 to 6 for the two row data, and at I from 6 to 12 for the one row data.

Summary and Conclusions

Experimental results are presented that describe the development and structure of flow downstream of one row of film-cooling holes with compound angle orientations. With this configuration, which is denoted number 3, holes are spaced $6d$ apart in the spanwise direction, inclined at 35 deg with respect to the test surface when projected into the streamwise/normal plane, and inclined at 30 deg with respect to the test surface when projected into the spanwise/normal plane. Results are presented for an injectant to free-stream density ratio near 1.0, x/d ranging from 6.8 to 98.7, injection blowing ratios from 0.5 to 1.50, and momentum flux ratios from 0.25 to 2.25. These results are compared to ones from configuration 2 to determine the effects of hole angle orientation for constant spanwise hole spacing, and with results from configuration 1 to determine the effects of spanwise hole spacing when the hole angle orientation is maintained constant.

The most important conclusion comes from a comparison of spanwise-averaged adiabatic effectiveness values measured downstream of injection hole configurations 2 and 3. From this, it is evident that the compound angle injection configuration 3 provides significantly improved protection compared to simple angle configuration 2 for the same spanwise hole spacing, normalized streamwise location x/d, and blowing ratio m, for $x/d<30$ when $m=0.5$, and for $x/d<60$ when m equals 1.0 and 1.5. At $x/d=6.8$ just downstream of the holes, the data measured downstream of injection hole configuration 3 lie 41 to 104 percent higher than data measured downstream of configuration 2, depending upon the blowing ratio. These differences at small x/d result mostly because the injectant from the compound angle holes is less likely to lift off of the test surface than the injectant from the simple angle holes. Lift-off influences cause $\overline{\eta}$ values downstream of configuration 3 to be highest for $m=0.5$ and generally decrease with blowing ratio at each x/d. Local η distributions show local maxima, which also decrease significantly with blowing ratio. Lift-off influences are also evident in injectant distribution surveys at x/d of 9.9, which show injectant concentrations located farther and farther from the test surface as m increases.

Lift-off is less likely with compound angle holes because: (1) Hole angles with respect to the test surface are 24 deg for the compound angle arrangement compared to 35 deg for the simple angle arrangement, and (2) the lateral component of momentum of the injectant from the compound angle holes causes the injectant to spread out much more in the lateral direction as it is convected downstream, which keeps larger concentrations of the injectant closer to the test surface. These same phenomena also account for higher injectant concentrations near the wall downstream of individual compound angle holes, as well as local adiabatic effectiveness values at $x/d=6.8$ which show greater spanwise periodicity than ones downstream of simple angle holes. Corresponding local effectiveness maxima shift to smaller Z/d as m increases because of injectant momentum, which causes injectant to move in the negative spanwise direction as it is convected downstream. At x/d larger than 60, spanwise-averaged adiabatic effectiveness data downstream of configuration 3 generally cover about the same range as the data measured downstream of the configuration 2 injection holes.

A comparison of results measured downstream of compound angle configurations 1 and 3 shows that spanwise-averaged effectiveness values are 20 to 39 percent higher when smaller hole spacing is employed (i.e., $6d$ compared to $7.8d$) provided data are compared at the same m and x/d, for $x/d<60$. At x/d greater than 60, differences between the two configurations range from 13 to 62 percent. Because of the large spanwise spacing between injection holes, coalescence of injectant distributions from adjacent holes does not occur until larger x/d. Consequently, spanwise-averaged effectiveness values are strongly dependent upon the density of the injectant distribution near the test surface and hence, the spanwise hole spacing.

Spanwise-averaged film effectiveness values measured downstream of one and two rows of holes from all three injection configurations tested (1, 2, and 3) show a reasonable collapse when plotted in $\bar{\eta}/m$ versus Xl/s coordinates. Within this collection of data points, results measured downstream of one row of holes collect together into a distribution that generally lies below the data measured downstream of two rows of holes. The results across the top of the two row distribution collect into a region that is believed to evidence film cooling that is approximately two dimensional, similar to that which would emanate from a slot or a porous strip.

Like the local η variations, local St_f/St_o data show spanwise periodicity. This periodicity is most evident at $x/d > 17.6$ and when present, is somewhat out of phase with the η distributions, with local St_f/St_o maxima that correspond to high velocity (and often high mixing) regions near the wall. These exist between streamwise velocity deficits, which are skewed and flattened in spanwise/normal planes with the largest gradients in the direction that film is ejected from the surface.

Spanwise-averaged iso-energetic Stanton number ratios measured downstream of compound angle configuration 3 range between 1.0 and 1.25 for $m < 1.6$. The data thus cover the same range of values and show the same trends with m and x/d as are measured downstream of two staggered rows of injection holes (Ligrani et al., 1992) and downstream of configurations 1 and 2, regardless whether one or two rows of injection holes are employed. For m values between 1 and 3, spanwise-averaged $\overline{St_f/St_o}$ data at $x/d = 6.7$–6.8 downstream of one row of holes are lower than the two row results, which indicates greater mixing and higher turbulence levels when the injectant emerges from two rows of holes.

Acknowledgment

This study was supported by: (1) the Naval Sea Systems Command, Job Order Numbers N622711-RGPLG and N622712-RTBPL (Dr. Dan Groghan and Dr. Sam Shepard were program monitors), and (2) the Aero-Propulsion Laboratory of Wright Patterson Air Force Base, MIPR Numbers FY 1455-89-N0670 and FY 1455-92-N0641 (Dr. Bill Troha was program monitor). Of the different portions of the study, the NSSC supported the portions of the investigation pertaining to configuration 3, and WPAFB supported the portions of the investigation pertaining to configurations 1 and 2.

References

Jabbari, M. Y., and Goldstein, R. J., 1978, "Adiabatic Wall Temperature and Heat Transfer Downstream of Injection Through Two Rows of Holes," ASME *Journal of Engineering for Power*, Vol. 100, pp. 303–307.

Ligrani, P. M., Ciriello, S., and Bishop, D. T., 1992, "Heat Transfer, Adiabatic Effectiveness, and Injectant Distributions Downstream of a Single Row and Two Staggered Rows of Compound Angle Film-Cooling Holes," ASME *Journal of Turbomachinery*, Vol. 114, pp. 687–700.

Ligrani, P. M., Wigle, J. M., Ciriello, S., and Jackson, S. M., 1994, "Film Cooling From Holes With Compound Angle Orientations, Part 1: Results Downstream of Two Staggered Rows With 3*d* Spanwise Spacing," ASME JOURNAL OF HEAT TRANSFER, Vol. 116, this issue, pp. 341–352.

Pedersen, D. R., Eckert, E. R. G., and Goldstein, R. J., 1977, "Film Cooling With Large Density Differences Between the Mainstream and the Secondary Fluid Measured by the Heat-Mass Transfer Analogy," ASME JOURNAL OF HEAT TRANSFER, Vol. 99, pp. 620–627.

Subramanian, C. S., Ligrani, P. M., Green, J. G., Doner, W. D., and Kaisuwan, P., 1992, "Development and Structure of a Film-Cooling Jet in a Turbulent Boundary Layer With Heat Transfer," *Rotating Machinery Transport Phenomena, Proceedings of the Third International Symposium on Transport Phenomena and Dynamics of Rotating Machinery* (*ISROMAC-3*), J. H. Kim and W.-J. Yang, eds., Hemisphere Publishing Corp., pp. 53–68.

Wigle, J. M., 1991, "Heat Transfer, Adiabatic Effectiveness and Injectant Distributions Downstream of Single and Double Rows of Film-Cooling Holes With Compound Angles," M. S. Thesis, Department of Mechanical Engineering, Naval Postgraduate School, Monterey, CA.

M. A. Habib
King Fahd University of
Petroleum and Minerals,
Dhahran, Saudi Arabia

A. M. Mobarak

M. A. Sallak

Cairo University,
Cairo, Egypt

E. A. Abdel Hadi

R. I. Affify

Zagazig University,
Cairo, Egypt

Experimental Investigation of Heat Transfer and Flow Over Baffles of Different Heights

The phenomenon of flow separation in ducts with segmented baffles has many engineering applications, for example, shell-and-tube heat exchangers with segmented baffles, labyrinth shaft seals, laser curtain seals, air-cooled solar collectors, and internally cooled turbine blades. In the present work, an experimental investigation has been done to study the characteristics of the turbulent flow and heat transfer inside the periodic cell formed between segmented baffles staggered in a rectangular duct. In particular, flow field, pressure loss, and local and average heat transfer coefficients were obtained. The experimental runs were carried out for different values of Reynolds numbers and baffle heights (window cuts) at uniform wall heat flux condition along the top and bottom walls. The results indicate that the pressure loss increases as the baffle height does, for a given flow rate. Also, the local and average heat transfer parameters increase with increasing Reynolds number and baffle height. However, the associated increase in the pressure loss was found to be much higher than the increase in the heat transfer coefficient.

Introduction

Since the heat transfer coefficients of gases flowing in ducts are relatively low, it is deemed advisable to use some kind of turbulence promoter, such as swirl, corrugated ducts, bluff bodies, and baffles, to improve the coefficients. Augmentation techniques usually employ baffles attached to the heated surfaces so as to provide an additional surface area for heat transfer and to improve the mixing process. The presence of these baffles causes the flow to separate, reattach and thus creates regions of reverse flow and high shearing rates. Rowley (cited by Kelkar and Patankar, 1987) studied the heat transfer in internal circumferential finned tubes in laminar flow. The study proved that, for fluids like air, such fins reduce the heat transfer as they cause the flow to detach from the tube wall and reduce the washing action on the tube surface. The rate of this reduction depends on the fin height and spacing. A similar behavior is expected if a duct is made of parallel plates with internal baffles placed on one side. If, however, the baffles are staggered, they will cause the flow to deflect and impinge upon the opposite walls, thereby increasing the washing action there. In applications to gas turbine and power plants such conditions can be anticipated over a wide range of scales, ranging from large flow obstructions to small ribs.

Segmented baffles may be employed in shell-and-tube heat exchangers that are used as coolers in large-scale, high-pressure, power plant installations. Fins in gas-cooled solar collectors may have components perpendicular to the main flow direction used to improve the heat transfer effects. Corrugated walls, with or without fins, may be used as passages in heat exchangers for the purpose of heat transfer augmentation (Amano et al., 1987). Small ribs are employed in the internal cooling passage of gas turbine blades for high-temperature service (Han et al., 1988). Hendricks and Stetz (1981, 1982) presented studies of flow patterns and local pressure drop over a range of thermophysical properties and Reynolds numbers for sequential orifices and Borda configurations. The results did not include heat transfer measurements and show jetting, unstable flows, and lack of flow development over the length of the configuration. Flows of sudden expansion in ducts were studied by many investigators, among them, Gooray et al. (1985) and Vogel and Eaton (1985). Ichimiya (1987) presented an investigation for velocity and turbulence profiles for the throughflow region above a series of fins in ducts.

The flow over baffles has different characteristics than those mentioned above. Berner et al. (1984) and Habib et al. (1984) obtained experimental results of mean velocity and turbulence distributions in flow around segmented baffles. Yu and Heinrich (cited by Berner et al., 1984) developed a transient numerical technique to predict spacewise periodic laminar flow around segmented baffles. Founti and Whitelaw (1981) measured the flow on the shell side of a model disk-and-doughnut heat exchanger. An axisymmetric streamwise-periodic flow complicated by a few axial supporting rods was considered. The flows in heat exchangers with segmented baffles were described by Knudsen and Katz (1958). Numerical predictions of the flow and heat transfer in channels with staggered fins were investigated by Kelkar and Patankar (1987), Webb and Ramadhyani (1985), and Habib et al. (1988). The flow visualization pictures made by Gunter et al. (1947) indicate the main features of the flow over baffles. The study covered wide ranges of velocity and baffle spacing and overlap. The results had not provided quantitative information about the flow velocity and turbulence patterns. The measurements of pressure drop and the evaluation of the average shell-side coefficients were studied by Bergelin et al. (1953), Gay and Williams (1968), and Gay et al. (1976, 1977, 1981).

From the above-mentioned analysis of the available literature, it is found that the previous investigations leave much to be desired concerning the heat transfer and turbulence for the flow through baffled ducts. The objective of the present work is to study the flow and heat-transfer behavior in a heated rectangular duct with segmented baffles, using air as the working fluid. The experimental measurements were performed to investigate the effect of the baffle height ratio (or window cut ratio) and flow rate (or Reynolds number) on the local and average heat transfer coefficients and pressure loss coefficient.

Experimental Test Rig and Instrumentation

A schematic diagram of the test rig is shown in Fig. 1. Air is forced through a circular tube, which is connected to an air

---

Contributed by the Heat Transfer Division for publication in the JOURNAL OF HEAT TRANSFER. Manuscript received by the Heat Transfer Division February 1991; revision received May 1993. Keywords: Augmentation and Enhancement, Finned Surfaces, Forced Convection. Associate Technical Editor: R. J. Simoneau.

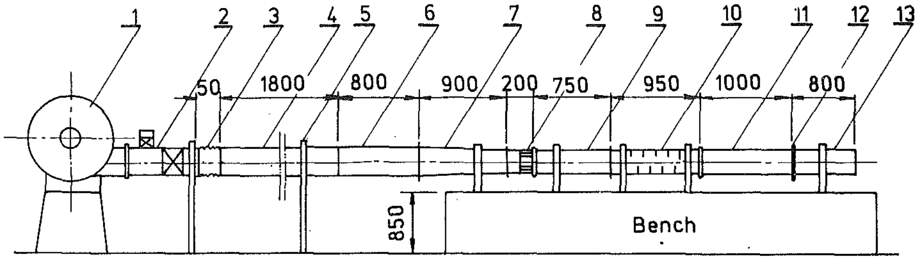

Dimensions in mms

1. Air blower
2. By pass section
3. Rubber joint
4. PVC circular tube
5. Wooden support
6. Diffuser
7. Converging section
8. Honeycomb
9. Straight duct
10. Test section
11. First segment of orifice meter
12. Orifice plate
13. Second segment of orifice meter

Fig. 1 Test rig

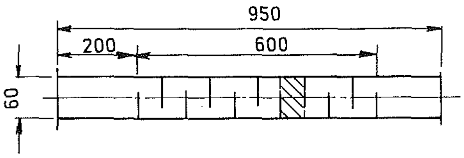

Dimensions in mms

Fig. 2(*a*) Test section

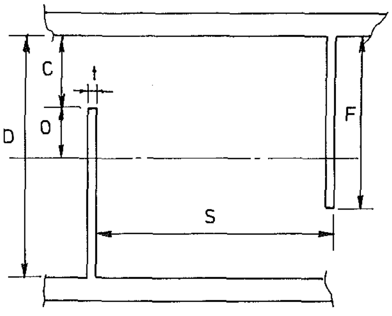

Fig. 2(*b*) Details of the cell

blower using a rubber joint to absorb the blower vibrations. The air then goes through a diffuser of rectangular cross section. The diffuser provides a geometric transmission from circular inlet, which has a diameter of 100 mm, to rectangular outlet of cross section of 80 × 300 mm. A converging section is connected to the diffuser to obtain uniformly distributed flow. Afterward, the air passes through a duct of constant rectangular cross section of 60 × 300 mm, which assists in providing a nearly two-dimensional flow at the inlet of the baffled test section. A screen and honeycomb were introduced between the converging section and the entrance section of the duct to reduce lateral velocity components. The end of the test section was connected to an orifice meter.

The test section, as shown in Fig. 2(*a*), consists of ten consecutive cells. Each cell, Fig. 2(*b*), has a depth D of 60 mm, baffle spacing S of 60 mm, baffle thickness t of 1.5 mm, and window cut C of 18, 30, and 42 mm. These give geometric ratios of $S/D = 1.0$, $t/D = 0.025$, and C/D of 0.3, 0.5, and 0.7 ($F/D = 0.7$, 0.5, and 0.3), respectively. Baffles were attached to the top and bottom walls using silicon rubber to eliminate leakage. The test section was made of aluminum plates of 6 mm thickness, 950 mm length, and forming a rectangular cross section of 60 × 300 mm. The top and bottom surface plates were heated by electric heaters. These electric heaters were wound on the top and bottom surfaces of the test section. The voltage across the heating elements was kept constant and the heat transfer to the surroundings was minimized by insulation and therefore, the heat flow, $\dot{q}$, remained unchanged through all the experiments. The test section was provided with 40 copper-constantan thermocouples distributed along and across the aluminum plates. A traverse thermocouple was used to measure the air-temperature distribution across the periodic cell #7. The temperature was recorded by the data logger (Fluke Model 2200 B).

Two pressure taps were used to measure the pressure drop across the periodic cell #7. As the flow is nearly two dimensional near the centerline, a five-hole hemispherical head probe of 3 mm diameter was used to measure the magnitude and

Nomenclature

A = duct cross-sectional area, m^2
C = window cut, m
c_P = specific heat at constant pressure, J/kg K
D = duct height, m
D_h = hydraulic diameter, m
F = baffle height, m
h = heat transfer coefficient, W/m^2 K
k = thermal conductivity, W/m K
L = duct length, m
$\dot{m}$ = mass flow rate, kg/s
O = baffle overlap, m
ΔP = pressure drop, N/m^2
$\dot{Q}$ = input heat, W
$\dot{q}$ = wall heat flux, W/m^2
S = spacing between baffles, m
T = temperature, °C
t = baffle thickness, m
U = average velocity, m/s
V = total velocity, m/s
u = horizontal mean velocity component, m/s
v = vertical mean velocity component, m/s
W = duct width, m
x = horizontal coordinate, m
y = vertical coordinate, m
μ = dynamic viscosity, Pa•s
ρ = density, kg/m^3

Dimensionless Groups

C/D = window cut ratio
F/D = baffle height ratio
K = pressure loss coefficient = $\Delta P/(1/2\ \rho U^2)$
Nu = Nusselt number = hD_h/k
Re = Reynolds number = $\rho U D_h/\mu$
S/D = baffle spacing ratio

direction of the velocity. The probe is provided with an electric traversing mechanism and a micromanometer (Model MDC FG001).

Calculation Procedure

The pressure loss coefficient was calculated from:

$$K = \Delta P/(1/2 \rho U^2) \tag{1}$$

where U is the bulk flow velocity and P is the pressure difference between two successive baffles on the same side.

The entrance temperature (T_{in}) of air was measured using two thermocouples located at the inlet of the baffled test section. The bulk temperature (T_b) of air was calculated from the equation:

$$T_b = \int_0^D |u| T dy \Big/ \int_0^D |u| dy \tag{2}$$

where u and T are the local velocity and temperature, respectively. The bulk temperature is calculated inside the periodic cell #7 and for five sections in the axial direction of the flow. Then the bulk temperature of the air at any arbitrary point inside the test section was calculated using the mass flow rate and the net heat flow at the same point. The total net heat flow, $\dot{Q}$, is defined as:

$$\dot{Q} = \dot{m} c_P (T_{bo} - T_{in}) \tag{3}$$

where T_{in} is the entrance temperature of the air, T_{bo} is the bulk temperature of air at the outlet of the baffled test section, and $\dot{m} = \rho A U$ is the mass flow rate that passes through the test section. The heat flux, $\dot{q}$, is calculated as follows:

$$\dot{q} = \dot{Q}/2WL \tag{4}$$

where $2WL$ represents the surface area of the top and bottom walls. The local heat transfer coefficient h is then evaluated from the following equation:

$$h = \dot{q}/(T_W - T_b) \tag{5}$$

where T_W is the wall temperature. Then, the Nusselt number Nu was calculated, based on the hydraulic diameter $D_h = 4A/2(W + D)$, as follows:

$$\mathrm{Nu} = hD_h/k \tag{6}$$

The average Nusselt number for a single wall in the typical cell is given by:

$$\overline{\mathrm{Nu}} = \bar{h} D_h/k \tag{7}$$

where $\bar{h} = (1/S) \int_0^S h dx$. To obtain the average Nusselt number for the cell, the heat transfer for both walls was taken into account.

The experiments were performed with aluminum baffles except for one experiment in which the baffles were made of wood for comparison reasons. The uncertainty estimation method of Kline and McClintock (1953) was used and indicates that the maximum uncertainties in the pressure loss coefficient and Nusselt number are 8.0 percent.

Results and Discussion

The results indicate thermally periodic fully developed flow after five cells for low Reynolds numbers and four cells for the higher Reynolds numbers. For short baffles at a medium Re of 11,500, a thermally periodic fully developed situation is obtained after 2, 3, or 5 cells for F/D values of 0.3, 0.5, and 0.7, respectively. Accordingly, all the results for the flow field and heat transfer coefficients were obtained in cell #7 as given in Fig. 2(a).

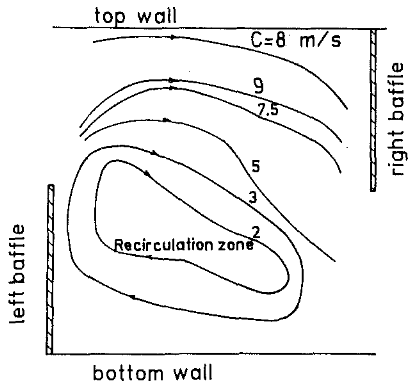

Fig. 3 Velocity contour lines (Re = 11,500, F/D = 0.5, S/D = 1.0)

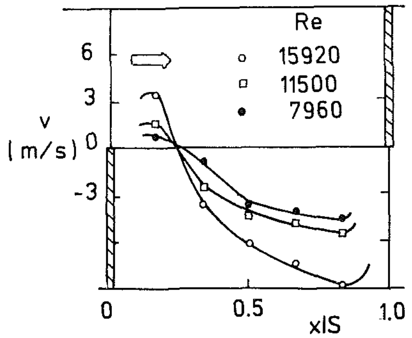

Fig. 4 Effect of Reynolds number on the vertical velocity component (F/D = 0.5, S/D = 1.0)

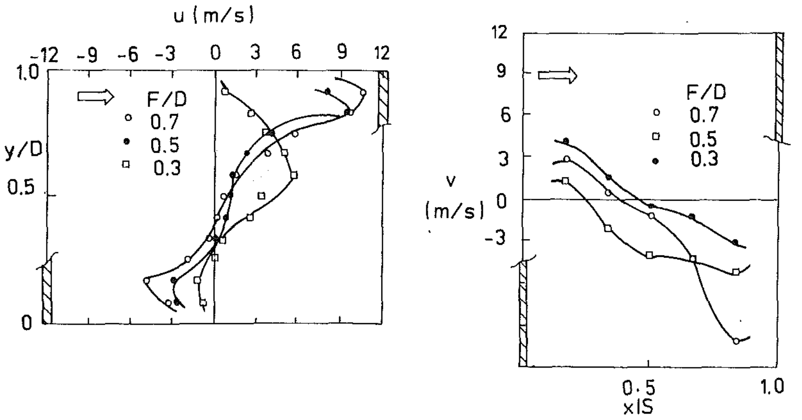

(a) Horizontal velocity component (b) Vertical velocity component

Fig. 5 Effect of baffle-height ratio on the velocity components (Re = 11,500, S/D = 1.0)

Flow Field. The velocity contour lines of the flow field at Re = 11,500, F/D = 0.5, and S/D = 1.0 inside the periodic cell #7 are plotted in Fig. 3. The flow is a turbulent shear flow, which is characterized by a large recirculation zone downstream of the left baffle with flow downward near the right baffle and upward near the left baffle of the cell. The flow is deflected due to the presence of the baffles and impinges on the top and bottom walls and on the upstream face of the baffles at different angles. The effect of Reynolds number on the vertical velocity component at the central plane in the x direction of the periodic cell #7 is shown in Fig. 4. It is noticed that the size and strength of the reversed flow region increase with the increase in Reynolds number. The effect of the baffle height on the velocity components is indicated in Fig. 5. The figure shows that the peak of the horizontal velocity component increases and its location shifts toward the vertical centerline of the downstream baffle with the increase in baffle-height ratio. It is noticed that the location of zero vertical velocity component is shifted toward the downstream baffle with the increase in window cut ratio.

Pressure Loss. The variation of the pressure drop for the turbulent, spatially periodic flow for three different baffle-height ratios with the Reynolds number for cell #7 is indicated in Fig. 6. It is observed that nearly constant values for the pressure loss coefficient are obtained for the same baffle-height ratio. The figure shows that a considerable increase in the pressure drop takes place as the baffle height ratio increases for the same flow rate.

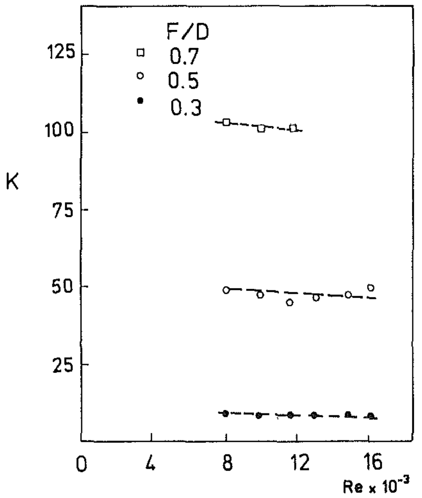

Fig. 6 Effect of baffle-height ratio on the pressure-loss coefficient

Local Heat Transfer. The heat transfer coefficient is presented here in terms of the ratio of Nusselt number for the baffled duct to those for the smooth one, Nu/Nu_o, where Nu_o is the value of Nusselt number of the smooth duct for laminar flow and equals 4.34 as given by Holman (1981).

The effect of the Reynolds number on the local heat transfer coefficient over the top and bottom walls of cell #7 is shown in Figs. 7(*a*) and 7(*b*). On the top wall, Fig. 7(*a*), the first flow impinges on it, resulting in high values of Nusselt numbers of maximum value at x/S = 0.4. Then, the flow gradually moves away from the top wall toward the tip of the next baffle as given in Fig. 3. This causes decrease in the flow intensity, which reflects a decrease in heat transfer coefficient. At x/S = 1.0, the heat transfer coefficient tends to increase where a large fraction of the energy is rerouted through the top wall into the baffle. On bottom wall, Fig. 7(*b*), the maximum Nusselt numbers occur at x/S = 0.0, i.e., at a point where the baffle is attached. This indicates that a large fraction of the energy is re-routed through the bottom wall into the baffle. The Nusselt number decreases sharply due to the recirculation region behind the left baffle and then increases again exhibiting a maximum value near x/S = 1.0, where the flow impinges on the bottom wall. The same phenomenon was observed by Kelkar and Patankar (1987) at F/D = 0.5 and S/D = 1.0 for laminar flow at Re = 500.

The effects of the baffle height ratio on the local heat transfer coefficient on the top and bottom walls are shown in Figs. 8(*a*) and 8(*b*) for Re = 11,500. The effect of the baffle height ratio on the heat transfer coefficient is shown to be similar to the effect of the Reynolds number, Figs. 7(*a*) and 7(*b*). It is found from the analysis of the flow patterns shown in Figs. 4 and 5, that the velocity of the throughflow increases with increasing the baffle-height ratio at fixed constant flow rate. Therefore, it is concluded that the heat transfer coefficient increases with the increase of the baffle-height ratio. The influence of the baffle material on the local Nusselt number is given in Fig. 9. The figure indicates a significant reduction in Nu for the wood baffle as compared to the aluminum baffle

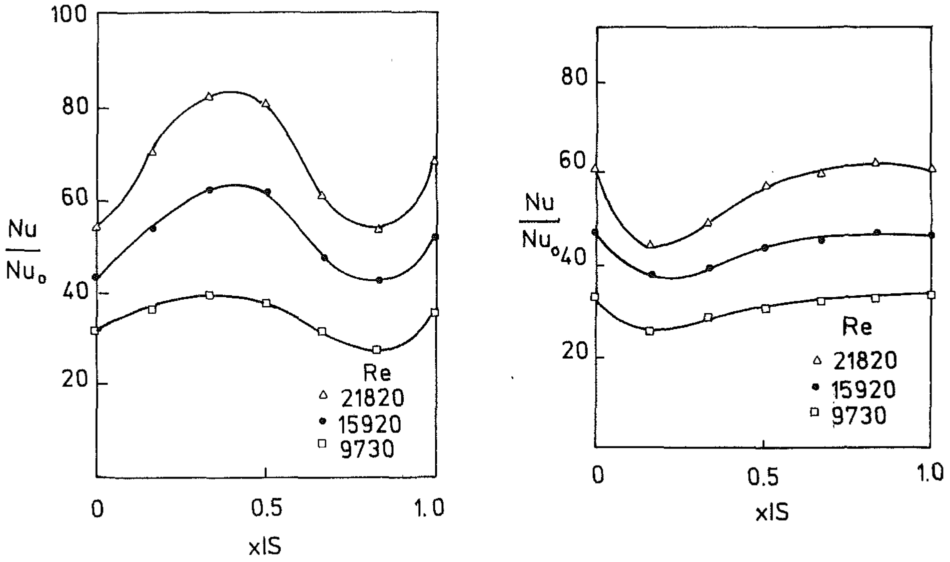

(a) On top wall

(b) On bottom wall

Fig. 7 Effect of Reynolds number on the local Nusselt number (F/D = 0.3, S/D = 1.0)

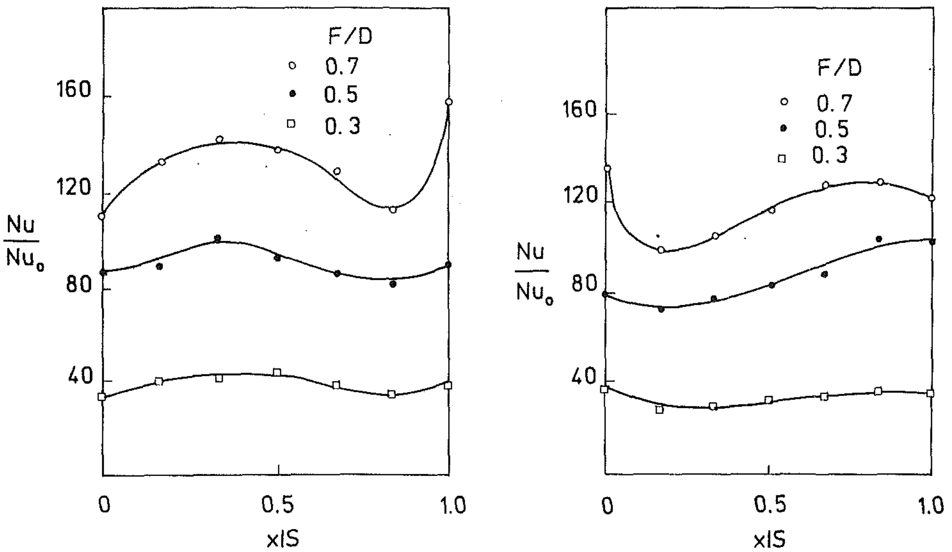

(a) On top wall

(b) On bottom wall

Fig. 8 Effect of baffle-height ratio on the local Nusselt number (Re = 11,500, S/D = 1.0)

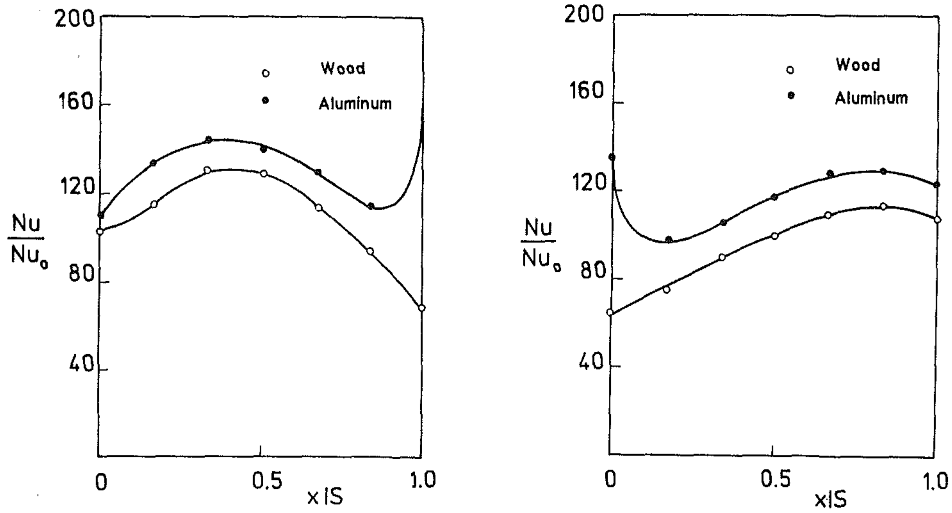

a) Top wall

b) Bottom wall

Fig. 9 Effect of the thermal conductivity of baffles on the local Nusselt number (Re = 11,500, F/D = 0.7, S/D = 1.0)

at the right-hand side of the cell for the top wall, Fig. 9(*a*), and at the left-hand side for the bottom wall, Fig. 9(*b*).

Average Heat Transfer. Figure 10 shows the variation of the average Nusselt number with Reynolds number for different baffle-height ratios. The Nusselt number for all values of the baffle-height ratios increases with increasing Reynolds number. The values of the heat transfer coefficient indicate that the augmentation is substantially higher for longer baffles, i.e., for high values of F/D. The figure presents a comparison between wood and aluminum baffles and indicates higher Nusselt numbers for the aluminum baffles more than wood baffles and confirms the results of Kelkar and Patankar (1987) and Webb and Ramadhyani (1985).

Comparison of Heat Transfer and Pressure Loss Coefficients. Figure 11 shows the effect of baffle height ratio at Reynolds number 11,500 on both average Nusselt number and pressure loss coefficient K. The pressure loss coefficient K increases rapidly with the increase in the baffle-height ratio.

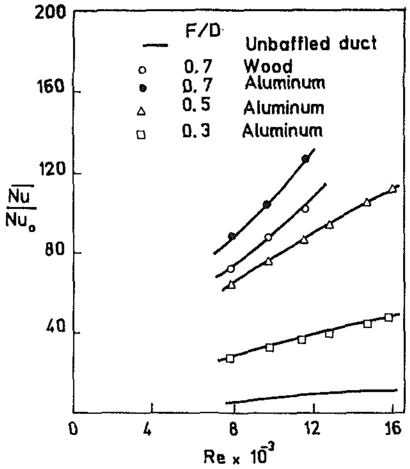

Fig. 10 Variation of the average Nusselt number with Reynolds number for different baffle-height ratios

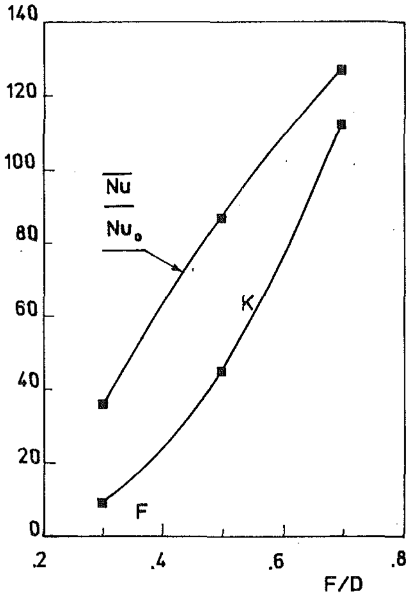

Fig. 11 Variation of the average Nusselt number and pressure loss coefficient cell with baffle-height ratio (Re = 11,500, *S/D* = 1.0)

It can be seen from the flow patterns shown in Figs. 4 and 5 that the velocity of the throughflow increases linearly with the baffle-height ratio. This is confirmed by the fact that the pressure drop is directly proportional to the square of the velocity.

It can be noticed that the Nusselt number increases, but at a lower rate than that of the pressure loss coefficient, with the increase in the baffle-height ratio. This is attributed to the increase in the thickness of the thermal boundary layer with velocity on the duct wall and front faces of the baffle as it is proportional to the square root of the through flow velocity (as in the case of flat plate boundary layer). Hence, a small rise in Nusselt number is found for large baffle height ratios. However, the increase in pressure loss coefficient is much higher than the increase in heat transfer coefficient.

The pressure loss coefficient data show that the baffle-height ratio $F/D > 0.3$ probably cannot be justified since a "knee" in the curve occurs there. The increase in pumping power requirement is too costly to justify the increase in heat transfer.

Conclusions

An experimental study was presented to provide a detailed investigation of the turbulent flow and the heat transfer in a rectangular duct with segmented baffles at a uniform wall-heat flux condition along the top and bottom walls. The experimental runs were carried out for different values of Reynolds number and baffle-height ratios. The flow is characterized by a large recirculation zone formed behind the obstructions and by regions of large velocity gradients. The results indicate that the heat transfer parameters increase with the increase of Reynolds number and baffle-height ratio. However, the increase in the pressure loss coefficient is much higher than the increase in heat transfer coefficient. The results indicate that for fluids of low heat transfer coefficient, such as gases, only marginal heat transfer augmentation may be expected.

Acknowledgments

The authors acknowledge the support by Cairo University and King Fahd University of Petroleum and Minerals for this research project.

References

Amano, R. S., Bagherle, A., Smith, R. J., and Niess, T. G., 1987, "Turbulent Heat Transfer in Corrugated Wall Channels With and Without Fins," ASME Journal of Heat Transfer, Vol. 109, pp. 62-67.

Bergelin, O. P., Brown, G. A., and Colburn, A. P., 1953, "Heat Transfer and Fluid Friction During Flow Across Banks of Tubes—V: A Study of a Cylindrical Baffles Exchanger Without Internal Leakage," ASME Journal of Heat Transfer, Vol. 75, pp. 841-850.

Berner, C., Durst, F., and McEligot, D. M., 1984, "Flow Around Baffles," ASME Journal of Heat Transfer, Vol. 106, pp. 743-749.

Founti, M. A., and Whitelaw, J. H., 1981, "Shell-Side Flow in a Model Disc-and-Doughnut Heat Exchanger," Tech. Report FS/81/37, Mech. Eng. Dept., Imperial College, London, United Kingdom.

Gay, B., and Williams, T. A., 1968, "Heat Transfer on the Shell-Side of a Cylindrical Shell-and-Tube Heat Exchanger Fitted With Segmental Baffles," *Trans. Inst. Chem. Engrs.*, Vol. 46, pp. T95-T100.

Gay, B., Mackley, N. V., and Jenkins, J.D., 1976, "Heat Transfer in Baffled Cylindrical Shell-and-Tube Exchangers. An Electrochemical Transfer Modelling Technique," *International Journal of Heat and Mass Transfer*, Vol. 19, No. 9, pp. 995-1002.

Gay, B., Jenkins, J. D., and Mackley, N. V., 1977, "Shell-Side Heat Transfer Coefficient in Cylindrical Heat Exchangers. The Influence of Geometrical Factors. I. The Non-leakage Case," *Letters in Heat and Mass Transfer*, Vol. 4, pp. 41-52.

Gay, B., Jenkins, J. D., and Mackley, N. V., 1981, "Shell-Sided Heat Transfer Coefficients in Cylindrical Heat Exchangers. The Influence of Geometrical Factors. II. The Leakage Case," *Letters in Heat and Mass Transfer*, Vol. 8, pp. 437-452.

Gooray, A. N., Watkins, G. B., and Aung, W., 1985, "Turbulent Heat Transfer Computations for Rearward Facing Steps and Sudden Pipe Expansions," ASME Journal of Heat Transfer, Vol. 107, pp. 70-76.

Gunter, A. Y., Sennstrom, H. R., and Kopp, S., 1947, "A Study of Flow Patterns in Baffled Heat Exchangers," ASME Paper No. 47-A-103.

Habib, M. A., Durst, F., and McEligot, D. M., 1984, "Streamwise-Periodic Flow Around Baffles," *Proc. 2nd Int. Conference on Applications of Laser Anemometry to Fluid Mechanics*, Lisbon, Portugal.

Habib, M. A., Attya, A. E., and McEligot, D. M., 1988, "Calculation of Turbulent Flow and Heat Transfer in Channels With Streamwise-Periodic Flow," ASME *Journal of Turbomachinery*, Vol. 110, pp. 405-411.

Han, J. C., Chandra, P. R., and Lau, S. C., 1988, "Local Heat/Mass Transfer Distribution Around Sharp 180 Degree Turn in Multipass Rib-Roughened Channels," ASME Journal of Heat Transfer, Vol. 110, pp. 91-98.

Hendricks, R. C., and Stetz, T. T., 1981, "Some Flow Phenomena Associated With Aligned Sequential Apertures With Borda Type Inlets," NASA TP-1972.

Hendricks, R. C., and Stetz, T. T., 1982, "Studies of Flows Through N-Sequential Orifices," presented at the ASME Winter Annual Meeting, Phoenix, AZ, Nov. 14-19.

Holman, J. P., 1981, *Heat Transfer*, McGraw-Hill, New York.

Ichimiya, K., 1987, "Effects of Several Roughness Elements on an Insulated Wall for Heat Transfer From the Opposite Smooth Heated Surface in a Parallel Plate Duct," ASME Journal of Heat Transfer, Vol. 109, pp. 68-73.

Kakac, S., Shah, R. K., and Aung, W., 1987, *Handbook of Single Phase Convective Heat Transfer*, Wiley, New York.

Kelkar, K. M., and Patankar, S. V., 1987, "Numerical Prediction of Flow and Heat Transfer in Parallel Plate Channel With Staggered Fins," ASME Journal of Heat Transfer, Vol. 109, pp. 25-30.

Kline, S. J., and McClintock, F. A., 1953, "Describing Uncertainties in Single Sample Experiments," *Mechanical Engineering*, Vol. 75, Jan., pp. 3-8.

Knudsen, W. W., and Katz, D. L., 1958, *Fluid Dynamics and Heat Transfer*, McGraw-Hill, New York.

Vogel, J. C., and Eaton, J. K., 1985, "Combined Heat Transfer and Fluid Dynamic Measurements Downstream of a Backward-Facing Step," ASME Journal of Heat Transfer, Vol. 107, pp. 922-929.

Webb, B. W., and Ramadhyani, S., 1985, "Conjugate Heat Transfer in a Channel With Staggered Ribs," *International Journal of Heat and Mass Transfer*, Vol. 28, No. 9, pp. 1679-1687.

Heat Transfer Predictions With Extended k–ϵ Turbulence Model in Radial Cooling Ducts Rotating in Orthogonal Mode

P. Tekriwal
GE Corporate Research and Development,
Schenectady, NY 12301
Assoc. Mem. ASME

Standard and extended k–ϵ turbulence closure models have been employed for three-dimensional heat transfer calculations for radially outward flow in rectangular and square cooling passages rotating in orthogonal mode. The objective of this modeling effort is to validate the numerical model in an attempt to fill the gap between model predictions and the experimental data for heat transfer in rotating systems. While the trend of heat transfer predictions by the standard k–ϵ turbulence model is satisfactory, the differences between the data and the predictions are approximately 30 percent or so in the case of high rotation number flow. The extended k–ϵ turbulence model takes an approach where an extra "source" term based on a second time scale of the turbulent kinetic energy production rate is added to the equation for the dissipation rate of turbulent kinetic energy. This yields a more effective calculation of turbulent kinetic energy as compared to the standard k–ϵ turbulence model in the case of high rotation number and high density ratio flow. As a result, comparison with the experimental data available in the literature shows that an improvement of up to a significant 15 percent (with respect to data) in the heat transfer coefficient predictions is achieved over the standard k–ϵ model in the case of high rotation number flow. Comparisons between the results of the standard k–ϵ model and the extended formulation are made at different rotation numbers, different Reynolds numbers, and varying temperature ratio. The results of the extended k–ϵ turbulence model are either as good or better than those of the standard k–ϵ model in all these cases of parametric study. Thus, the extended k–ϵ turbulence model proves to be more general and reduces the discrepancy between the model predictions and the experimental data for heat transfer in rotating systems.

1 Introduction

In order to increase the thermodynamic efficiency of a gas turbine engine, a high turbine inlet temperature is required. A high inlet temperature demands enhanced cooling of the turbine blade with minimum coolant flow rate. This is achieved in different ways such as film cooling and convective heat transfer to the gas flowing through the internal ducts (see Fig. 1). These internal ducts may be smooth or sometimes may have turbulators such as an array of cross-ribs to further enhance cooling. As shown in Fig. 1, the cross section of the internal ducts may vary from circular at the leading edge of the blade to rectangular or square in the middle section to triangular at the trailing edge.

In order to predict the operational life of the blade, stresses must be determined. The temperature distribution should also be known prior to the stress determination. A heat conduction analysis of the blade will require boundary conditions on its internal and external surfaces. To this end, therefore, heat transfer coefficient values must be determined either experimentally or analytically on the blade surfaces. Clearly, analytical predictive methods verified by experimental data will permit faster and more economic cooling design evaluation. Indeed, modern computerized methods of design evaluation have resulted in substantial reduction of development cost of design (Medwell et al., 1991).

In the current work an attempt has been made to model and predict heat transfer due to air flow in a radial cooling duct rotating about an axis perpendicular to its own—a condition known as orthogonal mode rotation. The duct is smooth and the flow is radially outward as shown in Fig. 2. The flow condition depicted in Fig. 2 is one encountered in gas turbine blades (see Fig. 1). Several researchers have carried out experimental and analytical studies for the fluid flow and/or heat transfer in radially rotating ducts or similar configurations. Mori et al. studied the fully developed turbulent (1971) and laminar (1968) convective heat transfer in radially rotating pipes by assuming velocity and thermal boundary layers along the wall. Heat transfer was found to increase due to rotation. Local Nusselt number had little variation in the circumferential direction. Ito and Nanbu (1971) measured the friction factor extensively for a fully developed flow in a radially rotating pipe for a wide range of Reynolds number and found that wall friction was enhanced by rotation. Johnston et al. (1972) experimentally investigated the effect of Coriolis force on the structure of turbulence in a rotating radial channel. The measured mean velocity profile indicated negative production of turbulence and increased stability on the suction side of the channel. The turbulence was amplified on the pressure side of the channel. Metzger and Stan (1977) experimentally investigated the effect of rotation on the entrance region heat transfer for different passage length-to-diameter ratios. They found that enhancement in overall rotational heat transfer increased with increasing L/d and decreased with increasing Reynolds number. However, the enhancement in the entry region was less than predicted for fully developed conditions. Kikuyama et al. (1986) found experimentally that due to Coriolis force, wall shear stress increased on the pressure side and decreased

---

Contributed by the Heat Transfer Division and presented at the ASME Winter Annual Meeting, Anaheim, California, November 8–13, 1992. Manuscript received by the Heat Transfer Division July 1992; revision received June 1993. Keywords: Rotating Flows, Turbines, Turbulence. Associate Technical Editor: R. J. Simoneau.

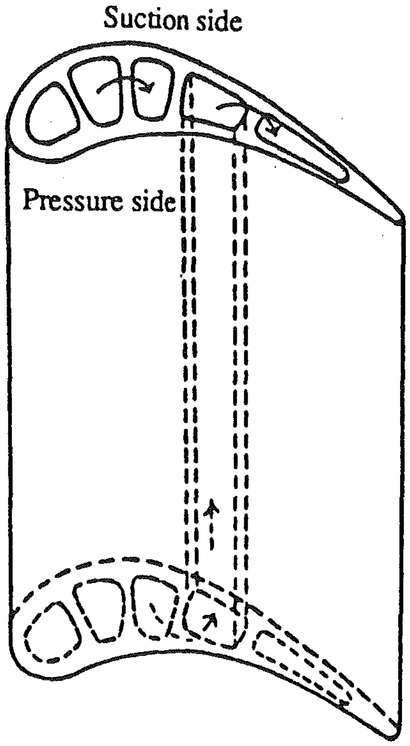

Fig. 1 Internal cooling passages in a turbine blade

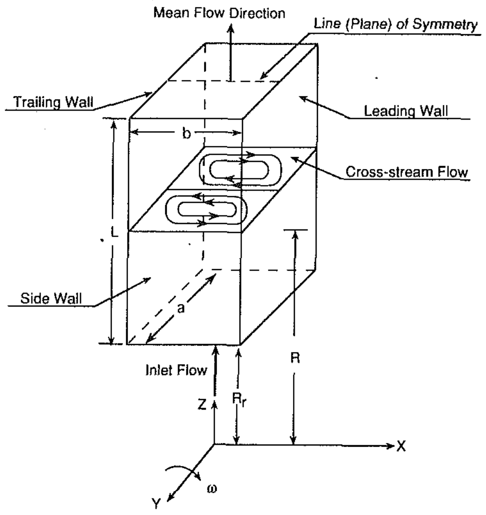

Fig. 2 Illustration of flow geometry

on the suction side of a diffuser rotating about a perpendicular axis.

Recently a number of investigators have studied and obtained heat transfer data in radially rotating ducts of different cross sections at varying flow and wall conditions. Morris and Ayhan (1979), Morris and Harasgama (1985), Morris and Ghavami-Nasr (1991), and Harasgama and Morris (1988) have obtained heat transfer measurements for circular, rectangular, and triangular ducts at relatively low rotation numbers (*Ro*). Morris and Ayhan (1979) observed that centrifugal buoyancy has an advantageous effect on heat transfer for radially inward flow but an adverse effect for radially outward flow. Guidez' (1989) geometry was rectangular with uniform wall heat flux condition and Wagner et al. (1991a, b) obtained a compre-

Nomenclature

AR = aspect ratio = a/b
a, b = duct dimensions in y and x directions
C_1, C_2, C_3, C_μ = turbulence model constants
C_p = specific heat
d = hydraulic diameter
E = wall roughness parameter
G_k = production rate of kinetic energy
H = enthalpy
H_b = bulk enthalpy
H_w = wall enthalpy
h = heat transfer coefficient
k = turbulent kinetic energy
k(Eke) = k computed from extended k–ϵ model
k(ke) = k computed from standard k–ϵ model
L = duct length
m = mass flow rate
Nu = Nusselt number
Nu_α or Nu_∞ = Nusselt number for nonrotating fully developed flow
P = a function
Pr = Prandtl number
Pr_ϵ, Pr_k = Prandtl numbers for ϵ and k, respectively

Pr_t = turbulent Prandtl number
p = pressure
q_w = average wall heat flux
R = midlength radius of the duct
Re = Reynolds number
Ro = rotation number = $\omega d/w_{\mathrm{in}}$ or $\omega dab/m$
R_r = root radius
$\mathbf{r}$ = position vector = $X\mathbf{i} + Y\mathbf{j} + Z\mathbf{k}$
S_H = additional enthalpy source term
St = Stanton number
s = skin friction
T = temperature
T_A, T_B, T_C = constants in $(T\sim H)$ relation
T_b = bulk temperature
T_f = film temperature = $(T_w + T_b)/2$
TKE = turbulent kinetic energy = k
T_{ref} = reference temperature
T_w = wall temperature
v = velocity of the fluid in near-wall cell
$\mathbf{w}$ = velocity vector
w_c = centerline velocity
w_{in} = inlet velocity
w_x, w_y, w_z = x-, y-, and z-direction velocity components

y^+ = nondimensional distance of near-wall cell center = $\delta C_\mu^{1/4} k^{1/2}/v$
z/d = nondimensional axial distance from inlet = $(Z - R_r)/d$
∇ = $\mathbf{i}\partial/\partial x + \mathbf{j}\partial/\partial y + \mathbf{k}\partial/\partial z$
ΔT = temperature difference = $T_w - T_b$
$\Delta\rho$ = density difference
δ = distance of near-wall cell center from the wall
ϵ = dissipation rate of turbulent kinetic energy
κ = von Karman constant
λ = thermal conductivity
μ = laminar viscosity
μ_f = laminar viscosity at film temperature
μ_{ref} = laminar viscosity at reference temperature
μ_t = turbulent viscosity
ν = kinematic viscosity
ρ = fluid density
τ_w = wall shear stress
$\mathbf{\Omega}$ = angular velocity vector
ω = angular speed

hensive heat transfer data on a square duct with uniform wall temperature at different values of flow parameters such as rotation number, density ratio, Reynolds number, and R/d ratio. They measured heat transfer in the first leg of four-leg serpentine flow passage for the radially outward flow condition (1991a) and then in three legs along with the connecting 180 deg bends (1991b) to study a turbine blade cooling passage flow more closely (see Fig. 1). Density ratio and rotation number were found to cause large changes in heat transfer for radially outward flow and relatively small changes for radially inward flow. Soong et al. (1991) obtained heat transfer data in radially rotating isothermal duct for varying aspect ratio, rotational speed, and Reynolds number. It was pointed out that the aspect ratio is a critical parameter in Coriolis-induced secondary flow formation. The secondary flow can provide a beneficial effect on the heat transfer enhancement, while the centrifugal buoyancy presents an adverse effect in the radially outward flow. Both of these effects diminish in a strong forced (high Re) flow.

It is clear from the literature review so far that the flow phenomenon in a radially rotating duct is very complex and is governed by various parameters such as forced convection (Re), rotation (Ro), buoyancy ($\Delta\rho/\rho = \Delta T/T_w$), aspect ratio ($a/b$), eccentricity ratio ($R_r/d$), and duct length parameter ($\bar{R}/d$). It requires expensive experimentation to study the effect of various parameters. An analytical approach supported by experimental data will be of significant assistance in the study of a flow of such complexity. Indeed, some investigators have made effort in the past and with the advent of ever-growing computing power more and more physics of the process is being taken into account in the current modeling work on radially rotating flow and heat transfer. Barua (1955) computed friction factor from an approximate series solution in a rotating pipe. Howard et al. (1980) employed a k–ϵ turbulence model with three Coriolis modifications to predict flow in rotating radial ducts. The Coriolis modification was confirmed to be useful in predicting the flow data of Johnston et al. (1972) for a high aspect ratio duct but the predictions were not very sensitive to the Coriolis modification of turbulence in the case of low aspect ratio duct flow. In the case of low aspect ratio duct flow the Coriolis-induced strong secondary flow was found to be the principal source of the modified wall shear stress. Iacovides and Launder (1987, 1991) used two-layer turbulence model to predict flow and heat transfer for fully developed flow in rotating radial ducts. A standard k–ϵ model was used in the outer boundary layer. Van Driest's (1956) mixing length model (Iacovides and Launder, 1987) and the one equation model within a thin band of $0.02d$ thickness (Iacovides and Launder, 1991) were employed in regions close to the walls. A uniform wall temperature condition was used at the solid boundary. Formation of two vortices was predicted at low rotation number flow and four vortices at high rotation number flow. A sudden jump in average Nusselt number was observed on the pressure side (trailing wall) due to onset of four vortices. Even at low rotation number there is strong augmentation of heat flux rate on the trailing wall and equally strong suppression on the leading wall. Hwang and Jen (1990) computed heat transfer for hydrodynamically and thermally fully developed laminar flow in a radially rotating duct of aspect ratio varying from 0.2 to 5 and Prandtl number equal to 0.7 and 7.0. A uniform wall temperature condition was employed. They also obtained a pair of pairs of vortices due to the Coriolis force. In all the analytical studies reviewed above, incompressible flow was assumed and the effect of centrifugal buoyancy was ignored.

Prakash and Zerkle (1991) included the effect of centrifugal buoyancy and found it to be significant in predicting the heat transfer in radially rotating duct. A standard k–ϵ model was employed and uniform temperature condition was used at the solid walls of the square-sectioned duct. Except near the inlet of the duct, prediction of heat transfer is within a range of 30 percent or so when compared with the data of Wagner et al. (1991a). Nusselt numbers are underpredicted over the trailing wall and near the exit on the leading wall. Skiadaressis and Spalding (1978) used the uniform wall heat flux condition for radially rotating ducts of aspect ratios 2:1, 1:1, 1:2. A comparison of different flow geometries tested showed that the effect of rotation on the flow and heat transfer was only weakly dependent on the aspect ratio.

In this paper standard and extended k–ϵ turbulence closure models have been employed for three-dimensional heat transfer calculations in rectangular- and square-sectioned smooth cooling passages rotating in orthogonal mode. The coolant (air) flow is in the radially outward direction. A finite difference method is used for the analysis. Effects of the Coriolis and centrifugal forces are included in the momentum equations. The effect of the centrifugal buoyancy is also incorporated. The heat transfer predictions from the two k–ϵ models are compared with the experimental data of Morris and Ghavami-Nasr (1991) for the rectangular duct and Wagner et al. (1991a) for the square duct at different rotation numbers, different Reynolds numbers, and varying density ratio. The model is capable of employing both the uniform wall heat flux and/or uniform wall temperature conditions. The objective of the modeling effort is to validate the numerical model in an attempt to fill the gap between model predictions and the experimental data for heat transfer in rotating systems. It is recognized that the Coriolis and centrifugal buoyancy force interactions will drive the flow in a radially rotating duct to nonequilibrium on the energy spectrum, especially at high rotation speeds. The extended k–ϵ model may be better able to capture the effects of nonequilibrium in the energy spectrum of the heat transfer.

2 Physics of the Problem

Figure 2 shows a rectangular duct of dimension $b \times a \times L$ rotating at a constant angular speed ω about the negative Y axis. Flow of the coolant (air) is radially outward as shown. The eccentricity or the root radius of the duct is given as R_r and the midheight of the duct is denoted by $\bar{R}$. The geometry and the flow conditions are symmetric about the longitudinal midplane of the duct, and therefore, flow in only one-half of the duct is discretized for computational economy.

As shown in Fig. 2, Coriolis forces produce a secondary flow in cross-stream planes, which causes the migration of flow from the central core region to the trailing wall of the duct with a return flow along the walls in order to maintain continuity. As a result, two symmetric vortices are formed in the planes perpendicular to the main flow direction. This secondary flow leads to an increase in wall friction and heat transfer at the trailing wall in comparison to those at the leading wall.

In the absence of density gradients in an incompressible flow the centrifugal force is hydrostatic and it only modifies the pressure. But in the case of heated walls, a temperature gradient exists from the wall region to the core, which gives rise to centrifugal buoyancy. In the case of radially outward duct flow, the radial velocity of the relatively cooler, and hence heavier, fluid near the trailing wall is increased while the radial velocity of the relatively warmer, and hence lighter, fluid near the leading wall is decreased. Consequently, the friction and heat transfer near the trailing wall are further promoted (Prakash and Zerkle, 1991).

3 Governing Equations

3.1 Conservation of Mass, Momentum, and Energy Equations. In the coordinate system rotating with the duct (see Fig. 2) the flow is steady. The mass, momentum, and energy equations derived from the conservation principles are given in the form of time-averaged mean flow variables as follows:

Mass:

$$\nabla \cdot \rho \mathbf{w} = 0 \tag{1}$$

Momentum:

$$(\mathbf{w} \cdot \nabla)\rho \mathbf{w} = -\nabla p + 2\rho \mathbf{w} \times \mathbf{\Omega} + \nabla \frac{1}{2} \rho(\mathbf{\Omega} \times \mathbf{r})^2 + \nabla \cdot [(\mu + \mu_t)\nabla]\mathbf{w} \tag{2}$$

Energy:

$$(\mathbf{w} \cdot \nabla)\rho H = \nabla \cdot \left[\left(\frac{\mu}{\mathrm{Pr}} + \frac{\mu_t}{\mathrm{Pr}_t} \right) \nabla \right] H + S_H \tag{3}$$

where $\mathbf{\Omega} = -\omega \mathbf{j}$ is the angular velocity vector.

The terms $2\rho \mathbf{w} \times \mathbf{\Omega}$ and $\nabla\ 1/2\ \rho(\mathbf{\Omega} \times \mathbf{r})^2$ in the momentum equation are due to the Coriolis and centrifugal forces per unit volume of the fluid (Landau and Lifshitz, 1987). S_H represents the unaccounted source terms of enthalpy such as the dissipation of mechanical energy. The following relationship can easily be proven:

$$\nabla \frac{1}{2} \rho(\mathbf{\Omega} \times \mathbf{r})^2 = -\rho \mathbf{\Omega} \times (\mathbf{\Omega} \times \mathbf{r}) \tag{4}$$

$\mathbf{\Omega} \times (\mathbf{\Omega} \times \mathbf{r})$ is the centripetal acceleration. In the component forms Eqs. (1) and (2) may be written in the left-handed coordinate system shown in Fig. 2 as follows:

Mass:

$$\frac{\partial}{\partial x} (\rho w_x) + \frac{\partial}{\partial y} (\rho w_y) + \frac{\partial}{\partial z} (\rho w_z) = 0 \tag{5}$$

x Momentum:

$$(\mathbf{w} \cdot \nabla)\rho w_x = -\frac{\partial p}{\partial x} - 2\rho\omega w_z + \rho\omega^2 x + \nabla \cdot [(\mu + \mu_t)\nabla] w_x \tag{6a}$$

y Momentum:

$$(\mathbf{w} \cdot \nabla)\rho w_y = -\frac{\partial p}{\partial y} + \nabla \cdot [(\mu + \mu_t)\nabla] w_y \tag{6b}$$

z Momentum:

$$(w \cdot \nabla)\rho w_z = -\frac{\partial p}{\partial z} - 2\rho\omega w_x + \rho\omega^2 z + \nabla \cdot [(\mu + \mu_t)\nabla] w_z \tag{6c}$$

In order to close the above system equations, the turbulent viscosity, μ_t, and the turbulent Prandtl number, Pr_t, must be specified. Specifying these two quantities is accomplished through what is known as turbulence modeling.

3.2 Standard and Extended k–ϵ model Turbulence Models. The turbulent viscosity is obtained from the following algebraic relationship (Launder and Spalding, 1974):

$$\mu_t = C_\mu \rho k^2/\epsilon \tag{7}$$

where $C_\mu = 0.09$ and the turbulent Prandtl number (Pr_t) is taken as a constant equal to 0.86. k and ϵ are known as the turbulent kinetic energy and the dissipation rate of the turbulent kinetic energy, respectively. They are computed from the following differential equations:

$$(\mathbf{w} \cdot \nabla)\rho k = -\nabla \left(\frac{\mu_t}{\mathrm{Pr}_k} \nabla k \right) + \rho(G_k - \epsilon) \tag{8}$$

$$(\mathbf{w} \cdot \nabla)\rho \epsilon = -\nabla \left(\frac{\mu_t}{\mathrm{Pr}_\epsilon} \nabla \epsilon \right) + C_1 \rho G_k \frac{\epsilon}{k} - C_2 \rho \frac{\epsilon^2}{k} + C_3 \rho \frac{G_k^2}{k} \tag{9}$$

where the turbulent kinetic energy production rate, G_k, is given by

$$G_k = \frac{\mu_t}{\rho} \left(\frac{\partial w_i}{\partial x_j} + \frac{\partial w_j}{\partial x_i} \right) \frac{\partial w_i}{\partial x_j} \text{ (summation convention implied)} \tag{10}$$

The buoyancy generation terms proportional to $(\mu_t/\rho)\beta\omega^2 x_i \partial T/\partial x_i$ are neglected in G_k. Note that the value of G_k depends upon the velocity gradients, which are of considerable magnitude in the regions close to the walls. The buoyancy contribution to the generation term is relatively small near the wall for the range of flow conditions considered in the present work.

The difference between the standard and the extended k–ϵ models lies in the values of various constants used in Eqs. (8) and (9). In the standard k–ϵ model the constants are given as (Launder and Spalding, 1974)

$$\mathrm{Pr}_k = 1.0,\ \mathrm{Pr}_\epsilon = 1.3,\ C_1 = 1.44,\ C_2 = 1.92, \text{ and } C_3 = 0.0 \tag{11}$$

whereas in the extended k–ϵ model, after Chen and Kim (1987), the following values are used:

$$\mathrm{Pr}_k = 0.75,\ \mathrm{Pr}_\epsilon = 1.15,\ C_1 = 1.15,\ C_2 = 1.9, \text{ and } C_3 = 0.25 \tag{12}$$

It should be noted that in addition to having different constant values, the ϵ equation in the "extended" version of the k–ϵ model has an additional "source" term $C_3 \rho G_k^2/k$, the constant C_3 being nonzero in the extended model as compared to zero in the standard model. The additional source term corresponds to an extra time scale based on the production rate. The two time scales included in the extended k–ϵ model are the dissipation rate time scale, k/ϵ, and the production rate time scale, k/G_k. In general, turbulence will comprise nonequilibrium-type fluctuating motions with a spectrum of multiple sizes and multiple time scales. The fact that the turbulence models based on single time scale (k/ϵ) have had successful predictions in numerous applications reflects that the flows considered have been close to a spectral equilibrium rather than that the single-time-scale formulation is adequate (Hanjalic et al., 1979). Chen and Kim (1987), by considering several flow examples, including a turbulent flow over a backward-facing step and a turbulent confined swirling flow, have shown that the extended k–ϵ formulation is more general than the standard k–ϵ model and yields better results by having the energy transfer mechanism respond to the mean strain more effectively. It is recognized that the Coriolis and centrifugal buoyancy force interactions will drive the flow in a radially rotating duct to nonequilibrium on the energy spectrum, especially at high rotation speeds. To see whether the heat transfer predictions benefit from the extended k–ϵ model constitutes one of the objectives of the present modeling effort.

In order to satisfy the consistency condition, the Prandtl number for the turbulent kinetic energy is modified to $\mathrm{Pr}_k = 0.8927$ in the extended k–ϵ model (see Eq. (12)). The consistency condition guarantees that the propagation speeds of the wave fronts of the turbulent kinetic energy (k) and its dissipation rate (ϵ) are the same. The condition is derived and discussed by Lele (1985). An interesting fact to note is that the recommended values of model constants in different turbulence closure models including the standard k–ϵ model do not satisfy the consistency condition exactly. However, a slight modification in these computer-optimized constants makes the model consistent (Lele, 1985). In the present work the value $\mathrm{Pr}_k = 0.8927$ was also employed and the change in heat transfer results was found to be negligible.

4 Facts, Features, and Assumptions

The present model employs the following facts, features, and assumptions to compute heat transfer in a radially rotating duct flow:

(*i*) On account of symmetry the flow in only one half of the duct is discretized for computational economy. A zero-normal-gradient condition is used for the flow variables at the plane of symmetry.

(*ii*) In order to verify model heat transfer predictions with the experimental data, a uniform wall temperature condition was used for the square-sectioned duct of Wagner et al. (1991a) and a uniform wall heat flux condition was used for the rectangular duct (aspect ratio 2:1) of Morris and Ghavami-Nasr (1991).

(*iii*) A generalized wall function approach (Rosten and Worrel, 1988; Prakash and Zerkle, 1991) is used to account for the boundary layer effects in the near-wall cells. Zero normal gradient for the turbulent kinetic energy (k) at the wall is used for the calculation of k from the transport equation at the near-wall cell center. The generation and the dissipation rate of the kinetic energy are calculated from analytical integration expressions. Recently, Djilali et al. (1989) employed two-layer and three-layer wall models and found improvement over the standard one-layer wall function in heat transfer predictions for recirculating turbulent flow.

(*iv*) Effect of centrifugal buoyancy is included. The effect of Coriolis forces is considered only in the momentum equations and no modification in the turbulence models is adopted due to rotation. The gravitational force is neglected in comparison with the centrifugal force.

(*v*) Uniform axial velocity profile at the inlet is assumed for the rectangular duct ($a/b = 2$) of Morris and Ghavami-Nasr (1991) and 1/7th power developed profile for the axial velocity (w_z) is used at the inlet of the square duct. Cross-stream components of velocity (w_x and w_y) are taken to be zero at the inlet. That is,

$$w_z = w_c(1-2|x|/b)^{1/7}(1-2|y|/a)^{1/7} \quad (13)$$

for the duct of Wagner et al. (1991a). A 4 percent turbulence intensity has been specified at the inlet (Wagner et al., 1991a).

(*vi*) A zero-gradient exit condition was used at the duct outlet. Prakash and Zerkle (1991) have found very little difference in the heat transfer results between the case of zero-gradient exit condition at the duct outlet and the case of zero-gradient exit condition when the duct outlet was placed much farther downstream including a 180 deg bend.

(*vii*) The coolant is air and the ideal gas law is used to calculate density at any state.

(*viii*) Laminar viscosity, μ, is calculated by using the Sutherland equation

$$\mu = \mu_{\text{ref}}(T/T_{\text{ref}})^{0.636} \quad (14)$$

where $\mu_{\text{ref}} = 3.018 \times 10^{-7}$ kg/cm s and $T_{\text{ref}} = 600$ K.

(*ix*) The specific heat is defined by the following ($T \sim H$) relationship:

$$T = T_A + T_B H + T_C H^2 \quad (15)$$

where $T_A = -4.4876$ K, $T_B = 1.0403 \times 10^{-7}$ K s^2/cm^2 and $T_C = -0.7478 \times 10^{-18}$ Ks^4/cm^4. The specific heat is then given as

$$C_p = dH/dT = 1/(T_B + 2T_C H). \quad (16)$$

(*x*) The laminar Prandtl number for air is taken to be constant (0.72).

5 Method of Solution

The commercial finite-difference code PHOENICS (Rosten and Spalding, 1987) is used to obtain the results in the present modeling effort. The option of hybrid interpolating scheme (Patankar, 1980) is chosen by default setting of the parameter DIFCUT = 0.5 (Rosten and Spalding, 1987). The standard two-equation k–ϵ turbulence model is available in PHOENICS for the users. PHOENICS provides a number of subroutines through which a modeler can effect a change and employ a new model suitable for a particular problem. CHAM, the owner of the code, also makes available to General Electric employees the source code describing any particular details so that any new modeling technique can be effectively employed. A new subroutine was developed to account for the source terms in the extended k–ϵ turbulence model equations described earlier and was employed in conjunction with the PHOENICS code to obtain the results with the extended k–ϵ model.

The hybrid scheme can generate false diffusion, especially in the case of strong secondary flow situation. However, if the grid size is fine enough, the effect of false diffusion is minimized or even eliminated. For the case of Morris and Ghavami-Nasr's duct (1991) a grid refinement study was made and a suitable grid size was chosen. Prakash and Zerkle (1991) carried out the grid sensitivity studies on the duct geometry of Wagner et al. (1991a) and determined that 20 × 10 × 50 cells were adequate. The other alternative is to use higher order schemes such as QUICK. The problem with this scheme is that the oscillations in the k computation may drive the values of the turbulent kinetic energy to being negative, thereby creating a computational overflow. So, the values of k have to be watched at every iteration. In the present computation the approach of a hybrid scheme in combination with adequate grid size has been taken. For adequately fine grid size first-order and higher order numerical schemes yield the same results. Unless specified otherwise, the number of control-volume cells taken in the symmetric half-duct is 20 × 10 × 50 for the geometry of Wagner et al. (1991a) and 14 × 14 × 50 for the geometry of Morris and Ghavami-Nasr (1991) in the x, y, and z directions. Effects of grid size and near-wall cell y^+ values on the Nusselt number computations are also studied. The control-volume cell size is decreased as the cell gets closer to the walls, with the ratio of cross-stream plane areas between two adjacent cells not dropping below 0.9. The cell size is increased in the z direction also as the location of cells moves away from the inlet.

6 Results and Discussion

Table 1 lists the geometric dimensions of the two ducts (Wagner et al., 1991a; Morris and Ghavami-Nasr, 1991) that were used to obtain heat transfer results. These results are presented in the form of variation of Nusselt number (Nu) for Morris and Ghavami-Nasr's duct (1991) and the Nusselt number ratio (Nu/Nu$_\alpha$) for Wagner's duct (1991a) with nondimensional axial (or radial) distance from the inlet of the duct (z/d):

$$\text{Nu} = \frac{hd}{\lambda} = \frac{q_w d}{(T_w - T_b)\lambda} \quad (17)$$

The bulk temperature, T_b, is calculated from the bulk enthalpy, H_b, by using Eq. (15). H_b at any axial location is obtained as

$$H_b = \frac{\iint \rho w_z H dx dy}{\iint \rho w_z dx dy} \quad (18)$$

Thermal conductivity λ ($= \mu C_p/\text{Pr}$) is evaluated at the film temperature, T_f, which is defined as the average of T_b and T_w.

Table 1 Geometric dimensions of the ducts

Parameter	Wagner et al. (1991a)	Morris & Ghavami-Nasr (1991)
a (cm)	1.27	1.10
b (cm)	1.27	0.55
L (cm)	18.16	15.00
R_r (cm)	53.21	17.50
d (cm)	1.27	0.73

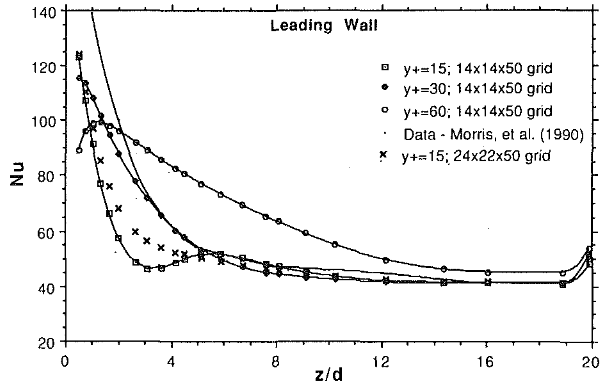

Fig. 3(*a*) Effect of y^+ and grid size on Nu computation

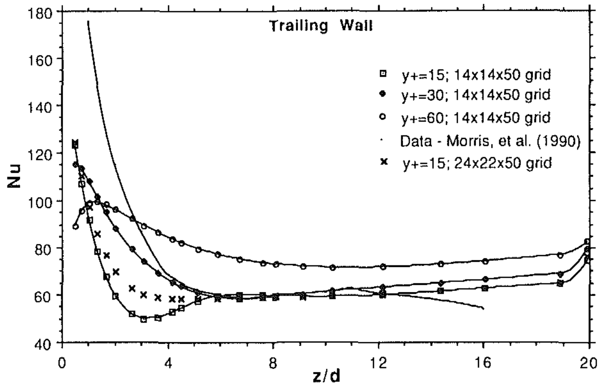

Fig. 3(*b*) Effect of y^+ and grid size on Nu computation

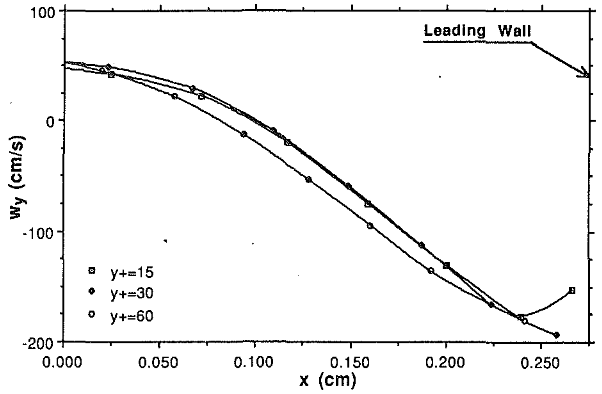

Fig. 3(*c*) Effect of near-wall grid size on the cross-stream velocity near leading wall, *z/d* = 12, *a/b* = 2:1

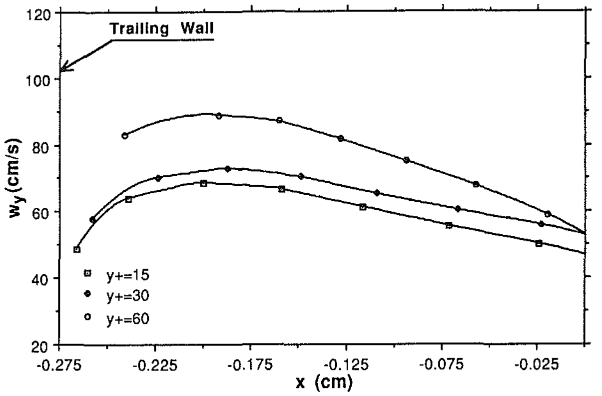

Fig. 3(*d*) Effect of near-wall grid size on the cross-stream velocity near trailing wall, *z/d* = 12, *a/b* = 2:1

Now, in order to compute Nu from Eq. (17) q_w and T_w both have to be known. One of these two quantities is usually known (either a uniform wall heat flux or a uniform wall temperature condition) and the other one is calculated from the following generalized wall function relations (Rosten and Worrel, 1988):

$$s=\frac{\tau_w}{\rho v^2}=\frac{\kappa C_\mu^{1/4}k^{1/2}}{\nu \ln(Ey^+)} \tag{19}$$

$$\mathrm{St}=\frac{q_w}{\rho v(H_w-H_b)}=\frac{1}{\mathrm{Pr}_t/s+\mathrm{Pr}_t Pv/C_\mu^{1/4}k^{1/2}} \tag{20}$$

where κ = 0. 435, E = 9 for smooth walls and the function P is given as

$$P=9(\mathrm{Pr}/\mathrm{Pr}_t-1)(\mathrm{Pr}_t/\mathrm{Pr})^{1/4} \tag{21}$$

Equation (21) was given by Jayatilleke (1969) and it accounts for the thermal resistance of the viscous sublayer. P = 0 corresponds to the Reynolds analogy.

Nu_α corresponds to the case of fully developed flow in a nonrotating duct and is given by:

$$\mathrm{Nu}_\alpha=0.022\ \mathrm{Re}^{0.8}\mathrm{Pr}^{0.6} \tag{22}$$

$$\mathrm{Re}=md/\mu_f ab \tag{23}$$

$\mathrm{Nu}/\mathrm{Nu}_\alpha > 1$ implies that heat transfer is enhanced due to rotation and $\mathrm{Nu}/\mathrm{Nu}_\alpha < 1$ indicates that heat transfer is impaired on the particular surface due to rotation. Unless specified otherwise, the percent quantities specified in the paper are percentages with respect to the experimental data.

In all the results presented in this paper the inlet turbulence intensity specified is 4 percent. In order to see the effect of inlet turbulence intensity, computations were made with 7 and 10 percent inlet turbulence intensity values for the square duct of Wagner et al. (1991a) at Ro = 0.24, $\Delta T/T_w$ = 0.13, Re = 25,000, and R/d = 49. A higher inlet turbulence intensity causes higher heat transfer near the inlet as expected. For instance, at a distance of two hydraulic diameters from the inlet (z/d = 2) the differences between the prediction and the data on the leading wall are 33.5, 27.5, and 22.2 percent for inlet turbulence intensity levels of 4, 7, and 10 percent, respectively. On the trailing wall these differences are 35.1, 31.2, and 28.5 percent, respectively. The effect diminishes downstream, becoming negligible after a distance of 4–5 hydraulic diameters from the inlet.

6.1 Effect of y^+ and Grid Size. Near-wall grid size has a significant effect on the heat transfer calculation if the wall function approach is used. Figures 3(*a*) and 3(*b*) show the effects of y^+ and grid size on Nusselt number calculations of leading and trailing walls, respectively. In order to study the effect of y^+ alone, a mesh of 14 × 14 × 50 cells is chosen and the size of only the cells adjacent to the walls is varied so that the typical values of y^+ are 15, 30, and 60. Nu versus z/d plots are shown in Figs. 3(*a*) and 3(*b*) for these values of y^+ and compared with the data of Morris and Ghavami-Nasr (1991) for the flow at Re = 25,000 and ω = 188.5 rad/s (Ro = 0.026). The curve corresponding to y^+ = 30 is in very good agreement with the data (within 6 percent) except near the inlet (z/d < 3). The prediction corresponding to y^+ = 15 is also in excellent agreement with the data at downstream locations away from the inlet (z/d > 5). The agreement with the y^+ = 60 predictions is not as good. It is found that a y^+ value in the range of 12 to 42 or so yields more accurate results.

In order to see the grid size effect, a numerical computation run is made for a 24 × 22 × 50 grid at y^+ = 15. On comparison of the two curves corresponding to 14 × 14 × 50 grid (y^+ = 15) and 24 × 22 × 50 grid (y^+ = 15) with the experimental data curve in Figs. 3(*a*) and 3(*b*), it is concluded that refining the mesh improves the predictions in the inlet region. But at downstream locations both the grid results are nearly the same. The coarser grid ($14 \times 14 \times 50$) results are slightly closer to the data for the leading wall than the fine grid ($24 \times 22 \times 50$) in Fig. 3(*a*). Notwithstanding the experimental errors in the data, this finding at locations away from the inlet is along the same line as that of Iacovides and Launder (1987) that successive grid refinement does not always lead to a monotonic approach to an asymptotic solution. Grid refinement studies ranging from 4000 cells to 40,000 by Prakash and Zerkle (1991) ensured that 10,000-cell grid was adequate for the geometry of Wagner et al. (1991a).

In order to see the effect of near-wall grid size on the secondary flow, the cross-stream velocity w_y is plotted near the leading and trailing walls in Figs. 3(*c*) and 3(*d*), respectively. It is noted in Fig. 3(*c*) that the maxima (or minima) of the velocity w_y are not captured for the larger near-wall grid sizes ($y^+ = 30$ and 60) whereas for the grid with $y^+ = 15$, the velocity reaches the maximum (minimum in the mathematical sense) and then starts approaching zero at the wall (no-slip condition). In Fig. 3(*d*) close to the wall a difference in velocity magnitude is noted due to grid size corresponding to $y^+ = 60$ when compared to the velocity magnitudes due the grids of $y^+ = 15$ and 30 both.

6.2 Comparison of Results With Data. Figures 4(*a*) and 4(*b*) compare the numerical model predictions with Morris and Ghavami-Nasr's experimental data (1991) at $Ro = 0.064$. The results from only standard k-ϵ model are plotted as the extended k-ϵ model yields almost identical results for low rotation number flows. For the leading wall, computed results of Nu using the k-ϵ turbulence model fall in the band of data reported by Morris and Ghavami-Nasr (1991) with the exception of the region near the inlet. For the trailing wall the computed results lie close to upper limit of the bandwidth shown in Fig. 4(*b*). Considering the error involved in experimental measurements, the agreement is good except in the inlet region of the duct. It is found in the present work that the numerically computed Nusselt numbers are consistently lower than the experimental data near the inlet. This can be attributed to the neglect of swirl in the flow at the inlet, the inability of wall function to predict heat transfer in the high gradient region, and the experimental error in the data. A swirl in the flow is expected to raise the level of turbulent kinetic energy and consequently the heat transfer. A 4 percent intensity of turbulence assumed at the inlet may be lower than the actual value in the experiment by Morris and Ghavami-Nasr (1991). In the experimental setup shown in the work of Wagner et al. (1991a) there is a plenum just before the duct inlet that will modify the turbulence and flow configuration. It is not clear from the paper what kind of swirl velocities exist at the inlet. Prakash and Zerkle (1991) extended the duct length fictitiously on the inlet side (without the heated wall condition) to simulate fully developed flow in a rotating environment and found that the computed results do have better agreement with the data. Experimental data with clearly and completely defined inlet conditions are needed to eliminate the contribution of unknown inlet condition to prediction-data disagreement in the inlet region.

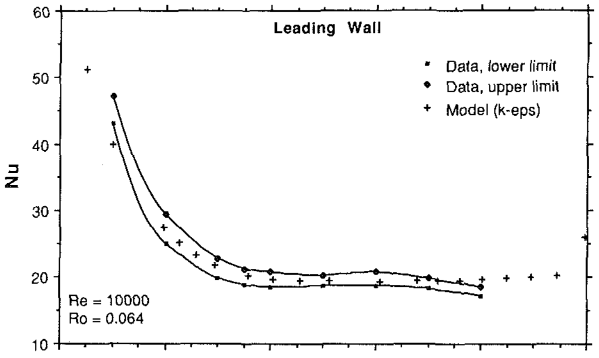

Fig. 4(*a*) Comparison of model predictions with data (Morris and Ghavami-Nasr, 1991) on leading wall, $a/b = 2:1$

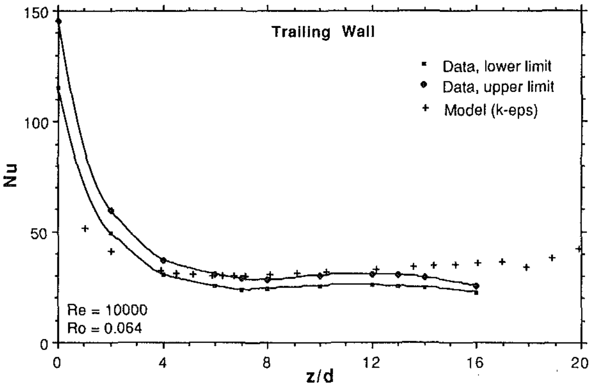

Fig. 4(*b*) Comparison of model predictions with data (Morris and Ghavami-Nasr, 1991) on trailing wall, $a/b = 2:1$

Figures 3(*a*), 3(*b*), 4(*a*), and 4(*b*) also show the correct trend of Nusselt number variation that its value is high near the inlet where the thermal boundary layer is thin and developing; and its value starts decreasing downstream as the thermal boundary layers starts thickening. The quantitative predictions are in good agreement except near the inlet for the reasons noted above.

6.3 Comparison at Varying Rotation Numbers (Ro). Figures 5(*a*) through 5(*c*) indicate that the two models do equally well in predicting heat transfer at no rotation (Fig. 5*a*) or at low rotation number ($Ro = 0.12$ in Figs. 5*b* and 5*c*). Nu/Nu_α is close to 1 at downstream locations and near the exit in the case of no rotation in Fig. 5(*a*). This validates the model since the flow is expected to be thermally fully developed after certain lengths in the duct, in which case the Nusselt number (Nu) should approach the value for fully developed flow (Nu_α). Figure 5(*d*) shows that at the leading wall the heat transfer predictions are the same by both the models near inlet, the value of z/d up to 4 or so. The difference in the two predictions starts developing near $z/d = 4$ and increases downstream to about 13 percent near the exit. Comparison with experimental data reveals that use of the extended k-ϵ model makes the predictions better, in general. Figure 5(*e*) indicates that the predictions from the two models are not much different for the trailing wall. However, the extended k-ϵ model improves the heat transfer predictions by about 10 percent at the trailing wall when the rotation number is increased to 0.48, as indicated by Fig. 5(*f*). In all the results the difference in the predictions and the data is relatively large near the inlet, which may be attributed to the reasons discussed earlier including the neglect of swirl at the inlet.

Figures 5(*b*) through 5(*f*) indicate that at downstream locations the heat transfer at the leading wall is impaired due to rotation, the ratio Nu/Nu_α being less than unity in Figs. 5(*b*) and 5(*d*); whereas the heat transfer at the trailing wall is enhanced due to rotation, Nu/Nu_α being greater than unity in Figs. 5(*c*), 5(*e*), and 5(*f*). This is consistent with a number of previously published works discussed during the literature review in the introduction.

Temperature-dependent thermophysical and transport properties of the fluid are used in the model. Since the temperature of the cooling medium is not uniform at any cross section normal to the flow direction (cross-stream plane), the variation in density causes centrifugal buoyancy effects. Due to the Coriolis force induced secondary flow in the cross-stream plane, relatively cooler and hence heavier fluid (higher density) is

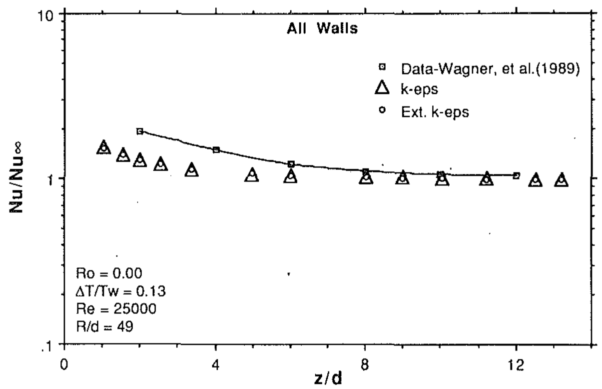

Fig. 5(*a*) Comparison of model predictions with data, a/b = 1:1, Ro = 0.0

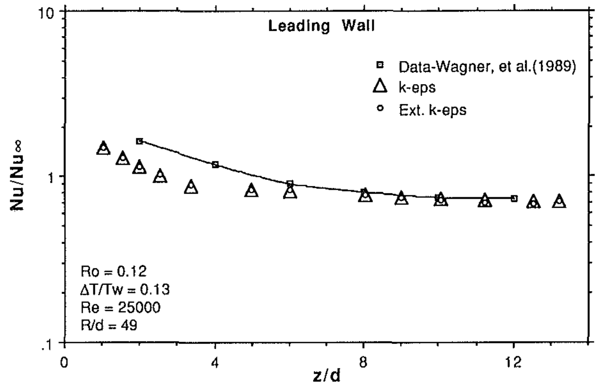

Fig. 5(*b*) Comparison of model predictions with data on leading wall, a/b = 1:1, Ro = 0.12

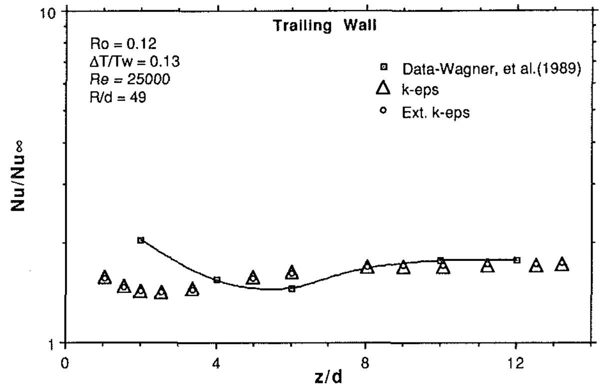

Fig. 5(*c*) Comparison of model predictions with data on trailing wall, a/b = 1:1, Ro = 0.12

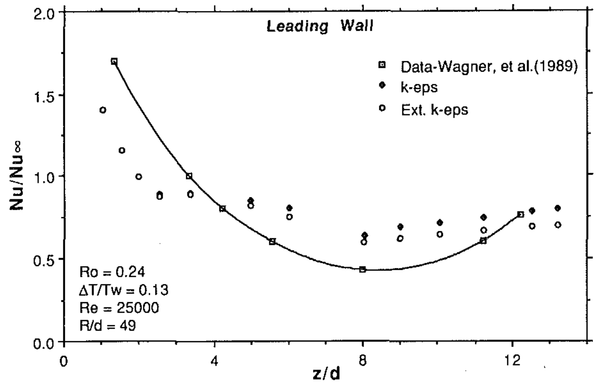

Fig. 5(*d*) Comparison of model predictions with data on leading wall, a/b = 1:1, Ro = 0.24

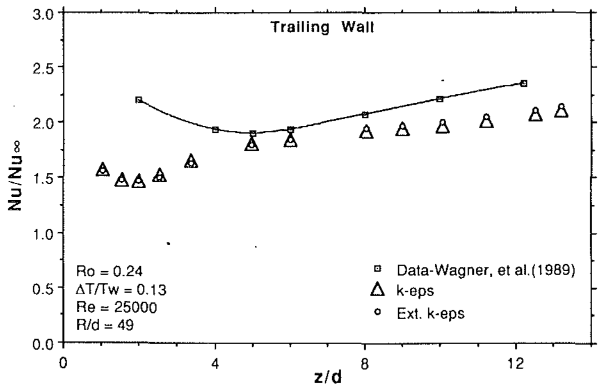

Fig. 5(*e*) Comparison of model predictions with data on trailing wall, a/b = 1:1, Ro = 0.24

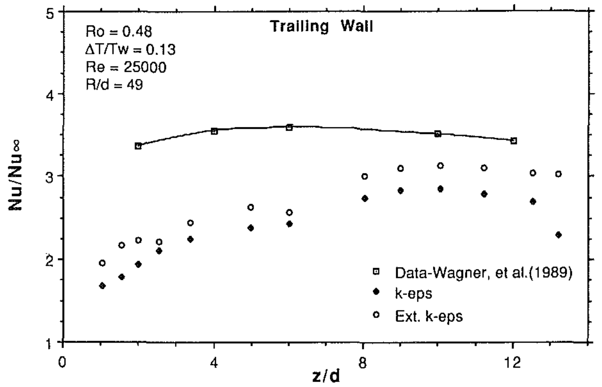

Fig. 5(*f*) Comparison of model predictions with data on trailing wall, a/b = 1:1, Ro = 0.48

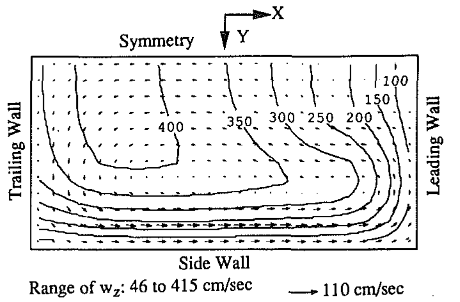

Fig. 5(*g*) Flow field at the cross-stream plane, Z = 63.4 cm (z/d = 8), a/b = 1:1, Ro = 0.12

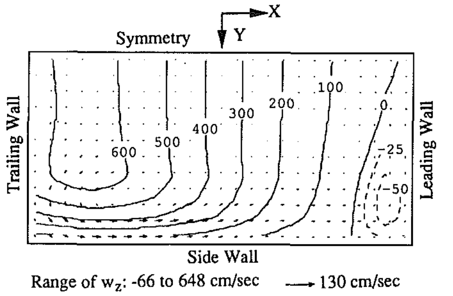

Fig. 5(*h*) Flow field at the cross-stream plane, Z = 63.4 cm (z/d = 8), a/b = 1:1, Ro = 0.48

transported from the central core region toward the trailing wall of the duct, thus enhancing the friction and heat transfer on the trailing wall. The effect of the centrifugal buoyancy is to increase the outward radial velocity of the coolant near the trailing wall, thereby raising the level of turbulent kinetic energy in the region. Consequently, further enhancement of the heat transfer at the trailing wall is obtained. On comparison of Figs. 5(*c*), 5(*e*), and 5(*f*) we find that as the rotation number is increased, the enhancement in heat transfer at the trailing wall is increased due to increase in Coriolis and centrifugal buoyancy forces at higher rotational speeds. Nu/Nu_α values are ~1.7, ~2.5, and ~3.5 for *Ro* equal to 0.12, 0.24, and 0.48, respectively. At the same time the drop in Nu/Nu_α below 1 for the leading wall is larger at rotation number 0.24 than at 0.12 (see Figs. 5*b* and 5*d*).

Another observation made in Fig. 5(*d*) is that the Nusselt number value after dropping at downstream locations picks up again near the exit. This trend is also captured by the numerical model. The increase in the leading wall heat transfer near the exit is due in part to buoyancy induced reverse axial flow. Prakash and Zerkle (1991) suggested that the reverse flow in the region causes mixing and higher turbulence, resulting in a local increase in heat transfer.

6.3.1 Flow Field. Figures 5(*g*) and 5(*h*) demonstrate the effect of rotation on the flow field. The cross-stream secondary velocity vector is shown by the arrows and the streamwise radial velocity component is shown by the contour lines. The flow field in only one half of the duct is shown because the flow field in the other half will be simply the mirror image across the symmetry line. The following observations are made in Figs. 5(*g*) and 5(*h*):

(*i*) *Secondary flow.* The existence of the Coriolis force induced secondary flow is noticed in both Figs. 5(*g*) and 5(*h*). As explained in Section 2 the secondary flow is from the leading wall toward the trailing wall in the center of the duct accompanied by a return to flow along the walls. This leads to formation of a pair of vortices (as shown in Fig. 2), one of which can be seen in Figs. 5(*g*) and 5(*h*). The transport of relatively cooler, and hence heavier (higher density), fluid from the central core region to the trailing wall enhances the heat transfer on the trailing wall as seen in Figs. 5(*c*), 5(*e*), and 5(*f*), Nu/Nu_α being greater than 1. On the other hand, the fluid near the leading wall is relatively warmer (after receiving heat from the trailing and side walls) and causes lower heat transfer, Nu/Nu_α being less than 1 in Fig. 5(*b*) at distances away from the inlet ($z/d > 5$).

(*ii*) *Shift in peak radial velocity.* At the inlet the nonrotating fully developed turbulent velocity profile is specified, that is, the maximum radial velocity occurs at the center of duct at the inlet. But at a downstream location ($z/d = 8$), as we can see from the contours in Figs. 5(g) and 5(*h*), a shift *in the peak radial velocity location toward the trailing wall is* caused. This is due to the Coriolis force causing the higher momentum fluid to be transported toward the trailing wall near the center of the duct. The shift is larger for higher rotation number flow (Fig. 5*h*) than for lower rotation number flow (Fig. 5*g*). (Note the term $2\rho\mathbf{w} \times \mathbf{\Omega}$ in Eq. (2).)

(*iii*) *Centrifugal buoyancy.* The centrifugal force $[\nabla\, 1/2\, \rho(\mathbf{\Omega} \times \mathbf{r})^2]$ depends upon density, rotational speed, and the radial position. The relatively cooler (higher density) fluid near the trailing wall experiences higher centrifugal force than the warmer fluid near the leading wall. The differential centrifugal force at the same radial (cross-stream) plane is known as the centrifugal buoyancy. This imbalance has a tendency to increase the outward radial velocity near the trailing wall and decrease it near the leading wall. The effect of centrifugal buoyancy increases with rotation number as well as density ratio ($\Delta\rho/\rho$). At high rotation number ($Ro = 0.48$) and high density ratio ($\Delta\rho/\rho = 0.13$) even a reverse radial flow is predicted near the leading wall (see dashed contour lines in Fig. 5*h*). The effect of the centrifugal buoyancy is to enhance the heat transfer further at the trailing wall.

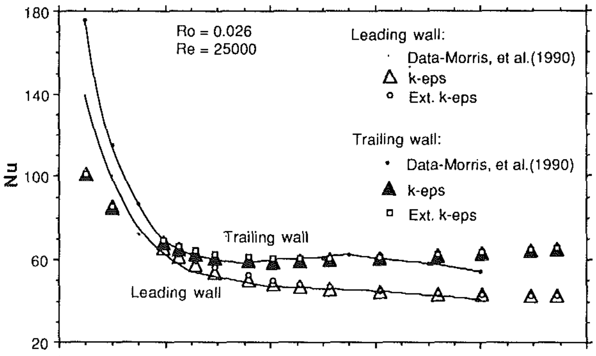

Fig. 6(*a*) Comparison of model predictions with data, *a/b* = 2:1, *Ro* = 0.026

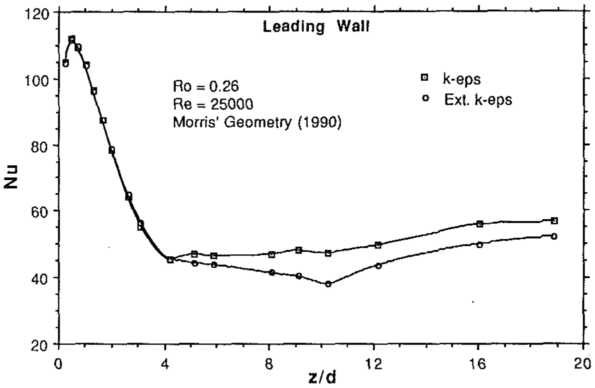

Fig. 6(*b*) Comparison of two model predictions, *a/b* = 2:1, *Ro* = 0.26

The occurrence of reverse radial flow was found to depend upon rotation number (*Ro*), density or temperature ratio ($\Delta\rho/\rho$), and the radius ratio (R/d). The product of these three quantities is equivalent to Gr/Re^2 where Grashof number (Gr) is defined as $Rd^3\Omega^2\Delta T/\nu^2 T_w$. Computations for several combination of *Ro*, Re, $\Delta\rho/\rho$, and R/d for the geometry of Wagner et al. (1991a) predicts the occurrence of reverse flow when Gr/Re^2 is 0.37 or higher. No reverse flow was predicted for Gr/Re^2 equal to 0.25 or lower. So, the cut-off point lies somewhere between 0.25 and 0.37.

6.3.2 Duct Geometry With AR = 2:1. The Nusselt number results from the two k-ϵ models are compared in Figs. 6(*a*) and 6(*b*) for the rectangular ($AR = 2:1$) duct geometry of Morris and Ghavami-Nasr (1991). Since Morris and Ghavami-Nasr's data are at a low rotation number ($Ro = 0.026$), the predictions from the two models are virtually the same and also in good agreement with the experimental data except near the inlet (Fig. 6*a*). However, if the rotation number is increased to a value of 0.26, a difference of up to 18 percent or so (with respect to the values from standard k-ϵ model) in Nu predictions by the two models is obtained at the leading wall, as seen in Fig. 6(*b*).

6.4 Comparison at Varying Temperature Ratio. In Figs. 5(*a*) through 5(*f*) the temperature ratio ($\Delta T/T_w$) was kept fixed at a value 0.13. Now, the temperature ratio is increased to 0.229 (Figs. 7*a* and 7*b*) and then decreased to 0.07 (Figs. 7*c* and 7*d*) while keeping all other parameters (*Ro*, Re, and R/d) fixed; and the results from the two models are plotted and compared with experimental data. In Fig. 7(*a*) for the leading wall the difference between the k-ϵ model prediction and the data, except near inlet, is within 35 percent, whereas this maximum difference is reduced to 26 percent between the extended k-ϵ model predictions and the data. In general, at

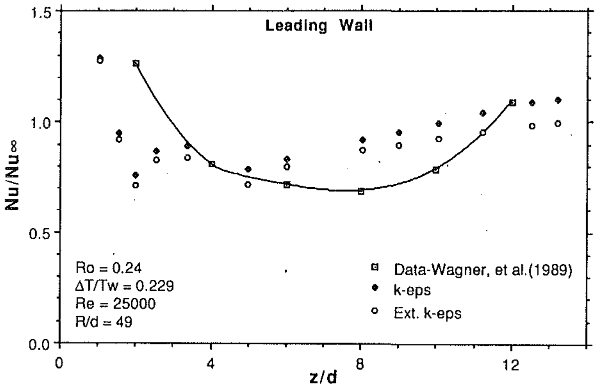

Fig. 7(*a*) Comparison of model predictions with data on leading wall, *a*/*b* = 1:1, Δ*T*/*T*

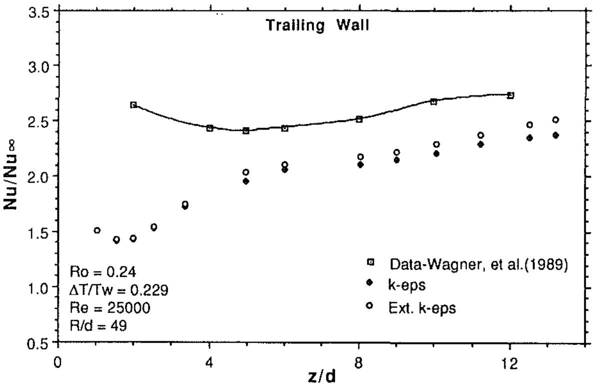

Fig. 7(*b*) Comparison of model predictions with data on trailing wall, *a*/*b* = 1:1, $\Delta T/T_w$ = 0.229

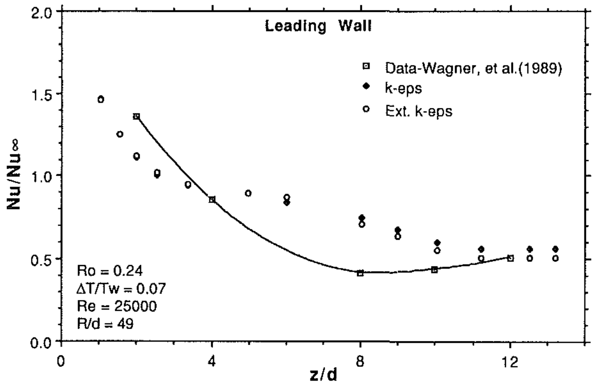

Fig. 7(*c*) Comparison of model predictions with data on leading wall, *a*/*b* = 1:1, $\Delta T/T_w$ = 0.07

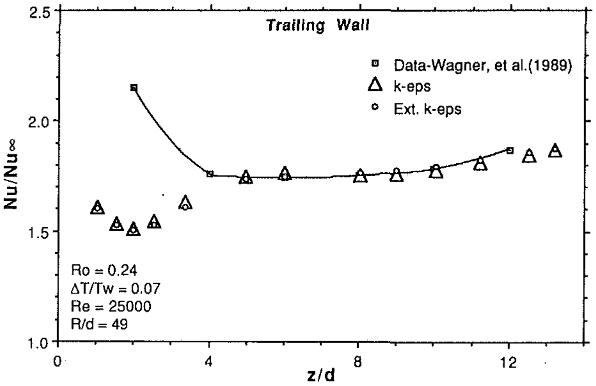

Fig. 7(*d*) Comparison of model predictions with data on trailing wall, *a*/*b* = 1:1, $\Delta T/T_w$ = 0.07

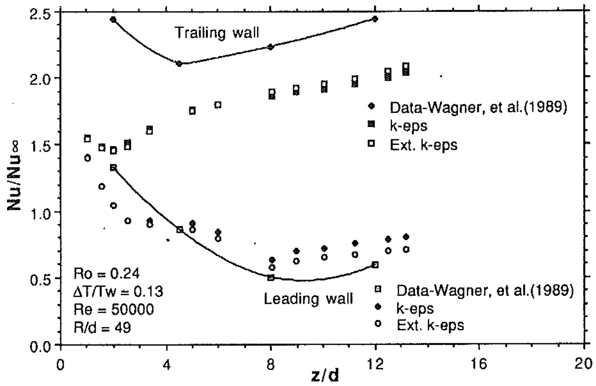

Fig. 8(*a*) Comparison of model predictions with data, *a*/*b* = 1:1, Re = 50,000

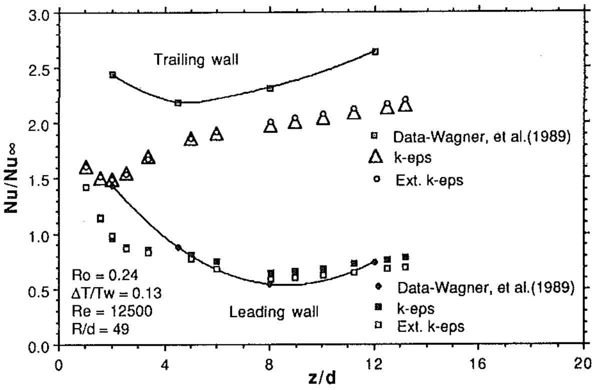

Fig. 8(*b*) Comparison of model predictions with data, *a*/*b* = 1:1, Re = 12,500

high temperature ratios the extended k-ϵ model improves the prediction by 10 percent or so at the leading wall (Figs. 7*a* and 7*c*) and by about 5 percent at the trailing wall (Figs. 7*b* and 7*d*). The model predictions are better for lower temperature ratios than for higher temperature ratios.

6.5 Comparison at Varying Reynolds Number. Figures 8(*a*) and 8(*b*) compare the two model predictions with the experimental data of Wagner et al. (1991a) at Reynolds number equal to 50,000 and 12,500, respectively, while the other parameters such as *Ro*, $\Delta T/T_w$, and R/d are fixed. In general, the k-ϵ model predictions are within 30 percent of the data and a slight improvement in heat transfer predictions by the use of extended k-ϵ model is observed at high as well as low Reynolds-number flows.

6.6 Comparison at Varying Radius Ratio (R/d). The comparison of the model predictions with data is also made for a different average radius ratio (R/d = 33) in Figs. 9(*a*) and 9(*b*) for the leading wall and the trailing wall, respectively. While the predictions from both (k-ϵ) models are close and in good agreement (within 8 percent) with the data at the trailing wall (Fig. 9*b*), the extended k-ϵ model does provide an improvement over the standard k-ϵ model by up to 15 percent in the prediction at the leading wall (Fig. 9*a*). The difference between the standard k-ϵ model predictions and the data is within 30 percent or so.

In order to see why the extended k-ϵ formulation predicts either a better result (or at least as good a result) than the standard k-ϵ model result, the ratio of turbulent kinetic energy from the two models near the wall is also plotted in Figs. 9(*a*) and 9(*b*). It may easily be seen in both Figs. 9(*a*) and 9(*b*) that the model predictions are close to each other if the kinetic energy ratio is close to 1 and they are different if the kinetic

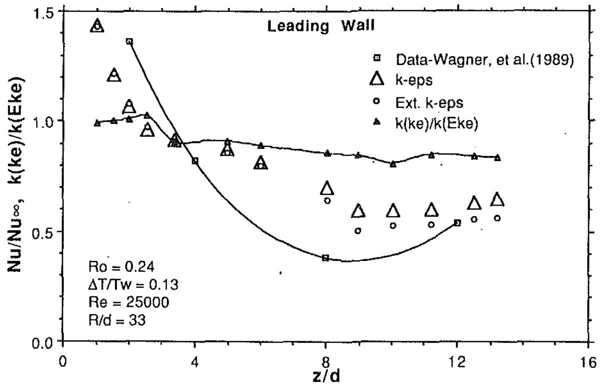

Fig. 9(*a*) Plots of Nu/Nu$_\alpha$ and TKE ratio from the two models on leading wall, *a/b* = 1:1

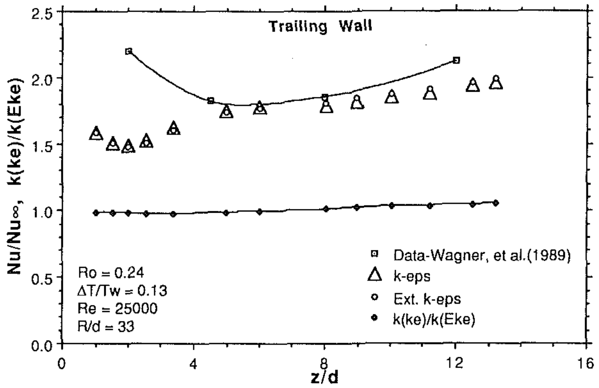

Fig. 9(*b*) Plots of Nu/Nu$_\alpha$ and TKE ratio from the two models on trailing wall, *a/b* = 1:1

energy ratio differs from 1. Inclusion of the production rate time scale in the governing equation of ϵ (Eq. (9)) allows the dissipation rate to respond to the mean strain more effectively (Chen and Kim, 1987). When the mean strain is strong, a higher production rate (see Eq. (10)) enhances the development of ϵ and when the mean strain is weak, ϵ is suppressed. Consequently, the turbulent kinetic energy is calculated more effectively, which, in turn, yields a more accurate value of heat transfer through "wall function" relationships (Eqs. (19) and (20)).

6.7 Observations and Comments. It is observed that the heat transfer is invariably underpredicted at the trailing wall and overpredicted at the leading wall by the k–ϵ turbulence models (Figs. 3–9). The phenomenon leads us to think that the effect of rotation should be somehow incorporated in the k–ϵ turbulence model. The higher the rotation number, the larger is the difference between the numerically predicted and experimentally measured Nu. Bertoglio's study (1982) indicates that the structure of homogeneous turbulence is affected by rotation. The magnitude as well as the direction of Coriolis force affect the turbulence structure (Lakshminarayana, 1985).

In addition to the Coriolis force effect, the effect of centrifugal buoyancy must also be incorporated to represent the effect of rotation on the turbulence structure more completely. It is evident from the study of heat transfer predictions at varying temperature ratio in this paper (Figs. 5*d*, 7*a*, and 7*c* for the leading wall and Figs. 5*e*, 7*b*, and 7*d* for the trailing wall) that a higher temperature ratio, leading to a larger centrifugal buoyancy effect, causes a larger deviation in the numerical predictions from the experimental data.

The merit of the results in the present work is dependent upon the suitability of the wall function. While the wall function approach certainly reduces the computational time (because the regions close to walls need not be resolved), it is not necessarily the most accurate approach. Computationally more intensive methods such as the low-Re model—in which case the governing equations are integrated all the way to the wall—and the Reynolds stress model (RSM) may provide better predictions, and therefore, need attention from the researchers. A compromise approach could be the use of a two-layer model in which the equations for k and ϵ are solved in the core region and the mixing length theory is used in the wall region.

7 Summary and Conclusions

Standard and extended k–ϵ turbulence models have been used to predict heat transfer for radially outward flow in rectangular and square ducts rotating in orthogonal mode. The effects of Coriolis forces have been considered in the momentum equations. The effect of centrifugal buoyancy is also considered in the mean flow equations. The numerical model predictions for heat transfer have been compared with the limited experimental data available in literature. The relative performance of the two k–ϵ models is also evaluated. The following conclusions are derived from the present modeling effort:

1 Near-wall grid size has a significant effect on the heat transfer calculations when the "wall function" treatment is used. Numerical experiment on the data of Morris and Ghavami-Nasr (1991) suggests that a y^+ ($=\delta C_\mu^{1/4} k^{1/2}/\nu$) value in the range of 12 to 42 or so yields more accurate results.

2 The qualitative agreement of the predictions with the data is very good. Heat transfer is enhanced at the trailing wall and impaired at the leading wall due to rotational effects (Coriolis force induced secondary flow and the centrifugal buoyancy effect).

3 Relatively large differences between the numerical predictions and the data near the inlet are believed to be due to neglect of the inlet swirl in the flow, inability of wall function to predict heat transfer in the high gradient regions, and measurement errors in the data.

4 A higher inlet turbulence causes higher heat transfer in the inlet region and has a diminishing effect on heat transfer downstream.

5 The extended k–ϵ turbulence model, while yielding heat transfer results virtually the same as those of the standard k–ϵ model for low rotation-number flows, provides an improvement over the standard k–ϵ model by up to 15 percent or so in heat transfer predictions for high rotation number flows.

6 Improvement in heat transfer predictions by the extended k–ϵ model is observed at high as well as low Reynolds number flows.

7 The need to represent properly the effect of Coriolis forces and centrifugal buoyancy in the k–ϵ model equations is realized. Other modeling methods aimed at enhancing the theory-data agreement are candidates for future investigations.

References

Barua, S. N., 1955, "Secondary Flow in a Rotating Straight Pipe," *Proc. Royal Soc., London*, Vol. 227A, pp. 133–139.

Bertoglio, J. P., 1982, "Homogeneous Turbulent Field Within a Rotating Frame," *AIAA Journal*, Vol. 20, p. 1175.

Chen, Y. S., and Kim, S. W., 1987, "Computation of Turbulent Flows Using an Extended k–ϵ Turbulence Closure Model," *NASA CR-179204*.

Djilali, N., Gartshore, I., and Salcudean, M., 1989, "Calculation of Convective Heat Transfer in Recirculating Turbulent Flow Using Various Near-Wall Turbulence Models," *Num. Heat Transfer*, Part A, Vol. 16, pp. 189–212.

Guidez, J., 1989, "Study of the Convective Heat Transfer in a Rotating Coolant Channel," ASME *Journal of Turbomachinery*, Vol. 111, pp. 43–50.

Hanjalic, K., Launder, B. E., and Schiestel, R., 1979, "Multiple-Time-Scale Concepts in Turbulent Transport Modeling," *2nd Intl. Symp. Turb. Shear Flows*, pp. 36–49.

Harasgama, S. P., and Morris, W. D., 1988, "The Influence of Rotation on the Heat Transfer Characteristics of Circular, Triangular, and Square-Sectioned Coolant Passages of Gas Turbine Rotor Blades," ASME *Journal of Turbomachinery*, Vol. 110, pp. 44–50.

Howard, J. H. G., Patankar, S. V., and Bordynuik, R. M., 1980, "Flow Prediction in Rotating Ducts Using Coriolis-Modified Turbulence Model," ASME *Journal of Fluids Engineering*, Vol. 102, pp. 456–461.

Hwang, G. J., and Jen, T. C., 1990, "Convective Heat Transfer in Rotating Isothermal Ducts," *Int. J. Heat Mass Transfer*, Vol. 33, No. 9, pp. 1817–1828.

Iacovides, H., and Launder, B. E., 1987, "Turbulent Momentum and Heat Transport in Square-Sectioned Ducts Rotating in Orthogonal Mode," *Num. Heat Transfer*, Vol. 12, pp. 475–491.

Iacovides, H., and Launder, B. E., 1991, "Parametric and Numerical Study of Fully Developed Flow and Heat Transfer in Rotating Rectangular Ducts," ASME *Journal of Turbomachinery*, Vol. 113, pp. 331–338.

Ito, H., and Nanbu, K., 1971, "Flow in Rotating Straight Pipes of Circular Cross-Section," ASME *Journal of Basic Engineering*, Vol. 93, pp. 383–394.

Jayatilleke, C. L. V., 1969, "The Influence of the Prandtl Number and Surface Roughness on the Resistance of the Laminar Sub-layer to Momentum and Heat Transfer," *Progress in Heat and Mass Transfer*, Vol. I, pp. 193–329, Pergamon Press.

Johnston, J. P., Halleen, R. M., and Lezius, D. K., 1972, "Effects of Spanwise Rotation on the Structure of Two-Dimensional Fully Developed Turbulent Channel Flow," *J. Fluid Mech.*, Vol. 56, Part 3, pp. 533–557.

Kikuyama, K., Murakami, M., Oshiro, M., Adachi, M., Hara, S., and Lee, K., 1986, "Effects of Coriolis Force on the Turbulent Boundary Layer With Pressure Gradients," *Bull. JSME*, Vol. 29, No. 254, Paper No. 85-0108.

Lakshminarayana, B., 1985, "Turbulence Modeling for Complex Flows," Invited Paper No. AIAA-85-1652.

Landau, L. D., and Lifshitz, E. M., 1987, *Fluid Mechanics*, 2nd ed., Pergamon Press, New York, p. 40.

Launder, B. E., and Spalding, D. B., 1974, "The Numerical Computation of Turbulent Flow," *Comp. Meth. App. Mech. Eng.*, Vol. 3, pp. 269–289.

Lele, S. K., 1985, "A Consistency Condition for Reynolds Stress Closures," *Phys. Fluids*, Vol. 28(1), pp. 64–68.

Medwell, J. O., Morris, W. D., Xia, J. Y., and Taylor, C., 1991, "An Investigation of Convective Heat Transfer in Rotating Coolant Channel," ASME *Journal of Turbomachinery*, Vol. 113, pp. 354–359.

Metzger, D. E., and Stan, R. L., 1977, "Entry Region Heat Transfer in Rotating Radial Tubes," *J. Energy*, Vol. 1, No. 5, pp. 297–300.

Mori, Y., and Nakayama, W., 1968, "Convective Heat Transfer in Rotating Radial Circular Pipes (1st Report, Laminar Region)," *Int. J. Heat Mass Transfer*, Vol. 11, pp. 1027–1040.

Mori, Y., Fukada, T., and Nakayama, W., 1971, "Convective Heat Transfer in Rotating Radial Circular Pipe (2nd Report)," *Int. J. Heat Mass Transfer*, Vol. 14, pp. 1807–1824.

Morris, W. D., and Ayhan, T., 1979, "Observation on the Influence of Rotation on Heat Transfer in the Coolant Channel of Gas Turbine Rotor Blade," *Proc. Inst. Mech. Engrs.*, Vol. 193, pp. 303–311.

Morris, W. D., and Harasgama, S. P., 1985, "Local and Mean Heat Transfer on the Leading and Trailing Surfaces of a Square-Sectioned Duct Rotating in the Orthogonal-Mode," *AGARD Conference on Heat Transfer and Cooling in Gas Turbines*, pp. 3-1 to 3-12.

Morris, W. D., and Ghavami-Nasr, G., 1991, "Heat Transfer Measurements in Rectangular Channels With Orthogonal Mode Rotation," ASME *Journal of Turbomachinery*, Vol. 113, pp. 339–345.

Patankar, S. V., 1980, *Numerical Heat Transfer and Fluid Flow*, Hemisphere Publishing Corp., Washington, DC.

Prakash, C., and Zerkle, R., 1991, "Prediction of Turbulent Flow and Heat Transfer in a Radially Rotating Square Duct," *Heat Transfer in Gas Turbine Engines*, ASME HTD-Vol. 188.

Rosten, H. I., and Spalding, D. B., 1987, *The PHOENICS Reference Manual*, CHAM TR/200.

Rosten, H. I., and Worrell, J. K., 1988, "Generalized Wall Functions for Turbulent Flow," *PHOENICS Journal*, Vol. 1, No. 1, pp. 81–109.

Skiadaressis, D., and Spalding, D. B., 1978, "Heat Transfer in Ducts Rotating Around a Perpendicular Axis," *Proc. 6th Int. Heat Transfer Conf.*, Part 2, Hemisphere Publishing Corp., pp. 91–95.

Soong, C. Y., Lin, S. T., and Hwang, G. J., 1991, "An Experimental Study of Convective Heat Transfer in Radially Rotating Rectangular Ducts," ASME JOURNAL OF HEAT TRANSFER, Vol. 113, pp. 604–611.

Van Driest, E. R., 1956, "On Turbulent Flow Near a Wall," *J. Aero. Sci.*, Vol. 23, p. 1007.

Wagner, J. H., Johnson, B. V., and Hajek, T. J., 1991a, "Heat Transfer in Rotating Passages With Smooth Walls and Radial Outward Flow," ASME *Journal of Turbomachinery*, Vol. 113, pp. 42–51.

Wagner, J. H., Johnson, B. V., and Kopper, F. C., 1991b, "Heat Transfer in Rotating Serpentine Passages With Smooth Walls," ASME *Journal of Turbomachinery*, Vol. 113, pp. 321–330.

An Experimental Investigation of the Augmentation of Tube-Side Heat Transfer in a Crossflow Heat Exchanger by Means of Strip-Type Inserts

Shou-Shing Hsieh
Professor and Chairman.
Mem. ASME

Ming-Tzung Kuo
Graduate Student.

Department of Mechanical Engineering,
National Sun Yat-Sen University,
Kaohsiung, Taiwan 80424

The results of an experimental investigation of the augmentation of heat transfer in a crossflow heat exchanger by means of strip-type inserts are presented and discussed. Three kinds of strip type inserts—longitudinal strip (LS), crossed-strip (CS), and regularly interrupted strip (RIS)—are studied. Correlations for friction factor and Nusselt number are also developed. It is shown that on the basis of both constant pumping power and constant heat duty, LS-inserts perform better than CS- and RIS-inserts for tube-side Reynolds numbers above 19,000. At tube-side Reynolds numbers below 12,000, CS-inserts perform better than LS- and RIS-inserts. Furthermore, flow visualization was made for shell-side hot air and cold air flow in the plenum to advance the qualitative understanding of the physical phenomena of this type of crossflow heat exchanger.

1 Introduction

Augmentation of heat transfer and improvement of the power efficiency of devices in which processes occur are the principal goals in the development of convective heat exchangers. Among the many techniques (both passive and active) investigated for augmentation of heat transfer rates inside circular tubes, a wide range of inserts has been utilized, particularly when turbulent flow is considered: tapered spiral inserts, packing, rings, disks, streamlined shapes, mesh inserts, and spiral brush inserts (Bergles, 1979). The mesh or spiral brush inserts were used by Megerlin et al. (1974) to enhance turbulent heat transfer in short channels subjected to high heat flux. The largest recorded improvements of up to 8.5 times in turbulent heat transfer coefficients were obtained. Maezawa and Lock (1978) reported the performance of a variety of "Everter" inserts, which mix wall and core flow, and several disk inserts. Large increases in local heat transfer coefficients are observed for air flowing in an electrically heated tube; however, there is no definite improvement beyond 10 diameters downstream of an insert. Average heat transfer coefficients are doubled, but friction factors are increased to 3-1/2 times. In general, it is found that these inserts are used in very few practical turbulent flow situations for reasons of pressure drop, plugging/or fouling, and structural considerations.

In this paper, instead of twisted tapes, strip-type inserts are considered as the enhancement devices within the crossflow heat exchanger tubes. Figures 1 and 2 show the schematic of the experimental setup and the positions for temperature and pressure measurements used in the present study, respectively. Three inserts including longitudinal strip (LS), crossed-strip (CS), and regularly interrupted strip (RIS) types are shown in Fig. 3. The objective of this paper is to examine whether the pressure drop associated with the strip type inserts can be reduced without seriously impairing the heat transfer augmentation rates. In addition, to examine the geometric dependence of the present study, experiments were also conducted for a single tube as shown in Fig. 1. Flow uniformity for both velocity and temperature measurements at the inlet and outlet of the test section has been examined for both tube bank and a single tube.

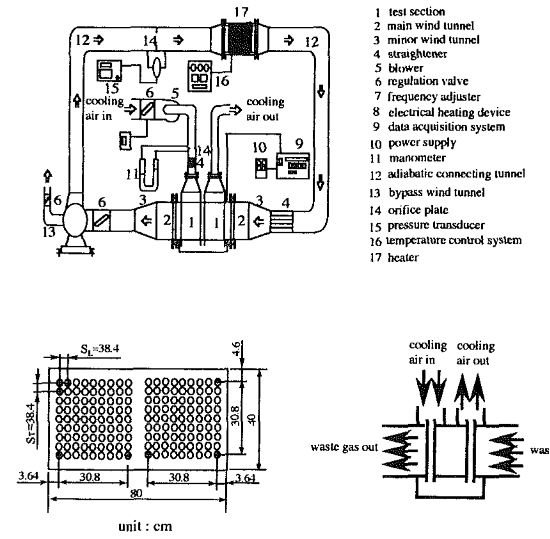

top view of test section (tube sheet) for multiple tubes

test section details of single tube

Fig. 1 Schematic view of experimental apparatus

Experimental investigations carried out with turbulent flow of air are presented and discussed. Experiments were conducted over the following ranges of independent parameters:

Cold air (tube side)	$T_{ci} = 30°C$
Hot air temperature (shell side)	(humidity level 56.8 percent)
Shell-side Reynolds number	$T_{hi} = 90°C, 100°C$
Tube-side Reynolds number	$1000 \leq Re_{max} \leq 4000$
Strip-type inserts	$5000 \leq Re_c \leq 33{,}000$
	LS, CS, RIS

2 Experimental Apparatus and Procedure

The experiments were performed in a closed-loop experimental facility as shown in Fig. 1. The loop consisted of two

---

Contributed by the Heat Transfer Division for publication in the JOURNAL OF HEAT TRANSFER. Manuscript received by the Heat Transfer Division April 1992; revision received July 1993. Keywords: Augmentation and Enhancement, Forced Convection, Heat Exchangers. Associate Technical Editor: T. W. Simon.

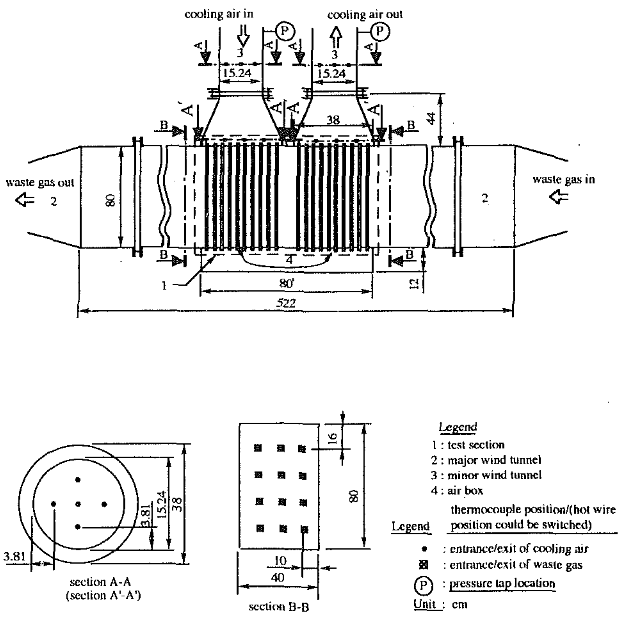

Fig. 2 Detailed position for quantitative temperature and pressure measurements for cross counterflow

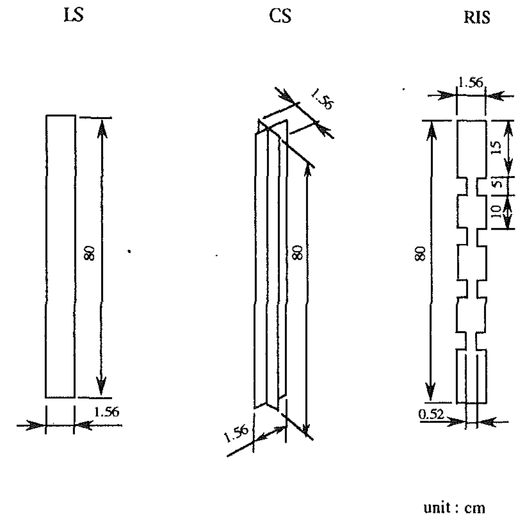

Fig. 3 Geometry of strip inserts

blowers (7.5 HP, 5 HP), a 15 KW electrical heater, the test section (see Fig. 2 for details) and a regulating valve. In all experiments, strip-type inserts were made from 1.5-mm-thick carbon steel strip, the width of which was 1 mm less than the inside diameter of the test section tube to keep no physical contact anywhere inside tube between the tube and insert. The crossed-strip-type inserts made out of spot-welded longitudinal strip inserts are shown in Fig. 3. The regularly interrupted strip-type inserts were made from interruptedly cut longitudinal strip inserts. All inserts were spot-welded to a steel rod (OD = 1.4 mm) length (22 mm) greater than the tube (OD = 21.7 mm) to keep the insert supported by the tube. The length of the entire closed loop for shell side wind tunnel was about 18 m; the tube-side tunnel was about 11 m. The electrical heating device consisted of 15 finned-type electrical heating rods with a total power output of 15 kW. The inlet temperature of hot air was controlled by the ON-OFF and proportional integral differential (PID) system, in which 12 kW was controlled by the ON-OFF system and the other 3 kW was controlled by the PID system. The variation of the inlet temperature of hot air was ± 1 percent about the temperature setting (90/100°C). The outer surface of the entire apparatus was insulated by fiber glass insulating material. The conduction and radiation losses, after careful calculations, were 2.7 and 2.6 percent of the net convective heat transfer rate, respectively.

The test section used in the present study was a rectangular wind tunnel (80 cm high and 40 cm wide). The test section consists of the shell-side and tube-side. Hot air flowing through the shell side and cold air through the tube-side were driven, respectively, by 7.5 HP and 5 HP frequency-adjusted, high-speed, centrifugal blowers. There were 81 tubes in each tube pass. Each tube was 21.7 mm in outside diameter and 2.64 mm wall thickness, and it was made out of carbon steel. The relative longitudinal and transverse pitches of the crossflow heat exchanger pitch ratios were both 1.77. The volume flow rates for the shell-side and tube-side were measured by orifice meters ($\beta = 0.7$) attached to a manometer and a pressure transducer. The inlet and outlet temperatures of hot and cold air were measured by 28 AWG K-type thermocouples, which were uniformly placed at the inlet and outlet cross section of the shell-side and tube-side wind tunnels, respectively. The thermocouple arrangements are shown in Fig. 2. The thermocouple outputs were fed to the data acquisition system coupled with an IBM 386 personal computer for data reduction and analysis.

Nomenclature

A = heat transfer area
A_i = total inside heat transfer area of tubes
A_m = mean heat transfer area $= (A_i + A_o)/2$
A_o = total outside heat transfer area of tubes
A_s = total outside surface area of test section
C_1, C_2 = correlation coefficients
C_p = heat capacity
D_h = hydraulic diameter
d_i = tube inner diameter
d_o = tube outer diameter
E = $1 - ((mc_p)_c(T_{co} - T_{ci}))/((mc_p)_h(T_{hi} - T_{ho}))$, percent, used in Table 1
f = friction factor $= (\Delta P_{\text{tube}}/1/2\rho V_c^2)(d_i/L)$
h_i = tube-side heat transfer coefficient
h_o = shell-side heat transfer coefficient
F = correction factor $= \Delta T_{lm}/\Delta T_{\text{LMTD}}$
K_f = thermal conductivity of fluid
K_s = thermal conductivity of fiberglass insulating material at test section
K_w = thermal conductivity of tubes
n_1, n_2 = exponents for Eqs. (12) and (13)
Nu_d = shell-side mean Nusselt number $= h_o d_o/k_f$
Nu_m = tube-side mean Nusselt number $= h_i d_i/k_f$
PR = pressure drop coefficient $= (\Delta p)_{\text{IN}}/(\Delta p)_{\text{BR}}$
Pr = Prandtl number $= \mu c_p/k$
Q_{act} = overall heat transfer rate $= ((mc_p)_h(T_{hi} - T_{ho}) + (mc_p)_c(T_{co} - T_{ci}))/2$
Q_c = conduction heat loss from test section to laboratory environment
Q_{net} = net convective heat flow rate $= Q_{\text{act}} - (Q_c + Q_r)/2$
Q_r = radiation heat loss from test section to its environment
R = ratio of $(mc_p)_c/(mc_p)_h$
Re = Reynolds number $= Vd_i/\nu$
$\text{Re}_{\max}$ = Reynolds number of main tunnel test section $= V_{\max} d_o/\nu$
Re_c = Reynolds number of tube tunnel test section $= V_c d_i/\nu$

In order to understand this type of crossflow heat exchanger better, flow visualization experiments were conducted for the surrounding field of the tube banks and plenum in the tube-side. The smoke generation method was applied with a $CCl_4 + TiCl_4$ mixture (mixing ratio 1:10) with air as the convection medium to visualize the flow. The illumination of the smoke was done by using a slide projector as a light source shining through a narrow slit so as to produce a plane of light. All photographs were taken with a Canon T70 camera on Fujicolor ISO 1600 film with exposure times of 1/8–1/30s.

3 Uncertainty Analysis

A Solartron Orion A automatic data acquistion system was used for data collection. Before the experiments, all the thermocouples were calibrated in a constant temperature bath to ensure the measurement accuracy of $\pm 0.1^\circ C$. The voltage input to each finned-type heater was measured with a sensitivity of ± 1 mV and an accuracy of ± 0.1 percent. The total power output of the electrical heating device was 15 kW, and a proportional integral differential (PID) control system was used. Several runs were conducted in which the voltage and the current for the circuit were measured, and the calculated power output was highly stable. This procedure resulted in a maximum uncertainty of ± 3 percent for the calculated power output. The thermophysical properties of the air were assigned an uncertainty of ± 3 percent. This was based on the latest values evaluated at proper temperature, pressure and humidity.

The estimated uncertainties in the $\mathrm{Re}_{\max}$, Re_c, f, Nu_m, and overall heat transfer coefficient U_o are 3.2–5.2, 1.3–1.4, 5.7–8.3, 8.9–11.8, and 7.4–9.7 percent, respectively, using the uncertainty estimation method of Kline and McClintock (1953). The energy losses by conduction and radiation are each 3 percent of the total energy output of the electrical heating device, respectively. It should be noted that the uncertainties in these parameters were calculated by the least-squares deviation method.

4 Data Reduction

The measuring data would be first calculated for pressure drop (f) and heat transfer coefficient (Nu) and then calculated for performance evaluation.

4.1 Pressure Drop Tests. The isothermal pressure drop tests were performed in the tube side wind tunnel. The tube side friction factor, f, was defined as follows:

$$f = \frac{\Delta P_{\text{tube}}}{\frac{1}{2}\rho V_c^2}\left(\frac{d_i}{L}\right) \tag{1}$$

where ΔP_{tube} equals the overall pressure drop divided by the number of flow passages (=2, in the present study); V_c and ρ are the inlet mean velocity and density of cold air in tube side channels.

4.2 Heat Transfer Tests. Since the flow properties in the shell/in tube side may change a bit while processing heat transfer between these hot and cold air streams, the overall heat transfer rate, Q_{act}, from the hot air to the cold air in the test channel, was calculated based on the mean value of the hot air heat transfer rate and cold air heat transfer rate. The temperatures and flow rates are measured quantities.

$$Q_{\text{act}} = \frac{(mc_p)_h(T_{hi} - T_{ho}) + (mc_p)_c(T_{co} - T_{ci})}{2} \tag{2}$$

Table 1 lists the measured (T_{hi}, T_{ci}, T_{ho}, T_{co}) results for the terms in the numerator of Eq. (2) and calculated ($\mathrm{Re}_{\max}$, Re_c, Nu_m) results for the reported tests. Furthermore, the net convective heat flow rate Q_{net} was calculated based on the following energy balance equation:

$$Q_{\text{net}} = Q_{\text{act}} - \frac{(Q_c + Q_r)}{2} \tag{3}$$

where Q_c is the conduction heat loss from the test section to the laboratory environment and Q_r is the radiative heat loss from the test seciton to its surroundings. The value of Q_c was evaluated by using $K_s A_s(\Delta T/\Delta X)$, in which ΔT stands for the difference of the wall temperature between the inside and outside surfaces of the fiberglass insulating material at the test section and ΔX indicates the thickness of the fiberglass insulating material. Therefore, after careful calculations, the maximum conduction heat loss from the test section was estimated to be 3 percent of the total power input for all the cases investigated. The value of Q_r was evaluated using a diffuse gray-surface network. The radiant heat was exchanged among all the side walls. The maximum radiative heat loss is less than 2.6 percent of the total power input for all the cases studied herein. After Q_c and Q_r were estimated, the net convective heat flow rate Q_{net} was calculated by Eq. (3). The terms Q_{net} and ΔT_{lm} have the following relationship:

$$Q_{\text{net}} = U_o A_o \Delta T_{lm} \tag{4}$$

$$= U_o A_o (F \Delta T_{\text{LMTD}}) \tag{5}$$

Nomenclature (cont.)

Rf_i = tube-side fouling resistance
Rf_o = shell-side fouling resistance
s = estimate of actual standard deviation
t = tube wall thickness
T_{ci} = inlet temperature of cooling air
T_{co} = outlet temperature of cooling air
T_{hi} = inlet temperature of heated air
T_{ho} = outlet temperature of heated air
U_a = analytical heat transfer coefficient calculated from Eq. (6)
U_o = experimental overall heat transfer coefficient
V_c = inlet mean velocity of tube side tunnel
$V_{\max}$ = velocity of main tunnel test section based on minimum free area available
β = contraction ratio
δ = strip thickness
ϵ = effectiveness
η_1 = effectiveness evaluation criterion, constant pumping power
η_2 = effectiveness evaluation criterion, constant heat duty
ν = kinematic viscosity
ρ = density
ΔT_{LMTD} = the logarithmic mean temperature difference for counter-current flow
ΔT_{lm} = the effective mean temperature difference
ΔX = wall thickness of fiberglass insulating material at test section

Subscripts

air = air
BR = tubes without inserts
c = cold air
CS = crossed-strip-type inserts
h = hot air
IN = insert
LS = longitudinal strip-type inserts
RIS = regularly interrupted-strip type inserts

where ΔT_{LMTD} is the logarithmic mean temperature difference for countercurrent flow. The value of the correction factor, F, of tubes with inserts was assumed to be the same as that obtained from analytical results (Bowman et al., 1940) of bare tubes at the same temperature. U_o can also be obtained from the following equation:

$$\frac{1}{U_o}=\frac{1}{h_o}+Rf_o+\frac{t}{K_w}\left(\frac{A_o}{A_m}\right)+\left(Rf_i+\frac{1}{h_i}\right)\frac{A_o}{A_i} \tag{6}$$

Rearranging Eq. (6) yields

$$h_i=\frac{1}{\dfrac{A_i}{A_o}\left(\dfrac{1}{U_o}-\dfrac{1}{h_o}\right)-\dfrac{t}{K_w}\left(\dfrac{A_i}{A_m}\right)} \tag{7}$$

and

$$\mathrm{Nu}_m=\frac{h_i d_i}{k_f} \tag{8}$$

where h_o is the outside (shell-side) heat transfer coefficient; Rf_o is the shell-side fouling resistance; t is tube wall thickness; K_w is the thermal conductivity of the tube material; A_m is the mean wall heat transfer area, usually taken to be the arithmetic mean $(A_i+A_o)/2$; Rf_i is the inside fouling resistance; h_i is the inside (tube-side) heat transfer coefficient. Both Rf_o and Rf_i could be neglected in the present study. The valve of h_o was found using a Wilson plot technique similar to that given by Bennett and Myers (1982) and it was checked with previous studies of Huge (1937), Pierson (1937) and Grimison (1937), and Zukauskas and Ulinskas (1985) within the maximum deviation of ±14 percent. With U_o from Eq. (5) and known h_o, h_i could be calculated through Eq. (7) and the value of the tube-side Nusselt number, Nu_m, was thus established, based on Eq. (8). In the course of the present calculations, the entrance length effects for the tube-side flow as well as the heating and cooling effects for the test section were not applied. The values of thermophysical properties of cold air were obtained using the average of inlet and outlet temperatures of cold air. Based on those calculations, the tube side Nusselt numbers, Nu_m, were evaluated for all the cases studied listed in Table 1 and correlated as a function of Re_c.

4.3 Performance Evaluation. Bergles et al. (1974) suggested several criteria for the performance evaluation of enhancement devices. The performance of the insert with the present geometry has been evaluated on the basis of two important criteria:

1. Basic geometry fixed, pumping power fixed—increase of heat transfer
2. Basic geometry fixed, heat duty fixed—reduced pumping power

These two criteria are used here to evaluate the performance of strip-type inserts within the crossflow heat exchanger tubes.

Criterion 1. The performance ratio, η_1, for this criterion is given by

$$\eta_1=\frac{(\mathrm{Nu}_m)_{\mathrm{IN}}}{(\mathrm{Nu}_m)_{\mathrm{BR}}} \tag{9}$$

where the subscripts "IN" and "BR" refer to tubes with/without inserts, respectively. For a given tube-side Reynolds number, $(\mathrm{Re}_c)_{\mathrm{IN}}$ and $(\mathrm{Nu}_m)_{\mathrm{IN}}$ are obtained from the correlation for tubes with strip-type inserts developed in this study (discussed later). For tubes without inserts, $(\mathrm{Nu}_m)_{\mathrm{BR}}$ is calculated for the tube-side Reynolds number, Re_c, where Re_c is calculated from the constant pumping power consideration (Bergles, 1974) as:

$$(\mathrm{Re})_{\mathrm{IN}}=\left[\left(\frac{f_{\mathrm{BR}}}{f_{\mathrm{IN}}}\right)\left(\frac{A_{\mathrm{BR}}}{A_{\mathrm{IN}}}\right)\right]^{1/3}(\mathrm{Re}_c)_{\mathrm{BR}} \tag{10}$$

where

$$(A)_{\mathrm{BR}}=\frac{\pi}{4}d_i^2$$

$$(A)_{\mathrm{LS}}=\frac{\pi}{4}d_i^2-\delta d_i$$

$$(A)_{\mathrm{CS}}=\frac{\pi}{4}d_i^2-2\delta d_i+\delta^2$$

$$(A)_{\mathrm{RIS}}=\frac{\pi}{4}d_i^2-\frac{\delta d_i}{3}$$

Criterion 2. The performance ratio, η_2, for this criterion (Bergles, 1974) is given by:

$$\eta_2=\frac{[f_{\mathrm{IN}}(\mathrm{Re}_c)^3_{\mathrm{IN}}A_{\mathrm{IN}}]}{[f_{\mathrm{BR}}(\mathrm{Re}_c)^3_{\mathrm{BR}}A_{\mathrm{BR}}]} \tag{11}$$

For a given tube-side Reynolds number $(\mathrm{Re}_c)_{\mathrm{IN}}$, the tube-side Nusselt number, $(\mathrm{Nu}_m)_{\mathrm{IN}}$, with inserts inside the tube is then obtained from the correlation. The tube-side Reynolds number, $(\mathrm{Re}_c)_{\mathrm{BR}}$, corresponding to the Nusselt number, $(\mathrm{Nu}_m)_{\mathrm{IN}}$, is finally obtained from the correlation for a bare tube.

5 Results and Discussion

An extensive study of the heat transfer augmentation effect in crossflow heat exchangers with strip-type inserts in the tubes was made. There were 120 different cases tested to gather extensive data and four flow field visualizations were made in this study. The flow uniformity for cold air (measured at the centerline of each tube) for both velocity and temperature was found to be valid at the inlet of the test section but did not exist at the outlet of the section. The statement above applies to the cross section of a single tube as well as tubes following a 180-deg return.

In order to make these experiments reliable, the experimental results of the crossflow heat exchanger without strip inserts in the tubes are compared with results obtained from the theoretical analysis through Eq. (6) directly using available heat transfer coefficients (h_i and h_o) for this unenhanced geometry. The overall heat transfer coefficient, U_o, ϵ, and R were obtained for each case. Figure 4 shows the results. The maximum difference between the overall heat transfer coefficient obtained from the theroretical analysis and the one obtained from the experiments based on strong mixing in the shell-side and in the plenum is about 16 percent. Therefore, the data from the experiments in this study were considered reliable, within the uncertainty of U_o. Table 1 shows the measured values of the relevant parameters, including T_{ci}, T_{co}, T_{ho} and the deduced results (R, ϵ, Nu_m) for bare tube, LS-insert, CS-insert, and RIS-insert under study.

5.1 Examination of Mixing Condition Effect of Shell-Side and Plenum on U_o. According to Eq. (5), the overall heat heat transfer coefficient, U_o, can be calculated after F is properly chosen. The correction factor F is found from any of several sources (Bowman et al., 1940) for cross heat transfer arrangements. The tube-side arrangement is two passes in series with each pass unmixed but assuming complete mixing/unmixing in the plenum. The shell-side flow was assumed to be ummixed through each pass across the tube bundle and across both passes. Similarly, the other possible cases of complete mixing in the bundle and in the gap between the two passes are also examined to determine the effect upon the value of U_o. One of the results at $\mathrm{Re}_{\max}=4000$ ($T_{hi}=100°\mathrm{C}$) and $\mathrm{Re}_c=19{,}000$ was shown in Fig. 5. The fourth case is not included because of a lack of support in the literature for the analysis. The maximum deviation from the worst case was less than 7.8 percent among these three cases. One mixed condition

Table 1 Measured/calculated values of relevant parameters

BR tube

Re_{max}	Re_c	T_{hi}	T_{ho}	T_{ci}	T_{co}	R	ε	Nu_m	E(%)
4000	33000	90.49	61.38	33.84	53.15	1.51	0.51	58.42	16.18
4000	26000	90.20	62.29	32.14	54.76	1.23	0.48	49.70	18.14
4000	19000	90.18	65.07	29.63	58.17	0.88	0.47	38.16	16.77
4000	12000	90.17	70.81	28.53	64.52	0.54	0.58	24.96	14.84
4000	5000	90.14	80.09	28.04	73.46	0.22	0.73	12.27	9.70
4000	33000	100.14	65.96	32.98	56.05	1.48	0.51	59.46	16.44
4000	26000	99.97	67.29	31.20	58.08	1.22	0.48	49.94	18.53
4000	19000	99.87	71.40	29.80	63.09	0.86	0.48	37.96	16.45
4000	12000	99.48	77.37	28.67	70.15	0.53	0.59	25.23	15.57
4000	5000	99.98	88.27	28.56	80.45	0.23	0.73	12.33	15.90
2000	33000	90.19	52.38	33.49	46.65	2.87	0.67	59.97	13.98
2000	26000	90.17	52.74	30.98	47.13	2.32	0.63	47.86	15.23
2000	19000	90.20	54.85	28.46	49.95	1.64	0.57	36.89	13.53
2000	12000	90.28	59.70	27.65	56.66	1.05	0.49	25.96	14.17
2000	5000	90.05	72.56	27.30	68.20	0.43	0.65	12.02	10.37
2000	33000	99.80	56.39	33.24	49.27	2.71	0.65	60.77	11.03
2000	26000	99.71	57.16	30.99	50.33	2.20	0.62	48.42	9.89
2000	19000	99.87	60.03	29.41	54.36	1.60	0.57	37.60	13.11
2000	12000	99.94	65.57	27.92	61.89	1.01	0.48	26.04	13.11
2000	5000	99.93	79.52	27.53	74.62	0.43	0.65	12.21	14.13
1000	33000	90.22	48.47	32.50	40.95	4.94	0.72	59.96	7.37
1000	26000	91.41	48.40	30.42	40.93	4.09	0.71	45.53	8.81
1000	19000	92.04	48.02	28.47	42.96	3.04	0.69	42.06	9.67
1000	12000	92.78	51.21	27.75	48.73	1.98	0.64	28.17	11.40
1000	5000	92.71	63.57	27.47	61.97	0.84	0.53	13.17	12.16
1000	33000	100.89	51.53	32.20	42.84	4.64	0.72	57.86	3.07
1000	26000	101.47	52.71	30.42	43.36	3.77	0.69	48.58	5.01
1000	19000	101.83	51.85	28.82	46.41	2.84	0.68	43.42	6.92
1000	12000	102.25	56.17	28.10	53.30	1.83	0.62	28.97	7.91
1000	5000	102.43	70.64	27.63	68.34	0.78	0.54	12.45	8.82

CS-insert

Re_{max}	Re_c	T_{hi}	T_{ho}	T_{ci}	T_{co}	R	ε	Nu_m	E(%)
4000	33000	90.10	61.54	36.30	57.21	1.37	0.53	86.06	12.11
4000	26000	89.94	61.85	34.58	57.78	1.21	0.51	65.29	17.15
4000	19000	89.96	63.73	31.61	61.85	0.87	0.52	54.08	18.29
4000	12000	89.86	68.53	30.07	69.44	0.54	0.66	38.86	17.41
4000	5000	89.83	81.13	29.58	83.98	0.16	0.90	20.06	9.21
4000	33000	99.98	66.89	37.28	61.89	1.34	0.53	89.31	12.56
4000	26000	99.88	67.06	34.58	62.14	1.19	0.50	66.38	17.45
4000	19000	99.84	69.06	31.60	67.32	0.86	0.52	57.17	12.04
4000	12000	99.66	75.35	30.08	76.28	0.53	0.66	38.94	16.98
4000	5000	99.65	89.60	29.77	92.92	0.16	0.90	19.56	7.67
2000	33000	89.76	55.24	36.38	50.06	2.52	0.65	83.60	7.11
2000	26000	89.75	54.17	33.78	49.46	2.27	0.64	61.64	16.07
2000	19000	89.86	54.00	30.37	52.36	1.63	0.60	59.09	14.90
2000	12000	90.34	57.45	28.57	59.83	1.05	0.53	44.51	16.07
2000	5000	90.44	74.12	27.84	80.23	0.31	0.84	20.61	10.84
2000	33000	99.94	59.74	37.12	53.38	2.47	0.64	84.98	7.24
2000	26000	99.84	58.01	33.55	52.80	2.17	0.63	68.14	14.72
2000	19000	99.87	58.50	30.47	56.70	1.58	0.60	62.27	15.94
2000	12000	99.97	62.94	28.92	65.72	1.01	0.52	45.68	14.63
2000	5000	100.25	81.91	28.12	89.27	0.30	0.85	20.04	12.28
1000	33000	87.94	50.27	38.11	46.20	4.66	0.76	89.64	4.65
1000	26000	87.94	49.48	34.69	44.44	3.94	0.72	66.01	7.45
1000	19000	90.67	51.09	31.43	45.56	2.80	0.67	51.76	5.22
1000	12000	92.72	52.87	30.41	51.95	1.85	0.64	39.98	8.27
1000	5000	93.58	65.78	29.66	75.46	0.61	0.72	23.44	11.98
1000	33000	97.57	53.08	37.08	47.54	4.25	0.74	92.58	7.72
1000	26000	99.31	52.60	34.19	46.65	3.75	0.72	62.21	12.03
1000	19000	101.75	54.13	30.86	48.84	2.65	0.67	59.34	5.99
1000	12000	102.30	56.29	28.91	55.73	1.72	0.63	42.94	9.81
1000	5000	103.00	72.18	29.02	82.85	0.57	0.73	23.14	15.36

LS- insert

Re_{max}	Re_c	T_{hi}	T_{ho}	T_{ci}	T_{co}	R	ε	Nu_m	E(%)
4000	33000	90.36	60.62	34.48	54.41	1.49	0.53	71.63	16.74
4000	26000	90.37	61.11	30.60	55.83	1.16	0.49	60.54	15.88
4000	19000	90.03	63.36	28.42	60.92	0.82	0.53	51.98	13.85
4000	12000	89.73	67.81	27.75	67.11	0.56	0.64	34.72	17.92
4000	5000	89.84	81.77	27.88	83.12	0.15	0.89	18.54	16.55
4000	33000	100.10	64.67	33.48	57.59	1.47	0.53	76.25	17.15
4000	26000	100.00	65.52	30.09	59.54	1.17	0.49	63.27	17.74
4000	19000	99.89	68.97	27.97	66.28	0.81	0.53	53.57	14.20
4000	12000	99.92	74.41	27.38	73.77	0.55	0.64	35.55	18.47
4000	5000	99.84	90.35	27.95	91.89	0.15	0.89	18.57	13.13
2000	33000	89.86	53.63	34.70	48.00	2.72	0.66	74.99	11.70
2000	26000	89.76	52.49	31.20	48.33	2.18	0.64	67.28	12.50
2000	19000	89.67	54.47	28.95	52.87	1.47	0.58	58.62	7.36
2000	12000	90.09	58.23	28.03	59.05	1.03	0.51	37.89	13.61
2000	5000	90.46	75.98	28.33	80.62	0.28	0.84	18.75	15.26
2000	33000	100.15	56.78	34.78	50.96	2.68	0.66	73.81	12.09
2000	26000	100.41	56.80	31.15	51.86	2.11	0.63	60.49	11.84
2000	19000	100.39	59.47	28.58	57.41	1.42	0.57	51.80	6.42
2000	12000	100.17	63.73	28.19	65.04	0.99	0.51	35.99	12.64
2000	5000	100.18	83.93	28.75	89.21	0.27	0.85	19.18	18.66
1000	33000	89.29	48.73	34.25	42.82	4.73	0.74	74.27	7.28
1000	26000	90.09	48.37	30.35	41.54	3.73	0.70	56.33	3.04
1000	19000	92.12	49.23	28.39	44.97	2.59	0.67	48.23	2.12
1000	12000	92.67	50.35	27.16	49.79	1.87	0.65	36.04	17.52
1000	5000	92.44	67.30	27.81	75.40	0.53	0.74	19.01	18.62
1000	33000	100.18	52.43	33.61	44.44	4.41	0.72	75.43	2.88
1000	26000	101.48	52.40	30.63	44.71	3.49	0.69	57.43	1.69
1000	19000	102.13	53.13	28.45	48.75	2.41	0.67	49.86	6.07
1000	12000	101.84	55.13	27.76	54.85	1.72	0.63	40.29	4.45
1000	5000	102.02	74.41	27.67	83.27	0.50	0.75	19.05	16.84

RIS -insert

Re_{max}	Re_c	T_{hi}	T_{ho}	T_{ci}	T_{co}	R	ε	Nu_m	E(%)
4000	33000	89.38	60.11	33.86	53.72	1.47	0.53	70.11	18.15
4000	26000	89.55	61.10	31.07	55.18	1.18	0.49	56.81	18.03
4000	19000	89.66	64.08	29.57	59.37	0.86	0.50	44.00	18.75
4000	12000	89.79	69.21	28.21	66.99	0.53	0.63	31.57	17.11
4000	5000	89.42	81.11	27.50	81.53	0.15	0.87	15.97	11.96
4000	33000	99.47	65.30	34.38	58.11	1.44	0.52	74.16	18.09
4000	26000	99.41	66.07	31.27	59.77	1.17	0.49	60.88	16.51
4000	19000	99.46	69.51	28.95	64.32	0.85	0.50	45.79	15.91
4000	12000	99.54	76.13	28.49	73.34	0.52	0.63	31.49	17.50
4000	5000	99.60	89.72	28.04	90.45	0.16	0.87	15.82	8.64
2000	33000	90.05	53.63	34.09	47.73	2.67	0.65	73.30	11.81
2000	26000	89.42	52.45	30.90	47.55	2.22	0.63	61.21	15.59
2000	19000	89.45	53.42	28.87	50.68	1.65	0.59	51.28	16.72
2000	12000	89.55	58.26	27.33	57.97	1.02	0.50	34.55	15.02
2000	5000	89.51	74.08	26.62	77.47	0.30	0.81	16.95	14.09
2000	33000	99.93	57.35	34.30	50.74	2.59	0.65	77.79	9.89
2000	26000	99.52	56.39	30.53	50.73	2.14	0.63	60.31	14.75
2000	19000	100.00	58.42	29.24	55.49	1.58	0.59	54.51	15.36
2000	12000	99.68	63.90	27.11	63.50	0.98	0.50	35.08	13.92
2000	5000	100.20	82.32	27.48	86.40	0.30	0.81	17.71	11.90
1000	33000	89.82	49.44	33.99	43.47	4.26	0.72	75.96	6.49
1000	26000	91.29	48.27	31.36	42.51	3.86	0.72	50.53	7.28
1000	19000	91.74	50.03	29.20	44.33	2.76	0.67	44.68	5.03
1000	12000	92.85	51.89	28.28	50.22	1.87	0.63	29.44	11.15
1000	5000	92.13	65.20	27.83	72.14	0.61	0.69	17.60	12.60
1000	33000	99.91	53.09	34.65	45.62	4.27	0.72	71.78	7.86
1000	26000	100.86	52.17	31.48	45.48	3.48	0.70	58.05	11.13
1000	19000	101.31	53.95	29.37	47.99	2.54	0.66	46.16	9.94
1000	12000	101.86	55.85	28.06	54.95	1.71	0.62	33.91	5.20
1000	5000	102.04	71.98	27.81	79.33	0.58	0.69	17.08	14.42

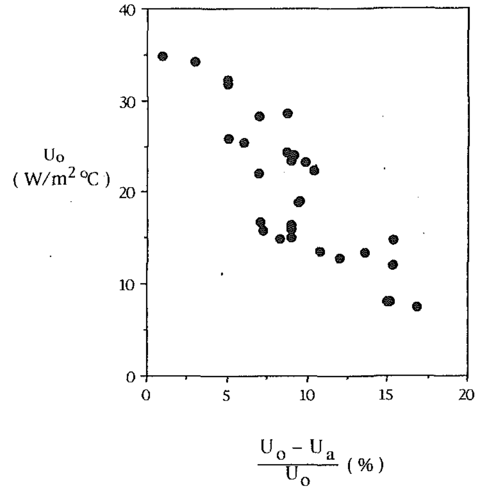

Fig. 4 Deviation of experimental data and analytical (with empirical correlation for h_i/h_o) data (bare tube)

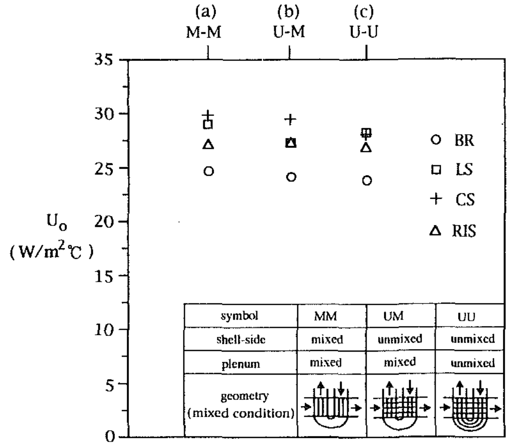

Fig. 5 Overall heat transfer coefficient U_o of three cases ($Re_{max} = 4000$ ($T_{hi} = 100$°C), $Re_c = 19{,}000$): (*a*) shell-side mixed and plenum mixed; (*b*) shell-side unmixed and plenum mixed; (*c*) shell-side unmixed and plenum unmixed

(shell-side mixed and plenum mixed) was chosen to present the results.

5.2 Flow Visualization. The flow visualization on the tube-side for single tube test can be found from Hsieh and Wen (1993), and the results of flow visualization on the outer field of tube banks are shown in Fig. 6. As the shell side Reynolds number Re_{max} in the test section equals or exceeds 500, the range of the closed vortex region behind the tube is reduced gradually. When Re_{max} equals 750, this tendency becomes more apparent. This result corresponds to the measurements indicated in Oka et al. (1974). However, in the paper reported by Oka et al. (1974), the nonuniform velocity distribution behind the in-line circular tube bank leads to an unstable flow pattern in the tube bank, especially when the shell side Reynolds number is larger. Moreover, as shown in Fig. 6, it is found that the separation point (*S*) of the first tube and the reattachment point (*R*) of the second tube agree with the experimental results reported by Oka et al. (1974). It indicates that there are two pairs of symmetric vortex cells in the closed vortex region. Figures 6(*a*), (*b*) show that the reattachment point would be affected and the separation point would be moved downstream due to a higher shell-side Reynolds number. The reattachment point moves to the leading stagnation point gradually and leads to the difference of flow pattern of fluid around each tube. Therefore, with the results of flow visualization experiments and the evidence provided earlier, it is believed that the pattern of flow around the tube is affected by the shell-side Reynolds number. The visualization also explains the different heat transfer characteristics for each tube. It has been long recognized that, at the reattachment point, the heat transfer coefficient reaches its peak value (Oka et al., 1974).

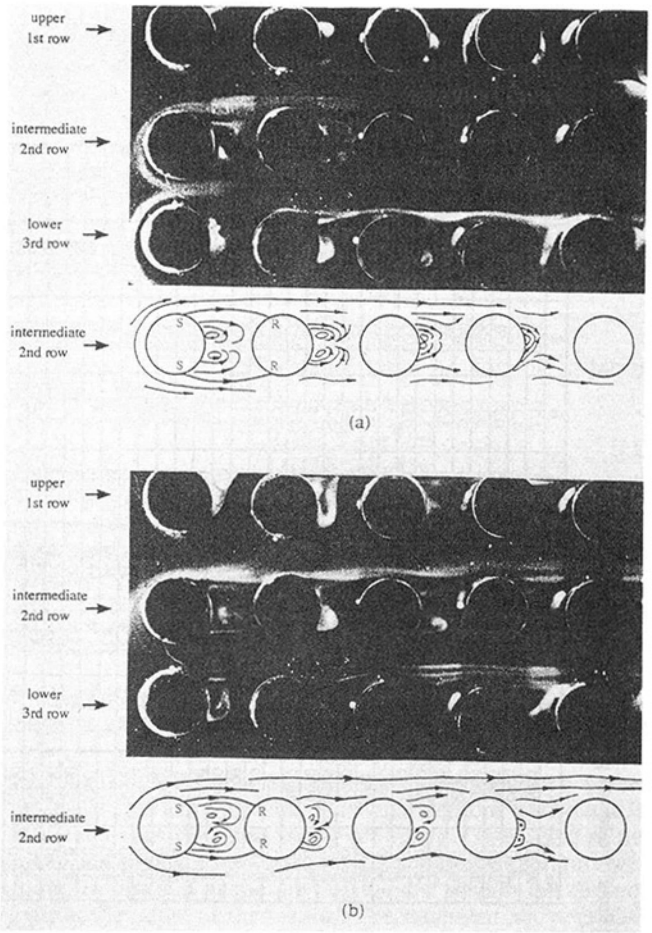

Fig. 6 Visualization of fluid surrounding of tube banks: (*a*) $Re_{max} = 500$; (*b*) $Re_{max} = 750$

Figure 7(*a*) shows the flow pattern of cold air from tube banks to the plenum when the tube-side Reynolds number, Re_c, equals 3000. From this figure, one may clearly find that *there is a vortex region at the left side of the inlet of the plenum*, ranging the entire left side of the plenum of the tube side tunnel. The flow intensity shown in Fig. 7(*a*) is not so stable in the vortex region at the left side because of the mutual influences of vortex cells between the tubes. Consequently, the flow pattern of cold air becomes very complicated after it collides with the base plate. When it flows to the outlet of the plenum as shown in Fig. 7(*a*), the flow pattern is not as regular as at the inlet, even though the fluid has entered the tube. Instead, a more complicated flow pattern results at the right side of the tube and two vortex regions are found at the right side of the plenum. Basically, the formation of these two vortex regions is due to the fluid flowing to the right side and colliding with the vertical wall of the plenum. Therefore, along the original flow direction, two vortex regions at the upper and lower sides are formed. Figure 7(*b*) shows that, when Re_c equals 5000, the flow pattern of cold air within the plenum is generally similar

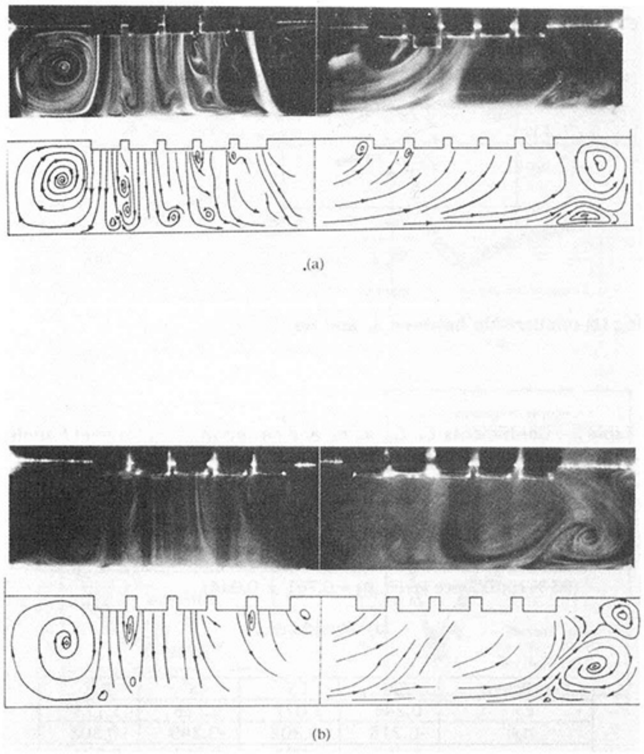

Fig. 7 Visualization of fluid in plenum: (*a*) $Re_{max} = 500$; (*b*) $Re_{max} = 750$

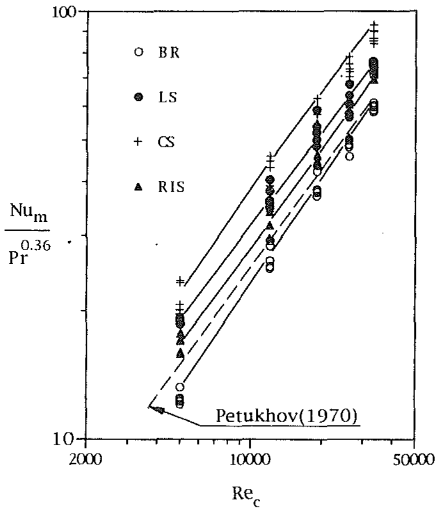

Fig. 8 The relationship between Nu_m and Re_c for BR (bare tube), LS (longitudinal strip), CS (crossed strip), and RIS (regularly interrupted strip) inserts

to the flow pattern when Re_c equals 3000. However, its intensity is higher due to a higher Re_c. In addition, in Fig. 7(*b*), the vortex region at the left side of the plenum is not exactly like the region at the left side of Fig. 7(*a*). Instead, the fluid at the lower left side moves slightly upward. The momentum of the fluid due to collision with the base plate becomes large with the increase of its kinetic energy. It flows slightly upward and a vortex region is thus formed. At the outlet of the plenum, the vortex flow at the right side of the plenum changes slightly due to an increase in Reynolds number Re_c. Because of the increase in the kinetic energy of fluid at $Re_c = 5000$, this causes the range of vortex region at the lower side to expand due to inertia when fluid collides with the base plate at the right side. Consequently, its region is larger than that for $Re_c = 3000$. Furthermore, the vortex region at the upper right side is reduced because of the squeeze effect caused by the expansion of vortex region at the lower right side. Based on flow visualization, in summary, it is found that the fluid forms a vortex region at the left and right sides of plenum when it enters and leaves the plenum. In addition, such a vortex region is expanded to the upper base plate of the plenum and its intensity is strengthened with the increase of Re_c. It is ascertained that the cold air in the plenum and the hot air in the shell-side frequently exchange heat at the upper base plate. Finally, this may result in poor heat transfer, which is discussed in the following section.

5.3 Heat Transfer Results. In the present study, 120 cases were tested by taking temperature measurements of crossflow heat exchanger with and without various strip-type inserts in tubes. The heat transfer correlation for each strip-type insert was developed. Figure 8 displays the relationships between tube-side mean Nusselt number Nu_m for different Re_c for all the cases studied herein. The influences due to the shell-side Reynolds number are insignificant, seen from Table 1 (maximum deviation about 12.8 percent). The deviation may be attributed to the present experimental uncertainty due to the measurements and the present plenum configuration. Nevertheless, the present result seems acceptable for the first time to explore such crossflow heat exchanger as far as the thermal performance as well as flow phenomena were concerned. From a tube-side Reynolds number, Re_c, the tube-side heat transfer is thus enhanced, which, consequently, increases the tube-side mean Nusselt number, Nu_m, as shown in Fig. 8. Further examination of Fig. 8 strongly suggests that the tubes with inserts have a better heat transfer rate than these without inserts. Furthermore, it strongly indicates that CS inserts have the best heat transfer performance among those three inserts (CS, RIS, and LS). Using computerized statistical analysis, four sets of correlations for Nu_m were developed in the following form (the exponent of Pr was assumed to be 0.36; see Zukauskas and Ulinskas, 1985):

$$Nu_m = C_1 Re_c^{n_1} Pr^{0.36} \tag{12}$$

The values of C_1, n_1 and standard deviation s_1 as tabulated in Table 2(*a*). The data for each case (the same insert type) can be correlated with a standard error on Nu_m of less than 0.5. These correlations represent the experimental data with an average deviation of 5 percent, based on the number of data points (30 data points for each case). At the 95 percent confidence level, $n_1 = 0.761 \pm 0.044$. This shows that Reynolds number dependence on heat transfer rates is the same in all the cases studied herein.

Figure 8 also indicates the correlation for mean Nusselt number developed by the Petukhov equation (Petukhov, 1970) for smooth tube for a comparison. It was found that the difference increases as Re_c decreases. This is because the heat transfer rates between the plenum and the shell-side decrease as Re_c increases. When tube-side air passes through the test section at high speed, the core heat transfer is far more effective than any plenum heat transfer. Thus, the Nu_m correlations developed for this case approximate the Petukhov correlation (Petukhov, 1970). The vortex flow formed at the two sides of the plenum, which is of the recirculation type, causes a heat transfer decrease. However, the intensity of this vortex region increases as Re_c increases. This results in a higher heat transfer coefficient at higher Re_c. A comparison indicates that the heat transfer augmentation of tube heat transfer with inserts is better than that of those without inserts, which corresponds to the calculations of Manglik and Bergles (1988), who regard the semicircular tube as a tube with an infinity twist ratio. In other words, they state that a semicircular tube is better for heat transfer because it has a larger heat transfer area for a given flow cross section. Further examination of Fig. 8 shows that the mean Nusselt number of tubes with any of the three

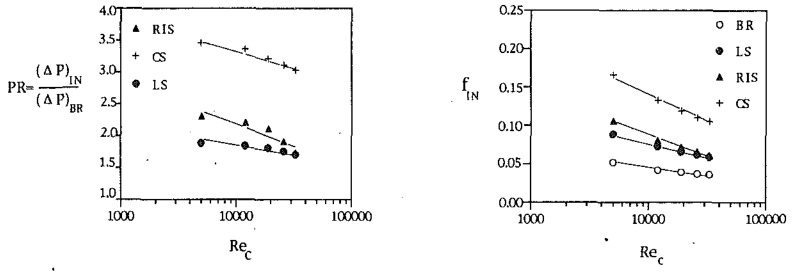

(a) (b)

Fig. 9 (*a*) Relationship between PR and Re_c; (*b*) relationship between f_{IN} and Re_c

strip inserts is higher than the mean Nusselt number of tubes without inserts. Among the three types of inserts, $(Nu_m)_{CS}$ has the highest Nusselt numbers, followed by $(Nu_m)_{LS}$ and $(Nu_m)_{RIS}$, respectively. Moreover, all three $(Nu_m)_{IN}$ increase as Re_c increases. Figure 8 shows that only when Re_c is higher than 10,000, is Nu_m for tubes with RIS higher than that with LS. Fluid flow in tubes with RIS is constantly developing. However, it is found that the increase in heat transfer coefficient due to developing flow is counterbalanced by the smaller heat transfer area of the RIS strip, compared to the continuous strips. Therefore, only when Re_c is high, could this effect be observed.

Mean Nusselt numbers with CS-inserts are the highest, followed by those for LS-inserts, while the RIS-insert results in the smallest mean Nusselt numbers. It is found that CS-inserts provide a larger tube-side heat transfer area than do LS-inserts. In fact, the ratios of surface area of the tubes with/without inserts are 2.16 (CS), 1.57 (RIS), 1.64 (LS), respectively. In addition, CS-inserts create more opportunities for boundary layer disturbances in the tubes and the thickness of this boundary layer is decreased, which promotes heat transfer augmentation. Because of their structure, CS-inserts generate secondary flows (two pairs of symmetric cells) on the plane perpendicular to the direction of flow, which improve heat transfer. The above confirms the positive impact of CS-inserts on heat transfer augmentation. When the temperature distribution and flow patterns are taken into consideration, the augmentation with CS-inserts is further confirmed. At this stage, the present enhancement seems strictly due to a combination of the higher heat transfer area and a difference in flow patterns when the tube was inserted. However, the magnitude for each contribution is difficult to quantify. In addition, the pressure drop caused by CS-inserts is almost twice as large as that caused by LS-inserts. Therefore, a pressure drop performance evaluation of CS-inserts must be conducted before employing these as heat transfer augmentation devices in crossflow heat exchangers.

Table 2 Coefficients C_1, C_2, n_1, n_2, and deviation S_1, S_2 for heat transfer correlation (Eq. (12)) and friction factor (Eq. (13))

Coefficient	BR	LS	CS	RIS
C_1	0.011	0.040	0.043	0.024
n_1	0.827	0.722	0.729	0.766
S_1	0.126	0.214	0.251	0.417

(95 % confidence level: $n_1 = 0.761 \pm 0.044$)

(a) Equation(12)

Coefficient	BR	LS	CS	RIS
C_2	0.243	1.077	1.118	1.175
n_2	-0.215	-0.302	-0.249	-0.308
S_2	0.008	0.038	0.012	0.004

(95 % confidence level: $n_2 = -0.269 \pm 0.034$)

(b) Equation(13)

5.4 Pressure Drop Results. A comparison of the tube-side channel overall pressure drop, ΔP, for tubes with different strip type inserts and for bare tubes was made. Figure 9(*a*) shows that the overall pressure drop $(\Delta P)_{CS}$ is 3.5 times that for bare tubes. This clearly reveals the large friction loss caused by the presence of the inserts. However, as Reynolds number, Re_c, increases, the pressure drop ratio reduces to 3. The overall pressure drop $(\Delta P)_{RIS}$ for tubes with RIS-inserts is 2.25 times that for bare tubes. This ratio reduces to 1.75 as Re_c increases. For tubes with LS-inserts, the overall pressure drop $(\Delta P)_{LS}$ was found to be 2 times that of bare tubes and reduces to 1.7 times as Re_c increases. This seems physically quite understandable since the inertial loss relative to friction loss is more significant at the higher Reynolds number, which results in a ΔP ratio decrease as Re_c increases. The overall pressure drop $(\Delta P)_{RIS}$ is higher than the overall pressure drop $(\Delta P)_{LS}$ for Reynolds number $Re_c \leq 30{,}000$, as shown in Fig. 9(*a*). The tube side friction factor, f_{IN}, for various inserts was correlated using:

$$f = C_2 Re_c^{n_2} \tag{13}$$

where values of C_2, n_2, and standard deviation, s_2, are in Table 2(*b*). The data for each case can be correlated with a standard error on f of less than 0.04. Moreover, these correlations represent the experimental data with an average deviation of 2 percent. As stated earlier for Nu_m, the percent average deviation in the f correlation represents the sum of the absolute percent deviation of the predicted value from the experimental values divided by the number of data points (30 data points for each insert). Figure 9(*b*) shows f-Re_c for tubes with, as well as without, inserts. Bare tubes show the smallest f-value and pressure drop for the same tube side Reynolds number Re_c. The value of pressure drop coefficient (PR) in Fig. 9(*a*) decreases slowly for all those cases shown, when tube side Reynolds number Re_c increases. Tubes with CS-inserts have a larger pressure drop coefficient when the Reynolds number Re_c is low (between 5000–6000). In Fig. 9(*b*) f_{CS} is 3-1/2 times that for bare tubes at $Re_c = 5000$. but, when tube side Reynolds number, Re_c, increases, these differences decrease. When Re_c equals 10,000, the difference reduces to a factor 2.5. However, f_{CS} decreases most rapidly when tube-side Reynolds number, Re_c, further increases. The values of f_{LS} and f_{RIS} are between those for tubes with CS-inserts and bare tubes. Furthermore, f_{RIS} is higher than f_{LS} when $Re_c \leq 30{,}000$. However, when $Re_c > 30{,}000$, pressure drop coefficients for tubes with RIS-inserts are slightly lower than those of tubes with LS-inserts. This may be attributed to the reason stated earlier that the inertial loss is dominant as Re_c increases.

5.5 Performance Evaluation Results. The performance evaluation using ϵ and the dimensionless parameters for tubes with different strip-type inserts are presented in this section. The contents are divided into two parts:

Figure 10(*a*)–(*c*) show the relation between effectiveness, ϵ,

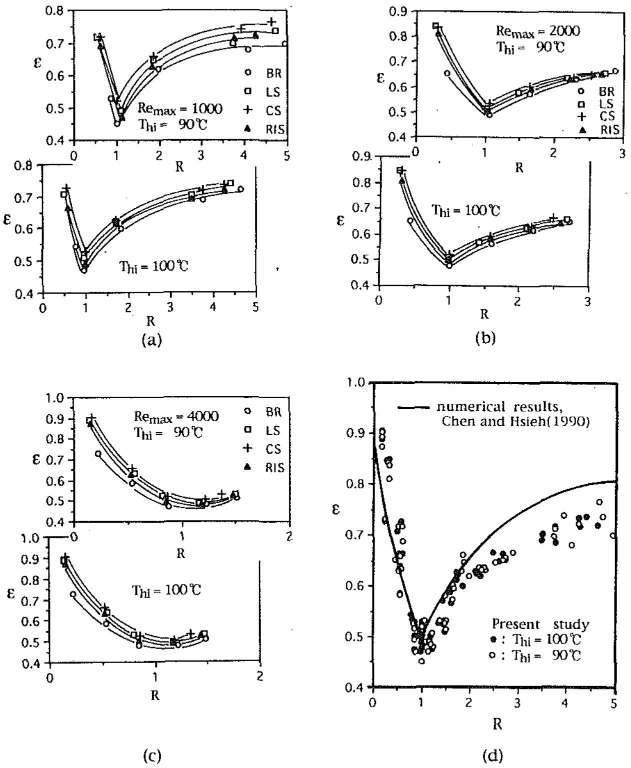

(a) (b) (c) (d)

Fig. 10 Relationship between effectiveness ϵ and ratio R: (*a*) $\mathrm{Re}_{\max} = 1000$; (*b*) $\mathrm{Re}_{\max} = 1000$; (*c*) $\mathrm{Re}_{\max} = 4000$; (*d*) comparison of the effectiveness ϵ and ratio R between experimental data and numerical results

and ratio, R, when shell side Reynolds number $\mathrm{Re}_{\max}$, is 1000, 2000, and 4000 at different shell-side hot air temperatures (90°C and 100°C). As shown in Fig. 10, CS inserts improve heat transfer the most for crossflow heat exchangers. The effectiveness with bare tubes is obviously the least. Any one of these inserts increases the effectiveness of crossflow heat exchangers. Taking a closer examination of Fig. 10, it is found that LS and CS have a better heat transfer augmentation than RIS. Figure 10 shows that when shell side Reynolds number, $\mathrm{Re}_{\max}$, increases, the effectiveness of a crossflow heat exchanger with bare tubes and tubes with strip type inserts also increases. So the effectiveness ϵ decreases to the lowest value when ratio R is 1, and increases when the ratio R increases. When the ratio, R, is below 1, heat capacity rate of cold air in tube side becomes smaller and the effectiveness is given by:

$$\epsilon = \frac{(mc_p)_c(T_{co} - T_{ci})}{(mc_p)_{\min}(T_{hi} - T_{ci})} = \frac{(T_{co} - T_{ci})}{(T_{hi} - T_{ci})} \tag{14}$$

When the ratio, R, is above 1, heat capacity rate of hot air in shell side becomes smaller and the effectiveness is given by:

$$\epsilon = \frac{(mc_p)_c(T_{co} - T_{ci})}{(mc_p)_h(T_{hi} - T_{ci})} = R \cdot \frac{(T_{co} - T_{ci})}{(T_{hi} - T_{ci})} \tag{15}$$

A numerical result for this type of heat exchanger, reported by Chen and Hsieh (1990), is also shown in Fig. 10(*d*). The present results show $R = 1$ as a critical value as reported earlier by Chen and Hsieh (1990). The differences between the numerical result and the data are relatively large for $R > 2$. The reason for this is not clearly understood at this stage. It is partly due to the experimental uncertainty, especially when $\mathrm{Re}_{\max}$ increases, and it is partly due to the existence of a plenum in the present experimental configuration.

Table 3 represents the effectiveness by the constant pumping power criterion (1), where $\eta_1 > 1$ represents enhanced performance, and the effectiveness by the constant heat duty criterion (2) where $\eta_2 < 1$ indicates enhanced performance. In the present study, according to criterion 1, the LS-insert is the best among the three types when $\mathrm{Re}_c \geq 19{,}000$. The CS-inserts provide better heat transfer augmentation than do the LS-inserts for $\mathrm{Re}_c \leq 12{,}000$. The RIS-inserts are the least effective among the three. Furthermore, when Reynolds number Re_c is higher than 26,000, RIS-inserts even reduce heat transfer where η_1 becomes smaller than 1. Table 3 indicates the effect of heat transfer augmentation of tube inserts as calculated by effectiveness criterion 2. The LS-inserts are most effective among the three for $\mathrm{Re}_c \geq 19{,}000$. The CS-inserts are more effective than LS-inserts for $\mathrm{Re}_c \leq 12{,}000$. It is clearly noted that when using CS-inserts as a heat transfer augmentation device, the tube-side Reynolds number Re_c must be low. The enhancement effects of RIS-inserts are the least effective among the three for all values studied herein. This is because, when the fluid flow in tubes with RIS-inserts is turbulent, the effect of reducing pressure drop by an interrupted region is rather limited. The interrupted region decreases the tube-side heat transfer, which, consequently, reduces the effect of tube-side heat transfer augmentation. This finding coincides with the results of Saha et al. (1990) on regularly spaced, twisted-tape inserts. This strongly suggests that, in turbulent flow at high Re_c, inserts with regularly spaced geometrical interruptives do not augment the heat transfer very effectively.

Table 3 Performance evaluation based on criterion 1 (η_1), pumping power fixed-increase heat transfer* and based on criterion 2 (η_2), heat duty fixed-reduction pumping power**

Re_c	performance	LS	CS	RIS
33000	η_1	0.9735	0.9624	0.8914
	η_2	1.0021	1.0687	1.5481
26000	η_1	1.0767	1.0723	0.9433
	η_2	0.8713	0.9031	1.4377
19000	η_1	1.0849	1.0874	0.8142
	η_2	0.7740	0.7968	1.3027
12000	η_1	1.1864	1.1965	0.7614
	η_2	0.6517	0.6437	1.2015
5000	η_1	1.2010	1.2674	0.5176
	η_2	0.5617	0.4623	1.0174

(* : If $\eta_1 > 1$ then heat transfer is enhanced)

(** : If $\eta_2 < 1$ then heat transfer is enhanced and pumping power is reduced)

Conclusion

The present study provides the results of tube-side heat transfer augmentation in the range $5000 \leq \mathrm{Re}_c \leq 33{,}000$, with different strip type inserts in a two-pass, inverted, crossflow heat exchanger. The effects on flow pattern and heat transfer characteristics in vertical tubes are also presented. The strip-type inserts include LS (longitudinal strip), CS (crossed strip), and RIS (regularly interrupted strip). One hundred twenty runs were tested and four sets of flow field visualizations were made. The results of heat transfer enhancement with several simple devices suitable for practical application were presented and discussed in detail. The conclusions obtained from the present study are as follows:

1 From the flow visualization of outer field of tube banks, it is found that the fluid flow through the tube banks and the range of closed vortices region behind tubes is gradually reduced as $\mathrm{Re}_{\max}$ increases. There are two symmetric vortex cells inside the closed vortex region. The reattachment point moves toward the stagnation point as Re_c increases. This is because a $\mathrm{Re}_{\max}$ increase causes the separation point to move downstream. Therefore, it makes the ambient flow pattern of each successive downstream tube different and results in different heat transfer characteristics for each tube. This strongly suggests that this kind of crossflow heat exchanger is geometry

dependent. In spite of this, the problem dealt with in this paper is of importance.

2 The fluid entering or leaving the plenum produces vortex regions in the plenum. This vortex region expands to the upper plate of the plenum and its strength is enhanced as Reynolds number, Re_{max}, is increased. Consequently, it also promotes heat transfer with shell-side hot air. Therefore, it is ascertained that the proportion of heat transfer across the upper plate between the cold air in the plenum and shell-side hot air is large. Moreover, due to the presence of the plenum, the flow would become nonuniform after a 180 deg return.

3 Four sets of correlations for Nu_m (Eq. (12)) for tubes with and without various strip-type inserts are developed. Similarly, four sets of correlations for friction factor (Eq. (13)) for tubes with and without various strip type inserts are also developed.

4 For tubes with or without inserts, the effectiveness of a crossflow heat exchanger gradually decreases with increases in the ratio R, when $R \leq 1$. The lowest value is found at the ratio $R = 1$. The effectiveness gradually increases with increases of the ratio, R, when $R \geq 1$. Thus, when a crossflow heat exchanger is operated normally, the value of the heat capacity ratio of shell-side hot air to tube-side cold air should be away from 1. It is found that, at this stage, the effectiveness of a crossflow heat exchanger is consistent with the need for basic economic efficiency requirements.

5 Based on the constant pumping power effectiveness criterion (1) (η_1), the LS-insert performed the best among the three inserts studied here when Re_c of tube-side cold air $\geq 19{,}000$. However, CS-insert showed a better heat transfer rate when Re_c of tube-side cold air $\leq 12{,}000$. When $Re_c \geq 26{,}000$, it was found that RIS-insert was the least effective. The constant heat duty effectiveness criterion (2) (η_2) shows similar results to those based on criterion (1) (η_1). This shows that CS insert is the best choice when Re_c is low. Moreover, the operating condition should be carefully chosen to keep $\eta_1 > 1$ and $\eta_2 < 1$.

Acknowledgments

The authors are grateful to the referees who provided detailed and constructive comments. This work was supported by the China Steel Corporation through Grant TRC-80-21 for which the authors express their sincere gratitude and thanks. The assistance in preparation of the manuscript from Mr. Jang-Ming Chyr is greatly appreciated.

References

Baclic, B. S., and Gvozdenac, D. D., 1981, "ϵ-NTU-R Relationships for Inverted Order Flow Arrangements of Two-Pass Crossflow Heat Exchangers," ASME HTD-Vol. 11, pp. 27–41.

Bennet, C. O., and Myers, J. E., 1982, *Momentum, Heat and Mass Transfer*, 3rd ed., McGraw-Hill, New York, p. 471.

Bergles, A. E., Blumenkrantz, A. R., and Taborek, J., 1974, "Performance Evaluation Criterion for Enhanced Heat Transfer Surfaces," *Proc. Int. Heat Mass Transfer Conference*, Vol. 2, pp. 239–243.

Bergles, A. E., 1979, "Augmentation of Forced-Convection Heat Transfer," in: *Turbulent Forced Convection in Channels and Bundles*, S. Kakac and D. B. Spalding, eds., Hemisphere Publishing Co., New York, pp. 883–909.

Bowman, R. A., Mueller, A. C., and Nagle, W. M., 1940, "Mean Temperature Difference in Design," *Trans. ASME*, Vol. 62, p. 283.

Chen, J. D., and Hsieh, S. S., 1990, "General Procedure for Effectiveness of Complex Assemblies of Heat Exchangers," *Int. J. Heat Mass Transfer*, Vol. 33, pp. 1667–1674.

Grimison, E. D., 1937, "Correlation and Utilization of New Data on Flow Resistance and Heat Transfer for Cross Flow of Gases Over Tube Banks," *Trans. ASME*, Vol. 59, pp. 583–594.

Hsieh, S.-S., and Wen, M.-Y., 1993, "Augmentative Heat Transfer for a Vertical 2-Pass Tube With Insert Connected an Air Box in a Crossflow Heat Exchanger," *Int. J. Heat Mass Transfer*, Vol. 36, pp. 3043–3057.

Huge, E. C., 1937, "Experimental Investigation of Effects of Equipment Size on Convection Heat Transfer and Flow Resistance in Cross Flow of Gases Over Tube Banks," *Trans. ASME*, Vol. 59, pp. 573–581.

Kline, S. J., and McClintock, F. A., 1953, "Describing Uncertainties in Single Sample Experiments," *Mechanical Engineering*, Vol. 75, Jan., pp. 3–8.

Maezawa, S., and Lock, G. S. H., 1978, paper presented at Sixth Int. Heat Transfer Conference, Toronto.

Manglik, E. M., and Bergles, A. E., 1988, "Laminar Flow Heat Transfer in a Semi-circular Tube With Unifom Wall Temperature," *Int. J. Heat Mass Transfer*, Vol. 31, pp. 625–636.

Megerlin, F. F., Murphy, R. W., and Bergles, A. E., 1974, "Augmentation of Heat Transfer in Tubes by Use of Mesh and Brush Inserts," ASME JOURNAL OF HEAT TRANSFER, Vol. 96, pp. 145–151.

Oka, S. N., Kostic, Z. G., and Sikmanovic, S., 1974, "Investigation of the Heat Transfer Processes in Tube-Banks in Cross Flow," in: *Heat Exchanger Design and Theory Sourcebook*, N. H. Afgan and E. U. Schlunder, eds., McGraw-Hill, New York, pp. 617–636.

Petukhov, B. S., 1970, "Heat Transfer and Friction in Turbulent Pipe Flow With Variable Physical Properties," in: *Advances in Heat Transfer*, J. P. Hartnett and T. F. Irvine, eds., Academic Press Inc., New York, Vol. 6, pp. 504–564.

Pierson, O. L., 1937, "Experimental Investigation of the Influence of Tube Arrangement on Convection Heat Transfer and Flow Resistance in Cross Flow of Gases Over Tube Banks," *Trans. ASME*, Vol. 59, pp. 563–572.

Saha, S. K., Gaitonde, U. N., and Date, A. W., 1990, "Heat Transfer and Pressure Drop Characteristics of Turbulent Flow in a Circular Tube Fitted With Regularly Spaced Twisted-Tape Elements," *Experimental Thermal and Fluid Science*, Vol. 3, pp. 632–640.

Stevens, R. A., Fernandes, J., and Woolf, J. R., 1957, "Mean Temperature Difference in One, Two and Three-Pass Cross Flow Heat Exchanger," *Trans. ASME*, Vol. 79, pp. 287–297.

Zukauskas, A. A., and Ulinskas, R. V., 1985, "Efficiency Parameters for Heat Transfer in Tube Banks," *Heat Transfer Engineering*, Vol. 6, No. 1, pp. 19–25.

Heat Exchange Effectiveness and Pressure Drop for Air Flow Through Perforated Plates With and Without Crosswind

C. F. Kutscher
National Renewable Energy Laboratory,
1617 Cole Boulevard,
Golden, CO 80401
Mem. ASME

Low-porosity perforated plates are being used as absorbers for heating ambient air in a new type of unglazed solar collector. This paper investigates the convective heat transfer effectiveness for low-speed air flow through thin, isothermal perforated plates with and without a crosswind on the upstream face. The objective of this work is to provide information that will allow designers to optimize hole size and spacing. In order to obtain performance data, a wind tunnel and small lamp array were designed and built. Experimental data were taken for a range of plate porosities from 0.1 to 5 percent, hole Reynolds numbers from 100 to 2000, and wind speeds from 0 to 4 m/s. Correlations were developed for heat exchange effectiveness and also for pressure drop. Infrared thermography was used to visualize the heat transfer taking place at the surface.

1.0 Introduction

Perforated plates have been used for multiple-plate heat exchangers, film cooling (e.g., of turbine blades), and most recently in a new type of solar collector used to heat ambient air (Kutscher et al., 1993). Despite numerous applications, few studies have been done on the heat transfer coefficients for air flowing through these plates. Sparrow and Ortiz (1982) used the naphthalene sublimation technique to deduce heat transfer coefficients on the upstream face for air flowing normal to perforated plates. They tested two plates containing holes arranged in a staggered array, one with 14 percent open area and the other with 22 percent open area. A hole Reynolds number range of 2000 to 20,000 was covered.

As part of a series of studies related to film cooling applications, Andrews and Bazdidi-Tehrani (1989) conducted transient cool-down tests on a wide range of 6.35-mm-thick perforated plates containing square arrays of holes with different hole diameters and pitches. They obtained a correlation for the overall Nusselt number for normal flow as follows:

$$\mathrm{Nu}_D = 2.44\left(\frac{P}{D}\right)^{-1.43} \mathrm{Re}_D^{0.57}\mathrm{Pr}^{0.33} \qquad (1)$$

which is said to cover $500 < \mathrm{Re}_D \leq 43{,}000$, $1.9 < P/D < 22$, and $0.8 < t/D < 9.9$. The range of suction mass flow rates covered was from 0.1 to 1.7 kg/m^2-s.

Transpired solar collectors consist of an unglazed black perforated plate through which outside air is drawn by a fan (see Fig. 1). The air is preheated as it passes through the irradiated plate and is subsequently used for applications such as building ventilation air or crop drying. A typical range of mass suction flow rates is $G = 0.01$ to 0.05 kg/m^2-s. (As shown by Kutscher et al., 1993, at an incident radiation level of 700 W/m^2, these suction rates would correspond to an air temperature rise of roughly 36°C at the low flow rate and 12°C at the high flow rate.) In order to predict the efficiency of this type of collector, one must know the heat exchange effectiveness for the transpired air stream. The heat transferred from the plate to the suction air stream and the heat exchange effectiveness can be written in terms of an overall heat transfer coefficient based on the difference between plate and inlet air temperatures or one based on the logarithmic mean temperature difference as follows. To make the distinction between these two definitions clear, this paper will call the former h (consistent with the papers by Sparrow and Ortiz and Andrews et al.) and the latter U (consistent with most heat exchanger texts). Thus the heat transferred and the heat exchange effectiveness can be written as follows:

$$Q = hA(T_s - T_{\mathrm{amb}}) = UA\,\frac{T_o - T_{\mathrm{amb}}}{\ln\dfrac{T_s - T_{\mathrm{amb}}}{T_s - T_o}} \qquad (2)$$

$$\epsilon_{HX} = \frac{T_o - T_{\mathrm{amb}}}{T_s - T_{\mathrm{amb}}} = \frac{hA}{\dot{m}C_p} = 1 - e^{-\frac{UA}{\dot{m}C_p}} \qquad (3)$$

Note that physically the heat exchange effectiveness is equal to the ratio of the heat transferred to the air stream to the maximum possible heat transfer (i.e., if the outlet air were

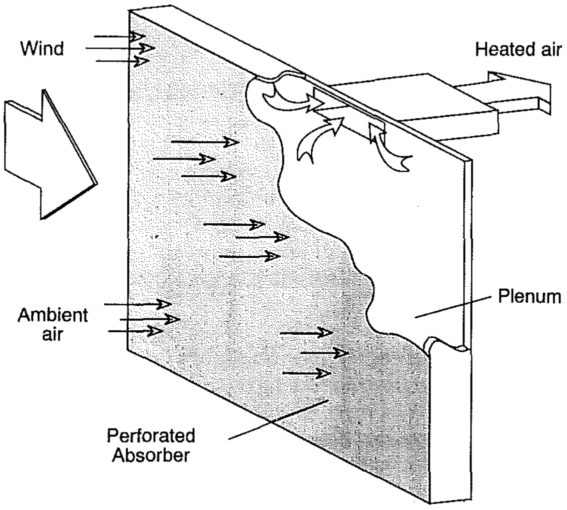

Fig. 1 Unglazed transpired solar collector oriented vertically for building ventilation preheat

---

Contributed by the Heat Transfer Division for publication in the JOURNAL OF HEAT TRANSFER. Manuscript received by the Heat Transfer Division April 1993; revision received July 1993. Keywords: Forced Convection, Heat Exchangers, Solar Energy. Associate Technical Editor: W. A. Fiveland.

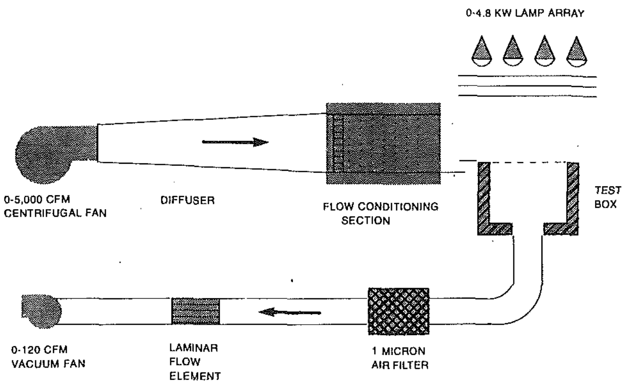

Fig. 2 Transpired collector test facility showing wind tunnel, test loop, and lamp array

heated to the plate surface temperature). Andrews and Bazdidi-Tehrani (1989) developed a correlation for Nusselt number based on h. In their correlation, h varies as the approach velocity raised to a power between 0 and 1. (The same is true for the work of Sparrow and Ortiz on front-surface-only heat transfer. They found that h for the front surface was proportional to $\mathrm{Re}_D^{0.476}$.) It readily can be seen that with such correlations, as suction velocity approaches zero, the heat exchange effectiveness is unbounded.

This was not necessarily a problem for their work, as their suction flow rates were high enough that the heat exchange effectiveness was always less than one. For the low flow rates used for transpired collectors, however, one must ensure that the correlation obtained yields physically realistic heat exchange effectiveness values. Although correlations can be developed for heat transfer coefficients based on either $(T_s - T_{\mathrm{amb}})$ or the log mean temperature difference, only the latter (U) can be correlated as a simple power law in mass flow rate. The purpose of this study was to develop a useful heat transfer correlation for flow through perforated plates under the conditions used for transpired collectors. These conditions are low porosity (typically less than 2 percent), low suction flow rates (0.01 to 0.05 kg/m^{2}s), staggered hole arrays, a thin aluminum plate (0.794 mm or 1/32 in.), and a crosswind on the upstream surface. (Some heat transfer enhancement can also occur on the back surface due to the flow in a plenum, but this is strongly dependent on the plenum used, and experimental tests at NREL have shown that this is a small effect.) Further details of the work presented here, including analytical and numerical modeling are contained in Kutscher (1992).

2.0 Experimental Apparatus

An overall schematic of the experimental setup is shown in Fig. 2. Rectangular perforated aluminum test plates of dimensions 30 cm × 50 cm were tested. The test plate dimensions were selected to allow sufficient length that measurements for crosswind tests could be taken in the region of asymptotic boundary layer thickness and sufficient width to allow plate centerline measurements to be undisturbed by edge effects. The plates were mounted atop an insulated and sealed plywood box. An additional perforated plate was used inside the box to ensure uniform flow through the test plate. Air exited the box through a 5.1 cm (2 in.) CPVC pipe, which penetrated the center of the floor of the box.

The top lid was essentially a frame that held the test absorber. The absorber to be tested was mounted on a series of plastic pins protruding from the inner edge of the frame that provided minimal conduction paths between the absorber and the frame. Tape was used to cover the gap between the metal absorber and the frame to prevent leakage around the edge of the absorber. Both the top and a long side of the box were removable for instrumentation access.

Suction through the box was provided by an Ametek 0-120 CFM vacuum fan driven by a universal AC-DC motor, and the motor speed was controlled by a 10 amp variable transformer. A combination of sliding gate dampers and a room air inlet pipe upstream of the fan (but downstream of the flow measuring section) was used to maintain operation at stable operating points for the suction fan and the transformer.

Electric resistance and radiative heating were considered as possible means for providing uniform heat flux to the test plates. Radiative heating was selected because its flux uniformity was not affected by the presence of holes, it lent itself well to testing a wide range of hole geometries, and it worked well with the aluminum plates generally used for solar collector applications. After testing a number of candidate lamps, GE R-40 300-watt flood lamps were chosen because they provided reasonably uniform illumination without local hot spots.

Obtaining uniform flux with an array of such lamps is not a trivial matter. A computer program was written to perform simulated tests of various lamp configurations. For simplicity, all lamps were aimed normal to the plane of the test absorber, which was located approximately 1 m away. The final array

Nomenclature

A = area of unit cell on plate less hole area, m^2
A' = area of unit cell on plate, m^2
c_p = air specific heat at constant pressure, J/kg-K
D = hole diameter, m
G = suction mass flow rate based on unit area A', kg/m^2-s
h = convective heat transfer coefficient based on $(T_s - T_{\mathrm{amb}})$ and area A, W/m^2-K
k = air thermal conductivity, W/m^2-K
L_s = starting length to establish asymptotic boundary layer, m
$\dot{m}$ = suction mass flow rate, kg/s
NTU = $UA/\dot{m}c_p$ = number of transfer units
NTS = plate orientation with narrow transverse (i.e., in the direction normal to the wind) spacing of holes
Nu_x = Ux/k or hx/k = Nusselt number
P = hole pitch, i.e., distance between center of hole and center of next closest hole, m
Pr = ν/α = Prandtl number
Re_x = vx/ν = Reynolds number, where v is relevant velocity scale
Q = heat transferred from plate to air stream, W
t = plate thickness, m
T_{amb} = ambient temperature $= T_\infty$, K
T_o = air outlet temperature, K
T_s = plate surface temperature, K
U = convective heat transfer coefficient based on log mean temperature difference and area A, W/m^2-K
U_∞ = free-stream velocity, wind speed, m/s
V = average suction face velocity, m/s
WTS = plate orientation with wide transverse (i.e., in the direction normal to the wind) spacing of holes
ΔP = pressure drop, Pa
α = air thermal diffusivity, m^2/s
δ = velocity boundary layer thickness, m
ϵ_{HX} = absorber heat exchange effectiveness
ζ = $(1/2)\rho V^2$ = nondimensional pressure drop
μ = air viscosity, kg/m-s
ν = air kinematic viscosity, m^2/s
σ = plate porosity, or open area fraction
ρ = air density, kg/m^3

configuration contained 16 lamps with a large open area in the middle of the array that eliminated a hot spot in the middle of the absorber that otherwise would be caused by the overlap there of the tails of all the lamp distributions. This configuration "wasted" some lamp energy compared with a scheme utilizing individual lamp tilting, but resulted in excellent flux uniformity of better than ±2 percent (measured by a Kipp & Zonen CM-11 pyranometer) with modest power requirements. The lamps were divided into two separate subarrays of 8 lamps each allowing the use of two 30-amp circuits. Each subarray was controlled by a separate 0-140 V output variable transformer, and these were kept at identical power settings by using two matched digital voltmeters. The transformers not only allowed the lamps to be adjusted to lower settings but also allowed much higher flux levels (exceeding 1200 W/m^2) by applying overvoltage to the 120 V lamps.

To provide a crosswind, a low-speed wind tunnel was built. An open circuit blow-through design was selected in order to provide easy access to the test section and to allow unobstructed viewing with an Inframetrics infrared camera. Because of the large amount of flow conditioning needed downstream of a fan, a high-head 2.36 m^3/s (5000 CFM) centrifugal unit was used in conjunction with considerable flow conditioning. A Fincor adjustable speed drive was used to allow the fan to be set from 0 to 1670 rpm. The flow conditioning consisted of a plastic honeycomb with one screen upstream of the honeycomb and seven screens downstream. The screen frames and honeycomb edge were seated into grooves routed into the inner styrofoam walls of the flow conditioning section.

The cross section of the flow conditioning section and tunnel exit was 0.362 m × 0.64 m (14.25 in. × 25 in.). This size allowed the test plate to be immersed in the inviscid core of undisturbed air exiting the tunnel. Tests were done with plates in both horizontal (face-up) and vertical orientations. To switch from one orientation to another, the entire assembly including test box, lamp array, and wind tunnel was rotated 90 deg. To remove boundary layer air along the edge (either floor or side) of the wind tunnel aligned with the test plate, a sharp leading edge was installed upstream of the test plate and extending 17 cm from the beginning of suction. Orginally, the boundary layer air was allowed to exit under the leading edge passively. It was found later that more precise splitting of streamlines could be obtained by adding active suction via a small fan and speed controller. Flow visualization was done via a smoke wire consisting of 10-mil constantan (from a 30 gage copper-constantan thermocouple wire), coated with oil, and heated with approximately 10 volts AC. Figure 3 shows smoke wire results indicating the effect of the boundary layer removal and the overall character of the flow.

3.0 Instrumentation

Absolute temperatures were measured with YSI 10,000 ohm thermistors. Temperature differences were measured both with the YSI thermistors and with special calibration type T (copper-constantan) thermocouples arranged in a thermopile circuit with voltages converted to temperature differences via a Newton-Raphson inversion routine in the software.

For surface temperature readings, sensors were glued to the underside of the plate with a high thermal conductivity epoxy, and lead wires were glued along the plate for a distance of 5 cm. It is important to note that for the aluminum plates tested, there was no measurable difference in temperature from the centerpoint between holes to the edge of a hole. This was verified by both multiple surface probes and by infrared thermography of the surface as well as by numerical simulations of the problem (to be reported in a separate paper). The ambient air temperature reading was taken several centimeters above the plate with sensors mounted in a double radiation shielded probe with both shields highly aspirated. Temperatures inside the test box were taken with an array of unshielded 30 gage type T thermocouples and with a thermistor mounted in a specially designed radiation shielded, low-aspiration-rate porous probe.

Suction flow rate was read with a calibrated Meriam laminar flow element with the pressure drop across the element measured by a calibrated MKS pressure transducer. This flow measuring device allowed a range of 10 to 1 on suction rates with a ±1 percent of reading accuracy. Wind tunnel velocity was determined by taking pitot tube measurements at speeds from 3 to 10 m/s and correlating these to fan rpm (measured by an optical tachometer). A plot of fan rpm versus wind tunnel speed was found to be extremely linear with no offset at zero, and so fan rpm was used to determine wind speed even at speeds less than 3 m/s. The test plate pressure drop was measured with a Dwyer point gage manometer having a range of 0-498 Pa (0-2 in. water) and readable to 2.29 Pa (0.001 in. water).

Data acquisition was done with an HP-75000 B-frame VXI bus data acquisition system with an internal HP-1326 5-1/2 digit digital voltmeter and several multiplexer/thermocouple cards. The data acquisition unit was controlled by an IBM PC-AT programmed in HT-Basic.

4.0 Normal Flow Effectiveness Results

Three different methods for determining heat exchange effectiveness were considered: transient cool-down (similar to the method used by Andrews et al.), energy balance method, and direct ΔT measurement. In the transient method, the plate is heated above ambient by the lamp array, and then the lamp radiation is blocked by a shield. The heat transfer coefficient can be determined from the slope of the temperature versus time curve as the plate cools down. In the energy balance method, the net radiation on the plate is measured, and this is assumed equal to the energy in the airstream.

In the direct temperature measurement method, the effectiveness is simply found from the definition:

$$\epsilon_{HX} = \frac{T_o - T_{\text{amb}}}{T_s - T_{\text{amb}}} \tag{4}$$

where T_o is the outlet air temperature in K.

An uncertainty analysis was done in accordance with ANSI/ASME PTC 19.1-1985. The uncertainties in temperature measurements (including installation effects) were estimated to be as follows: ±0.3 K for T_s, ±0.4 K for T_o, and ±0.5 K for T_{amb}. Figure 4 shows a comparison of the estimated experimental uncertainty for all three methods using an effectiveness model based on the final data correlation for zero wind results. (An approximate model used for initial assessment of the three experimental methods yielded similar relative results.) Note that the direct method has good accuracy at high effectiveness values. This is because ΔT's are high, and so the impact of uncertainties in the temperature measurements is low. At low values of effectiveness, the direct method is poor, although accuracy can be improved by turning the lamp array voltage up and reaching flux values of 1200 W/m^2 or more. (The curves in Fig. 4 are based on a flux of 800 W/m^2.)

For solar collector applications, high effectiveness values are mostly of interest, and the plates tested ranged in effectiveness from about 0.40 to about 0.90. The direct temperature measurement method has reasonably good accuracy over this region, and it has the additional advantage that it directly yields the quantity of interest without requiring any conversion. Because of these reasons, as well as the excellent repeatability found in the lab tests, it was chosen as the prime measurement technique, and the results reported here were obtained by this method.

To determine parameter sensitivities efficiently, the experimental work began with a full factorial test of 16 runs covering

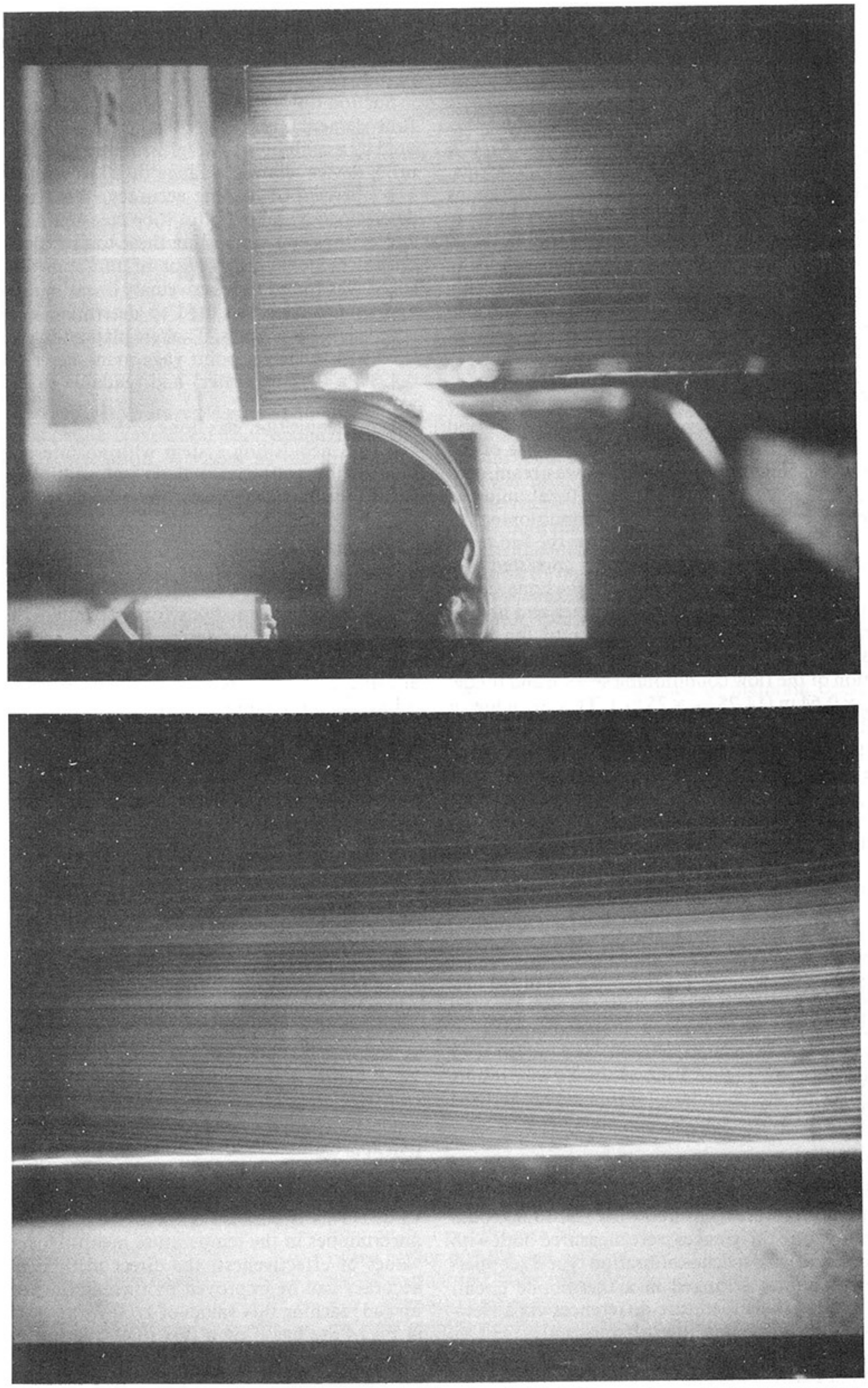

Fig. 3 Side view of smoke wire results for 1 m/s wind flow from left to right over a face-up horizontal absorber. Top: leading edge boundary layer removal. Bottom: effect of suction mass flow rate = 0.10 kg/m^2·s.

the three geometry parameters plus suction mass flow rate. When one of these parameters was found to have a low sensitivity (plate thickness), it was replaced first by wind speed and then by plate orientation (vertical versus horizontal) in additional factorial runs.

A series of eight original test plates were manufactured to perform the first full-factorial statistical experiment to determine the relative impact of varying hole size, spacing, and plate thickness over the ranges expected for transpired collector applications. A plot of all plate geometries (showing hole diameter and pitch, but not thickness) is shown in Fig. 5.

All plates were made of aluminum and painted on one side

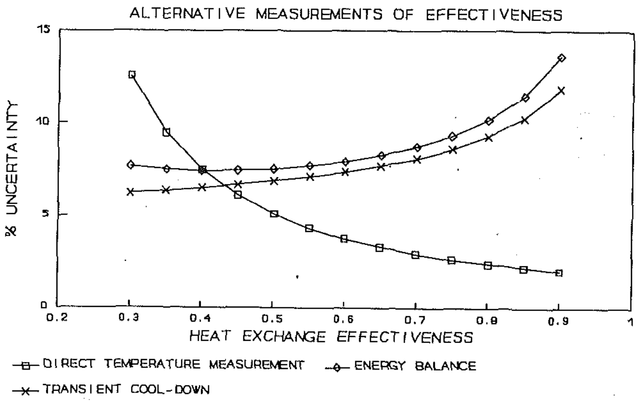

Fig. 4 Experimental uncertainty of effectiveness measurement versus effectiveness for three measurement methods

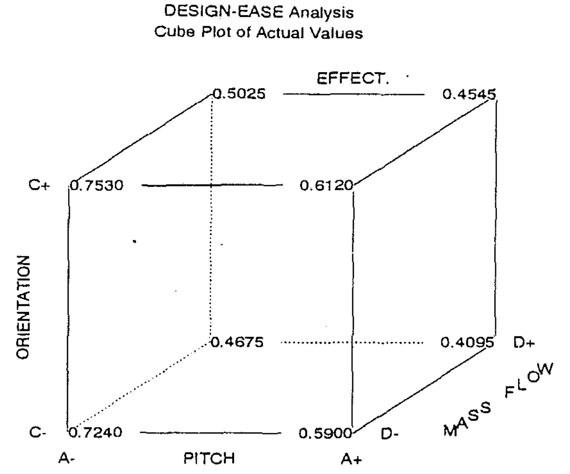

Fig. 6 Cube plot of measured effectiveness for investigation of orientation

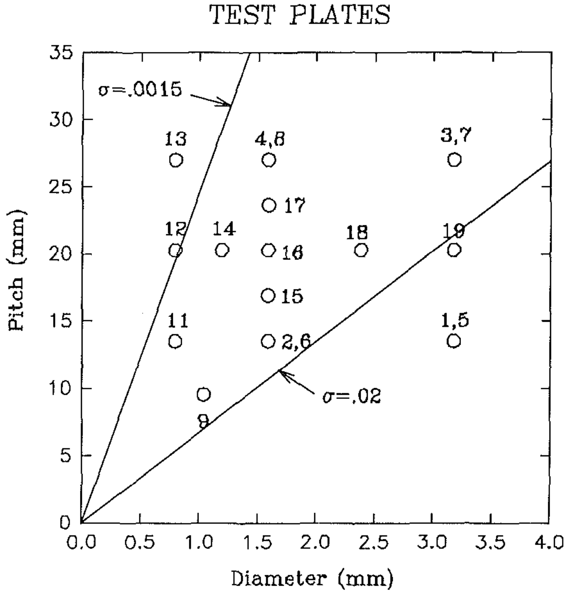

Fig. 5 Plot showing hole pitches and diameters for all test plates

with a flat black paint. Holes were then punched on a computer-controlled punching machine. The first eight test plates, numbers 1 through 8, form a cube in test space. (Note that plates 5, 6, 7, and 8 have the same hole diameters and pitches as plates 1, 2, 3, 4, respectively, but a different plate thickness. Plates 1-8 form a square in Fig. 5, since plate thickness is not plotted.)

Although the original test plates tend toward the high-porosity end of the range, this was necessary to meet the manufacturing constraint that hole diameter exceed plate thickness and still allow a 2 to 1 variation for hole diameter and for plate thickness. Plate 9 represents the geometry employed in a large outdoor test wall at NREL. The other plates were tested to provide additional data points for the correlation development.

The factorial tests revealed that the important parameters in determining heat exchange effectiveness are suction flow rate, wind speed, hole pitch, and hole diameter. Effectiveness increases with increasing wind speed and decreases with increasing suction flow rate, pitch, or diameter. For thin plates (1.588 mm [1/16 in.] or smaller), the actual plate thickness has a very small effect. The increase in effectiveness due to increasing plate thickness from 0.794 mm (1/32 in.) to 1.588 mm (1/16 in.) was only about 2 percent, or on the order of the experimental uncertainty. Plate orientation (vertical versus horizontal) had only a slightly larger effect as shown in the cube plot of Fig. 6. As a result of the factorial experiments, it was decided to test all plates at a thickness of 1/32 in. (the thickness typically employed in the field) and in a vertical orientation, as this orientation gave a slightly higher value and is the typical orientation for solar ventilation preheat applications.

All of the plates shown in Fig. 5 were tested over a range of suction mass flow rate, G, from 0.02 to 0.07 kg/m^2-s. (At G values less than 0.02, the outlet temperature measurement became sensitive to the outlet probe locations, and at G values greater than 0.07, the uncertainty in ΔT measurement became too high due to the low value of ΔT.) For each case, the effectiveness was directly measured, and an overall U based on the front surface area (excluding hole area) and the overall log mean temperature difference was determined. This overall U is related to effectiveness as follows:

$$\epsilon_{HX} = 1 - e^{-\mathrm{NTU}} \tag{5}$$

where

$$\mathrm{NTU} = \frac{UA}{\dot{m}C_p} = \frac{UA}{GA'C_p} = \frac{A}{A'}\frac{U}{GC_p}$$

Since A is the plate surface area minus the hole area and A' is the total frontal area (including holes), the ratio A/A' can be expressed in terms of the porosity, $\sigma = 0.907\ (D/P)^2$, as:

$$\frac{A}{A'} = 1 - \sigma \tag{7}$$

Various areas on which to base U, and various length scales for both Nusselt number and Reynolds number were tried in developing a satisfactory nondimensional correlation. The general form that collapsed the data best is similar to that used by Andrews and Bazdidi-Tehrani (1989), except that in this case the U value used in the Nusselt number is based on the log mean temperature difference rather than the difference between plate temperature and ambient temperature. All fluid properties were assumed constant and were based on the inlet (ambient) temperature (typically 27°C), since the temperature rises were small, and since the ambient temperature will most readily be known by the designer.

The best fit correlation equation for normal flow is

$$\mathrm{Nu}_D = 2.75\left(\frac{P}{D}\right)^{-1.2} \mathrm{Re}_D^{0.43} \tag{8}$$

This fit, shown in Fig. 7, has a coefficient of determination,

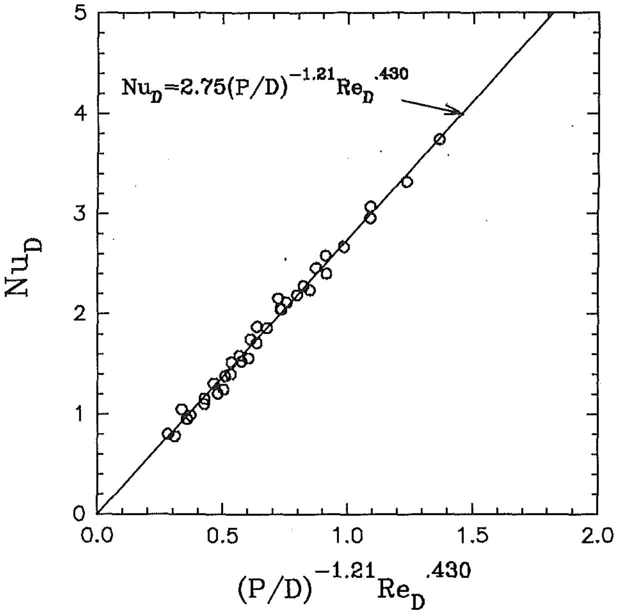

Fig. 7 Nu_D versus modified Re_D for vertical test plates

R^2, of 0.990. The coefficients of variation of the three parameters are as follows:

Leading coefficient:	2.7 ± 6.8 percent
(P/D) exponent:	− 1.2 ± 1.9 percent
Re_D exponent:	0.43 ± 3.5 percent

It should be pointed out that since heat transfer occurs in three regions (front surface, hole, and back surface), there was no guarantee a priori that a single term correlation would provide a good fit for the overall heat transfer. Note that D is not the only possible selection of length scale. An algebraically equivalent correlation for normal flow in terms of pitch-based nondimensional parameters is:

$$Nu_P=2.87\left(\frac{P}{D}\right)^{0.22}Re_P^{0.43} \tag{9}$$

but when the data are plotted in this form, they do not cluster as tightly.

5.0 Crosswind Effectiveness Results

As shown by Kutscher et al. (1993), for a flat plate in parallel flow with uniform suction, the theoretical starting length before the boundary layer reaches its final asymptotic state can be expressed as:

$$L_s\approx\frac{U_\infty\nu}{V^2} \tag{10}$$

Wind test data were taken under conditions in which the boundary layer could be considered at or very close to asymptotic. Suction mass flow rates were varied from 0.02 kg/m^2-s to a maximum of 0.07 kg/m^2-s, and the maximum wind speed tested was 4 m/s. The combination of minimum suction flow and maximum wind speed yields a maximum theoretical starting length of approximately 18 cm. This is based on a uniformly homogeneous suction surface and also does not account for the fact that a velocity boundary layer has already built up on a flat surface approximately 18–19 cm in length upstream of the absorber.

To test for the impact of downstream location, effectiveness measurements were taken both at the center of the absorber (25 cm downstream from the start of suction) and at a position 42 cm downstream from the start of suction. In each case, the local effectiveness was determined from measurements of the approaching air temperature (measured upstream from the absorber), the local surface temperature, and the local outlet temperature. It was found that the downstream measurement was always within 5 percent of the center plate measurement and usually much closer. Because results at the two locations were very close, and because the center location offered advantages such as direct comparison with zero-wind results (the same location and same surface and outlet sensors were used for the no-wind tests) and better isolation from plate edge losses, all of the wind results reported here are for the 25 cm location.

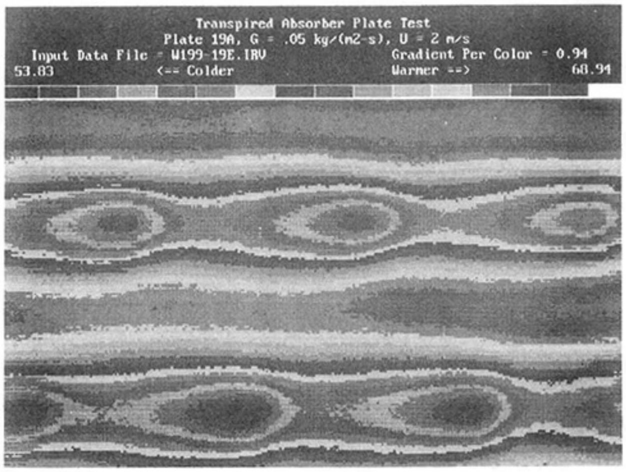

Fig. 8 Infrared image of black matboard absorber in WTS orientation; $G=0.05$ kg/m^2-s, wind speed = 2 m/s (from right to left)

For a staggered array of holes on a triangular pitch, it is important to note that the geometry presented to the wind depends on the major direction. Consider orientation WTS (wide transverse spacing) as the one in which the spacing between holes measured in a direction transverse to the wind is wide and the NTS direction as the one in which this distance is narrow. The effect of orientation on front surface heat transfer was visualized using infrared thermography images. (The numerical results given by Kutscher, 1992, show that the heat transfer that occurs on the front surface dominates heat transfer in the hole and on the back surface at the geometries and suction flow rates of interest.) Absorbers made of black matboard were perforated with the same hole pattern as plate 19 and used for thermal visualization. These absorbers have low thermal conductivity and hence, with a constant surface heat flux, variations in local heat transfer coefficient are manifested as variations in the local temperature.

Figure 8 shows the surface temperature distribution for the WTS orientation with a suction mass flow rate of 0.05 kg/m^2-s and wind speed (from *right to left*) of 2 m/s. Surface temperatures are lowest near the edges of holes where acceleration of the flow thins the local boundary layer, thus raising the local heat transfer coefficient. Note that for this orientation, warm bands aligned in the flow direction exist between rows of holes.

Figure 9 shows the same suction and wind condition but for the NTS orientation. Note that the downstream banding that occurs in the WTS orientation does not occur in the NTS orientation.

Tests of two versions of several plates with both the WTS and NTS orientations of holes indicated that the NTS direction has a somewhat higher heat exchange effectiveness than the WTS direction. This is shown in Fig. 10 for plate 15. The upper two curves show effectiveness versus wind speed for a suction mass flow rate of 0.02 kg/m^2-s, while the lower curves are for $G=0.07$ kg/m^2-s.

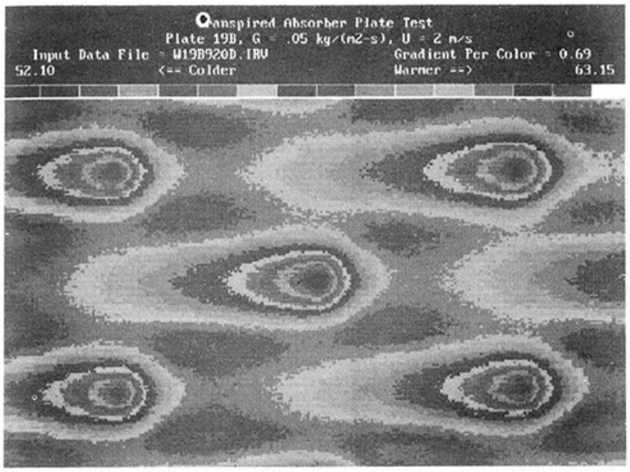

Fig. 9 Infrared image of black matboard absorber in NTS orientation; $G = 0.05$ kg/m^2-s, wind speed = 2 m/s (from right to left)

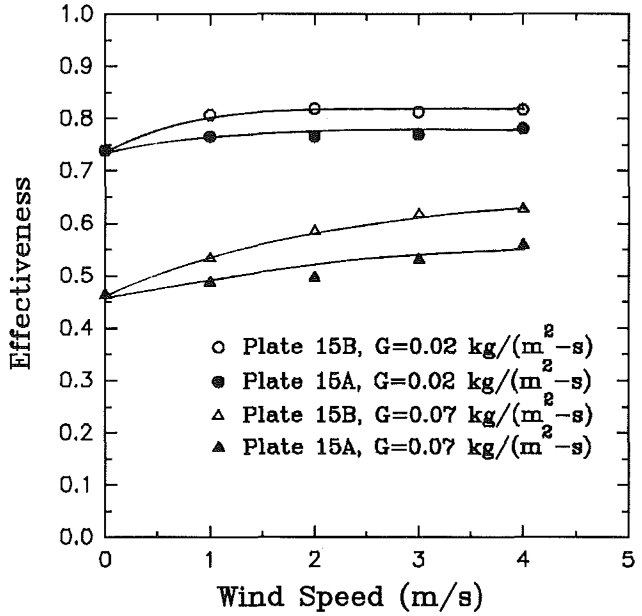

Fig. 10 Effect of hole orientation on wind test results. *A* denotes wide transverse spacing of holes and *B* denotes narrow transverse spacing

At each suction mass flow rate, a higher effectiveness is obtained for the NTS orientation of holes as compared with the WTS orientation. Because the higher performing orientation is of greater interest (one generally wants to maximize heat transfer), tests were run for seven different NTS orientation plates at all permutations of three suction mass flow rates ranging from $G = 0.02$ to $G = 0.07$ kg/m^2-s and at least three wind speeds (1, 2, and 4 m/s).

In seeking correlations for the wind results, it was found that at each individual wind speed, an accurate correlation could be obtained of the general form used for zero wind speed but with different values of coefficient and exponents. Various means were attempted for correlating all of the results into a single equation. The goal was to obtain a nondimensional correlation that reduced to the zero-wind case at zero wind and is zero at zero suction velocity. It appears reasonable to nondimensionalize the wind speed by dividing by the suction face velocity, V. This is because the asymptotic thermal boundary layer thickness is proportional to ν/V. Consider that the incremental heat transfer above the zero-wind value can be correlated in a form that relates a Nusselt number based on thermal boundary layer thickness to a Reynolds number based on the same length scale (and using wind speed as the velocity scale). Thus,

$$\mathrm{Nu}_\delta \sim \mathrm{Re}_\delta^x \tag{11}$$

Here the Nusselt number is based on an incremental heat transfer coefficient, $U' = U - U_0$, where U_0 is the value at zero wind and U is the value with nonzero wind. In terms of U' and δ,

$$\frac{U'\delta}{k} \sim \left(\frac{U_\infty \delta}{\nu}\right)^x \tag{12}$$

Noting that

$$\delta \sim \frac{\nu}{V} \tag{13}$$

the incremental heat transfer coefficient is:

$$U' \sim \frac{k}{\nu} V \left(\frac{U_\infty}{V}\right)^x \tag{14}$$

Note that if the exponent x is less than one, the incremental heat transfer coefficient goes to zero if wind speed or suction velocity go to zero.

Since the zero wind correlation is in the form of a Nusselt number based on hole diameter, it is convenient to multiply both sides of this equation by D/k, obtaining:

$$\mathrm{Nu}_D' \sim \sigma \mathrm{Re}_D \left(\frac{U_\infty}{V}\right)^x \tag{15}$$

and

$$\mathrm{Nu}_D = (\mathrm{Nu}_D)_0 + \mathrm{Nu}_D' \tag{16}$$

The wind data were thus fitted to a correlation of the form

$$\mathrm{Nu}_D' = a \sigma \mathrm{Re}_D \left(\frac{U_\infty}{V}\right)^b \tag{17}$$

Regression yielded:

$a = 0.0305$

$b = 0.48$

The coefficients of variation were ±18.3 percent for a and ±9.3 percent for b.

Thus the crosswind data for the narrow transverse spacing (NTS) were correlated as:

$$\mathrm{Nu}_D = 2.75 \left[\left(\frac{P}{D}\right)^{-1.2} \mathrm{Re}_D^{0.43} + 0.011 \sigma \mathrm{Re}_D \left(\frac{U_\infty}{V}\right)^{0.48} \right] \tag{18}$$

Note that for laminar flow over a plate, one expects an exponent on the wind speed of 1/2, and the fitted exponent is close to that. A plot of Nu_D for the nonzero wind data is shown in Fig. 11. When this correlation is used to determine heat exchange effectiveness, all measured heat exchange effectiveness values for the wind runs are predicted to within ±9 percent. The R^2 value for predicted versus measured effectiveness for wind runs was 0.926.

6.0 Pressure Drop

In the design of a transpired collector, it is necessary to know heat exchange effectiveness to determine thermal performance. It is also necessary to predict pressure drop to ensure that it is sufficient to provide good flow uniformity and prevent outflow and in order to minimize fan power. The most comprehensive source that could be found on pressure drop information is the Russian work edited by I. E. Idelchik, entitled *Handbook of Hydraulic Resistance* (Idelchik, 1986).

Data for the Reynolds number (based on hole diameter) range of interest (about 100 to 2000) are given on p. 406 of that book in the form of graphs and tables for a wide porosity range, but are stated as "tentative" for this flow regime. De-

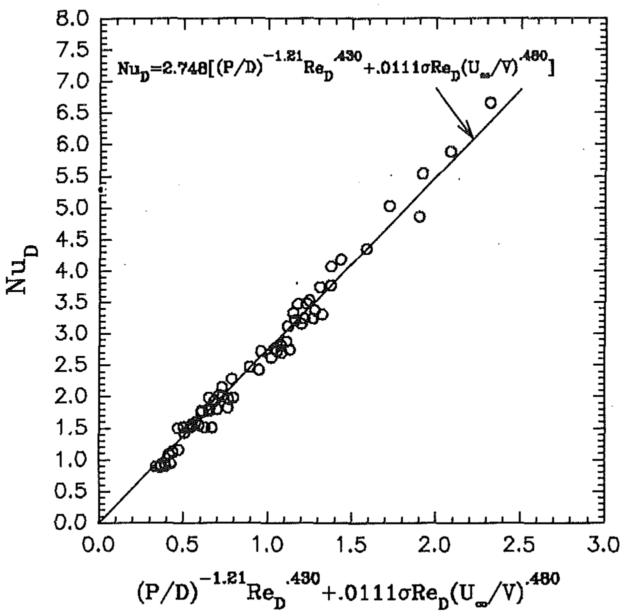

Fig. 11 General heat transfer correlation for nonzero wind tests

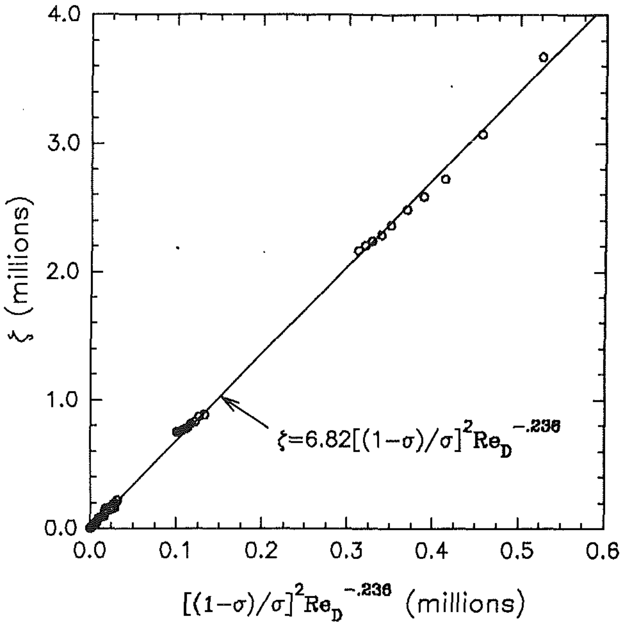

Fig. 12 Data and correlation for nondimensional pressure drop as a function of porosity and Reynolds number

termining the pressure drop for any given plate requires a complicated series of steps to evaluate various parameters and combine them into a final result.

In order to test the validity of the Idelchik data and to explore the possibility of a simpler correlation, all plates of 0.794 mm (1/32 in.) thickness were tested at suction mass flow rates from 0.01 to 0.08 kg/m^2-s. (Only data points with a minimum pressure drop of 5 Pa were recorded.) Flow rate was measured with the laminar flow element, and pressure drop was recorded by reading a Dwyer point gage manometer. This manometer has a range of 0-498 Pa (0-2 in. of water) and is readable to 2.29 Pa (0.001 in.).

The mean of the absolute value of the percentage error between the measured value and that calculated from the handbook was 14.6 percent with the highest error being 44 percent. Clearly there was room for improvement in predicting the pressure drop for these low-porosity plates.

The nondimensionalized pressure drop, ζ, is defined as:

$$\zeta\equiv\frac{\Delta P}{\frac{1}{2}\rho V^2} \quad (19)$$

where V is the approaching face velocity. An uncertainty analysis indicated that the nondimensionalized pressure drop could be measured with an overall experimental accuracy of ±6 percent. According to Idelchik (1986), ζ is a function of porosity, the Reynolds number based on hole diameter, and the friction factor. In seeking a simple single-term correlation for ζ, one can thus simply consider products of porosity and Reynolds number to unknown powers. In order not to prejudice the correlation, however, curve fits were done to determine dimensional pressure drop in terms of powers of hole pitch, hole diameter, and approach velocity. The resulting powers were highly consistent with the nondimensional variables given above.

When fitting the nondimensional variables, the power on porosity was very close to -2, that is, ζ was approximately proportional to $1/\sigma^2$. As shown by Batchelor (1967), the pressure drop across a perforated plate is analogous to a sudden enlargement in a pipe, and the decrease in the Bernoulli constant (i.e., the unrecoverable pressure drop) can be determined in nondimensional form from conservation of momentum as:

$$\zeta=\left(\frac{1-\sigma}{\sigma}\right)^2 \quad (20)$$

Batchelor points out that viscosity is not important unless the holes are very small. Note that for the plates tested here, which have very low porosity,

$$\left(\frac{1-\sigma}{\sigma}\right)^2\approx\frac{1}{\sigma^2} \quad (21)$$

so that it is not surprising that the data show an inverse dependence on the square of the porosity.

Expressing the porosity term in Batchelor's form is consistent with the physics and could be expected to make the correlation more extrapolatable to higher porosities. Because it did not decrease the accuracy of the fit, this term was used in the correlation. The fact that the curve fitting yields a nonzero exponent on the Reynolds number indicates that the holes are small enough for viscosity to play a role in the pressure drop. The best fit for normal flow pressure drop for the plates tested was:

$$\zeta=6.82\left(\frac{1-\sigma}{\sigma}\right)^2 Re_D{}^{-0.236} \quad (22)$$

When compared with the data, this fit yields an average value for the absolute magnitude of the error equal to 6.5 percent, but with a few considerably higher errors, the extreme being 26 percent. The coefficient of determination, R^2, for the fit is 0.9992. Thus this simple correlation fits the data better than the much more complicated procedure presented by Idelchik (1986). In fairness to Idelchik, the correlation presented here covers a much smaller range, namely the range suitable for transpired solar collectors. The correlation results together with the data are presented in Fig. 12.

All of the above-mentioned data were taken in the absence of a crosswind. A few runs were made to test the effect of a crossflow, and it was found that wind increases the pressure drop a small but significant amount. This can be seen in Fig. 13, which shows the increase in pressure drop for plate 17 as a function wind speed. Tests with both the WTS and NTS orientations showed no measurable effect of hole orientation on pressure drop.

Numerical analysis (Kutscher, 1992) shows that a separation

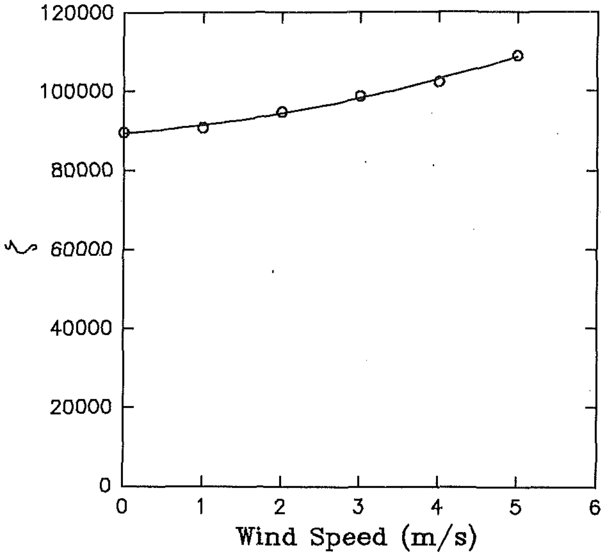

Fig. 13 Nondimensional pressure drop versus wind speed at $G = 0.023$ kg/m^2·s for plate 17

region occurs in the hole, and this likely has the effect of decreasing the effective hole size, thereby increasing the magnitude of the sudden enlargement. A detailed study of the effect of wind on pressure drop was beyond the scope of this study.

7.0 Summary and Conclusions

Perforated plates used for new solar collector applications are of low porosity and utilize very low flow rates at which the heat exchange effectiveness approaches its theoretical limit of one. In order to calculate the efficiency of such a device, the heat exchange effectiveness for the suction air stream must be known. This study showed that satisfactory heat transfer correlations can be developed if one defines an overall heat transfer coefficient based on the non-hole upstream surface area and the log mean temperature difference. It was shown that the major factors affecting heat transfer are suction flow rate, crosswind speed, hole pitch, and hole diameter. For thin plates, the actual thickness has little impact. Also, the enhancement associated with a vertical orientation as opposed to a horizontal orientation is slight. In the presence of a crosswind, the major orientation of the holes is important, with higher effectiveness values obtained in the case of the orientation with a lesser spacing in the cross-stream direction of hole rows. For plate porosities of 0.1 to 5 percent and hole Reynolds numbers of 100 to 2000, the following correlation for Nusselt number (for the narrow transverse hole spacing) predicts heat exchange effectiveness values to within ±9 percent:

$$\mathrm{Nu}_D = 2.75\left[\left(\frac{P}{D}\right)^{-1.2}\mathrm{Re}_D^{0.43} + 0.011\sigma\,\mathrm{Re}_D\left(\frac{U_\infty}{V}\right)^{0.48}\right] \tag{23}$$

Note that this correlation, even with U_∞ set to zero, cannot be directly compared with the results of Andrews and Bazdidi-Tehrani, since the correlation here is based on the log mean temperature difference, a necessity for the flow rate range for which this correlation is intended.

For plate porosities of 0.1 to 2.2 percent and hole Reynolds numbers of 100 to 2000, the following simple correlation for nondimensional pressure drop for normal flow yields an average error of 6.5 percent (but with some errors as high as 26 percent):

$$\zeta = 6.82\left(\frac{1-\sigma}{\sigma}\right)^2 \mathrm{Re}_D{}^{-0.24} \tag{24}$$

Acknowledgments

The author gratefully acknowledges the assistance provided by H. Doug Powell, Keith Gawlik, and Mark Lichtwardt at NREL, the advice given by Dr. John Daily of the University of Colorado at Boulder, and the financial support provided by Bob Hassett of the U.S. Department of Energy.

References

Andrews, G. E., and Bazdidi-Tehrani, F., 1989, "Small Diameter Film Cooling Hole Heat Transfer: The Influence of the Number of Holes," ASME Paper No. 89-GT-7.

ANSI/ASME PTC 19.1-1985, "ASME Performance Test Codes—Supplement on Instruments and Apparatus, Part 1: Measurement Uncertainty," American Society of Mechanical Engineers.

Batchelor, G. K., 1967, *An Introduction to Fluid Dynamics*, Cambridge University Press, Cambridge, United Kingdom.

Idelchik, I. E., 1986, *Handbook of Hydraulic Resistance*, Hemisphere Publishing Company, New York.

Kutscher, C. F., 1992, "An Investigation of Heat Transfer for Air Flow Through Low-Porosity Perforated Plates," Ph.D. thesis, Department of Mechanical Engineering, University of Colorado, Boulder, CO, Dec.

Kutscher, C. F., Christensen, C. B., and Barker, G. M., 1993, "Unglazed Transpired Solar Collectors: Heat Loss Theory," ASME *Journal of Solar Energy Engineering*, Vol. 115, pp. 182–188.

Sparrow, E. M., and Ortiz, M. C., 1982, "Heat Transfer Coefficients for the Upstream Face of a Perforated Plate Positioned Normal to an Oncoming Flow," *International Journal of Heat and Mass Transfer*, Vol. 25, No. 1, pp. 127–135.

Scaling of the Turbulent Natural Convection Flow in a Heated Square Cavity

R. A. W. M. Henkes

C. J. Hoogendoorn

J. M. Burgers Centre for Fluid Mechanics,
Faculty of Applied Physics,
Delft University of Technology,
P.O. Box 5046,
2600 GA Delft, The Netherlands

By numerically solving the Reynolds equations for air and water in a square cavity, with differentially heated vertical walls, at Rayleigh numbers up to 10^{20} the scalings of the turbulent natural convection flow are derived. Turbulence is modeled by the standard k-ϵ model and by the low-Reynolds-number k-ϵ models of Chien and of Jones and Launder. Both the scalings with respect to the Rayleigh number (based on the cavity size H) and with respect to the local height (y/H) are considered. The scalings are derived for the inner layer, outer layer, and core region. The Rayleigh number scalings are almost the same as the scalings for the natural convection boundary layer along a hot vertical plate. The scalings found are almost independent of the k-ϵ model used.

1 Introduction

Natural convection flows are flows driven by density differences. Density differences can result from temperature differences, from differences in concentration of chemical species in the fluid, or from the presence of multiple phases of a fluid. In this study only natural convection flows resulting from temperature differences will be considered. Two elementary classes of natural convection flows with temperature differences are: heating (or cooling) from a horizontal wall (*heating from below*) and heating (or cooling) from a vertical wall (*heating from the side*). The first class is characteristic for Rayleigh-Bénard convection and for the meteorology of the earth's atmospheric boundary layer. Both classes play a role in different technical applications, like solar collectors, climate conditioning of rooms, isolation by double glazing, heat removal in micro-electronics, and cooling of nuclear reactors.

The natural convection flow in a square cavity, differentially heated over the vertical walls and with adiabatic horizontal walls, has become a classical heat transfer problem. If the Rayleigh number, i.e., the dimensionless temperature difference between the vertical walls, becomes large, thin boundary layers are formed along the vertical walls and the core of the cavity becomes thermally stratified. De Vahl Davis and Jones (1983) have organized a workshop to obtain benchmark numerical results for the steady laminar flow of air for Rayleigh numbers up to 10^6. The initial phase of the transition to turbulence for air in this cavity (occurring at $\mathrm{Ra} \sim 10^8$) has been calculated by different authors (Le Quéré, 1987; Paolucci and Chenoweth, 1989; Henkes and Hoogendoorn, 1990a). If the Rayleigh number is further increased, the flow undergoes a transition to the fully turbulent state. Recently a workshop was organized to obtain benchmark numerical and experimental results for the weakly turbulent flow of air in the heated square cavity at a Rayleigh number of 5×10^{10} (Henkes and Hoogendoorn, 1993). Turbulence was modeled with the standard k-ϵ model. Besides that model, other turbulence models were also compared. In the present study the Rayleigh number is further increased to obtain the scalings for the fully turbulent state. In earlier studies (Henkes, 1991; Henkes and Hoogendoorn, 1990b) we derived the proper scalings and wall functions for the turbulent natural convection boundary layer along a hot vertical plate in an isothermal environment (the Rayleigh number was increased up to $\mathrm{Ra}_y = 10^{25}$). Knowledge of the proper scalings of a turbulent flow is important for the following reasons: (*i*) The scalings are closely related to the global physical structure of the flow; (*ii*) application of wall functions in computations bridges the large temperature and velocity gradients close to the wall, without using extra grid points, and thus saves CPU time; (*iii*) by using the scaling properties, experimental results obtained for one Rayleigh number can be extrapolated to a wider range of Rayleigh numbers. By comparison of the scalings for the cavity with the scalings for the plate we investigate whether the wall functions as derived for the plate also apply to the cavity.

The turbulent flow in the cavity is calculated by numerically solving the two-dimensional Reynolds equations, using the standard k-ϵ model and low-Reynolds-number k-ϵ models (the model of Chien and of Jones and Launder) for turbulence. The scalings are derived by increasing the Rayleigh number up to 10^{20}. Due to the thermal stratification in the core of the cavity, the scaling of the boundary layers along the cavity walls is more complicated than the scaling of the boundary layer along the plate in an isothermal environment; characteristic quantities in the boundary layers in the cavity depend on two variables, namely the (height-based) Rayleigh number Ra and the local height y/H (H is the height of the cavity), whereas quantities for the boundary layer along the plate depend on only one variable, namely the (y-based) Rayleigh number Ra_y.

We realize that for the large Rayleigh numbers as considered here, experimental data are not available. Therefore at this moment we cannot verify whether the scalings as derived from the k-ϵ models are also physically correct. However, at moderate Rayleigh numbers ($\mathrm{Ra}_y \sim 10^{11}$ for the plate, $\mathrm{Ra} \sim 4 \times 10^{10}$ for the cavity) experimental data exist. In our earlier studies (Henkes and Hoogendoorn, 1989; Henkes et al., 1991) these experimental data were used to determine the performance of the standard k-ϵ model and of low-Reynolds-number k-ϵ models. These studies showed that the k-ϵ models correctly predict the time-averaged velocity and temperature in the outer layer of the boundary layer (i.e., the part between the position of the maximum vertical velocity and the outer edge). In the inner layer (i.e., between the wall and the position of the maximum vertical velocity) a proper definition of the low-Reynolds-number terms (e.g., as in the models of Chien and Jones and Launder) is needed to predict the wall heat transfer and the wall shear stress accurately. For a detailed comparison of k-ϵ models with available experiments in the cavity, the

---

Contributed by the Heat Transfer Division for publication in the JOURNAL OF HEAT TRANSFER. Manuscript received by the Heat Transfer Division September 1992; revision received August 1993. Keywords: Enclosure Flows, Natural Convection, Turbulence. Associate Technical Editor: J. R. Lloyd.

reader is referred to the proceedings of the workshop (Henkes and Hoogendoorn, 1993).

Because the use of k-ϵ models was checked to make sense at moderate Rayleigh numbers, we also expect them to be physically relevant at larger Rayleigh numbers. Moreover, even at the moderate Rayleigh numbers for which experiments were available, the derived turbulent scalings for the plate showed a good agreement with the experimental scalings. Therefore we think that the turbulent scalings as derived here for the cavity are not just a peculiarity of the models used. More experimental data are needed for further verification.

2 Mathematical Formulation

We consider a two-dimensional square cavity with a hot left wall (temperature T_h) and a cold right wall (temperature T_c). The horizontal walls are adiabatic ($\partial T/\partial y = 0$). The height of the cavity is H. The flow in the cavity is described by the Reynolds equations, applying the Boussinesq approximation:

$$\frac{\partial u}{\partial x}+\frac{\partial v}{\partial y}=0$$

$$\frac{\partial u}{\partial t}+u\,\frac{\partial u}{\partial x}+v\,\frac{\partial u}{\partial y}=-\frac{1}{\rho}\,\frac{\partial p}{\partial x}+\frac{\partial}{\partial x}\,(\nu+\nu_t)\left(2\,\frac{\partial u}{\partial x}\right)+\frac{\partial}{\partial y}\,(\nu+\nu_t)\left(\frac{\partial u}{\partial y}+\frac{\partial v}{\partial x}\right)$$

$$\frac{\partial v}{\partial t}+u\,\frac{\partial v}{\partial x}+v\,\frac{\partial v}{\partial y}=-\frac{1}{\rho}\,\frac{\partial p}{\partial y}+g\beta\,(T-T_c)+\frac{\partial}{\partial x}\,(\nu+\nu_t)\left(\frac{\partial v}{\partial x}+\frac{\partial u}{\partial y}\right)+\frac{\partial}{\partial y}\,(\nu+\nu_t)\left(2\,\frac{\partial v}{\partial y}\right)$$

$$\frac{\partial T}{\partial t}+u\,\frac{\partial T}{\partial x}+v\,\frac{\partial T}{\partial y}\,\frac{\partial}{\partial x}\left(\frac{\nu}{\mathrm{Pr}}+\frac{\nu_t}{\sigma_T}\right)\frac{\partial T}{\partial x}+\frac{\partial}{\partial y}\left(\frac{\nu}{\mathrm{Pr}}+\frac{\nu_t}{\sigma_T}\right)\frac{\partial T}{\partial y} \qquad (1)$$

$$\frac{\partial k}{\partial t}+u\,\frac{\partial k}{\partial x}+v\,\frac{\partial k}{\partial y}=\frac{\partial}{\partial x}\left(\nu+\frac{\nu_t}{\sigma_k}\right)\frac{\partial k}{\partial x}+\frac{\partial}{\partial y}\left(\nu+\frac{\nu_t}{\sigma_k}\right)\frac{\partial k}{\partial y}+P_k+G_k-\epsilon+D$$

$$\frac{\partial \epsilon}{\partial t}+u\,\frac{\partial \epsilon}{\partial x}+v\,\frac{\partial \epsilon}{\partial y}=\frac{\partial}{\partial x}\left(\nu+\frac{\nu_t}{\sigma_\epsilon}\right)\frac{\partial \epsilon}{\partial x}+\frac{\partial}{\partial y}\left(\nu+\frac{\nu_t}{\sigma_\epsilon}\right)\frac{\partial \epsilon}{\partial y}+(c_{\epsilon1}f_1(P_k+c_{\epsilon3}G_k)-c_{\epsilon2}f_2\epsilon)\,\frac{\epsilon}{k}+E$$

with

$$P_k=\nu_t\left(2\left(\frac{\partial u}{\partial x}\right)^2+2\left(\frac{\partial v}{\partial y}\right)^2+\left(\frac{\partial u}{\partial y}+\frac{\partial v}{\partial x}\right)^2\right),$$

$$G_k=-\frac{\nu_t}{\sigma_T}\,g\beta\,\frac{\partial T}{\partial y},\ \nu_t=c_\mu f_\mu\,\frac{k^2}{\epsilon}.$$

In these equations x is the horizontal coordinate, y is the vertical coordinate, u is the horizontal velocity, v is the vertical velocity, ρ is the density, p is the pressure relatively to the hydrostatic pressure due to the reference temperature T_c, T is the temperature, g is the gravitational acceleration, β is the coefficient of thermal expansion, ν is the molecular viscosity, k is the turbulent kinetic energy, ϵ is the dissipation rate of turbulent kinetic energy, and ν_t is the turbulent viscosity.

To obtain formulation (1), the Reynolds stresses and the turbulent heat fluxes appearing in the Reynolds equations were modeled by the eddy viscosity concept, which introduces the turbulent viscosity ν_t. The turbulent viscosity itself is modeled by the k-ϵ model. The following versions of the k-ϵ model will be considered:

(*i*) *Standard k-ϵ model*

$c_\mu=0.09,\quad c_{\epsilon1}=1.44,\quad c_{\epsilon2}=1.92,\quad c_{\epsilon3}=\tanh|v/u|,$

$\sigma_T=0.9,\quad \sigma_k=1.0,$

$\sigma_\epsilon=1.3, f_\mu=f_1=f_2=1.0, D=E=0,$ and $k=0,$

$\epsilon=\infty$ at the wall.

(*ii*) *Low-Reynolds-number k-ϵ model of Chien* (*1980, 1982*)

$c_\mu=0.09,\quad c_{\epsilon1}=1.35,\quad c_{\epsilon2}=1.8,\quad c_{\epsilon3}=\tanh|v/u|,$

$\sigma_T=0.9,\quad \sigma_k=1.0,\quad \sigma_\epsilon=1.3,$

$f_\mu=1-\exp(-0.0115x^+),\quad f_1=1.0,$

$$f_2=1-\frac{2}{9}\exp(-(\mathrm{Re}_t/6)^2),$$

Nomenclature

c_f = wall shear stress coefficient = $2\nu(\partial v/\partial x)_w/g\beta\Delta TH$
g = gravitational acceleration
G_k = buoyant production of turbulent kinetic energy
H = height of cavity
k = turbulent kinetic energy
Nu = Nusselt number for cavity = $-(H/\Delta T)\,(\partial T/\partial x)_w$
$\overline{\mathrm{Nu}}$ = averaged Nusselt number in cavity = $\int_0^1 \mathrm{Nu}\; d(y/H)$
p = pressure
P_k = shear production of turbulent kinetic energy
Pr = Prandtl number
Ra = Rayleigh number for cavity = $g\beta\Delta TH^3\,\mathrm{Pr}/\nu^2$
Ra_y = Rayleigh number for plate = $g\beta\Delta Ty^3\mathrm{Pr}/\nu^2$
S = gradient of thermal stratification in cavity center = $(H/\Delta T)\,(\partial T/\partial y)$
t = time
Δt = numerical time step
T = temperature
ΔT = characteristic temperature difference = T_h-T_c for cavity, T_h-T_∞ for plate
T_c = temperature of cold cavity wall
T_h = temperature of hot cavity wall or plate
u = horizontal velocity component
v = vertical velocity component
x = horizontal coordinate
y = vertical coordinate
β = coefficient of thermal expansion
δ = boundary-layer thickness
ϵ = dissipation rate of turbulent kinetic energy
ν = molecular kinematic viscosity
ν_t = turbulent kinematic viscosity
ρ = density
σ_T = turbulent Prandtl number for T
Ψ = stream function, $u=-\partial\Psi/\partial y$, $v=\partial\Psi/\partial x$
Ψ_c = stream function at center of cavity

Subscripts

i = grid point in x direction
j = grid point in y direction
max = maximum of a quantity
trans = laminar–turbulent transition in Reynolds equations
w = wall condition
∞ = environment condition

$$D = -2\nu \frac{k}{x_n^2}, \quad E = -\frac{2\nu\epsilon}{x_n^2}\exp(-0.5x^+),$$

$$\text{and } k = \epsilon = 0 \text{ at the wall.}$$

(*iii*) *Low-Reynolds-number k-ε model of Jones and Launder (1972)*

$$c_\mu = 0.09, \quad c_{\epsilon 1} = 1.44, \quad c_{\epsilon 2} = 1.92, \quad c_{\epsilon 3} = \tanh|v/u|,$$

$$\sigma_T = 0.9, \quad \sigma_k = 1.0, \quad \sigma_\epsilon = 1.3, f_\mu = \exp\left(\frac{-2.5}{1 + \mathrm{Re}_t/50}\right),$$

$$f_1 = 1.0, \quad f_2 = 1 - 0.3\exp(-\mathrm{Re}_t^2),$$

$$D = -2\nu\left[\left(\frac{\partial\sqrt{k}}{\partial x}\right)^2 + \left(\frac{\partial\sqrt{k}}{\partial y}\right)^2\right],$$

$$E = 2\nu\nu_t\left[\left(\frac{\partial^2 u}{\partial y^2}\right)^2 + \left(\frac{\partial^2 v}{\partial x^2}\right)^2\right], \text{ and } k = \epsilon = 0 \text{ at the wall.}$$

These relations contain the following dimensionless variables: $x^+ = x_n v_\tau/\nu$, $v_\tau = (\nu(\partial v_t/\partial x_n)_w)^{1/2}$, and $\mathrm{Re}_t = k^2/(\nu\epsilon)$($x_n$ is the distance between the (x, y) position and the nearest fixed wall, and v_t is the velocity component tangential to that wall).

After nondimensionalization of the dependent and independent variables (with the help of H, $\Delta T = T_h - T_c$, $g\beta$, and ν), the solution of Eqs. (1) only depends on two characteristic numbers: the Prandtl number (Pr) and the Rayleigh number (Ra $= g\beta\Delta TH^3\ \mathrm{Pr}/\nu^2$). Calculations were made for both air (Pr = 0.71) and water (Pr = 7.0). The equations and boundary conditions give a solution that is centrosymmetric with respect to the cavity center. Therefore only half of the domain was calculated, applying the symmetry boundary conditions at $x = H/2$. The application of these boundary conditions is straightforward: Whenever an unknown with $x > H/2$ appears in the discretization, the value from the corresponding symmetric position with $x < H/2$ is substituted.

In order to solve the equations numerically, the spatial derivatives in the equations are discretized with the finite volume method on a staggered grid in the conventional way. The convection terms are discretized with either the hybrid scheme or the QUICK scheme. The hybrid scheme locally replaces the second-order central scheme by the first-order upwind scheme if the so-called mesh Reynolds number (i.e., $u\Delta x/\nu$ or $v\Delta y/\nu$) exceeds the value 2. The QUICK scheme approximates the convection flux through the side of a finite volume by fitting a parabola through three, not necessarily uniformly spaced, grid points (two upwind and one downwind point). In the present calculations the iteration procedure to solve the equations diverged if QUICK was used for the k and ϵ equations. Therefore QUICK results presented in this study actually only applied QUICK to the u, v, and T equations, whereas the hybrid scheme was applied to the k and ϵ equations.

A strongly nonuniform grid was used, positioning the x coordinates of the u unknowns and the y coordinates of the v unknowns according to

$$\frac{x_i}{H} = \frac{1}{2}\left(1 + \frac{\tanh[\alpha_1(i/i\max - 1/2)]}{\tanh(\alpha_1/2)}\right) \qquad i = 0, 1, \ldots, i\max$$

$$\frac{y_j}{H} = \frac{j}{j\max} - \frac{1}{2\pi}\sin\left(2\pi\frac{j}{j_{\max}}\right) \qquad j = 0, 1\ldots, j\max.$$

Here α_1 is given by $\alpha_2 = \alpha_1/\sinh(\alpha_1)$; for example we take $\alpha_2 = 1.5 \times 10^{-2}$ in the calculations for Ra $= 10^{11}$, whereas smaller α_2 values (giving even more grid refinement along the vertical walls) are used for larger Rayleigh numbers. For the largest Rayleigh number we considered (10^{20}) α_2 was set to 1.5×10^{-6}. The x and y coordinates of the scalar unknowns are taken as $(x_i + x_{i+1})/2$ and $(y_j + y_{j+1})/2$, respectively.

Table 1 Numerical accuracy for air at Ra = 10^{13} with standard k-ϵ model

scheme	grid	$\overline{Nu}$	$\frac{v_{\max}}{\sqrt{g\beta\Delta TH}}$	$\frac{\nu_{t,\max}}{\nu}$	$\frac{u_{\max}}{\sqrt{g\beta\Delta TH}}$	$\frac{H}{\Delta T}\left[\frac{\partial T}{\partial y}\right]_c$
hybrid	40×40	1690	0.131	479	0.00720	0.351
	80×80	1730	0.127	509	0.00695	0.352
	160×160	1736	0.126	509	0.00686	0.359
QUICK	40×40	1713	0.128	474	0.00689	0.372
	80×80	1739	0.126	504	0.00676	0.364
	160×160	1740	0.125	507	0.00680	0.366

An unsteady fully implicit time integration was performed to obtain the steady solution at large time. For each time step the discretized transport equations are iteratively solved by a line-Gauss-Seidel method. Alternating Gauss-Seidel sweeps are made from the west to east side and from the east to west side of the computational domain. After each sweep the pressure is calculated from a pressure correction equation (i.e., a discretized Poisson equation). The equation is solved by the MICCG solver (Modified Incomplete Choleksi Conjugate Gradient solver).

The calculation starts with a certain initial solution at $t = 0$ and the time integration is performed until a steady final solution is reached. For the initial solution we either take a previously obtained steady solution for a different Rayleigh number or we take the steady solution at the same Rayleigh number, but interpolated from a coarser grid. A convenient time step turned out to be $\Delta t\sqrt{g\beta\Delta TH}/H = 0.25$; a larger time step could lead to divergence of the numerical procedure. The steady solution is obtained after oscillations with a typical frequency of $fH/\sqrt{g\beta\Delta TH} = 0.05$–$0.09$ (depending on the turbulence model, Ra and Pr) have decayed. These are probably decaying internal gravity waves. The solution was considered to be converged to the steady state if during at least 1000 time steps the solution at some characteristic values did not change in 6 significant digits (among which the averaged wall heat transfer, the maximum vertical and horizontal velocity, and the vertical gradient of the center stratification). At each time level the Gauss-Seidel sweep procedure was stopped when both the pressure correction and the net heat flux through the boundaries were below a small criterion, or if 5 sweeps were made. In general about 5000 time steps were needed to reach the converged steady state.

Table 1 verifies the numerical accuracy of the results for air at Ra $= 10^{13}$ with the standard k-ϵ model, refining the grid to 40×40, 80×80, and 160×160 points, respectively ($\alpha_2 = 1.5 \times 10^{-3}$). Five characteristic quantities are given: the averaged wall heat transfer ($\overline{\mathrm{Nu}}$), the maximum vertical velocity and turbulent viscosity at half the cavity height, the maximum horizontal velocity at half the cavity width, and the vertical gradient of the thermal stratification at the cavity center. The averaged Nusselt number is defined by $\overline{\mathrm{Nu}} = \int_0^1 \mathrm{Nu}\ d(y/H)$, with $\mathrm{Nu} = -(H/\Delta T)(\partial T/\partial x)_w$. In the horizontal direction at half the cavity height, the 160×160 grid gives about 40 points in the core and about 60 points in each vertical boundary layer (with about 22 points between the wall and the position of the maximum vertical velocity). Table 1 shows that the results indeed seem to become grid independent for an increasing number of grid points. It is noted that even the coarse 40×40 grid gives a good accuracy. As differences between successive grids are smaller with the QUICK scheme than with the hybrid scheme, QUICK is slightly superior. The small difference is due to the fact that the solution is dominated by the vertical boundary layers; the large vertical convection and the alignment of the grid lines with the main boundary layer flow causes the false diffusion in the first-order hybrid scheme to be small. The results to be presented in the sequel typically used 60×60

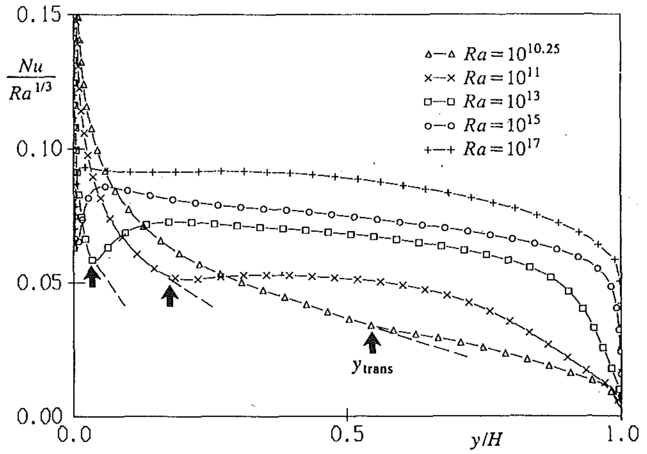

Fig. 1 Wall heat transfer for air at increasing Rayleigh number (Chien model)

points for Rayleigh numbers up to 10^{13} and 120×120 points for larger Rayleigh numbers.

The highest Rayleigh number we tried to calculate was 10^{20} for air and 10^{15} for water. With the standard k-ϵ model indeed a steady solution could be obtained at 10^{20}. In contrast to this, with the low-Reynolds-number models the low-frequency oscillations no longer decayed for $\mathrm{Ra}\geq10^{17}$. These oscillations also remained if the time step was refined up to $\Delta t\sqrt{g\beta\Delta TH/H}=1/32$. Further grid refinement (i.e., finer than 120×120 points) is required to decide whether this really refers to a mathematical bifurcation of the solution (e.g., a Hopf bifurcation from a steady to a periodic solution). Moreover, if it indeed is a bifurcation it remains to be checked whether its appearance also has a physical meaning; it might be that a low-frequency instability is generated in the flow, which is not modeled by the turbulence model.

3 Transition Effects

The low-Reynolds-number terms, which are meant to damp the turbulence, become active when the turbulence-based Reynolds number ($\mathrm{Re}_t=k^2/\nu\epsilon$) is small. This is always the case in the inner layer. It is also the case in the outer layer during the transition. As a consequence of the damping effect, low-Reynolds-number models give a later transition than the standard k-ϵ model (i.e., at a higher Rayleigh number or at a higher y/H position in the boundary layer along the hot wall). In the outer layer, the finding of the turbulent scalings requires that the full turbulent state be reached, i.e., transition effects (or low-Reynolds-number effects) must be absent. In particular for the Jones and Launder model, the Rayleigh number has to be increased quite far (beyond 10^{15}) before the full turbulent state is reached. For water the situation is even worse, as its transition starts at a Rayleigh number that is approximately 100 times larger than for air.

Figure 1 shows the development of the wall heat transfer along the hot cavity wall for increasing Rayleigh number, as obtained for air with the Chien model. The sudden increase of the wall heat transfer beyond a critical height (y_{trans}) indicates the start of the laminar to turbulent boundary layer transition. If the Rayleigh number is increased, y_{trans} moves to $y=0$.

A more detailed analysis of the transition regime (see Henkes, 1993) shows that the solution with the low-Reynolds-number models can be nonunique. No nonuniqueness was found for larger Rayleigh numbers in the fully turbulent regime. Because in the present study we are mainly interested in the full turbulent regime, an early transition with the low-Reynolds-number models may be achieved by triggering the boundary layer. We indeed obtained an earlier transition by prescribing some turbulent kinetic energy at the initial part of the boundary layer. With the help of this triggering the turbulent scalings were already obtained at lower Rayleigh numbers.

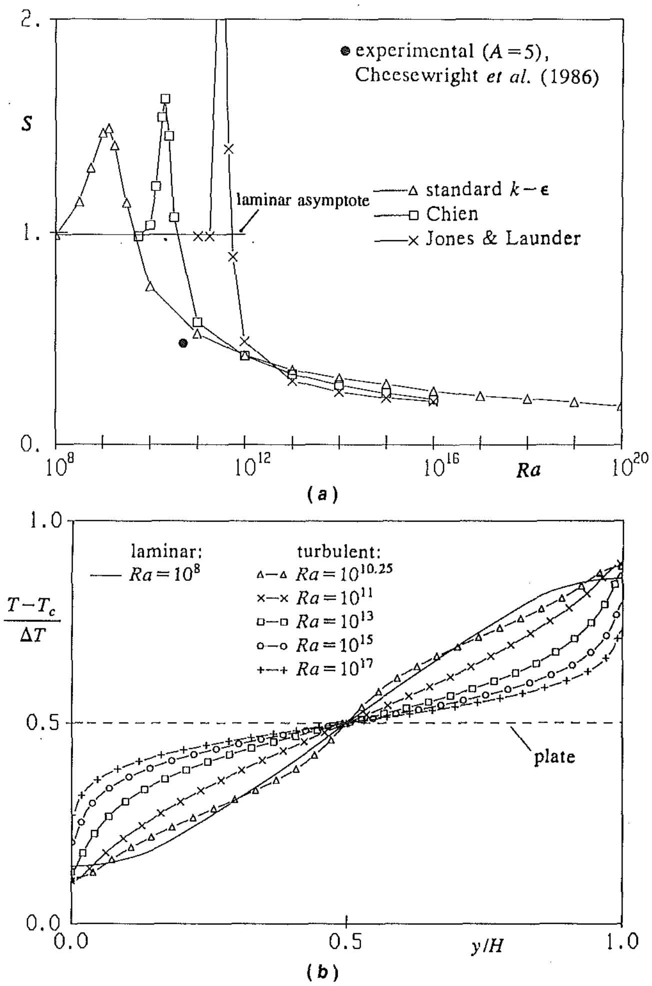

Fig. 2 Stratification for air: (a) gradient at the cavity center, (b) at half the cavity width (Chien model)

The scalings as will be derived in the next sections are most clearly detected with the standard k-ϵ model, because this model gives an early transition, even without triggering. The results with the low-Reynolds-number models in the next sections were all obtained without triggering of the transition, implying that, due to the late transition, small transition effects are even still present at the highest Rayleigh numbers we calculated. We verified, however, that if the low-Reynolds-number models were triggered, the turbulent scalings can be detected as clearly as for the standard k-ϵ model. Moreover, the scalings found turn out to be almost independent of the k-ϵ model used.

4 Comparison of the Cavity With the Plate

The vertical gradient of the temperature stratification in the cavity center ($S=(H/\Delta T)\partial T/\partial y$) for air at increasing Rayleigh number is shown in Fig. 2(a). S follows the laminar asymptote up to $\mathrm{Ra}_{\mathrm{trans}}$, after which it increases and reaches a maximum in the first part of the transition regime. The stratification strongly decreases in the second part of the transition regime until the fully turbulent asymptote is reached. Figure 2(b) gives the stratification at half the cavity width, as obtained with the Chien model for air at increasing Rayleigh number. The figure shows that the sudden increase of the gradient stratification for those Rayleigh numbers at the start of the transition is only a local behavior at heights close to $y=H/2$. For the larger Rayleigh numbers (10^{15}–10^{20}) we calculated with the standard

k–ϵ model that the turbulent asymptote for S decreases with increasing Rayleigh number according to $\text{Ra}^{-1/16}$. Figure 2(a) also gives an experimental value for S, as measured by Cheesewright et al. (1986) for air at $\text{Ra} = 5 \times 10^{10}$ in an $A = 5$ cavity. This value is close to the prediction of the k–ϵ model in the square cavity; both the experiment and the k–ϵ model have already reached the turbulent regime at $\text{Ra} = 5 \times 10^{10}$, whereas the low-Reynolds-number models give a later transition. Maybe, however, the good agreement between the measuring point and the standard k–ϵ model is fortuitous, as the stratification is known to be very sensitive to the realized experimental boundary conditions on the horizontal walls and on the front and back wall.

Figure 2(b) shows that the core of the cavity becomes almost isothermal for large Rayleigh numbers, with the exception of the parts of the core close to the horizontal walls. In the case of a *total* isothermal core the remaining difference between the cavity boundary layer and the boundary layer along the plate in an isothermal environment would be solely due to the presence of the horizontal boundary layers in the cavity. If we assume that the asymptotic theory of Gill (1966) for the laminar cavity flow (which was verified to be correct by Henkes, 1990) can also the applied to the turbulent cavity flow, the influence of these horizontal boundary layers on the development of the vertical cavity boundary layers vanishes in the limit $\text{Ra} \rightarrow \infty$. Gill's theory also says, however, that the core stratification is such that the normal velocity at the edge of the vertical cavity boundary layer is symmetric with respect to half the cavity height. Therefore the core can never become isothermal over the whole height, because this would give an *in*flow of mass at the boundary layer edge for all heights. The horizontal flow at the outer edge of the vertical boundary layer along the cavity walls and along the plate will thus remain essentially different, even for very high Rayleigh numbers.

5 Rayleigh Number Dependence

To derive the scalings for the turbulent flow in the cavity, the Rayleigh number dependence of different quantities in the calculated solutions of the Reynolds equations (1) are examined. The Ra dependence of a quantity ϕ is written as $\alpha \text{Ra}^{\gamma}$, with $\gamma = (\text{Ra}/\phi)[\partial\phi/\partial\text{Ra}]$. If γ becomes a constant in the limit $\text{Ra} \rightarrow \infty$, the proper scaling is found. Because the stratification in the core of the cavity is small, we expect that the scalings for the turbulent flow in the cavity will show a close analogy with the scalings for the turbulent boundary layer along the plate in the isothermal environment. Such an analogy would imply that the Ra scalings for the cavity approximately follow from the Ra_y scalings for the plate (see Henkes, 1991) by simply replacing y by H in Ra_y.

The scalings are determined in different regions of the cavity: (i) the inner layer (i.e., the part of the vertical boundary layer between the wall and the position of the maximum velocity); (ii) outer layer (i.e., the part of the vertical boundary layer beyond the position of the maximum velocity); (iii) core region. The resulting γ values are summarized in Table 2. The table also gives the scalings for the laminar cavity flow. The γ values for the turbulent flow only *approximately* give the proper scalings, as they could only be determined for Rayleigh numbers up to 10^{17} for the low-Reynolds-number models and up to 10^{20} with the standard k–ϵ model. The values may still show some Rayleigh number dependence when the Rayleigh number is further increased. The γ values as given for the inner layer quantities in the turbulent regime are not expected to be the right limits for $\text{Ra} \rightarrow \infty$, because we found for the plate that the inner layer quantities had not even reached limiting values at $\text{Ra}_y = 10^{25}$ (Henkes, 1991). Therefore only "best-fit" scalings seem to exist in the inner layer, which hold for a limited range of Rayleigh numbers.

Table 2 Rayleigh-number dependence

region	quantity	laminar	turbulent
inner layer	Nu	$Ra^{1/4}$	$\sim Ra^{3/8}$
	c_f	$Ra^{-1/4}$	$\sim Ra^{-1/4}$
	$\dfrac{v_{\max}}{\sqrt{g\beta\Delta TH}}$	Ra^{0}	$\sim Ra^{-1/24}$
	$x_{v\max}/H$	$Ra^{-1/4}$	$\sim Ra^{-1/8}$
outer layer	$\dfrac{\sqrt{2k_{\max}/3}}{v_{\max}}$	--	Ra^{0}
	$\dfrac{\delta}{H} = \dfrac{\psi_{x=H/2}}{v_{\max}H}$	$Ra^{-1/4}$	$\sim Ra^{-1/36}$
	$x_{k\max}/\delta$	--	Ra^{0}
	$\dfrac{v_{t,\max}}{v_{\max}\,\delta}$	--	Ra^{0}
core	S	Ra^{0}	$\sim Ra^{-1/16}$
	$\dfrac{u_{\max}}{\sqrt{g\beta\Delta TH}}$	$Ra^{-1/6}$	$\sim Ra^{-5/72}$

Figure 3 shows the Ra dependence of some quantities in the inner layer: the averaged wall heat transfer, the wall shear stress ($c_f = 2\nu(\partial v/\partial x)_w/(g\beta\Delta TH)$), and the maximum vertical velocity at $y = H/2$. The solid line in Fig. 3 (and in Figs. 4 and 5) denotes the laminar solution. This laminar solution was found from extrapolation of the laminar solution at lower Rayleigh numbers, using the scalings as summarized in Table 2. From the curve with the standard k–ϵ model for the averaged wall-heat transfer up to $\text{Ra} = 10^{20}$ in Fig. 3(a) it follows that γ in the expression $\overline{\text{Nu}} = \alpha \text{Ra}^{\gamma}$ remains dependent on the Rayleigh number. This suggests that a real scaling for $\overline{\text{Nu}}$ does not exist. For example, γ increases from about 3/8 at $\text{Ra} = 10^{12}$ up to 0.4 at $\text{Ra} = 10^{20}$. For the plate as well, we calculated that γ for Nu_y is about 3/8 at $\text{Ra}_y = 10^{12}$ and increases to 0.435 at $\text{Ra}_y = 10^{25}$. These γ values for the plate and cavity differ from the well-known 1/3-power wall heat transfer "law." We have to realize, however, that this experimental law was obtained for the plate at relatively low Rayleigh numbers. This experimental relation for the plate, $\overline{\text{Nu}} = 0.047\ \text{Ra}^{1/3}$, is also included in Fig. 3(a) (here $\overline{\text{Nu}}$ and Ra are based on twice the temperature difference between the hot wall and the isothermal environment). It is noted that the low-Reynolds-number models of Chien and Jones and Launder give a wall heat transfer that is much closer to this experimental curve than the standard k–ϵ model. In analogy with the $\text{Ra}_y^{-1/4}$ dependence of the wall shear stress at moderate Rayleigh numbers for the plate, the wall shear stress for the cavity in Fig. 3(b) also approximately scales with $\text{Ra}^{-1/4}$ in part of the turbulent regime. As for the wall heat transfer, γ for the wall shear stress does not become Ra independent: γ increases to -0.14 at $\text{Ra} = 10^{20}$. Also in analogy with the plate, the maximum vertical velocity at half the cavity height in Fig. 3(c) approximately scales with $(g\beta\Delta TH)^{1/2}\ \text{Ra}^{-1/24}$, which is close to the buoyant velocity scale $(g\beta\Delta TH)^{1/2}$. The buoyant velocity is the proper velocity scale for the laminar cavity flow. From Fig. 3 we conclude that for all the inner layer quantities $\phi = \alpha \text{Ra}^{\gamma}$ the kind of k–ϵ model used has only a small effect on γ, but a larger effect on α.

The scaling of the outer layer is illustrated in Fig. 4. As for the plate, also for the turbulent cavity, $v_{\max}$ turns out to be the proper velocity scale in the outer layer of the cavity. This is checked for $(2k_{\max}/3)^{1/2}$ at half the cavity height in Fig. 4(a). The proper length scale in the outer layer becomes clear from Figs. 4(b) and (c). Figure 4(b) shows the Ra dependence of δ/H. The boundary layer thickness δ is defined by $\delta(y) = \psi(H/2, y)/v_{\max}(y)$ (here ψ is the stream function with $\psi = 0$ at the wall). The Ra dependence for δ/H in the cavity closely resembles the Ra_y dependence for δ/y along the plate, namely $\delta/H \div \text{Ra}^{1/36}$ for the cavity and $\delta/y \div \text{Ra}_y^{0}$ for the plate. Figure 4(c) checks for $x_{k\max}$ (the position of $k_{\max}$) at half the cavity

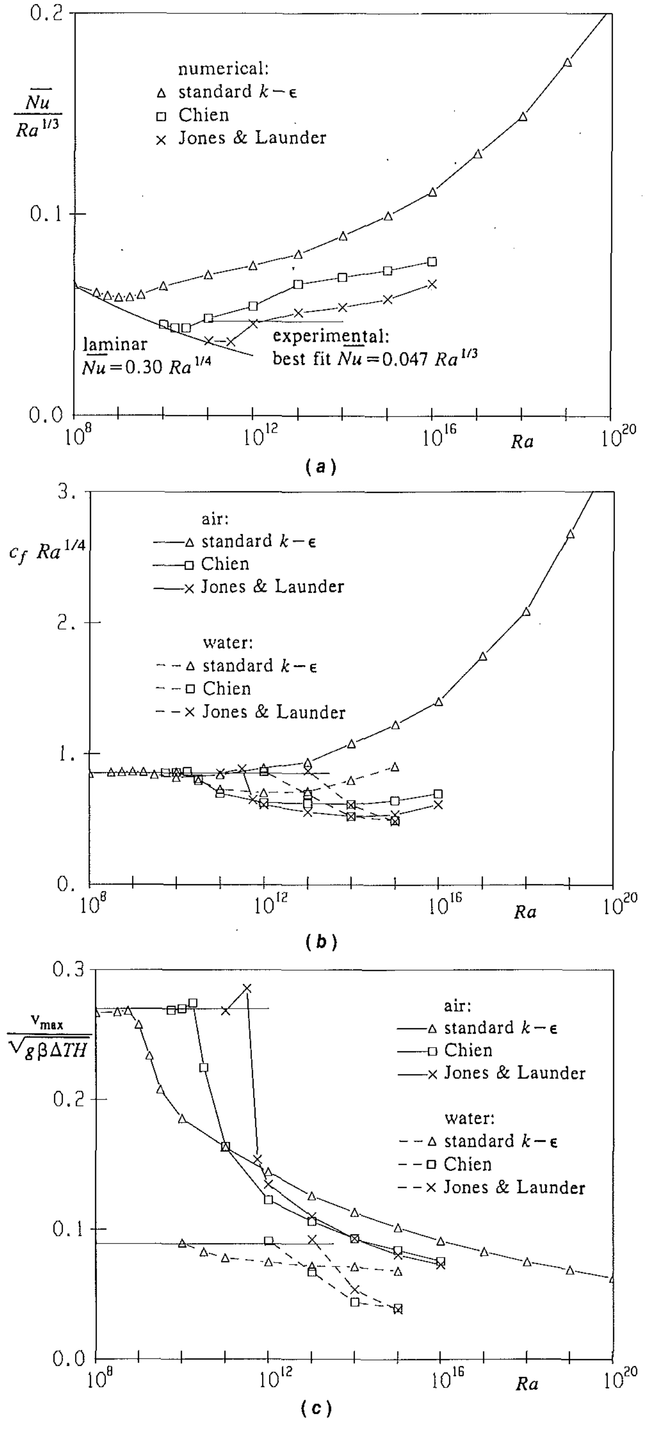

Fig. 3 Rayleigh-number dependence of some quantities in the inner layer: (*a*) averaged wall-heat transfer, (*b*) wall-shear stress at $y = H/2$, (*c*) maximum vertical velocity at $y = H/2$

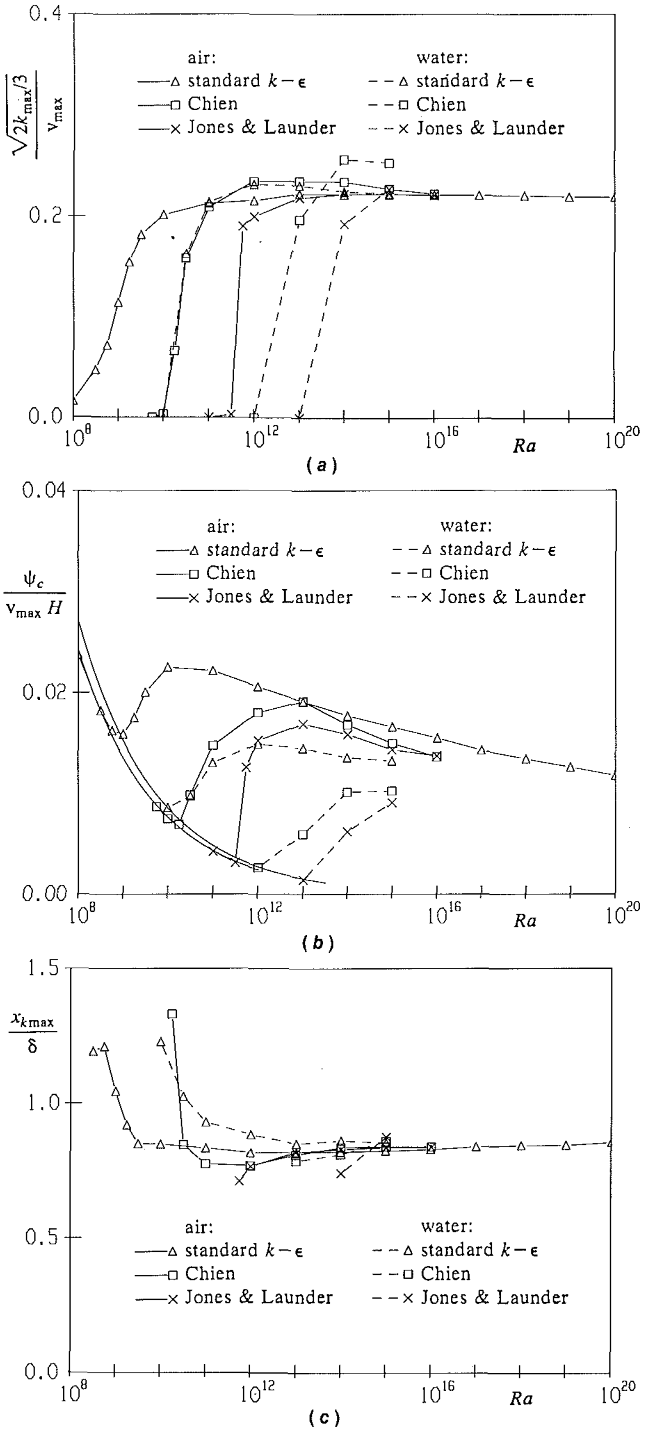

Fig. 4 Rayleigh-number dependence of some quantities in the outer layer: (*a*) maximum turbulent kinetic energy at $y = H/2$, (*b*) stream function at the center, (*c*) position of the maximum turbulent kinetic energy at $y = H/2$ with $\delta = \psi_c/(v_{max}H)$

height that δ is the proper length scale in the outer layer. For the plate we found that model differences in the outer layer quantities, scaled with v_{max} and δ, are small at sufficiently large Reyleigh numbers and only due to differences in the high-Reynolds-number constants. Moreover the scaled outer layer quantities for the plate are independent of the Prandtl number. The same behavior as for the plate is found here for the outer layer quantities in the turbulent cavity flow, as shown in Figs. 4(*b*) and 4(*c*). Differences between the models for the scaled outer layer quantities in the cavity almost disappear for increasing Rayleigh number, because the differences in the high-Reynolds-number constants are small.

The scaling for the core is illustrated in Fig. 5, showing the maximum horizontal velocity at $x = H/2$ (the behavior of the stratification gradient S was already given in Fig. 2*a*). In contrast to the laminar flow, for the turbulent flow in the cavity the maximum horizontal velocity does not fall in the horizontal boundary layer, but in the core. The Rayleigh number dependence of the horizontal core velocity is such that the mass transported through the upper half of the core ($\div H(g\beta\Delta TH)^{1/2}\mathrm{Ra}^{-5/72}$) balances the mass transported through the vertical boundary layer at half the cavity height ($\div v_{max}\delta$).

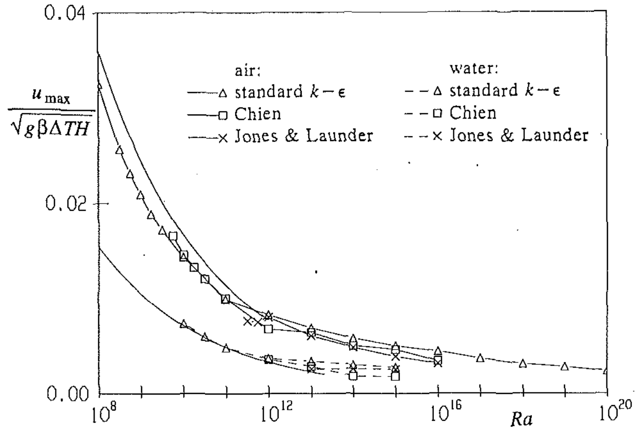

Fig. 5 Rayleigh-number dependence in the core; maximum horizontal velocity at $x = H/2$

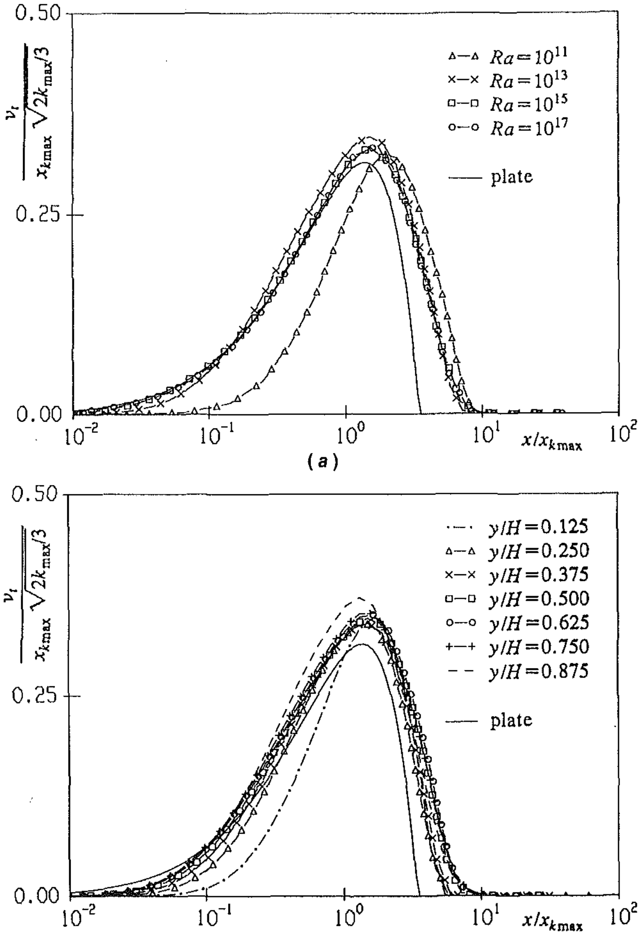

(*a*)

(*b*)

Fig. 6 Outer-layer profiles for the turbulent viscosity (air, Chien model): (*a*) at $y = H/2$ for increasing Rayleigh number, (*b*) at $Ra = 10^{13}$ for increasing height

6 Height Dependence

In the previous section it was found that the turbulent scalings with respect to Ra in the cavity closely resemble the turbulent scalings with respect to Ra_y for the plate, if y in Ra_y is replaced by H: Differences are only of the order $Ra^{-1/36}$. In contrast to this, less good agreement is found between the scalings in the cavity with respect to y/H on the one hand, and Ra_y scalings for the plate on the other hand. Actually, the resemblance is restricted to about $y/H = 0.3$ at the beginning of the turbulent boundary layer along the hot cavity wall; for larger y/H values the y/H scalings for the cavity are not simply found from the Ra_y scalings for the plate by splitting Ra_y into $Ra \times (y/H)^3$ and fixing Ra. For example, the maximum vertical velocity along the plate in an isothermal environment increases monotonically with the height, whereas the calculated maximum vertical velocity for the cavity reaches a maximum at a certain height and decreases to zero at $y = H$. Because this maximum is already reached at a height below $y = H/2$, the difference between the boundary layer along the cavity wall and along the plate is not just a local effect close to $y = H$ caused by the cavity corner: The difference must be caused by the small stratification in the core of the cavity. In the previous section we already mentioned that this small stratification is related to a horizontal velocity in the core, which is centro-symmetric with respect to half the cavity height. The mass leaving the boundary layer at $y > H/2$ corresponds to the decrease of the maximum vertical velocity. The same kind of difference between the cavity and the plate, as just shown for the maximum vertical velocity, also occurs for most of the other characteristic quantities (c_f, $k_{\max}$, $\nu_{t,\max}$). Only the y/H dependence for the wall heat transfer of the cavity gives a closer resemblance with the plate over almost the whole cavity height.

The height dependence of the Ra-scaled quantities complicates the application of the wall functions to the cavity flow. The wall functions for the turbulent natural convection flow were derived for the hot vertical plate in an isothermal envi-

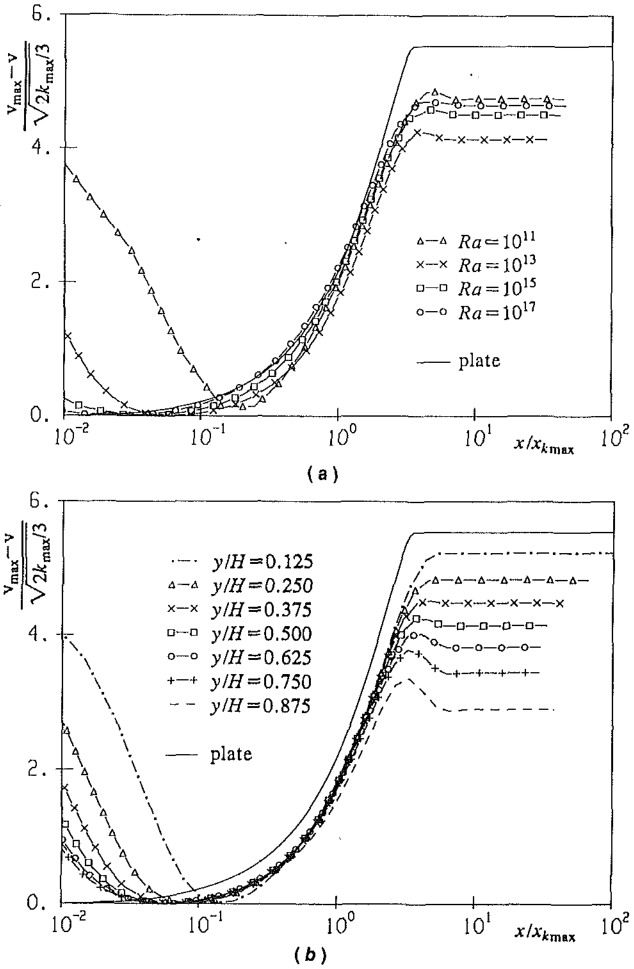

(*a*)

(*b*)

Fig. 7 Outer-layer profiles for the vertical velocity (air, Chien model): (*a*) at $y = H/2$ for increasing Rayleigh number, (*b*) at $Ra = 10^{13}$ for increasing height

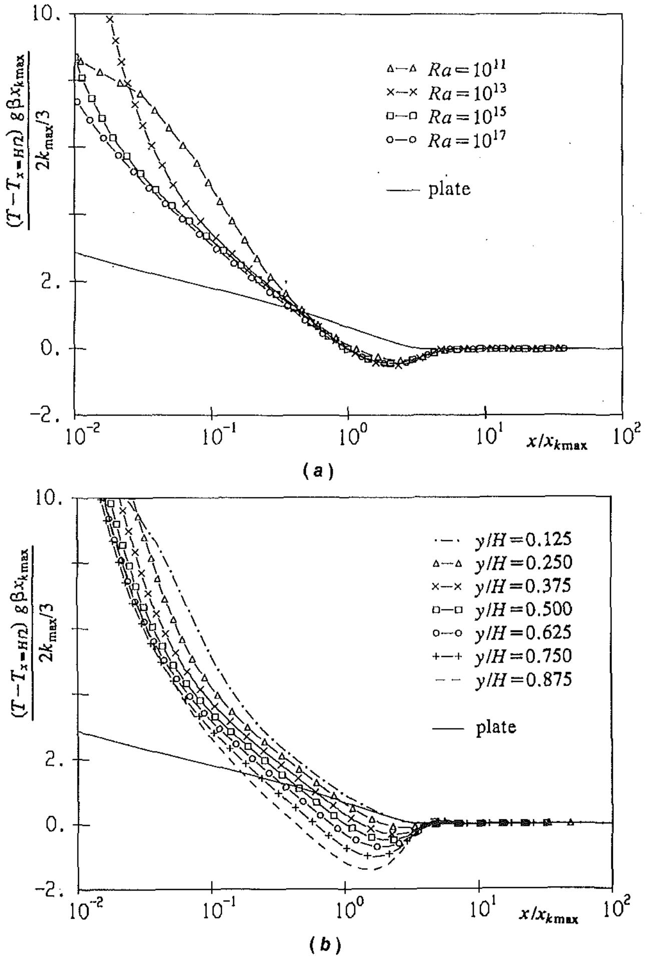

Fig. 8 Outer-layer profiles for the temperature (air, Chien model): (*a*) at $y = H/2$ for increasing Rayleigh number, (*b*) at $Ra = 10^{13}$ for increasing height

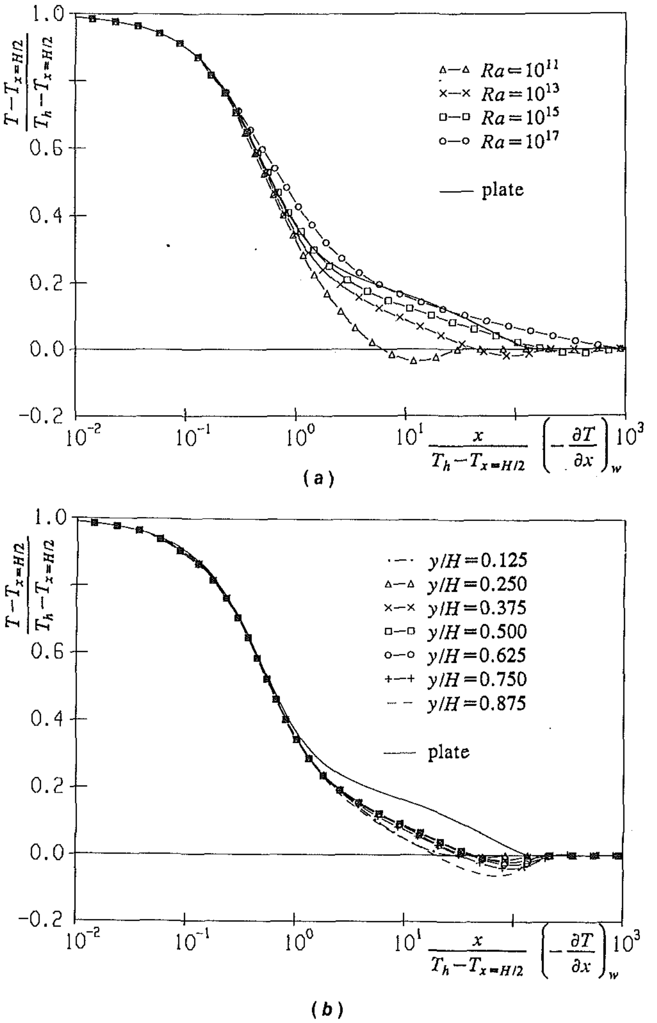

Fig. 9 Inner-layer profiles for the temperature (air, Chien model): (*a*) at $y = H/2$ for increasing Rayleigh number, (*b*) at $Ra = 10^{13}$ for increasing height

ronment in earlier studies (Henkes and Hoogendoorn, 1990; Henkes, 1991). Checking whether these wall functions also apply to the cavity (actually a boundary layer flow in a stratified environment) is the natural convection counterpart of checking whether the forced convection wall functions, as originally derived for a plate in an oncoming flow with zero pressure gradient, also apply to a plate in a flow with nonzero pressure gradient. To verify whether the natural convection wall functions apply with a reasonable accuracy to the cavity, first of all requires the finding of a velocity scale and a length scale in the outer layer of the vertical boundary layers in the cavity that not only give Ra independent but also give reasonably y/H independent profiles. The numerical solutions show that these scalings (being functions of Ra and y/H) indeed exist: $v_{\text{out}}=(2k_{\max}/3)^{1/2}$ is a proper velocity scale and $x_{\text{out}}=x_{k\max}$ is a proper length scale ($x_{k\max}$ is the position of the maximum turbulent kinetic energy). Figure 6, for example, shows that the profiles for the turbulent viscosity almost coincide if they are nondimensionalized with these scalings. Moreover, the profiles are close to the large-Rayleigh-number solution for the plate. We checked that these are also proper outer layer scalings for most of the other quantities: $(v_{\max}-v)/v_{\text{out}}$, k/v_{out}^2, and $\epsilon x_{\text{out}}/v_{\text{out}}^3$. As shown in Fig. 7 deviations for the scaled velocity only occur at the outer edge. Part of these deviations are due to the regions with flow reversal appearing at the outer edge of the boundary layer in the cavity. Only the scaled temperature profiles, $(T-T_{x=H/2})g\beta x_{\text{out}}/v_{\text{out}}^2$ versus x/x_{out}, do not coincide for increasing height (Fig. 8*b*). The scaled temperature profiles in the cavity almost coincide for increasing Rayleigh number (Fig. 8*a*), but these profiles do show a difference with the profile for the plate. This difference with the plate seems to be caused by the regions with temperature deficit that occur at the outer edge of the boundary layer in the cavity. Hence, the cavity calculations show that for all variables (except the temperature) the scalings $(2k_{\max}/3)^{1/2}$ and $x_{k\max}$ are more generally applicable than the scalings $v_{\max}$ and δ as appear in the wall functions for the plate.

For the plate we verified that the velocity profile $\frac{v}{v_{\max}}$ versus $\frac{x}{v_{\max}}\left(\frac{\partial v}{\partial x}\right)_w$ and the temperature profile $\frac{T-T_\infty}{T_h-T_\infty}$ versus $\frac{-x}{T_h-T_\infty}\left(\frac{\partial T}{\partial x}\right)_w$ are approximately independent of Ra_y in the inner layer of the plate, as long as $Ra_y \leq 10^{15}$. These profiles practically coincide in the inner layer of the boundary layers along the cavity walls as well (for the cavity ∞ is replaced by $H/2$, i.e., the local temperature difference is taken, $T_h-T(H/2, y)$). This is illustrated in Fig. 9 for the temperature profile, as calculated with the Chien model for air. Figure 9(*a*) shows the temperature at half the cavity height for increasing Rayleigh number, whereas Fig. 9(*b*) shows the temperature at $Ra=10^{13}$ for increasing height. These profiles for the cavity are also close to the results for the plate (as shown in the figure at the local Ra_y value at half the height of the cavity with $Ra = 10^{13}$). In analogy with the plate, the velocity profiles coincide as well (not shown here) and they also have the laminar scalings in part of the turbulent regime, because c_f turned out to scale with $\mathrm{Ra}^{-1/4}$ in part of the turbulent regime (Fig. 3*b*), whereas the maximum vertical velocity closely scales with the laminar velocity scale $(g\beta\Delta TH)^{1/2}$ (Fig. 3*c*).

8 Conclusions

Numerical solutions of the Reynolds equations were obtained for the turbulent natural convection flow of air and water in a heated square cavity at high Rayleigh numbers. The numerical accuracy was verified to be good by refining the grid up to 160×160 points. Steady solutions with the standard k-ϵ model were obtained for air up to $\mathrm{Ra} = 10^{20}$, whereas steady solutions with the low-Reynolds-number k-ϵ models could only be obtained up to $\mathrm{Ra} = 10^{17}$. With the low-Reynolds-number models transition effects occur over a relatively large Rayleigh number range. The standard k-ϵ model gives an early transition and quickly reaches the fully turbulent state, which clearly shows the turbulent scalings. For sufficiently large Rayleigh numbers these turbulent scalings (more precisely: the γ values in the expression $\phi = \alpha \mathrm{Ra}^{\gamma}$) are almost independent of the k-ϵ model used.

The turbulent scalings in the vertical boundary layers of the cavity show a large analogy with the scalings and wall functions for the boundary layer along a hot vertical plate in an isothermal environment. The scalings in the cavity with respect to Ra differ at most with a 1/36 power in Ra from the scalings with respect to Ra_y for the plate, when the coordinate y in Ra_y is replaced by H. On the contrary, the scalings in the cavity with respect to y/H follow from the Ra_y scalings for the plate only up to about $y/H = 0.3$. In particular $v_{\max}$ and δ, which are the outer layer scalings for the plate, are only the proper outer layer scalings for the cavity with respect to Ra but not with respect to y/H. Proper outer layer scalings for the cavity with respect to both Ra and y/H are $\sqrt{2k_{\max}/3}$ for the velocity and the x position of $k_{\max}$ for the length. The best-fit inner layer scalings as found for the velocity and temperature for the plate also hold for the cavity inner layer. As was also found for the plate, the wall heat transfer for the cavity does not follow the $\mathrm{Ra}^{1/3}$ dependence as measured at moderate Rayleigh numbers. The thermal stratification in the core of the cavity decreases with increasing Rayleigh number.

Accurate experiments at high Rayleigh numbers are required to verify further the scalings in the cavity as derived with k-ϵ models. It is also of interest to repeat the scaling analysis with more advanced turbulence models, like the differential Reynolds stress models.

Acknowledgments

The research of one of the authors (RAWMH) has been made possible by a fellowship from the Royal Netherlands Academy of Arts and Sciences.

References

Cheesewright, R., King, K. J., and Ziai, S., 1986, "Experimental Data for the Validation of Computer Codes for the Prediction of Two-Dimensional Buoyant Cavity Flows," ASME HTD-Vol. 60, pp. 75-81.

Chien, K.-Y., 1980, "Predictions of Channel and Boundary Layer Flows With a Low-Reynolds-Number Two-Equation Model of Turbulence," Paper No. AIAA-80-0134.

Chien, K-Y., 1982, "Predictions of Channel and Boundary-Layer Flows With a Low-Reynolds-Number Turbulence Model," *AIAA Journal*, Vol. 20, pp. 33-38.

De Vahl Davis, G., and Jones, I. P., 1983, "Natural-Convection in a Square Cavity; a Comparison Exercise," *International Journal of Numerical Methods in Fluids*, Vol. 3, pp. 227-248.

Gill, A. E., 1966, "The Boundary-Layer Regime for Convection in a Rectangular Cavity," *Journal of Fluid Mechanics*, Vol. 26, pp. 515-536

Henkes, R. A. W. M., and Hoogendoorn, C. J., 1989, "Comparison of Turbulence Models for the Natural Convection Boundary Layer Along a Heated Vertical Plate," *International Journal of Heat and Mass Transfer*, Vol. 32, pp. 156-169.

Henkes, R. A. W. M., 1990, "Natural-Convection Boundary Layers," PhD Thesis, Delft University of Technology, The Netherlands.

Henkes, R. A. W. M., and Hoogendoorn, C. J., 1990a, "On the Stability of the Natural Convection Flow in a Square Cavity Heated From the Side," *Applied Scientific Research*, Vol. 47, pp. 195-220.

Henkes, R. A. W. M., and Hoogdendoorn, C. J., 1990b, "Numerical Determination of Wall Functions for the Turbulent Natural Convection Boundary Layer," *International Journal of Heat and Mass Transfer*, Vol. 33, pp. 1087-1097.

Henkes, R. A. W. M., 1991, "Scaling of the Turbulent Natural-Convection Boundary Layer Along a Hot Vertical Plate," *Proceedings of the 8th Symposium on Turbulent Shear Flows*, Munich, Paper No. 24-2.

Henkes, R. A. W. M., Van der Vlugt, F. F., and Hoogendoorn, C. J., 1991, "Natural-Convection Flow in a Square Cavity Calculated With Low-Reynolds-Number Turbulence Models," *International Journal of Heat and Mass Transfer*, Vol. 34, pp. 377-388.

Henkes, R. A. W. M., 1993, "Application of k-ϵ Models to the Transition of Natural-Convection Boundary Layers," *Proceedings of the International Conference on Near-Wall Turbulent Flows*, R.M.C. So et al., eds., Elsevier, pp. 177-186.

Henkes, R. A. W. M., and Hoogendoorn, C. J., eds., 1993, "Turbulent Natural Convection in Enclosures," *Proceedings of the EUROTHERM/ERCOFTAC Workshop*, published by EETI, Paris.

Jones, W. P., and Launder, B. E., 1972, "The Prediction of Laminarization With a Two-Equation Model of Turbulence," *International Journal of Heat and Mass Transfer*, Vol. 15, pp. 301-314.

Le Quéré, P., 1987, "Etude de la Transition à l'Instationarité des Ecoulements de Convection Naturelle en Cavité Verticale Différentiellment Chauffée par Méthodes Spectrales Chebyshev," PhD Thesis, University of Poitiers, France.

Paolucci, S., and Chenoweth, D. R., 1989, "Transition to Chaos in a Differentially Heated Vertical Cavity," *Journal of Fluid Mechanics*, Vol. 201, pp. 379-410.

Structure of Round, Fully Developed, Buoyant Turbulent Plumes

Z. Dai
Graduate Student Research Assistant.

L.-K. Tseng
Research Fellow.

G. M. Faeth
Professor.
Fellow ASME

Department of Aerospace Engineering,
The University of Michigan,
Ann Arbor, MI 48109-2118

An experimental study of the structure of round buoyant turbulent plumes was carried out, emphasizing conditions in the fully developed (self-preserving) portion of the flow. Plume conditions were simulated using dense gas sources (carbon dioxide and sulfur hexafluoride) in a still air environment. Mean and fluctuating mixture fraction properties were measured using single-and two-point laser-induced iodine fluorescence. The present measurements extended farther from the source (up to 151 source diameters) than most earlier measurements (up to 62 source diameters) and indicated that self-preserving turbulent plumes are narrower, with larger mean and fluctuating mixture fractions (when appropriately scaled) near the axis, than previously thought. Other mixture fraction measurements reported include probability density functions, temporal power spectra, radial spatial correlations and temporal and spatial integral scales.

Introduction

Scalar mixing of round buoyant turbulent plumes in a still environment is an important fundamental problem that has attracted significant attention since the classical study of Rouse et al. (1952). However, recent work suggests that more information about the turbulence properties of scalar quantities within buoyant turbulent flows is needed to address turbulence/radiation interactions in fire environments (Kounalakis et al., 1991). In particular, the response of radiation to turbulent fluctuations is affected by the moments, probability density functions, and temporal and spatial correlations of scalar property fluctuations. In turn, scalar property fluctuations can be represented by mixture fraction (defined as the mass fraction of source fluid) fluctuations, using state relationships found from conserved-scalar concepts for both nonreactive and flame environments (Bilger, 1976; Sivathanu and Faeth, 1990). Thus, the objective of the present investigation was to measure mixture fraction statistics in round buoyant turbulent plumes in still environments. In order to simplify interpretation of the results, the experiments emphasized fully developed buoyant turbulent plumes, where effects of the source have been lost and both mean and fluctuating properties become self-preserving (Tennekes and Lumley, 1972).

The discussion of previous studies will be brief because several reviews of turbulent plumes have appeared recently (Kotsovinos, 1985; List, 1982; Papanicolaou and List, 1987, 1988). The earliest work concentrated on the scaling of flow properties within fully developed turbulent plumes (Rouse et al., 1952; Morton, 1959; Morton et al., 1956). Measurements of mean properties within plumes generally have satisfied the resulting scaling relationships; however, there are considerable differences among various determinations of centerline values, radial profiles, and flow widths (Abraham, 1960; George et al., 1977; Kotsovinos, 1985; List, 1982; Ogino et al., 1980; Peterson and Bayazitoglu, 1992; Shabbir and George, 1992; Rouse et al., 1952; Zimin and Frik, 1977). Aside from problems of experimental methods in some instances, List (1982) and Papanicolaou and List (1987, 1988) attribute these differences to problems of reaching fully developed plume conditions.

Two parameters are helpful for estimating when turbulent plumes become self-preserving. The first of these is the distance from the virtual origin normalized by the source diameter, $(x-x_o)/d$. Based on results for nonbuoyant round turbulent jets, values of $(x-x_o)/d$ greater than ca. 40 and 100 should be required for self-preserving profiles of mean and fluctuating properties, respectively (Tennekes and Lumley, 1972). By these measures, all past measurements over the cross section of plumes, which invariably used buoyant jets for the plume source, probably involve transitional plumes, e.g., they generally are limited to $(x-x_o)/d \leq 62$, aside from some limited measurements in liquids by Papantoniou and List (1989). The main reason for not reaching large values of $(x-x_o)/d$ for plumes, similar to jets, is that scalar properties decay much faster for plumes, e.g., proportional to $(x-x_o)^{-5/3}$ for plumes rather than $(x-x_o)^{-1}$ for jets. Thus, it is difficult to maintain reasonable experimental accuracy far from the source within the plumes. A contributing factor is that plume velocities are relatively small in comparison to jets so that controlling room disturbances far from the source is more difficult for plumes.

The second parameter useful for assessing conditions for self-preserving buoyant turbulent plumes is the distance from the virtual origin normalized by the Morton length scale, $(x-x_o)/l_{\rm M}$. The Morton length scale is defined as follows for a round plume having uniform properties at the source (Morton, 1959; List, 1982):

$$l_{\rm M} = (\pi/4)^{1/4}(\rho_\infty d u_o^2/(g|\rho_o-\rho_\infty|))^{1/2} \tag{1}$$

where an absolute value has been used for the density difference in order to account for both rising and falling plumes. Large values of $(x-x_o)/l_{\rm M}$ are required for buoyancy-induced momentum to become large in comparison to the source momentum so that the buoyant features of the flow are dominant. The ratio of $l_{\rm M}$ to d is proportional to the source Froude number, defined as follows (List, 1982):

$$\mathrm{Fr}_o = (4/\pi)^{1/4} l_{\rm M}/d = (\rho_\infty u_o^2/(g|\rho_o-\rho_\infty|d))^{1/2} \tag{2}$$

The source Froude number quantifies the initial degree of buoyant behavior of the source, e.g., $\mathrm{Fr}_o = 0$ for a purely buoyant source. Papanicolaou and List (1987, 1988) suggest that buoyancy-dominated conditions for mean and fluctuating quantities are reached for $(x-x_o)/l_{\rm M}$ greater than ca. 6 and 14, respectively. A greater proportion of existing data for mean properties exceed this criterion; however, the effect of transitional plume behavior (in terms of $(x-x_o)/d$) on these observations raises questions about the adequacy of this criterion.

Naturally, in instances where reaching self-preserving con-

Contributed by the Heat Transfer Division and presented at the National Heat Transfer Conference, Georgia, August 8-11, 1993. Manuscript received by the Heat Transfer Division March 1993; revision received July 1993. Keywords: Fire/Flames, Natural Convection, Turbulence. Associate Technical Editor: Y. Jaluria.

ditions for mean properties is questionable, it is likely that turbulent properties are transitional. Thus, the turbulence measurements of George et al. (1977) and Shabbir and George (1992) for x/d in the range 8–25, normally would not be thought to represent self-preserving conditions. The turbulence measurements of Papanicolaou and List (1987, 1988) for x/d in the range 12–62 probably represent transitional plumes as well with results at larger distances, x/d, of 20–62, subject to additional uncertainties due to systematic instrument errors (Papanicolaou and List, 1988). In contrast, the measurements of Papantoniou and List (1989) were carried out at x/d = 105, which should be within the self-preserving region; however, unusually large concentation fluctuations were observed, which they attribute to the large Schmidt numbers of the liquid plumes used in these tests, i.e., molecular mixing was inhibited at small scales that still could be resolved by their instrument system. Thus, the relevance of the Papantoniou and List (1988) turbulence measurements to gaseous plumes of interest for radiation processes in flame environments is questionable.

The preceding discussion suggests that existing measurements of mean and fluctuating properties within plumes probably involve either transitional plumes or liquid plumes exhibiting large Schmidt number effects that are not typical of gases. Thus, the objective of the present investigation was to complete measurements of the mean and fluctuating mixture fraction properties of buoyant turbulent plumes in gases, emphasizing conditions within the self-preserving turbulent plume region where the specific features of the source have been lost. The mixture fraction properties considered included mean and fluctuating values, probability density functions, temporal power spectra, radial spatial correlations, and temporal and spatial integral scales. The experiments involved source flows of carbon dioxide and sulfur hexafluoride in still air at atmospheric pressure and temperature, in order to provide a straightforward specification of the buoyancy flux within the test plumes. This approach yielded downward-flowing, negatively buoyant plumes. Measurements of mixture fraction properties were undertaken using laser-induced iodine fluorescene (LIF).

Experimental Methods

Test Apparatus. A sketch of the experimental apparatus is shown in Fig. 1. In order to minimize room disturbances and contamination of adjacent areas by iodine vapor, the plumes were observed in a double enclosure contained within a large, high-bay test area. The outer enclosure (3000 × 3000 × 3400 mm high) had plastic side walls with a screen across the top for air inflow in order to compensate for removal of air entrained by the plume. The plume itself was within a smaller enclosure (1100 × 1100 × 3200 mm high) with plastic screen walls (square pattern, 630 wires/m with a wire diameter of 0.25 mm). The small enclosure was mounted on linear bearings and could be traversed in one direction using a stepping motor driven linear positioner (5 μm positioning accuracy) in order to accommodate rigidly mounted instrumentation. The plume flow was removed through 300-mm-dia ducts that were mounted on the floor at the four corners of the outer enclosure. The exhaust flow was controlled by a bypass/damper system in order to match plume entrainment rates and to minimize flow disturbances. All components that might contact iodine vapor were plastic, painted, or sealed in plastic wrap, in order to prevent corrosion.

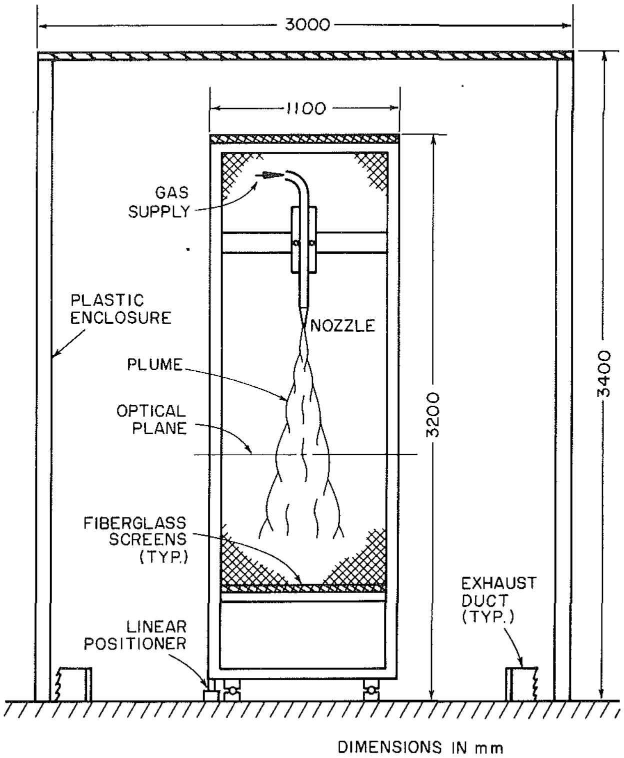

Fig. 1 Sketch of the buoyant turbulent plume apparatus

The plume sources consisted of rigid plastic tubes having inside diameters of 6.4 and 9.7 mm with flow straighteners at

Nomenclature

a, b = parameters in the Frenkiel function
d = source diameter
$E_f(n)$ = temporal power spectral density of f
f = mixture fraction
$F(r/(x-x_o))$ = scaled radial distribution of $\bar{f}$ in self-preserving region
Fr_o = source Froude number, Eq. (2)
g = acceleration of gravity
k_f = plume width coefficient, Eq. (8)
l_c = characteristic plume radius
l_f = characteristic plume radius based on mean mixture fraction
l_M = Morton length scale, Eq. (1)
n = frequency
PDF(f) = probability density function of mixture fraction
r = radial distance
Re_c = characteristic plume Reynolds number $= \bar{u}_c l_c/\nu_\infty$
Re_o = source Reynolds number $= u_o d/\nu_o$
u = streamwise velocity
x = streamwise distance
Δr = radial distance increment
Λ_{fr} = radial spatial integral scale of mixture fraction fluctuations
ν = kinematic viscosity
ρ = density
τ_f = temporal integral scale of mixture fraction fluctuations

Subscripts

c = centerline value
o = initial value or virtual origin location
∞ = ambient value

Superscripts

$(\overline{\ \ })$ = time-averaged mean value
$(\overline{\ \ })'$ = root-mean-squared fluctuating value

the inlet and length-to-diameter ratios of 50:1. The outside surface of the tubing exit was chamfered at an angle of 30 deg to reduce the separation disturbances of the plume-entrained flow. The source could be traversed in the vertical direction (0.25 mm positioning accuracy) to allow measurements at different streamwise positions. The source flows were either carbon dioxide or sulfur hexafluoride, stored under pressure in commercial cylinders. Gas flow rates were controlled and measured using pressure regulators in conjunction with critical flow orifices. All flow rates were calibrated using wet test meters. After metering and adding iodine vapor, the flow passed through a flexible plastic tube having a length-to-diameter ratio of 800 in order to obtain a uniform composition at the source exit.

The flow was seeded with iodine vapor by passing a portion of it though a bed of iodine crystals (bed diameter and depth of 100 × 200 mm). The bed operated at room temperature and the flow was saturated with iodine at the exit of the bed; therefore, the concentration of iodine vapor varied with changes of room temperature. Thus, the LIF signal was monitored with the fraction of flow entering the iodine bed periodically adjusted to control signal levels. The iodine crystals were reagent grade, with initial flake shapes having diameters of 2-8 mm and thicknesses of 0.5 mm.

Instrumentation. Mixture fractions were measured using LIF, similar to earlier studies of wall plumes in this laboratory (Lai and Faeth, 1987). The LIF signal was produced by the unfocused beam (beam diameter at the e^{-2} points of 1.5 mm) of an argon-ion laser having an optical power of roughly 1800 mW at the green (514.5 nm) line. This wavelength is absorbed by iodine and causes it to fluoresce at longer wavelengths in the visible yellow portion of the spectrum (Hiller and Hanson, 1990). The laser beam was horizontal and intersected the plume axis at roughly 1500 mm above the floor of the enclosure. The operation of the laser beam was monitored using two laser power meters: one measuring laser power before crossing the flow to detect laser power variations, the other measuring laser power after passing through the flow in order to correct the laser beam power at the measuring locations for absorption by iodine vapor.

The fluorescence signals were measured using two detectors (Hamamatsu R269), one mounted rigidly and the other traversable along the laser beam to provide measurements of two-point spatial correlations. Since the plume source could be traversed horizontally and vertically, all points in the flow could be addressed for two-point measurements. The fluorescence signals were observed at right angles to the laser beam with f4.1 collecting lenses having diameters of 80 mm. The apertures of the detectors were selected to give measuring volumes having diameters of 1 mm with lengths of 1.5 mm set by the laser beam diameter. The LIF signal was separated from light scattered at the laser line using long-pass optical filters (cut-off wavelengths of 520 nm). The detector outputs were amplified and then low-pass filtered to control alias signals using sixth-order Chebychev filters having break frequencies of 500 Hz. The signals were then sampled using an a/d converter and transferred to a computer for processing and storage. The detector signals were monitored using a digital oscilloscope as well.

Both the absorption and the LIF signals were calibrated based on measurements across the source exit, by mixing the source flow with air to vary the mixture fraction. These tests showed that fluctuations of iodine seeding levels were less than 1 percent. The LIF signal was not saturated for present conditions and varied linearly with laser power. The LIF signals also varied linearly with the number of iodine molecules present per unit volume (i.e., with the partial density of iodine) while reabsorption of scattered light was small (less than 10 percent). Thus, the relationship between the LIF signal level and the mixture fraction for signal processing was obtained from the state relationship for an ideal gas mixture. This relationship was nearly linear for the carbon dioxide source flow due to modest density variations but had significant nonlinearities for the sulfur hexafluoride source flow where the density variation was substantial. These calibrations were checked periodically by diverting the source flow through a plastic tube whose exit was mounted temporarily just above the measurement location. Final processing of the signals accounted for both absorption of the laser beam by iodine vapor and laser beam power variations.

Table 1 Summary of test conditions[a]

Source Properties	CO_2	SF_6
Density (kg/m^3)	1.75	5.87
Kinematic viscosity (mm^2/s)	8.5	2.6
Diameter (mm)	9.7	6.4
Average velocity (m/s)	1.74	1.89
Reynolds number	2000	4600
Froude number	7.80	3.75
Morton length scale, ℓ_M/d	7.34	3.53
Virtual origin, x_o/d	12.7	0.0

[a] Flow directed vertically downward in still air with an ambient pressure, temperature, density and kinematic viscosity of 99 ± 0.5 kPa, 297 ± 0.5 K, 1.16 kg/m^3 and 14.8 mm^2/s. Source passage length-to-diameter ratios of 50:1.

Differential diffusion between the source gas (carbon dioxide or sulfur hexafluoride) and the iodine vapor can be a significant source of error for LIF measurements. Effects of differential diffusion were evaluated analogous to the approach described by Stårner and Bilger (1983), noting that the binary diffusivities of carbon dioxide, sulfur hexafluoride, and iodine in air at normal temperature and pressure are 14.7, 8.6, and 7.7 mm^2/s (Bird et al., 1960). This yielded maximum errors of mean mixture fractions due to differential diffusion for the carbon dioxide and sulfur hexafluoride plumes less than 2 and 0.2 percent, respectively, with comparable values for mixture fraction fluctuations. The present measurements corroborated these results, based on the observation that the source gas had little effect on mixture fraction properties in the self-preserving region of the flow.

Gradient broadening errors were negligible (less than 1 percent) at the locations where measurements were made. Thus, signal sampling times were controlled to maintain experimental uncertainties (95 percent confidence) along the axis at less than 5 percent for mean mixture fractions and 10 percent for mixture fraction fluctuations, both being repeatable well within these ranges. These uncertainties were maintained up to $r/(x-x_o) = 0.15$ but increased at larger radial distances, roughly inversely proportional to $\bar{f}$.

Test Conditions. The test conditions for the carbon dioxide and sulfur hexafluoride plumes are summarized in Table 1. An attempt was made to keep source Froude numbers near current estimates of asymptotic Froude numbers in order to enhanced the development of the buoyancy properties of the flow (George et al., 1977). Additionally, source Reynolds numbers were made as large as possible, while satisfying the Froude number requirement, in order to enhance rates of development toward self-preserving turbulent plume conditions. Nevertheless, the Reynolds number of the carbon dioxide flow was relatively low, 2000, causing the virtual origin to be displaced a substantial distance downstream from the source exit. For $(x-x_o)/d$ greater than 87, where self-preserving plumes were reached, the turbulence microscales of mixture fraction fluctuations (the Batchelor scales) were less than 350 μm. Thus, although the previously stated experimental uncertainties were achieved, the spatial resolution of the LIF system was not

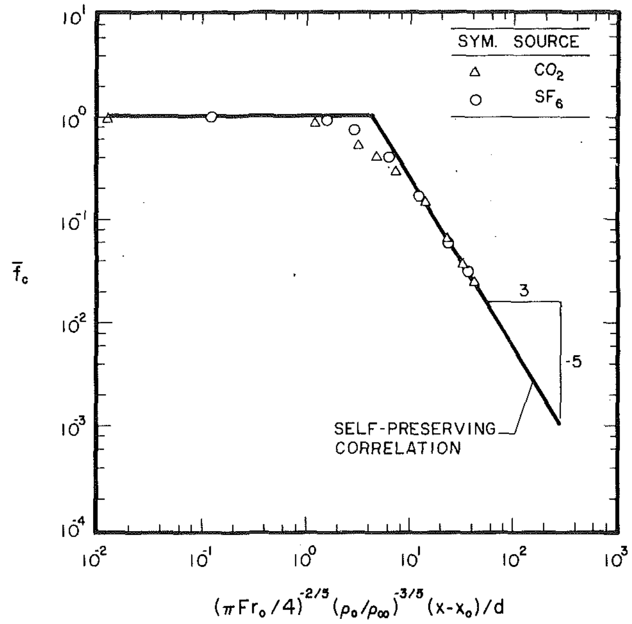

Fig. 2 Mean mixture fractions along the axis

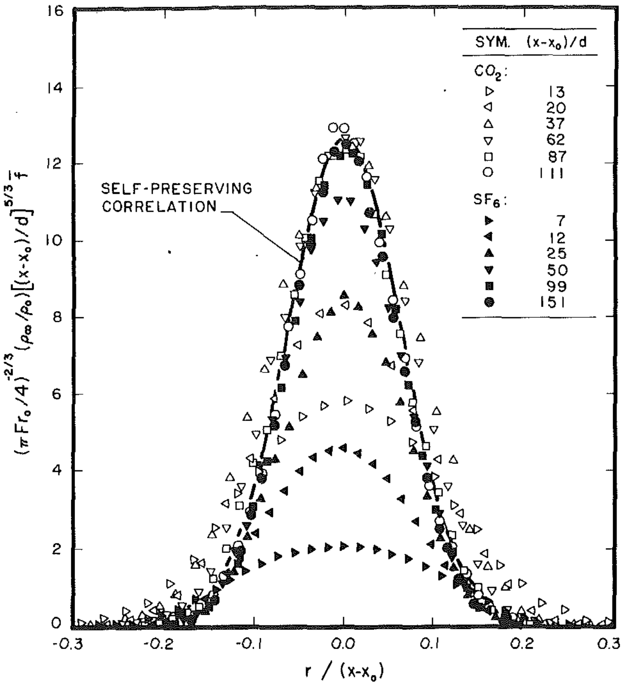

Fig. 3 Development of radial profiles of mean mixture fractions

sufficient to resolve the smallest scales of the turbulence within the self-preserving region of the plumes.

Self-Preserving Scaling

The state relationship for density as a function of mixture fraction is needed to relate the present measurements to properties in the self-preserving region. Assuming an ideal gas mixture, the exact state relationship for density becomes:

$$\rho = \rho_\infty/(1 - f(1 - \rho_\infty/\rho_o)) \qquad (3)$$

Additionally, far from the source in the self-preserving region, $f \ll 1$, and Eq. (3) can be linearized as follows:

$$\rho = \rho_\infty + f\rho_\infty(1 - \rho_\infty/\rho_o), \qquad f \ll 1 \qquad (4)$$

The measurements involved mean and fluctuating mixture fraction properties at various streamwise positions. Mean properties were then scaled in terms of the self-preserving variables of fully developed turbulent plumes, as follows (List, 1982):

$$\bar{f} = (\pi \mathrm{Fr}_o/4)^{2/3}(\rho_o/\rho_\infty)((x - x_o)/d)^{-5/3}F(r/(x - x_o)) \qquad (5)$$

$F(r/x - x_o))$ represents the appropriately scaled radial profile function of mean mixture fraction, which becomes a universal function in the self-preserving region far from the source where Eq. (4) applies. Equation (5) was used to extrapolate measurements of mean mixture fractions along the axis in order to identify the virtual origin that yielded the best fit of the data. As noted earlier, the location of the virtual origin is controlled by source properties like turbulence levels, ρ_o/ρ_∞, and the initial Froude numbers; however, it was beyond the scope of the present investigation to quantitatively study these relationships.

Finally, although velocity measurements were not made during the present study, it was of interest to find characteristic plume Reynolds numbers, $\mathrm{Re}_c = \bar{u}_c l_c/\nu_\infty$. This was done by adopting the expressions of Rouse et al. (1952) for $\bar{u}_c$ and l_c at self-preserving conditions to yield:

$$\mathrm{Re}_c = 0.43((x - x_o)/(d\,\mathrm{Fr}_o))^{2/3}u_o d/\nu_\infty \qquad (6)$$

Results and Discussion

Mean Properties. The variation of mean mixture fractions along the axis of the two test plumes is illustrated in Fig. 2. The measurements are plotted in terms of the variables of Eq. (5). In addition, lines showing the asymptotic behavior of the present measurements at small and at large distances from the source are shown on the plot. The limiting behavior at small distances, $(x - x_o)/d \ll 1$, is $\bar{f}_c = 1$ which the measurements satisfy by definition. The limit at large distances follows from Eq. (5) for conditions where $\bar{f}_c \ll 1$ and Eq. (4) applies. Then $F(0) = 12.6$ independent of source flow properties, based on the best fit of present measurements, and $\bar{f}_c \sim ((x - x_o)/d)^{-5/3}$. This latter condition is reached for values of the abscissa of Fig. 2 greater than 10, which implies $(x - x_o)/d$ and $(x - x_o)/l_M$ on the order of 100 and 10, respectively. Within the intermediate region, where the abscissa of Fig. 2 is in the range 0.1-10, results depend on source properties like Re_o, Fr_o, and ρ_o/ρ_∞ so that the differences in this region seen in Fig. 2 for the two sources are anticipated. Naturally, this implies that conditions required to reach self-preserving plume behavior depend on these variables as well.

A more complete picture of the development of transitional plumes toward self-preserving conditions can be obtained from the radial profiles of mean mixture fractions for the two sources illustrated in Fig. 3. In this case, the scaling parameters of Eq. (5) are used so that the ordinate is equal to $F(r/x - x_o))$. The measurements are plotted for various streamwise distances with $(x - x_o)/d \geq 7$. The radial mean mixture fraction profiles show progressive narrowing, with scaled values at the axis progressively increasing, as the streamwise distance increases. However, self-preserving conditions are observed for the present measurements when $(x - x_o)/d \geq 87$, which also corresponds to $(x - x_o)/l_M \geq 12$. The subsequent variation of the profiles with streamwise distance is well within experimental uncertainties over the range that was achieved during the present experiments: $87 \leq (x - x_o)/d \leq 151$ and $12 \leq (x - x_o)/l_M \leq 43$. This regime corresponds to characteristic plume Reynolds numbers of 2500-4200, which are reasonably high for unconfined turbulent flows. For example, this range is comparable to the highest characteristic wake Reynolds numbers where measurements of turbulent wake properties have been reported, while turbulent wakes exhibit self-preserving turbulence properties at characteristic wake Reynolds numbers as low as 70 (Wu and Faeth, 1993). The actual streamwise distance required

Table 2 Summary of self-preserving turbulent plume properties[a]

Source	Medium	$(x-x_o)/d$	$(x-x_o)/\ell_M$	k_f^2	$\ell_f/(x-x_o)$	F(0)	$(\bar{f}'/\bar{f})_c$
Present study	gaseous	87-151	12-43	125	0.09	12.6	0.45
Papantoniou and List (1989)	liquid	105	24,33	---	0.08-0.09	---	0.64
Papanicolaou and List (1988)	liquid	22-62	9-62	80	0.11	14.3	0.40
Papanicolaou and List (1987)	liquid	12-20	> 5	80	0.11	11.1	0.40
Shabbir and George (1992)	gaseous	10-25	6-15	68	0.12	9.4	0.40
George et al. (1977)	gaseous	8-16	6-12	65	0.12	9.1	0.40

[a]Round turbulent plumes in still, unstratified environments. Range of streamwise distances are for conditions where quoted self-preserving properties were found from measurements over the cross section of the plumes. Entries are ordered in terms of decreasing k_f.

to reach self-preserving conditions for mean mixture fractions, however, is likely to vary with source properties. For example, larger values of ρ_o/ρ_∞ and lower source Reynolds numbers tend to retard development toward self-preserving conditions, based on present findings during preliminary tests, while larger source Froude numbers require larger values of $(x-x_o)/d$ in order to achieve values of $(x-x_o)/l_M$ where buoyancy dominates flow properties.

Within the self-preserving region, present radial profiles of mean mixture fractions are reasonably approximated by a Gaussian fit, similar to past work (Rouse et al., 1952; George et al., 1977; List, 1982; Papanicolaou and List, 1987, 1988; Shabbir and George, 1992) as follows:

$$F(r/(x-x_o)) = F(0)\exp\{-k_f^2(r/(x-x_o))^2\} \tag{7}$$

where

$$k_f = (x-x_o)/l_f \tag{8}$$

Thus, l_f represents the characteristic plume radius where $\bar{f}/\bar{f}_c = e^{-1}$. The best fit of the present data in the self-preserving region yielded $F(0) = 12.6$ and $k_f^2 = 125$. This yielded the correlation illustrated in Fig. 3, which is seen to be a good representation of the measurements in the self-preserving region, i.e., $(x-x_o)/d \geq 87$ and $(x-x_o)/l_M \geq 12$. This yields a value of $l_f/(x-x_o)$ of roughly 0.09, which is in good agreement with the values of 0.08–0.09 found by Papantoniou and List (1989) for measurements at large distances from the source, $(x-x_o)/d = 105$ and $(x-x_o)/l_M$ of 24 and 33.

The present values of normalized streamwise distance required to reach self-preserving conditions within round buoyant turbulent plumes are similar to past observations for round turbulent jets (Hinze, 1975; Tennekes and Lumley, 1972); however, they are substantially larger than streamwise distances reached during past measurements of the self-preserving properties of turbulent plumes using buoyant jet sources, aside from the study of Papantoniou and List (1989). This behavior is quantified in Table 2, where the range of streamwise distances considered for measurements of radial profiles of self-preserving plume properties, and the corresponding reported values of k_f^2, $l_f/(x-x_o)$, and $F(0)$ are summarized for representative recent studies and associated earlier work from the same laboratories. Past measurements generally satisfy the criterion for buoyancy-dominated flow, i.e., $(x-x_o)/l_M > 6$ (Papanicolaou and List, 1987, 1988). Aside from the measurements of Papantoniou and List (1989) and the present study, however, the other results were obtained at values of $(x-x_o)/d$ that normally are not associated with self-preserving conditions for jetlike sources. Somewhat like the tendency for transitional plume conditions to have broader profiles than the self-preserving regime in Fig. 3, the values of k_f^2 tend to increase progressively as the maximum streamwise position is increased—almost doubling over the range of conditions given in Table 2. This yields a corresponding reduction of characteristic plume radius of 30 percent, and an increase of the scaled mean mixture fraction at the axis of 30 percent, when approaching self-preserving conditions over the range considered in Table 2 (ignoring the unusually large value of $F(0)$ reported by Papanicolaou and List (1988), which is thought to be due to a systematic instrument error, as noted earlier). Discrepancies between transitional and self-preserving plumes of this magnitude have a considerable impact on the empirical parameters obtained by fitting turbulence models to measurements. For example, Pivovarov et al. (1992) suggest that the standard set of constants used in empirical turbulence models is inadequate based on the assumption of self-preserving plumes in conjunction with past measurements for transitional plumes; however, their predictions using standard constants are in fair agreement with the present measurements of self-preserving plume properties under the same assumptions.

Root-Mean-Square Fluctuations. Radial profiles of mixture fraction fluctuations at various streamwise distances are plotted in Fig. 4 for the two sources. Near the source, the profiles are rather broad and exhibit a dip as the axis is approached, much like the behavior of nonbuoyant jets (Becker et al., 1967; Papanicolaou and List, 1987, 1988). The profiles evolve, however, with both the width and the magnitude of the dip near the axis gradually decreasing as the streamwise distance is increased. Eventually, self-preserving behavior is reached at conditions similar to the self-preserving conditions for mean mixture fractions in Fig. 3, e.g., $(x-x_o)/d \geq 87$ and $(x-x_o)/l_M \geq 12$. This behavior is not surprising because self-preserving conditions for mean properties are a generally necessary condition for self-preserving conditions for turbulence properties (Tennekes and Lumley, 1972). Within the self-preserving region, present measurements can be correlated reasonably well by the following empirical relationship:

$$\bar{f}'/\bar{f}_c = 0.45\ \exp(-40(r/(x-x_o))^{2.5}) \tag{9}$$

Analogous to mean mixture fractions, the measurements of rms mixture fraction fluctuations of Papanicolaou and List (1987, 1988), Shabbir and George (1992), and George et al. (1977) are similar to transitional plumes in the latter stages of development. Thus, although these profiles do not exhibit a dip near the axis, they are broader in terms of $r/(x-x_o)$ than the present measurements in the self-preserving region. Additionally, Papanicolaou and List (1987, 1988), Shabbir and George (1992), and George et al. (1977) find $(\bar{f}'/\bar{f})_c = 0.40$, rather than 0.45 for the present measurements, as summarized in Table 2. On the other hand, Papantoniou and List (1989) measure $(\bar{f}'/\bar{f})_c$ of roughly 0.64 at conditions that should be within the self-preserving region; however, as discussed earlier, this large value probably is caused by the large Schmidt number of their liquid plumes, which inhibits small-scale mixing in comparison to plumes in gases.

The gradual disappearance of the dip in mixture fraction fluctuations is an interesting feature of the results illustrated

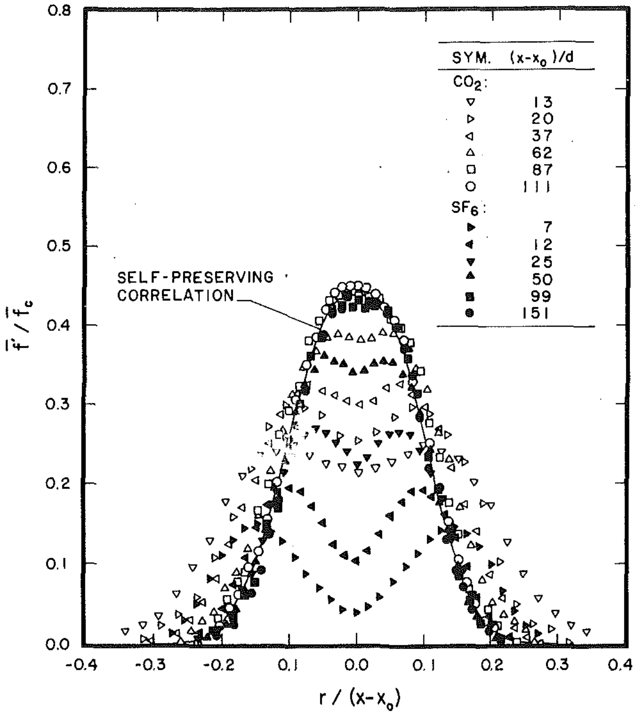

Fig. 4 Development of radial profiles of rms mixture fraction fluctuations

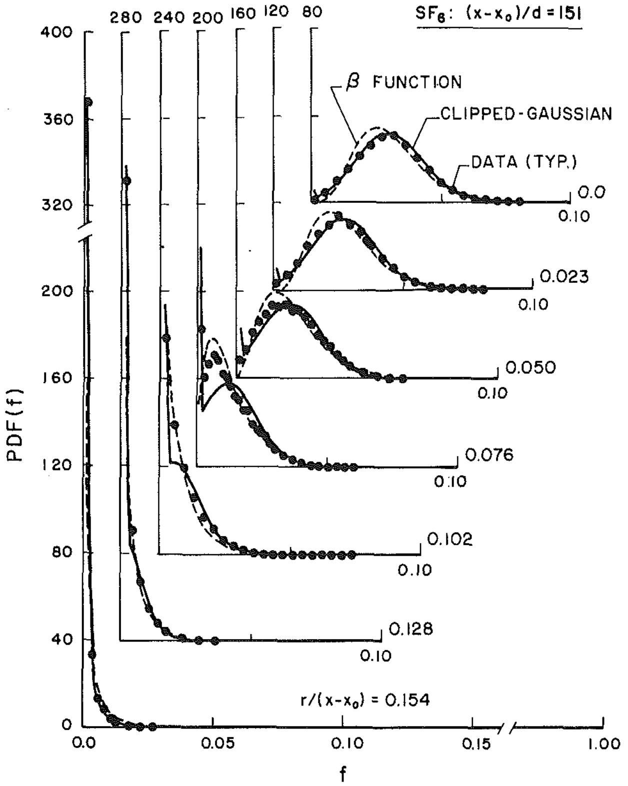

Fig. 5 Typical probability density functions of mixture fractions at self-preserving conditions: SF$_6$ soruce at $(x-x_o)/d$ = 151

in Fig. 4. The development of the flow from source conditions, where mixture fraction fluctuations are less than 1 percent, is certainly a factor in this behavior. However, the gradual disappearance of nonbuoyant dynamics as $(x-x_o)/l_M$ becomes large also is a factor. In particular, nonbuoyant jets have reduced mixture fraction fluctuations near the axis because turbulence production is small in this region in view of symmetry requirements (Becker et al., 1967; Papanicolaou and List, 1987, 1988). In contrast, effects of buoyancy provide turbulence production near the axis for plumes in spite of symmetry due to buoyant instability in the streamwise direction, i.e., the density approaches the ambient density in the streamwise direction. This added turbulence production accounts for increased mixture fraction fluctuation levels near the axis of plumes in comparison to jets in the self-preserving region, i.e., $(\bar{f}'/\bar{f})_c$ ca. 0.45 for plumes in comparsion to 0.15-0.18 for jets (Papanicolaou and List, 1987). Even maximum values of $\bar{f}'/\bar{f}_c$ in jets, ca. 0.25 at an $r/(x-x_o)$ of roughly 0.1, are substantially less than the maximum plume values (Papanicolaou and List, 1987). Thus, the contribution of buoyancy to turbulence is appreciable, with the large mixture fraction fluctuations of turbulent self-preserving plumes helping to explain the large radiation fluctuation levels observed in the plumes above buoyant turbulent diffusion flames (Kounalakis et al., 1991).

Probability Density Functions. Mean and fluctuating velocities are reasonably descriptive because the probability density functions of velocities in turbulent flows generally are well represented by a Gaussian distribution function that only has two moments. This is not the case for the probability density functions of mixture fracture, however, because the mixture fraction is limited to the finite range 0-1 by definition, so that finite range distribution functions must be used, e.g., the clipped-Gaussian function or the algebraically more convenient beta function; see Lockwood and Naguib (1975) for the properties of these two distributions. Thus, some typical probability density functions from present measurements are plotted along with these distribution in Fig. 5. Both distributions are defined by two moments; thus, the predicated distributions are based on the measured values of $\bar{f}$ and $\bar{f}'$ at each location considered.

The measured probability density functions illustrated in Fig. 5 are qualitatively similar to earlier measurements for flames, plumes, and jets (Kounalakis et al., 1991; Papanicolaou and List, 1987, 1988; Becker et al., 1967). At the axis, the probability density function is nearly Gaussian, although it still has a small spike at $f = 0$ representing some period when unmixed ambient fluid reaches the axis. With increasing radial distance, the spike at $f = 0$ increases and eventually dominates the distribution as the edge of the plume is approached. There is little to choose between representing the probability density functions by either clipped-Gaussian or beta functions although the ease of use of the beta function is helpful for reducing computation times during simulations (Lockwood and Naguib, 1975).

Temporal Power Spectral Densities. Temporal correlations, or temporal power spectral densities, which are their Fourier transform (Hinze, 1975; Tennekes and Lumley, 1972), must be known in order to simulate the temporal aspects of radiation fluctuations (Kounalakis et al., 1991). Some typical measurements of temporal power spectra for the sulfur hexafluoride plumes are illustrated in Fig. 6; results for the carbon dioxide plumes were similar. Spectra are plotted for $(x-x_o)/d$ in the range 25-151, considering radial positions over the full width of the flow at each streamwise position. The temporal spectra are relatively independent of radial position at at particular streamwise location. Similarly, the low-frequency portion of the spectra is relatively independent of streamwise distance when normalized in the manner of Fig. 6. However, there are systematic variations in the decaying portion of the spectra with streamwise distance that will be discussed next. Spectra of transitional plumes reported by Papanicolaou and List (1987, 1988) are qualitatively quite similar to the results illustrated in Fig. 6.

The decay of the spectra with increasing frequency is an interesting feature of the results illustrated in Fig. 6. The spectra initially decay according to the $-5/3$ power of frequency,

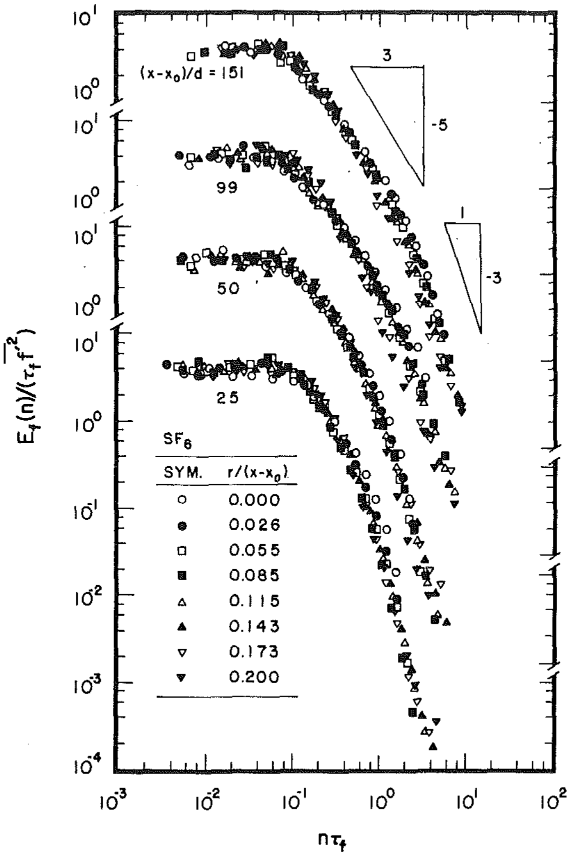

Fig. 6 Typical temporal power spectral densities of mixture fraction fluctuations: SF$_6$ source

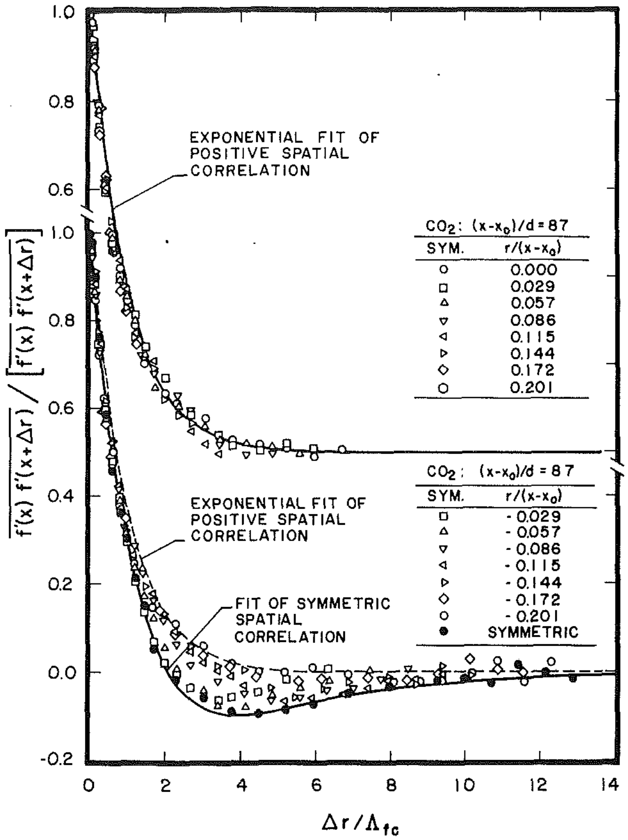

Fig. 7 Typical radial spatial correlations of mixture fraction fluctuations: CO$_2$ source

analogous to the well-known inertial region of the turbulence spectrum of velocity fluctuations which has been called the intertial-convective region for scalar property fluctuations (Tennekes and Lumley, 1972). Within this region, mixture fraction fluctuations simply are convected and effects of molecular diffusivities are small. This is followed by a region where the spectrum decays more rapidly, yielding a slope of roughly -3, that has been observed during several investigations of highly buoyant flows with molecular Prandtl/Schmidt numbers in the range 0.7–7, but not in nonbuoyant flows (Mizushima et al, 1979; Papanicolaou and List, 1987, 1988). Papanicolaou and List (1987) argue that this portion of the spectrum agrees with the behavior expected for the inertial-diffusive subrange, where the variation of the local rate of dissipation of mixture fraction fluctuations in buoyant flows is due to buoyancy-generated inertial forces rather than viscous forces. An effect of this type is plausible due to the progressive increase of the span of the inertial range as $(x-x_o)/d$ increases, e.g., the intersections of the $-5/3$ and -3 regions of the spectra occur at roughly $n\tau_f$ = 0.4, 0.8, 1.5, and 2.0 for $(x-x_o)/d$ = 25, 50, 99, and 151, respectively. This behavior is analogous to the anticipated reductions of microscales with increasing streamwise distance, which suggests a diffusive effect. However, understanding of the behavior of the spectra of buoyant turbulent flows in this region is very limited and clearly merits additional study. At higher frequencies, the mixture fraction microscale should be approached where the spectrum becomes small; unfortunately, existing measurements have had neither the spatial nor the temporal resolution needed to resolve this region.

Radial Spatial Correlations. Spatial correlations also must be known in order to simulate aspects of radiation fluctuations, due to effects of optical path lengths on radiation intensities (Kounalakis et al., 1991). Spatial correlations also are important fundamental properties of turbulence that have received significant attention in the past (Hinze, 1975; Tennekes and Lumley, 1972). Study of these properties was begun during the present investigation by measuring radial spatial correlations, which largely control radiation fluctuations in boundary layer flows, like plumes (Kounalakis et al., 1991).

The general properties of spatial correlations in turbulent shear flows vary depending on whether the two points considered are on the same or on opposites sides of planes or lines of symmetry. This orientation will be indicated for the present radial correlations by a coordinate system along the radial direction extending from $-\infty$ to ∞ with Δr always greater than zero and the left-most position denoting the position of the correlation. Thus, $r<0$ implies that both points are on the same side of the axis for $\Delta r < |r|$ and on the opposite side thereafter. If $r>0$, then both points are always on the same side of the axis. Finally, Corrsin and Uberoi (1950) introduced symmetric lateral spatial correlations for jets, where the two points are spaced equally on either side of the axis (at $-\Delta r/2$ and $\Delta r/2$), thus, there is only one correlation of this type at each streamwise position.

The present measurements of two-point radial and symmetric correlations are illustrated in Fig. 7. These results are for carbon dioxide plumes at $(x-x_o)/d$ = 87, which is within the self-preserving region. Other measurements within the self-preserving region were similar. The measurements are presented in two groups, with results for $r>0$ at the top, and results for $r<0$ and symmetric correlations at the bottom. The distance increment is normalized by Λ_{frc}; however, Λ_{fr} is relatively constant over the range of the measurements. The results for $r>0$ in Fig. 7 exhibit an exponential decay; however, this is an artifact of experimental limitations, e.g., the region near $\Delta r = 0$ should have a nonexponential (quadratic) behavior in terms of Δr as the microscale limit is approached (Becker et al., 1967; Hinze, 1975; Tennekes and Lumley, 1972). This is not seen in Fig. 7 because the present spatial resolution was not adequate to resolve the smallest scales. In terms of $\Delta r/\Lambda_{frc}$ the exponential fit of the radial spatial resolution was not adequate to resolve the smallest scales. In terms of $\Delta r/\Lambda_{frc}$ the exponential fit of the radial spatial correction is quite simple:

$$\overline{f'(r)f'(r+\Delta r)} \;/\; \overline{f'(r)}\;\overline{f'(r+\Delta r)} = \exp(-\Delta r/\Lambda_{frc}) \qquad (10)$$

where it should be understood that $\Delta r > 0$ as defined earlier. The results in Fig. 7 show that Eq. (10) provides a good fit of the measurements whenever both points of the correlation are on the same side of the axis, e.g., $r > 0$ or $\Delta r < |r|$ when $r < 0$. This approximation is effective because Λ_{fr} is relatively constant over the range of the measurements, as noted earlier. Notably, a radial spatial correlation at the plume axis in the self-preserving region, reported by Papantoniou and List (1989), has essentially the same shape as Eq. (10).

The symmetric spatial correlation provides the other limiting behavior of the radial spatial correlations seen in Fig. 7. These correlations exhibit a Frenkiel function shape as follows: similar to the exponential fit at small Δr; crossing to a region of negative correlations at $\Delta r/\Lambda_{frc} = 2.1$, which corresponds to $\Delta r/(x-x_o) = 0.07$; reaching a maximum negative value of -0.1 near $\Delta r/\Lambda_{frc} = 4$, which corresponds to $\Delta r/(x-x_o) = 0.13$; and finally decaying from the negative side toward zero as $\Delta r/\Lambda_{frc}$ becomes large. This behavior can be represented by the following empirical fit:

$$\overline{f'(\Delta r/2)f'(-\Delta r/2)} \;/\; \overline{f'(\Delta r/2)^2} = (1-0.11(\Delta r/\Lambda_{frc})^3)\exp(-\Delta r/\Lambda_{frc}) \qquad (11)$$

The present behavior is qualitatively similar to symmetric correlations observed in nonbuoyant jets, except that the negative correlation region is reached sooner in jets, $\Delta r/(x-x_o)$ in the range 0.04–0.06, and the maximum negative correlation is larger in jets, in the range -0.10 to -0.18 (Corrsin and Uberoi, 1950; Becker et al., 1967).

The Frenkiel function behavior of the symmetric correlation is probably caused by the requirement for conservation of scalar flux. In particular, fluctuations of one sign must be compensated by fluctuations of the other sign on opposite sides of the axis so that the mixture fraction flux is preserved as a whole. Similar behavior is well known for the lateral spatial correlations of velocity fluctuations in isotropic turbulence due to conservation of mass requirement (Hinze, 1975). The rather slow final decay of the negative portion of the symmetric correlation, in comparison to the exponential decay for $r > 0$, also tends to support a large-scale requirement of this type. Unfortunately, interpreting the Frenkiel function shape of the symmetric correlation will require information about velocities (or scalar fluxes) that currently is not available.

The measured spatial correlations for negative r in Fig. 7 generally are intermediate between the exponential and Frenkiel function limits. Naturally, the exponential correlation is retrieved exactly when $\Delta r < |r|$ and both points are on the same side of the axis. On the other hand, when $\Delta r \approx 2|r|$ for $r < 0$, the symmetric correlation is retrieved. Not surprisingly, other values of Δr generally represent an interpolation between these two limits. Most of the complexities of radial spatial correlations however, involve relatively small values of the correlations, which should not have a large effect on radiation fluctuations.

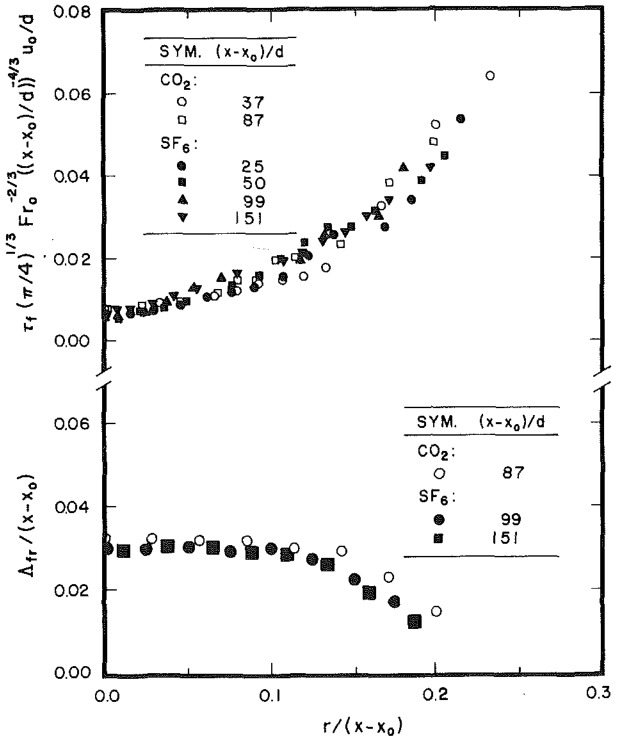

Fig. 8 Radial distributions of temporal and radial spatial integral scales

Integral Scales. The properties of the temporal power spectra and radial spatial correlations are completed by the corresponding temporal and spatial integral scales. Present measurements of the integral scales are plotted as a function of radial distance in Fig. 8 for both sources. The measurements extend into the self-preserving region, $25 \leq (x-x_o)/d \leq 151$; however, effects of streamwise distance are relatively small when plotted in the manner of Fig. 8.

The temporal integral scales at the top of Fig. 8 have been plotted by adopting Taylor's hypothesis for the relationship between spatial and temporal integral scales. Then the temporal integral scales have been normalized using self-preserving turbulent plume scaling relationships, i.e., length scales are proportional to $(x-x_o)$ and the velocity scales of the self-preserving region (Rouse et al., 1952; List, 1982). This approach seems robust and provides a good correlation of the temporal integral scales over the range of the present measurements. The results show a progressive increase of τ_f with radial distance. This follows from Taylor's hypothesis because spatial integral scales are relatively independent of radial position (see the lower part of Fig. 8) while streamwise mean velocities decrease as the edges of the plumes are approached.

The radial spatial integral scales for the plumes in the present self-preserving region, $(x-x_o)/d \geq 87$, are plotted in the lower part of Fig. 8. These integral scales were found from the correlations for positive values of r, as discussed previously. They have been normalized by $(x-x_o)$ to indicate scaling in the self-preserving region, similar to the temporal integral scales. The results indicate relatively little variation of Λ_{fr} for $r/(x-x_o) < 0.15$, followed by a reduction toward zero at large radial distances. This behavior follows from the intermittency of the flow at larger radial distances where the dimensions of turbulent fluid having mixture fractions greater than zero must decrease progressively. Present measurements yield $\Lambda_{fr}/(x-x_o) = 0.033$ near the axis $(r/(x-x_o) < 0.09)$ within the self-preserving region $((x-x_o)/d \geq 87)$. In contrast, Papantoniou and List (1989) report somewhat scattered and consistently lower values of $\Lambda_{fr}/(x-x_o)$ at comparable streamwise distances, in the range 0.011–0.022 for $r/(x-x_o) \leq 0.044$. The large Schmidt numbers of the liquid plumes considered by Papantoniou and List (1989) may be responsible for the differences between the two studies because this allows larger amounts of unmixed fluid to penetrate the flow than in gaseous plumes. Thus, large Schmidt numbers would tend to reduce spatial correlations, while increasing concentration fluctutaions as discussed earlier.

Conclusions

Mixture fraction statistics were measured in round buoyant turbulent plumes in still air. The test conditions involved buoyant jet sources of carbon dioxide and sulfur hexafluoride to give ρ_o/ρ_∞ of 1.51 and 5.06 and source Froude numbers of 7.80 and 3.75, respectively, with $(x-x_o)/d$ in the range 0-151 and $(x-x_o)/l_M$ in the range 0-43. The major conclusions are as follows:

1 The present measurements, supported by earlier findings of Papanicolaou and List (1989) for similar conditions, yielded distributions of mean mixture fractions in self-preserving plumes that were up to 30 percent narrower, with scaled values at the axis up to 30 percent larger, than other results found using buoyant jet sources in the literature, e.g., Papanicolaou and List (1987, 1988), Shabbir and George (1992), George et al. (1977), and Rouse et al. (1952), among others. Based on the observation that the earlier results were similar to behavior within the transitional plume region during the present study, it appears that the earlier results were not obtained at sufficient distances from the source to reach self-preserving conditions. In particular, self-preserving conditions were reached for $(x-x_o)/d \geq 87$ during the present measurements and those of Papantoniou and List (1989), while the earlier measurements, for comparable source Froude numbers, involved $(x-x_o)/d \leq 62$. Naturally, distances from the source to reach self-preserving conditions depend on source properties like Re_o, Fr_o, and ρ_o/ρ_∞, and may be much shorter for purely buoyant sources (Kotsovinos, 1985); quantifying these effects merits additional study.

2 Radial profiles of mixture fraction fluctuations in the self-preserving region for plumes do not exhibit reduced values near the axis similar to jets. Instead, effects of buoyancy cause mixture fraction fluctuations to be maximum at the axis with intensities of roughly 45 percent. These large intensities probably are responsible for the large radiation fluctuation levels observed in the near-overfire region of fires.

3 Probability density functions of mixture fractions can be approximated reasonably well by either clipped-Gaussian or beta functions. Unlike nonbuoyant turbulent jets, finite levels of intermittency are observed at the axis within the self-preserving region of turbulent plumes.

4 The low-frequency portion of the temporal spectra of mixture fraction fluctuations is a robust property of plumes, which scale in a relatively universal manner even in the transitional plume region. The spectra exhibit the well-known $-5/3$ power inertial decay region followed by a -3 power inertial-diffusive region. The latter region has been observed by others in buoyant flows but is not observed in nonbuoyant flows; thus, it is an interesting buoyancy/turbulence interaction that merits further study.

5 Radial spatial correlations were limited by correlations where both points were on the same side of the axis, which exhibited an exponential decay, and symmetric correlations, which approximated a Frenkiel function. This behavior probably follows from conservation of scalar flux considerations, but more measurements and study are required to understand the phenomena controlling spatial correlations. Behavior near microscales was not addressed during the present study due to the limited spatial resolution of the measurements.

6 Integral scales behaved as anticipated and provisional scaling relationships have been proposed that merit additional study. Temporal integral scales were smallest at the axis, which follows from Taylor's hypothesis noting than mean velocities are largest in this region. Radial spatial integral scales were largest at the axis, which follows from the topography of the flow, i.e., the streamwise extent of particular sections of partially mixed turbulent fluid must decrease as the intermittency increases toward the edge of the flow.

Acknowledgments

This research was supported by the United States Department of Commerce, National Institute of Standards and Technology, Grant No. 60NANB1D1175, with H. R. Baum of the Building and Fire Research Laboratory serving as Scientific Officer.

References

Abraham, G., 1960, "Jet Diffusion in Liquid of Greater Density," *ASCE J. Hyd. Div.*, Vol. 86, pp. 1-13.

Becker, H. A., Hottel, H. C., and Williams, G. C., 1967, "The Nozzle-Fluid Concentration Field of the Round, Turbulent, Free Jet," *J. Fluid Mech.*, Vol. 30, pp. 285-303.

Bilger, R. W., 1976, "Turbulent Jet Diffusion Flames," *Prog. Energy Combust. Sci.*, Vol. 1, pp. 87-109.

Bird, R. B., Stewart, W. E., and Lightfoot, E. N., 1960, *Transport Phenomena*, Wiley, New York, pp. 502-513.

Corrsin, H. Y., and Uberoi, M. S., 1950, "Further Experiments on the Flow and Heat Transfer in a Heated Turbulent Jet," NACA Rept. No. 998.

George, W. K., Jr., Alpert, R. L., and Tamanini, F., 1977, "Turbulence Measurements in an Axisymmetric Buoyant Plume," *Int. J. Heat Mass Trans.*, Vol. 20, pp. 1145-1154.

Hiller, B., and Hanson, R. K., 1990, "Properties of the Iodine Molecule Relevant to Laser-Induced Fluorescence Experiments in Gas Flows," *Expts. Fluids*, Vol. 10, pp. 1-11.

Hinze, J. O., 1975, *Turbulence*, 2nd ed, McGraw-Hill, New York, pp. 175-319.

Kotsovinos, N. E., 1985, "Temperature Measurements in a Turbulent Round Plume," *Int. J. Heat Mass Trans.*, Vol. 28, pp. 771-777.

Kounalakis, M. E., Sivathanu, Y. R., and Faeth, G. M., 1991, "Infrared Radiation Statistics of Nonluminous Turbulent Diffusion Flames," ASME JOURNAL OF HEAT TRANSFER, Vol. 113, pp. 437-445.

Lai, M.-C., and Faeth, G. M., 1987, "A Combined Laser-Doppler Anemometer/Laser-Induced Fluorescence System for Turbulent Transport Measurements," ASME JOURNAL OF HEAT TRANSFER, Vol. 109, pp. 254-256.

List, E. J., 1982, "Turbulent Jets and Plumes," *Ann. Rev. Fluid Mech.*, Vol. 14, pp. 189-212.

Lockwood, F. C., and Naguib, A. S., 1975, "The Prediction of Fluctuations in the Properties of Free, Round-Jet Turbulent Diffusion Flames," *Combust. Flame*, Vol. 24, pp. 109-124.

Mizushima, T., Ogino, F., Veda, H., and Komori, S., 1979, "Application of Laser-Doppler Velocimetry to Turbulence Measurements in Non-isothermal Flow," *Proc. Roy. Soc. London*, Vol. A366, pp. 63-79.

Morton, B. R., Taylor, G. I., and Turner, J. S., 1956, "Turbulent Gravitational Convection From Maintained and Instantaneous Sources," *Proc. Roy. Soc. London*, Vol. A234, pp. 1-23.

Mortion, B. R., 1959, "Forced Plumes," *J. Fluid Mech.*, Vol. 5, pp. 151-163.

Ogino, F., Takeuchi, H., Kudo, I., and Mizushima, T., 1980, "Heated Jet Discharged Vertically in Ambients of Uniform and Linear Temperature Profiles," *Int. J. Heat Mass Transfer*, Vol. 23, pp. 1581-1588.

Panpanicolaou, P. N., and List, E. J., 1987, "Statistical and Spectral Properties of Tracer Concentration in Round Buoyant Jets," *Int. J. Heat Mass Transfer*, Vol. 30, pp. 2059-2071.

Papanicolaou, P. N., and List, E. J., 1988, "Investigation of Round Vertical Turbulent Buoyant Jets," *J. Fluid Mech.*, Vol. 195, pp. 341-391.

Papantoniou, D., and List, E. J., 1989, "Large Scale Structure in the Far Field of Buoyant Jets," *J. Fluid Mech.*, Vol. 209, pp. 151-190.

Peterson, J., and Bayazitoglu, Y., 1992, "Measurements of Velocity and Turbulence in Vertical Axisymmetric Isothermal and Buoyant Plumes," ASME JOURNAL OF HEAT TRANSFER, Vol. 114, pp. 135-142.

Pivovarov, M. A., Zhang, H., Ramaker, D. E., Tatem, P. A., and Williams, F. W., 1992, "Similarity Solutions in Buoyancy-Controlled Diffusion Flame Modelling," *Combust. Flame*, Vol. 92, pp. 308-319.

Rouse, H., Yih, C. S., and Humphreys, H. W., 1952, "Gravitational Convection From a Boundary Source," *Tellus*, Vol. 4, pp. 201-210.

Shabbir, A., and George, W. K., 1992, "Experiments on a Round Turbulent Buoyant Plume," NASA Technical Memorandum 105955.

Sivathanu, Y. R., and Faeth, G. M., 1990, "Generalized State Relationships for Scalar Properties in Nonpremixed Hydrocarbon/Air Flames," *Combust. Flame*, Vol. 82, pp. 211-230.

Stårner, S. H., and Bilger, R. W., 1983, "Differential Diffusion Effects on Measurements in Turbulent Diffusion Flames by the Mie Scattering Technique," *Prog. Astro. and Aero.*, Vol. 88, pp. 81-104.

Tennekes, H., and Lumley, J. L., 1972, *A First Course in Turbulence*, MIT Press, Cambridge, MA.

Wu, J.-S., and Faeth, G. M., 1993, "Sphere Wakes in Still Surroundings at Intermediate Reynolds Numbers," *AIAA J.*, Vol. 31, pp. 1448-1455.

Zimin, V. D., and Frik, P. G., 1977, "Averaged Temperature Fields in Asymmetrical Turbulent Streams Over Localized Heat Sources," *Izv. Akad. Nauk. SSSR*, Mekhanika Zhidkosti Gaza, Vol. 2, pp. 199-203.

C. Harley

A. Faghri

Department of Mechanical and
Materials Engineering,
Wright State University,
Dayton, OH 45435

Complete Transient Two-Dimensional Analysis of Two-Phase Closed Thermosyphons Including the Falling Condensate Film

A transient two-dimensional thermosyphon model is presented that accounts for conjugate heat transfer through the wall and the falling condensate film. The complete transient two-dimensional conservation equations are solved for the vapor flow and pipe wall, and the liquid film is modeled using a quasi-steady Nusselt-type solution. The model is verified by comparison with existing experimental data for a low-temperature thermosyphon with good agreement. A typical high-temperature thermosyphon was then simulated to examine the effects of vapor compressibility and conjugate heat transfer.

Introduction

Two-phase thermosyphons are closed tubes that contain a small amount of working fluid. Evaporation occurs in the lower end of the tube due to heat input. Vapor travels upward to the cooled condenser section and rejects the latent heat of condensation to the ambient. The condensate falls back to the evaporator section in a thin film to begin the cycle again. This thin falling film was first studied by Nusselt (1916), who obtained an analytical solution for the condensate film thickness on a flat vertical plate by assuming that no shear stress was present at the liquid–vapor interface. This analysis has been extended by many other researchers (Sparrow and Gregg, 1959; Sparrow and Hartnett, 1961; Rohsenow, 1956) to account for the interfacial vapor shear stress, the momentum contribution of the condensing vapor, and the external vapor pressure drop.

Transient vapor condensation onto a vertical flat plate was examined by Reed et al. (1987). The falling film thickness determined from a complete transient numerical formulation using a variable grid geometry was compared with the film thickness determined from a quasi-steady solution of the problem. Reed et al. determined that when the Jakob number and the Jakob–Prandtl number ratio are of the order of unity, the inertial effects in the liquid film can be neglected since the quasi-steady solution results were within 2 percent of the more complete formulation.

When applying the Nusselt theory to a closed, two-phase thermosyphon, a variable vapor condensation rate must be considered. This approach was taken by Spendel (1984), who modeled a conventional thermosyphon condenser section with a two-dimensional incompressible formulation in the vapor space and an application of the Nusselt theory for the falling liquid film. With this model, Spendel performed a limited parametric study on the importance of including the interfacial shear stress and vapor pressure drop in determining the falling film thickness and the resulting Nusselt number for the thermosyphon. Based on these effects, the local Nusselt number in the condenser of a thermosyphon can vary as much as 60 percent from the approximate formulation derived by Nusselt.

An examination of conventional and concentric annular thermosyphons was performed by Faghri et al. (1989), where an improved flooding limit formulation was determined. Furthermore, in this study, the effects of the empirically obtained interfacial shear stress of the counterflowing vapor on the falling liquid film were considered in the condenser section alone.

The present model couples a general quasi-steady Nusselt-type solution of the falling film with the complete two-dimensional vapor solution to simulate the transient two-dimensional behavior of thermosyphons with variable properties. This model is significantly different from the previous models in that it simulates the entire thermosyphon, rather than only the condenser section. A two-dimensional transient formulation for the vapor is coupled to unsteady heat conduction in the pipe wall. Furthermore, the quasi-steady falling condensate film in the condenser, adiabatic, and evaporator sections are simulated by accounting for the variable vapor condensation rate, interfacial shear stress, and vapor pressure drop.

Mathematical Model

Conservation Equations for the Vapor and Wall. In a thermosyphon, the effect of gravity cannot be neglected, since the condensate is returned to the evaporator by gravity. However, the vapor velocity is often large enough to assume that forced convection is dominant over free convection, as is done in the present analysis. The coordinate system and labeling convention are shown in Fig. 1.

The differential conservation equations in cylindrical coordinates for transient, compressible, laminar flow in the vapor space of the thermosyphon with constant viscosity are as follows (Ganic et al., 1985):

Mass:

$$\frac{\partial \rho}{\partial t} + \nabla \cdot (\rho \mathbf{V}) = 0 \tag{1}$$

Momentum:

$$\rho \frac{D\mathbf{V}_v}{Dt} = -\nabla p + \frac{1}{3}\mu \nabla(\nabla \cdot \mathbf{V}_v) + \mu \nabla^2 \mathbf{V}_v + \rho \mathbf{g} \tag{2}$$

Energy:

$$\rho c_p \frac{DT_v}{Dt} - \nabla \cdot k \nabla T_v - \frac{Dp}{Dt} - \mu \Phi = 0 \tag{3}$$

Contributed by the Heat Transfer Division for publication in the JOURNAL OF HEAT TRANSFER. Manuscript received by the Heat Transfer Division April 26, 1993; revision received August 12, 1993. Keywords: Condensation, Evaporation, Heat Pipes and Thermosyphons. Associate Technical Editor: R. Viskanta.

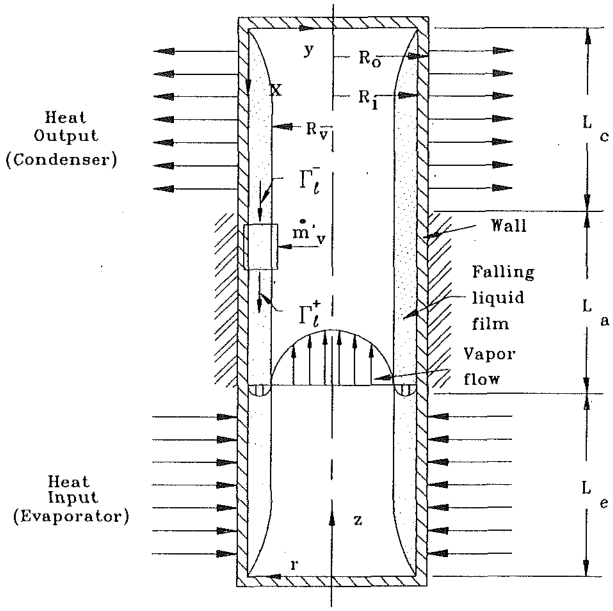

Fig. 1 Thermosyphon configuration and coordinate system (not to scale)

where

$$\Phi=2\left[\left(\frac{\partial v_v}{\partial r}\right)^2+\left(\frac{v_v}{r}\right)^2+\left(\frac{\partial w_v}{\partial z}\right)^2\right]+\left(\frac{\partial v_v}{\partial z}+\frac{\partial w_v}{\partial r}\right)^2-\frac{2}{3}\left[\frac{1}{r}\frac{\partial}{\partial r}(rv_v)+\frac{\partial w_v}{\partial z}\right]^2$$

The equation of state is given by

$$p=\rho_v R_g T_v \tag{4}$$

where R_g is the gas constant.

In the pipe wall, the transient two-dimensional energy conservation equation is

$$\rho_w c_{pw}\frac{\partial T}{\partial t}=k_w\left[\frac{1}{r}\frac{\partial}{\partial r}\left(r\frac{\partial T}{\partial r}\right)+\frac{\partial^2 T}{\partial z^2}\right] \tag{5}$$

where ρ_w and c_{pw} are the density and specific heat of the pipe wall material, respectively.

Falling Condensate Film Analysis. Assuming transient, laminar, incompressible liquid flow with constant properties, the two-dimensional conservation equations in cylindrical coordinates for a falling condensate film are

Mass:

$$\frac{1}{r}\frac{\partial}{\partial r}(rv_l)+\frac{\partial w_l}{\partial z}=0 \tag{6}$$

Radial Momentum:

$$\rho_l\left(\frac{\partial v_l}{\partial t}+v_l\frac{\partial v_l}{\partial r}+w_l\frac{\partial v_l}{\partial z}\right)=-\frac{\partial p_l}{\partial r}+\mu_l\left[\frac{1}{r}\frac{\partial}{\partial r}\left(r\frac{\partial v_l}{\partial r}\right)-\frac{v_l}{r^2}+\frac{\partial^2 v_l}{\partial z^2}\right] \tag{7}$$

Axial Momentum:

$$\rho_l\left(\frac{\partial w_l}{\partial t}+v_l\frac{\partial w_l}{\partial r}+w_l\frac{\partial w_l}{\partial z}\right)=-\frac{\partial p_l}{\partial z}+\mu_l\left[\frac{1}{r}\frac{\partial}{\partial r}\left(r\frac{\partial w_l}{\partial r}\right)+\frac{\partial^2 w_l}{\partial z^2}\right]+g\rho_l \tag{8}$$

Energy:

$$\rho_l c_{pl}\frac{\partial T_l}{\partial t}+v_l\frac{\partial T_l}{\partial r}+w_l\frac{\partial T_l}{\partial z}=\frac{1}{r}\frac{\partial}{\partial r}\left(rk_l\frac{\partial T_l}{\partial r}\right)+\frac{\partial}{\partial z}\left(k_l\frac{\partial T_l}{\partial z}\right) \tag{9}$$

where v_l and w_l are the radial and axial liquid velocity components, respectively, and g is the acceleration of gravity, assumed in the negative z direction for a vertical thermosyphon. These two-dimensional transient equations completely describe the condensate film under the influence of gravity. However, it is not necessary to solve this complex system of equations.

Reed et al. (1987) examined transient vapor condensation onto a flat plate using the simplified version of the boundary-layer equations to determine the importance of modeling the transient effects. A constant wall temperature was assumed but an allowance was made for the transient variation of the vapor temperature and interfacial shear stress. The condensation of water at atmospheric pressure onto a vertical plate with an axially variable mass condensation rate under the influence of gravity was examined. It was concluded that when the Jakob number and the Jakob-Prandtl number ratio are on the order of one, a quasi-steady analysis for the falling condensate film predicts a film thickness close to that of the complete transient analysis.

Nomenclature

c_p = specific heat at constant pressure, J/(kg-K)
g = gravitational acceleration, m/s^2
h = convective heat transfer coefficient, W/(m^2-K)
h_{fg} = latent heat of evaporation, J/kg
k = thermal conductivity, W/(m-K)
L = length, m
$\dot{m}$ = mass flow rate, kg/s
$\dot{m}'_v$ = vapor mass condensation rate per unit width, kg/(m-s)
p = pressure, N/m^2
Q = heat rate, W
q = heat flux, W/m^2
q_s = heat source, W/m^2
r = radial coordinate, m
R_i = inner pipe radius, m
R_o = outer pipe radius, m
R_v = vapor spacing radius $= R_i - \delta$, m
R_g = gas constant, J/(kg-K)
S = surface area, m^2
t = time, s
T = temperature, K
v = radial velocity component, m/s
$\mathbf{V}$ = velocity vector, m/s
w = axial velocity component, m/s
x = rectangular coordinate, m
y = rectangular coordinate, m
z = axial coordinate, m
Γ_l = liquid mass flow rate per unit width, kg/(m-s)
δ = film thickness, m
ϵ = emissivity
μ = dynamic viscosity, kg/(m-s)
ρ = density, kg/m^3
σ = Stefan-Boltzmann constant, W/(m^2-K^4)
τ = shear stress, N/m^2
Φ = viscous dissipation term

Subscripts

a = adiabatic
c = condenser
e = evaporator
l = liquid
o = outer wall
sat = saturation
t = total
v = vapor
w = wall
0 = reference
∞ = ambient
δ = liquid-vapor interface

Based on this conclusion, the present thermosyphon model uses a quasi-steady Nusselt-type solution procedure for the falling condensate film. This analysis assumes that

1 The vapor condensation is filmwise with no interfacial waves.
2 Liquid subcooling is negligible.
3 Inertial effects in the liquid are negligible.
4 Convection effects in the liquid are negligible.
5 The liquid film thickness is much smaller than the vapor space radius.
6 The vapor density is much smaller than the liquid density.
7 There are negligible circumferential liquid velocity and temperature gradients.

The general equations for the falling liquid film are further simplified through a coordinate transformation. Using the assumption that the liquid film thickness is much smaller than the vapor space radius, the equations are written in cartesian coordinates, as shown in Fig. 1. Based on these assumptions, the equations describing the thin liquid film simplify to

$$\frac{\partial^2 w_l}{\partial y^2}=\frac{1}{\mu_l}\frac{dp_l}{dx}-\frac{\rho_l g}{\mu_l} \tag{10}$$

and

$$\frac{\partial^2 T_l}{\partial y^2}=0 \tag{11}$$

where y is the distance from the pipe wall, and x is the distance from the condenser end cap.

At the liquid-wall interface ($y=0$), the no-slip condition is in effect:

$$w_l=0 \tag{12}$$

At the liquid–vapor interface ($y=\delta$), the shear stress in the liquid is equal to that in the vapor:

$$\mu_l\frac{\partial w_l}{\partial y}=-\mu_v\frac{\partial w_v}{\partial r} \tag{13}$$

The simplified liquid flow Eq. (10) can be further simplified with a boundary layer assumption on the radial pressure gradient in the liquid. If the liquid pressure is considered constant across the thickness, then the pressure gradient in the liquid can be approximated by the conditions at the liquid–vapor interface, or $(dp_l/dx)=-(dp_v/dz)$. Using these assumptions and integrating Eq. (10) twice with respect to y using Eqs. (12) and (13) gives

$$w_l(y)=\left(g\rho_l+\frac{dp_v}{dz}\right)\frac{\delta^2}{\mu_l}\left[\frac{y}{\delta}-\frac{1}{2}\left(\frac{y}{\delta}\right)^2\right]+\frac{\mu_v y}{\mu_l}\frac{\partial w_v}{\partial r}\bigg|_{r=R_v} \tag{14}$$

The liquid axial mass flow rate per unit width is defined as

$$\Gamma_l=\int_0^\delta \rho_l w_l(y)\,dy \tag{15}$$

The total liquid mass flow rate is found by multiplying Eq. (15) by the inner circumference of the pipe. Substituting Eq. (14) into Eq. (15), the liquid mass flow rate per unit width is

$$\Gamma_l=\left(g\rho_l+\frac{dp_v}{dz}\right)\frac{\rho_l\delta^3}{3\mu_l}+\frac{\rho_l\mu_v\delta^2}{2\mu_l}\frac{\partial w_v}{\partial r}\bigg|_{r=R_v} \tag{16}$$

At any axial position in the thermosyphon, mass enters a fixed control volume in the falling film by both condensation (or evaporation) of the vapor and liquid flow from above. This conservation of mass can be written as

$$\Gamma_l^+-\Gamma_l^-=\frac{d\Gamma_l}{dx}\,dx=\dot{m}_v' \tag{17}$$

where $\dot{m}_v'$ is the rate of vapor condensation (or evaporation) per unit width over the control volume, the superscript $(-)$ indicates conditions at the entrance to the control volume, and the superscript $(+)$ indicates conditions at the exit of the control volume (Fig. 1). The vapor condensation rate is related to the radial mass flow rates through

$$\dot{m}_v'=\rho_\delta v_\delta\,dx \tag{18}$$

where v_δ is the interfacial radial vapor velocity at the control volume. From Eqs. (17) and (18),

$$\Gamma_l=\int_0^x \rho_\delta v_\delta\,dx=\int_z^{L_t}\rho_\delta v_\delta\,dz \tag{19}$$

Combining Eqs. (16) and (19) gives

$$\left(g\rho_l+\frac{dp_v}{dz}\right)\frac{\rho_l\delta^3}{3\mu_l}+\frac{\rho_l\mu_v}{2\mu_l}\frac{\partial w_v}{\partial r}\bigg|_{r=R_v}\delta^2=\int_z^{L_t}\rho_\delta v_\delta\,dz \tag{20}$$

Equation (20) is a third-order polynomial in δ. The film thickness at the condenser end cap is identically zero:

$$\delta|_{x=0}=0 \tag{21}$$

If the interfacial shear stress and vapor pressure drop are neglected, a closed-form solution for the liquid film thickness can be found as

$$\delta=\left[\left(\int_z^{L_t}\rho_\delta v_\delta\,dz\right)\frac{3\mu_l}{g\rho_l^2}\right]^{1/3} \tag{22}$$

However, this closed-form solution for the falling film was not used in the present model since the effects of interfacial shear were considered.

The simplified energy Eq. (11) yields a linear temperature profile across the liquid film. This implies that the latent heat of the condensing vapor is removed only by conduction through the liquid.

It is important to mention that this falling film analysis is valid for only the "critical" liquid fill ratio, which is defined as the amount of liquid that produces a liquid film with a zero film thickness at $z=0$ and $z=L_t$. Therefore, this analysis neglects the possibility for working fluid to form a pool in the bottom of the evaporator. Evaporation or condensation only occurs from the surface of the condensate film.

It should also be noted that this model determines the mass of the film in the thermosyphon based on the vapor velocities to satisfy heat transfer requirements. Therefore, the mass of liquid in the thermosyphon is a function of the heat input. This is physically unrealistic because the mass of liquid in the thermosyphon should remain constant. As a result of this, the present formulation is not capable of predicting the entrainment or flooding limitation in a thermosyphon. However, the sonic limit can be determined since vapor flow compressibility has been accounted for. The falling liquid film model by Reed and Tien (1987) ensures a constant liquid mass with a varying heat input by employing a control-volume technique in body-fitting coordinates. In contrast, the present model uses an analytical method, which significantly reduces the computer requirements. The present approach, while being somewhat limited, is a significant improvement over previous models, which neglect the effects of counterflowing vapor and coupled heat conduction within the pipe wall.

Boundary Conditions. At the end caps of the thermosyphon ($z=0$, L_t), the no-slip condition for velocity and the adiabatic condition for temperature are applied. At the evaporator end cap, the falling film thickness cannot be specified due to the formulation used for the falling film. However, when the vapor condensation and evaporation rates are equal, such as at steady state, the condensate film thickness at the evaporator end cap will be zero.

$$z=0: \; v_v = w_v = \frac{\partial T}{\partial z} = 0 \tag{23}$$

$$z=L_t: \; \delta = v_v = w_v = \frac{\partial T}{\partial z} = 0 \tag{24}$$

At the centerline ($r=0$), the radial vapor velocity and the radial gradients of the axial velocity and temperature are zero.

$$v_v = \frac{\partial w_v}{\partial r} = \frac{\partial T}{\partial r} = 0 \tag{25}$$

To ensure saturation conditions at the liquid–vapor interface ($r=R_v$) in the evaporator section (and adiabatic section since the exact section transition point is determined iteratively), the Clausius–Clapeyron equation is used to determine the interface temperature as a function of pressure. The interface radial velocity is then found through the evaporation rate required to satisfy heat transfer requirements.

$$T_{\text{sat}} = \left(\frac{1}{T_0} - \frac{R_g}{h_{fg}} \ln \frac{p_v}{p_0} \right)^{-1} \tag{26}$$

$$v_\delta = \frac{\left(k_l \dfrac{T_\delta - T_w}{\delta} - k_\delta \dfrac{\partial T_v}{\partial r} \right)}{(h_{fg} + c_{p\delta} T_{\text{sat}}) \rho_\delta} \tag{27}$$

where T_δ is the temperature at the liquid–vapor interface, T_w is the temperature at the liquid–wall interface, k_δ is the harmonic average of the vapor and liquid thermal conductivities at the liquid–vapor interface, and T_0 and p_0 are the reference (saturation) vapor temperature and pressure, respectively.

Due to the no-slip condition, the vapor velocity at the liquid–vapor interface ($r=R_v$) must be the same as the condensate velocity at the interface. The mechanical force balance at the liquid–vapor interface must be also satisfied. It is important to notice that even though the shear stress is continuous across the liquid–vapor interface, the velocity gradients are discontinuous since there is a viscosity difference between the vapor and liquid phases:

$$w_v = -w_l(\delta) \tag{28}$$

$$\tau_l = -\tau_{v,\delta} = -\mu_v \left. \frac{\partial w_v}{\partial r} \right|_{r=R_v} \tag{29}$$

The interfacial liquid velocity is found from Eq. (14). The matching shear stress condition, Eq. (29), is implicitly satisfied in the formulation for the falling film thickness. The matching velocity condition at the liquid–vapor interface, Eq. (28), was first used by Spendel (1984) and is analogous to a no-slip condition for the vapor with a moving boundary. However, the validity of this boundary condition has been questioned since the change of phase is neglected at the liquid–vapor interface. However, this condition is implemented with the assumption that the phase-change jump condition is accounted for entirely in the radial vapor velocity formulation.

At the liquid–vapor interface ($r=R_v$) in the condenser section, vapor condenses releasing its latent heat energy. This process is simulated by applying a heat source to the cells in the wall at the liquid–vapor interface. To account for temperature continuity, the liquid temperature is set equal to the vapor temperature at the liquid–vapor interface:

$$q_s = (h_{fg} + c_{p\delta} T_\delta) \rho_\delta v_\delta \tag{30}$$

$$T_l = T_v |_{r=R_v} \tag{31}$$

At the liquid–wall interface ($r=R_i$), the heat flux into and out of the interface must be equal:

$$k_w \frac{\partial T}{\partial r} = -\frac{k_l}{\delta} (T_\delta - T_w) \tag{32}$$

At the outer pipe wall surface, the boundary conditions depend on both the axial position and the mechanism of heat transfer being studied (convection or radiation).

Evaporator:

$$k_w \left. \frac{\partial T}{\partial r} \right|_{r=R_o} = q_e \tag{33}$$

Adiabatic:

$$\left. \frac{\partial T}{\partial r} \right|_{r=R_o} = 0 \tag{34}$$

Condenser (convection):

$$-k_w \left. \frac{\partial T}{\partial r} \right|_{r=R_o} = h(T_o - T_\infty) \tag{35}$$

Condenser (radiation):

$$-k_w \left. \frac{\partial T}{\partial r} \right|_{r=R_o} = \sigma \epsilon (T_o^4 - T_\infty^4) \tag{36}$$

Initial Conditions. The temperature of the thermosyphon is assumed to be uniform at the initial temperature before the simulation begins. The initial temperature is assumed to be above the free molecular-continuum flow transition temperature based on the thermosyphon vapor space diameter (Cao and Faghri, 1993).

The falling liquid film is determined by the radial vapor velocity, so at the initial thermal equilibrium condition, there will be no liquid along the walls of the condenser and adiabatic sections. In reality, the working fluid will be pooled at the bottom of the evaporator section, but this model does not consider the possibility of a liquid pool.

This model also has the ability to determine the pulsed response of a thermosyphon. In this mode, the thermosyphon is initialized at the steady state of a lower heat input, with the film thickness determined by the radial vapor velocity at that state. The heat input is then suddenly increased to a higher value.

Numerical Procedure

The numerical procedure for the vapor flow and the coupling between the vapor and wall followed in this model is an application of the SIMPLE scheme (Patankar, 1980) and the conjugate analysis of Cao and Faghri (1990). However, the liquid flow is coupled to this solution through the condensation and evaporation rates at the liquid–vapor interface. This coupling is accounted for in the formulation of the governing equations for the liquid flow. After each iteration, the liquid flow is determined using the current field values of vapor velocity. Then, the liquid–wall interface temperature is updated to account for heat conduction across the thin liquid film. This process is continued until convergence is reached.

The sequence of numerical steps taken was:

1 Input the initial conditions.
2 Initialize the pressure, temperature, vapor density, and velocity fields.
3 For the first time step, find the falling film thickness using Eq. (20) assuming the vapor velocity and pressure drop are equal to zero.
4 Solve the momentum Eq. (2), using the vapor density and the average cross-sectional area to obtain v^* and w^*, which are the velocities based upon the guessed pressure field.
5 Solve for the new pressure field and update the guessed pressure field.
6 Calculate v and w from their starred values using the velocity correction formulas.
7 With the known vapor velocity fields, determine the con-

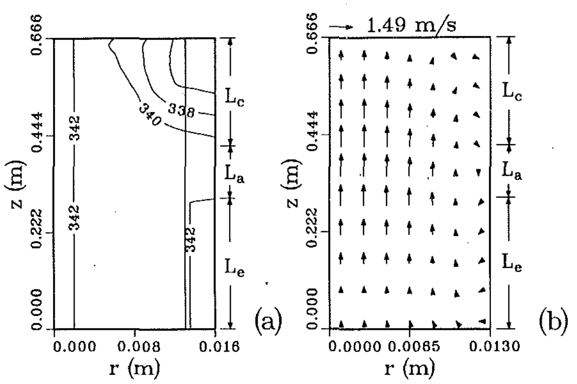

Fig. 2 Numerical simulation of the low-temperature thermosyphon experimentally studied by Mingwei et al. (1991): (*a*) temperature contours (K); (*b*) vapor velocity vectors (m/s)

densate film thickness using the quasi-steady Nusselt-type analysis, Eq. (20).

8 Solve the energy equation in the vapor, Eq. (3).
9 Solve the energy equation in the wall, Eq. (5).
10 Determine the new ρ from the equation of state.
11 Steps 4–10 are repeated for each time step until successive iterations differ by a small preassigned value, which is 0.1 percent of the maximum field value in this case.

The present study used a uniform axial grid system with a nonuniform radial grid. To account for the discontinuity of the physical properties at the liquid–vapor interface, the grid scheme discussed by Patankar (1980) was used, where the property values at the interface are based on the harmonic average of the adjacent cell values. It is important to mention that the variation of the thermosyphon cross-sectional area due to the variable thickness of the falling condensate film has been neglected in the vapor flow model. Instead, the average vapor-space cross-sectional area is determined at each iteration and used in determining the vapor velocities. This enables the falling condensate film to be modeled by a one-dimensional equation, not requiring body-fitted coordinates. However, Reed et al. (1987) determined that this assumption is valid and results in only minimal errors when compared to the full two-dimensional solution.

To achieve a convergent solution, linear underrelaxation was introduced into the procedure. Several different values of underrelaxation were used in this simulation, with the solution independent of relaxation factor. To enable rapid and stable convergence, the simulation used a linear relaxation value of 0.3.

Grid independence of the two-dimensional thermosyphon code was verified by systematically varying the number of axial and radial grids. It was found that varying the grid from 7 × 40 to 14 × 80 (radial × axial) resulted in less than a 2 percent variation in the field values but required nearly three times the CPU time for solution. The present grid (7 × 40) was chosen to optimize the accuracy of the result as compared with the required computational time.

Results and Discussion

To validate the numerical procedure, a low-temperature water/mild steel thermosyphon was simulated for a heat input of 268 W for comparison with the experimental data of Mingwei et al. (1991). Mingwei et al. state that the condenser section of the vertical thermosyphon was placed in a "low-temperature ambient." However, no specific values were given for this temperature, so an ambient temperature value of 0°C was assumed. Based on the steady-state temperature profiles and the known heat input to the thermosyphon, an effective convective heat transfer coefficient was determined to be 185 W/(m^2-K) for a heat input of 268 W. For this numerical simulation a uniform initial temperature of 400 K was used. The dimensions and properties of this thermosyphon are $L_t = 0.66$ m, $L_e = 0.30$ m, $L_a = 0.12$ m, $L_c = 0.24$ m, $R_i = 0.013$ m, $R_o = 0.016$ m, $t_w = 0.003$ m, $k_w = 60.5$ W/(m-K), $c_{pw} = 434$ J/(kg-K).

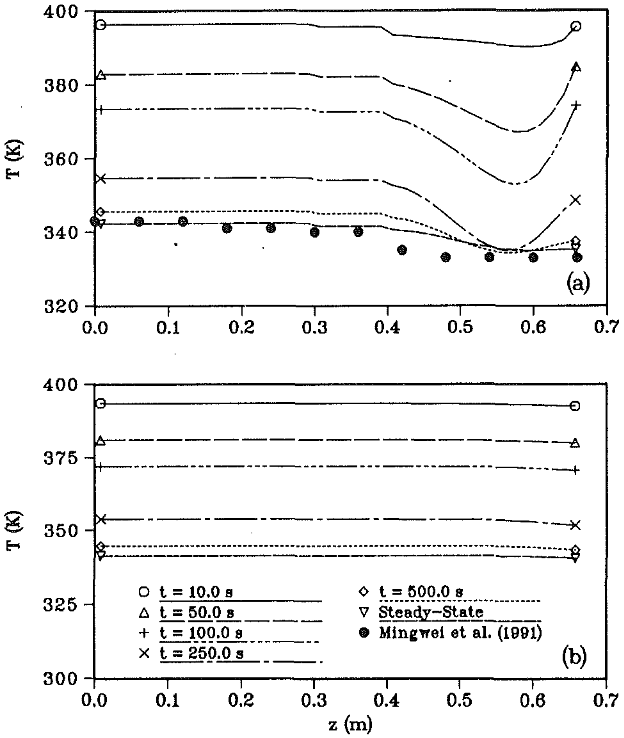

Fig. 3 Transient temperature profiles for the low-temperature thermosyphon experimentally studied by Mingwei et al. (1991): (a) transient outer wall temperature profiles; (b) transient centerline vapor temperature profiles

The temperature contour and vapor velocity vector plots for this case are shown in Fig. 2, where the isothermal nature of this low-temperature thermosyphon can be observed. In Fig. 2(*a*), the maximum temperature variation across the entire thermosyphon is only 6°C. The vapor velocity vector plot is as expected, where the highest axial velocities occur at the centerline at the exit of the adiabatic section and there is a small region of vapor flow reversal near the liquid–vapor interface due to the counterflowing falling liquid film.

The transient axial variations of the outer wall and centerline vapor temperatures are shown in Fig. 3, where the agreement with the steady-state experimental data of Mingwei et al. is quite good. The transient centerline axial vapor velocities for this low-temperature case are shown in Fig. 4 to be small and the axial pressure drop is negligible. The low axial vapor velocity is due in part to both the relatively high vapor density and latent heat of water, and the low heat flux input to the evaporator. Obviously, compressibility is not a factor for the low-temperature thermosyphon since the maximum Mach number is much less than 0.3. The negligible axial pressure variation is typical of low-temperature two-phase heat transfer devices due to the low vapor velocities.

The transient falling condensate film thickness for this case is shown in Fig. 5(*a*), where the coupled nature of the rate of film thickness developed with the entire thermosyphon can be seen. The steady-state mass flow rate comparison between the liquid and vapor for this case is shown in Fig. 5(*b*), where a reasonable agreement can be seen. At any axial cross section, the difference between the liquid and vapor mass flow rates is within 0.1 percent. This is expected since, at the steady state,

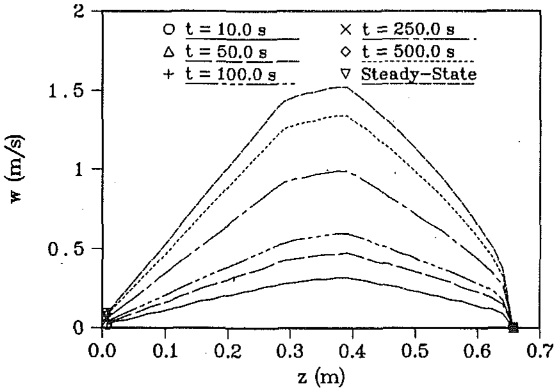

Fig. 4 Transient centerline axial vapor velocity profiles for the low-temperature thermosyphon experimentally studied by Mingwei et al. (1991)

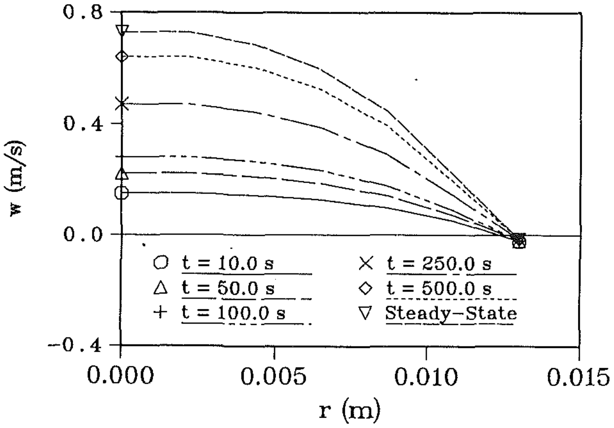

Fig. 6 Transient radial variation of axial vapor velocity for the low-temperature thermosyphon experimentally studied by Mingwei et al. (1991) at $z/L = 0.225$ (adiabatic)

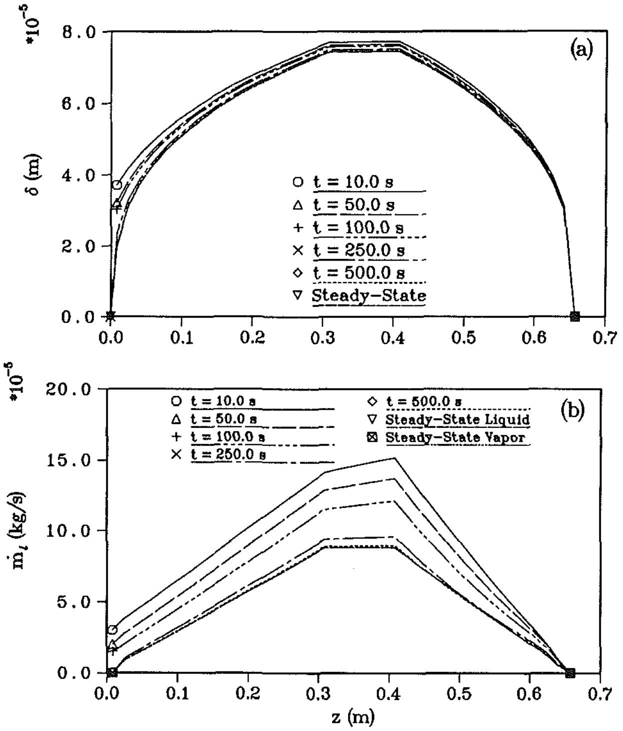

Fig. 5 Liquid dynamics for the low-temperature thermosyphon experimentally studied by Mingwei et al. (1991): (*a*) transient condensate film thickness profiles; (*b*) transient liquid mass flow rates

the mass flow rate entering the condenser must be the same as the liquid mass flowing back to the adiabatic and evaporator sections.

The transient radial variation of the axial vapor velocity profiles is shown in Fig. 6, where the vapor being pulled down by the counterflowing liquid can be seen. In this low-temperature case, both the vapor and the falling liquid film velocities are very small, so the effect of the counterflowing liquid and vapor phases is also small. At the liquid-vapor interface, the no-slip condition for the axial vapor velocity results in a small region of reverse vapor flow near the interface. At higher heat inputs, the vapor velocities would increase, resulting in a larger interfacial shear stress. This increased shear stress eventually results in a net upward (with respect to gravity) liquid velocity at the liquid-vapor interface. This trend continues until the flooding limit is reached, where the net liquid mass flow rate becomes zero, and evaporator dryout occurs. Faghri et al. (1989) determined that this phenomenon is periodic in nature, with the period of the dryout oscillations dependent on the magnitude of the heat input over the flooding limit.

To study high-temperature thermosyphon operation, a vertical stainless-steel/sodium thermosyphon was numerically simulated. Since sodium has a very high thermal conductivity, the temperature difference across the liquid film is very small. Also, the latent heat of vaporization for sodium is very large. As a result, $\mathrm{Ja}/\mathrm{Pr} < 0.1$ is satisfied although Pr for sodium is small. The condition $\rho_v/\rho_l \ll 0.1$ is also satisfied due to the extremely small sodium vapor density. The dimensions and properties of this thermosyphon are $L_t = 0.7$ m, $L_e = 0.105$ m, $L_a = 0.0875$ m, $L_c = 0.5075$ m, $R_i = 0.007$ m, $R_o = 0.009$ m, $t_w = 0.002$ m, $k_w = 20$ W/(m-K), and $c_w = 480$ J/(kg-K). The thermosyphon was simulated with a heat input of 500 W using a radiative condenser condition and an emissivity of 0.85. The high-temperature thermosyphon reached steady state in 350 s, or about 6 min. Steady state was determined when the heat output through radiation from the condenser was within 1 percent of the heat input to the evaporator.

The temperature contour plot for this high-temperature case is shown in Fig. 7(*a*), where a large temperature variation in the vapor can be observed. For this case, the vapor velocity, as shown in Fig. 7(*b*), is very high, resulting in significant compressibility effects. In the adiabatic section of the thermosyphon for this case, the Mach number is approximately 0.60. In addition, this plot shows the effect of axial conduction in the pipe wall since the radial temperature gradients are not constant across the pipe wall.

The transient axial variations of the outer pipe wall and centerline vapor temperatures are shown in Fig. 8. The vapor temperature drop caused by compressibility can be clearly seen in Fig. 8(*b*), with a slight temperature recovery in the condenser section. The vapor dynamics for this high-temperature case is shown in Fig. 9. As expected, the vapor velocities and pressure drop are significantly higher than in the low-temperature case. Both of these effects influence the falling film thickness, which will deviate significantly from the classical Nusselt theory for this case.

It has been suggested that the maximum vapor velocity, and thus the most likely occurrence of the sonic limit, occurs at the exit of the evaporator section. However, axial conduction in the pipe wall causes additional evaporation to occur in the adiabatic section, resulting in increased mass transfer at the exit of the adiabatic section. This model, since it accounts for axial conduction, shows that the maximum value occurs at the inlet to the condenser section.

The transient axial film thickness profiles including the effects of interfacial shear stress and vapor pressure drop are shown in Fig. 10. As vapor condenses on the inside of the

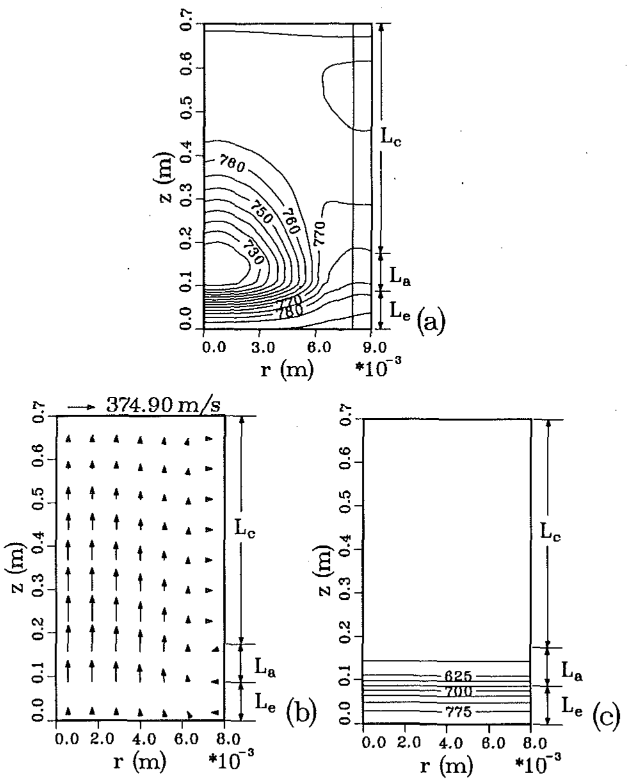

Fig. 7 High-temperature thermosyphon: (*a*) temperature contours (*K*); (*b*) vapor velocity vectors (m/s); (*c*) pressure contours (N/m^2)

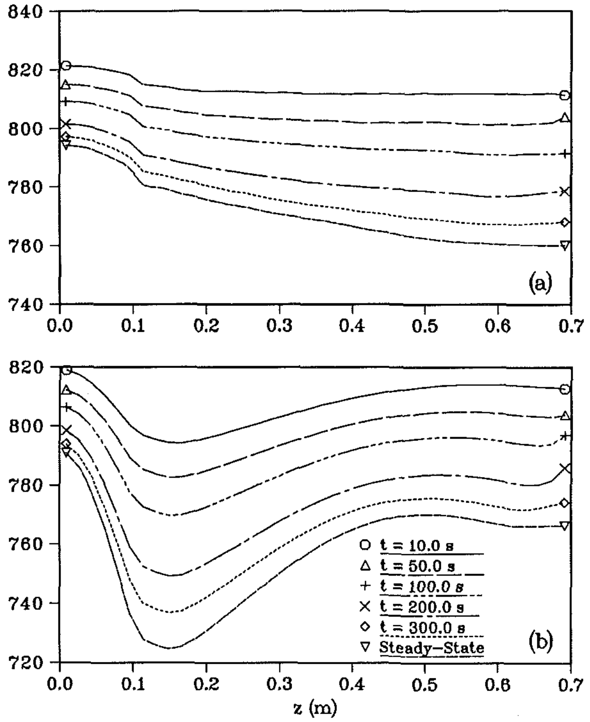

Fig. 8 Transient temperature profiles for the high-temperature thermosyphon: (*a*) transient outer wall temperature profiles; (*b*) transient centerline vapor temperature profiles

condenser section pipe wall, gravitational forces cause the condensate to form a thin film along the wall, which subsequently falls along the length of the thermosyphon. However, as the liquid film travels through the condenser, more condensate is added, resulting in a thicker film.

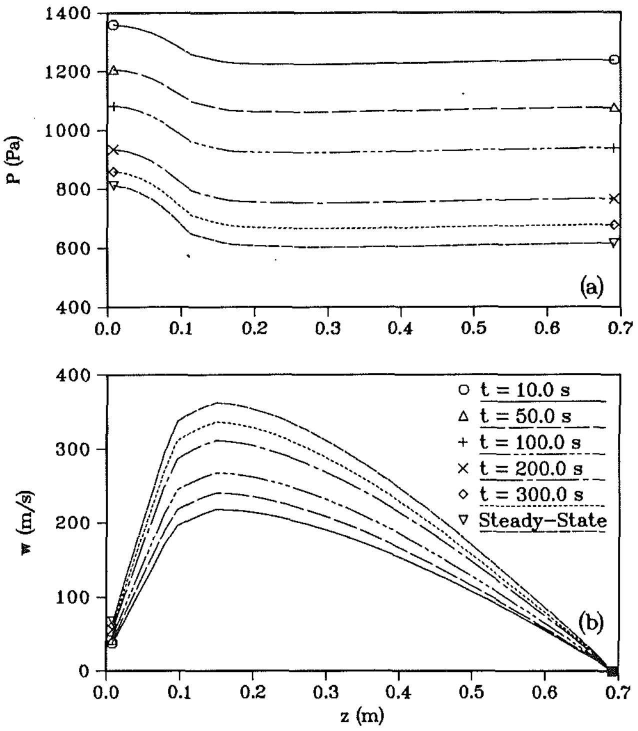

Fig. 9 Transient vapor dynamics for the high-temperature thermosyphon: (*a*) transient centerline pressure profiles; (*b*) transient centerline axial vapor velocity profiles

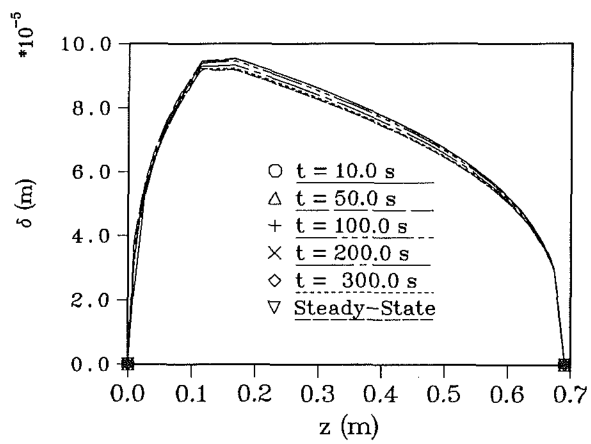

Fig. 10 Transient liquid film thickness for the high-temperature thermosyphon

When the condensate film enters the adiabatic section, no additional mass is added to the film through condensation. However, the film does not maintain a constant thickness through this region due to the interaction between interfacial shear stress, vapor pressure drop, and axial heat conduction in the pipe wall. In fact, a small amount of evaporation occurs in the adiabatic section due to axial heat condition. Physically, this is justified since only the outer pipe wall is insulated; i.e., heat transfer is only restricted at the outer pipe surface.

In the evaporator section, the liquid in the thin film evaporates, removing its latent heat from the evaporator pipe wall. As this evaporation process occurs, the condensate film must become thinner, since mass is being removed from the film. It is important to point out that this analysis is applicable only to the critical liquid fill ratio, or the maximum amount of liquid that does not allow a pool to form in the evaporator section. Thus, the phase change in the evaporator is by film

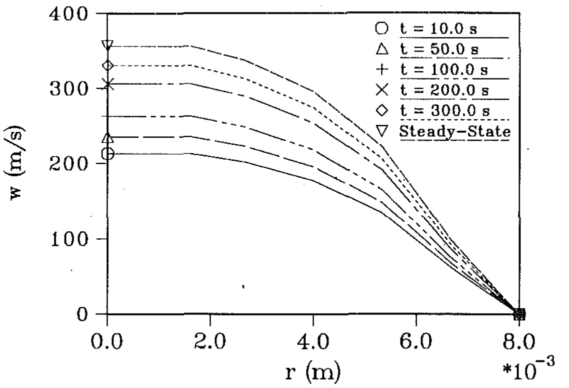

Fig. 11 Transient radial variation of axial vapor velocity for the high-temperature thermosyphon at $z/L = 0.225$ (adiabatic)

evaporation only, rather than also through nucleate boiling in the liquid pool. Like the low-temperature thermosyphon, the steady-state liquid and vapor mass flow rates at any axial locations for the high-temperature thermosyphon are within 0.01 percent.

The radial variations of the axial vapor velocity profiles are shown in Fig. 11. It should be mentioned that the resolution of the graphics routine does not allow the relatively small interfacial liquid velocity to be seen on the radial profiles of the axial velocity. However, there is still a net downward flow of liquid as the thermosyphon has not yet reached the entrainment heat flux limitation.

Finally, the results of the Nusselt-type quasi-steady falling film analysis previously developed are compared to the results of the classical Nusselt theory with a constant wall temperature and with a constant heat flux. The classical Nusselt theory for a condensing vapor on a flat plate that assumes a constant temperature difference between the saturated vapor and the vertical wall is

$$\delta(x) = \left[\frac{4k_l\mu_l(T_{\text{sat}} - T_w)x}{g\rho_l(\rho_l - \rho_v)h_{fg}}\right]^{1/4} \tag{37}$$

where T_{sat} is the saturation temperature of the vapor and T_w is the wall temperature. The classical Nusselt theory with constant heat flux is

$$\delta(x) = \left[\frac{3\mu_l Qx}{Sg\rho_l(\rho_l - \rho_v)h_{fg}}\right]^{1/3} \tag{38}$$

where Q is the total heat input, S is the condensation surface area (equal to $2\pi R_i L_c$ for a thermosyphon), and x is the distance from the condenser end cap. When predicting the film thickness in the condenser section of a thermosyphon, the characteristic length is L_c and when determining the film thickness in the evaporator section, the length is L_e. Furthermore, when applying this theory to evaporation from a thin film, the axial coordinate x is replaced with $(L_e - x)$.

The three theories are shown in Fig. 12(*a*) for the low-temperature thermosyphon with a heat input of 269 W, and the agreement between the three theories can be seen to be reasonable. It should be noted here that the two existing Nusselt theories predict slightly different film thickness variations. For a constant wall temperature, the film thickness varies with $x^{1/4}$. However, for the constant heat flux case, due to the differences in formulation, the thickness varies with $x^{1/3}$. In most conventional flat-plate-type condensation problems, the constant heat flux case consistently predicts a larger film thickness than the constant wall temperature case. However, the axial film thickness profile predicted with the constant heat flux theory includes the effects of a variable vapor condensation rate. The numerical solution of Eq. (20) accounts for both a nonconstant temperature difference and nonconstant heat flux. More importantly, the numerical solution is not limited to the steady state since the liquid mass flow rates are found from the transient radial vapor condensation and evaporation rates.

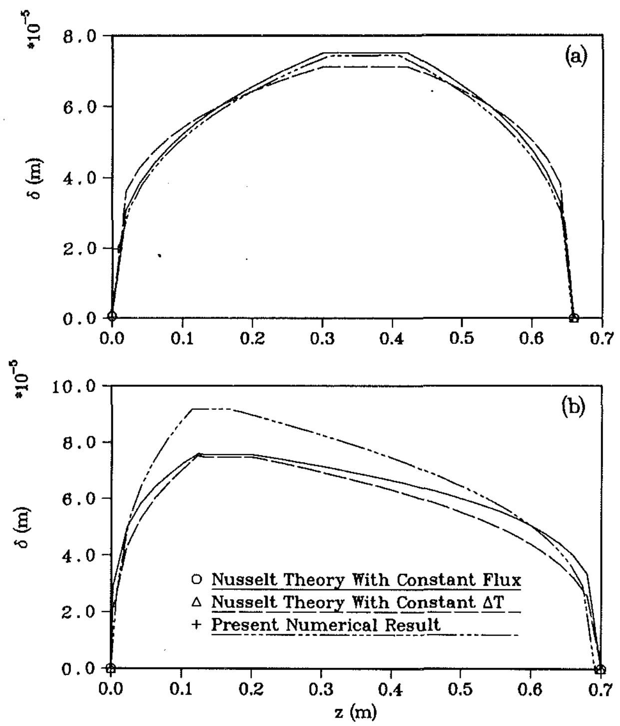

Fig. 12 Comparison of predicted falling film thickness profiles with Nusselt theory for: (*a*) low-temperature thermosyphon; (*b*) high-temperature thermosyphon

The three theories are compared for the high-temperature thermosyphon in Fig. 12(*b*), where the agreement is not as good as in the low-temperature case. This disagreement is due to the very high vapor velocities in the high-temperature thermosyphon and the resulting large interfacial shear stresses, which result in a thicker condensate film. In the classical Nusselt analysis, this interfacial shear stress is neglected, which, for this high-temperature case, creates a significant error in the predicted film thickness profile.

Conclusions

A complete two-dimensional transient thermosyphon model has been presented. This model simulates the entire thermosyphon, rather than only the condenser section, and solves the complete two-dimensional transient compressible governing equations in the vapor space, which are coupled to unsteady heat conduction in the pipe wall. The falling condensate film is modeled with a quasi-steady Nusselt-type analysis, which is implicitly coupled to the solution of the momentum equation in the vapor space. Using this model, a low-temperature thermosyphon was simulated and the results are compared to existing experimental data with good agreement. The Nusselt-type approximation can predict reasonably well the heat transfer coefficient in the condenser and evaporator sections for low-temperature two-phase closed thermosyphons. Compressibility effects in a high-temperature thermosyphon were also investigated and found to be significant in some cases.

References

Cao, Y., and Faghri, A., 1990, "Transient Two-Dimensional Compressible Analysis for High-Temperature Heat Pipes With Pulsed Heat Input," *Numerical Heat Transfer*, Part A, Vol. 18, pp. 483–502.

Cao, Y., and Faghri, A., 1993, "Simulation of the Early Startup Period of High-Temperature Heat Pipes From the Frozen State by a Rarefied Vapor Self-Diffusion Model," ASME JOURNAL OF HEAT TRANSFER, Vol. 115, pp. 239–246.

Faghri, A., Chen, M.-M., and Morgan, M., 1989, "Heat Transfer Characteristics in Two-Phase Closed Conventional and Concentric Annular Thermosyphons," ASME JOURNAL OF HEAT TRANSFER, Vol. 111, pp. 611–618.

Ganic, E. N., Hartnett, J. P., and Rohsenow, W. M., 1985, "Basic Concepts of Heat Transfer," in: *Handbook of Heat Transfer Fundamentals*, W. M. Rohsenow et al., eds., McGraw-Hill, New York.

Mingwei, T., Li, C., Hongji, Z., and Qingming, T., 1991, "Start-Up Behavior of the Frozen Two-Phase Closed Steel-Water Thermosyphons," *Proc. 8th Int. Heat Pipe Conf.*, Paper B-P2.

Nusselt, W., 1916, "Die Oberflaechenkondensation des Wasser-Dampfes," *Z. Ver. Dt. Ing.*, Vol. 60, pp. 541.

Patankar, S. V., 1980, *Numerical Heat Transfer and Fluid Flow*, Hemisphere, Washington, DC.

Reed, J., Gerner, F., and Tien, C., 1987, "Transient Condensation of a Laminar Film Onto a Vertical Plate," *Proc. AIAA 22nd Thermophysics Conf.*, Honolulu, Hawaii.

Reed, J., and Tien, C., 1987, "Modeling of the Two-Phase Closed Thermosyphon," ASME JOURNAL OF HEAT TRANSFER, Vol. 109, pp. 722–730.

Rohsenow, W., 1956, "Heat Transfer and Temperature Distribution in Laminar Film Condensation," *Trans. ASME*, Vol. 78, pp. 1645–1648.

Sparrow, E., and Gregg, J., 1959, "A Theory of Rotating Condensation," ASME JOURNAL OF HEAT TRANSFER, Vol. 81, pp. 113–120.

Sparrow, E., and Hartnett, J., 1961, "Condensation on a Rotating Cone," ASME JOURNAL OF HEAT TRANSFER, Vol. 83, pp. 101–102.

Spendel, T., 1984, "Laminar Film Condensation Heat Transfer in Closed Two-Phase Thermosyphons," *Proc. 5th Int. Heat Pipe Conf.*, Tsukuba, Japan.

A Two-Fluid Model for Reacting Turbulent Two-Phase Flows

S. H. Chan

M. M. M. Abou-Ellail

Department of Mechanical Engineering,
University of Wisconsin—Milwaukee,
P.O. Box 784,
Milwaukee, WI 53201

A reacting two-fluid model, based on the solution of separate transport equations for reacting gas–liquid two-phase flow, is presented. New time-mean transport equations for two-phase mixture fraction $\bar{f}$ *and its variance* g *are derived. The new two-fluid transport equations for* $\bar{f}$ *and* g *are useful for two-phase reacting flows in which phases strongly interact. They are applicable to both submerged and nonsubmerged combustion. A pdf approach to the reaction process is adopted. The mixture fraction pdf assumes the shape of a beta function while the instantaneous thermochemical properties are computed from an equilibrium model. The proposed two-fluid model is verified by predicting turbulent flow structures of an n-pentane spray flame and a nonreacting bubbly jet flow for which experimental data exist. Good agreement is found between the predictions and the corresponding experimental data.*

Introduction

Presently, very few combustion models can be used to predict the turbulence structure of multiphase (gas, liquid, and solid phases) submerged reacting plumes. Such multiphase submerged reacting plumes can be formed, for example, as a result of the reaction of an oxidant gaseous jet that is injected into a liquid fuel pool. These complex multiphase submerged reacting plumes can be found in closed liquid metal fuel combustors (Hughes et al., 1983; Parnell et al., 1987; Chen and Faeth, 1983; Chan et al., 1990a, 1990b), in steel making and metal extraction processes (Turkoglu and Farouk, 1993), in steam generator safety analysis (steam jets submerged in liquid sodium) of liquid metal-cooled reactors (Greene, 1987), in the recent innovative gas injection technique for in-situ synthesis of metal composites (Sahoo and Koozak, 1993) and other chemical and metallurgical processes (Chan et al., 1988). Practically all the contemporary models (such as the deterministic or stochastic separated-flow model) developed for nonsubmerged reacting flows (like spray flames) are inapplicable to the submerged reacting plumes due to the change in the flow regime and the condensation of excess evaporated fuel and products in the plume. Besides, these stochastic models require that the initial condition of, say, the droplets be known *a priori* at the inlet condition to proceed with the stochastic simulation. However, in submerged combustion, droplets are entrained, as part of the solution procedure, from the rather unspecified plume boundary, making stochastic simulation very difficult, if not impossible, to use. The only applicable model (Chen and Faeth, 1983; Chan et al., 1988, 1990a, 1990b) for the prediction of the submerged plume structure is the locally homogeneous flow (LHF) (with single-fluid k-ϵ-f-g) model developed in the 1970s. The LHF model has been used to predict spray flames (Mao et al., 1980) and the submerged combustion in liquid metal fuel combustors (Chen and Faeth, 1983; Chan et al., 1990a, 1990b). It implies that interphase transport rates for momentum, energy, and mass are infinitely fast, so that both phases have the same velocity and are in the thermodynamic equilibrium at each point in the flow at any instant of time. It treats a two-phase flow more like a single-phase flow with mixture properties. It simplificity made is popular as a computational tool for predicting highly complex reacting two-phase flow. However, effects of droplet size in spray flames of bubble/droplet size in submerged reacting flows cannot be considered in an LHF model of combustion.

In view of the deficiencies in the existing LHF model, there is a strong need to develop a better model for multiphase submerged combustion. In the following, a two-fluid reacting model is developed. It is known (Ishii, 1975) that the existing classic, nonreacting, two-fluid model (TFM) can appropriately accommodate the effect of the slip velocity between the two phases, the droplet/bubble size, and the difference in turbulent diffusivities of the phases. The two-fluid model has been used successfully to predict nonreacting turbulent two-phase flows (Abou-Ellail and Abou-Arab, 1985; Mostafa and Elghobashi, 1986). The two-fluid model is essentially equivalent to the stochastic, separated-flow model when a large number of trajectories is considered for an initially uniform droplet-size spray (Gosman et al., 1980). In order for the nonreacting TFM model to be applied to reacting two-phase flow, two transport equations must be introduced, namely, the two-phase mixture fraction ($\bar{f}$) and its variance (g). Such transport equations are currently not available for two-phase flow. The new transport equations for $\bar{f}$ and g for two-phase reacting flow based on separate transport equations for each phase are presented in this paper. They are needed for the development of a two-fluid model for reacting flows. These transport equations can be incorporated in existing two-phase codes such as the PHOENICS code (Ludwig et al., 1989) to account for species fluctuation in reacting flows.

In the absence of experimental data for turbulent plume structure of submerged reacting jets, it is necessary to compare the proposed two-fluid reacting models using other available data. Since the submerged reacting plume contains, among others, two main flow regimes (i.e., the droplet flow regime near the nozzle injector and the bubble flow regime away from the injector), the experimental data of the reacting droplet spray flame (Mao et al., 1980), and the nonreacting bubbly jet flow (Sun and Faeth, 1986a, 1986b) are employed here for comparison to the proposed two-fluid reacting model.

Theoretical Formulation for Two-Fluid Combustion Model

In the present two-fluid model, separate transport equations are formulated for each phase, and the interaction between the phases is accounted for by including interfacial drag and mass exchange source terms. For compactness, all the time-averaged, steady-state conservation equations for mass and momentum are summarized in Appendix A and expressed in Cartesian tensor notation, although they are actually solved

---

Contributed by the Heat Transfer Division and based on papers presented at 1992 National Heat Transfer Conference, San Diego, California, August 9–12, 1992 and the 1991 ASME/JSME Thermal Engineering Conference, Reno, Nevada, March 1991. Manuscript received by the Heat Transfer Division July 1992; revision received July 1993. Keywords: Combustion, Multiphase Flows, Reacting Flows. Associate Technical Editor: W. L. Grosshandler.

in their cylindrical polar form. The required two-fluid turbulence model for these conservation equations is summarized in Appendix B.

Combustion of turbulent two-phase diffusion flames is characterized by relatively fast chemistry and large mixture fraction fluctuations. Chemistry and evaporation are assumed to be fast enough so that the two-phase reacting mixture is in thermodynamic equilibrium. Therefore, the instantaneous state relationship is a function of a two-phase mixture fraction, f, similar to the case of single-phase combustion. The two-phase mixture fraction transport equation will be derived later.

The combustion model above is used to obtain the time-averaged value of any thermophysical property ($\bar{\phi}$) solely dependent on f as follows:

$$\bar{\phi}=\int_0^1 \phi(f)P(f)df \tag{1}$$

where $P(f)$ is a probability density function, which may be characterized by the mean two-phase mixture fraction, $\bar{f}$, and its variance, $g(\equiv\overline{f'f'})$. A transport equation for reacting two-phase flow mean square fluctuations, g, also needs to be derived from the transport equation of $\bar{f}$. The main modeling assumptions and the governing equations of $\bar{f}$ and g are presented below.

1 Two-Phase Mixture Fraction. Without loss of generality, the following conservation equations are written assuming that gas is the carrier phase (droplet flow). However, they are also applicable to bubbly flow if the g subscript is interchanged with the l subscript; in this case, the liquid is the carrier phase.

An exact instantaneous mixture fraction conservation equation is to be derived from the following instantaneous conservation equations for mass and any element (k), namely, for the gas phase,

$$\frac{\partial}{\partial t}(\rho_g\alpha_g)+\frac{\partial}{\partial x_i}(\rho_g u_{gi}\alpha_g)=\dot{m}_v'''\alpha_l \tag{2}$$

$$\frac{\partial}{\partial t}(\rho_g\alpha_g Y_g^{(k)})+\frac{\partial}{\partial x_i}\left(\rho_g\alpha_g u_{gi}Y_g^{(k)}-\Gamma_g^{(k)}\alpha_g\frac{\partial Y_g^{(k)}}{\partial x_i}\right)=\dot{m}_v'''\alpha_l Y_l^{(k)} \tag{3}$$

and for the liquid phase

$$\frac{\partial}{\partial t}(\rho_l\alpha_l)+\frac{\partial}{\partial x_i}(\rho_l u_{li}\alpha_l)=-\dot{m}_v'''\alpha_l \tag{4}$$

$$\frac{\partial}{\partial t}(\rho_l\alpha_l Y_l^{(k)})+\frac{\partial}{\partial x_i}\left(\rho_l\alpha_l u_{li}Y_l^{(k)}-\Gamma_l^{(k)}\alpha_l\frac{\partial Y_l^{(k)}}{\partial x_i}\right)=-\dot{m}_v'''\alpha_l Y_l^{(k)} \tag{5}$$

where $Y_g^{(k)}$ and $Y_l^{(k)}$ are the mass fractions of an element (k) in the gas and liquid phases (mass of element (k) per unit mass of the phase in question), and $\Gamma_g^{(k)}$ and $\Gamma_l^{(k)}$ are the diffusion coefficients of element (k) in the gas and liquid phases, respectively.

Nomenclature

C_1, C_2, C_3, C_μ = two-phase k-ϵ model constants
C_{g1}, C_{g2} = two-phase g equation constants
d = diameter of injector
d_{l0} = initial Sauter mean droplet (or bubble) diameter (SMD)
d_l = SMD at any cross section normal to flame axis
f = two-phase mixture fraction (injector fluid mass fraction)
g = variance of mixture fraction
g_j = j component of the acceleration of gravity
G = generation term of turbulence kinetic energy
k = turbulence kinetic energy
$\dot{m}_v'''$ = evaporation rate per unit dispersed phase volume
L = loading ratio = $(\rho_l\alpha_l)/(\rho_g\alpha_g)$
$\dot{m}_{l0}$ = inlet liquid fuel flow rate
$\dot{n}_g''$ = bubble number intensity (number of bubbles flowing per unit area)
p = pressure
p^c = pressure correction
r = radius/radial coordinate
Sc = Schmidt number
T = temperature
u = axial mixture velocity
u_i = mixture velocity in the i direction
u_g = axial gas velocity
u_{gi} = gas velocity in the i direction
u_l = axial liquid velocity
u_{li} = liquid velocity in the i direction
u_{lgi} = slip velocity in the i direction = $(u_{li}-u_{gi})$
x = axial coordinate
x_i = i-direction coordinate
Y = mass fraction
$Y^{(k)}$ = k-element mass fraction in each phase
α = volume fraction
β, θ = exponents of the beta function
$\Delta\bar{\mu}_{gc}$ = the difference between the centerline axial gas velocity ($\bar{u}_{gc}$) and the free stream axial velocity ($\bar{u}_{g\infty}$)
Δr = width of the jet
δ_{ij} = Kronecker delta tensor
ϵ = dissipation rate of k
Γ = transport coefficient
μ = dynamic viscosity $\equiv \rho\nu$
μ_t = turbulent viscosity of the carrier phase
ν = kinematic viscosity
ν_t = turbulent kinematic viscosity of the carrier phase
ρ = density
σ = Prandtl/Schmidt number
ϕ = flow variable

Subscripts

c = centerline
eff = effective
g = gas phase or variance g
i, j = i and j directions
k = turbulence kinetic energy
l = liquid phase
m = m direction
t = turbulent
0 = injector exit
ϵ = dissipation rate of k
∞ = free stream

Superscripts

$\bar{}$ = mean value
$'$ = fluctuating component
(k) = element k

Combining, Eqs. (2) and (4) leads to

$$\frac{\partial}{\partial t}(\rho)+\frac{\partial}{\partial x_i}(\rho u_i)=0 \tag{6}$$

where $\rho(\equiv\rho_g\alpha_g+\rho_l\alpha_l)$ is a mixture density, and u_i $(\equiv[\rho_g\alpha_g u_{gi}+\rho_l\alpha_l u_{li}]/\rho)$ is a mixture velocity.

Let the mixture fraction be defined as the percentage of mass originating from the nozzle stream,

$$f=(\phi^{(k)}-\phi_\infty^{(k)})/(\phi_0^{(k)}-\phi_\infty^{(k)}) \tag{7}$$

such that $f=1$ at the nozzle exit ("0" is the stream jet fluid) and $f=0$ at the free stream ("∞" is the co-flowing surrounding fluid). $\phi^{(k)}$ is the mass fraction of element (k) in the mixture defined as

$$\phi^{(k)}=(\rho_g\alpha_g Y_g^{(k)}+\rho_l\alpha_l Y_l^{(k)})/\rho \tag{8}$$

$\phi_0^{(k)}$ and $\phi_\infty^{(k)}$ are the values of $\phi^{(k)}$ at the nozzle exit and the surrounding fluid; they are constant and are actually the mixture mass fractions of element (k) in the jet and surrounding fluids, respectively. Adding Eqs. (3) and (5) yields

$$\frac{\partial(\rho\phi^{(k)})}{\partial t}+\frac{\partial}{\partial x_i}(\rho u_{gi}\phi^{(k)})+\frac{\partial}{\partial x_i}(\rho_l\alpha_l u_{lgi}Y_l^{(k)})-\frac{\partial}{\partial x_i}\left(\alpha_g\Gamma_g^{(k)}\frac{\partial Y_g^{(k)}}{\partial x_i}+\alpha_l\Gamma_l^{(k)}\frac{\partial Y_l^{(k)}}{\partial x_i}\right)=0 \tag{9}$$

Multiplying Eq. (6) by ϕ_0 yields

$$\frac{\partial}{\partial t}(\rho\phi_0^{(k)})+\frac{\partial}{\partial x_i}(\rho u_{gi}\phi_0^{(k)})+\frac{\partial}{\partial x_i}(\rho_l\alpha_l u_{lgi}\phi_0^{(k)})=0$$

Using Eq. (7), the equation above and the definition of the mixture fraction in the liquid phase only for element k, $f_l\equiv(Y_l^{(k)}-\phi_\infty^{(k)})/(\phi_0^{(k)}-\phi_\infty^{(k)})$, the mixture fraction equation can be derived as,

$$\frac{\partial(\rho f)}{\partial t}+\frac{\partial}{\partial x_i}(\rho u_{gi}f)+\frac{\partial}{\partial x_i}(\rho_l\alpha_l u_{lgi}f_l)-\frac{\partial}{\partial x_i}\left[\alpha_g\Gamma_g^{(k)}\frac{\partial f_g}{\partial x}+\alpha_l\Gamma_l^{(k)}\frac{\partial f_l}{\partial x_i}\right]=0 \tag{10}$$

in which $u_{lgi}\equiv u_{li}-u_{gi}$ is a slip velocity and

$$f_g\equiv(Y_g^{(k)}-\phi_\infty^{(k)})/(\phi_0^{(k)}-\phi_\infty^{(k)})=f+(f-f_l)(\rho_l\alpha_l/\rho_g\alpha_g)$$

$$\frac{\partial f_g}{\partial x_i}=\frac{\rho}{\rho_g\alpha_g}\frac{\partial f}{\partial x_i}-\frac{\rho_l\alpha_l}{\rho_g\alpha_g}\frac{\partial f_l}{\partial x_i}+(f-f_l)\frac{\partial L}{\partial x_i} \tag{11}$$

where $L\equiv(\rho_l\alpha_l)/(\rho_g\alpha_g)$ is a loading ratio ($\equiv$liquid mass/gas mass). Substituting Eq. (11) into Eq. (10) and noting that

$$\rho u_{gi}=\rho u_i-\rho_l\alpha_l u_{lgi};\quad \rho\gamma_g^{(k)}=\Gamma_f^{(k)}-\rho_l\alpha_l\gamma_{lg}^{(k)}$$

and

$$\Gamma_f^{(k)}=\alpha_g\Gamma_g^{(k)}+\alpha_l\Gamma_l^{(k)};\quad \gamma_{lg}^{(k)}\equiv(\Gamma_l^{(k)}/\rho_l)-(\Gamma_g^{(k)}/\rho_g)$$

the instantaneous transport equation of the mixture fraction is finally obtained,

$$\frac{\partial}{\partial t}(\rho f)+\frac{\partial}{\partial x_i}\left(\rho u_i f-\Gamma_f\frac{\partial f}{\partial x_i}\right)+\frac{\partial}{\partial x_i}\left[\rho_l\alpha_l u_{lgi}(f_l-f)-\rho_l\alpha_l\gamma_{lg}\frac{\partial}{\partial x_i}(f_l-f)\right]+\frac{\partial}{\partial x_i}\left[\Gamma_g\alpha_g(f_l-f)\frac{\partial L}{\partial x_i}\right]=0 \tag{12}$$

in which equal molecular diffusion coefficients have been assumed, namely, $\Gamma_f^{(k)}=\Gamma_f$ and $\gamma_{lg}^{(k)}=\gamma_{lg}$. In turbulent flows, those laminar diffusion coefficients Γ_f, Γ_g, and "slip" diffusivity γ_{lg} are small, as compared to the turbulent counterpart and can be neglected.

The liquid mixture fraction, f_l, will remain constant in reacting two-phase systems with no condensation, because the fuel evaporated from the liquid phase containing pure fuel reacts in the gaseous phase and the liquid phase remains "pure." In this case f_l is equal to 1.0, where the liquid phase is injected in a gas phase (spray flames), or 0.0 for liquid metal fuel systems, where the liquid phase is the surrounding fluid. In both cases f_l remains constant everywhere inside the flame.

Equation (12) is used to derive the time-mean, two-phase mixture fraction transport equation. For evaporating systems, f_l is equal to zero. Terms involving only molecular diffusion, such as the last term in Eq. (12), are neglected. In this work, the liquid volume fraction is assumed to be nonfluctuating and consequently, the gas volume fraction is also nonfluctuating. Furthermore, as in the single-fluid Reynolds averaging technique, the fluctuating terms involving the density fluctuations are neglected in the present two-fluid Reynolds-averaged equations. Therefore, terms involving ρ', α_l', or α_g' are neglected. The final form of the steady-state, time-mean, "two-phase mixture fraction" transport equation is

$$\frac{\partial}{\partial x_i}\left(\bar\rho\bar u_i\bar f-\Gamma_{f,\mathrm{eff}}\frac{\partial\bar f}{\partial x_i}\right)+\frac{\partial}{\partial x_i}\left[\bar\rho_l\bar\alpha_l\bar u_{lgi}(\bar f_l-\bar f)-\bar\rho_l\bar\alpha_l\gamma_{lg,\mathrm{eff}}\frac{\partial}{\partial x_i}(\bar f_l-\bar f)\right]=0 \tag{13}$$

The effective exchange coefficients are defined by

$$\Gamma_{f,\mathrm{eff}}-\Gamma_f+[(\bar\alpha_l\bar\rho_l/\bar\rho_g\sigma_l)+\bar\alpha_g]\mu_t/\sigma_f \tag{14}$$

$$\gamma_{lg,\mathrm{eff}}=\gamma_{lg}+[\nu_{tl}-\nu_t]/\sigma_f \tag{15}$$

where $\sigma_f=0.7$ if the turbulent Schmidt number taken from the existing LHF model, ν_t is defined in Eq. (A12), and σ_l is given in Eq. (A20).

Equation (13) indicates that $\bar f$ is transported by two mechanisms, namely, the bulk flow as well as a slipping relative flow. It is interesting to note that when the slipping flow effect is neglected ($\bar u_{lg}\approx 0$ and $\gamma_{lg}\approx 0$), the $\bar f$ equation correctly reduces to the existing single-phase mixture fraction conservation equation.

2 Two-Phase Mixture Fraction Fluctuations. The transport equation for the mean square fluctuations of the mixture fraction for two-phase reacting flows is derived from Eq. (12). This is done by multiplying Eq. (12) by f' and then performing time-averaging on the resulting equation. Following the same assumptions that led to Eq. (13), the steady-state, time-mean, modeled transport equation for g $(\equiv\overline{f'f'})$ can be readily shown, with considerable manipulation, as,

$$\frac{\partial}{\partial x_i}\left[\bar\rho\bar u_i g-\Gamma_{g,\mathrm{eff}}\frac{\partial g}{\partial x_i}\right]=C_{g1}\mu_t\left[\left(\frac{\partial\bar f}{\partial x_i}\right)^2+\bar\rho_l\bar\alpha_l\left(\frac{1}{\bar\rho_l\sigma_l}-\frac{1}{\bar\rho_g}\right)\frac{\partial\bar f}{\partial x_i}\frac{\partial}{\partial x_i}(\bar f_l-\bar f)\right]+\bar\rho_l\bar\alpha_l\bar u_{lgi}\frac{\partial g}{\partial x_i}-\frac{\partial}{\partial x_i}\left(\bar\rho_l\bar\alpha_l\gamma_{lg,g}\frac{\partial g}{\partial x_i}\right)-C_{g2}\bar\rho g\epsilon/k \tag{16}$$

In the above, C_{g1} and C_{g2} are constants of the order $2/\sigma_f$ and 2.0; their values of 2.8 and 1.84 from the LHF model are used. $\Gamma_{g,\mathrm{eff}}$ and $\gamma_{lg,g}$ are turbulent exchange coefficients defined as

$$\Gamma_{g,\mathrm{eff}}=(\bar\alpha_g\mu_g+\bar\alpha_l\mu_l)/\mathrm{Sc}+\left(\bar\alpha_g+\frac{\bar\rho_l}{\bar\rho_g}\frac{\bar\alpha_l}{\sigma_l}\right)\mu_t/\sigma_g \tag{17}$$

$$\gamma_{lg,g}=\gamma_{lg}+[\nu_{tl}-\nu_t]/\sigma_g \tag{18}$$

where $\sigma_g=0.7$ (from LHF) is a turbulent Schmidt number and $\mathrm{Sc}=0.7$. In deriving Eq. (16), the continuity equations for mean and fluctuating flow of the mixture (i.e., $\partial(\bar\rho\bar u_i)/\partial x_i=\partial(\rho u_i')/\partial x_i=0$) were used. Terms involving laminar diffusion, with no turbulent counterpart, were ignored. Also, terms involving $\partial(\bar\rho_l\bar\alpha_l u_{lgi}')/\partial x_i=-\partial(\bar\rho u_{gi}')/\partial x_i$ if α_l' can be

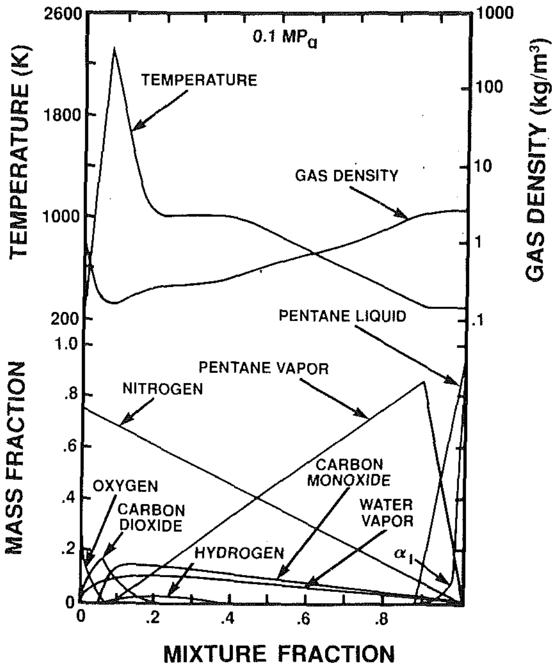

Fig. 1 State relationships for *n*-pentane burning in air at atmospheric pressure (Mao et al., 1980)

neglected) were ignored due to their small contribution relative to other terms in the g transport equation (Elghobashi and Abou-Arab, 1983). In the limit when two fluids are identical without a slipping velocity between them, the present g equation again reduces correctly to the existing single-fluid equation.

3 The Probability Density Function. Different shapes of pdf's have been used in modeling turbulent diffusion flames. In addition to the clipped Gaussian pdf (Chen and Faeth, 1983; Chan et al., 1990a, 1990b; Lockwood and Naguib, 1975; Kent and Bilger, 1976), the beta function has recently been used, as it is appropriately bound between zero and one (Correa et al., 1984; Abou-Ellail and Salem, 1990). The beta function pdf is used here,

$$P(f)=f^{\theta-1}(1-f)^{\beta-1}\Big/\int_0^1 f^{\theta-1}(1-f)^{\beta-1}df \qquad (19)$$

The exponents θ and β can be related to the mean mixture fraction $\bar{f}$ and its variance g by:

$$\theta=\bar{f}\left[\frac{\bar{f}(1-\bar{f})}{g}-1\right]$$

$$\beta=(1-\bar{f})\left[\frac{\bar{f}(1-\bar{f})}{g}-1\right]$$

The values of $\bar{f}$ and g are computed from the transport equations discussed above.

Comparison With Experimental Data

In the absence of detailed turbulence plume structure data of submerged combustion, the present two-fluid model is used to predict the cases for which experimental data are available, namely, an *n*-pentane free jet spray flame (Mao et al., 1980) and a bubbly jet flow (Sun and Faeth, 1986a, 1986b). The equilibrium state relationships, namely ϕ in Eq. (1), for the combustion of *n*-pentane spray in atmospheric air (0.1 MPa) are depicted in Fig. 1, giving temperature and the species mass fractions as function of f, and thus eliminating the need to include the energy equation in the present calculation when radiation is neglected. A complete description of the state relationships is given by Mao et al. (1980). With the state relationships given by Fig. 1, the evaporation rate can be calculated from the mean liquid phase volume fraction ($\overline{\alpha}_l$) and Eq. (A2). The mean liquid phase volume fraction $\overline{\alpha}_l$ can be calculated at any point inside the flame from the instantaneous value of α_l, obtained from Fig. 1, and Eq. (1), namely,

$$\overline{\alpha}_l=\int_0^1 \alpha_l(f)f^{\theta-1}(1-f)^{\beta-1}df\Big/\int_0^1 f^{\theta-1}(1-f)^{\beta-1}df \qquad (20)$$

where θ and β are calculated from $\bar{f}$ and g obtained from solution of their transport equations. Using Eqs. (A2) and (A17), the evaporation rate per unit volume of liquid phase can be calculated from the following equation:

$$\dot{m}_v''' = -\left[\frac{\partial}{\partial x_i}\left(\overline{\rho}_l\overline{\alpha}_l\overline{u}_{li}-(\mu_{tl}/\sigma_{\alpha l})\frac{\partial\overline{\alpha}_l}{\partial x_i}\right)\right]\Big/\overline{\alpha}_l \qquad (21)$$

The mean liquid volume fraction $\overline{\alpha}_l$ is obtained from Eq. (20) while $\overline{u}_{li}$ is computed from Eq. (A4). The equation above is simply a mass balance of the liquid phase resulting from the changes in $\overline{\alpha}_l$. With the present two-fluid model, only one mean droplet diameter can be computed at any section normal to the flame axis as follows:

$$d_l/d_{l0}=\left[\left(\int_0^{r_0}2\pi r\overline{\rho}_l\overline{\alpha}_l\overline{u}_l dr\right)\Big/\dot{m}_{l0}\right]^{1/3} \qquad (22)$$

where d_{l0} and d_l are "mean droplet diameters" at the fuel nozzle and any particular cross section downstream, $\dot{m}_{l0}$ is the inlet liquid fuel flow rate, and r_0 is the outer radius of the fuel spray at a particular cross section. The present model can easily be applied to include discrete droplet (or bubble) sizes. In this case, two equations similar to Eqs. (A2) and (A4) have to be included for each size group. However, for the carrier phase, only the drag force and evaporation rate terms in Eqs. (A1) and (A3) will be replaced by a summation over all droplet/bubble size groups. Details are reported elsewhere (Chan and Abou-Ellail, 1992).

Equations (20)–(22) are only used for the combusting *n*-pentane spray, since for the nonreacting bubbly jet flow in $\dot{m}_v'''$ is equal to zero; hence, the bubble volume fraction can be directly computed from Eq. (A2).

1 Experimental Data and Boundary Conditions. A good number of data sets for combusting sprays flames exist (Mao et al., 1980; Khalil and Whitelaw, 1976). The data (Mao et al., 1980) of an upwardly directed free jet, *n*-pentane spray flame are used here. The Reynolds number for this flame was 36,000. A Spray Systems Co. air atomizing injector (Model I/4J2050 fluid nozzle, No. 67147 air nozzle, outlet diameter 1.194 mm) was used. Both liquid phase and gas phase mean velocities were equal to 11.6 m/s. The loading ratio at the injector exit was 4.4. The surface-volume mean droplet diameter was 48 μm for the combusting spray (Mao et al., 1980). The pressure and temperature at the injector exit were 97 kPa and 296 K, respectively. The initial turbulence intensity ($(2k/3)^{1/2}/\overline{u}_{go}$) is taken to be about 5 percent, while the turbulent length scale ($C_\mu^{3/4}k^{3/2}/\epsilon$) is taken as 3 percent of the injector radius, which is nearly equivalent to fully developed pipe flow, for $\bar{f}=1$ and $g=0$. The effect of the assumed turbulence intensity diminishes rapidly downstream of the injector (Abou-Ellail and Salem, 1990; Razdan and Stevens, 1985). At the outer boundaries of the two-phase jet, $\overline{u}_l=0.001\ \overline{u}_{lo}$, $\overline{u}_g=0.001\ \overline{u}_{go}$, and $\bar{f}=g=0$, while the turbulence intensity is taken as 5 percent.

For the case of bubbly flow, the experimental data (Sun and Faeth, 1986) with nearly uniform bubble size are suitable for the validation of the present TFM model, although the flow is nonreacting. In this case, a dilute bubble air–water turbulent round jet is injected vertically upward at a speed of 1.65 m/s in still water. The mean bubble diameter is approximately 1000 μm and its volume fraction at the nozzle exit is 0.024.

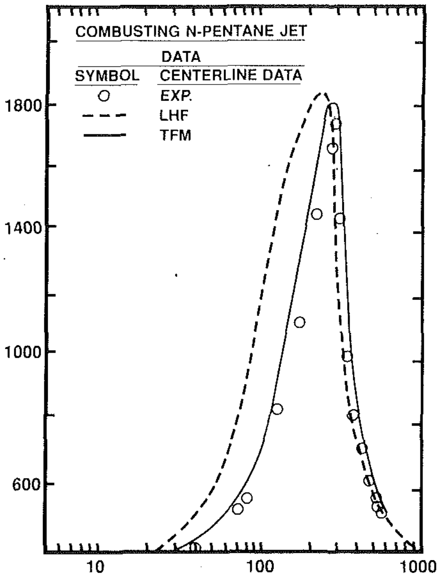

Fig. 2 Predicted axial mean gas temperature profile using two-fluid model (TFM) together with corresponding experimental data and LHF results of Mao et al. (1980) for *n*-pentane spray flame

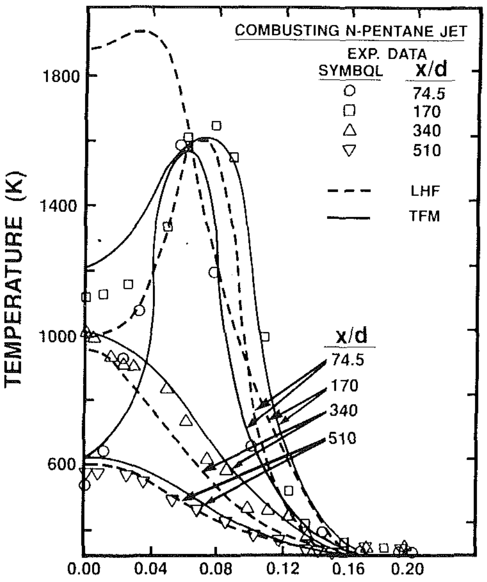

Fig. 3 Two-fluid model (TFM) predictions for radial mean gas temperature profiles for *n*-pentane spray flame together with corresponding measurements and LHF results of Mao et al. (1980)

The nozzle diameter is 5.08 mm. The initial k and ϵ are calculated in the same way as the reacting *n*-pentane spray. Since the mixture fraction was not measured, the $\overline{f}$ and g transport equations will not be solved for the case of the bubbly flow.

2 Solution Procedure. The solution procedure is based mainly on an iterative-marching integration algorithm as described in detail elsewhere (Abou-Ellail and Abou-Arab, 1985; Warda and Abou-Ellail, 1984). The main dependent variables are $\overline{u}_{gi}$, $\overline{u}_{li}$, p^c, k, ϵ, $\overline{f}$, g, and $\dot{m}_v'''$ for the reacting case or $\overline{\alpha}_g$ for the bubble flow, where p^c is computed from a combined equation derived from Eqs. (A1) and (A2). The remaining variables, k, ϵ, $\overline{f}$, g, and $\dot{m}_v'''$ (or $\overline{\alpha}_g$ for the bubbly flow) are computed from Eqs. (A13), (A14), (13), (16), and (21) (or Eq. (A2) for the bubble flow). The solution domain is overlaid with a nonuniform, two-dimensional, axisymmetric grid. The governing transport equations are formally integrated, over control volumes surrounding each grid node, to obtain their finite-difference counterpart (Abou-Ellail and Abou-Arab, 1985). Since the obtained difference equations are nonlinear and coupled, a few iterations are performed at each cross-stream plane, until the error in each equation is less than 1 percent of a representative reference value (e.g., for the momentum equations, the inlet momentum of each phase is used as the reference value), before marching downstream to the next plane. The present predictions were computing using 1200 (axial) grid nodes, and a maximum of 80 radial nodes, covering an axial distance of 600 jet diameters for the *n*-pentane flame of 100 jet diameters for the bubbly flow. The number of radial grid nodes was increased in proportion to the jet spreading rate as one marches downstream. The grid above gave nearly grid-independent results, since increasing the number of grid nodes by 20 percent resulted in changes of less than 1 percent in the computed variables.

Results and Discussion

1 Reacting Droplet Flow. The predicted axial variation of the mean centerline gas temperature for the combusting *n*-pentane spray is depicted in Fig. 2, together with the existing experimental data and the LHF model predictions (Mao et al., 1980). It is clear from Fig. 2 that the two-fluid model gives a better simulation of the reacting *n*-pentane spray flame, and that predicted results are much closer to the measured centerline temperature profile than the LHF model results. According to the present two-fluid model, no appreciable chemical reaction occurs along the centerline before $x/d = 30$, which agrees better with the experimental value of 40, compared to the LHF result of approximately 22. It seems that the new two-phase transport equations for $\overline{f}$ and g properly model the radial spreading rate of the *n*-pentane spray flame.

The predicted radial profiles of the mean gas temperature are shown in Fig. 3. The corresponding measurements and the existing LHF model results (Mao et al., 1980) are also shown. At low values of x/d, the improvement caused by the two-fluid model, which incorporates the new $\overline{f}$ and g equations, is more pronounced. Also, the improvement is more apparent near the centerline of the spray where there is more liquid fuel. For $x/d \geq 340$, the two-fluid model and the LHF model results essentially agree due to the possible absence of liquid unburned fuel at large values of x/d. The improvement in the present predicted temperature profiles is not likely a result of using a beta function pdf instead of clipped gaussian pdf used by Mao et al. (1980). It is known that the pdf shape has little effect on the predicted temperature profiles, provided that the shape satisfies the mean values of $\overline{f}$ and g (Jones and Whitelaw, 1984).

The normalized axial mean profiles of the centerline mixture fraction $\overline{f}_c$, liquid volume fraction $\overline{\alpha}_{lc}$, and gas and liquid velocities $\overline{u}_{gc}$ and $\overline{u}_{lc}$ are depicted in Fig 4. The corresponding measurements and LHF model results for $\overline{u}_c/\overline{u}_0$ are also shown. The measured $\overline{u}_c/\overline{u}_0$ lies between $\overline{u}_{gc}/\overline{u}_{g0}$ and $\overline{u}_{lc}/\overline{u}_{l0}$ computed in the present work. The profile of $\overline{\alpha}_{lc}$ indicates that the liquid fuel is essentially absent for x/d larger than 200. However, chemical reaction is still occurring with the evaporated fuel, since $\overline{f}_c$ reaches its stochiometric value at $x/d = 280$.

Figure 5 shows the predicted radial profiles of the normalized gas and liquid axial velocities $\overline{u}_g/\overline{u}_{gc}$ and $\overline{u}_l/\overline{u}_{lc}$, for combusting *n*-pentane spray, and the corresponding experimental data and LHF model predictions. At 74.5 jet diameters, the gas phase spreads more radially than the liquid phase. The liquid phase spreads radially only to a value of r/x, approximately equal to 0.1, while for the gas phase, the jet spreading reached a value of $r/x = 0.17$. The two phases approach the same axial velocity for values of $x/d > 170$. The agreement is general for all values of x/d is fairly good.

2 Bubbly Air-Water Flow. The predicted axial profiles

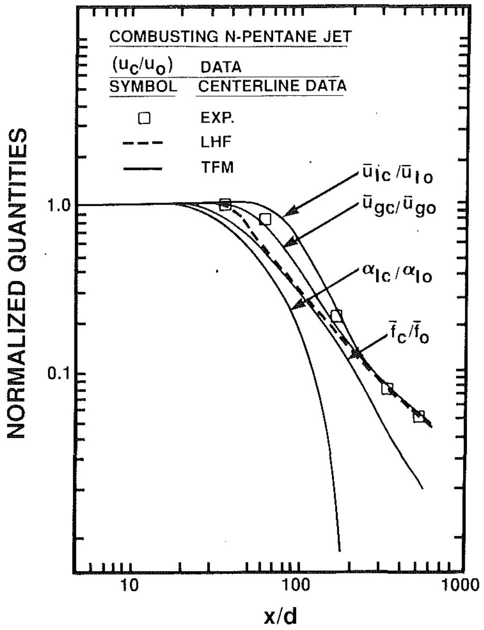

Fig. 4 Predicted mean normalized quantities along spray axis (TFM) together with measurements and LHF results of Mao et al. (1980) for $(\bar{u}/\bar{u}_c)$

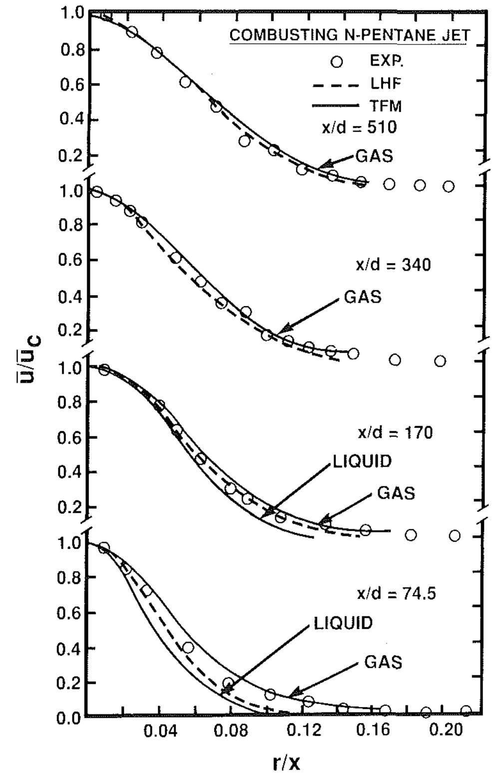

Fig. 5 Predicted radial profiles of gas and liquid axial velocities using two-fluid model (TFM) together with measurements and LHF results of Mao et al. (1980) for mean axial mixture velocity

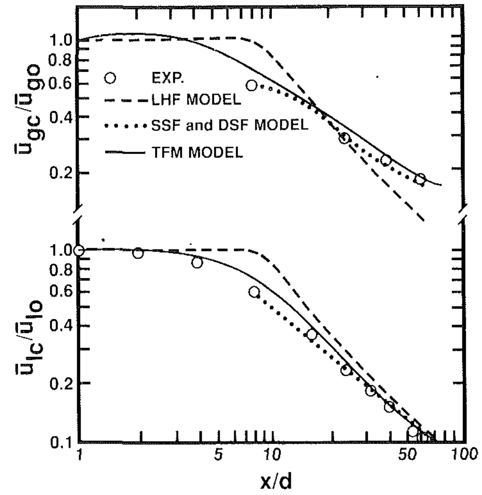

Fig. 6 Axial profiles of liquid-phase and gas-phase mean axial velocities (Exp., LHF, SSF, and DSF from Sun and Faeth, 1986)

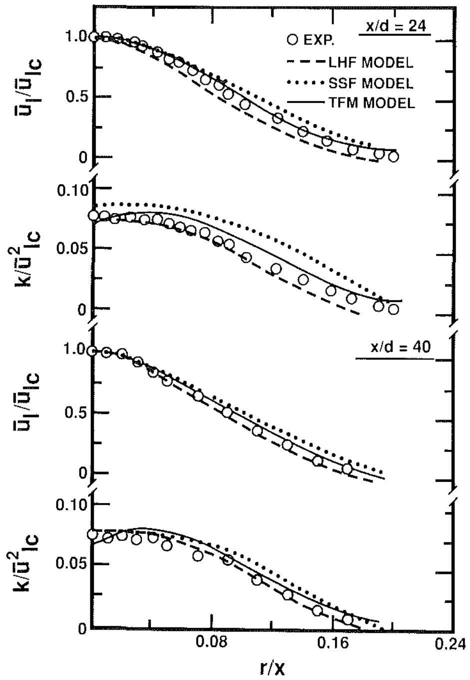

Fig. 7 Liquid-phase radial profiles of the normalized axial velocity $(\bar{u}_l/\bar{u}_{lc})$ and turbulence energy $(k/\bar{u}_{lc}^2)$

of the mean centerline liquid-phase and gas-phase normalized axial velocities ($\bar{u}_{lc}/\bar{u}_{l0}$ and $\bar{u}_{gc}/\bar{u}_{g0}$) are depicted in Fig. 6 for the upward bubbly jet (Sun and Faeth, 1986a, 1986b). In addition to the present TFM predictions, the corresponding experimental data, LHF predictions, deterministic separated flow (DSF) and stochastic separated flow (SSF) results of Sun and Faeth (1986a, 1986b) are also shown in Fig. 6 and all subsequent figures. The main difference between the DSF and SSF models is that the former uses the mean flow properties to calculate the bubble trajectories while the SSF model invokes "instantaneous random flow properties." Figure 6 shows that the present TFM accurately predicts the liquid phase axial velocity for all values of x/d, while the LHF model overpredicts $\bar{u}_{lc}$ for most of the two-phase jet. Although the SSF and DSF model results by Sun and Faeth (1986b) agree well with the measurements, no predictions were reported before $x/d = 8$ because they used the experimental data at $x/d = 8$ as the initial inlet condition for computation. Figure 6 shows clearly that while the TFM predicts the axial variation of the bubble axial velocity $\bar{u}_{gc}$, the LHF model is unable to predict the general trend of the axial variation of $\bar{u}_{gc}$.

The predicted radial profiles of the liquid-phase normalized axial velocity ($\bar{u}_l/\bar{u}_{lc}$) and turbulence energy ($k/\bar{u}_{lc}^2$), for $x/d = 24$ and 40, are shown in Fig. 7. The normalized radial profiles of $\bar{u}_l$ are predicted well by the TFM, LHF, and SSF models, while the turbulence energy results predicted by the TFM model show better agreement with the experimental data than that of the SSF model.

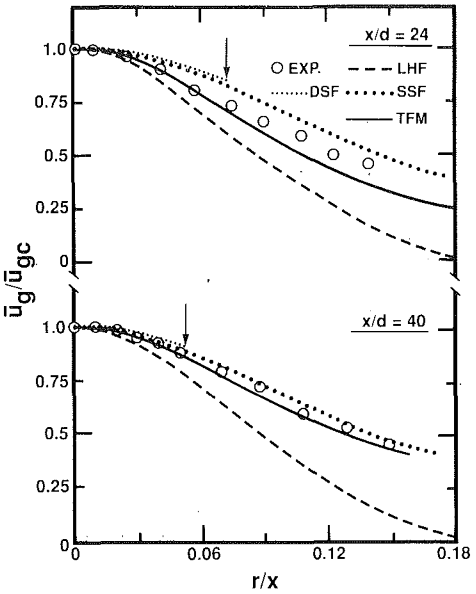

Fig. 8 Gas-phase radial profiles of the normalized mean bubble velocity ($\bar{u}_g/\bar{u}_{gc}$), for $x/d=24$ and 40

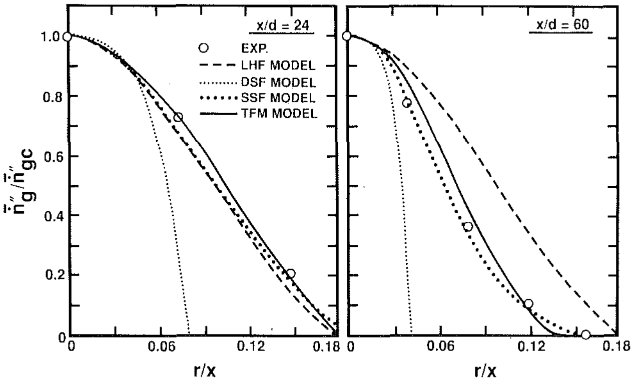

Fig. 9 Radial profiles of the normalized mean bubble number intensity ($\overline{\dot{n}_g''}/\overline{\dot{n}_{gc}''}$), for $x/d=24$ and 60

The radial profiles of the mean bubble axial velocity, for $x/d=24$ and 40, are depicted in Fig. 8. Here also, unlike the TFM and SSF, and LHF model cannot accurately predict the radial profile of $\bar{u}_g$. However, the TFM results are in slightly better agreement with the experimental data than the SSF model predictions, especially at $x/d=24$.

Radial profiles at $x/d=24$ and 60 for the mean bubble number intensity, $\overline{\dot{n}_g''}$, are shown in Fig. 9. The normalized mean bubble number intensity, $\overline{\dot{n}_g''}/\overline{\dot{n}_{gc}''}$, is predicted well by the TFM and SSF models at $x/d=24$ and 60. The LHF model overpredicts $\overline{\dot{n}_g''}$ for $x/d=60$, while the DSF model underpredicts $\overline{\dot{n}_g''}$ for both values of x/d.

In the calculations above, the TFM model predicts with reasonable accuracy the reacting droplet flow as well as the bubbly flow; with care, it could be used for a wide range of engineering applications, including the multiphase submerged combustion to which the SSF and DSF models are inapplicable. The application of the present study to the submerged combustion with a droplet size distribution is reported elsewhere (Chan and Abou-Ellail, 1992).

Conclusions

The present two-fluid combustion model presents new transport equations for the mean mixture fraction $\bar{f}$ and its variance g for the two-phase reacting flows. They are equally applicable to any reacting two-phase system, including multiphase submerged combustion as in liquid metal fuel combustors, and nonsubmerged combustion, as in spray flame applications. Comparison of the present reacting two-fluid model has been made to an n-pentane spray flame and a bubbly jet upward flow for which experimental data exist. The two-fluid model, in general, agrees more with the experimental data for both cases than alternative modeling approaches investigated.

Acknowledgment

This research was sponsored by the U.S. Office of Naval Research, Grant No. NOOO14-89-J-1267, under the technical management of Dr. G. Roy.

References

Abou-Ellail, M. M. M., and Abou-Arab, T. W., 1985, "Prediction of Two-Phase Flow and Heat Transfer in Vertical Pipes," *Proc. 5th Symp. on Turbulent Shear Flows*, Ithaca, NY, pp. 8.1–8.7.

Abou-Ellail, M. M. M., and Salem, H., 1990, "A Skewed PDF Combustion Model for Jet Diffusion Flames," ASME JOURNAL OF HEAT TRANSFER, Vol. 112, pp. 1002–1007.

Chan, S. H., Janke, P. J., and Shen, T. R., 1988, "Equilibrium Computations of Multi-phase Non-ideal Electrolytic Systems and Structure of Turbulent Reacting Dissolving Jets," *22nd Symp. (Int.) on Combustion*, pp. 721–729.

Chan, S. H., Zhao, Y. G., Janke, P. J., and Tan, C. C., 1990a, "Combustion of Turbulent Gaseous Fluorine Jets Submerged in Molten Lithium Fuel," *AIAA/ASME Thermophysics and Heat Transfer Conf.*, ASME HTD-Vol. 142, pp. 23–31.

Chan, S. H., Tan, C. C., Zhao, Y. G., and Janke, P. J., 1990b, "Li-SF$_6$ Combustion in Stored Chemical Energy Propulsion System," *23rd Symp. (Int.) on Combustion*, pp. 1139–1146.

Chan, S. H., and Abou-Ellail, M. M. M., 1992, "A Multi-fluid Model of Turbulence of Li-SF$_6$ Submerged Combustion," presented at AIAA/SAE/ASME/ASEE 28th Joint Propulsion Conf., Nashville, TN, July.

Chen, L. D., and Faeth, G. M., 1983, "Structure of Turbulent Reacting Gas Jets Submerged in Liquid Metals,"*Combustion Sci. and Tech.*, Vol. 11, pp. 111–131.

Correa, S. M., Drake, M. C., Pitz, R. W., and Shyy, W., 1984, "Prediction and Measurement of a Non-equilibrium Turbulent Diffusion Flame," *20th Symp. (Int.) on Combustion*, pp. 337–343.

Elghobashi, S. E., and Abou-Arab, T. W., 1983, "Two-Equation Turbulence Model for Two-Phase Flows," *J. Physics of Fluids*, Vol. 26, No. 4, pp. 931–938.

Gosman, A. D., Ioannides, E., Lever, D. A., and Cliffe, K. A., 1980, "A Comparison of Continuum and Discrete Droplet Finite-Difference Models Used in the Calculation of Spray Combustion in Swirling Turbulent Flows," AERE Harwell Report TP865.

Greene, D., 1987, "Summary of Small and Intermediate Sodium/Water Reaction Programs in the United States," *Proc. of 22nd IECEC*, Vol. 3, pp. 1630–1637.

Hughes, T. G., Smith, R. B., and Kiley, D. H., 1983, "Stored Energy Propulsion System for Underwater Applications," *J. Energy*, Vol. 7, pp. 128–133.

Ishii, M., 1975, *Thermo-Fluid Dynamic Theory of Two-Phase Flow*, Eyrolls, Paris.

Jones, W. P., and Whitelaw, J. H., 1984, "Modelling and Measurements in Turbulent Combustion," *20th Symp. (Int.) on Combustion*, pp. 233–249.

Kent, J. H., and Bilger, R. W., 1976, "The Prediction of Turbulent Diffusion Flame Fields and Nitric Oxide Formation," *16th Symp. (Int.) on Combustion*, pp. 1643–1656.

Khalil, E. E., and Whitelaw, J. H., 1976, "Aerodynamic and Thermodynamic Characteristics of Kerosene-Spray Flames," *16th Symp. (Int.) on Combustion*, pp. 569–576.

Lockwood, F. C., and Naguib, A. S., 1975, "The Prediction of the Fluctuations in the Properties of Free, Round-Jet, Turbulent Diffusion Flames," *Combustion and Flame*, Vol. 24, pp. 109–124.

Lockwood, F. C., and Stolakis, P., 1983, "Assessment of Two Turbulence Models for Turbulent Round Diffusion Jet With Combustion," *Proc. of Turbulent Shear Flows Conf.*, pp. 10.25–10.31.

Ludwig, J. C., Qin, H. Q., and Spalding, D. B, 1989, *The PHOENICS Reference Manual*, CHAM TR/200.

Mao, C. P., Szekely, G. A., Jr., and Faeth, G. M., 1980, "Evaluation of a Locally Homogeneous Flow Model of Spray Combustion," *J. Energy*, Vol. 4, No. 2, pp. 78–87.

Markatos, N. C., and Singhal, A. K., 1982, "Numerical Analysis of One-Dimensional Two-Phase Flow in a Vertical Cylindrical Passage," *J. Advances in Engrg. Software*, Vol. 4, No. 3, pp. 99–106.

Mostafa, A. A., and Elghobashi, S. E., 1986, "Effect of Liquid Droplets on Turbulence in a Round Gaseous Jet," NASA Contractor Report 175063.

Parnell, L. A., Katz, D. L., Gilchrist, J. T. Bryant, L. E., Lucero, J. P., and Zerwekh, W. D., 1987, "Radiography of Liquid Metal Fuel Combustion," *Proc. 22nd Intersoc. Energy Conversion Eng. Conf.*, Philadelphia, PA.

Razdan, M. K., and Stevens, J. G., 1985, "Co/Air Turbulent Diffusion Flame: Measurement and Modeling," *Combustion and Flame*, Vol. 59, pp. 289–301.

Rizk, M. A., and Elghobashi, S. E., 1989, "A Two-Equation Turbulence Model for Dispersed Dilute Confined Two-Phase Flows," *Int. J. Multiphase Flow*, Vol. 15, No. 1, pp. 119–133.

Rodi, W., 1979, "Influence of Buoyancy and Rotation on Equations for the Turbulent Length Scale," *2nd Symp. on Turbulent Shear Flows*, London, pp. 10.37–10.42.

Sahoo, P., and Koozak, M. J., 1993, "Analysis of In-Situ Formation of Titanium Carbide in Aluminum Alloys," *J. Mat. Sc. and Tech.*, in press.

Simonin, O., and Viollet, P. L., 1989, "Numerical Modeling of Devolatilization in Pulverised Coal Injection Inside a Hot Co-flowing Air Flow," *Lecture Notes in Engrg.* (*Turbulent Reaction Flows*), Vol. 40, pp. 824–846.

Sun, T.-Y., and Faeth, G. M., 1986a, "Structure of Turbulent Bubbly Jets—I. Methods and Centerline Properties," *Int. J. Multiphase Flow*, Vol. 12, No. 1, pp. 99–114.

Sun, T.-Y., and Faeth, G. M., 1986b, "Structure of Turbulent Bubbly Jets—II. Phase Property Profiles," *Int. J. Multiphase Flow*, Vol. 12, No. 1, pp. 115–126.

Turkoglu, H., and Farouk, B., 1993, "Numerical Computations of Fluid Flow and Heat Transfer in Gas Injected Iron Baths," *ISIJ Int.*, in press.

Warda, H. A., and Abou-Ellail, M. M. M., 1984, "Computer Simulation of Two-Phase Flow in Oil Wells Using Gas-Lift," *Engrg. Software for Microcomputers, Proc. 1st Inf. Conf.*, Venice, pp. 567–581.

APPENDIX A

The Two-Fluid Mean Mass and Momentum Equations

Following the work of Mostafa and Elghobashi (1986) and Elghobashi and Abou-Arab (1983), the time-averaged, steady-state, conservation equations for mass and momentum may be written as follows:

$$\frac{\partial}{\partial x_i}(\bar{\rho}_g\bar{\alpha}_g\bar{u}_{gi})+\frac{\partial}{\partial x_i}(\bar{\rho}_g\overline{\alpha'_g u'_{gi}})=\dot{m}_v'''\,\bar{\alpha}_l \qquad \text{(A1)}$$

$$\frac{\partial}{\partial x_i}(\bar{\rho}_l\bar{\alpha}_l\bar{u}_{li})+\frac{\partial}{\partial x_i}(\bar{\rho}_l\overline{\alpha'_l u'_{li}})=-\dot{m}_v'''\,\bar{\alpha}_l \qquad \text{(A2)}$$

$$\frac{\partial}{\partial x_i}(\bar{\rho}_g\bar{\alpha}_g\bar{u}_{gi}\bar{u}_{gj}-\bar{\alpha}_g\bar{\tau}_{gij}+\bar{\rho}_g\bar{\alpha}_g\overline{u'_{gi}u'_{gj}}+\bar{\rho}_g\bar{u}_{gj}\overline{\alpha'_g u'_{gi}}+\bar{\rho}_g\bar{u}_{gi}\overline{\alpha'_g u'_{gj}})$$
$$=-\bar{\alpha}_g\frac{\partial\bar{p}}{\partial x_j}+f_D\bar{\alpha}_l(\bar{u}_{lj}-\bar{u}_{gj})+\dot{m}_v'''\,(\bar{\alpha}_l\bar{u}_{lj}+\overline{\alpha'_l u'_{lj}})$$
$$+f_D\overline{\alpha'_l(u'_{lj}-u'_{gj})}+\bar{\alpha}_g(\bar{\rho}_g-\bar{\rho}_0)g_j \qquad \text{(A3)}$$

$$\frac{\partial}{\partial x_i}(\bar{\rho}_l\bar{\alpha}_l\bar{u}_{li}\bar{u}_{lj}-\bar{\alpha}_l\bar{\tau}_{lij}+\bar{\rho}_l\bar{\alpha}_l\overline{u'_{li}u'_{lj}}+\bar{\rho}_l\bar{u}_{lj}\overline{\alpha'_l u'_{li}}+\bar{\rho}_l\bar{u}_{li}\overline{\alpha'_l u'_{lj}})$$
$$=-\bar{\alpha}_l\frac{\partial\bar{p}}{\partial x_j}+f_D\bar{\alpha}_l(\bar{u}_{lj}-\bar{u}_{gj})+\dot{m}_v'''\,(\bar{\alpha}_l\bar{u}_{lj}+\overline{\alpha'_l u'_{lj}})$$
$$+f_D\overline{\alpha'_l(u'_{lj}-u'_{gj})}+\bar{\alpha}_l(\bar{\rho}_l-\bar{\rho}_0)g_j \qquad \text{(A4)}$$

and the global continuity is

$$\bar{\alpha}_g+\bar{\alpha}_l=1 \qquad \text{(A5)}$$

In the above, the subscripts "g" and "l" denote gas and liquid phases, respectively. $\bar{u}_i$ is the mean velocity in the i direction and u'_i is its fluctuating component. f_D is a momentum exchange coefficient, which is mainly dominated by interfacial drag for free two-phase jet flow (other forces such as the Saffman lift forces are only important near pipe walls), $\bar{p}$ is the mean pressure, g_j is the j-component of the gravitational acceleration, and α is the volume fraction. τ_{ij} is the mean laminar stress tensor. For the gas phase, it is given by

$$\bar{\tau}_{gij}=\mu_g\left[\frac{\partial\bar{u}_{gi}}{\partial x_j}+\frac{\partial\bar{u}_{gj}}{\partial x_i}-\left(\frac{2}{3}\right)\frac{\partial\bar{u}_{gm}}{\partial x_m}\delta_{ij}\right] \qquad \text{(A6)}$$

and similarly for the liquid phase. However, μ_l in this case is caused by the carrier phase molecular motion (Rizk and Elghobashi, 1989). To express the equation above in cylindrical coordinates is straightforward. For example, in the continuity Eqs. (A1) and (A2), the term $(\partial/\partial x_i)(c\phi_i)$ becomes $(1/r)(\partial/\partial r)(r\phi_r)+(\partial/\partial z)(\phi_z)$, while in the momentum Eqs. (A3) and (A4), the shear term $(\partial/\partial z_i)(\bar{\alpha}_g\tau_{gij})$ should be replaced by $(1/r)(\partial/\partial r)(r\bar{\alpha}_g\tau_{g_{rr}})+(\partial/\partial z)(\bar{\alpha}_g\tau_{gzz})$, and the shear term $(\partial/\partial x_i)(\bar{\alpha}_l\tau_{lij})$ needs to be replaced by $(1/r)(\partial/\partial r)(r\bar{\alpha}_l\tau_{lrr})+(\partial/\partial z)(\bar{\alpha}_l\tau_{lzz})$.

The moment exchange coefficient f_D is given by (Abou-Ellail and Abou-Arab, 1985)

$$f_D=18Z\mu_g/d_l^2 \qquad \text{(A7)}$$

where d_l is the mean droplet (or bubble) diameter and μ_g is the gas laminar viscosity. Z may be calculated for deformable droplets (Markatos and Singhal, 1982)

$$Z=1+0.15\,\mathrm{Re}_l^{0.687}+0.02\,\mathrm{Re}_l/(1+42{,}500/\mathrm{Re}_l^{1.16}) \qquad \text{(A8)}$$

where Re_l is the liquid droplet (or bubble) Reynolds number, in the j direction, defined as

$$\mathrm{Re}_l=\bar{\rho}_g d_l|\bar{u}_{gj}-\bar{u}_{lj}|/\mu_g \qquad \text{(A9)}$$

In the above equations, some terms involving α' have been neglected due to their relatively small contribution (Mostafa and Elghobashi, 1986; Elghobashi and Abou-Arab, 1983). Moreover, terms involving ρ' were also ignored (Lockwood and Stolakis, 1983). The remaining time-averaged fluctuation terms and the required two-fluid turbulence model are presented in Appendix B.

APPENDIX B

The Turbulence Model

The Reynolds stresses ($\overline{u'_{gi}u'_{gj}}$ and $\overline{u'_{li}u'_{lj}}$) are calculated by way of a two-phase k–ϵ model (Elghobashi and Abou-Arab, 1983) using the concept of eddy diffusivity,

$$-\overline{u'_{gi}u'_{gj}}=\nu_t\left[\frac{\partial\bar{u}_{gi}}{\partial x_j}+\frac{\partial\bar{u}_{gj}}{\partial x_i}-\left(\frac{2}{3}\right)\frac{\partial\bar{u}_{gm}}{\partial x_m}\delta_{ij}\right]-\frac{2}{3}k\delta_{ij} \qquad \text{(A10)}$$

for the gas phase, and

$$-\overline{u'_{li}u'_{lj}}=(\nu_t/\sigma_l)\left[\frac{\partial\bar{u}_{li}}{\partial x_j}+\frac{\partial\bar{u}_{lj}}{\partial x_i}-\left(\frac{2}{3}\right)\frac{\partial\bar{u}_{lm}}{\partial x_m}\delta_{ij}\right]-\frac{2}{3}k_l\delta_{ij} \qquad \text{(A11)}$$

for the liquid phase. The last term in Eq. (A11) is included to balance the equation (namely, to satisfy the condition $\overline{u'_{li}u'_{li}}/2=k_l$) but it is usually negligible. $\sigma_l\,(\equiv\nu_t/\nu_{tl})$ is the liquid phase turbulent Schmidt number of the order of unity; its value for spray flames is expected to be higher than 1.0 (see Eq. (A20)), reflecting the reduced effect of turbulent diffusion of the droplets relative to the gas phase. ν_t and ν_{tl} are turbulent kinematic viscosities of gas and liquid. The carrier phase turbulent kinematic viscosity ν_t is defined as

$$\nu_t=C_\mu k^2/\epsilon \qquad \text{(A12)}$$

Here, k is ($\overline{u'_{gi}u'_{gi}}/2$) and ϵ is its dissipation rate. C_μ is a constant of the model. The last term in Eqs. (A10)–(A11) is too small to affect the momentum equations significantly and can be neglected in later computations.

The kinetic energy of turbulence k and its dissipation rate ϵ are to be calculated from their transport equations (Mostafa and Elghobashi, 1986), namely

$$\bar{\rho}_g\bar{\alpha}_g\bar{u}_{gi}\frac{\partial k}{\partial x_i}-\frac{\partial}{\partial x_i}\left[\left(\frac{\mu_t\bar{\alpha}_g}{\sigma_k}\right)\frac{\partial k}{\partial x_i}\right]=\bar{\alpha}_g(G+\Delta G)$$
$$-\bar{\rho}_g\bar{\alpha}_g(\epsilon+\Delta\epsilon) \qquad \text{(A13)}$$

$$\rho_g\bar{\alpha}_g\bar{u}_{gi}\frac{\partial \epsilon}{\partial x_i}-\frac{\partial}{\partial x_i}\left[\left(\frac{\mu_t\bar{\alpha}_g}{\sigma_\epsilon}\right)\frac{\partial \epsilon}{\partial x_i}\right]=\bar{\alpha}_g\left(\frac{\epsilon}{k}\right)C_1(G+\Delta G)$$
$$-\bar{\rho}_g\bar{\alpha}_g\left(\frac{\epsilon}{k}\right)(C_2\epsilon+C_3\Delta\epsilon) \qquad \text{(A14)}$$

where C_1, C_2, and C_3 are constants of the two-phase k–ϵ model. ΔG and $\Delta\epsilon$ are additional generation and dissipation terms due to slip between the two phases, volume fraction fluctuations, and evaporation of the liquid phases. The full expressions for ΔG and $\Delta\epsilon$ are available for nonevaporating two-phase flow (Elghobashi and Abou-Arab, 1983) and the flow modified to account for evaporation (Mostafa and Elghobashi, 1986). The standard generation term G is given, as for single-phase, by

$$G=\mu_t\left(\frac{\partial\overline{u}_{gi}}{\partial x_j}+\frac{\partial\overline{u}_{gj}}{\partial x_i}\right)\frac{\partial\overline{u}_{gi}}{\partial x_j}-\frac{2}{3}\frac{\partial\overline{u}_{gm}}{\partial x_m}\left(\mu_t\frac{\partial\overline{u}_{gm}}{\partial x_m}+\overline{\rho}_g k\right) \qquad \text{(A15)}$$

The remaining correlation terms in Eqs. (A1)–(A4) are modeled using the Boussinesq approximation similar to single-phase flow (Abou-Ellail and Abou-Arab, 1985)

$$-\overline{\alpha_g' u_{gi}'}=\overline{\alpha_l' u_{gi}'}=\left(\frac{\nu_t}{\sigma_{\alpha g}}\right)\frac{\partial\overline{\alpha}_g}{\partial x_i} \qquad \text{(A16)}$$

$$-\overline{\alpha_l' u_{li}'}=\overline{\alpha_g' u_{li}'}=\left(\frac{\nu_{tl}}{\sigma_{\alpha l}}\right)\frac{\partial\overline{\alpha}_l}{\partial x_i} \qquad \text{(A17)}$$

where $\sigma_{\alpha g}=1$ and $\sigma_{\alpha l}=1$ are the turbulent Schmidt numbers in the gas and liquid phases, respectively, and $\mu_t=\overline{\rho}_g\nu_t$. Equations (A16)–(A17) make use of the fact that $\alpha_g'=-\alpha_l'$ at any time. For any variable ϕ, the following relations (Abou-Ellail and Abou-Arab, 1985) can be used:

$$-\overline{u_{gi}'\phi_g'}=\frac{\nu_t}{\sigma_\phi}\frac{\partial\overline{\phi}_g}{\partial x_i} \qquad \text{(A18)}$$

$$-\overline{u_{li}'\phi_l'}=\frac{\nu_{tl}}{\sigma_\phi}\frac{\partial\overline{\phi}_l}{\partial x_i}=(\nu_t/\sigma_l\sigma_\phi)\frac{\partial\overline{\phi}_l}{\partial x_i} \qquad \text{(A19)}$$

where σ_l reflects the coupling effect between the gas and liquid momentum fields and can be calculated as (Simonin and Viollet, 1989),

$$\sigma_l=1+\frac{2}{3}\overline{\rho}_l\epsilon/[C_\mu k f_D(1+\overline{\alpha}_l\overline{\rho}_l/\overline{\rho}_g\overline{\alpha}_g)] \qquad \text{(A20)}$$

The model constants used are: $C_\mu=0.09-0.04F$, $C_1=1.44$, $C_2=1.92-0.0667F$, $C_3=1.2$, σ_l is given by Eq. (A20), $\sigma_k=1.0$, $\sigma_\epsilon=1.3$, $\mathrm{Sc}=0.7$, and $\sigma_{\alpha l}=\sigma_{\alpha g}=1.0$, where F is a correction factor to account for jet spreading rate given by (Rodi, 1979),

$$F=\left|\left(\frac{d\overline{u}_{gc}}{dx}-\left|\frac{d\overline{u}_{gc}}{dx}\right|\right)\Delta r/(1.6\Delta\overline{u}_{gc})\right|^{0.2} \qquad \text{(A21)}$$

Here x is the axial direction, $d(\overline{u}_{gc})/dx$ is the axial velocity gradient of the gas phase, Δr is the width of the turbulent region in the spreading jet, i.e., r (at $\Delta\overline{u}_g=0.1\ \Delta\overline{u}_{gc}$) $-\,r$ (at $\Delta\overline{u}_g=0.9\ \Delta\overline{u}_{gc}$) and $\Delta\overline{u}_{gc}$ is the maximum velocity difference in the radial plane across the turbulent region of the jet. The above was also used for two-phase, nonreacting flow (Mostafa and Elghobashi, 1986). It is noted that all model constants are the same as those in the existing LHF model except $C_3=1.2$, which was determined by Elghobashi and Abou-Arab (1983). Thus, the only new constants introduced are $\sigma_{\alpha l}=\sigma_{\alpha g}=1$, since the turbulent transports of momentum and mass are of the same order in each phase. As mentioned before, the above equations are also applicable to bubbly flow if the g subscript is interchanged with the l subscript.

Solidification of Liquid Metal Droplets Impacting Sequentially on a Solid Surface

B. Kang

Z. Zhao

D. Poulikakos

Department of Mechanical Engineering,
University of Illinois at Chicago,
842 West Taylor St.,
Chicago, IL 60607-7022

In this paper, a combined theoretical and experimental study is reported on the process of solidification of two liquid metal droplets impacting sequentially one on top of the other on a cold substrate. The process of interest is directly related to the splat-quenching regime in the spray deposition of metal droplets. The theoretical part of the study is focused on the heat transfer aspects of the solidification process and the difference in the behavior of the solidification of the first and second droplet. The experimental part of the study aims at the characterization of the structure of solidified splats composed of one or two droplets. It is found that the solidification of the second droplet exhibits drastically slower cooling rates compared to the first droplet. As a result, the grain structure of the top of a two-droplet splat is considerably coarser than the structure of the top of a single droplet splat. The findings of the present study imply that in splat cooling severe limitations need to be imposed on the thickness of the resulting solid product (ribbon or coating, for example) to ensure rapid solidification and fine grain structure. In addition, it is shown that the temperature field in the substrate is two dimensional and radial conduction in the substrate should not be neglected in the modeling of the process.

1 Introduction

Splat-quenched solidification is a rapid solidification process that involves the impingement, spreading, and ensuing solidification of a liquid metal droplet on a solid substrate. Contrary to traditional manufacturing processes where the quenching is performed on solid material specimens, Rapid Solidification Processes (RSP) represent a separate category of quenching in which the initial state of the material is liquid. In the case of quenching an alloy from the liquid state, the liquidus and solidus become critical phase boundaries, introducing the potential for novel nonequilibrium phases to be captured provided quenching is very rapid. Because the atomic mobility in a liquid is far greater than in a solid, the quenching rate must be much faster to arrest a nonequilibrium state residing in the liquid phase than to secure one residing in the solid phase. This brings up a defining characteristic of RSP, which is that cooling rates imposed on the melt are typically many orders of magnitude faster than conventional quenching methods.

Splat-quenched solidification is one member of a family of spray deposition regimes (Jones, 1982; Gutierrez-Miravete, 1985; Annavarapu et al., 1990). These regimes are distinguished by the conditions existing on the deposition surface as well as the state of the impinging spray itself. In the case of splat-quenched solidification, consecutive generations of entirely liquid molten droplets impact upon a completely solidified surface. This situation occurs when the mechanism of heat transfer (principally conduction) away from the deposition layer is capable of removing heat much faster than it is deposited by the molten material.

Manufacturing has taken an interest in spray deposition technology because of its near-net shaping capability, rapid preform production, as well as improved material properties (Annavarapu et al., 1990; Bricknell, 1986; Brooks et al., 1977). With reference to the process of splat-quenched solidification, one of the most frequently utilized rapid solidification processes, it is easy to discover that a significant amount of work has been performed to study the basic mechanisms of this process especially from the materials science standpoint. In addition, the great majority of existing studies deals with splat-quenching of a single droplet. A representative cross section of existing studies is presented in the following paragraphs.

Jones (1982) and Anatharaman and Suryanarayana (1971) have summarized the first decade of developments resulting from the application of the splat-quenching technique. Predecki et al. (1965) performed a study to determine solidification rates, heat transfer coefficients, and cooling rates in splats. They studied not individual droplets but a spray produced from a few tenths of a gram of molten metal with the "gun" technique. The impingement of the spray on the substrate was recorded using high-speed silhouette photography, and the thermal histories of the splats were measured by a variation of the usual thermocouple device. Although they did not make any direct conversion to temperatures from the thermoelectric potential established by the thermocouple, Predecki et al. (1965) were able to estimate cooling rates, the splat-substrate heat transfer coefficient, and solidification rates, by assuming that the potential varied linearly with temperature and that the cooling of the splat was Newtonian (no temperature gradients were established within the splat). Predecki et al. (1965) demonstrated a couple of defining characteristics of the splat-quenching process, the first being that cooling rates imposed on the splat are extremely high, and the second, that the freeze propagates very rapidly through the melt. However, they made no effort to establish the effect of the substrate material and/or temperature on the cooling and solidification of the splats.

Brower et al. (1970) performed a comparative study of the relative cooling rate and its effect on microstructure, for cooling imposed by gas quenching, liquid quenching, chill casting, and splat quenching. They found that typical cooling rates were: 1–10°C/s for gas quenching, 30–200°C/s for liquid quenching, 10^3–10^4°C/s for chill casting, and 10^5–10^6°C/s for splat quenching. They also investigated the effect of splat thickness on the cooling rate and determined that the cooling rate of the splat would be increased by faster thinning of the melt.

Scott (1974) made comparative measurements of the average and maximum cooling rate exhibited by aluminum copper alloy

---

Contributed by the Heat Transfer Division for publication in the JOURNAL OF HEAT TRANSFER. Manuscript received by the Heat Transfer Division April 1993; revision received August 1993. Keywords: Materials Processing and Manufacturing Processes, Phase-Change Phenomena, Sprays/Droplets. Associate Technical Editor: A. Faghri.

splats quenched on copper and glass (soda glass) substrates. He used an existing approach based on a theoretically developed relationship between lamellar spacing and the freezing rate of a eutectic alloy. He found the surprising result that the cooling rate of a splat on glass substrate was higher than the cooling rate of the same splat on a copper substrate. He explained his results by suggesting that the thermal contact between the splat and the substrate was much better for the glass substrate than the copper substrate and supported this claim by citing evidence that the splats had melted the surface of the glass substrate slightly, thereby improving the thermal contact.

Wang and Matthys (1991, 1992) have investigated the interface velocity as a function of propagation distance, with and without undercooling of the melt, using a one-dimensional conduction model. With undercooling, the velocity of the interface is seen to decrease rapidly as the freeze propagates. Without undercooling of the melt, the velocity of the interface is heat transfer limited, realizing a less drastic change in interface velocity as the front propagates forward. Naturally, the quality of thermal contact between splat and substrate is influential in sustaining the interface velocity in an undercooled melt and critical if there is no undercooling. They focused on a single droplet having completed the spreading process before the initiation of heat transfer. They modeled the splat as a thin disk.

Relevant to the splat quenching process was the work of Shingu and Ozaki (1975) who numerically investigated rapid solidification occurring by conduction cooling. Rosnar and Epstein (1975) studied theoretically the simultaneous kinetic and heat transfer limitations in the crystallization of highly undercooled melts. Evans and Greer (1988) developed a one-dimensional numerical solution for the rapid solidification of an alloy melt in order to investigate solute trapping. Their model employed two equations relating the interface velocity and solid composition to the temperature and liquid composition at the freezing interface. They found that the heat extraction rate was the principal determinant of the freezing interface velocity and therefore of the degree of solute trapping. Changes in initial alloy composition slightly altered the interface temperature; however, this change in temperature did not have a large enough effect on the diffusivity of the liquid to alter the amount of solute trapping substantially.

The work presented in this paper aims at improving our understanding of the rapid solidification of a splat formed by two liquid metal droplets quenched sequentially one on top of the other on a substrate. Since we are interested in the splat cooling regime, the impact of the second droplet takes place after the first droplet has completed its solidification. It is the main goal of the study to compare the solidification phenomenon in the first and second droplets. In doing so, conclusions will be drawn relevant to the final thickness of the splat versus the desired fine grain structure characteristic of rapid solidification processes. The study consists of two parts: In the first part, a theoretical heat transfer model examines the heat transfer aspects of the solidification process accounting for freezing kinetics considerations. In the second part, an experiment is performed to create metal splats from one or two liquid metal droplets. The grain structure of these splats is examined with electron microscopy to determine the effect of the cooling rate on the grain structure.

2 Mathematical Model and Numerical Solution

The theoretical part of the study consists of an approximate heat transfer model of the solidification processes in the two-droplet splat. Invoking a simple order of magnitude analysis, it can be easily shown that the time scale of the spreading process of a droplet impacting on a surface is much shorter than the time scale of the heat transfer process from the splat to the substrate. This result practically implies that the droplets forming the splat spread first and cool down subsequently. To construct a relatively simple and easy to use model of the solidification process, we make use of the aforementioned result and model each droplet in the splat as a thin metal disk initially in the liquid phase and finally, after the solidification is completed, in the solid phase. The simplification of modeling a splat as a thin metal disk has been used successfully in earlier investigations of single droplet splats (Madejski, 1976, 1983; Wang and Matthys, 1991, 1992).

Since we are investigating the splat cooling regime, it is

Nomenclature

c = specific heat, J/kgK
d = diameter of spherical droplet, mm
D = diameter of splat, mm
g = gravitational acceleration, m/s^2
h = heat transfer coefficient for free falling spheres, W/m^{2}K
h_a = convective heat transfer coefficient, W/m^{2}K
h_c = contact heat transfer coefficient, W/m^{2}K
H = height of splat, μm
I = number of nodes in axial direction in splat
k = thermal conductivity, W/mK
K_f = freezing kinetics coefficient, m/sK
L = latent heat, J/kg
M = number of nodes in radial direction in substrate
N = number of nodes in axial direction in substrate
Nu_d = Nusselt number for free falling spheres
Pr = Prandtl number
r = radial coordinate, mm
R = radius of splat, mm
Re = Reynolds number
Δr = increment of radial coordinate, mm
t = time, s
t' = time lapsed since the contact of the second splat with the first splat
t_c = flight time of impacting droplet, s
T = temperature, °C
T_f = equilibrium freezing temperature, °C
T_o = initial temperature of splat, °C
T_∞ = initial temperature of substrate or ambient air temperature, °C
V = interface velocity, m/s
z = axial coordinate, mm
Δz = increment of axial coordinate, mm
Z = distance between release point and substrate, m
α = thermal diffusivity, m^2/s
θ = temperature difference between droplet and ambient air
θ_a = initial temperature difference between droplet and ambient air
ν = kinematic viscosity, m^2/s
ξ = spread factor
ρ = density, kg/m^3

Superscripts

l = liquid
m = index taking on the values s for solid or l for liquid
s = solid

Subscripts

b = bottom of control volume containing freezing interface
i = interface
j = index taking on the values 1 for the first (bottom) splat or 2 for the second (top) splat
t = top of control volume containing freezing interface
1 = first splat
2 = second splat

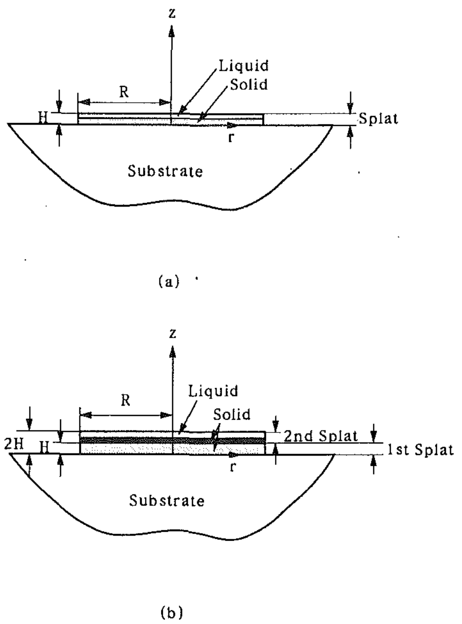

Fig. 1 Schematic of the system of interest: (*a*) single-droplet splat; (*b*) two-droplet splat

assumed that the second disk (splat) contacts the first disk (splat) a short time after the solidification process of the first splat is completed. Figure 1(*a*) shows a schematic of the model of a single droplet splat and Fig. 1(*b*) a schematic of the model of a two-droplet splat according to the aforementioned simplifications. The exact dimensions of each disk are determined from the experiments, as will be discussed in detail in section 4.

Owing to the fact that the thickness to diameter ratio of the splat is very small (typically of the order of 0.1 to 0.05) the heat conduction process in the splat is practically unidirectional. Earlier studies of the heat conduction process in a single droplet splat (Bennett, 1993) have shown that neglecting the effect of radial conduction in the splat has minimal impact on the resulting temperature field. On the other hand, the present model will account for both radial and axial conduction in the substrate. Note that in earlier studies of the freezing of single droplet splats (Madejski, 1976, 1983; Wang and Matthys, 1991, 1992), the effect of radial conduction in the substrate was neglected.

The first droplet in the splat is assumed to be a thin metal disk at uniform temperature, which is suddenly brought into contact with a large (by comparison) substrate of initial temperature considerably lower than the freezing temperature of the disk metal, T_f. Heat is conducted away from the splat to the substrate. Solidification ensues and progresses until the entire splat is solidified. After a short time, the second droplet of the splat is deposited on top of the first droplet. The modeling and the initial condition of the second droplet (disk) are identical to those of the first droplet. Heat is conducted from the second splat to the first splat and eventually to the substrate. Solidification of the second splat ensues and progresses until the entire region solidifies.

Following the discussion above, the heat conduction equation for both the first droplet and the second droplet in the splat reads

$$(\rho c)_j^m \frac{\partial T_j^m}{\partial t} = \frac{\partial}{\partial z}\left(k_j^m \frac{\partial T_j^m}{\partial z}\right) \qquad (1)$$

where the subscript j takes on the values 1 or 2 corresponding to the first (bottom) or the second (top) disk and the superscript m takes on the values s or l denoting solid or liquid region. The temperature is denoted by T, the time by t, the axial coordinate by z (Fig. 1), and the density, specific heat, and thermal conductivity of the solidifying material by ρ, c, and k, respectively. The heat conduction equation in the substrate is

$$\rho c \frac{\partial T}{\partial t} = k\left(\frac{\partial^2 T}{\partial r^2} + \frac{1}{r}\frac{\partial T}{\partial r} + \frac{\partial^2 T}{\partial z^2}\right) \qquad (2)$$

where the notation is analogous to what was defined above with the added clarification that r stands for the radial coordinate (Fig. 1).

The initial conditions for the splat and the substrate are

$$T_1^l(z, t=0) = T_o \qquad (3)$$

$$T_2^l(z, t'=0) = T_o \qquad (4)$$

$$T(r, z, t=0) = T_\infty \qquad (5)$$

It is worth clarifying that t is the time from the contact of the first splat with the substrate and t' is the time from the contact of the second splat with the first splat.

The boundary and matching conditions accompanying the above are:

$$T(r \to \infty, z=0, t) = T_\infty \qquad (6)$$

$$T(r, z \to -\infty, t) = T_\infty \qquad (7)$$

$$-k_1^m \frac{\partial T_1^m}{\partial z}\bigg|_{z=H,\, t} = h_a[T_1^m(z=H, t) - T_\infty], \quad m=s \text{ or } l \qquad (8)$$

$$-k_2^m \frac{\partial T_2^m}{\partial z}\bigg|_{z=2H,\, t'} = h_a[T_2^m(z=2H, t') - T_\infty], \quad m=s \text{ or } l \qquad (9)$$

$$-k \frac{\partial T}{\partial z}\bigg|_{r>R,\, z=0,\, t} = h_a[T(r>R, z=0, t) - T_\infty] \qquad (10)$$

Boundary conditions (6) and (7) simply state the fact that the temperature inside the substrate far away from the surface as well as the temperature of the substrate surface far away from the splat region remain unaffected by the solidification process and retain their initial value. Boundary conditions (8)-(10) account for convective losses through the top of the first splat, the top of the second splat, and the top of the substrate surrounding the splat, respectively. Clearly, boundary condition (8) is in effect prior to the deposition of the second splat. After the second splat is deposited on top of the first splat, boundary condition (8) is replaced by

$$-k_1^s \frac{\partial T_1^s}{\partial z}\bigg|_{z=H,\, t} = h_c[T_1^s(z=H, t') - T_2^m(z=H, t')], \quad m=s \text{ or } l \qquad (11)$$

where h_c is the contact heat transfer coefficient (the reciprocal of the contact resistance) between the two splats. A matching condition analogous to Eq. (11) is utilized at the interface to couple the substrate with the first splat:

$$-k \frac{\partial T}{\partial z}\bigg|_{r<R,\, z=0,\, t} = h_c[T(r<R, z=0, t) - T_1^m(z=0, t)], \quad m=s \text{ or } l \qquad (12)$$

It has been found in studies of single droplet splats (Wang and Matthys, 1991, 1992; Bennett, 1993) that it is important to account for the presence of contact resistance in the heat transfer modeling of the splat cooling process.

The next issue to be discussed is that of the freezing interface separating the solid from the liquid region. At this interface the following energy balance is satisfied:

$$\rho_j^s L V = k_j^s \frac{\partial T_j^s}{\partial z}\bigg|_{z=z_i} - k_j^l \frac{\partial T_j^l}{\partial z}\bigg|_{z=z_i}, \quad j=1 \text{ or } 2 \qquad (13)$$

The subscript i denotes the freezing interface, V is the velocity of this interface, and L is the latent heat of fusion.

In the classical equilibrium treatment of a freezing front, this front is defined by the freezing temperature of the material (T_f) and its propagation velocity is limited by Eq. (13) (the rate at which the heat generation at the interface is conducted away in the liquid and solid regions). This treatment, however, does not account for the presence of undercooling in the melt, which is of great importance to rapid solidification processes such as the splat quenching problem under investigation. To model the undercooling, a freezing kinetics relationship between the amount of undercooling and the velocity of propagation of the freezing front is needed. A common relationship of this kind postulates a linear dependence between the freezing front propagation velocity and the amount of undercooling (Levi and Mehrabian, 1982; Clyne, 1984; Wang and Matthys, 1991, 1992; Bennett, 1993)

$$V = K_f(T_f - T_i) \tag{14}$$

where K_f is a freezing kinetics coefficient, T_f is the equilibrium freezing temperature of the material, and T_i is the actual interface temperature. Obviously, the difference $T_f - T_i$ defines the amount of undercooling. If undercooling exists and T_i is below T_f, Eq. (14) will result in a rate of latent heat release in excess of that which can be conducted away from the interface (Eq. (13)). In this limit, the propagation of the solidification front is said to be controlled by the freezing kinetics. The rapid propagation of the freezing interface will cause its heating and subsequent retardation. As the freezing interface temperature approaches the equilibrium freezing temperature, the solidification becomes heat transfer limited.

The numerical solution of the aforementioned mathematical model was obtained with the finite difference method. To this end, the substrate was overlaid with a network of M points in the radial direction and N points in the axial direction. Both the grid sizes Δr and Δz were allowed to vary depending on the spatial position. The finite differencing of the heat conduction model in the substrate was obtained with the control volume formulation (Patankar, 1981; Wang and Matthys, 1991, 1992; Bennett, 1993) and solved by utilizing the ADI method (Anderson et al., 1984). No further details on the control volume formulation or the ADI method are included here for brevity; they can be found in the aforementioned literature.

The control volume method was also used to discretize the unidirectional heat conduction model in the splat, first for the case when only one droplet is deposited and next for the case when the second droplet is added. The splat was overlaid with a unidirectional uniform grid (in the axial direction) consisting of I grid points when only one droplet was present. An identical grid of I points was used to discretize the conduction in the second droplet of the splat once it was deposited on top of the first droplet. The discretized equations of the splat were cast in tridiagonal form and solved with the Thomas algorithm (Anderson et al., 1984).

To account for the sudden change in the value of the thermophysical properties across the freezing interface, the following procedure (Goodrich, 1978) was adopted. The control volume containing the freezing interface was subdivided into two regions, a solid region and a liquid region as shown in Fig. 2. Three (instead of one) grid points were placed in this control volume: one at the interface location, one at the center of the solid region, and one at the center of the liquid region (Fig. 2). These three points satisfied the following equations (which are discretized utilizing the control volume method, as well):

$$-k_j^s \frac{\partial T_j^s}{\partial z}\bigg|_b + k_j^s \frac{\partial T_j^s}{\partial z}\bigg|_i = \rho_j^s c_j^s \frac{\partial T_j^s}{\partial t}, \quad j = 1 \text{ or } 2 \tag{15}$$

$$-k_j^s \frac{\partial T_j^s}{\partial z}\bigg|_i + k_j^l \frac{\partial T_j^l}{\partial z}\bigg|_i = -\rho_j^s V L, \quad j = 1 \text{ or } 2 \tag{16}$$

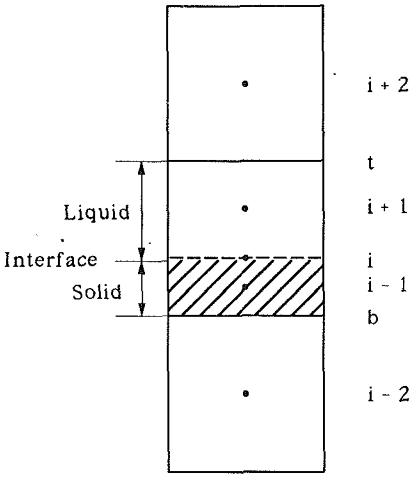

Fig. 2 Grid points in the control volume containing the freezing interface

$$-k_j^l \frac{\partial T_j^l}{\partial z}\bigg|_i + k_j^l \frac{\partial T_j^l}{\partial z}\bigg|_t = \rho_j^l c_j^l \frac{\partial T_j^l}{\partial t}, \quad j = 1 \text{ or } 2 \tag{17}$$

In the equations above the subscripts i, b, and t stand for interface, the bottom of the control volume containing the interface, and the top of the control volume containing the interface. Equations (15) and (17) are energy balances in the solid and liquid regions of the control volume containing the interface, respectively. Equation (16) is the interface energy balance.

Based on previous studies (Bennett, 1993), $M \times N = 70 \times 70$ grid points in the substrate and $I = 100$ points in each of the two droplets of the splat were chosen. Adding five points in each direction of the substrate left the results unaltered. Regarding the time step, a very fine time step ($\Delta t = 10^{-9}$ s for $h_c = 1.5 \times 10^4$ W/m^{2}K and $\Delta t = 10^{-12}$ s for $h_c = 1.5 \times 10^5$ W/m^{2}K) was used at the earlier stages of the transient phenomenon initiated by the deposition of the first droplet on the substrate as well as the deposition of the second droplet on top of the first droplet. At later times the time step was gradually increased to reflect the fact that the heat transfer process had slowed down. This task was performed by trial and error. The initial size of the time step was chosen to be small enough so that the maximum change in temperature within one time step is within 0.1 percent.

The numerical computation marched forward in time as follows: First, the current thermal and phase conditions of the one-droplet splat were checked. Freezing of the splat was initiated when the temperature of the bottom surface of the splat reached below the prescribed degree of undercooling. If freezing was present in the current time step, the freezing interface was moved forward a distance equal to the product of the interface velocity and one time step. The velocity of the freezing interface was determined from Eq. (14), using the temperature of the freezing interface obtained from the previous time step. Utilizing the updated physical conditions, the solution was advanced by one time step using the ADI method and Thomas algorithm. If the change of the temperature field between the current time step and the previous time step was very small, the size of the future time step was increased accordingly to speed up the calculation and the cycle was repeated.

This procedure was followed until the first droplet in the splat solidified entirely (the interface reached the top of the droplet). A short time thereafter (typically 11 μs for $h_c = 1.5 \times 10^4$ W/m^{2}K and 0.1 μs for $h_c = 1.5 \times 10^5$ W/m^{2}K) the second droplet was introduced and the numerical simulation was re-initiated covering now the entire domain consisting of the substrate, the first droplet, and the second droplet in the

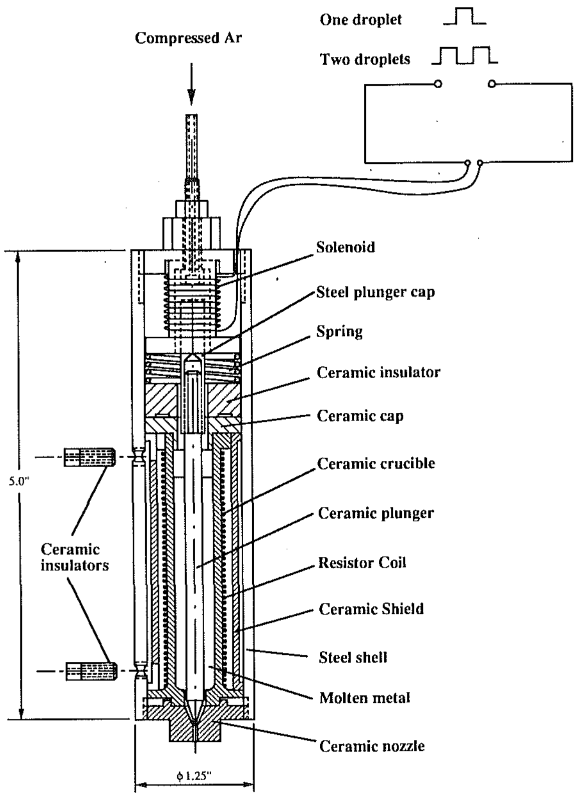

Fig. 3 Schematic diagram of the molten metal droplet generator

splat. The freezing of the second droplet was treated in a manner identical to that of the first droplet. The computation was terminated some time after the solidification of the second droplet was completed.

The numerical code typically required about 10 CPU hours to run on an IBM 3090/300J. This rather large time requirement is due to the very fine grid and time step sizes necessary for the accurate simulation of the rapid solidification of the two-droplet splat.

3 The Experimental Setup and Procedures

The main goal of the experimental part of the study was to determine whether the significant differences in the cooling rates between the first and second droplets in the splat (these differences will be discussed in the following section) affect the microstructure of the resulting solid splat. The main requirement, therefore, of the experimental setup was the successful generation of one or two (in a sequence) liquid metal droplets that would impact on a solid surface.

The solid surface upon which the droplets impacted was a copper plate of sufficient thickness (12.0 mm) to act as an infinitely thick substrate for the duration of the splat cooling process. The main component (and challenge) of the experimental set was to devise and build the generator of the liquid metal droplets. This generator should perform two functions: first, melt the metal under investigation and superheat it up to a desired temperature and, second, generate one, or a sequence of, liquid metal droplets. Several alternatives were considered. The final design is shown in Fig. 3.

The metal is melted inside a cylindrical ceramic crucible. On the outside of the crucible a resistor coil is wound. Connecting this resistor coil to a power supply provides the thermal energy necessary for the melting of the metal. The coil is constructed utilizing a nickel/chromium alloy wire that can be operated safely at temperatures up to 1200°C. These temperatures are well above the melting point of lead (327.5°C), which was the metal utilized in the present study, since its low melting point facilitates the experiments and limits oxidation. As seen in Fig. 3, a ceramic shield (sleeve) is placed outside the resistor coil. The droplets are generated utilizing the ceramic plunger shown in Fig. 3. This plunger is machined out of ceramic. The oscillation of the plunger is driven by a solenoid connected to a pulse generator. In its initial position, the tip of the plunger seals the nozzle of the droplet generator. To generate a liquid-metal droplet, after the metal in the crucible is melted, an electrical pulse is passed through the solenoid, creating an electromagnetic force and temporarily lifting the plunger upward. This allows for the escape of a liquid metal droplet through the nozzle at the bottom of the generator. Subsequently, the plunger returns to its original position by the action of the gravitational force, Fig. 3. The temperature of the melted metal in the crucible is monitored with a thermocouple. The temperature of the droplet at impact is estimated according to the simple heat transfer model outlined in the appendix. The diameter of the droplet is controlled by the size of the exit nozzle (Fig. 3) as well as by the duration of the pulse driving the plunger up and down. It is worth noting that a sequence of two droplets is generated if a sequence of two pulses is passed through the solenoid. A special pulse generator timing device was designed and built that allowed the control of both the pulse duration time and the pulse separation time in the case of a sequence of pulses. The height of the entire liquid metal droplet generator assembly (Fig. 3) was 107.0 mm and its diameter 31.8 mm.

After the liquid-metal droplets are released from the droplet generator, they require some time to attain a spherical shape. This time is an important parameter for the experimental design of this study. An approximate analysis was performed to determine the characteristic time required for a protruding liquid ligament to be incorporated in the liquid spherical mass of a droplet due to surface tension. The simple model employed by Goedde and Yuen (1970) was used for order of magnitude calculations. It was found that the characteristic time is shorter than a millisecond. The discussion above suggests that no additional considerations will be needed for non-sphericity effects during impact on the substrate.

The structure of the solidified splats (both their top surface and their bottom surface in contact with the substrate) was examined and recorded with electron microscopy. To this end, the IEOL JSM-35 C scanning electron microscope of the Research Resources Center of the University of Illinois at Chicago was utilized. This microscope provides magnifications up to 180,000 × with a point to point resolving power of 5 nm, which was more than adequate resolution for the observation of the important morphological details of the solidified splats.

4 Results and Discussion

In all the numerical simulations lead splats were utilized. As mentioned earlier, each droplet in the splat was approximated with a disk. The two-droplet splat consisted of two identical disks. The dimensions of each disk were decided based on the experimental observations. To this end, the spread factor (the ratio of the disk diameter, D, to the spherical droplet diameter, d, prior to impact) $\xi = D/d = 4.1$ was utilized. Equating the mass of the spherical droplet to the mass of the disk for this value of ξ yielded the height to diameter ratio of the disk for the numerical simulation $H/D = 0.02$.

The initial temperature of the substrate was room temperature ($T_\infty = 25°\text{C}$). The initial temperature of each disk prior to the initiation of the cooling process was assumed to be $T_o = 460°\text{C}$ (a value chosen based on experimental measurements, Bennett, 1993). This is equivalent to 133°C of superheat of the liquid lead, a realistic amount to achieve good fluidity for the droplet to be generated easily.

As mentioned in the previous section, severe undercooling is present in the process of splat cooling. Based on earlier

Table 1 Values of all the parameters used in numerical study

	copper	solid lead	liquid lead
k (W/m K)	397.0	34.9	15.4
ρ (kg/m^3)	8960	11680	10678
. c (J/kg K)	386.0	129.8	152.0
d	3.0 (mm)		
D	12.3 (mm)		
H	119.0 (µm)		
h_a , for top surface of splat	20.0 (W/m^{2}K)		
h_a , for top surface of substrate	8.0 (W/m^{2}K)		
h_c	1.5×10^4, 1.5×10^5 (W/m^{2}K)		
K_f	0.05 (m/s K)		
L of lead	23220 (J/ kg)		

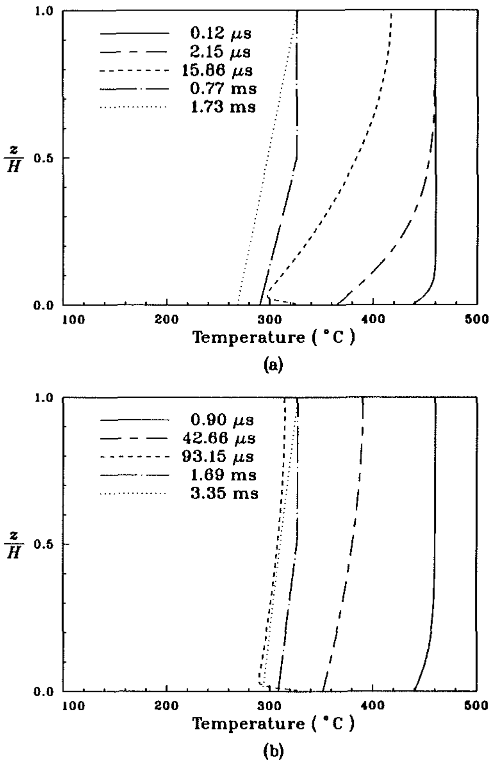

Fig. 4 The temperature distribution across the splat thickness for $h_c = 1.5 \times 10^5$ W/m^{2}K: (*a*) bottom splat; (*b*) top splat

experimental measurements (Bennett, 1993; Wang and Matthys, 1991, 1992), the initial value of undercooling $(T_f - T_i)_{t=0} = 40°$C was assigned for all numerical experiments. According to the literature (Bennett, 1993; Wang and Matthys, 1991, 1992), the value of the contact coefficient between the splat and the substrate is in the range 10^4 W/m^{2}K $< h_c < 2.0 \times 10^5$ W/m^{2}K. Low and high values of h_c were examined in the present work to cover the above range. Identical values of h_c were utilized to describe both the contact resistance between the splat and the substrate and the contact resistance between the two disks composing the splat.

The values of all the parameters (thermophysical properties and transport coefficients) utilized in the numerical study are listed in Table 1. These are all realistic values and they are held fixed throughout this study since the main goal of the study is to identify the differences between the solidification of the first and the second droplet in the two droplet splat.

The temperature distribution across the splat thickness for both the bottom and the top droplet in the splat in case of $h_c = 1.5 \times 10^5$ W/m^{2}K is shown in Fig. 4. The temperature field of the bottom droplet (Fig. 4*a*) differs markedly from the temperature field in the top droplet (Fig. 4*b*). Note that in both figures as well as in all the remaining figures in this paper, unless otherwise specified, the times $t = 0$ or $t' = 0$ correspond to the moment at which the first or the second disk simulating the flattened droplets come into thermal contact with the substrate (in the case of the bottom disk) or the bottom disk (in the case of the top disk). For example, the solid curve in Fig. 4(*a*) corresponds to the temperature distribution in the bottom disk 0.12 µs after the contact of this disk with the substrate. On the other hand, the solid curve in Fig. 4(*b*) represents the temperature distribution in the top disk 0.9 µs after this disk come into contact with the bottom disk. Throughout this study it was assumed that the second disk contacts the first disk in the splat very shortly (11 µs for $h_c = 1.5 \times 10^4$ W/m^{2}K, 0.1 µs for $h_c = 1.5 \times 10^5$ W/m^{2}K) after the solidification of the first disk is terminated.

Returning to Fig. 4(*a*) we observe that the cooling of the first droplet is initially localized in the vicinity of the splat/substrate interface in the form of a thermal boundary layer ($t = 0.12$ µs). Subsequently, the cooling effect propagates through the splat until solidification ensues. A solid/liquid interface exists in the splat at $t = 15.86$ µs and it is marked by the minimum in the temperature curve. This minimum is a direct result of the undercooling existing in the system. This undercooling was 40°C at the initiation of the freezing and it is about 30°C at $t = 15.86$ µs as shown in Fig. 4(*a*) (recall that the equilibrium freezing temperature of lead is $T_f = 327.5°$C).

As time progresses, the freezing front propagates upward and the undercooling diminishes. At $t = 0.77$ ms the freezing interface (marked by the cusp in the respective temperature curve) is practically at the equilibrium freezing temperature. The rapid solidification process of the first droplet has been completed by $t = 1.73$ ms and the temperature variation across the thickness of the splat is linear.

The temperature distributions in Fig. 4(*b*), corresponding to the top droplet in the splat, exhibit temperature gradients that are not as sharp as those of Fig. 4(*a*). As a result, the cooling process of the second droplet is considerably slower than that of the first droplet. It takes 93.15 µs to observe a solid/liquid interface in the top droplet (Fig. 4*b*) similar to the one observed in the bottom droplet at 15.86 µs (approximately one sixth of the earlier time).

Severe undercooling exists early in the freezing process. The undercooling diminishes later and the interface temperature becomes identical to the equilibrium freezing temperature. Owing to the heat released upon freezing, especially at the earlier stages, the splat warms up temporarily (compare the curves for $t = 93.15$ µs and 1.69 ms in Fig. 4*b*) before it cools down eventually and exhibits a linear temperature distribution at the termination of the freezing process ($t = 3.35$ ms).

Figure 5 pieces together the temperature history of the entire

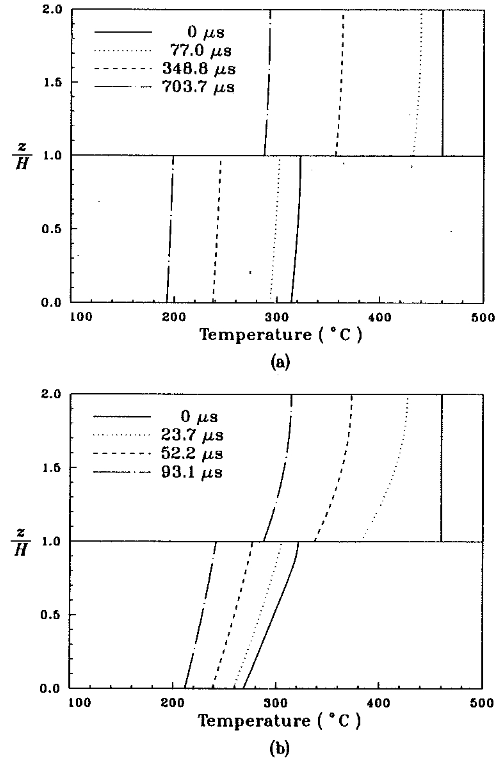

Fig. 5 The temperature profile in the entire two droplet splat: (*a*) $h_c = 1.5 \times 10^4$ W/m^{2}K; (*b*) 1.5×10^5 W/m^{2}K.

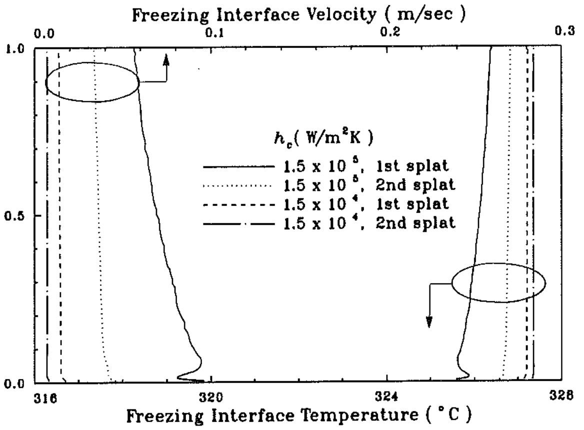

Fig. 6 The freezing interface temperature and velocity

two-droplet splat for two values of the contact coefficient: $h_c = 1.5 \times 10^4$ W/m^{2}K (Fig. 5*a*), $h_c = 1.5 \times 10^5$ W/m^{2}K (Fig. 5*b*). The times for all curves in this figure are measured from the initiation of the cooling of the second (top) droplet of the splat. By this time the solidification of the bottom droplet has been completed. The behavior of the two droplets in the splat is qualitatively similar. In both cases (Fig. 5*a*, *b*) the temperature jump caused by the imperfect thermal contact at the interface decreases as the cooling process progresses. The large contact coefficient (Fig. 5*b*) yields larger temperature gradients in the splat and much faster conduction cooling. For example, the temperature range of the splat at $t = 348.8$ μs in Fig. 5(*a*) is of similar magnitude with the temperature range of the splat at only $t = 93.1$ μs in Fig. 5(*b*). The presence of a small contact coefficient results in small temperature variations in the splat (of the order of 10°C in Fig. 5*a*), an indication of largely Newtonian cooling.

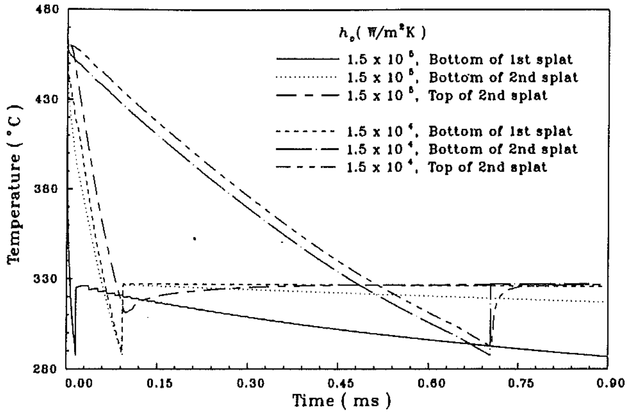

Fig. 7 The temperature history of top and bottom surface of each splat

The freezing interface temperature and velocity are shown in Fig. 6. Only the bottom splat for $h_c = 1.5 \times 10^5$ W/m^{2}K exhibits a behavior that is controlled by the freezing kinetics expressed in Eq. (14). In this case, the freezing interface temperature gradually approaches the equilibrium value. In all other cases, it remains almost constant except at the initial stage of the solidification. This fact is due to the large heat extraction capability for $h_c = 1.5 \times 10^5$ W/m^{2}K at the splat/substrate interface relative to all the other cases. The heat released at the freezing interface is not fully used for the increase of the freezing interface temperature because it is rapidly conducted away. A considerable amount of undercooling, which controls the freezing interface velocity, exists in the solid curves of Fig. 6. On the other hand, the heat transfer limited behavior is present for all the other cases in Fig. 6. This indicates an equilibrium between the heat released at the freezing interface and the heat conducted away from the freezing interface. As soon as the solidification starts, the heat released at the freezing interface cannot be conducted away rapidly enough due to poor thermal contact. Therefore, the freezing interface temperature is increased almost to the value of the equilibrium freezing temperature. Subsequently, the freezing temperature remains constant due to the establishment of the aforementioned balance between heat generation and removal at the freezing interface. It is worth noting that this constant interface temperature is not exactly equal to the equilibrium freezing temperature of the splat material. This result was also observed by Wang and Matthys (1992) for single droplet splats. The freezing interface temperature becomes higher as the thermal contact at the splat/substrate interface deteriorates. The behavior of the freezing velocity can be explained in a manner analogous to that of the freezing temperature because the shape of the freezing velocity curve is practically a mirror image of that of the freezing interface temperature curve (Fig. 6).

The temperature history of the bottom of both the first and the second droplet (disk) in the splat for characteristic values of the contact coefficient is shown in Fig. 7. The onset of the solidification is marked by the cusps in the temperature versus time curves. Prior to the initiation of the freezing, the temperature of the splat/substrate interface decreased very rapidly with time. The same was true, to a lesser extent, for the temperature of the interface between the top and the bottom droplet for the case of the large contact coefficient ($h_c = 1.5 \times 10^5$ W/m^{2}K). The results for the low contact coefficient exhibit a less drastic dependence of the temperature on time prior to the freezing initiation, markedly so for the interface between the top and the bottom droplet in the splat. After the freezing front has departed from the splat/substrate interface, or the interface between the two droplets, the temperature dependence on time is very weak. In the case of the large contact coefficient ($h_c = 1.5 \times 10^5$ W/m^{2}K) the cooling of the two aforementioned locations continues (albeit in a very slow fashion). In the case of the small contact coefficient ($h_c = 1.5 \times 10^4$ W/m^{2}K) the temperature is practically independent of time. An

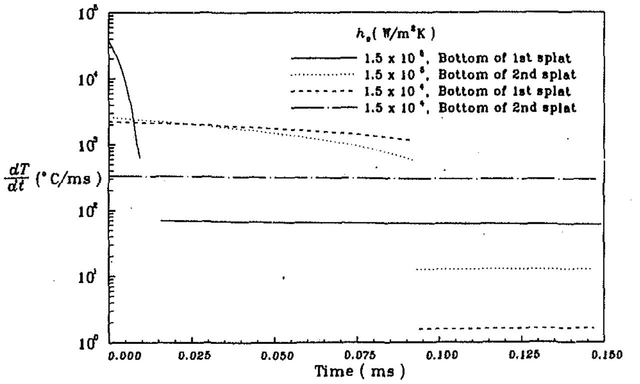

Fig. 8 The cooling rate history of the bottom surface of the first and second droplets in the splat

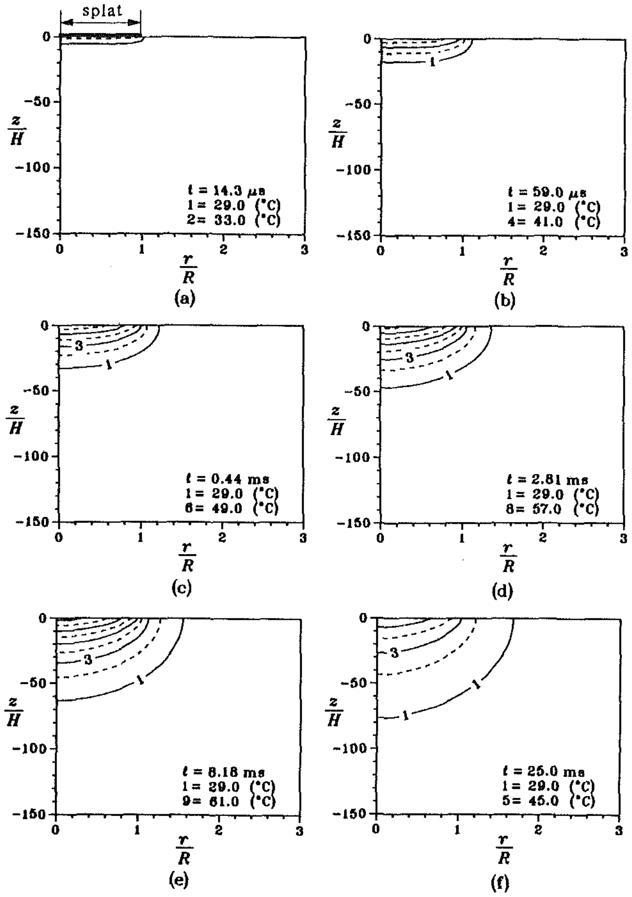

Fig. 9 Transient isotherms in the substrate for $h_c = 1.5 \times 10^4$ W/m²K: (a) 14 μs; (b) 59 μs; (c) 0.44 ms; (d) 2.81 ms; (e) 8.18 ms; (f) 25 ms

additional important finding in Fig. 7 is that it takes much longer for the freezing of the top droplet in the splat to ensue compared to the bottom droplet in the splat (a direct result of the different cooling rates prior to solidification). For example, in the case of $h_c = 1.5 \times 10^5$ W/m²K the freezing of the bottom droplet is initiated at $t = 0.015$ ms while it takes about 0.09 ms for the freezing of the top droplet to occur from the time it is placed into contact with the bottom droplet.

The variation of the bottom temperature gradient of each splat with respect to time is shown in Fig. 8. The extremely steep variation of the cooling rate at the onset of freezing is not shown to aid the clarity of this figure. This explains the gap existing in the curves identifying the freezing initiation at the substrate surface. The temperature gradient is very large before the solidification ensues ranging from 2×10^5 °C/s to 4×10^7 °C/s for all cases, which causes the very sharp temperature drop observed earlier in Fig. 7 during the same time period. After the onset of solidification, the temperature gradient remains almost constant. The independence of the cooling rate of time during this period is due to the establishment of equilibrium between the heat generated at the freezing interface and the heat conducted to the substrate at the splat/substrate interface. The cooling rate of the second splat is much lower than that of the first splat after the solidification is initiated. This is due to the added thermal resistance caused by the existence of the first splat. It is worth noting that except for the case of $h_c = 1.5 \times 10^5$ W/m²K, the cooling rate of the bottom of the splat is weakly dependent on time even prior to the onset of solidification. This is in agreement with the practically linear shape of the temperature distribution in Fig. 7.

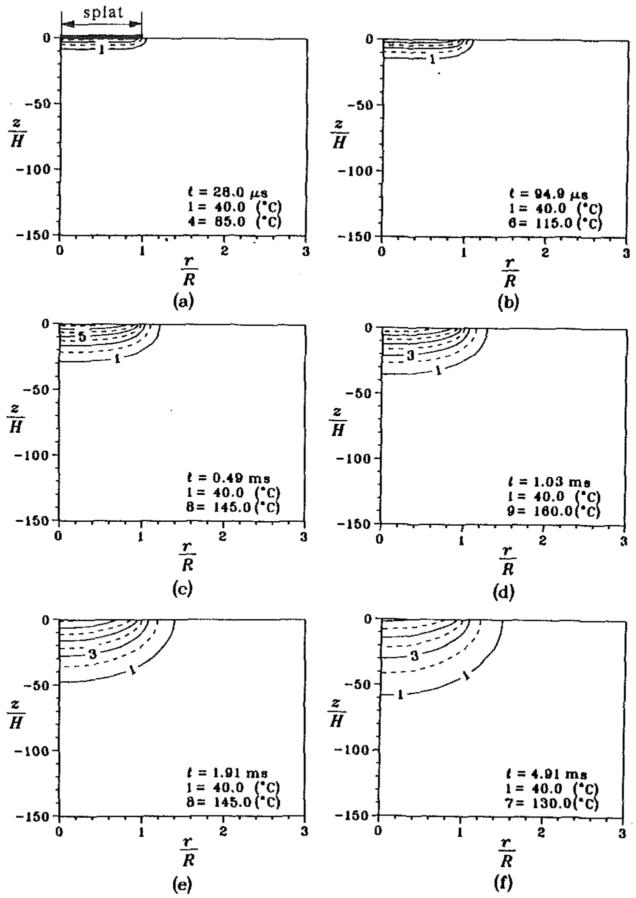

Fig. 10 Transient isotherms in the substrate for $h_c = 1.5 \times 10^5$ W/m²K: (*a*) 28 μs; (*b*) 94.9 μs; (*c*) 0.49 ms; (*d*) 1.03 ms; (*e*) 1.91 ms; (*f*) 4.91 ms

The transient temperature field in the substrate is shown in Fig. 9 for $h_c = 1.5 \times 10^4$ W/m²K and Fig. 10 for $h_c = 1.5 \times 10^5$ W/m²K. It should be clarified that the isotherms in Fig. 9 are equally spaced every 4.0°C. The isotherms in Fig. 10 are also equally spaced but every 15.0°C, almost four times the spacing of Fig. 9. Hence, clearly, the heating effect of the droplet penetrates much deeper in the substrate at any given time in the case of the large contact coefficient (Fig. 10). An important finding in the results of Figs. 9 and 10 is the two-dimensional nature of the temperature field in the substrate. Only at very small times, $t \leq 14$ μs in Fig. 9 and $t \leq 28$ μs in Fig. 10, can the radial dependence of the temperature field in the substrate, perhaps, be considered negligible. Taking into account Figs. 4 and 7, we conclude that the two-dimensional nature of the temperature field in the substrate is in effect well before the solidification of the two-droplet splat is completed and should be taken into account in efforts of theoretical modeling of the process.

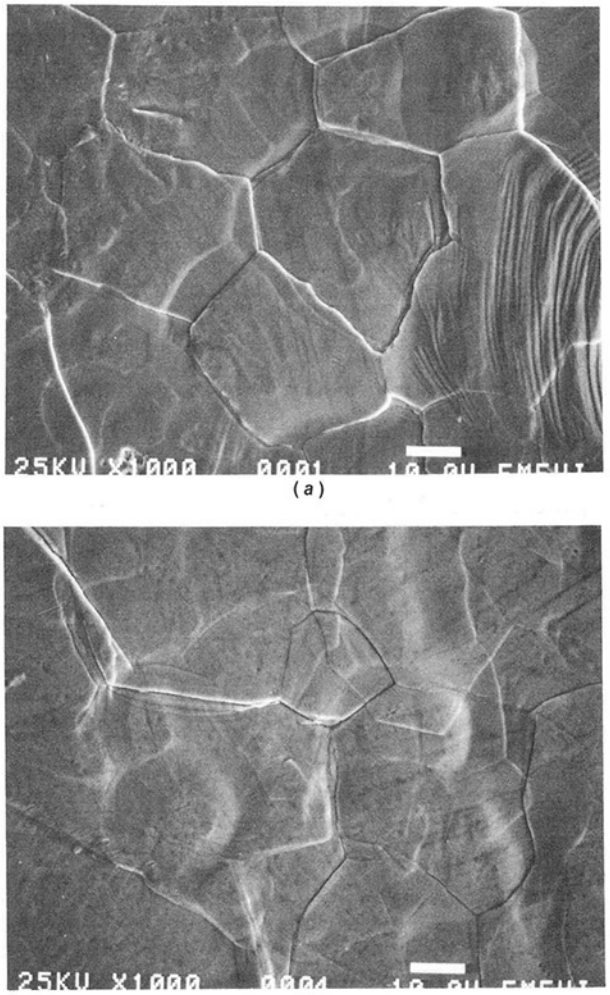

Fig. 11 Electron micrographs of the bottom of the splat: (*a*) single-droplet splat; (*b*) double-droplet splat

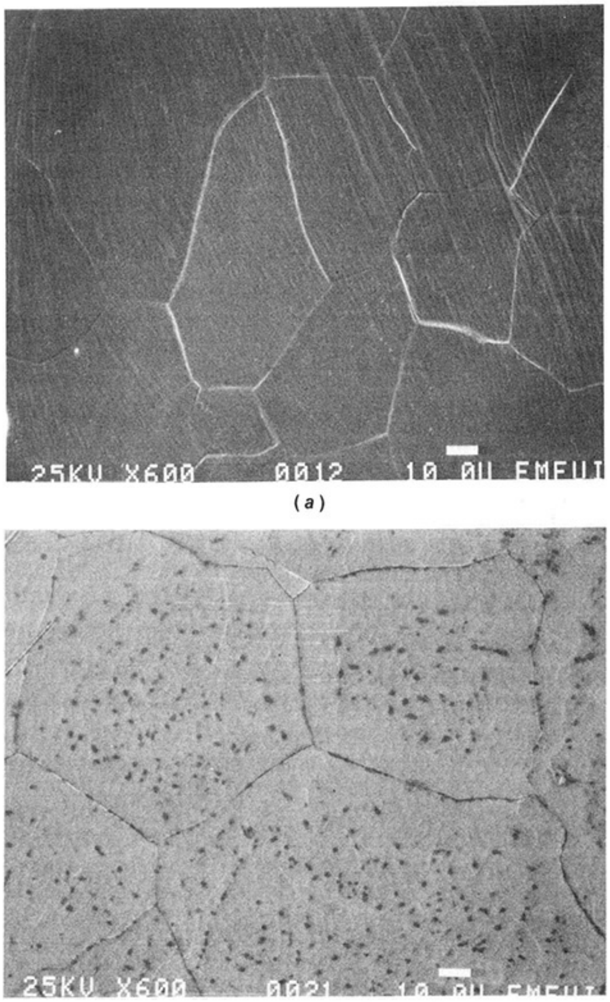

Fig. 12 Electron micrographs of the top of the splat: (*a*) single-droplet splat; (*b*) double-droplet splat

The results of the experimental portion of this work aim at examining the effect of the difference in cooling rates between the first and second droplets in the splat on the microstructure of the solidified metal. Lead was used as the working metal in all the experiments. The substrate temperature was maintained at 22.8°C. The droplet temperature at impact was 359°C estimated from the measured temperature at the droplet generator (360.6°C) according to the appendix. The impinging speed of the droplet on the substrate was 2.15 m/s. The resulting spread ratio for the two-droplet splat was $\xi = 3.972$. The standard deviation of the ξ measurement was 0.249 for the double droplet splats. The centerline height to diameter ratios of the splats analyzed in this study were 0.0173 for the single droplet splat and 0.0213 for the case of the double droplet splat. The pulse separation time in the case of the double-droplet splat cooling experiments was set to be 20 μs. The droplet release separation time was about one order of magnitude longer due to the mechanical inertia and the electromagnetic retardation of the droplet release mechanism.

Figure 11 shows scanning electron micrographs of the bottom surfaces of a single droplet splat, Fig. 11(*a*), and a double droplet splat, Fig. 11(*b*). The two micrographs reveal essentially similar microstructural features. The average grain sizes of the bottom of both splats were found to be basically the same. Predendritic structures are visible inside the grains in Fig. 11. In Fig. 12 electron micrographs of the top of a single-droplet splat (Fig. 12*a*) and a double-droplet splat (Fig. 12*b*) are shown. The impact of the retardation on the cooling rate is immediately visible in the grain size of the top of the two-droplet splat (Fig. 12*b*), which is visibly larger than the grain size of the top of the single-droplet splat. An order of magnitude estimation of the grain size of the splats was calculated as the diameter of a circle of area equal to that of a grain measured from the electron micrographs. The top surface grain size was typically 45 μm for a single-droplet splat, Fig. 12(*a*), and 85 μm for a double-droplet splat, Fig. 12(*b*). The grain shapes at the top surface of the double-droplet splat are primarily equiaxed (Fig. 12*b*). On the other hand, enlongated grains are observed at the top surface of the single-droplet splat (Fig. 12*a*). The enlongated grains were found to exist mainly near the rim of the top surface of a single-droplet splat. These elongated grains are indicative of the fact that some outward spreading is still in progress when solidification is initiated. They are not observed on the two-droplet splat (Fig. 12*b*) where due to lower cooling rates there is enough time for the outward spreading to be practically terminated before the solidification of the rim region.

5 Conclusions

In this paper a combined theoretical and experimental study was reported on the problem of splat cooling of two liquid metal droplets impacting sequentially on a substrate. The theoretical part of the study clearly showed that the cooling rate of the top droplet is significantly lower than the cooling rate of the bottom droplet. In addition, the early part of the freezing progress is described by nonequilibrium crystallization kinetics due to the severe undercooling present at the onset of solidification. The effect of contact resistance both at the splat/substrate interface and at the interface between the two splats is important and it affects the results quantitatively. The findings of the theoretical model also clearly demonstrated the presence of a two-dimensional temperature field in the substrate during the solidification of the splat. The experimental part of the study clearly indicated that the aforementioned reduced cooling rate of the second droplet in the splat yields a considerably coarser grain structure. From a practical standpoint this finding implies that in splat cooling severe limitations need to be imposed on the thickness of the resulting solid product (ribbon or coating, for example) to ensure rapid solidification and fine grain structure in addition to the net shape forming.

References

Anantharaman, T. R., and Suryanarayana, C., 1971, "Review: A Decade of Quenching From the Melt," *Journal of Material Science*, Vol. 6, pp. 1111-1135.

Anderson, D. A., Tannehill, J. C., and Pletcher, R. H., 1984, *Computational Fluid Mechanics and Heat Transfer*, Hemisphere Publishing Co., New York.

Annavarapu, S., Apelian, D., and Lawley, A., 1990, "Spray Casting of Steel Strip: Process Analysis," *Metallurgical Transactions A*, Vol. 21A, pp. 3237-3256.

Bennett, T. D., 1993, "Splat-Quench Solidification: An Investigation Into Influential Parameters," M.S. Thesis, University of Illinois at Chicago.

Bricknell, R. H., 1986, "The Structure and Properties of a Nickel-Base Superalloy Produced by Osprey Atomization Deposition," *Metallurgical Transactions A*, Vol. 7A, pp. 583-590.

Brooks, R. G., Moore, C., Leatham, A. G., and Coombs, J. S., 1977, "Osprey Process," *Powder Metallurgy*, Vol. 2, pp. 100-102.

Brower, W. E., Jr., Strachan, R., and Flemings, M. C., 1970, "Effect of Cooling Rate on Structure of Ferrous Alloys," *AFS Cast Metals Research Journal*, Vol. 6, pp. 176-180.

Clyne, T. W., 1984, "Numerical Treatment of Rapid Solidification," *Metallurgical Transactions B*, Vol. 15B, pp. 369-381.

Evans, P. V., and Greer, A. L., 1988, "Modeling of Crystal Growth and Solute Redistribution During Rapid Solidification," *Material Science and Engineering*, Vol. 98, pp. 357-361.

Goedde, E. F., and Yuen, M. C., 1970, "Experiments on Liquid Jet Instability," *Journal of Fluid Mechanics*, Vol. 40, pp. 495-511.

Goodrich, L. E., 1978, "Efficient Numerical Technique for One-Dimensional Thermal Problems With Phase Change," *International Journal of Heat and Mass Transfer*, Vol. 21, pp. 615-621.

Gutierrez-Miravete, E., 1985, "The Mathematical Modeling of Rapid Solidification," Ph.D. Thesis, Massachusetts Institute of Technology, Cambridge, MA.

Jones, H., 1982, "Rapid Solidification of Metals and Alloys," *The Institution of Metallurgists*, Monograph 8, Great Britain Institution of Metallurgists.

Levi, C. G., and Mehrabian, R., 1982, "Heat Flow During Rapid Solidification of Undercooled Metal Droplets," *Metallurgical Transactions A*, Vol. 13A, pp. 221-234.

Madejski, J., 1976, "Solidification of Droplet on a Cold Surface," *International Journal of Heat and Mass Transfer*, Vol. 19, pp. 1009-1013.

Madejski, J., 1983, "Droplets on Impact With a Cold Surface," *International Journal of Heat and Mass Transfer*, Vol. 26, pp. 1095-1098.

Patankar, S. V., 1981, *Numerical Heat Transfer and Fluid Flow*, Hemisphere Publishing Co., New York.

Predecki, P., Mullendore, A. W., and Grant, N. G., 1965, "A Study of the Splat Cooling Technique," *Transactions of the Metallurgical Society of AIME*, Vol. 233, pp. 1581-1587.

Ranz, W., and Marshall, W., 1952, "Evaporation From Drops, Part I," *Chemical Engineering Progress*, Vol. 48, pp. 141-146.

Rosnar, D. E., and Epstein, M., 1975, "Simultaneous Kinetic and Heat Transfer Limitations in the Crystallization of Highly Undercooled Melts," *Chemical Engineering Science*, Vol. 30, pp. 511-520.

Scott, M. G., 1974, "The Effect of Glass Substrate on Cooling Rate in Splat-Quenching," *Journal of Material Science*, Vol. 9, pp. 1372-1974.

Shingu, P. A., and Ozaki, R., 1975, "Solidification Rate in Rapid Conduction Cooling," *Metallurgical Transactions A*, Vol. 6A, pp. 33-37.

Wang, G.-X., and Matthys, E. F., 1991, "Modelling of Heat Transfer and Solidification During Splat Cooling: Effect of Splat Thickness and Splat/Substrate Thermal Contact," *International Journal of Rapid Solidification*, Vol. 6, pp. 141-174.

Wang, G.-X., and Matthys, E. F., 1992, "Numerical Modelling of Phase Change and Heat Transfer During Rapid Solidification Processes: Use of Control Volume Integrals With Element Subdivisions," *International Journal of Heat and Mass Transfer*, Vol. 35, pp. 141-153.

A P P E N D I X

Convective Cooling of the Droplet During Free Fall

The initial droplet temperature at the time of release can be measured directly; however, there is no simple way of accurately measuring the impact temperature of the droplet. Therefore, in order to estimate the initial conditions of the splat on the substrate surface, the amount of cooling undergone by the droplet during free fall must be calculated.

Assuming lumped heat capacity and Newtonian cooling, the governing differential equation for the droplet temperature during free fall is given by

$$\frac{d}{dt}(\rho c\theta) = -h\theta \qquad \text{(A1)}$$

where θ is the instantaneous temperature difference between the droplet and the isothermal ambient air.

The convective coefficient can be found from the Ranz and Marshall (1952) Nusselt number correlation for free falling spheres:

$$\mathrm{Nu}_d = \frac{hd}{k} = 2 + 0.6\ \mathrm{Re}^{1/2}\mathrm{Pr}^{1/3} \qquad \text{(A2)}$$

where, although the Prandtl number (Pr) can be considered a constant, the Reynolds number (Re) is a function of velocity, hence of time:

$$\mathrm{Re} = \frac{ud}{\nu} = \frac{gtd}{\nu} \qquad \text{(A3)}$$

Combining Eqs. (A1) and (A2) yields

$$\frac{d\theta}{dt} + \frac{\alpha \mathrm{Nu}_d}{d}\theta = 0 \qquad \text{(A4)}$$

Equation (A4) is a first-order, linear, differential equation, which has the initial condition:

$$\theta(t=0) = \theta_a \qquad \text{(A5)}$$

where θ_a is the initial temperature difference between the droplet and ambient air.

The solution of Eq. (A4) subject to the initial condition (A5) reads

$$\theta = \theta_a \exp\left\{-(2+0.4\ \mathrm{Re}^{1/2}\mathrm{Pr}^{1/3})\ \frac{\alpha t}{d}\right\} \qquad \text{(A6)}$$

Equation (A6) can be used to estimate the droplet temperature at any time during its flight. If the distance between the release point of the droplet and the substrate is denoted by Z, the time elapsed between release and initial contact with the substrate is

$$t_c = \sqrt{\frac{2Z}{g}} \qquad \text{(A7)}$$

The temperature at impact is then estimated by evaluating Eq. (A6) at $t = t_c$ from Eq. (A7) after taking into account the time dependence of Re (Eq. (A3)).

Xin Zeng

A. Faghri

Department of Mechanical and
Materials Engineering,
Wright State University,
Dayton, OH 45435

Experimental and Numerical Study of Microwave Thawing Heat Transfer for Food Materials

A combined experimental and numerical study of microwave thawing of a food analog material is reported. The objective of this study is to determine thawing histories and temperature profiles for cylindrically shaped samples. Microwave thawing experiments of samples with different aspect ratios were performed to collect time–temperature data for various power levels. These measured thawing times were utilized in a comparative analysis with the numerical predictions. The heat transfer phenomena due to the interaction between phase change and heat generation was analyzed. A two-dimensional mathematical model was developed to deal with the complicated thawing process, which includes the frozen, mushy, and thawed phases, and the evaporation of water. The present study is anticipated to form a fundamental understanding of the interactions between microwave irradiation and phase-change heat transfer.

Introduction

A significant amount of food is frozen for preservation and further processing. While freezing presents a convenient means of preserving foods, the time required to thaw the frozen material presents a significant constraint on industrial applications. A common approach to thawing frozen products is convective thawing, which needs long processing times, large space requirements, and may cause chemical and biological deterioration (Mudgett, 1989; Rosenberg and Bogl, 1987; Decareau, 1968). Research on microwave thawing suggests the possibility of replacing the existing convective thawing technique in the future. The most attractive aspects of microwave processes are rapid and uniform heating effects, and high energy efficiency. Although microwave thawing has many advantages over convective thawing, there are few practical applications in the food industry. The major problems associated with the development of industrial microwave processing are the lack of understanding of the interactions between microwave radiation and food materials undergoing phase change (Zeng and Faghri, 1992), the lack of predictive models relating physical, thermal, and electrical properties of food materials to the transient temperature field distribution, which determines microbial safety and product quality (Mudgett, 1986), and the lack of systematic experiments that can accommodate most common food shapes. Essentially, the microwave food process design assumes a trial-and-error approach, which frequently results in failure in practical industrial applications.

Ohlsson and Bengtsson (1971) studied microwave heating profiles in slabs of food and food substitutes. A one-dimensional heat conduction model was developed for heat transfer in an infinite slab of prescribed thickness. The importance of internal heat conduction during microwave heating was emphasized. A comparison between numerically simulated and experimentally determined heating profiles in rectangular slabs of food and phantom meat showed good agreement. A detailed outline of experimental procedures and numerical results was given by Nykvist and Decareau (1976) in their investigation of the feasibility of using microwaves to cook beef roasts. A two-dimensional model of microwave heating, excluding thawing, was developed in which both radial and axial microwave dissipation within cylindrically shaped samples were assumed separately. Good agreement between the experimental data and the predicted results was reported for operating conditions of 300 W at 915 MHz and the combination of 600 W at 915 MHz for the first 20 min and 300 W at 915 thereafter. The study determined that a frequency of 915 MHz performed better than 2450 MHz due to the increased penetration depth. The influences of sample geometry, heating power, and microwave frequency on the temperature distribution were examined.

In order to avoid local runaway heating effects during microwave thawing of foods, Bialod et al. (1978) experimentally conducted microwave thawing combined with surface cooling for thawing of large-sized products. The cooling system consisted of spraying a cryogenic liquid under a high electrostatic voltage, which prevented overheating at the surface. Their experimental study determined the amount of cooling required as a function of the thickness of the product and the final temperature.

Taoukis et al. (1987) modeled microwave thawing of slabs and cylinders experimentally and numerically. In their experiments, there was some evidence of nonuniform heating at the area near the top end of the cylinder across the entrance of the microwave field. The average experimental thawing time of the sample was 22 percent less than the predicted value based on the modified isotherm migration method. The authors stated that at higher powers a localized overheating around the thermocouples due to microwave-thermocouple interactions was evident and the use of the thermocouples at these powers was impossible. Komoprasert and Ofoli (1989) developed a dimensional analysis method to predict microwave heating of water. To determine the validity of their predictive model, time–temperature data of water were collected using a Luxtron fluoroptic temperature sensor equipped with fiberoptic probes. Two household microwave cavities (Tappan and Litton) with a frequency of 2450 MHz and variable power outputs were used. Although the results of the model showed good agreement with the experimental data, use of the model may be limited to water and other materials that have properties similar to water. Zeng (1991) experimentally and numerically studied the microwave thawing heat transfer of a food analog material (Tylose) of simple shapes. In the experiments, the frozen cylindrical samples were suspended in the center of the microwave cavity with aluminum foil covering both ends to

---

Contributed by the Heat Transfer Division for publication in the JOURNAL OF HEAT TRANSFER. Manuscript received by the Heat Transfer Division November 1992; revision received July 1993. Keywords: Conduction, Materials Processing and Manufacturing Processes, Phase-Change Phenomena. Associate Technical Editor: Y. Bayazitoglu.

ensure one-dimensional radial heating. A periodic power input was used and temperature data were recorded during the "off" cycle. The agreement between the predicted and experimental thawing times was within 30 percent. Recently, Zeng and Faghri (1992) proposed a new mathematical model of microwave thawing heat transfer for food and biological materials. Based on an analysis of the phase-change characteristics of food and biological materials, a relationship between the local liquid fraction and temperature was derived as a piecewise quadratic function of temperature. Accordingly, an apparent heat capacity formulation was developed to solve the highly nonlinear phase-change heat conduction problem including the effects of the mushy region and heat generation. However, the effects of microwave irradiation in the axial direction and mass transfer due to the moisture evaporation through the surface were neglected. The proposed mathematical model and numerical method were applied to one- and two-dimensional microwave thawing problems of food and biological materials. A comparison between the numerical solutions and the existing experimental data showed a good agreement.

Modeling of the microwave thawing of food and biological materials raises a very interesting class of phase-change problems, which include the effects of a mushy region. The objective of the present work is to measure and collect microwave thawing data for cylindrically shaped Tylose food analog material samples with different aspect ratios, and to validate the present numerical model with the measured data. The heat transfer within the Tylose samples under the interaction of microwave energy is examined in detail. Special attention is paid to the phase-change evolution and heat generation with the mushy region. A simple treatment of the strong evaporation of water within the runaway heat region is proposed. The data collected can be utilized in comparative analyses with mathematical models of microwave thawing heat transfer. The research presented here provides a basis for a fundamental understanding of microwave thawing of food and biological materials.

Heat Transfer Analysis

Heat transfer during microwave thawing by conduction, convection, and evaporation are externally governed by the input power level, which provides a volumetrically distributed, time-varied heat source, and are internally constrained by the absorption of latent heat within the mushy region. The physical, thermal, and electrical properties of the material subjected to microwave irradiation vary considerably with temperature over the mushy region where the frozen and thawed phases coexist. Modeling of microwave thawing of food and biological materials can present special difficulties due to nonlinearities stemming from the evolution of latent heat within the mushy region, the nonuniform energy distribution within the thawed materials, and the interaction between these two phenomena during the thawing process.

Microwave heating effects of food and biological materials are attributed to the coupling of electrical energy from an electromagnetic field generated by a magnetron in a microwave cavity and the dissipation within the material. The heat generation is mainly related to a number of interrelated electrical properties, which vary substantially with the processing frequency and temperature (Mudgett, 1986). The heat transfer analysis of microwave thawing involves Maxwell's equations coupled with the heat conduction equation including phase change, for which all physical, thermal, and electrical properties of the material are nonlinear (Zeng and Faghri, 1992). As electrical energy is converted into thermal energy within the material, the attenuation factor, which determines the en-

Nomenclature

a = coefficient in Eq. (24)
b = coefficient in Eq. (24)
C_p, C_{ps}, $C_{p\ell}$ = specific heat at constant pressure of mixture, solid and liquid phases, respectively, J/(kg-K)
$C^*(T)$ = apparent heat capacity in Eq. (12), J/(m^3-K)
D = diameter, m
f = frequency, Hz
f_ℓ = liquid fraction, Eq. (10)
H = height, m
I = microwave intensity, W/m^2
I_0 = microwave intensity at surface, W/m^2
k, k_s, k_ℓ = thermal conductivity of mixture, solid and liquid phases, respectively, W/(m-K)
L = latent heat of melting, J/kg
L_v = latent heat of evaporation, J/kg
M = mass, kg
m_v = mass transfer rate due to evaporation, kg/s
P = power, W
q = heat generation term in Eq. (7), W/m^3
Q = heat generation in Eq. (22), W
r = radial coordinate
Δr = radial step, m
R = radius, m
S = source term in Eq. (25)
t = time, s
T = temperature, K
T_f = final phase change temperature of thawing, K
T_i = initial phase change temperature of thawing, K
T_m = temperature corresponding to the peak value of latent heat evolution, K
x = axial coordinate, m
Δx = axial step, m
Z = penetration depth, m
α, α_s, α_ℓ = attenuation factor of mixture, solid, and liquid phases, respectively, 1/m
ϵ' = relative dielectric constant
ϵ'' = relative dielectric loss
λ_0 = wavelength in free space, m
ρ, ρ_s, ρ_ℓ = density of mixture, solid, and liquid phases, respectively, kg/m^3

Subscripts

b = bottom
f = final
ℓ = liquid phase, or left
nb = neighbor of the grid node P
P = grid node P
r = right, or radial direction
s = solid phase
t = top
w = wall
x = in x direction
0 = initial

Superscript

old = previous time level

ergy distribution within the material, may vary significantly with temperature. According to von Hipple (1954), the attenuation factor can be defined as:

$$\alpha=\frac{2\pi}{\lambda_0}\sqrt{\frac{\epsilon'\{[1+(\epsilon''/\epsilon')^2]^{1/2}-1\}}{2}} \tag{1}$$

where ϵ' is the relative dielectric constant, which is a measure of the ability of a material to store electric energy. The relative dielectric loss ϵ'' is a function of the ability of the material to convert electrical energy to heat energy. λ_0 is the wavelength in vacuum. Freezing or thawing has a profound effect upon the heating ability of foods with moderate or high moisture contents. This is due to the differences between the dielectric properties of water and ice. Water is a highly absorptive medium, while ice is highly transparent. Since the outer layer of the material absorbs most of the incident energy, overheating on the material surface or corner frequently occurs for relatively large geometries and high power inputs.

The attenuation factor α is inversely related to the penetration depth Z, which is the depth from the surface at which $(1-1/e^2)$ of the power of the incident microwaves is absorbed.

$$Z=\frac{1}{\alpha} \tag{2}$$

The interaction of microwave energy with a biological material is a very complex phenomenon. The basic assumption concerning the microwave radiation in the present study are:

1 The microwave field is a planar wave propagating perpendicularly to the material surface.
2 The microwave field at the material surface is uniform.
3 The microwave energy entering from different sides (radial and axial directions) decreases exponentially and is considered separately.
4 The total amount of absorbed power within the material subjected to microwave irradiation is constant

Based on the assumptions above, the intensity of the transmitted microwave radiation, expressed as an energy flux, I, at some depth from the surface into the material, is determined from its attenuation factor according to Lambert's absorption relationship (von Hipple, 1954).

$$I_r(r,x,t)=I_0(t)\exp[-2\alpha(R-r)], \quad -R<r<R \tag{3}$$

$$I_\ell(r,x,t)=I_0(t)\exp[-2\alpha(R+r)], \quad -R<r<R \tag{4}$$

$$I_t(r,x,t)=I_0(t)\exp\left[-2\alpha\left(\frac{H}{2}-x\right)\right], \quad -\frac{H}{2}<x<\frac{H}{2} \tag{5}$$

$$I_b(r,x,t)=I_0(t)\exp\left[-2\alpha\left(\frac{H}{2}+x\right)\right], \quad -\frac{H}{2}<x<\frac{H}{2} \tag{6}$$

Shown schematically in Fig. 1, I_r, I_ℓ, I_t, and I_b are the intensities of transmitted microwave radiation at depth from the right, left, top, and bottom locations, and $I_0(t)$ is the intensity of the microwave field at the surface. Considering the microwave penetration from both sides of the radial and axial directions, the heat generation term is

$$q(r,x,t)=q_r(r,x,t)+q_x(r,x,t), -R<r<R, \quad -\frac{H}{2}<x<\frac{H}{2} \tag{7}$$

where

$$q_r(r,x,t)=\frac{1}{r}\frac{\partial}{\partial r}[r(I_r-I_\ell)], \quad -R<r<R \tag{8}$$

$$q_x(r,x,t)=\frac{\partial}{\partial x}[I_t-I_b], \quad -\frac{H}{2}<x<\frac{H}{2} \tag{9}$$

q_r and q_x represent the heat generation terms due to radial and axial microwave radiation, respectively.

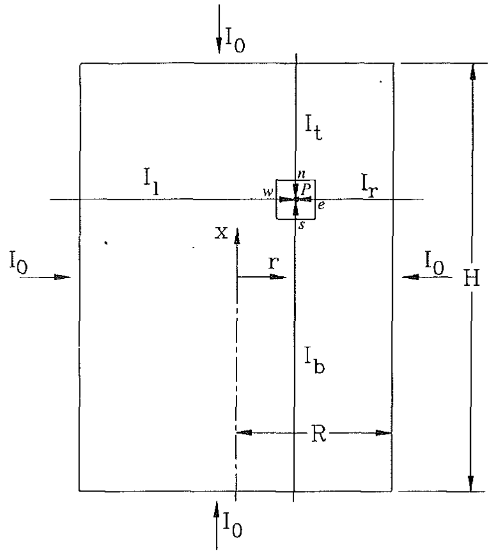

Fig. 1 Microwave radiation from the axial and radial directions

Thawing of food and biological materials is a phase transformation process that is accompanied by absorption of thermal energy over a range of temperatures in which the frozen and thawed phases coexist. The mushy region phase change is characterized by the presence of a liquid fraction, which depends primarily on temperature. The relationship between liquid fraction, f_ℓ, and temperature can be expressed as (Zeng and Faghri, 1992):

$$f_\ell=\begin{cases} 0 & T<T_i \\ \dfrac{(T-T_i)^2}{(T_f-T_i)(T_m-T_i)} & T_i\le T<T_m \\ 1-\dfrac{(T-T_f)^2}{(T_f-T_i)(T_f-T_m)} & T_m\le T\le T_f \\ 1 & T>T_f \end{cases} \tag{10}$$

where T_i represents the initial thawing temperature, which is the lower limit of the mushy region, T_f is the final thawing temperature, which accounts for the upper limit of the mushy region, and T_m is the temperature corresponding to the peak evolution of latent heat.

In convective thawing, the latent and sensible heat required to thaw the material is conducted from the boundaries. During microwave thawing, however, the heat required to thaw the material is mainly supplied by a volumetrically distributed, time-varied heat source due to microwave dissipation. Although the total amount of the input power is assumed to be constant, the heat source function varies with space and time. On one hand, since the attenuation factor is temperature dependent, the uneven temperature field results in uneven attenuation factors, which translates to a nonuniform distribution of the heat source within the sample. On the other hand, the nonuniform distribution of heat source influences the temperature field. The interaction between the phase change and heat generation makes the thawing process highly nonlinear.

Mathematical Model

Since symmetry about the two center axes of the cylinder is assumed, determination of the temperature pattern in a 1/4 cross section, as shown in Fig. 2, is representative of the temperature distribution throughout the entire cylinder. The temperature-transforming formulation for modeling microwave thawing (Zeng and Faghri, 1992) has been adopted in the

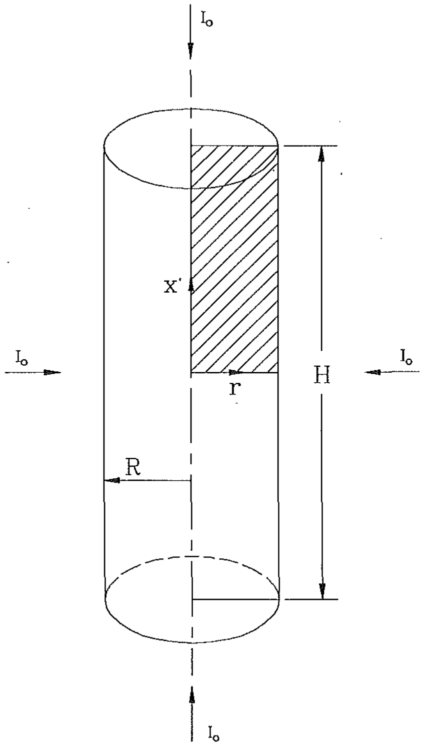

Fig. 2 Computational domain for the cylindrical sample

present study. For a two-dimensional cylindrical geometry, the apparent heat capacity can be written as:

$$C^*(T)\frac{\partial T}{\partial t}=\frac{1}{r}\frac{\partial}{\partial r}\left(kr\frac{\partial T}{\partial r}\right)+\frac{\partial}{\partial x}\left(k\frac{\partial T}{\partial x}\right)+q \tag{11}$$

The heat generation term $q(r, x, t)$ in Eq. (11) accounts for the conversion of microwave energy to heat energy, which is given in Eqs. (7)–(9). The apparent heat capacity $C^*(T)$ is defined as:

$$C^*(T)=\rho C_p+\left[\frac{\rho(\rho_\ell-\rho_s)}{\rho_\ell-f_\ell(\rho_\ell-\rho_s)}\times(C_pT+f_\ell L)+\rho(C_{p\ell}-C_{ps})T+\rho L\right]\frac{df_\ell}{dT} \tag{12}$$

Incorporation of the apparent heat capacity $C^*(T)$ into Eq. (11) to account for the evolution of latent heat within the mushy region requires that the liquid-fraction/temperature relation Eq. (10) be introduced. The derivative of liquid fraction fraction f_ℓ with respect to temperature from Eq. (10) is

$$\frac{df_\ell}{dT}=\begin{cases}0 & T<T_i \text{ or } T>T_f\\[1ex] \dfrac{2(T-T_i)}{[(T_f-T_i)(T_m-T_i)]} & T_i\le T<T_m\\[1ex] \dfrac{2(T_f-T)}{[(T_f-T_i)(T_f-T_m)]} & T_m\le T\le T_f\end{cases} \tag{13}$$

The mean mixture theory is used to define the continuum physical and thermal properties:

$$\rho=\rho_s+f_\ell(\rho_\ell-\rho_s)\ \rho/\rho_\ell \tag{14}$$

$$k=k_s+f_\ell(k_\ell-k_s)\rho/\rho_\ell \tag{15}$$

$$C_p=C_{ps}+f_\ell(C_{p\ell}-C_{ps}) \tag{16}$$

while the relation between attenuation factor α and liquid fraction f_ℓ can be expressed using a harmonic approximation (Taoukis et al., 1987):

$$\alpha=\frac{\alpha_s\alpha_\ell}{\alpha_\ell+f_\ell(\alpha_s-\alpha_\ell)} \tag{17}$$

In the present study, when the transient temperature within the sample was lower than 100°C, an insulating boundary condition was assumed because the samples were placed in Pyrex cylinders and thawing was completed in a short time. Therefore, for $T<100°\mathrm{C}$:

$$\left.\frac{\partial T}{\partial r}\right|_{r=R}=0 \tag{18}$$

$$\left.\frac{\partial T}{\partial x}\right|_{x=H/2}=0 \tag{19}$$

The symmetric condition gives:

$$\left.\frac{\partial T}{\partial r}\right|_{r=0}=0 \tag{20}$$

$$\left.\frac{\partial T}{\partial x}\right|_{x=0}=0 \tag{21}$$

When the temperature within the material reaches 100°C, the effects of strong surface moisture migration and evaporation should be considered. In practice, the highest temperature within the moderate and high water content materials cannot exceed 100°C. Higher temperatures are possible when the material has completely dried, especially near the surface or corner. Since no experimental data are available for the attenuation factor α and no other simple models have been proposed that indicate how to deal with the mass transfer effects when the temperature is equal to or greater than 100°C, some simplifying assumptions are made in the current model to account for the mass transfer involved during microwave thawing:

1 When the temperature within the material reaches 100°C, the temperature in the area remains constant at 100°C until the water content in the area is completely evaporated.

2 The heat of evaporation is equal to the heat absorbed by the material in the local area, that is

$$Q=m_v\,L_v \tag{22}$$

For a given heat generation in the local area, since the latent heat of evaporation of water, L_v, is large (for water, $L_v=2.2572\times10^6$ J/kg), the mass transfer rate due to evaporation, m_v, is relatively small. In most cases, the mass transfer occurs near the top-right corner, as shown in Fig. 2, which is the location of maximum power incidence from the axial and radial directions.

The initial temperature T_0 is uniform:

$$T=T_0,\quad t=0 \tag{23}$$

A numerical discretization of the apparent heat capacity formulation, Eq. (11), based on control volume finite difference method (Patankar, 1980) has the following form:

$$A_pT_p=\Sigma\,a_{nb}\,T_{nb}+bT_P^{\text{old}}+S \tag{24}$$

where the subscript P indicates the value at node point P, and nb indicates a neighbor of the node P (the summation being over all neighbors). The heat generation term S can be discretized as

$$S=S_r+S_x \tag{25}$$

S_x and S_r are the heat source terms due to microwave irradiation in the axial and radial directions, which are considered separately. Because the attenuation factor α is a function of temperature, the source terms S_x and S_r in terms of Eqs. (8) and (9) are:

$$S_r=\Delta x[r_e(I_r-I_\ell)_e-r_w(I_r-I_\ell)_w] \tag{26}$$

$$S_x=\Delta r\ r_p[I_t-I_b] \tag{27}$$

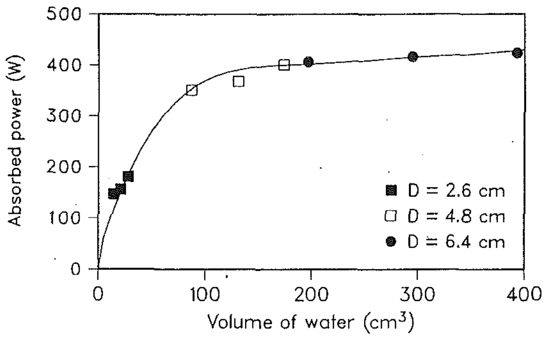

Fig. 3 Variation of absorbed power with volume for cylindrically shaped water samples ($H/D = 1.0, 1.5, 2.0$)

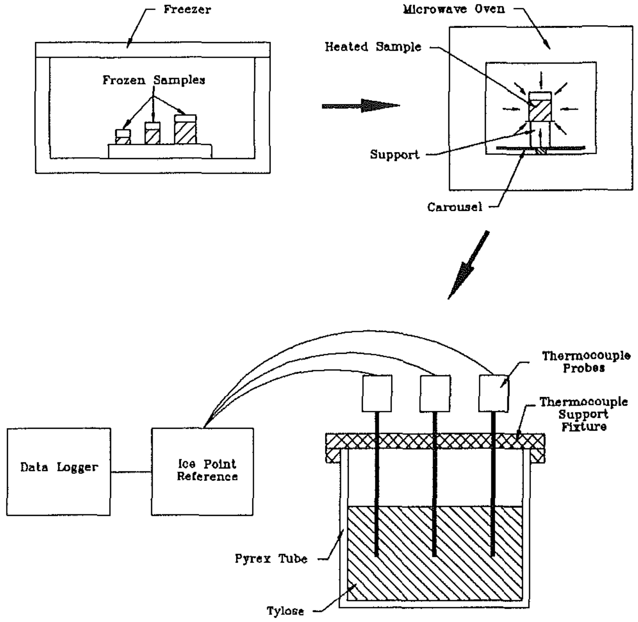

Fig. 4 Schematic diagram of experimental setup

where the subscripts e, w, n, and s represent east, west, north, and south, respectively (see Fig. 1).

Results that were independent of the grid size were obtained by simulating the microwave thawing of a $D \times H = 48 \times 72$ mm cylindrical sample using 5×7, 10×14, and 20×28 grids. Comparison of temperature profiles revealed an excellent agreement for the frozen and mushy regions. Slightly less favorable agreement (maximum error < 5 percent) was obtained for temperature prediction within the thawed region. Therefore, a grid size of 10×14 was used in all the runs. The iterative procedure has been discussed in detail by Zeng and Faghri (1992). The essential feature of the numerical solution is the iteration of the liquid fraction field until the predicted temperature field and heat source distribution are in agreement according to the liquid-fraction/temperature relation and the given input power.

Experimental Method

Cylindrical samples of Tylose, a 23 percent solid methylcellulose gel, were used in all of the thawing experiments. Because its thermal properties are similar to those of lean beef, Tylose has been widely used in food freezing and thawing investigations (Cleland et al., 1986, 1987). Pyrex glass cylinders 0.2 cm thick of different inner diameters ($D = 2.6$, 4.8 cm) were filled with Tylose. The cylinders were cut to a height of twice their respective diameters. Holes were drilled axially in the frozen Tylose samples for insertion of thermocouples. All temperature measurements were made with copper/constantan thermocouples connected to a Fluke 2280-A datalogger to record the output voltages produced by the thermocouples. The thermocouples were calibrated in a Lauda constant-temperature bath, which resulted in an uncertainty of ±0.2°C.

Table 1 Experimental design of microwave thawing experiments

Test No.	$P(W)$	D(cm)	H(cm)	H/D
1	147.5	2.6	2.6	1.0
2	157	2.6	3.9	1.5
3	181.5	2.6	5.2	2.0
4	351	4.8	4.8	1.0
5	367	4.8	7.2	1.5
6	400	4.8	9.6	2.0

Thawing experiments were carried out using a Tappan microwave oven (2450 MHz, 500 W at level 10) in which a carousel rotated the sample to improve the heating uniformity. The calorimetric technique of Nykvist and Decareau (1976) was used to indirectly estimate the microwave energy absorbed by the sample. In this method, the power absorbed by distilled water at the same volume and geometry at a given transmitted microwave power was measured. The amount of power absorbed by a sample is:

$$P = MC_{p\ell}\frac{\Delta T}{\Delta t} \tag{28}$$

where P is the power, M is the mass, $C_{p\ell}$ is the specific heat of water, ΔT is the temperature increase, and Δt is the time interval.

Figure 3 shows the variation of microwave power absorbed with volume for cylindrical water samples. Three different sample diameters ($D = 2.6$, 4.8, and 6.4 cm) and three height-to-diameter ratios for each diameter ($H/D = 1.0$, 1.5, and 2.0) were used. The power was limited by the rated cooking power of the microwave oven, which accounts for the smaller changes in power as the volume increased above approximately 200 cm^3. Based on the least-squares method, a fifth-degree polynomial was used to fit the experimental data. An error analysis showed that the measured power was accurate to within ±5.1 percent. These experimental power levels were incorporated into the numerical simulation. In terms of the experimental results reported by Taoukis et al. (1987), frozen and thawed foods, whose penetration depths fall between 1.2 to 12 cm, were assumed to absorb the total power during thawing, which was approximately constant. For Tylose, the penetration depth in the frozen phase is approximately 5.9 cm, while the depth in the thawed phase is 1.45 cm.

Figure 4 shows the experimental setup. Before the microwave thawing experiments could be performed, Tylose samples were prepared and frozen in the same dimensions as those used for water in the power testing. The sample was frozen to the prescribed initial temperature, $T_0 = -20 \pm 1\,^\circ\mathrm{C}$, transferred to the microwave oven, and the power was turned on. The sample was removed from the microwave oven after the desired heating time interval, and then thermocouples were inserted into the sample. The voltage readings were recorded by the datalogger when thermal equilibrium between the sample and the thermocouples was reached. The sample was then returned to the freezer and completely frozen for the next test. This same procedure was repeated for several time intervals until each sample was completely thawed. Parametric data for the experimental cases examined in the present study are listed in Table 1. The time–temperature data were recorded at selected locations ($R/2$ and center for 26 mm diameter samples, and $3R/4$, $R/2$, and center for 48 mm diameter samples).

Results and Discussions

The freezing or thawing of Tylose, which is a binary mixture,

Table 2 Thermal property data of Tylose (Cleland et al., 1986)

	Frozen phase	Thawed phase
Thermal conductivity (W/m-K)	1.65	0.55
Heat capacity (MJ/m^3-K)	1.90	3.71
Enthalpy difference (MJ/m^3) (from − 10 to 0°C)	226	

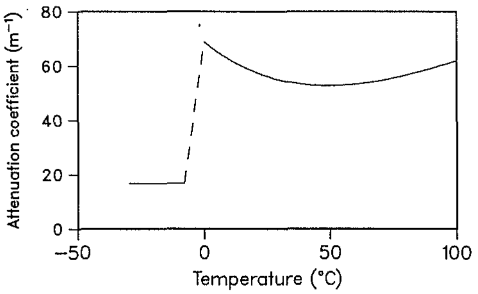

Fig. 5 Attenuation coefficient versus temperature

does not occur at a specific phase-change temperature, but occurs over a range of temperatures. A rational estimate of the mushy region temperature, as suggested by Rebellato et al. (1978) and Cleland and Earle (1984), ranges from $T_i = -8°$ to $T_f = -0.6°C$. We chose $T_m = -3°C$ as the temperature corresponding to the peak evolution of latent heat. The thermal and dielectric properties of Tylose can vary significantly within the mushy phase-change temperature range. Table 2 lists thermal property data of Tylose used in the calculations (Cleland et al., 1986). According to Mudgett (1989), the dielectric properties of food and biological material are primarily determined by moisture and salt contents. The greater the moisture and salt contents, the shallower the microwave penetration depth, while the solids of the materials are considered to absorb no microwave energy for moderate and high moisture content products. The attenuation factor is the only dielectric property used in the present numerical model. Since no experimental data are available for the dielectic properties of Tylose, beyond the mushy region the attenuation factor was calculated using Eq. (1) from the dielectric data of lean beef at a frequency of 2800 MHz (Bengtsson and Risman, 1971; Nykvist and Decareau, 1976). Within the mushy region the attenuation factor was estimated by Eq. (17). The relation between the attenuation factor and temperature is shown in Fig. 5, in which the dashed line shows the assumed variation of attenuation factor within the mushy region.

Comparisons between the experimental data and the predicted results of the thawing history at different radial locations for three $D = 26$ mm samples are shown in Fig. 6. In Fig. 6(*a*) ($H/D = 1$), for $t = 5$ *s*, the predicted temperature values of both the centerline and $r = R/2$ locations were larger than the experimental data and varied sharply with heating time. The discrepancy at the early time results from the assumption in the model that a constant power is absorbed in the sample. In the completely frozen phase, the attenuation factor is very small, which suggests that part of the incident power passes completely through the sample and reflects back to the magnetron. The penetration depth of the frozen phase is 5.9 cm, which is larger than the diameter and height of the samples. In this case, the actual absorbed power of the frozen sample is less than the given power, which is measured using water. For the time interval of $5 < t < 25$ *s*, the temperatures at the centerline and $R/2$ vary slowly with the heating time because of the absorption of latent heat within the mushy region. In addition, the temperature values of the numerical and experimental results at different locations are approximately the same, which means that the heating effect is uniform in the frozen and mushy phases. For $t > 25$ s, however, evident temperature variations occur between the centerline and $R/2$ locations. Since the outer layer of the sample is thawed first, more power is absorbed within the thawed layer due to the increase in attenuation factor. It is assumed that a constant power is absorbed in the sample, so less microwave power energy reaches the inner layer. As a result, the temperature gradient between the centerline and $r = R/2$ are large as the thawed front appears.

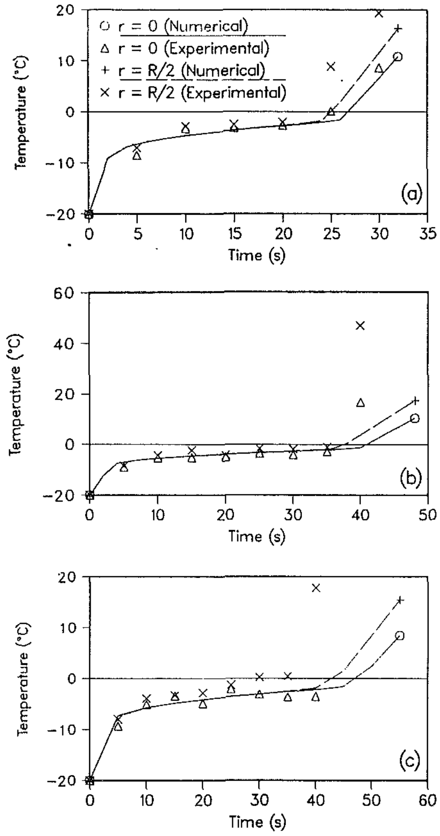

Fig. 6 Comparison of numerical and experimental temperatures during microwave thawing of a short Tylose cylinder ($D = 2.6$ cm): (*a*) $H/D = 1.0$, $P = 147.5$ W; (*b*) $H/D = 1.5$, $P = 157.0$ W; (*c*) $H/D = 2.0$, $P = 181.5$ W

The transient temperature and liquid fraction distributions within the $D \times H = 26 \times 26$ mm sample are plotted in Fig. 7. Conditions at $t = 10$ s are shown in Figs. 7(*a*) and 7(*b*). Since the temperature of the whole domain is limited to the mushy region temperature range (−8 to −0.6°C), the temperature field in Fig. 7(*a*) is nearly isothermal. As seen in Fig. 7(*b*), the liquid fraction within the sample is almost constant. Similar trends can be found in Figs. 7(*c*) and 7(*d*) at $t = 20$ s. Since the temperature rise causes an increase in the attenuation factor within the mushy region, more power is absorbed within the outer layer of the sample as phase change advances. In turn, increased temperature and liquid fraction gradients can be found near the top-right corner, where microwaves enter the top and side faces of the sample. After $T > T_f$, the liquid fraction is identically unity, which means the thawing process is complete. In Fig. 7(*e*), the isotherms show that greater temperature gradients appear from the top-right to the bottom-left corner because of the completion of phase change.

The temperature histories of the $D \times H = 26 \times 39$ mm sample at the centerline and $r = R/2$ are illustrated in Fig. 6(*b*). For the time interval of $0 < t \leq 35$ *s*, the numerical solution and experimental data agree well. However, the experimental data are significantly higher than the predicted results at $t = 40$ s.

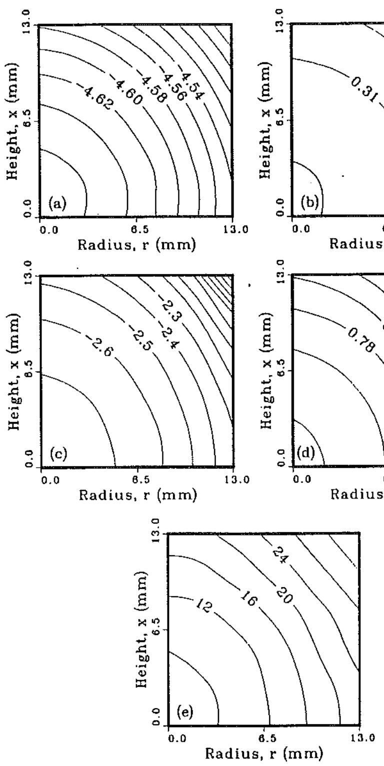

Fig. 7 Temperature and liquid fraction contours at different times for a cylindrical Tylose sample ($D\times H=26.0$ mm $\times$ 26.0 mm, $P=147.5$ W): (*a*) temperature (°C), $t=10$ s; (*b*) liquid fraction, $t=10$ s; (*c*) temperature (°C), $t=20$ s; (*d*) liquid fraction, $t=20$ s; (*e*) temperature (°C), $t=30$ s

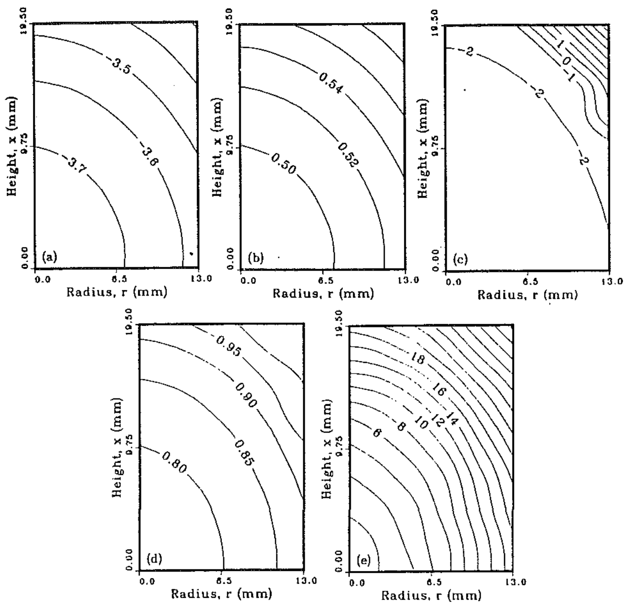

Fig. 8 Temperature and liquid fraction contours at different times for a cylindrical Tylose sample ($D\times H=26.0$ mm $\times$ 39.0 mm, $P=157.0$ W): (*a*) temperature (°C), $t=20$ s; (*b*) liquid fraction, $t=20$ s; (*c*) temperature (°C), $t=30$ s; (*d*) liquid fraction, $t=30$ s; (*e*) temperature (°C), $t=40$ s

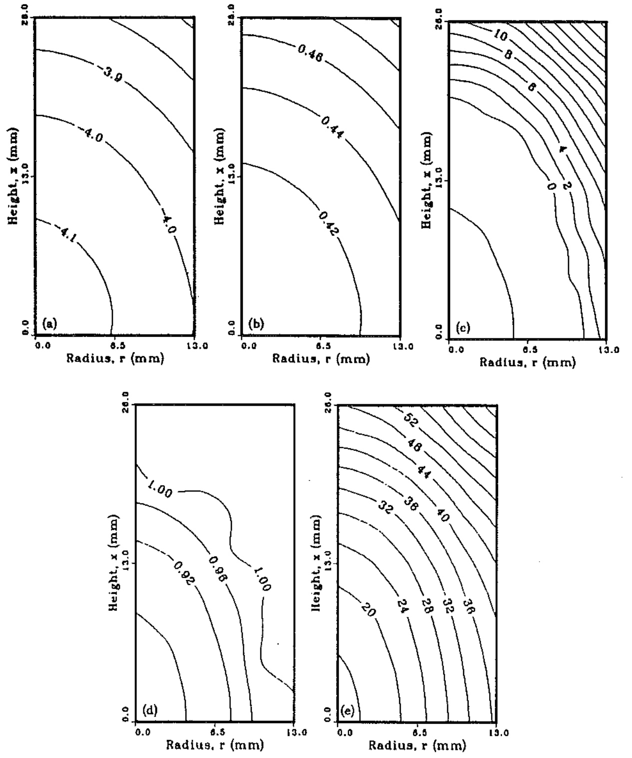

Fig. 9 Temperature and liquid fraction contours at different times for a cylindrical Tylose sample ($D\times H=26.0$ mm $\times$ 52.0 mm, $P=181.5$ W): (*a*) temperature (°C), $t=20$ s; (*b*) liquid fraction, $t=20$ s; (*c*) temperature (°C), $t=40$ s; (*d*) liquid fraction, $t=40$ s; (*e*) temperature (°C), $t=60$ s

The source of the discrepancy is the nonuniform heating effect along the axis, which accounts for the fact that the microwave field at the sample surface is nonuniform. This effect increased with the height of the sample, but was decreased by rotating the sample. Numerically, the discrepancy may be attributed to uncertainties in the thermal and electric property data base. In spite of these discrepancies, the predicted thawing time is close to the experimental thawing time. The experimental time was 35 s, which was 14 percent less than predicted. The predicted temperature and liquid fraction contours for $t=20$, 30, and 40 s are plotted in Fig. 8 to illustrate the different heating patterns during the thawing process. At $t=20$ s, the temperature within the calculated domain is between the mushy region temperature range, so the temperature field (Fig. 8(*a*)) and liquid fraction distribution (Fig. 8(*b*)) were relatively uniform. By $t=30$ s, local thawing occurred. Within the thawed top-right corner, due to the completion of phase transformation and the absorption of the higher microwave energy, the temperature rose quickly, while the rest of the sample remained nearly isothermal (Fig. 8(*c*)). The dense isotherms in the top-right corner demonstrate the existence of large temperature gradients. Because of the rapid change of temperature near the final thawing temperature, $T_f=-0.6$°C, unstable temperature and liquid fraction contours can be observed in Figs. 8(*c*) and 8(*d*) near the final thawing temperature. Isotherms at $t=40$ s are plotted in Fig. 8(*e*). At this time, the phase-change process was completed, resulting in relatively even temperature gradients within the sample.

The thawing histories at selected locations within the $D\times H=26\times 52$ mm sample are shown in Fig. 6(*c*). Good agreement is restricted to $t<40$ *s*. Disagreement is most pronounced at $r=R/2$ at $t=40$ s. At this location, the experimental temperature data exceeded the predicted value by nearly 20°C. In addition to the above-mentioned nonuniformity of the microwave irradiation, another source of discrepancy could be induced by a localized overheating around the thermocouple holes, which may result in higher temperature readings during the test. The temperature and liquid fraction contours with heating time are shown in Fig. 9. The propagation of the thawing front along the axial direction is faster than in the radial direction (see Figs. 9(*c*) and 9(*d*)), even though a uniform incident microwave intensity at the surface is assumed. This

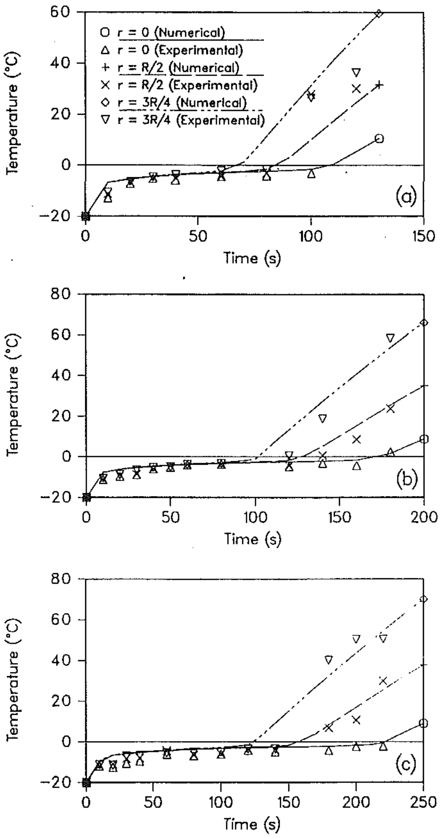

Fig. 10 Comparison of numerical and experimental temperatures during microwave thawing of a short Tylose cylinder ($D = 4.8$ cm): (*a*) $H/D = 1.0$, $P = 351.0$ W; (*b*) $H/D = 1.5$, $P = 367.0$ W; (*c*) $H/D = 2.0$, $P = 400.0$ W

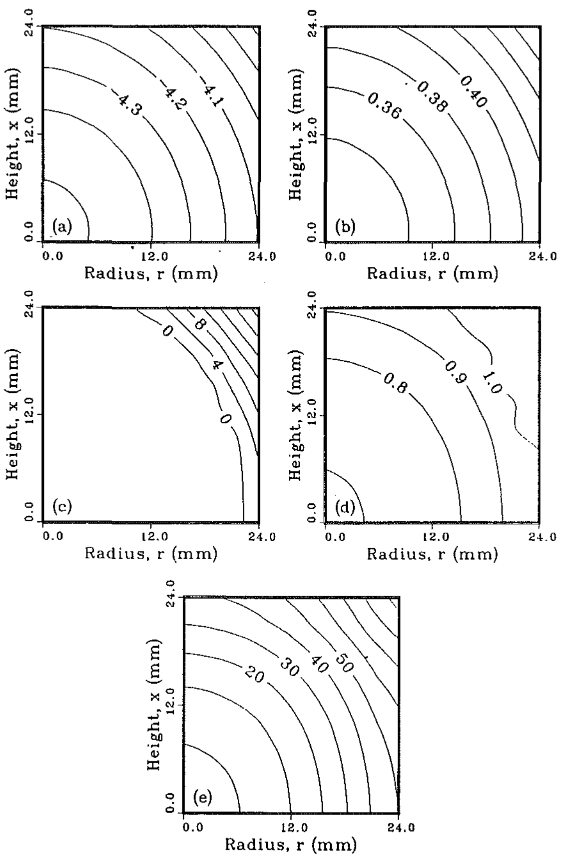

Fig. 11 Temperature and liquid fraction contours at different times for a cylindrical Tylose sample ($D \times H = 48.0$ mm × 48.0 mm, $P = 351.0$ W): (*a*) temperature (°C), $t = 30$ s; (*b*) liquid fraction, $t = 30$ s; (*c*) temperature (°C), $t = 60$ s; (*d*) liquid fraction, $t = 60$ s; (*e*) temperature (°C), $t = 100$ s

phenomenon can be explained by the difference in the successive shell volumes along in the radial direction. In the cylindrical coordinate system, the equal radial space steps Δr result in an increase in the volume of the shell along the radial axis. With increasing time, the slope of the isotherms becomes steeper (Figs. 9(*c*) and 9(*e*)). Fluctuating temperature and liquid fraction contours near the final thawing temperature T_f are seen in Figs. 9(*c*) and 9(*d*), which can be attributed to the sharp temperature variations resulting from the completion of phase change.

A comparison of Figs. 7, 8, and 9 disclose that in the frozen state of the sample, the large penetration depth results in an even distribution of the heat generation. In addition, the large thermal conductivity and small heat capacity yield a high thermal diffusivity within the frozen phase. In the mushy region, the absorption of latent heat imposes some limits on the temperature variation. The attenuation factor increases with the liquid fraction, but the thermal diffusive capacity decreases with the liquid fraction. Owing to the governing effects of the mushy phase-change process, the even temperature and liquid fraction fields can be anticipated. As partial thawing takes place in the sample, the temperature in the thawed region increases rapidly because the effects of latent heat are removed.

Figure 10 presents the thawing history for the 48-mm-dia sample with $H/D = 1$, 1.5, and 2. In Fig. 10(*a*), $H/D = 1$, for the time interval of $0 < t \leq 10$ s, the predicted temperatures vary rapidly with time. As mentioned previously, this is attributed to the constant absorbed power assumption in the mathematical model. For the time interval of $10 < t \leq 80$ s, the temperature data at the three locations are nearly the same, which suggests the temperature at $r = 0$, $R/2$, and $3R/4$ range from -8 to -0.6°C, which is defined as the mushy region temperature range. As the thawing process is completed in the outer layer of the sample, the predicted and measured temperatures differ more significantly. Temperature and liquid fraction contours at $t = 30$ s are shown in Figs. 11(*a*) and 11(*b*). The uniform distributions of temperature and liquid fraction exhibit characteristics indicative of the mushy region. At $t = 60$ s, the top-right corner is completely thawed (Figs. 11(*c*) and 11(*d*)), which results in large temperature gradients and fluctuating temperature and liquid fraction contours near the thawing front. By $t = 100$ s, the maximum isotherm is 90°C, while the minimum isotherm is 0°C (Fig. 11(*e*)). Since most of the microwave energy is absorbed in the outer layer, the inner layer near the bottom-left corner forms a cold core. It should be noted that runaway heating occurs as the attenuation factor increases with temperature when the temperature is higher than 50°C (Fig. 5).

Figure 10(*b*) compares the experimental and numerical results for $D \times H = 48 \times 72$ mm at selected locations. From $t = 20$ to 100 s, the temperatures indicate the existence of the mushy region at $r = 0$, $R/2$, and $3R/4$. Achievement of better accuracy is limited by the local completion of thawing. In the case of 2450 MHz, the penetration depth of the microwaves in the frozen sample is approximately 5.9 cm. However, in thawed Tylose the penetration depth is approximately 1.45 cm. As time progresses and temperatures increases, the thawed layer absorbs larger amounts of energy, while less energy reaches the mushy or frozen regions. Figures 12(*a*) and 12(*b*) show the conditions at $t = 60$ s. The mushy region spread within the entire domain, which led to uniform temperature and liquid fraction distributions. Fluctuating temperature and liquid fraction contours were again found near the thawing fronts in Figs. 12(*c*) and 12(*d*). At $t = 180$ s, the temperature near the top-right corner reached 100°C, as shown in Fig. 12(*e*). Overheating

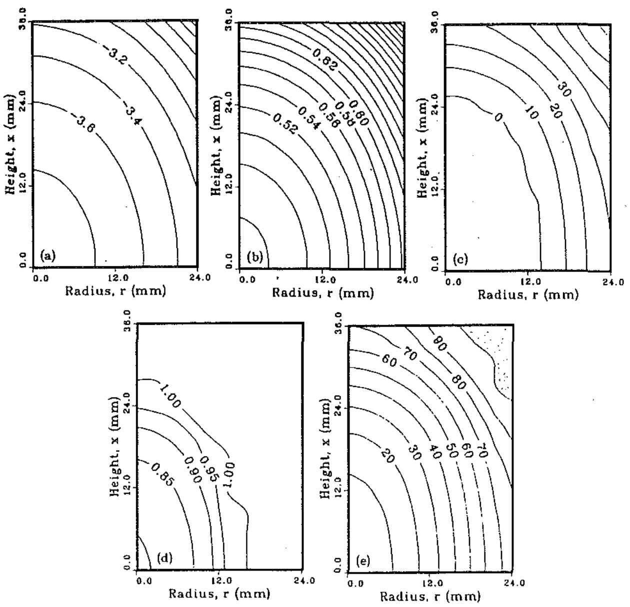

Fig. 12 Temperature and liquid fraction contours at different times for a cylindrical Tylose sample ($D \times H = 48.0$ mm × 72.0 mm, $P = 367.0$ W): (*a*) temperature (°C), $t = 60$ s; (*b*) liquid fraction, $t = 60$ s, (*c*) temperature (°C), $t = 120$ s; (*d*) liquid fraction, $t = 120$ s; (*e*) temperature (°C), $t = 180$ s

effects in the corner region of the tested sample were also observed experimentally for this case. Runaway heating is characterized by the formation of voids within the Tylose at the corners because the temperature reaches the boiling point of water. As the water in the sample evaporates, a stabilizing temperature zone occurs in the top-right corner. The decrease of the water content in the sample brings about a decrease in the absorptive ability in the outer layer. In turn, an improved agreement between the predictions and measurements, as shown in Fig. 10(*b*), is obtained.

Similar trends in the thawing history can be found in Fig. 10(*c*) for $D \times H = 48 \times 96$ mm. The comparison between the predicted and experimental thawing times show a good agreement. At $t = 60$ s, the mushy region extended over the entire domain. The smooth temperature and liquid fraction contours and small increments of the contours account for uniform, stable temperature and liquid fraction fields (Figs. 13(*a*) and 13(*b*)). With increasing time, a completely thawed region appeared near the top-right corner of the sample (Figs. 13(*c*) and 13(*d*)). The mushy and the thawed regions coexisted within the sample. At the thawing front, the unstable behavior of temperature and liquid fraction contours appeared, as previously noted. By $t = 220$ s, the mushy, thawed, and strong evaporation regions co-existed within the domain (Fig. 13(*e*)). The temperature at the top-right corner reached 100°C, while that at the bottom-left corner remained at 0°C.

For a frequency of 2450 MHz, the penetration depth of the microwaves in the frozen Tylose is approximately 5.9 cm. However, in the thawed state the penetration depth is approximately 1.45 cm. The smaller samples of 2.6 cm in diameter and height to diameter ratios of 1.0, 1.5, and 2.0 heated evenly. For the larger samples, the microwaves only penetrated and heated the outer layer of the sample, while the centers of the samples were heated partially by the microwaves and conduction from the outer layer.

Conclusions

To assess and develop mathematical models relating time-temperature profiles during microwave thawing and heating, accurate experimental data are required. The experimental data and numerical results presented in this work demonstrate the transient thawing characteristics of cylindrical Tylose samples subject to microwave irradiation from the axial and radial directions. The essential features of the microwave thawing heat transfer are as follows:

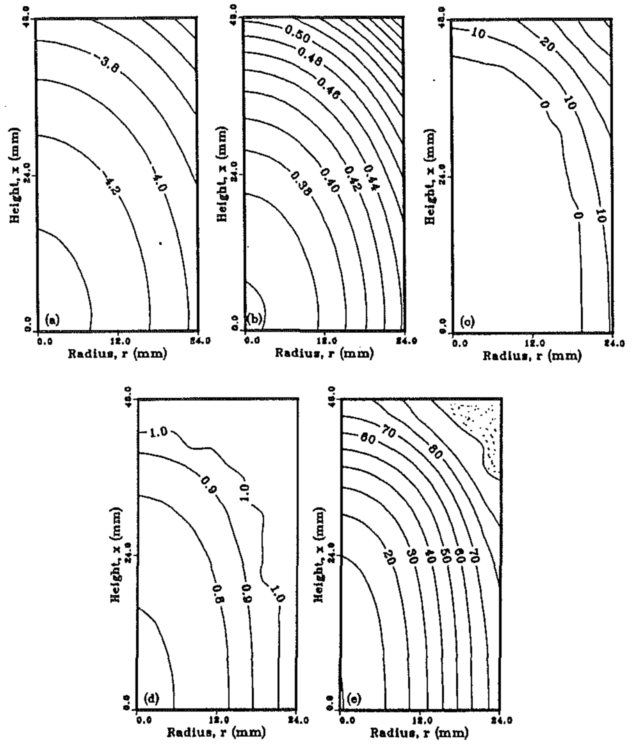

Fig. 13 Temperature and liquid fraction contours at different times for a cylindrical Tylose sample ($D \times H = 48.0$ mm × 96.0 mm, $P = 400.0$ W): (*a*) temperature (°C), $t = 60$ s; (*b*) liquid fraction, $t = 60$ s, (*c*) temperature (°C), $t = 120$ s; (*d*) liquid fraction, $t = 120$ s; (*e*) temperature (°C), $t = 220$ s

1 Although the microwave thawing curves display trends similar to conventional convective thawing curves, which have distinct phase-change characteristics, the time required for microwave thawing is greatly decreased due to the different method of power input as well as higher power delivered to the samples than convective thawing.

2 Due to the variations of the attenuation factor and thermal diffusivity between the frozen and thawed phases, uniform heating effects can be anticipated when the temperature within the entire sample is below the final thawing temperature. As soon as local thawing occurs, large temperature gradients appear between the thawed and mushy region.

3 Variations in the diameter and the length significantly affect the resulting temperature profiles and thawing profiles and thawing times. For the $D \times H = 48 \times 72$ mm and $D \times H = 48 \times 96$ mm samples, runaway heating effects were observed experimentally and simulated numerically.

4 The numerical model accounted for mushy region phase change, heat generation due to microwave irradiation, simple mass transfer during runaway heating, and variable thermal and electrical properties. The model predicted thawing times for cylindrical Tylose samples with good agreement with the experimental data.

References

Bengtsson, N. E., and Risman, P. O., 1971, "Dielectric Properties of Foods at 3 GHz as Determined by a Cavity Perturbation Technique. II: Measurements on Food Materials," *J. Microwave Power*, Vol. 6, No. 2, pp. 107–123.

Bialod, D., Jolion, M., and LeGoff, R., 1978, "Microwave Thawing of Food

Products Using Associated Surface Cooling," *J. Microwave Power*, Vol. 13, No. 3, pp. 269–274.

Cleland, A. C., and Earle, R. L., 1984, "Assessment of Freezing Time Prediction Methods," *J. Food Sci.*, Vol. 49, pp. 1034–1042.

Cleland, D. J., Cleland, A. C., Earle, R. L., and Byrne, S. J., 1986, "Prediction of Thawing Times for Foods of Simple Shape," *Int. J. Refrig.*, Vol. 9, pp. 220–228.

Cleland, D. J., Cleland, A. C., Earle, R. L., and Byrne, S. J., 1987, "Experimental Data for Freezing and Thawing of Multidimensional Objects," *Int. J. Refrig.*, Vol. 10, pp. 23–31.

Datta, A. K., 1990, "Heat and Mass Transfer in the Microwave Processing of Food," *Chemical Engineering Process*, Vol. 86, No. 6, pp. 47–53.

Decareau, R., 1968, "High Frequency Thawing of Foods," *Microwave Energy Appl. Newsletter*, Vol. 1, No. 2, p. 3.

Komoprasert, V., and Ofoli, R. Y., 1989, "Mathematical Modeling of Microwave Heating by the Method of Dimensional Analysis," *J. Food Processing and Preservation*, Vol. 13, pp. 87–106.

Mudgett, R. E., 1986, "Microwave Properties and Heating Characteristics in Foods," *Food Technology*, Vol. 40, No. 1, pp. 84–93.

Mudgett, R. E., 1989, "Microwave Food Processing," *Food Technology*, Vol. 43, No. 1, pp. 117–126.

Nykvist, W. E., and Decareau, R. V., 1976, "Microwave Meat Roasting," *J. Microwave Power*, Vol. 11, No. 1, pp. 3–24.

Ohlsson, T., and Bengtsson, N. E., 1971, "Microwave Heating Profiles in Foods," *Microwave Energy Appl. Newsletter*, Vol. IV, No. 6, pp. 3–8.

Patankar, S. V., 1980, *Numerical Heat Transfer and Fluid Flow*, Hemisphere, Washington, DC.

Rebellato, L., Del Guidice, S., and Comini, G., 1978, "Finite Element Analysis of Freezing Processes in Foodstuffs," *J. Food Sci.*, Vol. 43, pp. 239–250.

Rosenberg, U., and Bogl, W., 1987, "Microwave Thawing, Drying and Baking in the Food Industry," *Food Technology*, Vol. 41, No. 6, pp. 85–91.

Taoukis, P., Davis, E. A., Davis, H. T., Gordon, J., and Talmon, Y., 1987, "Mathematical Modeling of Microwave Thawing by the Modified Isotherm Migration Method," *J. Food Science*, Vol. 52, No. 2, pp. 455–463.

von Hipple, A. R., 1954, *Dielectrics and Wave*, MIT Press, Cambridge, MA.

Zeng, X., 1991, "Mathematical Modeling, Numerical Method, and Experiment of Freezing and Thawing Heat Transfer in a Food Analog Material," Ph.D. Dissertation, Chongqing University, Chongqing, PRC.

Zeng, X., and Faghri, A., 1992, "Mathematical Modeling of Microwave Thawing Heat Transfer for Food and Biological Materials," submitted to the *Int. J. Heat Mass Transfer*.

Heat Transfer Measurement and Analysis for Sintered Porous Channels

G. J. Hwang
Professor.
Mem. ASME

C. H. Chao[1]

Department of Power Mechanical Engineering,
National Tsing Hua University,
Hsinchu, Taiwan, 30043

This paper presents the results of heat transfer measurement and analysis for two $5 \times 5 \times 1$ cm porous channels. The channels were made of sintered bronze beads with two different mean diameters, $d_p = 0.72$ and 1.59 mm. The local wall temperature distribution, inlet and outlet pressures and temperatures, and heat transfer coefficients were measured for heat flux of 0.8, 1.6, 2.4, and 3.2 W/cm^2 with air velocity ranging from 0.16 to 5 m/s and inlet air pressure of 1 ~ 3 atm. The measurement covers the data in both thermal entrance and thermally fully developed regions. The local Nusselt numbers were correlated in the fully developed region. The fully developed Nusselt numbers were analyzed theoretically by using a non-Darcy, two-equation flow model. Heat transfer between the solid and fluid phases was modeled by a relation of the form $h_{loc} = ARe^n$. A wall function was introduced to model the transverse thermal dispersion process for the wall effect on the lateral mixing of fluid. The predicted fully developed Nusselt numbers are in good agreement with the measured values.

Introduction

The increasing demand for execution speed and memory capacity in modern computers has increased circuit density per unit chip and power dissipation per unit volume. Therefore, the heat flux at the chip may be raised to a certain high level, e.g., the typical average power densities at the chip level for plastic DIPs and PGA ceramic package are about 10 and 25 W/cm^2, respectively (Mahalingam and Berg, 1984; Mahalingam, 1985). For reliable operation, the electronic package must be maintained at a reasonable temperature level, e.g., below 130°C. Generally speaking, natural and forced convection can only remove a small amount of heat per unit area per unit temperature difference about 0.001 W/cm^2°C by natural convection, 0.01 W/cm^2°C in forced air, and 0.1 W/cm^2 in forced liquid (Simon, 1983). Compared to the heat flux levels at the chip, heat removal from the package's surface by common heat transfer technique is quite low. Therefore, efficient cooling schemes must be developed to remove the heat to the environment.

While heat flow internal to the package is primarily by thermal conduction, heat removal from the surface of the package is usually by convection. The heat transfer between the coolant and the package surface contributes a significant fraction of the total thermal resistance. Accordingly, an adequate surface area for heat disposal and a large heat transfer coefficient are pursued in package cooling. It has been widely recognized that the heat transfer can be increased by increasing the area of the heat sink in contact with the coolant. Tuckerman and Pease (1981, 1982) point out that for laminar flow in confined channels, the heat transfer coefficient is inversely proportional to the width of the channel since the limiting Nusselt number is constant. They built a water-cooled integral heat sink with microscopic flow channels, typically 50 μm wide and 300 μm deep, and demonstrated that extremely high power density circuits could be cooled with a surface flux of 790 W/cm^2 or more. Mahalingam (1985) confirmed the superiority of microchannel cooling on a silicon substrate of 5×5 cm by using water and air as coolants. These correspond to a heat removal of 3.6 W/cm^2°C for water and 0.1 W/cm^2°C for air at the silicon substrate level. It is interesting to note that for the thermal entrance region problem (Graetz problem), the local Nusselt number attains an asymptotic value (a constant minimum value) for fully developed flow. This fact in forced convection has been known since 1883 but was not utilized for about a hundred years until Tuckerman and Pease's novel development in forced cooling in the 1980's.

Another cooling technique is heat transfer augmentation by using a porous medium. Kuo and Tien (1981) and Hunt and Tien (1988) utilized foam to enhance liquid forced convective cooling for potential application to electronics cooling. The results show that an increase of two to four times in heat transfer is achievable as compared to that of laminar slug flow in a clear duct. Thermal dispersion caused by the presence of the solid matrix play a key role in their heat transfer augmentation. Koh and Colony (1974) and Koh and Stevens (1975) studied the problem of forced convection in a porous channel by using Darcy flow model and found that under the boundary condition of a constant heat flux, the wall temperature and also the temperature difference between the wall and the coolant can be drastically reduced by the insertion of a high-conductivity porous material in the channel.

A porous medium will provide a solid–air contact area many times greater than the duct surface area. The total heat transfer rate will be increased drastically regardless of its lower heat transfer coefficient at the solid–air contact surface. Using this idea, an experimental investigation is conducted to examine the feasibility of using a high-conductivity porous channel as a heat sink for high-performance forced air cooling in microelectronics. The porous channel, $5 \times 5 \times 1$ cm, was made of sintered bronze beads with two difference mean diameters, $d_p = 0.72$ and 1.59 mm. In electronic cooling, the micro-electronic devices may be damaged by a local excess high temperature of the heat sink instead of the average one; therefore the local wall temperature distribution and heat transfer coefficient are presented. The data were measured for heat fluxes of 0.8, 1.6, 2.4, and 3.2 W/cm^2 with air velocity ranging from 0.16 to 5 m/s and inlet air pressure of 1 ~ 3 atm. The results show that the high-conductivity porous channel enhances the

---

[1] Current address: Energy & Resources Laboratories, ITRI, Chutung, Taiwan 310.

Contributed by the Heat Transfer Division and presented at the ASME Winter Annual Meeting, Anaheim, California, November 8-13, 1992. Manuscript received by the Heat Transfer Division July 1992; revision received July 1993. Keywords: Electronic Equipment, Forced Convection, Porous Media. Associate Technical Editor: C. E. Hickox, Jr.

heat transfer and the maximum wall temperature could be reduced drastically. For example, the forced air cooling can be extended from 0.01 to 0.5 W/cm^2°C by a porous heat sink with a maximum wall temperature less than 100°C. Also, the present study shows that porous heat sinks of $5\times5\times1$ cm using air as the cooling fluid can keep the temperature rise of 250 W chips below 100°C for $\mathrm{Re}_d=425$ and reduce thermal resistance to 0.4°C/W. Finally, the local and fully developed Nusselt numbers are correlated, and the full developed Nusselt number is also analyzed theoretically.

Experimental Apparatus and Procedure

Experimental Apparatus. An experimental setup for heat transfer measurement of a sintered copper beads porous channel is shown in Fig. 1. It was composed of four major parts: (*a*) coolant air supply, (*b*) test section, (*c*) porous media, and (*d*) data acquisition system. The details of the apparatus are depicted as follows:

(*a*) *Coolant Air Supply.* The coolant air flow with gage pressure ranging from 0 to 6 kg/cm^2 was supplied by an air compressor. A valve was installed to regulate the air pressure and flow rate. A thermocouple was located at the inlet of the plenum space to measure the temperature of the inlet air flow. To pick up the bulk temperature reading at the exit, a mixing chamber made of teflon was attached to the exit plane as shown in Fig. 1. A stagger rod bundle was installed in the chamber to provide a well-mixed condition. After passing the test section, the outlet of coolant air flow was connected to a flow meter. Two flow meters with different ranges (0.12 ~ 2.16 and 1.0 ~ 10 m^3/h) were installed for indicating the air flow rate.

(*b*) *Test Section.* The test section and the entrance region were made of a teflon cylinder 8 cm in diameter and thermally insulated from the outside environment by a cylindrical composite wall consisting of an inner layer of fiberglass and outlet acrylic plastic tube. The porous channel $5\times5\times1$ cm was fixed inside the test section. Three pressure taps are located at inlet plenum, before and after the test section of porous channel. A $5\times5\times0.2$ cm copper plate was also sintered together with the porous channel and heated by a 0.01 mm thickness film heater of 108.2 ohms to simulate a heat sink with a constant heat flux condition for electronic cooling. A 300 W DC power supply for the film heater was measured with a digital multimeter. As shown in Fig. 1, the copper plate was cut into 12 sections to reduce the wall heat conduction along the flow direction. Three T-type copper-constantan thermocouples were spot welded in each section for measuring the local temperature. To have a fully developed flow before entering the porous channel, an unheated section $5\times5\times1$ cm of the same material was also installed.

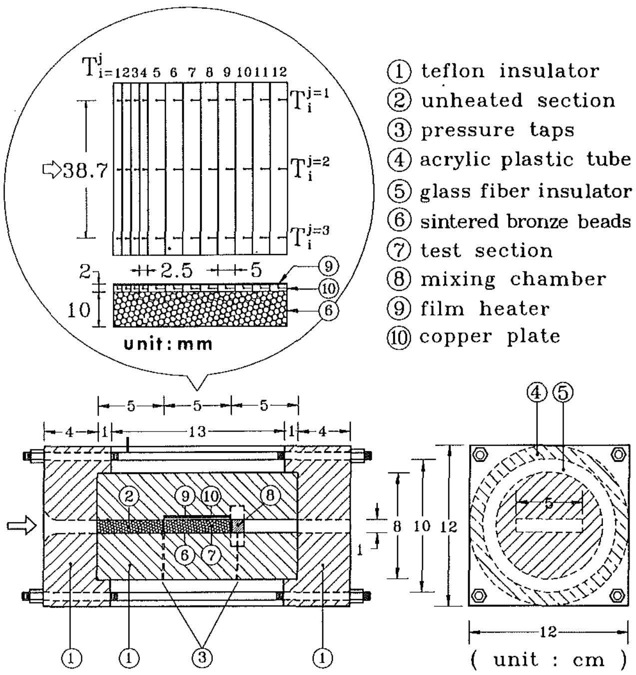

Fig. 1 Experimental apparatus and installation of thermocouples

(*c*) *Porous Medium.* The porous media were made of sintered bronze beads (89 percent Cu + 11 percent Sn) and two test sections were employed in the present investigation. The average bead diameters were 0.72 and 1.59 mm. This type of porous medium in sintered metals has been used extensively in industrial applications such as heat exchangers, fluid filters, and many others. It is essential to measure carefully the corresponding flow and thermophysical properties of these materials. The measurements for the sintered beads channel are:

1 Void fraction—The void fraction or porosity, ϵ, was evaluated by using $\epsilon=(v_t-v_s)/v_t$, where v_t and v_s are the total porous channel and particle volumes, respec-

Nomenclature

A = area, m^2, or empirical constant
a = specific surface area per unit volume, m^{-1}
Bi = modified Biot number $=h_{\mathrm{loc}}aH^2/k_s^*$
C = constant or dimensionless pressure drop defined in Eq. (8)
c = isobaric specific heat, J/kgK
c_e = effective isobaric specific heat of porous media $=\rho_e[\epsilon\rho_f c_f+(1-\epsilon)\rho_s c_s]$, J/kgK
Da = Darcy number $=K/\epsilon H^2$
D_e = hydraulic diameter $=4A/S$
D_t = thermal dispersion constant
d_i = diameter of the beads in a particular size range
d_p = average bead diameter, m
d_v = average void diameter $=4\epsilon/a$, m
F = inertia coefficient constant or variables
Fs = Forchheimer number $=\dot{m}F\sqrt{K}/\mu_f$
H = channel height, m
h = local heat transfer coefficients $=q/(T_{wi}-T_{fb})$, W/mK
h_{loc} = internal heat transfer coefficient, W/mK
J = integer
K = permeability, m^2
k = thermal conductivity
k_e = effective thermal conductivity of porous media, W/mK
l = wall function defined in Eq. (7)
$\dot{m}$ = mass flow rate of fluid per unit sectional area, kg/m^{2}s
Nu_{fx} = local Nusselt number for the rectangular channel $=h(5/3\,H)/k_f$
Nu_{fx}^+ = local Nusselt number $=hD_e/k_e$
$\mathrm{Nu}_{f\infty}$ = fully developed Nusselt number $=h_\infty(5/3\,H)/k_f$
$\mathrm{Nu}_{f\infty}^*$ = fully developed Nusselt number for parallel plate channel $=h_\infty(2H)/k_f^*$
P = pressure, N/m^2; or nodal point
Pe_d = particle Peclet number $=c_f\dot{m}d_p/k_f^*$
Pe^+ = Peclet number $=\rho_e c_e\overline{U}D_e/k_e$

tively. The volume v_t is measured by its geometry, while v_s is determined by the volume of filling liquid.

2 Bead size distribution—The mean diameter of sintered bronze beads was measured by using a set of standard sized screens. The mean particle diameter was calculated from the equations, $d_p = 1/[\Sigma_i(w_i/d_i)]$ where w_i is the weight fraction in a given size interval and d_i is the diameter of the beads in a particular size range.

3 Permeability and inertia constant—They were determined from adiabatic data by using a pressure tap, flow meter, and Hg-manometer. The quantity $(-1/\mu_f U)(dP/dX)$ versus $\rho_f U/\mu_f$ for a range of flow rate was plotted. The permeability and inertial coefficients for the porous channel were calculated using a rearranged version of the modified Darcy equation (Hunt and Tien, 1988)

$$-\frac{dP}{dX}\frac{1}{\mu_f U}=\frac{1}{K}+\rho_f\frac{FU}{\sqrt{K}\mu_f} \tag{1}$$

4 Effective thermal conductivity—It was measured by an experimental apparatus made by Tokyo Meter Co., Ltd., Model: HVS-40-200-SD. By performing a number of one-dimensional conduction heat transfer experiments, the effective thermal conductivity was found. It is noted that the sintered bronze bead porous media were nearly isotropic and uniform in pore spacing near wall region. Table 1 lists the corresponding flow and thermal properties of the two porous media. Noted that the K and F values from the Ergun model for packed spheres are larger than that for the sintered beads. This indicated that the packed spheres gives a smaller low-speed flow resistance but shows a larger high-speed flow inertia resistance.

(*d*) *Data Acquisition System.* A digital micromanometer for low-pressure differences (less than 0.2 atm) and *U*-tube Hg manometer for higher pressure difference (less than 1 atm) connected to pressure taps were used measure the pressure drop across the test channel. A standard voltmeter and ammeter were used to measure the DC voltage across the heating element and the current passing through it. The temperature readings of the wall thermocouples were transmitted from the test section to the hybrid recorder (Yogokawa Model HR2500). The raw data were recorded until the criterion of steady state—that the variations of the wall temperature were less than 0.2°C in ten minutes—was satisfied. In the experiment procedure, the wall heat flux and the mass flow rate were kept constant.

Table 1 Physical parameters for sintered bronze beads

SAMPLE	1	2
average diameter, d_p [mm]	0.72	1.59
porosity, ϵ	0.37	0.38
permeability, $K \times 10^{10}$ [m^2]	2.9 (4.4)*	10.0 (24.1)*
inertial coefficient, F	0.242 (0.635)*	0.118 (0.610)*
thermal conductivity, k_e^0 [W/mK]	10.565	10.287

* Ergun model $K=\epsilon^3 d^2/[150(1-\epsilon)^2]$, $F=1.75/(\sqrt{150}\,\epsilon^{1.5})$

Procedure. Preliminary tests were performed for data calibration and error estimations. The errors in the temperature measurement were due to the inaccuracies in the initial calibration of the thermocouples, and the reading of recorder. The wall temperature and bulk mean air temperatures entering and leaving the test channel were measured by thermocouples. The maximum error was within ±0.2°C for the temperature measurement. The effect of axial wall temperature variation on the local film resistance was relatively small. The maximum errors both in the flow rate and pressure drop across the test section were less than 5 percent.

The test generally proceeded by increasing the power input to the test section while maintaining a constant flow rate and an inlet temperature. The flow rate, inlet and outlet fluid bulk temperatures, the local wall temperatures, and electrical power input were also recorded. The local wall temperatures were read from the outputs of the 36 thermocouples on the copper plates. By using the three-point Gauss integral rule, the local mean wall temperature T_{wi} was calculated by using the measured data of three thermocouples at an axial location. Therefore, the local average wall temperature, T_{wi}, was calculated by using the following equation:

$$T_{wi}=(5T_i^{j=1}+8T_i^{j=2}+5T_i^{j=3})/18 \tag{2}$$

where the subscript i and superscript j are shown in Fig. 1. The local bulk air temperature, T_{bx}, at each measuring section was calculated by assuming a linear air temperature variation along the flow channel. The net heat input to the test section

Nomenclature (cont.)

Q, q = power input, W, and wall heat flux per unit area, W/cm^2
R_h = channel height to average particle diameter ratio $=H/d_p$
Re = modified Reynolds number $=\dot{m}d_v/\mu_f$
Re_d = particle Reynolds number $=\dot{m}d_p/\mu_f$
St* = modified Stanton number $=h_{\mathrm{loc}}aH^2/c_f\dot{m}d_p$
T = temperature, K
U, u = volume average velocity, m/s, and dimensionless volume average velocity
v = volume, cm^3
w_i = weight fraction
X, Y = Cartesian coordinates
x^+ = nondimensional distance (inverse Graetz number) $=X/(D_e\mathrm{Pe}^+)$
ϵ = void fraction or porosity
η = variable $=X/[(C\mathrm{Re}_d)^n D_e]$
θ = dimensionless temperature difference $=(T-T_w)/(q/h_{\mathrm{loc}}aH)$
μ = viscosity, kg/ms
ρ = density, kg/m^3
ρ_e = effective density of porous media $=\epsilon\rho_f+(1-\epsilon)\rho_s$, kg/m^3
ω = empirical constant

Superscripts

$\bar{\ }$ = average value
$*$ = equivalent value
k = number of iteration
n = empirical constant

Subscripts

a = energy difference between power generated by foil heater and heat loss
b = bulk quantity
d = quantity based on Darcy's law
e = power generated by film heater
f = quantity based on fluid
i, j = position of thermocouple
in = measured position at inlet
out = measured position at exit
s = quantity based on solid
t = total
w = quantity based on the wall
∞ = fully developed value

Q_a was computed as the difference between the electric power input Q_e and the heat loss Q_{loss} through the insulation material. By performing tests without the coolant air flow, a relatively small heat loss for the test section was determined. The maximum heat loss from the test section was less than 4 percent for the power input Q_e ranging from $20 \sim 80$ W. In the present study, the difference between total net power input to the test section, and cooling air enthalpy rise along the test channel was within 5 percent.

The local heat transfer coefficient, h, and Nusselt number, Nu_{fx}, at a specific axial location were then calculated as

$$h = q/(T_w - T_{fb})$$

$$\text{Nu}_{fx} = hD_e/k_f \tag{3}$$

where $q = Q_a/A_{\text{heated}} = (Q_e - Q_{\text{loss}})/A_{\text{heated}}$ is the heat input per unit area, $D_e = 5H/3$ is the hydraulic diameter, and k_f is the thermal conductivity of fluid evaluated at local film temperature, $T_{\text{film}} = 1/2\ (T_b + T_w)$.

An analysis of the general validity of experimental measurements was performed using an uncertainty analysis (Kline and McClintock, 1953). The accuracy of the thermocouple temperature reading is within $\pm 0.1°\text{C}$, thus the accuracy of $(T_w - T_b)$ is within $\pm 0.2°\text{C}$. In the experimental measurements, the values of $(T_w - T_b)$ are about 5°C near the inlet region and 50°C near outlet region, therefore the percentage accuracy of $(T_w - T_b)$ is about ± 4 percent and ± 0.4 percent, respectively, near the inlet and outlet regions. The maximum errors in determining the heat flux q, fluid conductivity k_f, and hydraulic diameter D_e are estimated with 2, 1, and 1 percent, respectively. Therefore, the uncertainties of the values of h and Nu_{fx} by using the root mean square method are within 8.3 and 8.4 percent, respectively, in the present experimental study.

Fully Developed Flow Analysis

Thermal transport in porous channels involves a complex mechanism between the coolant and sintered metal beads with an irregular arrangement. Exact solutions concerning local velocity and temperature fields are impossible. Models for heat and flow in porous media were found by volume averaging the governing equations. This averaging process may obscure local pore phenomena that contribute to the global transport. Therefore it requires the use of empirical relation for closure.

To simulate the present experimental results in the fully developed region of large-aspect-ratio porous channels with upper wall heated and three sides insulated, it may be reasonable to use plane poiseuille flow analysis (Chao and Hwang, 1992). The steady volume-averaged momentum equation for forced convection can be written as follows (Hunt and Tien, 1988):

$$0 = -\frac{dP}{dX} - \frac{\mu}{K} U - \frac{\rho F}{\sqrt{K}} U^2 + \frac{\mu}{\epsilon} \frac{d^2U}{dY^2} \tag{4}$$

where K is the permeability and F the inertia coefficient. The momentum equation neglects the convective term since the velocity is fully developed. At low velocities, Forchheimer's effect become insignificant and boundary viscous drag term can be neglected with small particles. Consequently, Darcy's law is resumed (Hunt and Tien, 1988). The inertia effect, which is proportional to the square of the velocity, become important because the present experimental flow region covers the laminar, transitional, and turbulent flow regimes.

Due to the high solid to fluid conductivity ratio, the temperature difference between the solid and the coolant, in general, is not small. Therefore, the volume-averaging as applied to the solid phase, T_s, and the fluid phase, T_f, is (Bories, 1987)

$$0 = h_{\text{loc}} a (T_f - T_s) + k_s^* \frac{d^2T_s}{dY^2} \tag{5}$$

$$(\rho c)_f U \frac{dT_f}{dX} = h_{\text{loc}} a (T_s - T_f) + (k_f^* + k_t^*) \frac{d^2T_f}{dY^2} \tag{6}$$

where h_{loc} is the internal heat transfer coefficient, k_t^* is the dispersion conductivity, $k_t^* = D_t(\rho c)_f d_p U l$, where D_t is the thermal dispersion constant, and l is the wall function. The previous work on heat transfer in porous media almost exclusively employed local thermal equilibrium between the solid and fluid phase. This assumption may not be satisfactory for the present problem. By substituting the convective term in Eq. (5) into Eq. (6), the temperature difference between the solid and fluid phase is clearly observable for the large difference between the solid and fluid thermal conductivities. Experimental measurements for porous media related to the heat transfer between the solid and fluid phases were modeled by the relation $h_{\text{loc}} = A\text{Re}^n$ where A and n are empirical constants. The equivalent conductivity of the solid k_s^* is a function of the geometry and the solid conductivity k_s. Similarly, the equivalent conductivity of fluid k_f^* is simply ϵk_f. If a Van Driest type of wall function is introduced, the expression for l (Schroeder et al., 1981; Cheng and Hsu, 1986; Cheng et al., 1988) is

$$\begin{aligned} l &= 1 - \exp[-Y/(\omega d_p)] & 0 \le Y \le \tfrac{1}{2} H \\ &= 1 - \exp[-(H-Y)/(\omega d_p)] & \tfrac{1}{2} H \le Y \le H \end{aligned} \tag{7}$$

where ω is the empirical constant to be determined. Because of large Reynolds number and thermal dispersion, the diffusive flux due to molecular conduction is omitted in energy Eq. (6). Equations $(4) \sim (7)$ can be nondimensionalized by introducing the following variables:

$$\begin{gathered} Y = y[H], \quad U = u[\overline{U}], \quad T_s - T_w = \theta[\theta_c], \quad T_f - T_w = \theta[\theta_c], \\ \theta_c = [q/h_{\text{loc}} a H], \quad C = [-(dP/dX)K/\mu_f \overline{U}], \\ \text{Da} = [K/\epsilon H^2], \quad \text{Fs} = [\dot{m} F \sqrt{K}/\mu_f], \quad \text{Bi} = [h_{\text{loc}} a H^2/k_s^*], \\ \text{St}^* = [h_{\text{loc}} a H^2/c_f \dot{m} d_p], \text{ and } R_h = [H/d_p] \end{gathered} \tag{8}$$

where $\dot{m}$ is the mass flow rate of fluid per unit sectional area, Da is the Darcy number, Fs is the Forchheimer number, Bi is the modified Biot number, St^* is the modified Stanton number, and R_h is the ratio of channel height to average particle diameter. For the fully developed plane poiseuille flow subjected to constant wall heat flux, the temperature gradient along the flow direction is constant, and energy balance performed on a differential control volume yields $dT_f/dX = dT_s/dX = dT_w/dX = q/c_f \dot{m} H = \text{const}$. The nondimensionalized equations are then expressed as follows:

$$0 = C + \text{Da} \frac{d^2u}{dy^2} - (1 + \text{Fs}u)u \tag{9}$$

$$0 = \text{Bi}(\theta_f - \theta_s) + \frac{d^2\theta_s}{dy^2} \tag{10}$$

$$u = (\theta_f - \theta_s) + \frac{D_t u l}{\text{St}^*} \frac{d^2\theta_f}{dy^2} \tag{11}$$

where

$$\begin{aligned} l &= 1 - \exp[-(R_h/\omega)y] & 0 \le y \le \tfrac{1}{2} \\ &= 1 - \exp[-(R_h/\omega)(1-y)] & \tfrac{1}{2} \le y \le 1 \end{aligned} \tag{12}$$

with the boundary conditions:

$$\text{at } y = 0, \ u = 0, \ \theta_s = \theta_f = 0 \tag{13}$$

$$\text{at } y = 1, \ u = 0, \ \frac{d\theta_s}{dy} = \frac{d\theta_f}{dy} = 0 \tag{14}$$

For the present asymmetric heating problem, the fully developed Nusselt number is given by

Table 2 Numerical experiments for grid size

number of grid	20	40	60	80	100
St*=0.1	6.661	6.022	5.991	6.090	6.100
St*=100	0.4715	0.4744	0.4765	0.4775	0.4776

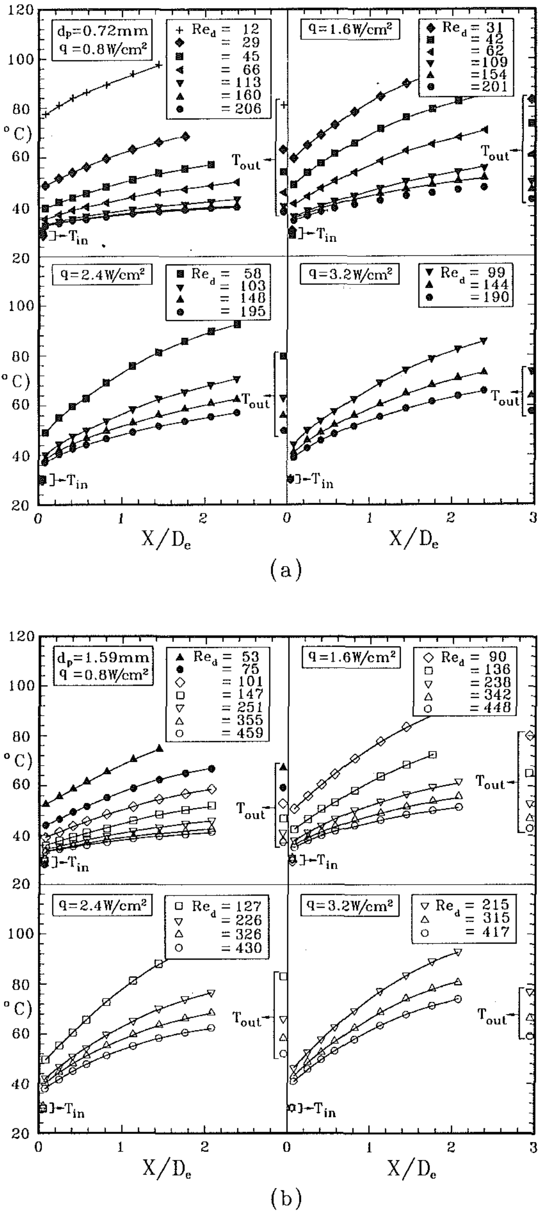

(a)

(b)

Fig. 2 Wall temperature distributions for two pieces of porous channels

$$\mathrm{Nu}^*_{f\infty} = q(2H)/[k^*_f\,(T_w - T_{fb})] = -2\mathrm{St}^*\mathrm{Pe}_d/\theta_{fb} \qquad (15)$$

where T_{fb} is the fluid mixing mean temperature and Pe_d is the particle Peclet number.

For prescribed values of Da, Fs, Bi, St*, D_t, R_h, and ω, Eqs. (9) ~ (12) can be used to compute the local volume-averaging velocity, solid and fluid temperature profiles, and the fully developed Nusselt numbers. The finite difference scheme for solving a tridiagonal system of equations by using the Thomas algorithm were employed (Anderson et al., 1984). In order to predict the flow and temperature fields accurately, particularly for low Darcy number, a large number of nodes is required near the walls. Hence, a coordinate stretching transformation has been introduced to distribute a reasonably large number of grid points near the walls. Accordingly, the x and y coordinates are transformed by using a simple algebraic relationship $\overline{P_1P_J} = \overline{P_1P_N}\,(J-1/\overline{N-1})^n$, for $1 \le J \le N$ and $1 \le n \le 2$ (e.g., $n=1$, for the case of uniform grid), where P_1 and P_N are the positions of the end points and P_J is the position of an intermediate point. The details regarding the formulation of finite difference equations are omitted here for simplicity. The constant C of dimensionless pressure drop is guessed, first, and adjusted by considering the relation:

$$C_{\mathrm{new}} = C_{\mathrm{old}}/(\textstyle\int u dy) \qquad (16)$$

It is noted that the value of C will be unchanged if the global continuity equation $\int u dy = 1$ is satisfied. With the converged velocity distributions, the energy Eqs. (10) and (11) together with wall function (12) and boundary conditions (13) and (14) are solved simultaneously. The criterion of convergence for u, θ_s, and θ_f is:

$$\mathrm{Max}|F_i^{k+1} - F_i^k|/\mathrm{Max}|F_i^{k+1}| \le 10^{-5} \qquad (17)$$

The results of numerical experiments for grid size are listed in Table 2. Finally, 80 grids across the channel height are chosen throughout the numerical computation.

Results and Discussion

Local Wall Temperature and Nusselt Number Distributions. In micro-electronics, devices can be damaged by excess local high temperature instead of the average one; therefore the temperature distribution along the flow direction of the test section is of practical interest in design. For reliable and efficient operation, the electronic package must be maintained at a reasonable temperature level, e.g., below 130°C. Figure 2(a,b) presents the local wall temperature distribution along the flow direction and the bulk mean temperature at inlet and outlet with the effect of particle Reynolds number for $d_p = 0.72$ and 1.59 mm, and $q = 0.8$, 1.6, 2.4, and 3.2 W/cm². It is seen that the local wall temperature increases with the increase in the axial position X/D_e, the decrease in the particle Reynolds number, or the increase in heat flux q. The inlet temperature was between 28 ~ 31°C. The outlet bulk mean temperature increases with the increase in the value of heat flux q but decreases with increase in the particle Reynolds number. As depicted in the figure, the wall temperature gradient approaches a constant value in the fully developed region. It is shown that higher particle Reynolds number and smaller bead sizes will keep the temperature distribution uniform.

Figure 3(a,b) depicts Nu_{fx} versus X/D_e for $d_p = 0.72$ mm and 1.59 mm, respectively. The local Nusselt number, Nu_{fx}, was calculated by using Eq. (5). It is interesting to note that for the thermal entrance region problem (Graetz problem), the local Nusselt number attains an asymptotic value (a constant minimum value) for fully developed flow. A similar trend is also observed here. At a given particle Reynolds number, the local Nusselt numbers decreases with the increase in the axial distance and then reaches its fully developed value. It is also seen that for a given Re_d and q the results of the smaller particles size ($d_p = 0.72$ mm) give higher values of the local Nusselt number than for the larger particle size.

Local and Fully Developed Nusselt Number Correlations. Figure 4(a, b) shows the distribution of local Nusselt number at four dimensionless axial positions versus particle Reynolds number for $d_p = 0.72$ and 1.59 mm, respectively. As seen from this figure, the local Nusselt number increases with the increase in the particle Reynolds number and approaches limiting maximum values. Moreover, the variation of local Nusselt number at all dimensionless axial positions is distinctly small at lower particle Reynolds number. Obviously, the thermal entrance length is shorter for the small-particle Reynolds number than

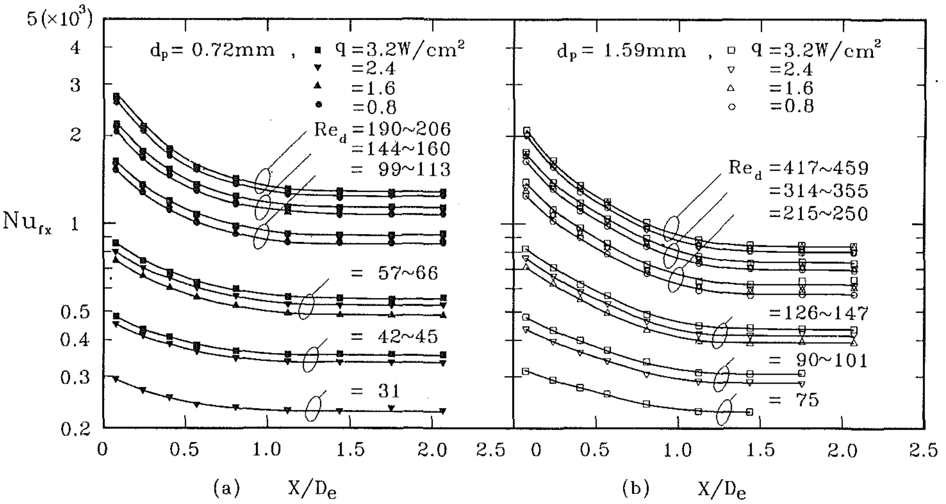

Fig. 3 Local Nusselt number at different axial location with the effect of particle Reynolds number

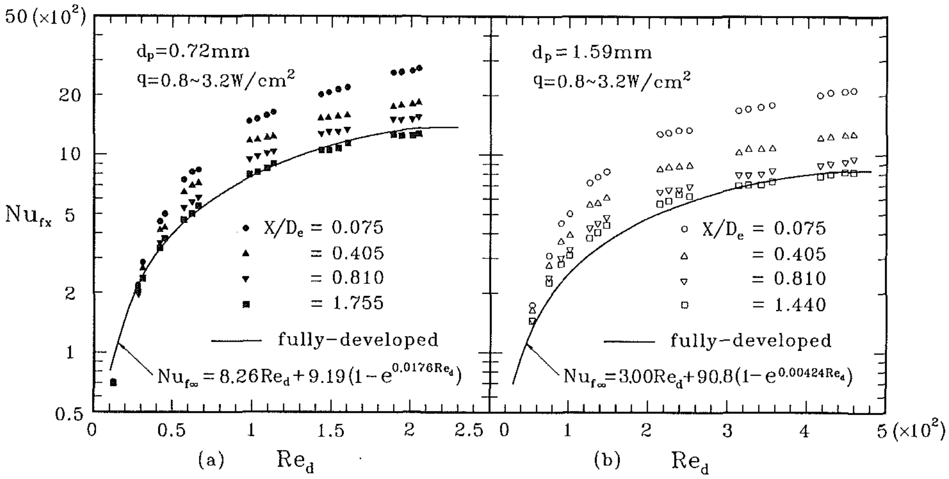

Fig. 4 Predicted local Nusselt number as a function of particle Reynolds number at different axial location

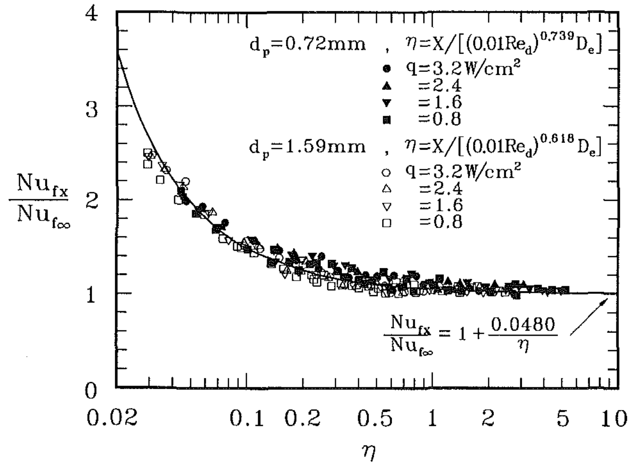

Fig. 5 Comparison of the prediction of Dittus and Boelter (1930) with experimental data

for the large-particle one. At higher particle Reynolds number, the fully developed Nusselt number curves reach some limiting values. At a given particle Reynolds number, the fully developed Nusselt number, $\mathrm{Nu}_{f\infty}$, decreases with the increase in the particle size. Over the range of particle Reynolds numbers presented in this figures, the fully developed Nusselt number can be correlated with an accuracy of ±16 percent by the following empirical equation:

$$\overset{*}{\mathrm{Nu}}_{f\infty} = C_o\mathrm{Re}_d + C_1[1 - \exp(C_2\mathrm{Re}_d)] \qquad (18)$$

Values of the constants C_0, C_1, and C_2 are given in Fig. 4.

Furthermore, the local Nusselt number in Fig. 3 can be replotted in Fig. 5 (Dittus and Boelter, 1930) by using the coordinates $Nu_{fx}/Nu_{f\infty}$ and η where $\mathrm{Nu}_{f\infty}$ is the fully developed Nusselt number, $\eta = X/[0.01\mathrm{Re}_d)^{0.739}D_e]$ for $d_p = 0.72$ mm and $\eta = X/[(0.01\mathrm{Re}_d)^{0.618}D_e]$ for $d_p = 1.59$ mm. It is interesting to see that almost all the data lie near a single curve within a maximum difference of 18 percent.

Calculated Solutions and Comparisons. The values of Da and Fs were determined from the adiabatic measurement. Heat transfer between the solid and fluid phases, h_{loc}, was modeled (Kar and Dybbs, 1982) for sintered metal beads by the following relation:

$$h_{\mathrm{loc}} = 0.0040 \times (k_f/d_v) \times \mathrm{Pr}_f^{0.333} \times \mathrm{Re}^{1.35} \quad \mathrm{Re}_d < 100$$

$$h_{\mathrm{loc}} = 0.0156 \times (k_f/d_v) \times \mathrm{Pr}_f^{0.333} \times \mathrm{Re}^{1.04} \quad \mathrm{Re}_d \geq 100$$

and

$$a = 20.346 \times (1 - \epsilon)\epsilon^2/d_p \qquad (19)$$

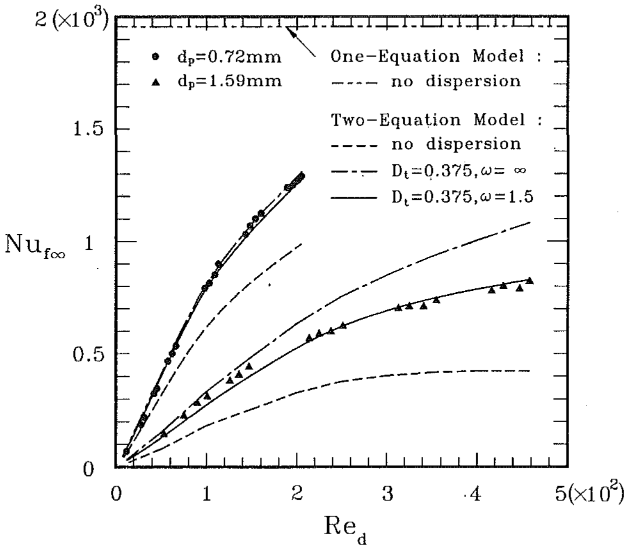

Fig. 6 Comparison of the fully developed Nusselt numbers by the effect of dispersion

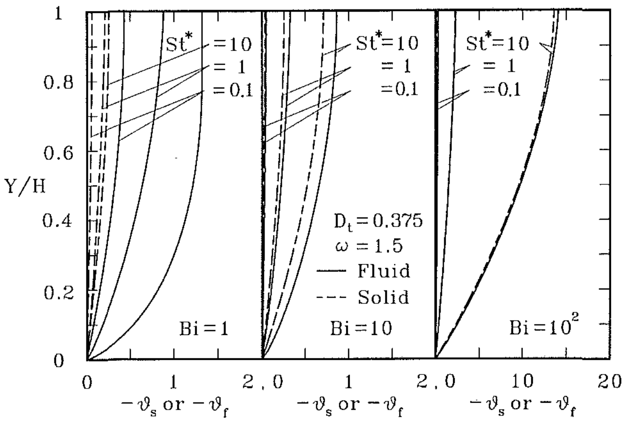

Fig. 7 $-\theta_s$ and $-\theta_f$ distributions for $Da=10^{-6}$, $Fs=10^{-1}$, and $R_h=20$

where Pr_f is the Prandtl number of the fluid, the Reynolds number is based on the average void diameter, and a is internal surface area per unit volume. Therefore the values of Bi and St* can be calculated. The Van Driest type of the wall function l in Eq. (12) for transverse thermal dispersion introduced by Cheng and his co-workers (1986, 1988) to account for the wall effect on the reduction of lateral mixing of fluid. In their papers the value of $\omega \cong 1.5$ was obtained by matching the predicted heat transfer characteristics with experimental data of Schroeder et al. (1981). With the determined values Da, Fa, Bi, St*, and l, the dispersion constant D_t can be determined from the computation of Eqs. (9) ~ (14) by matching the present experimental data. Figure 6 shows the predicted and the experimental fully developed Nusselt numbers versus the particle Reynolds number for dispersion constant $D_t=0.375$ and no dispersion. It shows that the predicted results are in good agreement with the experimental data by considering the wall effect in the transverse fluid mixing. If the inertia and boundary viscous terms in Eq. (4) and the temperature difference between solid and fluid phases in Eqs. (5) and (6) are neglected, the governing equation reduces to Darcy's law and one-equation model as follows:

$$U_d = -\frac{K}{\mu}\frac{dP}{dX} \tag{20}$$

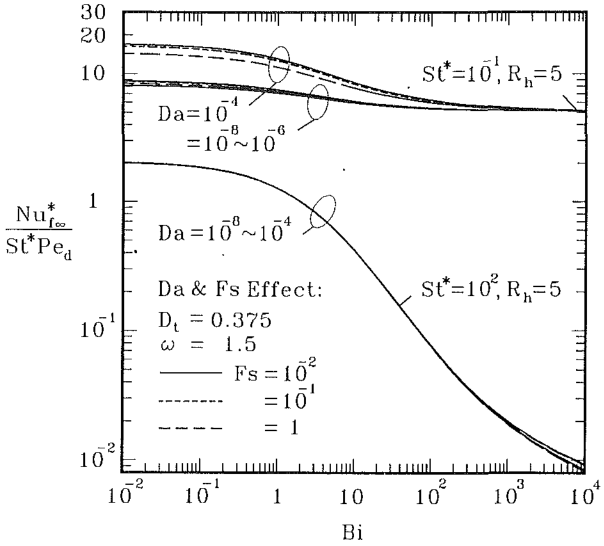

Fig. 8 $Nu^*_{f\infty}/St^*Pe_d$ versus Bi with the effects of Da and Fs

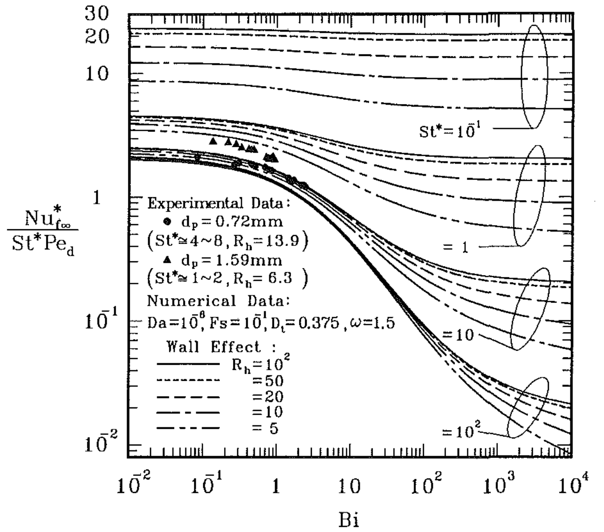

Fig. 9 $Nu^*_{f\infty}/St^*Pe_d$ versus Bi with the effects of St and R_h

$$(\rho c)_f U_d \frac{dT}{dX} = k_e \frac{d^2T}{dY^2} \tag{21}$$

where $T=T_s=T_f$ and k_e is the effective conductivity of porous media, which may or may not contain dispersion effect. The Nusselt number for Darcy's law and one-equation model in a porous channel of aspect ratio 5 ($D_e=5/3H$) is then

$$Nu_{e\infty} = \frac{q(D_e)}{k_e(T_w-T_b)} = 5 \text{ and } Nu_{f\infty} = Nu_{e\infty}\left(\frac{k_e}{k_f}\right) \cong 1.95 \times 10^3 \tag{22}$$

It may be concluded that the conventional thermal equilibrium one-equation model will over predict the Nusselt number for sintered porous channels.

Figure 7 shows the full developed dimensionless temperature profiles for $Bi=1$, 10, and 10^2 and $St^2=0.1$, 1, and 10 with $Da=10^{-6}$, $Fs=10^{-1}$, and $R_h=20$. The solid lines represent temperatures of the fluid phase, while the dashed lines represent those of the solid phase. It is clear from the figure that when Bi number is large, the solid and fluid temperature profiles literally coincide with each other. As the Bi number decreases, the fluid and solid temperature profiles are gradually

Table 3 Experimental parameters for sintered bronze beads

(a)

sample 1 $Da=7.84\times10^{-6}$, $R_h=13.89$, $D_t=0.375$, $\omega=1.5$

P_{in}	$\dot{m}$	Fs	Bi	St^*	$\frac{Nu_f^*}{St^*Pe_d}$
1.023×10^5	0.335	0.069	0.083	3.862	2.127
1.038×10^5	0.776	0.160	0.260	5.195	1.846
1.041×10^5	0.859	0.177	0.298	5.383	1.900
1.053×10^5	1.165	0.240	0.450	5.987	1.846
1.057×10^5	1.247	0.257	0.494	6.133	1.791
1.072×10^5	1.582	0.326	0.679	6.662	1.761
1.078×10^5	1.723	0.355	0.761	6.861	1.682
1.084×10^5	1.834	0.378	0.828	7.013	1.651
1.133×10^5	2.723	0.561	1.411	8.054	1.434
1.149×10^5	2.858	0.589	1.513	8.214	1.376
1.151×10^5	3.023	0.623	1.605	8.233	1.356
1.159×10^5	3.135	0.646	1.666	8.245	1.380
1.217×10^5	3.970	0.818	2.128	8.323	1.263
1.228×10^5	4.111	0.847	2.206	8.334	1.262
1.241×10^5	4.276	0.881	2.299	8.347	1.246
1.254×10^5	4.441	0.915	2.392	8.360	1.223
1.324×10^5	5.246	1.081	2.844	8.416	1.132
1.339×10^5	5.411	1.115	2.938	8.427	1.104
1.355×10^5	5.581	1.150	3.032	8.437	1.088
1.366×10^5	5.693	1.173	3.095	8.443	1.081

(b)

sample 2 $Da=2.63\times10^{-5}$, $R_h=6.289$, $D_t=0.375$, $\omega=1.5$

P_{in}	$\dot{m}$	Fs	Bi	St^*	$\frac{Nu_f^*}{St^*Pe_d}$
1.019×10^5	0.670	0.125	0.134	1.377	2.819
1.022×10^5	0.943	0.176	0.214	1.555	2.768
1.024×10^5	1.136	0.212	0.274	1.658	2.681
1.026×10^5	1.270	0.237	0.324	1.746	2.519
1.030×10^5	1.587	0.296	0.408	1.762	2.446
1.031×10^5	1.715	0.320	0.441	1.767	2.414
1.033×10^5	1.849	0.345	0.479	1.773	2.418
1.046×10^5	2.696	0.503	0.707	1.799	2.104
1.048×10^5	2.835	0.529	0.745	1.803	2.067
1.051×10^5	2.996	0.559	0.769	1.760	2.036
1.054×10^5	3.162	0.590	0.791	1.717	2.059
1.069×10^5	3.945	0.763	0.869	1.512	2.113
1.072×10^5	4.095	0.764	0.878	1.471	2.116
1.077×10^5	4.293	0.801	0.890	1.422	2.089
1.086×10^5	4.470	0.834	0.901	1.381	2.141
1.098×10^5	5.242	0.978	0.916	1.199	2.229
1.102×10^5	5.403	1.008	0.916	1.163	2.286
1.108×10^5	5.628	1.050	0.916	1.114	2.259
1.112×10^5	5.767	1.076	0.916	1.086	2.355

$Fs=\dot{m}F\sqrt{K}/\mu_f$, $Bi=h_{loc}aH^2/k_s^*$, $St^*=h_{loc}aH^2/c_f\dot{m}d_p$, $Pe_d=c_f\dot{m}d_p/k_f^*$
$Nu_{f\infty}^*=h_\infty(2H)/k_f^*$, and $P_{out}=1.013\times10^5$ N/m^2

separated and the local thermal equilibrium assumption becomes invalid. The large difference between the solid and fluid temperatures clearly observed due to the "fin effect" for the small Biot number. It is noted that the one-equation model is valid only for large Biot number regardless of the change of modified Stanton number.

Figure 8 shows the dimensionless ratio of $Nu_{f\infty}^*/St^*Pe_d$ versus Bi with the effects of Da and Fs numbers for $St^*=10^{-1}$ and 10^2, and $R_h=5$. It is seen in the figure that for $Da\leq10^{-6}$ the lines of $Nu_{f\infty}^*/St^*Pe_d$ nearly overlap regardless the change of Fs. Even when $St^*=10^{-1}$, $R_h=5$, and $Da=10^{-4}$, the maximum differences of $Nu_{f\infty}^*/St^*Pe_d$ between $Fs=1$ and 10^{-2} are less than 20 percent. It is also seen that for $St^*=0.1$ and $Bi\leq10$ the effect of Da plays a significant role in the prediction of heat transfer rate.

Figure 9 shows the dimensionless values of $Nu_{f\infty}^*/St^*Pe_d$ versus Bi number with the effects of St^* and R_h for $Da=10^{-6}$, and $Fs=10^{-1}$. It is seen in the figure that at a given St^*, the value of $Nu_{f\infty}^*/Pe_d$ decreases with the increase in the value of Bi and the value of $Nu_{f\infty}^*/St^*Pe_d$ increases with the decrease in St^*. It is seen from Eq. (13) the thermal dispersion term and the wall effect of R_h can be magnified by a small St^*. This phenomenon can be observed in this figure also. Finally, the experimental fully developed data are replotted and shown in Table 3. A good agreement is also observed here.

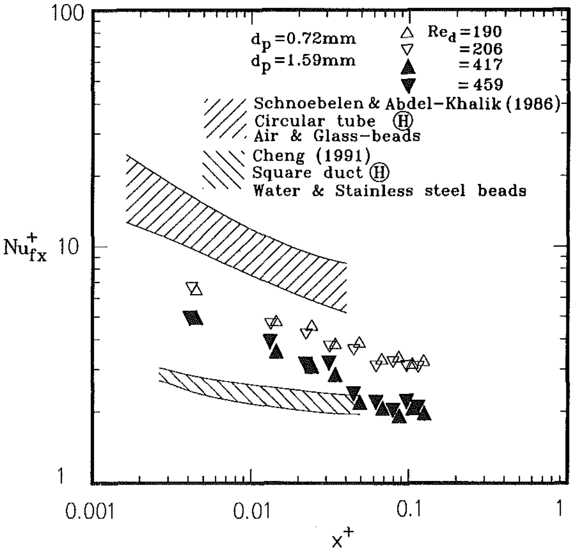

Fig. 10 Comparison of local Nusselt numbers with other experimental data

The comparison of Nusselt numbers with varying dimensionless longitudinal distance between the results of the present study and those of Schnoebelen and Abdel-khalik (1986) and Cheng (1991) is shown in Fig. 10. Schnoebelen and Abdel-khalik measured the local heat transfer coefficient for gravity flowing glass-beads in the entrance region of a circular tube with constant wall heat flux and the fluid was air. Cheng carried out the measurement for packed stainless steel beads in a square duct with water as a working medium. It is seen in the figure that the data of the present study for sintered beads fall between them. The difference in the Nusselt numbers may be due mainly to the different porous structures used in these experiments.

Conclusions

1 This paper presents the results of heat transfer measurement for two $5 \times 5 \times 1$ cm porous channels. The measurement covers the data in both thermal entrance and thermally fully developed regions. The local Nusselt numbers can be correlated by $\mathrm{Nu}_{fx}/\mathrm{Nu}_{f\infty} = 1 + 0.048/[X/(A\mathrm{Re}_d^n D_e)]$, and the fully developed Nusselt numbers can be correlated by $\mathrm{Nu}_{f\infty} = C_0\mathrm{Re}_d + C_1[1 - \exp(C_2\mathrm{Re}_d)]$.

2 The fully developed Nusselt numbers were analyzed theoretically by using a non-Darcy, two-equation flow model. The predicted fully developed Nusselt numbers are in good agreement with the measured values. The present analysis leads to a result of non-thermal equilibrium with different fluid and solid temperatures that was also observed experimentally. It is also obtained that the conventional thermal equilibrium one-equation model overpredicts the Nusselt number for the sintered porous channel flow.

3 The porous channels under study can be used as a heat sink for high-performance forced air cooling in micro-electronics. The electronic devices may be damaged by a local excess high temperature of the heat sink instead of the average one. Therefore the measurement of local wall temperature distribution and the local Nusselt number were focused. The results showed that the high-conductivity porous channel enhances the local heat transfer rate or reduced maximum wall temperature of the heat sink. For example, the forced air heat transfer coefficient can be increased from 0.01 to 0.5 W/cm°C by using the porous heat sink of $d_p = 0.72$ mm.

Acknowledgments

The authors would like to thank the National Science Council, ROC for the financial support through Grant No. NSC-80-0404-E007-01. One of the authors, C. H. Chao, is also indebted to the NSC, for a scholarship.

References

Anderson, D. A., Tannehill, J. C., and Pletcher, R. H., 1984, *Computation Fluid Mechanics and Heat Transfer*, Hemisphere Publishing Corp., pp. 551-557.

Bories, S., 1987, "Natural Convection in Porous Media," in: *Advances in Transport Phenomena in Porous Media*, J. Bear and M. Y. Corapcioglu, eds., Martinus Nijhoff Publishers, pp. 79-141.

Chao, C. H., and Hwang, G. J., 1992, "Laminar Mixed Convection in a Horizontal Rectangular Darcy Porous Channel," *Chinese Society of Mechanical Engineering*, Vol. 13, No. 5, pp. 430-437.

Cheng, C. J., 1991, "Heat Transfer Experiment and Flow Visualization of Non-Darcian Mixed Convection in Horizontal Square Packed-Sphere Channels," Master's Thesis, National Central University, Chung-Li, Taiwan.

Cheng, P., and Hsu, C. T., 1986, "Applications of Van Driest's Mixing Length Theory to Transverse Thermal Dispersion in Forced Convective Flow Through a Packed Bed," *Int. Comm. Heat Mass Transfer*, Vol. 13, pp. 613-625.

Cheng, P., Hsu, C. T., and Chowdhury, A., 1988, "Forced Convection in the Entrance Region of a Packed Channel With Asymmetric Heating," ASME JOURNAL OF HEAT TRANSFER, Vol. 110, pp. 946-954.

Dittus, F. W., and Boelter, L. M. K., 1930, "Heat Transfer in Automobile Radiators of the Tubular Type," University of California Publications in Engineering, Vol. 2, No. 13, pp. 443-461.

Hunt, M. L., and Tien, C. L., 1988, "Effects of Thermal Dispersion on Forced Convection in Fibrous Media," *Int. J. Heat Mass Transfer*, Vol. 31, pp. 301-309.

Kar, K. K., and Dybbs, A., 1982, "Internal Heat Transfer Coefficients of Porous Metals," ASME *Proceedings of the Winter Annual Meeting*, Phoenix, AZ, pp. 81-91.

Kline, S. J., and McClintock, F. A., 1953, "Describing Uncertainties in Single-Sample Experiments," *Mechanical Engineering*, Jan., pp. 3-8.

Koh, J. C. Y., and Colony, R., 1974, "Analysis of Cooling Effectiveness for Porous Material in a Coolant Passage," ASME JOURNAL OF HEAT TRANSFER, Vol. 96, pp. 324-330.

Koh, J. C. Y., and Stevens, R. L., 1975, "Enhancement of Cooling Effectiveness for Porous Material in a Coolant Passages," ASME JOURNAL OF HEAT TRANSFER, Vol. 97, pp. 324-330.

Kuo, S. M., and Tien, C. L., 1981, "Heat Transfer Augmentation in a Foam-Material Filled Duct With Discrete Heat Sources," *Proceedings of IEEE Thermal Phenomena in Electronic Components Conference*, Los Angeles, CA, pp. 87-91.

Mahalingam, M., and Berg, H. M., 1984, "Thermal Trend in Component Level Packaging," *Int. J. Hybrid Microelectron*, Vol. 7, pp. 1-9.

Mahalingam, M., 1985, "Thermal Management in Semiconductor Device Packaging," *Proc. IEEE*, Vol. 73, pp. 1396-1404.

Schnoebelen, K. S., and Abdel-Khalik, S. I., 1986, "Local Nusselt Numbers for Flowing Packed Particle Beds in Circular Tubes With Constant Wall Heat Flux," ASME JOURNAL OF HEAT TRANSFER, Vol. 108, pp. 466-469.

Schroeder, K. J., Renz, V., and Elegeti, K., 1981, "Forschungsberichte des Landes Nordrhein-Westfalen," No. 3037.

Simons, R. E., 1983, "Thermal Management of Electronic Packages," *Solid State Tech.*, Vol. 26, pp. 131-137.

Tuckerman, D. B., and Pease, R. F., 1981, "High-Performance Heat Sinking for VLSI," *Electron Device Lett.*, Vol. 2, pp. 126-129.

Tuckerman, D. B., and Pease, R. F., 1982, "Ultra High Thermal Conductance Microstructures for Cooling Integrated Circuits," IEEE CH781-4, pp. 145-149.

Forced Convection in a Porous Channel With Localized Heat Sources

A. Hadim
Department of Mechanical Engineering,
Stevens Institute of Technology,
Hoboken, NJ 07030

A numerical study is performed to analyze steady laminar forced convection in a channel filled with a fluid-saturated porous medium and containing discrete heat sources on the bottom wall. Hydrodynamic and heat transfer results are reported for two configurations: (1) a fully porous channel, and (2) a partially porous channel, which contains porous layers above the heat sources and is nonporous elsewhere. The flow in the porous medium is modeled using the Brinkman–Forchheimer extended Darcy model. Heat transfer rates and pressure drop are evaluated for wide ranges of Darcy and Reynolds numbers. Detailed results of the evolution of the hydrodynamic and thermal boundary layers are also provided. The results indicate that as the Darcy number decreases, a significant increase in heat transfer is obtained, especially at the leading edge of each heat source. For fixed Reynolds number, the length-averaged Nusselt number reaches an asymptotic value in the Darcian regime. In the partially porous channel, it is found that when the width of the heat source and the spacing between the porous layers are of the same magnitude as the channel height, the heat transfer enhancement is almost the same as in the fully porous channel while the pressure drop is significantly lower. These results suggest that the partially porous channel configuration is a potentially attractive heat transfer augmentation technique for electronic equipment cooling, an end that motivated this study.

Introduction

Fundamental studies related to thermal convection in porous media have increased significantly during recent years. This interest is due to the presence of porous media in diverse engineering applications including geothermal systems, building thermal insulation, enhanced oil recovery, nuclear waste disposal, packed bed chemical reactors, and solid-matrix heat exchangers. Earlier investigations were based on the Darcy flow model and comprehensive reviews were provided by Combarnous and Bories (1975), Cheng (1978), and Catton (1985). Lately, non-Darcy effects on thermal convection in porous media have been considered by several investigators, including Vafai and Tien (1981), Poulikakos and Bejan (1985), Beckermann et al. (1988), and Lauriat and Prasad (1989) among others and more recent reviews of this subject are provided by Kakac et al. (1991) and Nield and Bejan (1992).

The problem of forced convection in porous media is mostly relevant in flow through packed beds and in solid matrix heat exchangers. Koh and his co-workers (1974, 1975) investigated the performance of a heat exchanger containing a conductive porous matrix. They used a slug flow model that was limited to porous media with very low permeability. In a study based on the Brinkman-extended Darcy flow model, Kaviany (1985) reported analytical and numerical results for forced convection in a porous channel bounded by isothermal parallel plates. A similar problem was solved numerically by Poulikakos and Renken (1987) who used a general flow model, which included the effects of flow inertia, variable porosity, and Brinkman friction. Cheng et al. (1988) reported results for a thermally developing forced convective flow in a packed channel heated asymmetrically. Renken and Poulikakos (1989) conducted an experimental study of boundary-layer forced convection from a flat isothermal plate placed in a packed bed of spheres. Analytical solutions of fully developed forced convection in a porous channel were presented by Vafai and Kim (1989) and later by Lauriat and Vafai (1991). Most of these studies relate to understanding the fundamental aspects of forced convection in porous media.

Some investigations have been conducted on thermal convection in fluid/porous composite systems. A study of fully developed forced convection in a channel partially filled with a porous matrix (Poulikakos and Kazmierczack, 1987) showed the existence of a critical thickness of the porous layer at which the Nusselt number reaches a minimum. Vafai and Thiyagaraja (1987) derived an analytical solution of fully developed forced convection for the interface region between a fluid layer and a porous medium. Vafai and Kim (1991) analyzed boundary layer flow and heat transfer through a composite system in which a fluid layer overlaid a porous substrate, which was attached to the surface of an isothermal plate. Tong and Sharatchandra (1990) investigated the use of porous inserts for heat transfer enhancement in a rectangular channel. More recently, the problem of forced convection in a channel partially filled with a porous medium and bounded by two isothermal plates was investigated numerically by Jang and Chen (1992). They studied the effects of inertia and thermal dispersion on convective heat transfer in the channel for various open space thickness ratios.

Of particular interest to the present work, some studies have explored the innovative use of a porous matrix as a potential heat transfer augmentation technique in electronic cooling. Hunt and Tien (1988a, 1988b) have demonstrated the feasibility of this heat transfer enhancement technique. Their work indicated that a heat transfer increase by several times was achievable with the use of a ''foam-material'' system. They attributed this increase mostly to thermal dispersion effects, which were significant at large Reynolds number. Kuo and Tien (1988) solved the problem of forced convection in a porous channel with discrete heat sources assuming hydrodynamically fully developed flow. They reported an increase of two to four times in heat transfer as compared to the case with laminar slug-flow in a clear duct. Rizk and Kleinstreuer (1991) analyzed

---

Contributed by the Heat Transfer Division and presented at the ASME Winter Annual Meeting, Dallas, Texas, November 25–30, 1990. Manuscript received by the Heat Transfer Division November 1992; revision received July 1993. Keywords: Electronic Equipment, Forced Convection, Porous Media. Associate Technical Editor: C. E. Hickox, Jr.

laminar forced convection on discrete heated blocks in a porous channel. They reported empirical correlations for pressure drop due to the porous material and the solid blocks. Their study also resulted in an increase in heat transfer when compared with the nonporous channel.

The objective of the present work was to perform a detailed numerical study of forced convection in a porous channel with discrete heat sources flush-mounted on the bottom wall. For practical application to electronic cooling, it is necessary to consider the effect of the porous matrix on the total pressure drop in the channel. In this study, the heat transfer augmentation and pressure drop in a partially porous channel are evaluated, and the results are compared with the fully porous channel case.

Mathematical Formulation

A schematic of the physical model and coordinate system is shown in Fig. 1(*a*) for the fully porous channel and Fig. 1(*b*) for the partially porous channel, which contains porous layers located above the heat sources and is nonporous elsewhere. For convenience, the latter case is identified simply as "the partially porous channel." It is assumed that the flow in the channel is steady, laminar incompressible, and two dimensional. The porous medium is considered to be homogeneous and isotropic and is saturated with a single-phase fluid, which is in thermal equilibrium with the solid matrix. The thermophysical properties of the solid matrix and of the fluid are assumed to be constant. Although for certain porous media such as spherical beads the porosity may vary due to channeling near the walls (Vafai, 1984), in the current study, fibrous media are considered for which the porosity and permeability are constant even close to the walls (Hunt and Tien, 1988a). Finally, viscous dissipation is neglected in the energy equation. The governing equations can then be written separately for the fluid and porous layers. For the fluid layers:

Continuity:

$$\nabla \cdot \mathbf{V} = 0 \tag{1}$$

Momentum:

$$\rho(\mathbf{V} \cdot \nabla)\mathbf{V} = -\nabla p + \rho g + \mu \nabla^2 \mathbf{V} \tag{2}$$

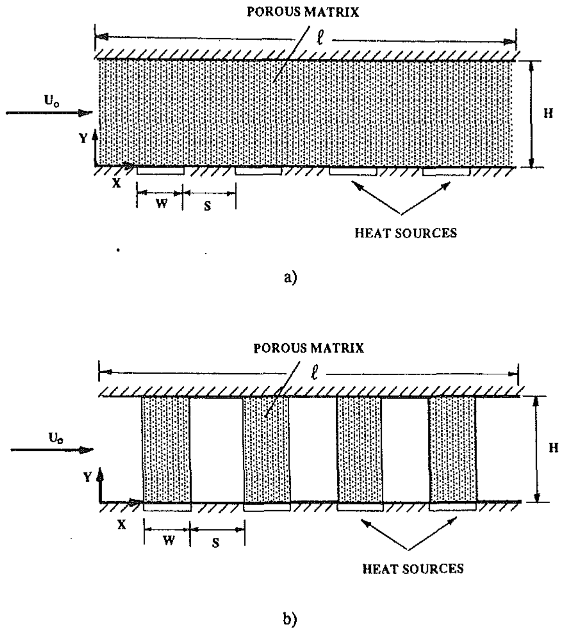

Fig. 1 Schematic of the physical models and coordinate system: (*a*) fully porous channel; (*b*) partially porous channel

Energy:

$$(\rho c)_f(\mathbf{V} \cdot \nabla T) = k_f \nabla^2 T \tag{3}$$

For the porous layers:

Continuity:

$$\nabla \cdot \mathbf{V} = 0 \tag{4}$$

Momentum:

$$\frac{\rho}{\epsilon^2}(\mathbf{V} \cdot \nabla)\mathbf{V} = -\nabla p + \rho g - \left[\frac{\mu}{K} + \frac{\rho C}{\sqrt{K}}|\mathbf{V}|\right]\mathbf{V} + \mu' \nabla^2 \mathbf{V} \tag{5}$$

Energy:

$$(\rho c)_f(\mathbf{V} \cdot \nabla T) = k_e \nabla^2 T \tag{6}$$

Nomenclature

c = specific heat, J/kg-K
C = inertia coefficient
Da = Darcy number $= K/H^2$
g = acceleration of gravity, m/s^2
h = heat transfer coefficient, W/m^2-K
H = channel height, m
k_f = thermal conductivity of the fluid, W/m-K
k_e = effective thermal conductivity of the fluid-saturated porous medium, W/m-K
K = permeability of the porous medium, m^2
l = channel length, m
L = dimensionless channel length $= l/H$
Nu = local Nusselt number $= hH/k_f$
Nu$_s$ = average Nusselt number over one heat source
Nu$_L$ = length-averaged Nusselt number
p = pressure, Pa
p_o = pressure at channel inlet
P = dimensionless pressure $= p/(\rho U_o^2)$
Pe = Peclet number = RePr
Pr = Prandtl number $= \nu/\alpha$
q = uniform heat flux from each heat source, W/m^2
Re = Reynolds number $= U_o H/\nu$
R_k = thermal conductivity ratio $= k_e/k_f$
s = spacing between heat sources, m
T = temperature, K
T_o = uniform inlet temperature, K
u = velocity in x direction, m/s
U_o = uniform inlet velocity, m/s
U = dimensionless velocity in x direction $= u/U_o$
v = velocity in y direction, m/s
V = dimensionless velocity in y direction $= v/U_o$
$\mathbf{V}$ = velocity vector, m/s
w = width of heat source, m
x = horizontal distance, m
X = dimensionless distance in x direction $= x/H$
y = vertical distance, m
Y = dimensionless distance in y direction $= y/H$
α = thermal diffusivity of the fluid $= k_f/(\rho c_p)_f$, m^2/s
β = thermal expansion coefficient of the fluid, K^{-1}
ϵ = porosity
ζ = vorticity
Θ = dimensionless temperature $= (T - T_o)/(qH/k_f)$
λ = binary parameter defined in Eq. (8)
μ = dynamic viscosity, kg/m-s
μ' = effective dynamic viscosity, kg/m-s
ν = kinematic viscosity, m^2/s
ψ = stream function

Subscripts

e = effective (i.e., fluid-saturated porous medium)
f = fluid
o = inlet
w = wall

where

$$|\mathbf{V}| = \sqrt{u^2 + v^2} \tag{7}$$

In Eqs. (2) and (5), the convective term on the left-hand side of the momentum equations is included in order to account for the development of the hydrodynamic boundary layer, which may be significant especially in the case when the channel is partially porous. The momentum equations for the porous region are enhanced by the use of the Brinkman–Forchheimer-extended Darcy model, which accounts for both viscous and inertia effects (Vafai and Tièn, 1981; Beckermann et al., 1988; Lauriat and Prasad, 1989). In the energy equation, axial conduction is accounted for since it is significant at low Reynolds number (Hadim, 1994). The apparent viscosity μ', in the Brinkman extension of the momentum equations, may have a different value than the fluid viscosity but for most porous media, setting $\mu' = \mu$ provides good agreement with experimental data (Lundgren, 1972). Thermal dispersion in the porous matrix is assumed to be constant and it is incorporated in the effective thermal conductivity. This assumption is reasonable for low Reynolds number (Hunt and Tien, 1988a).

The boundary conditions for the configurations shown in Fig. 1 are such that no slip occurs at the impermeable walls. At the bottom wall, there is a uniform heat flux q, which is distributed over each heat source and the portion of the wall between heat sources is adiabatic. The top wall is entirely adiabatic. At the channel inlet, the fluid has a uniform velocity U_o, and a uniform temperature T_o. The boundary conditions at the exit are obtained by extrapolation and will be discussed later in this section.

In the case of a partially porous channel, the two sets of equations are coupled by the matching conditions at the fluid/porous-layer interface. These conditions express continuity of normal and tangential velocities, pressure, normal and shear stresses, temperature, and heat flux. The inclusion of the Brinkman extension in the momentum Eqs. (5) for the porous layer allows for continuity of velocity and shear at the fluid/porous-layer interface and a no-slip condition on the solid walls.

For the partially porous channel case, instead of solving the two sets of describing equations separately, the equations can be combined into one set by introducing the binary parameter (Poulikakos, 1987a, b; Beckermann et al., 1988)

$$\lambda = \begin{cases} 1 & \text{in the porous layers, } 0 < \epsilon < 1 \\ 0 & \text{in the fluid layers, } \epsilon = 1 \end{cases} \tag{8}$$

In the fully porous channel case, λ is set equal to 1 throughout the channel. With the use of this binary parameter, the matching conditions at the fluid/porous-layer interface are automatically satisfied; thus, the numerical solution procedure is greatly simplified.

The numerical model is based on a vorticity-stream function formulation in which the stream function (ψ) and vorticity (ζ) are defined in the usual was as

$$-\frac{\partial \psi}{\partial Y} = U, \quad \frac{\partial \psi}{\partial X} = V, \quad \zeta = \frac{\partial V}{\partial X} - \frac{\partial U}{\partial Y} \tag{9}$$

The resulting dimensionless governing equations are (Poulikakos, 1987a, b):

$$\nabla^2 \psi = \zeta \tag{10}$$

$$\left[\frac{\lambda}{\epsilon^2} - (\lambda - 1)\right]\left[-\frac{\partial \psi}{\partial Y}\frac{\partial \zeta}{\partial X} + \frac{\partial \psi}{\partial X}\frac{\partial \zeta}{\partial Y}\right] = -\frac{\lambda}{\mathrm{ReDa}}\zeta$$
$$+\frac{\lambda C}{\sqrt{\mathrm{Da}}}\left[\frac{\partial}{\partial X}|\mathbf{V}|V - \frac{\partial}{\partial Y}|\mathbf{V}|U\right] + \frac{1}{\mathrm{Re}}\nabla^2 \zeta \tag{11}$$

$$-\frac{\partial \psi}{\partial Y}\frac{\partial \theta}{\partial X} + \frac{\partial \psi}{\partial X}\frac{\partial \theta}{\partial Y} = \frac{1}{\mathrm{Pe}}[\lambda(R_k - 1) + 1]\nabla^2 \theta \tag{12}$$

The relevant dimensionless boundary conditions are:

$$\text{at } X = 0, \quad \zeta = 0, \quad \frac{\partial \psi}{\partial Y} = -1, \quad \theta = 0 \tag{13a}$$

$$\text{at } Y = 0, \quad \zeta = \frac{\partial^2 \psi}{\partial Y^2}, \quad \psi = 0, \quad \frac{\partial \theta}{\partial Y} = \begin{cases} 0 & \text{at insulated area} \\ -1 & \text{at heat source} \end{cases} \tag{13b}$$

$$\text{at } Y = 1, \quad \zeta = \frac{\partial^2 \psi}{\partial Y^2}, \quad \psi = 1, \quad \frac{\partial \theta}{\partial Y} = 0 \tag{13c}$$

For the fully porous channel case, the boundary conditions at the exit are given by the following conditions for hydrodynamically fully developed flow (Roache, 1982):

$$\text{at } X = L, \quad \frac{\partial \zeta}{\partial X} = 0, \quad \frac{\partial^2 \psi}{\partial X^2} = 0 \tag{13d}$$

The temperature at the exit is determined by extrapolation of the values at the inner two nodes (Tomimura and Fujii, 1988). For the partially porous channel, the vorticity, the stream function, and the temperature are determined by extrapolation. Because the flow is strongly parabolic, an extended computational domain was used in order to find accurate results for the physical domain. The outflow boundary condition is placed sufficiently downstream of the fourth heater such that its effects on flow and heat transfer in the inlet section of the channel are negligible. The validity and accuracy of the exit boundary conditions used was verified by comparing velocity and temperature profiles obtained for $L = 9$ with those obtained for $L = 15$ at the same Re and Da. Very good agreement was found between the two cases.

The local Nusselt number is defined as

$$\mathrm{Nu} = \frac{qH}{(T_w - T_0)k_f} \tag{14}$$

With this definition, the local Nusselt number is the reciprocal of the dimensionless wall temperature.

The local dimensionless pressure drop is calculated as

$$\Delta P = \frac{\Delta p}{1/2\rho U_0^2} \tag{15}$$

where Δp is the pressure drop between the channel inlet and the average pressure at a cross section along the axial direction. The average Nusselt number and pressure drop in the channel are obtained by integrating the local values over the channel length, which includes the first four heaters as shown in Fig. 1.

Numerical Procedure

Equations (10)–(13) were transformed into algebraic, finite-difference equations using the control volume formulation outlined by Gosman et al. (1969). The method ensures that the conservation laws are obeyed over each control volume. The nonlinear Forchheimer term in the momentum equations was modeled as a source term. The resulting nonlinear, simultaneous, algebraic equations were solved using the Gauss–Seidel point iterative scheme, which uses new values as soon as they become available. Relaxation parameters for vorticity, stream function, and temperature were used to yield more rapid convergence. The iteration procedure was terminated when the dependent variables agreed to four significant digits.

The mesh required in order to obtain acceptable accuracy was found by trial and error. In this analysis, the grid size varied with the magnitude of Darcy number. The harmonic mean formulation suggested by Patankar (1980) was used to handle abrupt changes in thermophysical properties across the fluid/porous interface without requiring an excessively fine grid. A skewed mesh was used along both coordinates such that the node density was higher in the vicinity of the channel walls in the y direction, at the leading edge of each heat source in the x direction for the fully porous channel, and at the fluid/porous interface in the partially porous channel. In general, in the partially porous channel, it was found that a 51 by 271 grid yielded results with less than 2 percent error from those obtained using a 71 by 351 grid. Furthermore, energy balance was preserved to within 2.5 percent in all calculations.

The accuracy of the numerical model was verified by comparing results for various segments of the present model with corresponding results reported in the literature. Results for the fully developed centerline velocity and fully developed Nusselt number in a fully porous channel with constant heat flux at the walls were compared with the analytical solutions reported by Lauriat and Vafai (1991) and Vafai and Kim (1989) as shown in Fig. 2. It is noteworthy that when inertia effects are included, the results presented by Vafai and Kim (1989) are valid only when $Da/\epsilon < 0.01$. Results for the limiting case of a nonporous channel with discrete heat sources on one wall were compard with those obtained by Tomimura and Fujii (1988). The model for the case when the channel is filled with a composite fluid/porous-layer system was validated by comparing the results with those obtained by Beckermann et al. (1988) for natural convection in an enclosure in which a vertical porous layer was superposed between two vertical fluid layers. At all locations, the discrepancy between the temperatures obtained with the present model and the measurements of Beckermann et al. (1988) was less than 5 percent of the total temperature difference across the test cell.

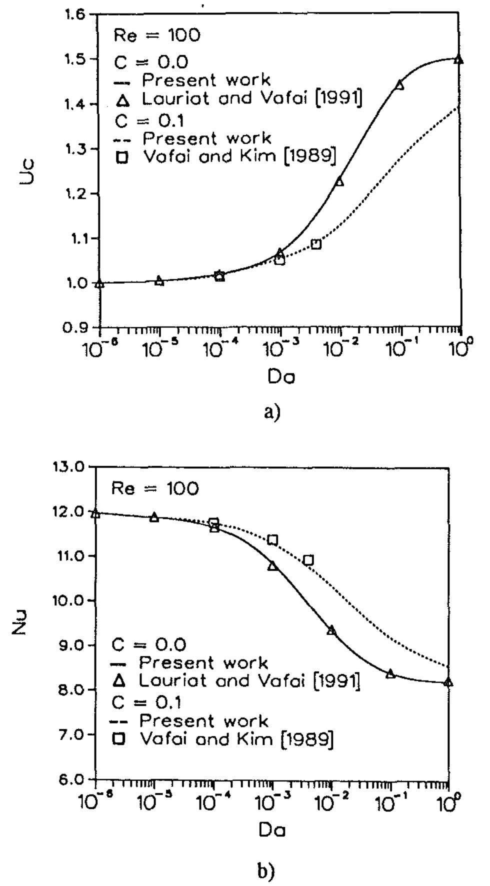

a)

b)

Fig. 2 Comparison with results from the literature: (*a*) fully developed centerline velocity; (*b*) fully developed Nusselt number

Results and Discussion

Data for the physical parameters of the fluid and porous matrix were selected for the potential application to electronics cooling. Based on the measurements reported by Hunt and Tien (1988a) for a dielectric fluid and a foam material made of carbon, the typical values selected for the physical parameters were: $Pr = 10$, $C = 0.1$, and $\epsilon = 0.97$. Furthermore, the thermal conductivity ratio R_k was set equal to 1.0 in order to eliminate the effects of conduction within the solid matrix. Hunt and Tien (1988a) reported a value of 1.05 from their measurements. All calculations were performed for $w/H = 1.0$ and $s/H = 1.0$ (Fig. 1). Parametric studies were conducted to analyze the effects of Darcy number and Reynolds number on velocity and temperature profiles, local and average Nusselt number, and pressure drop in the channel.

The flow in the channel is analyzed by considering the relevant physical mechanisms consisting of bulk damping resistance of the porous matrix, inertial resistance in the porous medium, and viscous effects at the boundary. Forced convection in the porous channel can be classified as either Darcian or non-Darcian. The Darcy flow regime occurs when the inertia effects are negligible. The criteria that characterize each flow regime depend on Da and Re. However, in the present study, since the results obtained with $Da = 10^{-6}$ differ from the results with $Da = 10^{-7}$ by less than 3 percent for the considered range of Re, the Darcy flow regime is identified as $Da \leq 10^{-6}$.

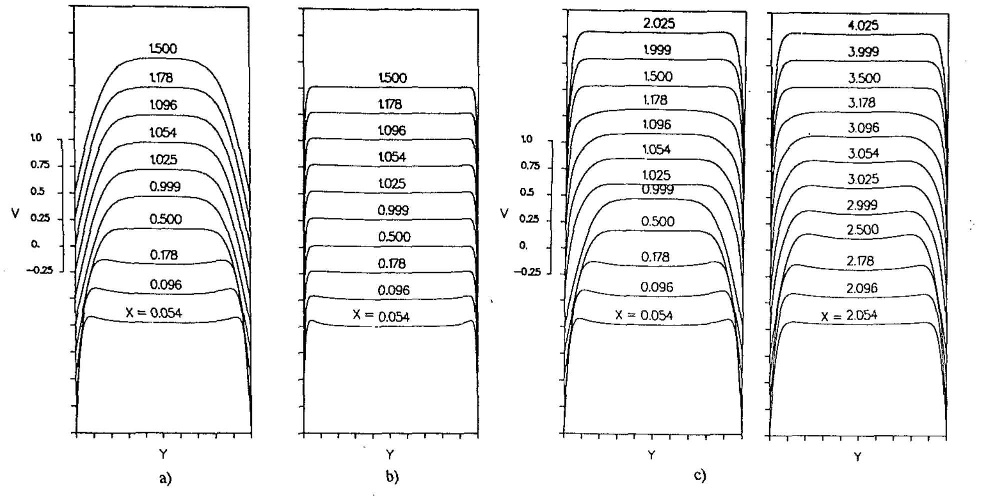

a)

b)

c)

Fig. 3 Development of the velocity profile for Re = 250 and $Da = 10^{-3}$: (*a*) nonporous channel; (*b*) fully porous channel; (*c*) partially porous channel

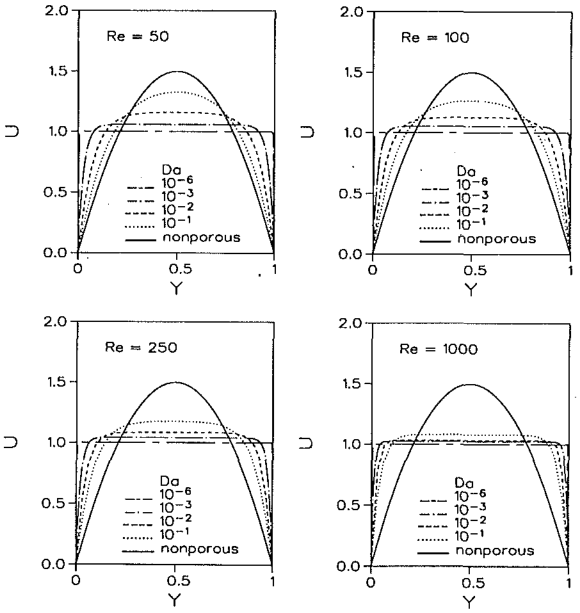

Fig. 4 Effects of Darcy and Reynolds numbers on the fully developed velocity profile in the fully porous channel

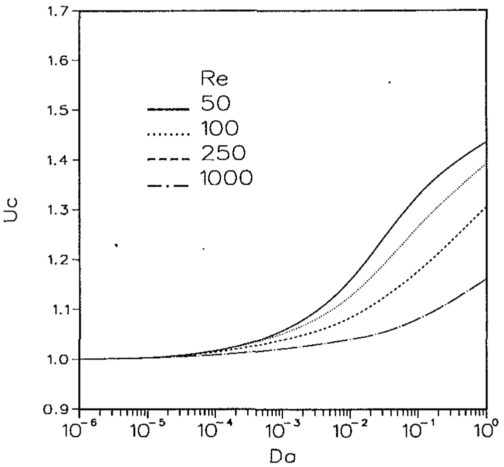

Fig. 5 Effects of Darcy and Reynolds numbers on the axial centerline velocity variation in the fully porous channel

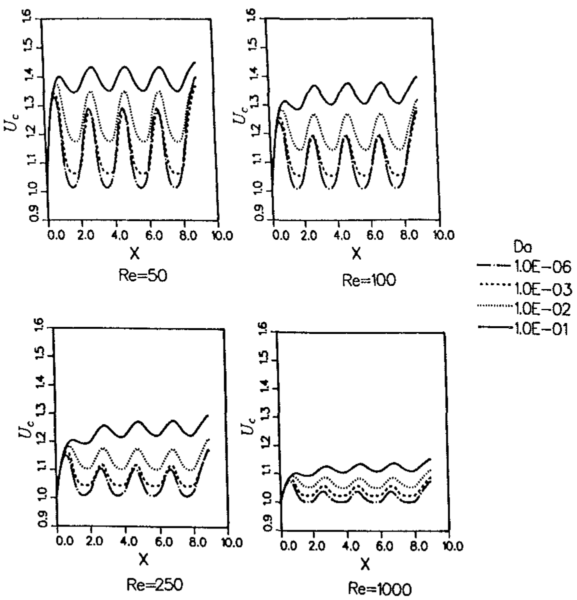

Fig. 6 Effects of Darcy and Reynolds numbers on the axial centerline velocity variation in the partially porous channel

Hydrodynamic Results. The velocity profiles in the channel are illustrated in Fig. 3 for $\mathrm{Re}=250$ and $\mathrm{Da}=10^{-3}$. In the nonporous channel (Fig. 3*a*), it is known that the velocity distribution develops from a flat profile at the inlet to a fully developed parabolic profile beyond the entrance region. At a very short distance from the channel entrance, a dip in the velocity profile is observed in Fig. 3(*a*) and it is evident that the maximum velocity does not occur at the centerline. This central concavity diminishes with increasing axial distance and eventually vanishes completely within a short distance from the channel entrance. This phenomenon was also reported by Wang and Longwell (1964) and Zeldin and Schmidt (1972) in their numerical solutions. In the fully porous channel (Fig. 3*b*), due to the bulk damping caused by the presence of the porous matrix, the viscous effects are confined to the region near the walls. This results in a flat profile of the velocity in the core region. As the Darcy number is decreased, the boundary layer thickness decreases and the flat portion of the velocity profile extends gradually toward the solid surfaces. This trend was reported by Vafai and Tien (1981) and Kaviany (1985) who showed that the boundary layer thickness was of the order of $(K/\epsilon)^{1/2}$. The development of the velocity profile in the partially porous channel is shown in Fig. 3(*c*). In the first nonporous layer ($0 \leq X < 1$), the profiles are identical to the ones shown in Fig. 3(*a*). As the fluid progresses through the first porous layer ($1 \leq X < 2$), the hydrodynamic boundary layer thickness decreases and a flat profile is obtained similar to the one shown in Fig. 3(*b*) for the fully porous channel. When the flow passes through the nonporous layers, it is shown in Fig. 3(*c*) that for $s/H = 1$, the viscous effects do not penetrate deeply into the core region. Thus, even at low Reynolds number, the development of the velocity profile does not reach a parabolic shape in the fluid layers and as the flow progresses through the next porous layer, the velocity profile flattens after a short distance and closely approaches that of the fully porous channel even at relatively high Darcy number. Such flow behavior has an important bearing on the heat transfer as discussed in the next section. The hydrodynamic development length decreases significantly as the Darcy number is decreased. This result was discussed in more detail by Hadim (1994).

The effects of Darcy and Reynolds numbers on the fully developed velocity profile in the fully porous channel are illustrated in Fig. 4. As the Darcy number is decreased, the centerline velocity decreases and the velocity profile changes from a parabolic shape to a flatter shape. In the Darcian regime ($\mathrm{Da} \leq 10^{-6}$) the velocity profile is virtually that of slug flow. As the Reynolds number increases, it is shown in Fig. 4 that the porous matrix has a greater effect on the velocity profile, which becomes less parabolic at high Darcy number.

The variation of the axial centerline velocity with Darcy and Reynolds numbers is presented in Fig. 5 for the fully porous channel. It is observed that the magnitude of the centerline velocity decreases either when the Darcy number decreases or when the Reynolds numbers increases. In the extreme cases of nonporous channel and Darcy flow regime ($\mathrm{Da} \leq 10^{-6}$), the centerline velocity approaches asymptotic values of 1.5 and 1.0 respectively, independent of the Reynolds number. In the partially porous channel, as shown in Fig. 6, the centerline velocity increases to a maximum in the nonporous layers and decreases to a minimum in the porous layers due to the effects of the porous matrix as explained earlier. In this case, the velocity profile attains a periodically fully developed behavior. The amplitude of oscillation of the centerline velocity decreases with decreasing Darcy number or with increasing Reynolds number. It is shown in Fig. 6 that for the entire ranges of

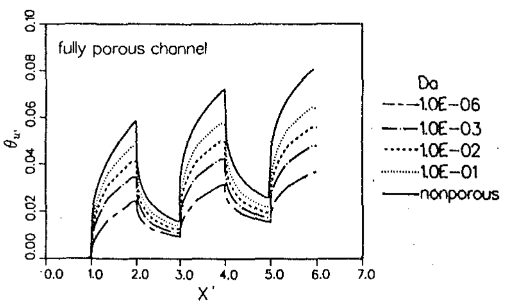

Fig. 7 Effects of Darcy number on the bottom wall temperature variation in the fully porous channel for Re = 250

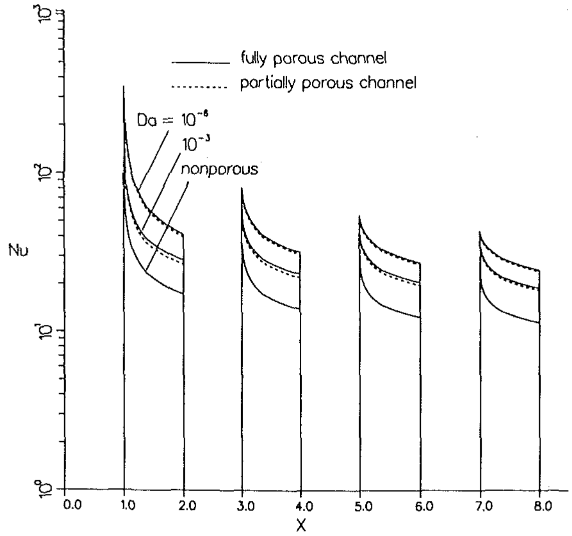

Fig. 8 Effects of Darcy number on the local Nusselt number variation for Re = 250

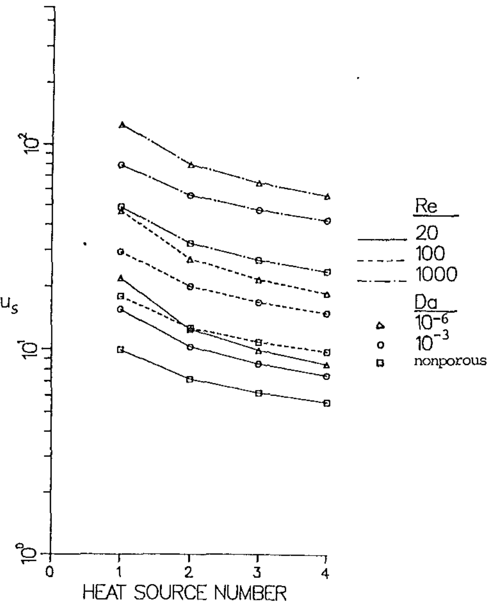

Fig. 9 Variation of Nusselt number averaged over each heat source with Darcy and Reynolds numbers

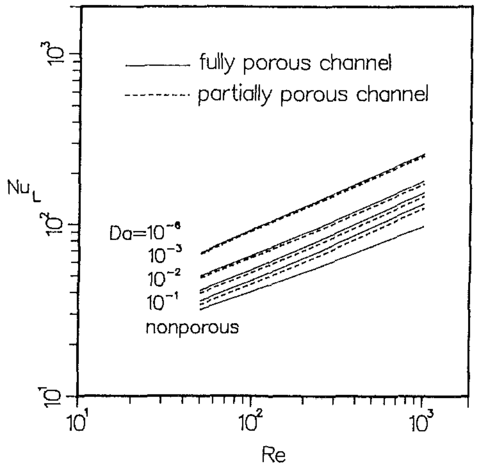

Fig. 10 Length-averaged Nusselt number versus Reynolds number at various Darcy numbers

Darcy and Reynolds number investigated, periodically fully developed flow is reached shortly after the first set of fluid and porous layers (i.e., for $X > 2$).

Heat Transfer Results. The effects of Darcy number on the bottom wall temperature variation are shown in Fig. 7 for the fully porous channel. Due to the discrete heating condition, an intermittent development of the thermal boundary layer is observed. Clearly, the temperature over each heat source increases with increasing distance along the channel, while in the adiabatic portion, the temperature decreases with increasing axial distance due to heat transfer from the wall to the bulk of the flow. As shown in Fig. 7, the wall temperature decreases with increasing Darcy number. This decrease in wall temperature is more significant at the leading edge of each heat source.

The results presented so far for velocity and temperature suggest that as the Darcy number decreases, the heat transfer in the channel increases. This is more clearly shown in Fig. 8 where the effects of Darcy number on the local Nusselt number variation for Re = 250 are displayed. For a fixed Da, it is shown in Fig. 8 that the Nusselt number distribution is sharply peaked at the upstream edge of each heat source and drops less steeply toward the downstream edge. A sudden decline to a very small value (which was found to be infinitesimally greater than zero in order to avoid numerical divergence) of the Nusselt number occurs in the insulated region separating the heat sources. A similar behavior characterizes the other heaters such that a large Nusselt number occurs at the leading edge of the heater where the intermittent thermal boundary layer begins to grow and the Nusselt number decays upstream along the heater due to boundary layer growth. As the Darcy number is decreased from the limiting case of a nonporous channel, the local Nusselt number increases over each heat source, and this increase is more pronounced at the leading edge of each heat source. This increase is caused by the relatively high velocities near the walls of the porous channel as explained in the previous section. The heat transfer results obtained for the partially porous channel are shown in Fig. 8 superposed with those of fully porous channel. For the present configuration, it is found that the magnitude of the local Nusselt number in the partially porous channel is almost the same as in the fully porous channel, especially at low Darcy number. This is justified by the nature of the intermittent development of the velocity profile as discussed earlier. For the present configuration, differences in the velocity profiles within the porous layers between the fully porous channel and the partially porous channel are not significant enough to cause any substantial changes in the Nusselt number.

The combined effects of Darcy and Reynolds numbers on the Nusselt number averaged over each heat source are shown in Fig. 9. As the Darcy number decreases, at low Reynolds number, there is a small increase in Nusselt number. At higher values of the Reynolds number, the increase in Nusselt number

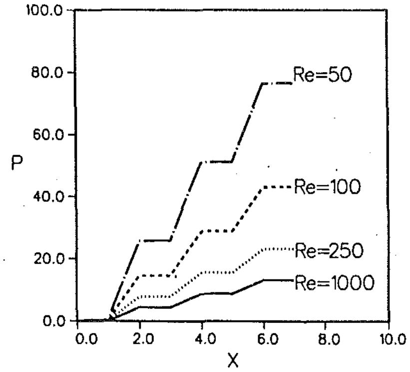

Fig. 11 Local pressure distribution in the partially porous channel for $Da = 10^{-3}$ and various Reynolds numbers

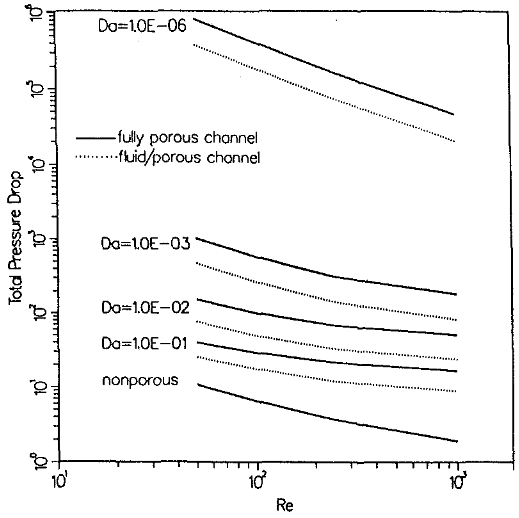

Fig. 12 Total dimensionless pressure drop in the channel versus Reynolds number at various Darcy numbers

is more significant, especially over the upstream heat sources. For example, when $Re = 1000$, more than a twofold increase in Nusselt number is obtained in a porous channel with $Da = 10^{-6}$ compared with the nonporous channel. The heat transfer results are summarized in Fig. 10 by displaying the effects of Darcy and Reynolds numbers on the length-averaged Nusselt number in the channel. With increasing Darcy number, the rate of increase of the Nusselt number is significantly higher as the flow in the porous channel approaches Darcian regime. For fixed Re, it was found that the length-averaged Nusselt number reached an asymptotic value in the Darcy regime similar to the case of a fully porous channel with uniform heat flux at the walls (Fig. 2*b*).

Pressure Drop Calculations. When using a porous matrix for heat transfer enhancement, an important factor to consider is the penalty arising from increased pressure drop. The pressure drop calculations were first verified by comparing the results with the exact solution of Lauriat and Vafai (1991) for the case of fully developed flow in a porous channel and with Kaviany (1985) for developing flow. The normalized axial pressure distribution in the partially porous channel is presented in Fig. 11 for $Da = 10^{-3}$ and various Reynolds numbers. In the partially porous channel, the pressure drop in the nonporous layers is negligible compared with that of the porous layers. Since the hydrodynamic development length is very short, especially at low Darcy number, it is found that the pressure varies linearly with axial distance in the porous layers (Kaviany, 1985). Comparison of pressure drop in the partially porous channel with that of the fully porous channel is presented in Fig. 12 where the variation of the average dimensionless pressure drop with Darcy and Reynolds numbers is displayed. It is obvious in both cases that the pressure drop increases as the Darcy number decreases. The pressure drop in the partially porous channel is significantly lower than in the fully porous channel and this difference increases as the Darcy number decreases. In the Darcian regime, for the case when the spacing between heat sources is equal to the width of the heat source, the pressure drop in the partially porous channel was found to be approximately one half of the pressure drop in the fully porous channel.

Conclusions

A numerical study of laminar forced convection in a porous channel with discrete heat sources on the bottom wall was performed. Hydrodynamic and heat transfer results are reported for two cases: (1) a fully porous channel and (2) a partially porous channel, which contains porous layers located above the heat sources and is nonporous elsewhere. In both cases, the Nusselt number increases as the Darcy number decreases. The increase in heat transfer is more significant at higher Reynolds number, and at the leading edge of each heat source.

Results for the partially porous channel indicate that almost the same increase in heat transfer (especially at low Darcy number) and a significantly reduced pressure drop can be obtained compared with the fully porous channel. Therefore, this technique appears to be promising for application to electronics cooling, especially in applications characterized by large power dissipation.

Further experimental and numerical studies are needed in order to demonstrate clearly the feasibility of the proposed heat transfer augmentation technique and to optimize the configuration of the partially porous channel for maximum heat transfer and minimum pressure drop.

Acknowledgments

The author would like to thank Mr. Angel Bethancourt and Mr. Guoqi Chen, graduate research assistants, for their help with some of the numerical computations.

References

Beckermann, C., Viskanta, R., and Ramadhyani, S., 1988, "Natural Convection in Vertical Enclosures Containing Simultaneously Fluid and Porous Layers," *J. Fluid Mechanics*, Vol. 186, pp. 257–284.

Catton, I., 1985, "Natural Convection Heat Transfer in Porous Media," in: *Natural Convection: Fundamentals and Applications*, Hemisphere, New York.

Cheng, P., 1978, "Heat Transfer in Geothermal Systems," *Advances in Heat Transfer*, Vol. 14, pp. 1–105.

Cheng, P., Hsu, C. T., and Choudhury, A., 1988, "Forced Convection in the Entrance Region on a Packed Channel With Asymmetric Heating," ASME JOURNAL OF HEAT TRANSFER, Vol. 110, pp. 946–954.

Combarnous, M. A., and Bories, S. A., 1975, "Hydrothermal Convection in Saturated Porous Media," *Advances in Hydroscience*, Vol. 10, pp. 231–307.

Gosman, A. D., Pun, W. M., Runchal, A. K., Spalding, D. B., and Wolfshtein, M., 1969, *Heat and Mass Transfer in Recirculating Flows*, Academic Press, New York.

Hadim, A., 1994, "Numerical Study of Laminar Mixed Convection in a Vertical Porous Channel," *AIAA J. of Thermophysics and Heat Transfer*, Vol. 8, No. 2, in press.

Hong, J. T., Tien, C. L., and Kaviany, M., 1985, "Non-Darcian Effects on Vertical Plate Natural Convection in Porous Media With High Porosities," *Int. J. Heat Mass Transfer*, Vol. 28, pp. 2149–2157.

Hunt, M. L., and Tien, C. L., 1988a, "Effects of Thermal Dispersion on Forced Convection in Fibrous Media," *Int. J. Heat Mass Transfer*, Vol. 31, pp. 301–310.

Hunt, M. L., and Tien, C. L., 1988b, "Diffusion and Dispersion Regimes for Boundary-Layer Flow in a Porous Medium," *Proc. ASME 25th National Heat Transfer Conference*, Vol. 1, pp. 635–641.

Jang, J. Y., and Chen, J. L., 1992, "Forced Convection in a Parallel Plate Channel Partially Filled With a High Porosity Medium," *Int. Comm. Heat Mass Transfer*, Vol. 19, pp. 263–273.

Kakac, S., Kilkis, B., Kulacki, F. A., and Arinc, F., 1991, *Convective Heat and Mass Transfer in Porous Media*, Kluwer Academic, Dordrecht.

Kaviany, M., 1985, "Laminar Flow Through a Porous Channel Bounded by Isothermal Parallel Plates," *Int. J. Heat Mass Transfer*, Vol. 28, pp. 851–858.

Koh, J. C. Y., and Colony, R., 1974, "Analysis of Cooling Effectiveness for Porous Material in Coolant Passage," ASME JOURNAL OF HEAT TRANSFER, Vol. 96, pp. 324–330.

Koh, J. C. Y., and Stevens, R. L., 1975, "Enhancement of Cooling Effectiveness by Porous Materials in Coolant Passage," ASME JOURNAL OF HEAT TRANSFER, Vol. 97, pp. 309–311.

Kuo, S. M., and Tien, C. L., 1988, "Heat Transfer Augmentation in a Foam-Material Filled Duct With Discrete Heat Sources," *Proc. Thermal Phenomena in Electronics Components Conference*, Los Angeles, CA, May 11–13, pp. 87–91.

Lundgren, T. S., 1972, "Slow Flow Through Stationary Random Beds and Suspensions of Spheres," *J. Fluid Mechanics*, Vol. 51, pp. 273–299.

Lauriat, G., and Prasad, V., 1989, "Non-Darcian Effects on Natural Convection in a Vertical Porous Enclosure," *Int. J. Heat Mass Transfer*, Vol. 32, pp 2135–2147.

Lauriat, G., and Vafai, K., 1991, "Forced Convection and Heat Transfer Through a Porous Medium Exposed to a Flat Plate or a Channel," in: *Convective Heat and Mass Transfer in Porous Media*, S. Kakac, B. Kilkis, F. A. Kulacki, and F. Arinc, eds., Kluwer Academic, Dordrecht, pp. 289–327.

Nield, D. A., and Bejan, A., 1992, *Convection in Porous Media*, Springer-Verlag, New York.

Patankar, S. V., 1980, *Numerical Heat Transfer and Fluid Flow*, Hemisphere, New York.

Poulikakos, D., and Bejan, A., 1985, "The Departure From Darcy Flow in Natural Convection in a Vertical Porous Layer," *Physics of Fluids*, Vol. 28, pp. 3477–3484.

Poulikakos, D., 1987a, "Buoyancy Driven Convection in a Horizontal Fluid Layer Extending Over a Porous Substrate," *Physics of Fluids*, Vol. 29, pp. 3949–3957.

Poulikakos, D., 1987b, "Thermal Instability in a Horizontal Fluid Layer Superposed on a Heat Generating Porous Bed," *Numerical Heat Transfer*, Vol. 12, pp. 83–100.

Poulikakos, D., and Renken, K., 1987, "Forced Convection in a Channel Filled With a Porous Medium, Including the Effects of Flow Inertia, Variable Porosity, and Brinkman Friction," ASME JOURNAL OF HEAT TRANSFER, Vol. 109, pp. 880–888.

Poulikakos, D., and Kazmierczak, M., 1987, "Forced Convection in a Duct Partially Filled With a Porous Material," ASME JOURNAL OF HEAT TRANSFER, Vol. 109, pp. 653–662.

Renken, K., and Poulikakos, D., 1989, "Experiments on Forced Convection From a Horizontal Heated Plate in a Packed Bed of Glass Spheres," ASME JOURNAL OF HEAT TRANSFER, Vol. 111, pp. 59–65.

Rizk, T. A., and Kleinstreuer, C., 1991, "Forced Convective Cooling of a Linear Array of Blocks in Open and Porous Matrix Channels," *Heat Transfer Engineering*, Vol. 12, pp. 40–47.

Roache, P. J., 1982, *Computational Fluid Dynamics*, Hermosa Publishers, Albuquerque, NM.

Tomimura, T., and Fujii, M., 1988, "Laminar Mixed Convection Between Parallel Plates With Localized Heat Sources," in: *Cooling Technology for Electronic Equipment*, W. Aung, ed., Hemisphere, Washington, DC, pp. 233–247.

Tong, T. W., and Sharatchandra, M. C., 1990, "Heat Transfer Enhancement Using Porous Inserts," in: *Heat Transfer and Flow in Porous Media*, ASME HTD-Vol. 156, pp. 41–46.

Vafai, K., and Tien, C. L., 1981, "Boundary and Inertia Effects on Flow and Heat Transfer in Porous Media," *Int. J. Heat Mass Transfer*, Vol. 24, pp. 195–203.

Vafai, K., 1984, "Convective Flow and Heat Transfer in Variable Porosity Media," *J. Fluid Mechanics*, Vol. 147, pp. 233–259.

Vafai, K., and Thiyagaraja, R., 1987, "Analysis of Flow and Heat Transfer at the Interface Region of a Porous Medium," *Int. J. Heat Mass Transfer*, Vol. 30, pp. 1391–1405.

Vafai, K., and Kim, C. L., 1989, "Forced Convection in a Channel Filled With a Porous Medium: An Exact Solution," ASME JOURNAL OF HEAT TRANSFER, Vol. 111, pp. 1103–1106.

Vafai, K., and Kim, C. L., 1991, "Analysis of Surface Enhancement by a Porous Substrate," ASME JOURNAL OF HEAT TRANSFER, Vol. 112, pp. 700–706.

Wang, Y. L., and Longwell, P. A., 1964, "Laminar Flow in the Inlet Section of Parallel Plates," *AIChE Journal*, Vol. 10, pp. 323–329.

Zeldin, B., and Schmidt, F. W., 1972, "Developing Flow With Combined Forced-Free Convection in an Isothermal Vertical Tube," ASME JOURNAL OF HEAT TRANSFER, Vol. 94, pp. 211–221.

Journal of Heat Transfer
Technical Notes

This section contains shorter technical papers. These shorter papers will be subjected to the same review process as that for full papers.

Reducing the Heat Transfer From a Hot Pipe Buried in a Semi-infinite, Saturated, Porous Medium

G. N. Facas[1]

Nomenclature

d, w = distance from center of cylinder in the y and x directions, respectively
h = burial depth
l = baffle length
Nu = Nusselt number based on the cylinder radius $= (\bar{h}R)/\lambda'$
R = pipe radius
Ra = Rayleigh number based on the cylinder radius $= (g\rho_o\rho_f c_f\beta_f RK\Delta T)/\lambda'\mu$
γ = circumferential (angle) coordinate [see Fig. 1]
δ = baffle thickness
θ = dimensionless temperature
λ' = equivalent thermal conductivity
ξ, η = body-fitted coordinates
ψ^* = dimensionless streamfunction

Introduction

In recent years, the problem of a pipe buried in a semi-infinite, saturated, porous medium has become the subject of investigation because of its considerable practical interest. This problem arises in power plant steam lines, industrial and agricultural water distribution lines, buried electrical cable, oil and gas transmission lines, and in the storage of nuclear waste.

The early studies that considered the problem of buried pipes and cables assumed the surrounding medium to be purely conductive (see Eckert and Drake, 1972; Thiyagarajan and Yovanovich, 1978; Bau and Sadhal, 1982). However, the assumption that the heat losses from a buried pipe can be calculated using only a conduction model may not be valid for high-permeability saturated soils.

The problem of a hot pipe buried in a semi-infinite, saturated, porous medium has been revisited lately in order to account for convection. Schrock et al. (1970) and Fernandez and Schrock (1982) carried out experiments and numerical calculations for a cylinder buried beneath a permeable, horizontal surface. Farouk and Shayer (1988) solved the same problem numerically. However, their results were significantly different from the predictions of Fernandez and Schrock (1982), especially at high Ra values. They attributed this to the fact that the boundary condition that was used along the permeable surface was different in the two studies.

Bau (1984) considered the problem of a pipe buried beneath both a permeable and an impermeable, horizontal surface. Both the cylinder and the medium surface were assumed to be maintained at constant temperature. Himasekhar and Bau (1987) extended the work presented for the impermeable case by Bau (1984) to include a convective boundary condition at the medium's surface. An optimal burial depth was found to exist for which the heat losses from the pipe are minimized.

Mathematical Formulation

The problem considered in this study is a pipe buried a distance h beneath an impermeable surface of a semi-infinite, saturated, porous medium with two baffles attached on the pipe's surface, as depicted schematically in Fig. 1. The surface of the pipe is assumed to be maintained at a constant temperature T_1, whereas the top horizontal impermeable surface is maintained at a constant temperature T_2, with $T_1 > T_2$. Since it is very difficult to treat an infinite domain numerically, the physical domain will be truncated by assuming that the two far boundaries at infinite x and negative infinite y are at a large distance w and d away from the center of the cylinder, respectively. A new body-fitted curvilinear coordinate system (ξ, η) is introduced to represent the truncated domain such that the various surfaces coincide with constant values of ξ and η. From the various techniques available, the PDE method presented by Thompson et al. (1982) is chosen. The computational plane consists of the rectangle $\xi_1 \leq \xi \leq \xi_2$, and $\eta_1 \leq \eta \leq \eta_2$.

For low Rayleigh numbers, the governing equations and corresponding boundary conditions for steady natural con-

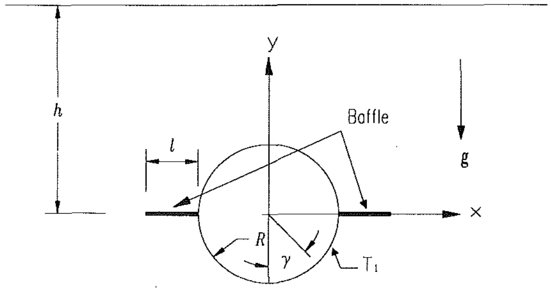

Fig. 1 Geometry and configuration

---

[1] Department of Engineering, Trenton State College, Trenton, NJ 08650.

Contributed by the Heat Transfer Division and based on a paper presented at the ASME Winter Annual Meeting, New Orleans, Louisiana, November 28–December 3, 1993. Manuscript received by the Heat Transfer Division April 1993; revision received July 1993; Keywords: Natural Convection, Numerical Methods, Porous Media. Associate Technical Editor: R. Viskanta.

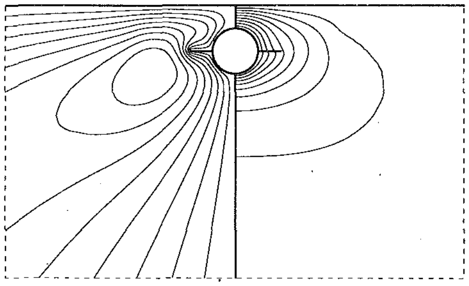

Fig. 2 Uniformly spaced streamlines (left-hand side) and isotherms (right-hand side) corresponding to $l/R=1$, $h/R=2$, and $\mathrm{Ra}=10$

vection with the Boussinesq, Darcy flow, and negligible inertia approximations in dimensionless form expressed in body-fitted curvilinear coordinates are (Facas, 1993):

$$\alpha_1\psi^*_{\xi\xi}-2\alpha_2\psi^*_{\xi\eta}+\alpha_3\psi^*_{\eta\eta}+\mathbf{J}^2\{P\psi^*_\xi+Q\psi^*_\eta\}$$
$$=-\mathrm{Ra}\,\mathbf{J}\{y_\eta\theta_\xi-y_\eta\theta_\eta\} \quad (1)$$

$$\alpha_1\theta_{\xi\xi}-2\alpha_2\theta_{\xi\eta}+\alpha_3\theta_{\eta\eta}+\mathbf{J}^2\{P\theta_\xi+Q\theta_\eta\}=\mathbf{J}\{\psi^*_\eta\theta_\xi-\psi^*_\xi\theta_\eta\} \quad (2)$$

$$\frac{\lambda_b}{\lambda'}\frac{\delta}{R}\left(\frac{y_\eta^2\theta_{\xi\xi}-2y_\xi y_\eta\theta_{\xi\eta}+y_\xi^2\theta_{\eta\eta}}{\mathbf{J}^2}+\frac{[y_\eta^2y_{\xi\xi}-2y_\xi y_\eta y_{\xi\eta}+y_\xi^2y_{\eta\eta}][x_\eta\theta_\xi-x_\xi\theta_\eta]}{\mathbf{J}^3}\right)$$
$$+\frac{\lambda_b}{\lambda'}\frac{\delta}{R}\left(\frac{[y_\eta^2x_{\xi\xi}-2y_\xi y_\eta y_{\xi\eta}+y_\xi^2x_{\eta\eta}][y_\xi\theta_\eta-y_\eta\theta_\xi]}{\mathbf{J}^3}\right)$$
$$+\frac{x_\eta\{\theta_\xi\}_2-x_\eta\{\theta_\xi\}_1}{\mathbf{J}}=0 \quad (3)$$

The energy equation along the baffle [Eq. (3)] has been derived assuming negligible thermal resistance across the thickness of the baffle and negligible thermal capacitance. The corresponding boundary conditions become

Cylinder surface:

$$\theta=1,\ \psi^*=0 \quad \text{at} \quad \xi_1\le\xi\le\xi_2,\ \eta=\eta_1 \quad (4a)$$

Impermeable surface:

$$\theta=\psi^*=0 \quad \text{at} \quad \xi_1\le\xi\le\xi_a;\ \eta=\eta_2 \quad (4b)$$

Symmetry axis:

$$\begin{aligned}\psi^*=\theta_\xi=0 \quad &\text{at} \quad \xi=\xi_1;\ \eta_1\le\eta\le\eta_2\\ \psi^*=\theta_\xi=0 \quad &\text{at} \quad \xi=\xi_2;\ \eta_1\le\eta\le\eta_2\end{aligned} \quad (4c)$$

Far-right surface:

$$y_\eta\psi^*_\xi-y_\xi\psi^*_\eta=y_\eta\theta_\xi-y_\xi\theta_\eta=0 \quad \text{at} \quad \xi_a\le\xi\le\xi_b;\ \eta=\eta_2 \quad (4d)$$

Far bottom surface:

$$x_\eta\psi^*_\xi-x_\xi\psi^*_\eta=x_\eta\theta_\xi-x_\xi\theta_\eta=0 \quad \text{at} \quad \xi_b\le\xi\le\xi_2;\ \eta=\eta_2 \quad (4e)$$

Numerical Solution

The solution to Eqs. (1)–(3) subject to the boundary conditions specified by Eq. (4) is obtained numerically using finite differences. Central differences are used to approximate the diffusive terms, whereas the upwind differencing scheme was introduced with the convective terms (Roache, 1976). The resulting algebraic equations were solved iteratively using the method of overrelaxation (S.O.R.). The dimensionless baffle thickness (δ/R) was for simplicity taken to be 1/60; higher values for the baffle thickness are not expected to alter the results significantly for the low baffle thermal conductivities considered in this study.

The numerical results for the problem under consideration will, in general, be sensitive to the values set for (w/R) and (d/R). As a result, a considerable effort has been directed to select values for (w/R) and (d/R) such that the solution is independent of the value selected for these two quantities. The results predicted with the present code were also compared to the results presented for the same problem by Bau (1984). Based on these calculations, it was concluded that the solution becomes independent of (w/R) and (d/R) when values larger than 31 are selected for these quantities; see Facas (1993) for details. The minimum value considered in this analysis for (w/R) and (d/R) was about 38 and, in some cases, values as large as 57 were used. For $(h/R)\le 10$, a grid size of 60×90 was found to yield solutions that are reasonably grid independent and in good agreement with the results presented for a pipe buried in a semi-infinite porous medium by Bau (1984).

Results and Discussion

In view of the complexity and the large number of parameters involved in this problem, the present study was restricted to three baffle lengths: $(l/R)=0.5$, 1.0, and 2.0, where l and R represent the baffle length and pipe radius, respectively. It is important to note here that the baffle does not have to be an integral part of the pipe and it can be made of any material (such as a thin sheet of plastic) that is impermeable to fluid flow. The thermal conductivity of the baffle was assumed to be equal (representing an optimistic case for nonmetallic baffles, see Facas, 1993, for details) to the equivalent thermal conductivity of the porous medium. It is important to note that for nonmetallic baffles the thermal conductivity of the baffle is not expected to influence the effectiveness of the baffle significantly because the objective of the baffle is not a fin (fins are frequently used in order to increase the surface area across which the convection occurs) but the alteration of the hydrodynamic characteristics of the problem.

Figure 2 illustrates the effects on the fluid flow in terms of isotherm and streamline plots when a baffle of length $l/R=1$ is attached along the surface of the pipe, $h/R=2$ and $\mathrm{Ra}=10$. Clearly, the presence of the baffle forces the ascending hot fluid to travel around it. As the fluid travels around the baffle, the overall strength of the convective flow is weakened (compared to the case of pipe buried without any baffles) due to the additional resistance that the baffle imposes on the fluid flow. The result of this weaker fluid flow is an overall reduction in the heat transfer from the pipe. Moreover, as the fluid flow is diverted away from the pipe by the baffle, a lower temperature gradient is produced on the surface of the pipe near the baffle (as evidenced by the "bulging" of the isotherms), which tends of reduce both the local and the average heat transfer from the pipe further. At this time, it is important to note that the physical domain shown in Fig. 2 represents only a small portion of the domain that was considered in the analysis in order to be able to show details near the pipe.

As the baffle length increases to 2, the fluid flow is now characterized by a primary circulation—consisting of the stream that ascends along the pipe surface from the bottom—and a secondary circulation located between the baffle and the top, horizontal surface; see Facas (1993). With the development of this secondary flow, the primary flow is further weakened (compared to the case of $l/R=1$) and, as a result, the heat transfer from the surface of the pipe is reduced even further.

Results in terms of isotherm and streamline contour plots for $l/R=2$ for a pipe buried at a depth $h/R=8$ and $\mathrm{Ra}=10$ are given by Facas (1993). In this case the fluid flow exhibits a plume structure, whereas no such structure is observed when $h/R=2$. This difference can be attributed to the fact that the top, horizontal surface generally tends to constrain the fluid flow and, as a result, it prevents the development of a plume at small burial depths. The streamline contour plots show that no secondary flow exists at this burial depth for the baffle lengths considered. For $\mathrm{Ra}=10$ and $l/R=2$, the minimum burial depth beyond which the secondary flow does not exist was determined to be between 3 and 4.

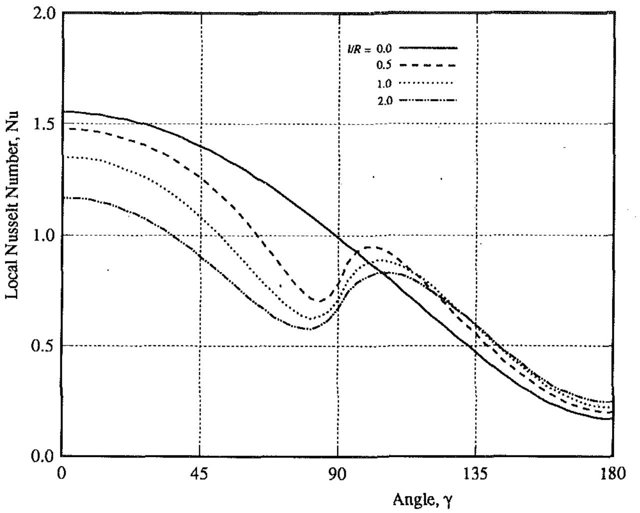

Fig. 3 Local Nusselt number distributions corresponding to various baffle lengths, $h/R = 5$ and $\mathrm{Ra} = 10$

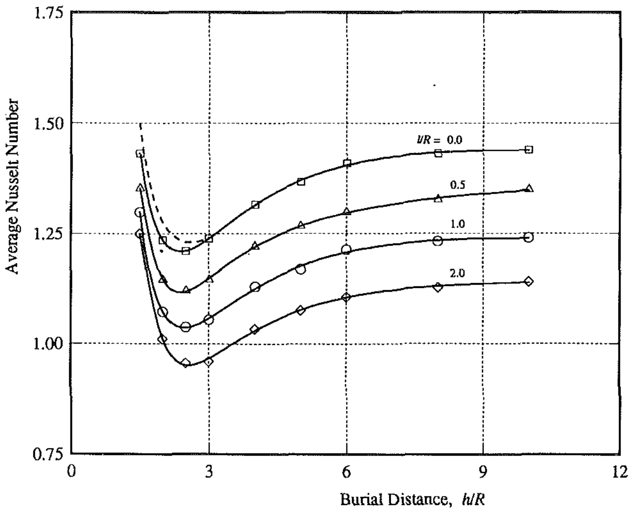

Fig. 5 Average Nusselt number as a function of h/R and l/R; $\mathrm{Ra} = 20$

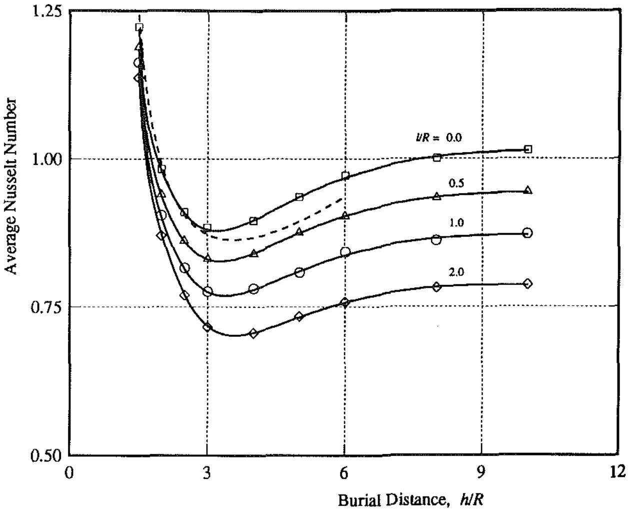

Fig. 4 Average Nusselt number as a function of h/R and l/R; $\mathrm{Ra} = 10$

Figure 3 depicts local Nusselt number distributions when a baffle is attached along the pipe surface, $h/R = 5$ and $\mathrm{Ra} = 10$. Comparing these distributions to the distribution that was obtained when no baffle is attached (also shown in Fig. 3), the presence of the baffle yields a large reduction in heat transfer along the lower half of the pipe surface and a slight increase along the top half surface of the pipe with a large variation near the baffle.

Plots of the average Nusselt number associated with a pipe (with and without a baffle) buried beneath a cold, horizontal surface are presented as a function of h/R, l/R, and Ra in Figs. 4 and 5. Similar results are presented by Facas (1993) for $\mathrm{Ra} = 5$. The symbols in Figs. 4 and 5 denote the results of the numerical simulation, whereas the solid lines represent the best fit through the data. The dashed line—plotted up to an effective Rayleigh number, ($\mathrm{Ra}\ h/R$), of 60—represents the analytical solution (converted to the notation used in this study) that was obtained by Himasekhar and Bau (1987) using Shanks' transformation. The heat transfer profile associated with a pipe with a baffle attached along its surface is similar to the profile exhibited by a pipe (without a baffle) buried in a semi-infinite medium; the heat transfer decreases initially as the burial depth increases, reaches a minimum, and then begins to increase again. As the burial depth becomes very large, the heat transfer reaches asymptotically a value that corresponds to the case of a pipe buried in an infinite medium. Heat transfer values for a pipe buried in an infinite medium were presented by Cheng (1984). Clearly, the optimal burial depth at which the minimum heat loss occurs decreases as the Ra number increases. For the range of Ra numbers considered in this study, the minimum heat loss (from a pipe without a baffle) occurs at burial depths between 2.5 and 5 and it appears to increase slightly when a baffle is attached along the pipe surface.

Although the optimal burial depth does not change significantly when a baffle is used, the overall heat transfer characteristic of the problem is greatly altered with the use of a baffle. Clearly, the heat loss from a pipe with a baffle is always much lower than the heat loss from a pipe without one. Moreover, the use of a baffle can in some cases (depending on the baffle length) yield a heat transfer rate that, for burial depths greater than 2, is lower than the "optimal heat loss" from a pipe without a baffle.

Finally, for demonstration purposes, the potential for energy savings will be examined for a pipe with a baffle buried beneath an impermeable cold, horizontal surface. Consider, as an example, a pipe of radius 0.25 m buried a distance of 2 m below the impermeable cold, horizontal surface. Let's assume that the soil is silica sand with an average grain size of 2.54×10^{-4} and that it is saturated with water. Let's further assume that the porosity is 0.4 and that the temperature difference between the pipe and the top surface is 60°C. The permeability, $K \sim 6.3 \times 10^{-11}\ \mathrm{m}^2$, is calculated using the Karman–Kozeny formula (Nield and Bejan, 1992). If the water properties are evaluated at 40°C, the corresponding Rayleigh number is $\mathrm{Ra} \sim 10$. For a pipe buried a distance of 2 m ($h/R = 8$) beneath the horizontal surface, the average Nusselt number is $\overline{\mathrm{Nu}} \sim 1.0$. Let's now consider the case where a baffle of length 0.25 m ($l/R = 1$) is used. The average Nusselt number corresponding to this case is 0.86. Clearly, the use of this size baffle would yield approximately a 14 percent energy savings. On the other hand, if the length of the baffle was assumed to be 0.5 m ($l/R = 2$), energy savings of about 22 percent would be realized. It is interesting to note that the heat loss is lower for both examples considered than the heat loss from a pipe buried at the optimal depth (for $\mathrm{Ra} = 10$, the average Nusselt number at the optimal burial depth is approximately 0.88).

At this time it is very important to note that the energy savings that a baffle generates could be realized at a very nominal cost. Since the baffle does not really need to be attached to the pipe, it could generally be as wide as the pipe trench and it could simply be a thin sheet of nonbiodegradable plastic or other impermeable material laid on top of the pipe before backfilling the trench.

Conclusion

A numerical investigation has been performed to solve for the flow and temperature fields for a pipe with two baffles attached along its surface buried in a saturated porous medium. Results are presented for three baffle lengths and a range of burial depths and Rayleigh numbers. The numerical simulations indicate that substantial energy savings can be realized if baffles are used. The heat losses from a pipe with baffles are predicted to be much lower than the heat losses from a pipe without baffles. Moreover, the use of baffles can in some cases (depending on the baffle length) yield a heat transfer rate that for burial depths greater than 2, is lower than the "optimal heat loss" from a pipe without baffles.

References

Bau, H. H., and Sadhal, S. S., 1982, "Heat Losses From a Fluid Flowing in a Buried Pipe," *Int. J. Heat Mass Transfer*, Vol. 25, No. 11, pp. 1621-1629.

Bau, H. H., 1984, "Convective Heat Losses From a Pipe Buried in a Semi-infinite Porous Medium," *Int. J. Heat Mass Transfer*, Vol. 27, No. 11, pp. 2047-2056.

Cheng, P., 1984, "Natural Convection in a Porous Medium: External Flows," presented at NATO Advanced Study Institute, July 16-27.

Eckert, E. R. G., and Drake, R. M., 1972, *Analysis of Heat and Mass Transfer*, McGraw-Hill, New York.

Facas, G. N., 1993, "Reducing the Heat Transfer From a Hot Pipe Buried in a Semi-infinite, Saturated, Porous Medium," *Multiphase Transport in Porous Media*, ASME FED-Vol. 173/HTD-Vol. 265, pp. 127-135.

Farouk, B., and Shayer, H., 1988, "Natural Convection Around a Heated Cylinder in a Saturated Porous Medium," ASME JOURNAL OF HEAT TRANSFER, Vol. 110, pp. 642-648.

Fernandez, R. T., and Schrock, V. E., 1982, "Natural Convection From Cylinders Buried in a Liquid-Saturated Porous Medium," *Proc. of the International Heat Transfer Conference*, Munich, Vol. 2, pp. 335-340.

Himasekhar, K., and Bau, H. H., 1987, "Thermal Convection Associated With Hot/Cold Pipes Buried in a Semi-infinite, Saturated, Porous Medium," *Int. J. Heat Mass Transfer*, Vol. 2, pp. 335-340.

Nield, D. A., and Bejan, A., 1992, *Convection in Porous Media*, Springer-Verlag, New York.

Roache, P. J., 1972, *Computational Fluid Dynamics*, Hermosa Publishers, Albuquerque, NM.

Schrock, V. E., Fernandez, R. T., and Kesavan, K., 1970, "Heat Transfer From Cylinders Embedded in a Liquid Filled Porous Medium," *Proc. of the International Heat Transfer Conference*, Paris, Vol. VII, CT 3.6.

Thiyagarajan, R., and Yovanovich, M. M., 1974, "Thermal Resistance of a Buried Cylinder With Constant Flux Boundary Condition," ASME JOURNAL OF HEAT TRANSFER, Vol. 96, pp. 249-250.

Thompson, J. F., Warsi, Z. U. A., and Mastin, C. W., 1982, "Boundary-Fitted Coordinate System for Numerical Solution for Partial Differential Equations—A Review," *Journal of Computational Physics*, Vol. 47, pp. 1-108.

A Note on Heat Conduction in Liquid Metals: A Comparison of Laminar and Turbulent Flow Effects[1]

G. Talmage[2]

Nomenclature

a = dimensionless width of the free surface
b = dimensionless half-width of the rotor face
B_0 = applied magnetic-field strength
I = total dimensionless current per unit depth
$\mathbf{j}$ = electric current density vector
k = thermal conductivity of the liquid metal
L = dimensional width of the radial gap
M = Hartmann number
N = interaction parameter
R = dimensionless rotor radius
Pr = Prandtl number
Re = Reynolds number
s = dimensionless width of the side stator
T = dimensionless temperature difference
T_o = temperature of the solid at the coolant channel
t_r = dimensionless length between the rotor face and the coolant channel
t_s = dimensionless length between the liquid metal-axial stator interface and the coolant channel in the stator
u = primary azimuthal velocity
x = azimuthal coordinate
y = radial coordinate
z = axial coordinate
θ = angle between the y axis and magnetic field vector
κ = thermal diffusivity of the liquid metal
ν = viscosity of the liquid metal
ρ = density of the liquid metal
σ = electrical conductivity of the liquid metal
Ω = angular velocity of the rotor

Subscripts

LM = quantity associated with the liquid metal
t = turbulent quantity
0 = molecular quantity

Superscripts

$*$ = dimensional quantity

Introduction

Heat transfer in liquid metals with electric currents and magnetic fields differs considerably from heat transfer in electrically insulating fluids and in conducting solids, because both Joulean heating and viscous dissipation act as volumetric heat sources. The relative significance of viscous dissipation to Joulean heating depends on, among other parameters, the total current as well as the strength and orientation of the magnetic field (Talmage et al., 1990). Unlike ordinary hydrodynamic (OHD) flows, the velocity field is determined, in part, by the electromagnetic (EM) body forces. As a consequence, the viscous dissipation is increased over that for OHD flows due to the magnetohydrodynamic-enhanced velocity gradients. There are instances in which the Joulean heating and viscous dissipation are so large that significant temperature gradients arise in spite of the large thermal conductivity of liquid metals. Liquid-metal sliding electrical contacts for homopolar machines are a technologically important example in which large temperature gradients can develop within a small region of liquid metal.

A homopolar motor or generator is a high-current low-voltage DC electromechanical energy converter. Typically, a homopolar device consists of a set of copper disks (rotors) mounted on an axle. Each disk is shrouded by a stationary concentric copper surface (the stator). A sliding electrical contact completes an electric circuit between the rotor and stator. The device operates in the presence of superconducting coils, which produce a strong, complex, and axisymmetric magnetic field. Pairs of rotors with opposite axial magnetic field orientations are electrically connected along the shaft.

A liquid metal, such as the eutectic mixture of sodium and potassium (NaK), has an extremely low electrical resistance, forms an excellent electrical contact with copper, and produces

---

[1] The opinions and conclusions are solely those of the author and do not necessarily reflect the opinions and conclusions of the US Government.

[2] Department of Mechanical Engineering, The Pennsylvania State University, University Park, PA 16802.

Contributed by the Heat Transfer Division and presented at the National Heat Transfer Conference, Atlanta, Georgia, August 8-11, 1993. Manuscript received by the Heat Transfer Division December 1992; revision received August 1993. Keywords: Conduction, Liquid Metals, Turbulence. Associate Technical Editor: Y. Bayazitoglu.

Conclusion

A numerical investigation has been performed to solve for the flow and temperature fields for a pipe with two baffles attached along its surface buried in a saturated porous medium. Results are presented for three baffle lengths and a range of burial depths and Rayleigh numbers. The numerical simulations indicate that substantial energy savings can be realized if baffles are used. The heat losses from a pipe with baffles are predicted to be much lower than the heat losses from a pipe without baffles. Moreover, the use of baffles can in some cases (depending on the baffle length) yield a heat transfer rate that for burial depths greater than 2, is lower than the "optimal heat loss" from a pipe without baffles.

References

Bau, H. H., and Sadhal, S. S., 1982, "Heat Losses From a Fluid Flowing in a Buried Pipe," *Int. J. Heat Mass Transfer*, Vol. 25, No. 11, pp. 1621-1629.

Bau, H. H., 1984, "Convective Heat Losses From a Pipe Buried in a Semi-infinite Porous Medium," *Int. J. Heat Mass Transfer*, Vol. 27, No. 11, pp. 2047-2056.

Cheng, P., 1984, "Natural Convection in a Porous Medium: External Flows," presented at NATO Advanced Study Institute, July 16-27.

Eckert, E. R. G., and Drake, R. M., 1972, *Analysis of Heat and Mass Transfer*, McGraw-Hill, New York.

Facas, G. N., 1993, "Reducing the Heat Transfer From a Hot Pipe Buried in a Semi-infinite, Saturated, Porous Medium," *Multiphase Transport in Porous Media*, ASME FED-Vol. 173/HTD-Vol. 265, pp. 127-135.

Farouk, B., and Shayer, H., 1988, "Natural Convection Around a Heated Cylinder in a Saturated Porous Medium," ASME JOURNAL OF HEAT TRANSFER, Vol. 110, pp. 642-648.

Fernandez, R. T., and Schrock, V. E., 1982, "Natural Convection From Cylinders Buried in a Liquid-Saturated Porous Medium," *Proc. of the International Heat Transfer Conference*, Munich, Vol. 2, pp. 335-340.

Himasekhar, K., and Bau, H. H., 1987, "Thermal Convection Associated With Hot/Cold Pipes Buried in a Semi-infinite, Saturated, Porous Medium," *Int. J. Heat Mass Transfer*, Vol. 2, pp. 335-340.

Nield, D. A., and Bejan, A., 1992, *Convection in Porous Media*, Springer-Verlag, New York.

Roache, P. J., 1972, *Computational Fluid Dynamics*, Hermosa Publishers, Albuquerque, NM.

Schrock, V. E., Fernandez, R. T., and Kesavan, K., 1970, "Heat Transfer From Cylinders Embedded in a Liquid Filled Porous Medium," *Proc. of the International Heat Transfer Conference*, Paris, Vol. VII, CT 3.6.

Thiyagarajan, R., and Yovanovich, M. M., 1974, "Thermal Resistance of a Buried Cylinder With Constant Flux Boundary Condition," ASME JOURNAL OF HEAT TRANSFER, Vol. 96, pp. 249-250.

Thompson, J. F., Warsi, Z. U. A., and Mastin, C. W., 1982, "Boundary-Fitted Coordinate System for Numerical Solution for Partial Differential Equations—A Review," *Journal of Computational Physics*, Vol. 47, pp. 1-108.

A Note on Heat Conduction in Liquid Metals: A Comparison of Laminar and Turbulent Flow Effects[1]

G. Talmage[2]

Nomenclature

a = dimensionless width of the free surface
b = dimensionless half-width of the rotor face
B_0 = applied magnetic-field strength
I = total dimensionless current per unit depth
$\mathbf{j}$ = electric current density vector
k = thermal conductivity of the liquid metal
L = dimensional width of the radial gap
M = Hartmann number
N = interaction parameter
R = dimensionless rotor radius
Pr = Prandtl number
Re = Reynolds number
s = dimensionless width of the side stator
T = dimensionless temperature difference
T_o = temperature of the solid at the coolant channel
t_r = dimensionless length between the rotor face and the coolant channel
t_s = dimensionless length between the liquid metal-axial stator interface and the coolant channel in the stator
u = primary azimuthal velocity
x = azimuthal coordinate
y = radial coordinate
z = axial coordinate
θ = angle between the y axis and magnetic field vector
κ = thermal diffusivity of the liquid metal
ν = viscosity of the liquid metal
ρ = density of the liquid metal
σ = electrical conductivity of the liquid metal
Ω = angular velocity of the rotor

Subscripts

LM = quantity associated with the liquid metal
t = turbulent quantity
0 = molecular quantity

Superscripts

$*$ = dimensional quantity

Introduction

Heat transfer in liquid metals with electric currents and magnetic fields differs considerably from heat transfer in electrically insulating fluids and in conducting solids, because both Joulean heating and viscous dissipation act as volumetric heat sources. The relative significance of viscous dissipation to Joulean heating depends on, among other parameters, the total current as well as the strength and orientation of the magnetic field (Talmage et al., 1990). Unlike ordinary hydrodynamic (OHD) flows, the velocity field is determined, in part, by the electromagnetic (EM) body forces. As a consequence, the viscous dissipation is increased over that for OHD flows due to the magnetohydrodynamic-enhanced velocity gradients. There are instances in which the Joulean heating and viscous dissipation are so large that significant temperature gradients arise in spite of the large thermal conductivity of liquid metals. Liquid-metal sliding electrical contacts for homopolar machines are a technologically important example in which large temperature gradients can develop within a small region of liquid metal.

A homopolar motor or generator is a high-current low-voltage DC electromechanical energy converter. Typically, a homopolar device consists of a set of copper disks (rotors) mounted on an axle. Each disk is shrouded by a stationary concentric copper surface (the stator). A sliding electrical contact completes an electric circuit between the rotor and stator. The device operates in the presence of superconducting coils, which produce a strong, complex, and axisymmetric magnetic field. Pairs of rotors with opposite axial magnetic field orientations are electrically connected along the shaft.

A liquid metal, such as the eutectic mixture of sodium and potassium (NaK), has an extremely low electrical resistance, forms an excellent electrical contact with copper, and produces

---

[1] The opinions and conclusions are solely those of the author and do not necessarily reflect the opinions and conclusions of the US Government.

[2] Department of Mechanical Engineering, The Pennsylvania State University, University Park, PA 16802.

Contributed by the Heat Transfer Division and presented at the National Heat Transfer Conference, Atlanta, Georgia, August 8-11, 1993. Manuscript received by the Heat Transfer Division December 1992; revision received August 1993. Keywords: Conduction, Liquid Metals, Turbulence. Associate Technical Editor: Y. Bayazitoglu.

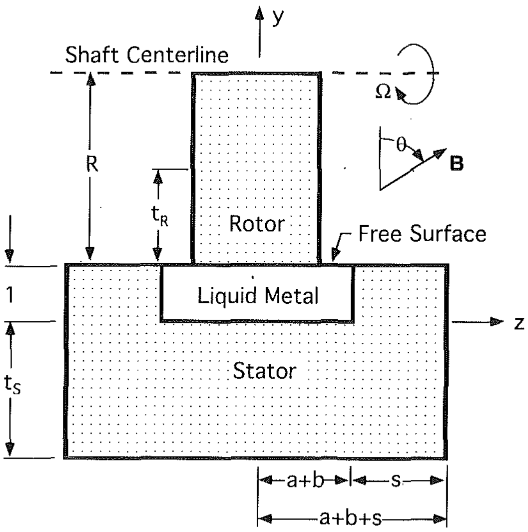

Fig. 1 Schematic of a liquid-metal sliding electrical contact. All lengths are dimensionless.

very little drag on the disk because of its low viscosity. These properties make a liquid metal an excellent sliding electrical contact. When the disk begins to rotate, the liquid metal is carried by viscous drag to fill the gap around the entire periphery of the disk. As the speed increases, centrifugal forces produce a relatively uniform distribution of liquid around the periphery. The angular velocity of the rotor determines the flow regime. For the lower operating speeds, the flow is laminar; for the higher speeds, it is turbulent. Several technical issues must be resolved before homopolar devices with liquid-metal sliding electrical contacts can be designed for operation on an industrial scale (Stevens et al., 1977). Here, we address one issue: the effect of the flow regime on the temperature distribution within the liquid metal and solid parts of a homopolar device.

Problem Formulation

A model of a liquid-metal sliding electrical contact is shown in Fig. 1. All lengths shown in Fig. 1 are nondimensionalized by L, the dimensional radial gap width. To remove heat from the liquid metal region, coolant channels are used in the stator and, possibly, the rotor. For modeling purposes, we will assume that coolant channels are located in the stator at $y=-t_s$ and in the rotor at $y=1+t_r$. We assume a steady, uniform axisymmetric magnetic field with radial and axial components; a steady, axisymmetric flow; temperature-independent transport properties; and perfect electrically conducting solid parts. The inertial effects are negligible, and the primary azimuthal flow decouples from the secondary flow. Here, the primary flow is in the azimuthal direction, with the secondary flow in the radial and axial directions. The secondary-flow quantities are significantly smaller than the primary-flow quantities and will be neglected from further consideration. The Peclet number is based on the characteristic velocity of the secondary flow and is small, indicating that the transport of energy by the secondary flow is negligible. (For the lower operating speeds and higher magnetic-field strengths, the Peclet number is between 0.001 and 0.1.) The rationale for these assumptions has been discussed elsewhere (Talmage et al., 1989; Kalkan and Talmage, 1993). Under these assumptions, the energy equation decouples from the other equations, and secondary-flow transport of energy is neglected. The dimensionless governing equation for the temperature distribution within the liquid metal reduces to:

$$\frac{\partial}{\partial y}\left(k_t\frac{\partial T_{LM}}{\partial y}\right)+\frac{\partial}{\partial z}\left(k_t\frac{\partial T_{LM}}{\partial z}\right)=-\mathrm{M}^{-2}\nu_t\left[\left(\frac{\partial u}{\partial y}\right)^2+\left(\frac{\partial u}{\partial z}\right)^2\right]-[j_y^2+j_z^2], \quad (1)$$

where k_t and ν_t are the turbulent thermal conductivity and turbulent viscosity of the liquid metal, respectively, T_{LM} denotes the dimensionless temperature difference of the liquid metal, u is the primary azimuthal velocity, j_y and j_z are the electric current densities directed radially inward and axially, respectively, and M is the Hartmann number. The Hartmann number is the square root of the ratio of the EM body force to the "viscous force,"

$$\mathrm{M}=B_0L\sqrt{\frac{\sigma}{\rho\nu_0}},$$

where B_0 is the magnetic field strength; σ, ρ, and ν_0 are the electrical conductivity, density, and molecular kinematic viscosity of the liquid metal. The temperature is normalized by

$$T_{LM}^*-T_0=\frac{\sigma(\Omega RL)^2B_0^2L^2}{k_0}T_{LM},$$

where T_{LM}^* is the dimensional liquid-metal temperature, T_0 is the temperature of the solid part at the coolant channel, ΩRL is the velocity of the rotor face, and k_0 is the molecular thermal conductivity of the liquid metal. The first term on the right-hand side of Eq. (1) is the viscous dissipation, and the second term is the Joulean heating. Once the velocity and electric current density distributions are known, the viscous dissipation and Joulean heating can be determined. The velocity and electric current density distributions have been treated previously and will not be reviewed here (Talmage et al., 1991). However, it should be noted that the velocity and electric current density are not constant but functions of y and z.

If we assume that the solid parts are perfect electrical conductors and that the transport properties of the solid parts are not functions of temperature, then the temperature distribution equation within both the stator and rotor reduces to Laplace's equation. The free surfaces at $y=1$, for $b<|z|<(a+b)$; the side walls of the rotor at $z=\pm b$, for $1\le y\le 1+t_r$; the external side walls of the stator at $z=\pm(a+b+s)$, for $-t_s\le y\le 1$; and the stator surfaces at $y=1$, for $(a+b)\le|z|\le(a+b+s)$ are taken to be adiabatic. Here, b is the dimensionless half-width of the rotor, a is the dimensionless length of the free surface, and s is the thickness of the stator side wall. The dimensionless temperature difference is set to zero at the coolant channels. Finally, at the liquid-metal–solid interfaces, both the temperature and heat flux are continuous.

The primary focus of this work is not the turbulence model. We have chosen a turbulence model that is relatively easy to implement, but any model would have been appropriate at this stage. The term k_t that appears in Eq. (1) can be related to the turbulent Prandtl number. For locally isotropic fully developed turbulent flow, a formula for the thermal diffusivity was developed by Yakhot and Orszag (as described by Branover et al., 1986):

$$\left(\frac{\frac{1}{\mathrm{Pr}}-1.1703}{\frac{1}{\mathrm{Pr}_0}-1.1703}\right)^{0.65}\left(\frac{\frac{1}{\mathrm{Pr}}+2.1793}{\frac{1}{\mathrm{Pr}_0}+2.1793}\right)^{0.35}=\frac{\nu_0}{\nu}, \quad (2)$$

where $\mathrm{Pr}=(\nu/\kappa)$ and $\mathrm{Pr}_0=(\nu_0/\kappa_0)$ are the Prandtl numbers associated with the turbulent and laminar flows, respectively. Here, $\kappa=\kappa_0\kappa_t$ is the thermal diffusivity, where κ_0 is the molecular thermal diffusivity and κ_t is the turbulent thermal diffusivity. The viscosity, $\nu=\nu_0\nu_t$, is based on the molecular kinematic viscosity, ν_0, and the turbulent viscosity, ν_t (Sukoriansky, 1987, provides a discussion on the appropriate formulation of ν_t for magnetohydrodynamic flows. Details on the calculation of ν_t can be found from Talmage et al., 1992). Finally, the turbulent thermal conductivity is determined from the Prandtl numbers and the turbulent viscosity:

$$k_t=\frac{\mathrm{Pr}_0\nu_t}{\mathrm{Pr}}, \qquad (3)$$

where Pr is obtained from Eq. (2). It must be noted that for sufficiently large M, there will be large-scale anisotropic mixing, so the effect of the magnetic field on the thermal conductivity must be incorporated into Eq. (2). For the operating conditions considered here, Eq. (2) suffices.

A control-volume finite-difference approach on a nonuniform mesh was used to solve this problem. The solutions were verified using standard procedures. Once the solution converged, the residual of the governing equation was checked: For each node, the residual was less than 10^{-7}. The mesh was refined until no changes were observed in the temperature distributions. Finally, because no experimental data exist for the temperature distribution within a homopolar device, a second code that employs a hybrid technique (Moon and Walker, 1990) was developed. The results from the finite-difference code and the hybrid code were in complete agreement.

Results and Discussion

Here we consider the effects of the Reynolds number on the temperature distribution. Typical parameter values for a liquid-metal sliding electrical contact are used: $\mathrm{M}=5$, $\theta=\pi/4$, $\mathrm{Re}=150$ and 13,333, and $\mathrm{Pr}_0=0.024$. θ represents the angle between the y axis and the magnetic-field vector. The Reynolds number is defined in terms of the characteristic velocity of the primary flow, $\mathrm{Re}=(\Omega RL)L/\nu_0$. A Reynolds number of 150 represents a laminar flow, and $\mathrm{Re}=13{,}333$ represents a turbulent flow. The total dimensionless current per unit depth, I, is taken to be -100. The ratio of the thermal conductivity of the solid parts to that of the liquid metal is 15. Values for a, b, s, t_r, and t_s are 3.04, 9.96, 3.0, 2.0, and 3.1, respectively.

Figures 2(*a*) and 2(*b*) contain the isotherms for the laminar and turbulent flow regimes, respectively. Both sets of isotherms have similar structure: a hot spot is associated with the right rotor corner. For the laminar flow, the maximum dimensionless temperature difference is 23.05 at $y=0.5$ and $z=8.75$. For the turbulent flow, the maximum dimensionless temperature difference is 19.75 on the free surface, just to the right of the rotor corner. The maximum dimensionless temperature difference has decreased by 15 percent. For both flow regimes, there is a "hot" spot near the left rotor corner; however, the contour intervals are too coarse to resolve the details. In the side stators, as $|z|$ goes from $(a+b)$ to $(a+b+s)$, the temperature, which is an order of magnitude smaller than that in the hot spots, decreases. Again, the contour interval is so coarse that this feature is not seen in the figures but is found in the data. There are no volumetric heat sources in the solid parts, and energy is transferred from the liquid metal to the solid parts via conduction. The temperature is continuous at the liquid-metal-solid interfaces, but the temperature gradient is not because the thermal conductivity of the liquid metal and the solid parts are not equal. This is seen in Figs. 2(*a*, *b*): The isotherms have "kinks" at the liquid-metal-solid interface. The local behavior of the velocity and the electric current density determines the structure of the isotherms (Kalkan and Talmage, 1993).

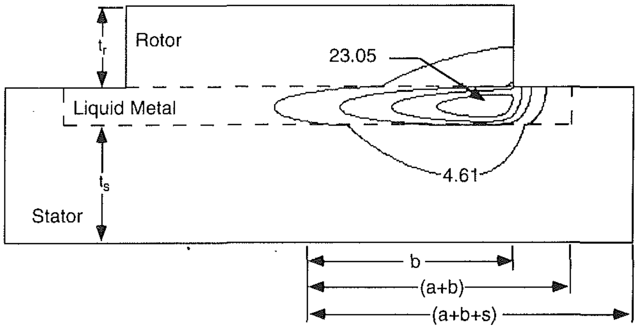

Fig. 2(*a*) **Isotherms for Re = 150 and $I=-100$. The contour interval is 4.61.**

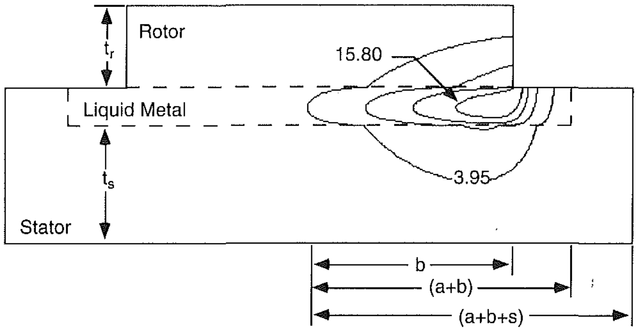

Fig. 2(*b*) **Isotherms for Re = 13,333 and $I=-100$. The contour interval is 3.95.**

In comparison to the laminar flow regime, the magnitude of the velocity and its gradients for the turbulent flow are significantly reduced in the central-core region of the flow while near the rotor face and the stator surface parallel to the rotor, they are enhanced. In spite of the fact that ν_t is several orders of magnitude larger for a turbulent flow than for a laminar flow, this increase is not sufficient to overcome the reduction in the velocity gradients, and the total viscous dissipation decreases for turbulent flows. Since the total current is fixed at $I=-100$, the total Joulean heating is approximately the same for both the laminar and turbulent flow regimes. Given the trends of the viscous dissipation and Joulean heating, it is not surprising that the maximum dimensionless temperature difference decreases for the turbulent flow.

The turbulent thermal conductivity, k_t, could also contribute to the decrease in the maximum dimensionless temperature difference for the turbulent flow. From Eqs. (2) and (3), we see that the turbulent thermal conductivity is greater than one for turbulent flows and equal to one for laminar flows. With a larger thermal conductivity, energy is more easily transferred from regions of higher temperature to regions of lower temperature, resulting in a more uniform temperature distribution. However, k_t is based on Pr_0, which is small for liquid metals. Therefore, while k_t is greater than one, it remains an order one quantity, and its effect on the temperature distribution is small.

Typical parameter values are $\sigma=2.38\times10^6$ S/m at 311 K, $k_0=22$ W/m-K (the average value of the molecular thermal conductivity between 20°C and 100°C), $L=10^{-4}$ m, and B_0 is between $0.5T$ and $6T$. With these typical values, $T^*_{LM}-T_0=1.08\times10^{-4}(\Omega RL)^2B_0^2T_{LM}$, where the results are in °C. For a smaller magnetic-field strength, say, $B_0=0.83T$, the dimensional temperature difference at the maximum dimensionless temperature is 0.02°C for the laminar flow, with $\Omega RL=1.125$ m/s and 147.2°C for the turbulent flow, with $\Omega RL=100$ m/s. Note that the maximum dimensional temperature difference is significantly larger for the turbulent flow than for the laminar flow. The saturation temperature for NaK is $T_{SAT} = 825°C$ at 760 mm Hg, so if $T_0 = 20$ to 100°C, then the maximum dimensional temperature differences are far below T_{SAT} when $B_0 = 0.83T$.

We are confronted with two problems. The dimensionless temperature difference is proportional to the magnetic-field strength squared. So, as the magnetic-field strength increases, the temperature differences will increase, and the assumption that the transport properties are not functions of temperature becomes weak for the turbulent flow regime. With temperature differences of over 100°C, this approximation is even questionable here with $B_0 = 0.83T$. Furthermore, if the saturation temperature is exceeded, which is entirely possible for the larger magnetic-field strengths, then the flow is not a single-phase flow but a two-phase flow.

Conclusions

For the cases studied, we have found that while it appears that the laminar flow regime provides a conservative estimate of the maximum dimensionless temperature difference, when it comes to determining the maximum dimensional temperature difference, the flow regime is of critical importance. This agrees with previous work where we found that to reasonably estimate the total Joulean heating and total viscous dissipation, a full model, which includes turbulence, is necessary. Furthermore, from this study, it appears that for turbulent flows with large net currents and certain magnetic-field orientations the temperature dependence of the transport properties of the liquid metal must be taken into account.

Acknowledgments

The author would like to thank Dr. Samuel H. Brown and Dr. Neal A. Sondergaard of the Carderock Division, Naval Surface Warfare Center, for their insights and support. This research was sponsored by the Defense Advanced Research Projects Agency (DOD), Naval Technology Office, Submarine Technology Program.

References

Branover, H., Greenspan, E., Sukoriansky, S., and Talmage, G., 1986, "Turbulence and the Feasibility of Self-Cooled Liquid-Metal Blankets for Fusion Reactors," *Fusion Technology*, Vol. 10, No. 3, pp. 882–829.

Kalkan, A. K., and Talmage, G., 1993, "Heat Transfer in Liquid Metals With Electric Currents and Magnetic Fields: the Conduction Case," *International Journal of Heat and Mass Transfer*, in press.

Moon, T. J., and Walker, J. S., 1990, "Liquid Metal Flow Through a Sharp Elbow in the Plane of a Strong Magnetic Field," *Journal of Fluid Mechanics*, Vol. 213, pp. 397–418.

Stevens, O. H., Superczynski, M. J., Doyle, T. J., Harrison, H. J., and Messinger, H., 1977, "Superconducting Machinery for Naval Ship Propulsion," *IEEE Trans. Mag.*, Vol. 13, pp. 269–274.

Sukoriansky, S., 1987, "Local and Integral Characteristics of Turbulence in the Presence of a Magnetic Field and Without It," Ph.D. dissertation, Ben-Gurion University of the Negev, Israel.

Talmage, G., Walker, J. S., Brown, S. H., and Sondergaard, N. A., 1989, "Liquid-Metal Flows in Current Collectors for Homopolar Machines: Fully-Developed Solutions for Primary Azimuthal Velocity," *Physics of Fluids*, Vol. A1, No. 7, pp.1268–1278.

Talmage, G., Walker, J. S., Brown, S. H., Sondergaard, N. A., Branover, H., and Sukoriansky, S., 1990, "Magnetohydrodynamic Liquid-Metal Flows in a Rectangular Channel With an Axial Magnetic Field, a Moving Conducting Wall and Free Surfaces," *J. Appl. Phys.*, Vol. 68, No. 9, pp. 4446–4460.

Talmage, G., Walker, J. S., Brown, S. H., Sondergaard, N. A., Branover, H., and Sukoriansky, S., 1991, "Liquid-Metal Flows in Sliding Electrical Contacts With Arbitrary Magnetic Field Orientations," *Physics of Fluids*, Vol. 6, pp. 1657–1665.

Talmage, G., Walker, J. S., Brown, S. H., Sondergaard, N. A., Branover, H., and Sukoriansky, S., 1992, "Liquid-Metal Flows in Sliding Electrical Contacts: Solutions for Turbulent Primary Azimuthal Velocity," *Advances in Turbulence Studies*, H. Branover and Y. Unger, eds., *Progress in Astronautics and Aeronautics*, Vol. 149, pp. 165–189.

Impingement Cooling of an Isothermally Heated Surface With a Confined Slot Jet

Y. J. Chou[1,3] and Y. H. Hung[2,3]

Introduction

Jet impingement cooling is of importance in a variety of industrial applications, such as annealing of metal and plastic sheets, tempering of glass, cooling of electronics components, turbine blades, and drying of textiles, veneer, and paper. Detailed reviews of flow and heat transfer between impinging jets and solid surface have been given by Martin (1977), Downs and James (1987), and Polat et al. (1989). According to the literature survey, most of the existing research puts much emphasis on heat transfer characteristics of two-dimensional stagnation flow and impinging jets without confinement plate. Little information on laminar local heat transfer and fluid flow of impinging slot jets with confinement plate is presented; and the various factors affecting the local heat transfer behaviors along the heated target surface have not been systematically investigated. Therefore, the objectives of this study include: (1) to explore the effects of jet Reynolds number, ratio of separation distance to jet width, and jet exit-velocity profile on stagnation and local heat transfer characteristics in confined slot-jet impingement problems; and (2) to propose new Nu correlations for predicting stagnation and local heat transfer characteristics.

Theoretical Analysis

A confined slot jet normally impinging on an isothermally heated surface is considered in the present study. Two-dimensional, incompressible laminar forced convection is employed in the analysis. A Newtonian fluid with constant properties is assumed. Furthermore, the viscous dissipation and the compressibility effect in the energy equation are neglected.

Let

$$X = \frac{x}{W} \quad Y = \frac{y}{W} \quad U = \frac{uW}{\nu} \quad V = \frac{vW}{\nu}$$

$$P = \frac{pW^2}{\rho\nu^2} \quad \tau = \frac{\nu t}{W^2} \quad \theta = \frac{T - T_j}{T_w - T_j} \tag{1}$$

where x and y represent the coordinates parallel to and normal to the heated surface, respectively. u and v are the fluid velocity components in the x and y directions, respectively. W is the slot jet width. T_j and T_w are the jet exit temperature and the heated surface temperature, respectively.

With the above-mentioned assumptions, the general expression of the governing equations can be written in dimensionless form as follows:

$$\frac{\partial \psi}{\partial \tau} + \frac{\partial (U\psi)}{\partial X} + \frac{\partial (V\psi)}{\partial Y} = \frac{\partial}{\partial X}\left(\Gamma^* \frac{\partial \psi}{\partial X}\right) + \frac{\partial}{\partial Y}\left(\Gamma^* \frac{\partial \psi}{\partial Y}\right) + S^{\psi} \tag{2}$$

---

[1] Graduate Student.

[2] Professor.

[3] Department of Power Mechanical Engineering, National Tsing Hua University, Hsinchu, Taiwan 30043.

Contributed by the Heat Transfer Division of THE AMERICAN SOCIETY OF MECHANICAL ENGINEERS. Manuscript received by the Heat Transfer Division January 1993; revision received July 1993. Keywords: Augmentation and Enhancement, Electronic Equipment, Jets. Associate Technical Editor: F. P. Incropera.

cantly larger for the turbulent flow than for the laminar flow. The saturation temperature for NaK is $T_{SAT} = 825°C$ at 760 mm Hg, so if $T_0 = 20$ to 100°C, then the maximum dimensional temperature differences are far below T_{SAT} when $B_0 = 0.83T$.

We are confronted with two problems. The dimensionless temperature difference is proportional to the magnetic-field strength squared. So, as the magnetic-field strength increases, the temperature differences will increase, and the assumption that the transport properties are not functions of temperature becomes weak for the turbulent flow regime. With temperature differences of over 100°C, this approximation is even questionable here with $B_0 = 0.83T$. Furthermore, if the saturation temperature is exceeded, which is entirely possible for the larger magnetic-field strengths, then the flow is not a single-phase flow but a two-phase flow.

Conclusions

For the cases studied, we have found that while it appears that the laminar flow regime provides a conservative estimate of the maximum dimensionless temperature difference, when it comes to determining the maximum dimensional temperature difference, the flow regime is of critical importance. This agrees with previous work where we found that to reasonably estimate the total Joulean heating and total viscous dissipation, a full model, which includes turbulence, is necessary. Furthermore, from this study, it appears that for turbulent flows with large net currents and certain magnetic-field orientations the temperature dependence of the transport properties of the liquid metal must be taken into account.

Acknowledgments

The author would like to thank Dr. Samuel H. Brown and Dr. Neal A. Sondergaard of the Carderock Division, Naval Surface Warfare Center, for their insights and support. This research was sponsored by the Defense Advanced Research Projects Agency (DOD), Naval Technology Office, Submarine Technology Program.

References

Branover, H., Greenspan, E., Sukoriansky, S., and Talmage, G., 1986, "Turbulence and the Feasibility of Self-Cooled Liquid-Metal Blankets for Fusion Reactors," *Fusion Technology*, Vol. 10, No. 3, pp. 882–829.

Kalkan, A. K., and Talmage, G., 1993, "Heat Transfer in Liquid Metals With Electric Currents and Magnetic Fields: the Conduction Case," *International Journal of Heat and Mass Transfer*, in press.

Moon, T. J., and Walker, J. S., 1990, "Liquid Metal Flow Through a Sharp Elbow in the Plane of a Strong Magnetic Field," *Journal of Fluid Mechanics*, Vol. 213, pp. 397–418.

Stevens, O. H., Superczynski, M. J., Doyle, T. J., Harrison, H. J., and Messinger, H., 1977, "Superconducting Machinery for Naval Ship Propulsion," *IEEE Trans. Mag.*, Vol. 13, pp. 269–274.

Sukoriansky, S., 1987, "Local and Integral Characteristics of Turbulence in the Presence of a Magnetic Field and Without It," Ph.D. dissertation, Ben-Gurion University of the Negev, Israel.

Talmage, G., Walker, J. S., Brown, S. H., and Sondergaard, N. A., 1989, "Liquid-Metal Flows in Current Collectors for Homopolar Machines: Fully-Developed Solutions for Primary Azimuthal Velocity," *Physics of Fluids*, Vol. A1, No. 7, pp.1268–1278.

Talmage, G., Walker, J. S., Brown, S. H., Sondergaard, N. A., Branover, H., and Sukoriansky, S., 1990, "Magnetohydrodynamic Liquid-Metal Flows in a Rectangular Channel With an Axial Magnetic Field, a Moving Conducting Wall and Free Surfaces," *J. Appl. Phys.*, Vol. 68, No. 9, pp. 4446–4460.

Talmage, G., Walker, J. S., Brown, S. H., Sondergaard, N. A., Branover, H., and Sukoriansky, S., 1991, "Liquid-Metal Flows in Sliding Electrical Contacts With Arbitrary Magnetic Field Orientations," *Physics of Fluids*, Vol. 6, pp. 1657–1665.

Talmage, G., Walker, J. S., Brown, S. H., Sondergaard, N. A., Branover, H., and Sukoriansky, S., 1992, "Liquid-Metal Flows in Sliding Electrical Contacts: Solutions for Turbulent Primary Azimuthal Velocity," *Advances in Turbulence Studies*, H. Branover and Y. Unger, eds., *Progress in Astronautics and Aeronautics*, Vol. 149, pp. 165–189.

Impingement Cooling of an Isothermally Heated Surface With a Confined Slot Jet

Y. J. Chou[1,3] **and Y. H. Hung**[2,3]

Introduction

Jet impingement cooling is of importance in a variety of industrial applications, such as annealing of metal and plastic sheets, tempering of glass, cooling of electronics components, turbine blades, and drying of textiles, veneer, and paper. Detailed reviews of flow and heat transfer between impinging jets and solid surface have been given by Martin (1977), Downs and James (1987), and Polat et al. (1989). According to the literature survey, most of the existing research puts much emphasis on heat transfer characteristics of two-dimensional stagnation flow and impinging jets without confinement plate. Little information on laminar local heat transfer and fluid flow of impinging slot jets with confinement plate is presented; and the various factors affecting the local heat transfer behaviors along the heated target surface have not been systematically investigated. Therefore, the objectives of this study include: (1) to explore the effects of jet Reynolds number, ratio of separation distance to jet width, and jet exit-velocity profile on stagnation and local heat transfer characteristics in confined slot-jet impingement problems; and (2) to propose new Nu correlations for predicting stagnation and local heat transfer characteristics.

Theoretical Analysis

A confined slot jet normally impinging on an isothermally heated surface is considered in the present study. Two-dimensional, incompressible laminar forced convection is employed in the analysis. A Newtonian fluid with constant properties is assumed. Furthermore, the viscous dissipation and the compressibility effect in the energy equation are neglected.

Let

$$X = \frac{x}{W} \quad Y = \frac{y}{W} \quad U = \frac{uW}{\nu} \quad V = \frac{vW}{\nu}$$

$$P = \frac{pW^2}{\rho\nu^2} \quad \tau = \frac{\nu t}{W^2} \quad \theta = \frac{T - T_j}{T_w - T_j} \tag{1}$$

where x and y represent the coordinates parallel to and normal to the heated surface, respectively. u and v are the fluid velocity components in the x and y directions, respectively. W is the slot jet width. T_j and T_w are the jet exit temperature and the heated surface temperature, respectively.

With the above-mentioned assumptions, the general expression of the governing equations can be written in dimensionless form as follows:

$$\frac{\partial \psi}{\partial \tau} + \frac{\partial (U\psi)}{\partial X} + \frac{\partial (V\psi)}{\partial Y} = \frac{\partial}{\partial X}\left(\Gamma^* \frac{\partial \psi}{\partial X}\right) + \frac{\partial}{\partial Y}\left(\Gamma^* \frac{\partial \psi}{\partial Y}\right) + S^{\psi} \tag{2}$$

---

[1] Graduate Student.

[2] Professor.

[3] Department of Power Mechanical Engineering, National Tsing Hua University, Hsinchu, Taiwan 30043.

Contributed by the Heat Transfer Division of THE AMERICAN SOCIETY OF MECHANICAL ENGINEERS. Manuscript received by the Heat Transfer Division January 1993; revision received July 1993. Keywords: Augmentation and Enhancement, Electronic Equipment, Jets. Associate Technical Editor: F. P. Incropera.

Table 1 Dimensionless coefficients and source terms in Eq. (2)

Equation	ψ	Γ^*	S^ψ
Continuity	1	0	0
X-momentum	U	1	$-\partial P/\partial X$
Y-momentum	V	1	$-\partial P/\partial Y$
Energy	θ	1/Pr	0

where ψ represent dimensionless transported scalar properties. All the dimensionless coefficients and sources terms of Eq. (2) are defined in Table 1.

Since the present computational domain is symmetric, only half of the configuration is needed to simulate the problem. The corresponding dimensionless boundary conditions over all boundaries of the domain are briefly described in the following.

Temperature at the jet exit is taken to be uniform, i.e., $\theta = 0$. In addition, three types of velocity distribution such as uniform, Gaussian, and parabolic profiles at jet exit ($0 < X \leq 0.5$, $Y = H/W$) are employed in the present study, i.e.,

$$U=0,\ V=\begin{cases} -\mathrm{Re}_w & \text{(uniform)} \\ -V_{\max}\, e^{-4bX^2} & \text{(Gaussian)} \\ -1.5\ \mathrm{Re}_w\,(1-4X^2) & \text{(parabolic)} \end{cases} \tag{3}$$

where Re_w is defined as $\bar{v}_j W/\nu$; and $\bar{v}_j$ and W represent the average jet-exit velocity and jet width, respectively. H is the separation distance measured normally from the target surface to the slot jet.

Similar to the Gaussian profile presented by van der Meer (1987) for circular jets, a Gaussian profile, which stretches itself over the region of jet exit, is proposed in Eq. (3) and considered as another developing profile for study. The value of b is chosen such that $V = V_{\max}/2$ at $X = 0.5$, where $V_{\max}$ is the centerline velocity of the slot jet. Thus, under the condition of same mass flow rate for different jet-exit velocity profiles, the values of $V_{\max}$ and constant b in Eq. (3) can be obtained as 1.236 Re_w and 0.693, respectively, in the present study.

No-slip, no suction/blowing conditions, and zero temperature gradient are used at the insulated confinement surface ($X > 0.5$, $Y = H/W$). The conditions of transported properties are assumed to be invariant in the flow direction at the outflow boundary ($X = L/2W$, $0 < Y < H/W$), where L is the heated length of the target surface. In addition, no-slip, no suction/blowing and isothermal conditions are imposed at the heated target surface ($0 \leq X \leq L/2W$, $Y = 0$), i.e., $U = V = 0$, $\theta = 1$. At the axis of symmetry ($X = 0$, $0 < Y < H/W$), the U velocity is set to 0, and the gradients of all other variables are set to 0.

The above-mentioned governing equations can be integrated over the control volume and then discretized by using the power-law scheme with staggered grids. A time-marching procedure with a semi-implicit iterative algorithm, SIMPLEC, presented by van Doormaal and Raithby (1984), is implemented for steady-state solution in the present study.

Once the flow and thermal fields are obtained, the local Nusselt number can be evaluated with the following equations:

$$\mathrm{Nu}_x = \frac{h_x W}{\kappa} = -\left.\frac{\partial\theta}{\partial Y}\right|_{Y=0} \tag{4}$$

where h_x represents the local heat transfer coefficient on the target surface.

To achieve an acceptable numerical accuracy and to save CPU time, three different heated-surface lengths and four grid sizes were tested. From a comparison of the Nu_x results in the region of $0 \leq X \leq 10$, the dimensionless heated-surface length $L/W = 20$ and grid size 35 (in the X direction) × 46 (in the Y direction) were chosen for providing numerical results of high accuracy.

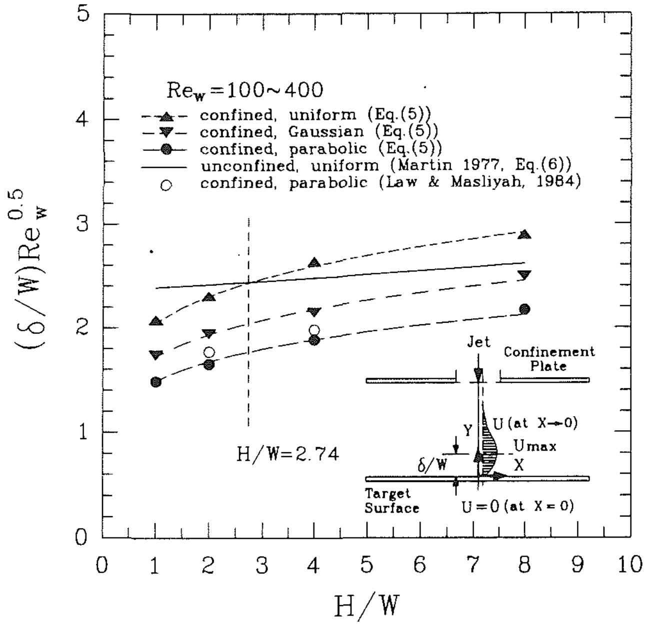

Fig. 1 Viscous boundary-layer thickness at stagnation line in confined jet impingement

Results and Discussion

The parameters studied are Prandtl number, Pr = 0.7, jet Reynolds numbers, Re_w = 100–400, and ratios of separation distance to jet width ranging from 1 to 8 in the present study.

Boundary Layer Thickness at Stagnation Line. As we know, it is very difficult to define a free-stream velocity just beyond the boundary layer, as the same used for two-dimensional flows or unconfined impinging-jet flows, in the present confined impinging-jet flows. To the authors' knowledge, the viscous boundary-layer thickness at the stagnation line for "confined" impinging-jet studies was defined only by Law and Masliyah (1984) in the existing literature. Law and Masliyah defined the thickness of the viscous boundary layer in the stagnation flow region as the distance from the impingement surface where the lateral velocity reaches 99 percent of $U_{\max}$, the maximum value of velocity component in the X direction for an individual profile of velocity component U. Therefore, based on Law and Masliyah's concept, a similar definition of viscous boundary-layer thickness at the stagnation line for the present confined-jet impingement study can be used. The boundary-layer thickness may be determined by the location of $Y = \delta/W$ where the value of U is maximum when $X \rightarrow 0$.

From the present numerical results for 48 cases, it is obvious that the δ/W distribution is a function of Re_w, H/W, and jet-exit velocity profile. The relationship among δ/W, Re_w, H/W, and jet-exit velocity profile can be found in the following expression:

$$\delta/W = C_1\ \mathrm{Re}_w^{-0.5}(H/W)^{0.17} \tag{5}$$

where C_1 = 2.048, 1.721, and 1.490 for the uniform, Gaussian, and parabolic velocity profiles, respectively.

As shown in Fig. 1, the average deviation of the predictions using Eq. (5) from the present numerical results is 5.75 percent. Besides, the numerical data for laminar confined slot-jet cases with a parabolic jet exit velocity profile presented by Law and Masliyah (1984) are chosen for comparison. The average de-

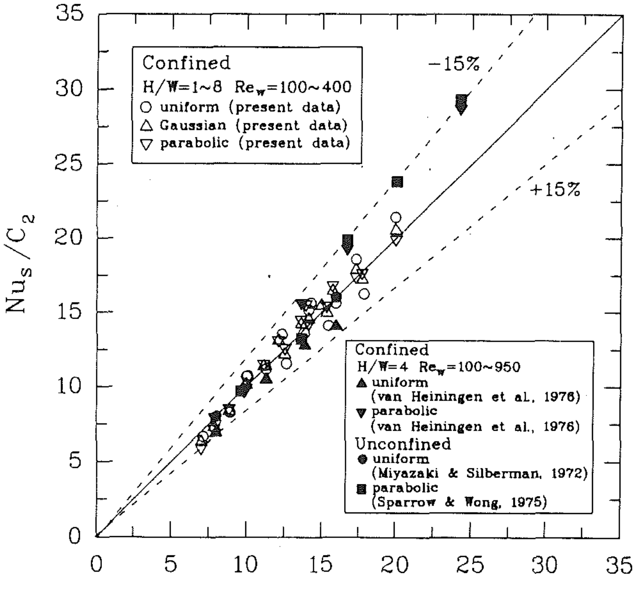

Fig. 2 Comparison of stagnation Nusselt numbers between confined and unconfined jet impingement cases

viation of the predictions using Eq. (5) for parabolic profile from Law and Masliyah's data is 7.89 percent. Furthermore, for real stagnation flows due to an impinging jet of finite jet width without plate confinement, the relative boundary-layer thickness, δ/W, was experimentally found and expressed in the following form (Martin, 1977):

$$\delta/W = 2.38/[\mathrm{Re}_w(1.02 - 0.024\ H/W)]^{1/2}, \qquad 1 \le H/W \le 10 \tag{6}$$

It is interesting to point out that when the ratio of separation distance to jet width is less than 2.74, the δ/W values for the present confined slot-jet cases under various jet-exit velocity profiles are usually smaller than those evaluated by Eq. (6) for unconfined slot-jet cases. The main reason is that the effect of the confinement plate will become significant on the flow acceleration right after the impingement when the ratio of separation distance to jet width is smaller than a certain value, say 2.74 in the present study.

Stagnation Heat Transfer. With the present numerical data, the Nusselt number at the stagnation line (Nu_s) can be correlated into the following two expressions:

$$\mathrm{Nu}_s = 1.176(\delta/W)^{-1} \tag{7}$$

and

$$\mathrm{Nu}_s = C_2\ \mathrm{Re}_w^{0.5}\ (H/W)^{-0.17} \tag{8}$$

where C_2 = 0.574, 0.683, and 0.789 for the uniform, Gaussian, and parabolic velocity profiles, respectively.

Equation (7) is exactly the same as that derived from the correlations for two-dimensional stagnation flow (Schlichting, 1979; Kays and Crawford, 1980). Additionally, all the present numerical results, the data reported by other researchers (Miyazaki and Silberman, 1972; Sparrow and Wong, 1975; van Heiningen et al., 1976), as well as the predictions using Eq. (8), are plotted in Fig. 2. From the results, it is notable that the average deviation for cases of uniform, Gaussian, and parabolic profiles are 6.45, 4.65, and 5.09 percent, respectively. The range of parametric validity for using Eq. (8) in the present study under three different jet-exit velocity profiles is $7 \le \mathrm{Re}_w^{0.5}\ (H/W)^{-0.17} \le 20$.

Furthermore, to explore the effect of jet exit velocity profile on heat transfer enhancement at the stagnation line, Eq. (8) clarifies that relative to results for a uniform velocity profile, both the Gaussian and parabolic profiles are found to enhance significantly Nu_s by about 19 and 37 percent, respectively. The enhancement of stagnation heat transfer due to nonuniform jet-exit velocity profile in the present cases of laminar submerged slot jet with confinement is lower than 44–48 percent, which was shown experimentally by Wolf et al. (1990) for turbulent free-surface slot water jet without confinement.

New Composite Nu_x Correlations. From the present results, the local Nusselt number in the wall jet region may be proposed to be composed of two limiting distributions, that is, one due to flow stagnation effect, and the other due to downstream wall effect. Therefore, a bell-like distribution, representing the heat transfer characteristics in the vicinity of stagnation line, may be proposed as

$$(\mathrm{Nu}_x)_s = \mathrm{Nu}_s \exp(-0.05\ X^2) \tag{9}$$

All the numerical data are fitted by Eq. (9) with a maximum deviation less than 5.5 percent in the region of $X \le 0.5$.

In addition, to investigate the local Nusselt number in the wall jet region, Pohlhausen's solution of local Nusselt number for a flat plate (Kays and Crawford, 1980) is used to compare with the present results. Pohlhausen's solution used in the present study can be expressed as

$$\mathrm{Nu}_x = 0.332\ \mathrm{Pr}^{1/3}\ (\mathrm{Re}_w/X)^{1/2} \tag{10}$$

As considering the wall jet region affected by the impinging jet, a scaling position in the X direction, where the velocity component perpendicular to the target surface drops to its mean value, is proposed effectively to render the plot independent of Pohlhausen's solutions for various jet-exit velocity profiles in the present study. Therefore, the scaling positions S_x, which can be evaluated from Eq. (3), are 0.50, 0.28, and 0.29 for the uniform, Gaussian, and parabolic velocity profiles, respectively. Consequently, the modified Pohlhausen solution, representing the characteristics in the downstream region, say $X \ge 3.5$, for different air jet-exit velocity profiles in the present study (Pr = 0.7), can be expressed as

$$(\mathrm{Nu}_x)_p = 0.295\ [\mathrm{Re}_w/(X - S_x)]^{1/2}, \quad X \ge 3.5 \tag{11}$$

Moreover, in the present confined slot-jet flow, as the flow changes its direction and the main flow motion becomes transverse, this is similar to a boundary-layer growth on a flat surface. Nevertheless, this is not true at the farther downstream location where the flow pattern indeed becomes a developed channel flow. The modified Pohlhausen solution may be considered to be valid for $3.5 \le X \le 10$ in the present study.

Using an approximate composite relation suggested by Churchill and Usagi (1972), a form for representing new Nu_x correlations in the wall jet region of confined slot-jet flow may hereby be expressed as

$$\mathrm{Nu}_x/\mathrm{Re}_w^{0.5} = [(\mathrm{Nu}_x/\mathrm{Re}_w^{0.5})_s^n + (\mathrm{Nu}_x/\mathrm{Re}_w^{0.5})_p^n]^{1/n} \tag{12}$$

where $(\mathrm{Nu}_x)_s$ and $(\mathrm{Nu}_x)_p$ are expressed in Eqs. (9) and (11), respectively.

As fitted with the present numerical results in the region of $0 \le X \le 10$, the optimum value of n shown in Eq. (12) can be found as −5, i.e., Eq. (12) becomes

$$\mathrm{Nu}_x/\mathrm{Re}_w^{0.5} = [(\mathrm{Nu}_x/\mathrm{Re}_w^{0.5})_s^{-5} + (\mathrm{Nu}_x/\mathrm{Re}_w^{0.5})_p^{-5}]^{-1/5} \tag{13}$$

Comparisons between the present data and the predictions with Eq. (13) are made and shown in Fig. 3. Satisfactory agreements have been achieved. The average deviations for cases with uniform, Gaussian, and parabolic velocity profiles (294 data points) are 3.48, 5.61, and 6.86 percent, respectively.

Concluding Remarks

The main conclusions from the present results can be sum-

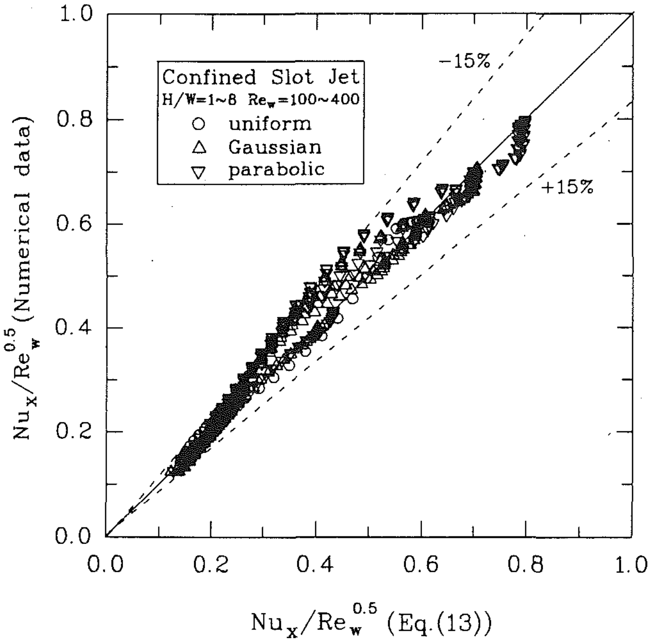

Fig. 3 Comparison of local Nusselt numbers between numerical results and Eq. (13)

marized as follows: (1) The ratio of viscous boundary-layer thickness at the stagnation line to jet width is inversely proportional to jet Reynolds number in a 0.5 power, while it is proportional to the ratio of separation distance to jet width in a 0.17 power. Among three different jet-exit velocity profiles, the case with a parabolic profile has the minimum viscous boundary-layer thickness. (2) New correlations of Nusselt number at the stagnation line for different jet-exit velocity profiles are proposed in terms of Re_w and H/W for confined impinging slot jets. The range of parametric validity for using these correlations is $7 \leq \mathrm{Re}_w^{0.5} (H/W)^{-0.17} \leq 20$. (3) New composite Nu_x correlations in the wall jet region of confined slot-jet flow under different jet-exit velocity profiles are postulated. Comparisons between the present data and the predictions are made with a satisfactory agreement.

Acknowledgments

The authors wish to thank Professors I. Mudawar and R. Viskanta at Purdue University for their valuable comments in this study.

References

Churchill, S. W., and Usagi, R., 1972, "A General Expression for the Correlation of Rates of Transfer and Other Phenomena," *AIChE J.*, Vol. 18, pp. 1121-1128.

Doormaal, J. P. van, and Raithby, G. D., 1984, "Enhancement of the SIMPLE Method for Predicting Incompressible Fluid Flow," *Numerical Heat Transfer*, Vol. 7, No. 2, pp. 147-163.

Downs, S. J., and James, E. H., 1987, "Jet Impingement Heat Transfer—a Literature Survey," ASME Paper No. 87-HT-35.

Heiningen, A. R. P. van, Mujumdar, A. S., and Douglas, W. J. M., 1976, "Numerical Prediction of the Flow Field and Impingement Heat Transfer Caused by a Laminar Slot Jet," ASME JOURNAL OF HEAT TRANSFER, Vol. 98, pp. 654-658.

Kays, W. M., and Crawford, M. E., 1980, *Convective Heat and Mass Transfer*, 2nd ed., McGraw-Hill, New York.

Law, H. S., and Masliyah, J. H., 1984, "Numerical Prediction of the Flow Field Due to a Confined Laminar Two-Dimensional Submerged Jet," *Computers & Fluids*, Vol. 12, pp. 199-215.

Martin, H., 1977, "Heat and Mass Transfer Between Impinging Gas Jets and Solid Surfaces," in: *Advances in Heat Transfer*, Academic Press, New York, Vol. 13, pp. 1-60.

Meer, T. H. van der, 1987, "Heat Transfer From Impinging Flame Jets," Doctoral Thesis, Technical University of Delft, The Netherlands.

Miyazaki, H., and Silberman, E., 1972, "Flow and Heat Transfer on a Flat Plate Normal to a Two-Dimensional Laminar Jet Issuing From a Nozzle of Finite Height," *Int. J. Heat Mass Transfer*, Vol. 15, pp. 2097-2107.

Polat, S., Huang, B., Mujumdar, A. S., and Douglas, W. J. M., 1989, "Numerical Flow and Heat Transfer Under Impinging Jets: A Review," in: *Annual Review of Numerical Fluid Mechanics and Heat Transfer*, C. L. Tien and T. C. Chawla, eds., Vol. 2, Hemisphere Publishing Corp., pp. 157-197.

Schlichting, H., 1979, *Boundary Layer Theory*, 7th ed., McGraw-Hill, New York.

Sparrow, E. M., and Wong, T. C., 1975, "Impingement Transfer Coefficients Due to Initially Laminar Slot Jets," *Int. J. Heat Mass Transfer*, Vol. 18, pp. 597-605.

Wolf, D. H., Viskanta, R., and Incropera, F. P., 1990, "Local Convective Heat Transfer From a Heated Surface to a Planar Jet of Water With a Nonuniform Velocity Profile," ASME JOURNAL OF HEAT TRANSFER, Vol. 112, pp. 899-905.

Correlating Equations for Impingement Cooling of Small Heat Sources With Multiple Circular Liquid Jets

D. J. Womac,[1] F. P. Incropera,[1] and S. Ramadhyani[1]

Nomenclature

A = heater surface area $= L^2$
A_r = ratio of impingement zone surface area to total area
d_i = diameter of free-surface jet in the impingement plane
d_n = nozzle diameter
g = gravitational acceleration
$\bar{h}$ = average heat transfer coefficient
k = thermal conductivity
L = heater length
L_e = length of nozzle unit cell for an array
L_n = nozzle length
L^* = characteristic length given by Eq. (2) or (3)
N = number of jets in an array
$\overline{\mathrm{Nu}}$ = average Nusselt number
P_n = nozzle pitch
Pr = Prandtl number
q = heat transfer rate
r = radial coordinate
Re_{d_i} = impingement Reynolds number $= V_i d_i/\nu$
Re_{d_n} = nozzle Reynolds number $= V_n d_n/\nu$
Re_{L^*} = wall jet Reynolds number $= V_i L^*/\nu$
S = nozzle-to-heater separation distance
$\bar{T}_s$ = average surface temperature
T_n = fluid temperature at nozzle discharge
V_i = impingement velocity
V_n = nozzle exit velocity
$\dot{V}$ = volumetric flow rate
ν = kinematic viscosity

---

[1] Heat Transfer Laboratory, School of Mechanical Engineering, Purdue University, West Lafayette, IN 47907.

Contributed by the Heat Transfer Division of THE AMERICAN SOCIETY OF MECHANICAL ENGINEERS. Manuscript received by the Heat Transfer Division June 1993; revision received September 1993. Keywords: Electronic Equipment, Forced Convection, Jets. Associate Technical Editor: R. Viskanta.

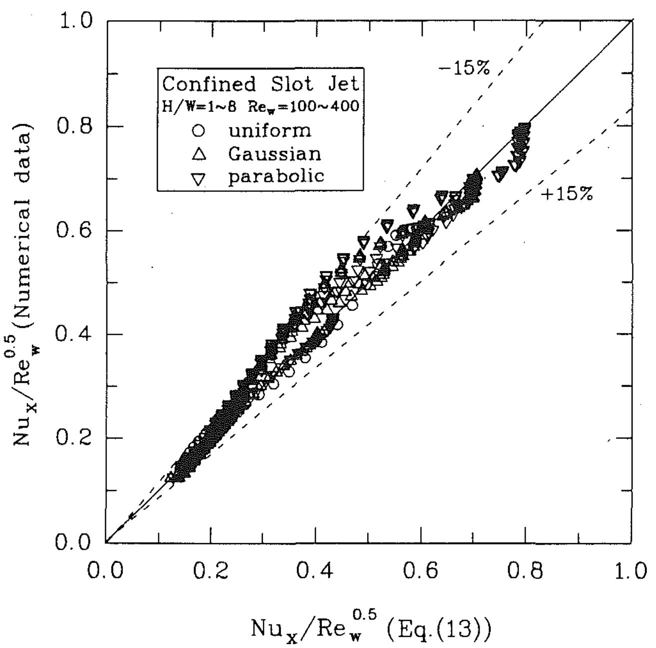

Fig. 3 Comparison of local Nusselt numbers between numerical results and Eq. (13)

marized as follows: (1) The ratio of viscous boundary-layer thickness at the stagnation line to jet width is inversely proportional to jet Reynolds number in a 0.5 power, while it is proportional to the ratio of separation distance to jet width in a 0.17 power. Among three different jet-exit velocity profiles, the case with a parabolic profile has the minimum viscous boundary-layer thickness. (2) New correlations of Nusselt number at the stagnation line for different jet-exit velocity profiles are proposed in terms of Re_w and H/W for confined impinging slot jets. The range of parametric validity for using these correlations is $7 \leq \mathrm{Re}_w^{0.5}\,(H/W)^{-0.17} \leq 20$. (3) New composite Nu_x correlations in the wall jet region of confined slot-jet flow under different jet-exit velocity profiles are postulated. Comparisons between the present data and the predictions are made with a satisfactory agreement.

Acknowledgments

The authors wish to thank Professors I. Mudawar and R. Viskanta at Purdue University for their valuable comments in this study.

References

Churchill, S. W., and Usagi, R., 1972, "A General Expression for the Correlation of Rates of Transfer and Other Phenomena," *AIChE J.*, Vol. 18, pp. 1121-1128.

Doormaal, J. P. van, and Raithby, G. D., 1984, "Enhancement of the SIMPLE Method for Predicting Incompressible Fluid Flow," *Numerical Heat Transfer*, Vol. 7, No. 2, pp. 147-163.

Downs, S. J., and James, E. H., 1987, "Jet Impingement Heat Transfer—a Literature Survey," ASME Paper No. 87-HT-35.

Heiningen, A. R. P. van, Mujumdar, A. S., and Douglas, W. J. M., 1976, "Numerical Prediction of the Flow Field and Impingement Heat Transfer Caused by a Laminar Slot Jet," ASME JOURNAL OF HEAT TRANSFER, Vol. 98, pp. 654-658.

Kays, W. M., and Crawford, M. E., 1980, *Convective Heat and Mass Transfer*, 2nd ed., McGraw-Hill, New York.

Law, H. S., and Masliyah, J. H., 1984, "Numerical Prediction of the Flow Field Due to a Confined Laminar Two-Dimensional Submerged Jet," *Computers & Fluids*, Vol. 12, pp. 199-215.

Martin, H., 1977, "Heat and Mass Transfer Between Impinging Gas Jets and Solid Surfaces," in: *Advances in Heat Transfer*, Academic Press, New York, Vol. 13, pp. 1-60.

Meer, T. H. van der, 1987, "Heat Transfer From Impinging Flame Jets," Doctoral Thesis, Technical University of Delft, The Netherlands.

Miyazaki, H., and Silberman, E., 1972, "Flow and Heat Transfer on a Flat Plate Normal to a Two-Dimensional Laminar Jet Issuing From a Nozzle of Finite Height," *Int. J. Heat Mass Transfer*, Vol. 15, pp. 2097-2107.

Polat, S., Huang, B., Mujumdar, A. S., and Douglas, W. J. M., 1989, "Numerical Flow and Heat Transfer Under Impinging Jets: A Review," in: *Annual Review of Numerical Fluid Mechanics and Heat Transfer*, C. L. Tien and T. C. Chawla, eds., Vol. 2, Hemisphere Publishing Corp., pp. 157-197.

Schlichting, H., 1979, *Boundary Layer Theory*, 7th ed., McGraw-Hill, New York.

Sparrow, E. M., and Wong, T. C., 1975, "Impingement Transfer Coefficients Due to Initially Laminar Slot Jets," *Int. J. Heat Mass Transfer*, Vol. 18, pp. 597-605.

Wolf, D. H., Viskanta, R., and Incropera, F. P., 1990, "Local Convective Heat Transfer From a Heated Surface to a Planar Jet of Water With a Nonuniform Velocity Profile," ASME JOURNAL OF HEAT TRANSFER, Vol. 112, pp. 899-905.

Correlating Equations for Impingement Cooling of Small Heat Sources With Multiple Circular Liquid Jets

D. J. Womac,[1] F. P. Incropera,[1] and S. Ramadhyani[1]

Nomenclature

A = heater surface area $= L^2$
A_r = ratio of impingement zone surface area to total area
d_i = diameter of free-surface jet in the impingement plane
d_n = nozzle diameter
g = gravitational acceleration
$\bar{h}$ = average heat transfer coefficient
k = thermal conductivity
L = heater length
L_e = length of nozzle unit cell for an array
L_n = nozzle length
L^* = characteristic length given by Eq. (2) or (3)
N = number of jets in an array
$\overline{\mathrm{Nu}}$ = average Nusselt number
P_n = nozzle pitch
Pr = Prandtl number
q = heat transfer rate
r = radial coordinate
Re_{d_i} = impingement Reynolds number $= V_i d_i/\nu$
Re_{d_n} = nozzle Reynolds number $= V_n d_n/\nu$
Re_{L^*} = wall jet Reynolds number $= V_i L^*/\nu$
S = nozzle-to-heater separation distance
$\bar{T}_s$ = average surface temperature
T_n = fluid temperature at nozzle discharge
V_i = impingement velocity
V_n = nozzle exit velocity
$\dot{V}$ = volumetric flow rate
ν = kinematic viscosity

---

[1] Heat Transfer Laboratory, School of Mechanical Engineering, Purdue University, West Lafayette, IN 47907.

Contributed by the Heat Transfer Division of THE AMERICAN SOCIETY OF MECHANICAL ENGINEERS. Manuscript received by the Heat Transfer Division June 1993; revision received September 1993. Keywords: Electronic Equipment, Forced Convection, Jets. Associate Technical Editor: R. Viskanta.

Introduction

With heat fluxes in microelectronic devices approaching 100 W/cm^2, there is growing interest in cooling by means of single-phase, liquid jet impingement. Jiji and Dagan (1988), for example, considered impingement of a circular free-surface jet (fluorocarbon liquid 3M FC-77 and water) on a 12.7 mm × 12.7 mm surface, and heat transfer data were correlated in terms of the nozzle diameter and exit velocity, the heater length, and the fluid properties. The correlation overpredicted data obtained by Womac et al. (1993), who were able to collapse their results by using an area-weighted combination of separate correlations for the impingement and wall jet regions of the surface. For small nozzle diameters and exit velocities, Womac et al. (1993) found heat transfer to be attenuated by bulk warming of the thin fluid sheet flowing over the surface. Moreover, for small diameters and large exit velocities, fluid splashed from the free surface near the impingement region and the attendant removal of fluid from the radial flow was, in certain cases, sufficient to reduce convection heat transfer. For large diameters and small exit velocities, the effect of gravitational acceleration on the velocity and diameter of the impinging jet was significant and heat transfer was enhanced.

Womac et al. (1993) also obtained heat transfer data for submerged jets, and results were influenced by location of the heater surface relative to the potential core of the jet. However, if the surface was well within the potential core ($S/d_n \lesssim 4$), heat transfer was only weakly dependent on S. For $\mathrm{Re}_{d_n} \gtrsim 4000$, turbulence generated in the shear layer of the submerged jet yielded convection coefficients that exceeded those associated with the free-surface jet. Results for the submerged jets were also correlated by superimposing separate correlations for the impingement and wall jet regions.

Multiple jet impingement on a single surface has the potential to enhance cooling effectiveness and to improve temperature uniformity across the surface. However, local surface conditions are influenced by jet interactions which occur after impingement. Experiments have largely been performed for arrays of air (submerged) jets.

Gardon and Cobonpue (1961) measured local heat transfer coefficients for 5×5 and 7×7 arrays of circular air jets and found maxima at locations midway between adjoining jets and minima at the midpoints of diagonals between jets. Kercher and Tabakoff (1970) investigated the effects of nozzle diameter, d_n, pitch, P_n, separation distance, S, and crossflow for air jet impingement on a surface that was constrained on three sides, thereby forcing spent fluid to exit in a single direction. Due to increasing crossflow effects, local heat transfer coefficients were found to decrease in the direction of the exiting fluid. For fixed V_n, the average Nusselt number increased with decreasing P_n and d_n. From measurements performed with a 4×4 array of air jets, Hollworth and Berry (1978) also found the average Nusselt number to increase with decreasing P_n but to be independent of d_n. For the large nozzle pitches of the study ($P_n/d_n \geq 10$), jet interaction effects were negligible.

Jiji and Dagan (1988) experimentally investigated arrays of four or nine free-surface jets impinging on a single heat source and on 2×2 and 3×3 heat source arrays. The jets emerged from nozzles consisting of straight tubes of diameters $d_n = 0.5$ mm and 1.0 mm and length $L_n = 6.4$ mm. For the same total flow rate and nozzle diameter, surface temperature uniformity was observed to increase with an increase in the number of jets, and the average Nusselt number was correlated by the expression

$$\frac{\overline{\mathrm{Nu}}_L}{\mathrm{Pr}^{1/3}} = 3.84\left[0.008\,\frac{L}{d_n}\,N+1\right]\mathrm{Re}_{d_n}^{1/2} \tag{1}$$

where N is the number of jets. The effect of jet spacing in the array was not considered.

The objective of this study is to consider the efficacy of using arrays of free-surface or submerged liquid jets to cool a small, chip-like heat source. The data are correlated by obtaining area-weighted combinations of separate correlations associated with impingement and wall jet regions.

Experimental Methods

Nozzles were machined to provide 2×2 and 3×3 arrays of circular jets. The nozzles consisted of straight tubes with a contoured inlet and a fixed length of $L_n = 4.78$ mm. Two nozzle diameters were tested for both arrays ($d_n = 0.513$, 1.02 mm), with a single pitch for the 3×3 array ($P_n = 5.08$ mm). For the 2×2 array, a single pitch ($P_n = 10.16$ mm) was tested for $d_n = 0.513$ mm and two pitches ($P_n = 6.35$, 10.16 mm) were tested for $d_n = 1.02$ mm. The length-to-diameter ratio of the nozzles, L_n/d_n, ranged from 4.69 to 9.32, providing partially developed laminar or turbulent velocity profiles at the nozzle exit for Reynolds numbers in the range $500 \lesssim \mathrm{Re}_{d_n} \lesssim 20{,}000$. Experiments were performed for water ($\mathrm{Pr} \approx 7$) and a fluorocarbon liquid (3 M FC-77, $\mathrm{Pr} \approx 24$), with volumetric flow rates in the range $0.2 \lesssim \dot{V} \lesssim 5.0$ liters/min.

The heater module consisted of a 12.7-mm-square, 3-mm-thick copper block, which was flush mounted to a fiberglass substrate. Omegatherm 201, a thermal paste of $k = 2.4$ W/m•K, was used to provide good thermal contact between a 12.7-mm-square electric resistance heater and the back surface of the block. Seven copper-constantan thermocouples were routed through the block to measure temperature at various locations on the surface. The average heat transfer coefficient

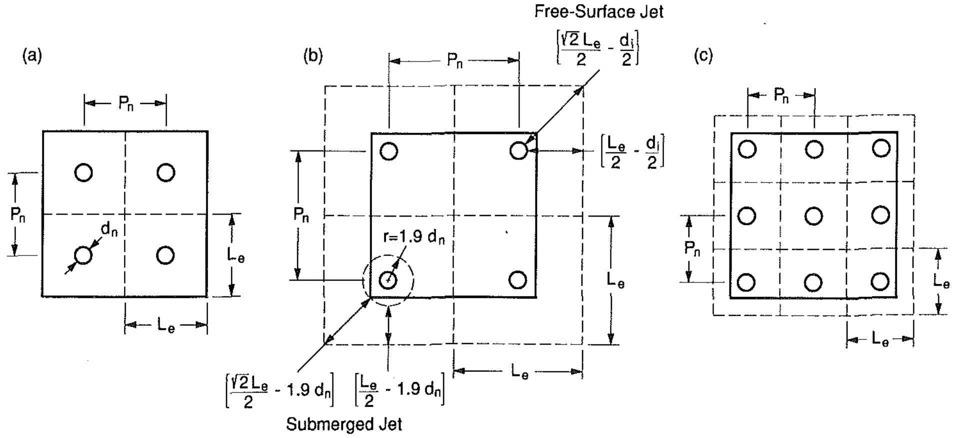

Fig. 1 Unit cells for nozzle arrays: (*a*) 2 × 2 array with $P_n = L_e = 6.35$ mm; (*b*) 2 × 2 array with $P_n = L_e = 10.16$ mm; (*c*) 3 × 3 array with $P_n = L_e = 5.08$ mm

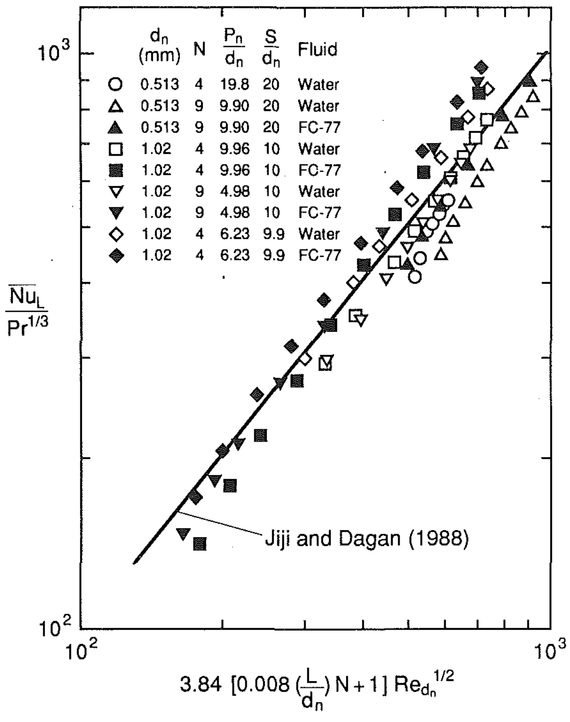

Fig. 2 Comparison of data for the free-surface jet arrays with the correlation of Jiji and Dagan (1988)

was determined from $\overline{h}=q/A(\overline{T}_s-T_n)$, where q is the power supplied to the heater (substrate losses were predicted to be less than 2 percent). A complete discussion of the experimental apparatus and procedures is provided elsewhere (Womac et al., 1993).

As shown in Fig. 1, an effective heater length L_e was used to characterize a unit cell for the multiple jet arrangements. In each case the length of the unit cell for a nozzle is equivalent to the nozzle pitch ($P_n=L_e$), and in two cases unit cells for outer jets extend beyond the edge of the heater. The effective heater length may be used to obtain a reasonable first estimate of the average distance L^* associated with radial flow in the wall-jet regions of the heater. It may be expressed as

$$L^*=\frac{[(\sqrt{2}L_e/2)-(d_i/2)]+[(L_e/2)-(d_i/2)]}{2} \tag{2}$$

for the free-surface jets, and

$$L^*=\frac{[(\sqrt{2}L_e/2)-1.9d_n]+[(L_e/2)-1.9d_n]}{2} \tag{3}$$

for the submerged jets. Under submerged conditions, the jet spreads radially as its momentum is transferred to the ambient fluid, and the extent of the impingement region exceeds the nozzle diameter. Gardon and Cobonpue (1961) observed a marked increase in the local heat transfer coefficient for a submerged jet at $r=1.9\,d_n$, and the increase was attributed to termination of the favorable pressure gradient in the impingement region and the onset of turbulence in the wall jet region. Hence, in this study the impingement region is assumed to extend to a radial location of $1.9\,d_n$.

Experimental Results

Free-Surface Jets. Experiments in which S/d_n was varied over the range from 5 to 10 revealed that, to within the experimental uncertainty, heat transfer was unaffected by the nozzle separation distance S (Womac, 1989). However, as shown by Womac (1989), for a prescribed volumetric flow rate, the largest average convection coefficients corresponded to arrays with the smallest nozzle diameter ($d_n=0.513$ mm) and, for a fixed diameter, to arrays with the smallest number of nozzles ($N=4$). The increase in heat transfer with decreasing d_n and N is due to an increase in the jet velocity. Similarly, if, for fixed $\overline{V}$ and d_n, results for $N=4$ are contrasted with those previously obtained for a single jet (Womac et al., 1993), an increase in $\overline{h}$ is found to correspond to the increased value of V_n resulting from a reduction in N.

In all cases, $\overline{h}$ decreased with decreasing $\overline{V}$, and at low flow rates for the smallest nozzle diameter, the reduction became more pronounced due to bulk heating of the fluid (a condition that occurs when the thermal boundary layer reaches the free surface of the wall jet). At high flow rates of FC-77 for $N=4$ and $d_n=0.513$ mm, fluid splattered from the free surface near the impingement region, reducing the thickness of the liquid film and allowing the thermal boundary layer to reach the free surface, thereby reducing $\overline{h}$. Bulk heating and splattering effects have been reported for impingement by a single jet (Womac et al., 1993).

For fixed values of $\overline{V}$, $N=4$, and $d_n=1.02$ mm, larger values of $\overline{h}$ were obtained for the smaller pitch (Fig. 2a), and hence the smaller value of L^*. In fact, for a prescribed value of V_n, the general trend was one of increasing $\overline{h}$ with decreasing L^*. The trend is attributed to an increase in jet interference due to the smaller P_n and/or to a reduction in the wall jet region.

In a first attempt to collapse the data of this study, results that were unaffected by bulk warming were compared with the correlation developed by Jiji and Dagan (1988). As shown in Fig. 2, the data deviate from the correlation by ±30 percent, and for the same configuration and nozzle diameter, the data are not collapsed by a Prandtl number exponent of 1/3. The deviation is unlikely to be due to differences in nozzle geometries, which are virtually identical for the two studies.

An alternative correlation was obtained by adopting the superposition procedure previously used for a single jet (Womac et al., 1993). In particular, the Nusselt number was evaluated as an area-weighted combination of correlations associated with the impingement and wall jet regions. Respectively, the correlations are of the form

$$\overline{\mathrm{Nu}}_{d_i}=C_1\mathrm{Re}_{d_i}^{m}\,\mathrm{Pr}^{0.4} \tag{4}$$

and

$$\overline{\mathrm{Nu}}_L{}^*=C_2\mathrm{Re}_L^{n}{}^*\mathrm{Pr}^{0.4} \tag{5}$$

where $V_i=(V_n^2+2\,gS)^{1/2}$, $d_i=(d_n^2V_n/V_i)^{1/2}$, and L^* is given by Eq. (2). The area-weighted combination of these expressions is

$$\frac{\overline{\mathrm{Nu}}_L}{\mathrm{Pr}^{0.4}}=C_1\mathrm{Re}_{d_i}^{m}\left(\frac{L}{d_i}\right)A_r+C_2\mathrm{Re}_{L^*}^{n}\left(\frac{L}{L^*}\right)(1-A_r) \tag{6}$$

where $A_r=N\pi d_i^2/4L^2$. Since flow conditions in proximity to the stagnation point should be equivalent for single and multiple free-surface jet impingement, values of $C_1=0.516$ and $m=0.5$ were chosen from previous results for a single jet (Womac et al., 1993). Using a least-squares technique, values of $C_2=0.344$ and $n=0.579$ were then found to fit all of the multiple jet data unaffected by bulk warming to within ±17 percent (Fig. 3). The average error is ±5.83 percent, and the standard deviation is 7.52 percent.

Submerged Jets. Several trends were consistent with those observed for the free-surface jets. For example, for fixed $\overline{V}$, $\overline{h}$ increased with decreasing N, d_n and L^*. Since submerged jets spread radially with axial distance from the nozzle exit, mutual interactions may occur before impingement, inducing turbulence and enhancing heat transfer. The increase in $\overline{h}$ with decreasing L^* is consistent with the findings of Kercher and Tabakoff (1970) for arrays of circular air jets. Again the trend

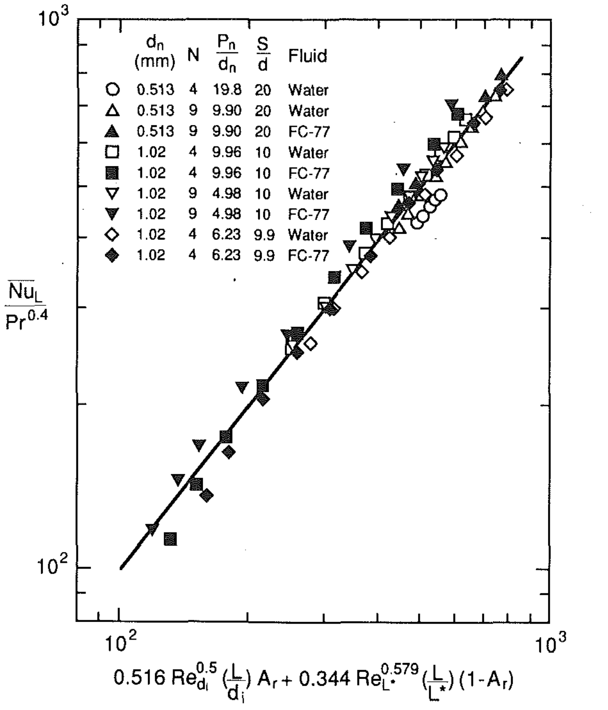

Fig. 3 Area-weighted correlation of data for an array of free-surface jets

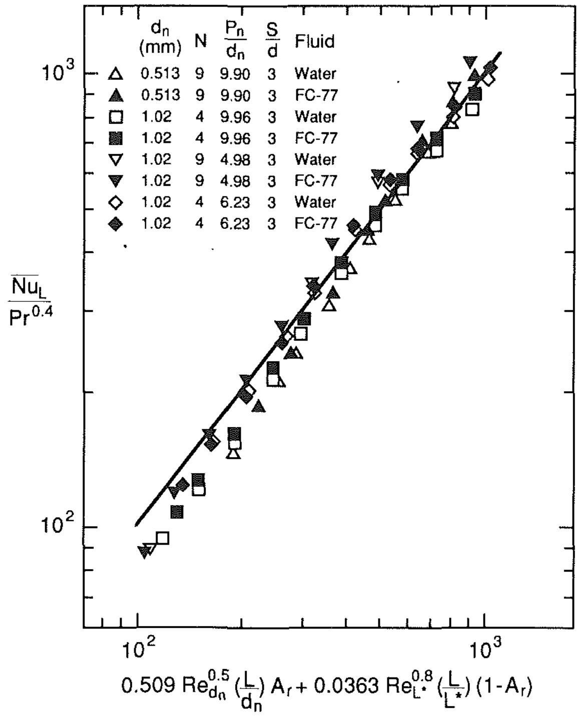

Fig. 4 Area-weighted correlation of data for an array of submerged jets

may be attributed to the increased interference caused by smaller jet-to-jet spacing and/or to the shorter wall jet region.

The effect of jet spacing was examined for $1 \leq S/d_n \leq 10$, and the general trend was one of reduced heat transfer at small separation distances for widely spaced jets and at a large separation distances for closely spaced jets (Womac, 1989). Specifically, heat transfer was adversely affected for $P_n/d_n \gtrsim 7$, $S/d_n \approx 1$; $P_n/d_n \gtrsim 19$, $S/d_n \lesssim 2$; and $P_n/d_n \lesssim 7$, $S/d_n \gtrsim 10$.

For $d_n = 0.513$ mm and equivalent values of V_n, heat transfer data for submerged jets of FC-77 with $S/d_n = 3$ were in good agreement with results for the free-surface jets, except for the upper range of velocities in FC-77 ($Re_{d_n} \gtrsim 4500$), where splattering reduced heat transfer for the free-surface jets. For water, heat transfer for the submerged jets slightly exceeded that for the free surface jets over the entire Reynolds number range. For the lower Reynolds number range ($Re_{d_n} \lesssim 4500$), the effect is attributed to a reduction in $\bar{h}$ for the free-surface jets due to bulk warming. For $Re_{d_n} \gtrsim 4500$, the effect is attributed to heat transfer enhancement associated with turbulence produced by enhanced jet spreading and jet-to-jet interactions. Similar trends characterized results for the larger nozzle diameter, although for most conditions differences between results obtained for the free-surface jets and submerged jets (with $S/d_n = 3$) were small (Womac, 1989).

As with the free-surface jet, an attempt was made to correlate data through an area-weighted combination of correlations for the impingement and wall jet regions.

$$\overline{Nu}_L = C_1 Re_{d_n}^m \left(\frac{L}{d_n}\right) A_r + C_2 Re_{L^*}^{\,n} \left(\frac{L}{L^*}\right)(1-A_r) \qquad (7)$$

where $A_r = N\pi\,(1.9\,d_n)^2/L^2$ and the average length of the wall jet region in a unit cell is given by Eq. (3). Because the impingement zone of a particular jet is assumed to extend to $r = 1.9\,d_n$, A_r may exceed unity and L^* may be less than zero. In such cases, values of 1 and 0 were assigned to A_r and C_2, respectively. Consistent with the approach taken for a single jet (Womac et al., 1993), values of $m = 0.5$ and $n = 0.8$ were selected on the presumption that laminar and turbulent flows characterized the impingement and wall jet regions, respectively. Working only with data (Womac, 1989) for which $\bar{h}$ was independent of nozzle separation ($2 \leq S/d_n \leq 4$), a least-squares technique was used to obtain values of $C_1 = 0.509$ and $C_2 = 0.0363$. The correlation is plotted in Fig. 4 with data obtained for $S/d_n = 3$. The correlation is within ±30 percent of all of the data for which it was determined, although it consistently overpredicts the data in the lower range of Reynolds numbers. The average error is ±9.93 percent, and the standard deviation is 12.23 percent. For a prescribed Reynolds number, Nusselt numbers obtained for $N = 4$ and $d_n = 0.513$ mm were up to a factor of two smaller than those obtained for the other operating conditions and could not be satisfactorily correlated. Pending the availability of additional data, Eq. (7) should not be used outside the limited range of conditions for which it was obtained.

Summary

Experiments were performed to investigate single-phase heat transfer from a 12.7 mm × 12.7 mm heat source to 2×2 and 3×3 arrays of free-surface and submerged jets. Based on data reported elsewhere (Womac, 1989), average heat transfer coefficients $\bar{h}$ for the free-surface jets were independent of nozzle spacing, while heat transfer to the submerged jets was degraded for small ($S/d_n \lesssim 2$) and large ($S/d_n \gtrsim 10$) separations, depending on the nozzle pitch (P_n/d_n). Moreover, results for the submerged jets exceeded or were approximately equal to those for the free-surface jets, depending on operating conditions. For a fixed volumetric flow rate, $\bar{h}$ increased with decreasing nozzle diameter and nozzle pitch for both the free-surface and submerged cases. Using an area-weighted combination of expressions for the impingement and wall jet regions, separate correlations were developed for the free-surface and submerged jets.

Acknowledgments

Appreciation is expressed to the IBM Corporation for its support of this work and to the 3M Corporation for supplying the test fluid (FC-77).

References

Gardon, R., and Cobonpue, J., 1961, "Heat Transfer Between a Flat Plate and Jets of Air Impinging on It," *Proc. Second Int. Heat Transfer Conf.*, pp. 454-460.

Hollworth, B. R., and Berry, R. D., 1978, "Heat Transfer From Arrays of Impinging Jets With Large Jet-to-Jet Spacing," ASME JOURNAL OF HEAT TRANSFER, Vol. 100, pp. 352-357.

Jiji, L. M., and Dagan, Z., 1988, "Experimental Investigation of Single Phase Multi-jet Impingement Cooling of an Array of Microelectronic Heat Sources," *Cooling Technology for Electronic Equipment*, W. Aung, ed., Hemisphere Publishing Corporation, Washington, DC, pp. 333-351.

Kercher, D. M., and Tabakoff, W., 1970, "Heat Transfer by a Square Array of Round Air Jets Impinging Perpendicular to a Flat Surface Including the Effect of Spent Air," ASME *Journal of Engineering for Power*, Vol. 92, pp.73-82.

Womac, D. J., 1989, "Single Phase Axisymmetric Liquid Jet Impingement Cooling of Discrete Heat Sources," MS Thesis, Purdue University, W. Lafayette, IN.

Womac, D. J., Ramadhyani, S., and Incropera, F. P., 1993, "Correlating Equations for Impingement Cooling of Small Heat Sources With Single Circular Liquid Jets," ASME JOURNAL OF HEAT TRANSFER, Vol. 115, pp. 106-115.

Enhancement of Liquid Jet Impingement Heat Transfer With Surface Modifications

D. Priedeman,[1] V. Callahan,[1] and B. W. Webb[1]

Introduction

Jet impingement is a common method of heating or cooling solid surfaces because of its high transport characteristics. While impinging jets have been studied extensively, the use of extended surfaces with impinging jets has attracted only minimal attention. Extended surfaces are successfully used to enhance convective heat transfer in a wide variety of applications through both an increase in the convecting surface area and the modification of the heat transfer coefficient due to the presence of the surface modifications. The body of impinging jet literature is large. Most early work concentrated on jets impinging on smooth, flat surfaces. Work in the area has been summarized in recent reviews (Downs and James, 1987; Hrycak, 1981; Martin, 1977; Livingood and Hrycak, 1973). Previous work reporting techniques for the enhancement of jet impingement heat transfer is limited. A variety of schemes designed to enhance the heat transfer have been used with varying degrees of success (Downs and James, 1987). The few investigations of jet impingement combined with extended surfaces have reported generally promising results. Several studies investigating the use of surface modifications for air jet impingement include those of Ali Khan et al. (1982), Hrycak (1984), Obot and Trabold (1987), and Hansen and Webb (1993), while others have reported enhancement of liquid jets using jet or surface modifications (Fleishman and Yuen, 1988; Sullivan et al., 1992; Heindel et al., 1993). This study reports experimental results of liquid jet impingement heat transfer from several different configurations of arrays of extended surfaces using both water and FC-77 as coolant.

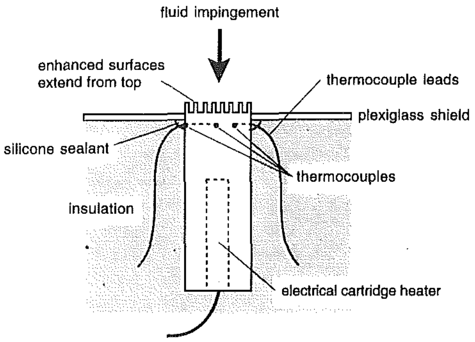

Fig. 1 Schematic of heater module

Experimental Method

The experimental apparatus consisted of a closed-loop liquid delivery system, flow meters, heat exchanger, jet nozzle, and heater assembly with test surface. The heater assembly was housed in a large sealed containment vessel, which was also used to collect the spent fluid and redirect it back to the heat exchanger and pump. The heat exchanger consisted of cooling coils through which cooling water from the building supply was circulated. The fluids used in this study were circulated around the cooling coils prior to being directed back to the pump. Two rotameter-type flow meters with different ranges were connected in parallel to optimize the flow rate measurement accuracy. The flow meters were calibrated accurate to within 5 percent. The nozzle used primarily in the experiments was an aluminum tube of 7.0 mm inside diameter. The tube was 70 diameters long, insuring fully developed flow over the range of Reynolds numbers studied.

The heater assembly consisted of a cylindrical, aluminum heater module wrapped in fiber-glass insulation to prevent heat loss, as shown in Fig. 1. A heater assembly was constructed for each test surface, including the smooth reference surface. Without the surface modifications, each cylindrical heater module was 19.1 mm in diameter and 50.8 m long. The upper surface of the module served as the impingement test surface, and its base was positioned flush with a 6.3-mm-thick plexiglass shield into which the aluminum heater was pressed. This fit was sealed with silicone sealant on its underside to prevent liquid from penetrating the fiberglass insulation and electrical and instrumentation wiring beneath the wetted surface. The bottom of the aluminum cylinder was bored to accept a 225 W cartridge heater, which was powered by a HP 6030A DC power supply.

The heater module temperature was determined from three T-type thermocouples positioned 3.2 mm below the test base surface at the centerline, half-radius, and outer edge of each heater module. Those thermocouples on the interior of the module were inserted and epoxied in blind holes drilled just large enough to accommodate the 32 gage thermocouple wires and insulation. The actual test surface base temperature was determined from these measurements made below the surface using a one-dimensional Fourier conduction approximation at each radial location. In addition to the surface temperature correction, there was non-negligible radial variation in temperature. The test surface base temperature variation was approximated by fitting the three calculated base surface temperatures to a parabola. The average module base temperature, $\overline{T}_b$, was then determined from an area average of this parabolic temperature variation. The liquid jet temperature, T_j, was measured with a single thermocouple inserted into the tubing upstream of the jet nozzle. The minimum average temperature difference, $\overline{T}_b - T_j$, in all experiments was 9.0 °C, although this temperature difference was more typically 12-15 °C.

---

[1] Department of Mechanical Engineering, Brigham Young University, Provo, UT 84602.

Contributed by the Heat Transfer Division and presented at the ASME Winter Annual Meeting, New Orleans, Louisiana, November 28-December 3, 1993. Manuscript received by the Heat Transfer Division June 1993; revision received September 1993. Keywords: Finned Surfaces, Forced Convection, Jets. Associate Technical Editor: A. Faghri.

References

Gardon, R., and Cobonpue, J., 1961, "Heat Transfer Between a Flat Plate and Jets of Air Impinging on It," *Proc. Second Int. Heat Transfer Conf.*, pp. 454-460.

Hollworth, B. R., and Berry, R. D., 1978, "Heat Transfer From Arrays of Impinging Jets With Large Jet-to-Jet Spacing," ASME JOURNAL OF HEAT TRANSFER, Vol. 100, pp. 352-357.

Jiji, L. M., and Dagan, Z., 1988, "Experimental Investigation of Single Phase Multi-jet Impingement Cooling of an Array of Microelectronic Heat Sources," *Cooling Technology for Electronic Equipment*, W. Aung, ed., Hemisphere Publishing Corporation, Washington, DC, pp. 333-351.

Kercher, D. M., and Tabakoff, W., 1970, "Heat Transfer by a Square Array of Round Air Jets Impinging Perpendicular to a Flat Surface Including the Effect of Spent Air," ASME *Journal of Engineering for Power*, Vol. 92, pp. 73-82.

Womac, D. J., 1989, "Single Phase Axisymmetric Liquid Jet Impingement Cooling of Discrete Heat Sources," MS Thesis, Purdue University, W. Lafayette, IN.

Womac, D. J., Ramadhyani, S., and Incropera, F. P., 1993, "Correlating Equations for Impingement Cooling of Small Heat Sources With Single Circular Liquid Jets," ASME JOURNAL OF HEAT TRANSFER, Vol. 115, pp. 106-115.

Enhancement of Liquid Jet Impingement Heat Transfer With Surface Modifications

D. Priedeman,[1] V. Callahan,[1] and B. W. Webb[1]

Introduction

Jet impingement is a common method of heating or cooling solid surfaces because of its high transport characteristics. While impinging jets have been studied extensively, the use of extended surfaces with impinging jets has attracted only minimal attention. Extended surfaces are successfully used to enhance convective heat transfer in a wide variety of applications through both an increase in the convecting surface area and the modification of the heat transfer coefficient due to the presence of the surface modifications. The body of impinging jet literature is large. Most early work concentrated on jets impinging on smooth, flat surfaces. Work in the area has been summarized in recent reviews (Downs and James, 1987; Hrycak, 1981; Martin, 1977; Livingood and Hrycak, 1973). Previous work reporting techniques for the enhancement of jet impingement heat transfer is limited. A variety of schemes designed to enhance the heat transfer have been used with varying degrees of success (Downs and James, 1987). The few investigations of jet impingement combined with extended surfaces have reported generally promising results. Several studies investigating the use of surface modifications for air jet impingement include those of Ali Khan et al. (1982), Hrycak (1984), Obot and Trabold (1987), and Hansen and Webb (1993), while others have reported enhancement of liquid jets using jet or surface modifications (Fleishman and Yuen, 1988; Sullivan et al., 1992; Heindel et al., 1993). This study reports experimental results of liquid jet impingement heat transfer from several different configurations of arrays of extended surfaces using both water and FC-77 as coolant.

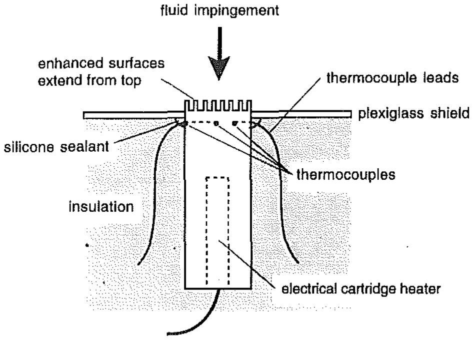

Fig. 1 Schematic of heater module

Experimental Method

The experimental apparatus consisted of a closed-loop liquid delivery system, flow meters, heat exchanger, jet nozzle, and heater assembly with test surface. The heater assembly was housed in a large sealed containment vessel, which was also used to collect the spent fluid and redirect it back to the heat exchanger and pump. The heat exchanger consisted of cooling coils through which cooling water from the building supply was circulated. The fluids used in this study were circulated around the cooling coils prior to being directed back to the pump. Two rotameter-type flow meters with different ranges were connected in parallel to optimize the flow rate measurement accuracy. The flow meters were calibrated accurate to within 5 percent. The nozzle used primarily in the experiments was an aluminum tube of 7.0 mm inside diameter. The tube was 70 diameters long, insuring fully developed flow over the range of Reynolds numbers studied.

The heater assembly consisted of a cylindrical, aluminum heater module wrapped in fiber-glass insulation to prevent heat loss, as shown in Fig. 1. A heater assembly was constructed for each test surface, including the smooth reference surface. Without the surface modifications, each cylindrical heater module was 19.1 mm in diameter and 50.8 m long. The upper surface of the module served as the impingement test surface, and its base was positioned flush with a 6.3-mm-thick plexiglass shield into which the aluminum heater was pressed. This fit was sealed with silicone sealant on its underside to prevent liquid from penetrating the fiberglass insulation and electrical and instrumentation wiring beneath the wetted surface. The bottom of the aluminum cylinder was bored to accept a 225 W cartridge heater, which was powered by a HP 6030A DC power supply.

The heater module temperature was determined from three T-type thermocouples positioned 3.2 mm below the test base surface at the centerline, half-radius, and outer edge of each heater module. Those thermocouples on the interior of the module were inserted and epoxied in blind holes drilled just large enough to accommodate the 32 gage thermocouple wires and insulation. The actual test surface base temperature was determined from these measurements made below the surface using a one-dimensional Fourier conduction approximation at each radial location. In addition to the surface temperature correction, there was non-negligible radial variation in temperature. The test surface base temperature variation was approximated by fitting the three calculated base surface temperatures to a parabola. The average module base temperature, $\overline{T}_b$, was then determined from an area average of this parabolic temperature variation. The liquid jet temperature, T_j, was measured with a single thermocouple inserted into the tubing upstream of the jet nozzle. The minimum average temperature difference, $\overline{T}_b - T_j$, in all experiments was 9.0 °C, although this temperature difference was more typically 12-15 °C.

---

[1] Department of Mechanical Engineering, Brigham Young University, Provo, UT 84602.

Contributed by the Heat Transfer Division and presented at the ASME Winter Annual Meeting, New Orleans, Louisiana, November 28-December 3, 1993. Manuscript received by the Heat Transfer Division June 1993; revision received September 1993. Keywords: Finned Surfaces, Forced Convection, Jets. Associate Technical Editor: A. Faghri.

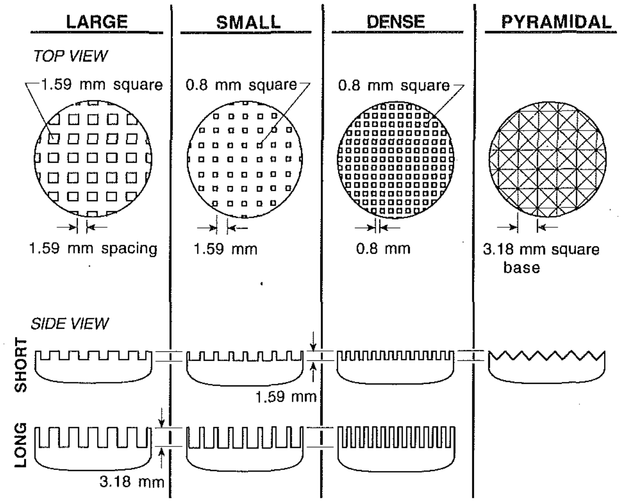

Fig. 2 Schematic of modified surfaces investigated

All thermocouple voltages were acquired digitally to an accuracy of 1 μV. The total heat transfer, Q, was determined from the electrical dissipation in the cartridge heaters, which was calculated from Ohm's law using voltage and current measurements recorded during each test run. Conduction losses from the heater module were estimated from a numerical model of the system, and were found to be negligible.

The surface modifications investigated were machined as integral parts of each cylindrical aluminum module and protruded beyond the base length. The surface modifications studied here are illustrated schematically in Fig. 2. Seven different extended surface configurations were studied. Six of the extended surface configurations studied featured fins of square cross section. Two different fin sizes of 1.59 mm and 0.8 mm square cross section with 1.59 mm interfin spacing were studied. These will be hereafter referred to as *large* and *small* fins, respectively. The smaller fins (0.8 mm square) were also studied for 0.8 mm interfin spacing, and will be termed *dense*. For each of these square cross-sectional fins two different fin lengths (1.59 mm and 3.18 mm) were investigated, and will be described as *short* and *long*. Hence, the designation *short small fins* will refer to the 0.8 mm square-cross-section fins spaced 1.59 mm apart and of 1.59 mm length; *long dense fins* refer to 0.8 mm square fins spaced 0.8 mm apart and of 3.18 mm length. The seventh extended surface element, termed *pyramidal*, consisted of an array of pyramids 1.59 mm tall with a square base 3.18 mm on a side. Data were also collected for a smooth surface (without fins) to serve as reference against which the heat transfer for the modified surface configurations were compared. The ratio of total surface area of each extended surface configuration (A_t) to the reference smooth surface area ($A_{t,s}$) is shown in Table 1.

Table 1 Ratio of total surface area (A_t) to the smooth surface area ($A_{t,s}$) for the surface modification configurations studied

Surface	$A_t/A_{t,s}$
Smooth	1.0
Short large	2.13
Long large	3.26
Short small	1.80
Long small	2.56
Short dense	2.92
Long dense	4.84
Pyramidal	1.55

Data were obtained to report average heat transfer coefficient and system effectiveness and efficiency as a function of jet Reynolds number (Re $= \rho V_j d/\mu$ where V_j is the average jet exit velocity) for all test surfaces. Heat transfer results for each test surface are presented in terms of an average Nusselt number based on the liquid jet exit diameter, d, defined as

$$\overline{\mathrm{Nu}} = \overline{h}d/k \tag{1}$$

The average Nusselt number as defined here is not indicative of *total* heat transfer rate from the fin/base system, but is a measure of the average heat transfer *coefficient*, which prevails over the entire fin/base surface. For the smooth surface, the average heat transfer coefficient was determined from

$$h = Q/A_t(\overline{T}_b - T_j) \tag{2}$$

where A_t for the smooth reference surface is $A_t = A_{t,s} = \pi D^2/4$, where D is the diameter of the heater module. For the modified test surfaces the average heat transfer coefficient was approximated from an iterative solution of an expression for the total heat transfer from the fin/base system:

$$Q = \overline{h}A_b(\overline{T}_b - T_j) + \sum_{i=1}^{N} M_i \frac{\sinh(m_i H) + (\overline{h}/m_i k_f)\cosh(m_i H)}{\cosh(m_i H) + (\overline{h}/m_i k_f)\sinh(m_i H)} \tag{3}$$

where $M_i = (\overline{h}P_i A_{c,i})^{1/2}(\overline{T}_b - T_j)$, $m_i = (\overline{h}P_i/k_f A_{c,i})^{1/2}$, and H and P_i are the height and perimeter of each fin, respectively. The index, i, in the summation of Eq. (3) varies from 1 to n, the total number of fins on the test surface. Thus, the first term in Eq. (3) represents the heat transfer from the exposed base (non-fin) area, and the second term accounts for heat transfer from the N fins using the fin equation for each. For the square cross-sectional fins studied, the non-square cross section of the fins on the test surface perimeter was accounted for through modification of the coefficients M_i and m_i. It should be emphasized that the use of Eq. (3) is only an approximation, since this equation assumes a one-dimensional temperature distribution in the fin. This assumption may not be accurate for the high liquid jet heat transfer coefficients and some of the relatively large cross-sectional fins studied. Nevertheless, the value of $\overline{h}$ determined from Eq. (3) sheds light on the influence of the several fin configurations studied on the transport mechanisms. Total heat transfer enhancement for each extended surface geometry was evaluated in terms of an overall system effectiveness, ϵ. This is defined as the ratio of system heat transfer with extended surfaces (Q) to heat transfer without extended surfaces (Q_{smooth}) for the same base surface-to-jet temperature difference:

$$\epsilon = Q/Q_{\mathrm{smooth}} \tag{4}$$

The smooth surface heat transfer was determined as a least-squares regression of experimental average Nusselt number data for the smooth surface, which took the form $\overline{\mathrm{Nu}} = a\mathrm{Re}^m$. The value of Q_{smooth} was then calculated for any Reynolds number of interest from the correlation for $\overline{\mathrm{Nu}}$ using Eq. (2). Equation (4) reflects the overall effectiveness of the fin/base system, and should not be confused with the effectiveness of the individual fins. Note again that while the average Nusselt number characterizes the influence of surface modifications on average heat transfer coefficient, the overall system effectiveness illustrates the effect of modifications on total heat transfer from the fin/base system. The overall efficiency of the fin-base system was estimated and is reported elsewhere (Priedeman et al., 1993).

The maximum uncertainty in the average Nusselt numbers is dominated by the uncertainty in the test surface base temperature, and is estimated to be 10 percent at 20:1 odds (Kline and McClintock, 1953). The maximum uncertainty for jet Reynolds numbers was determined to be 6 percent.

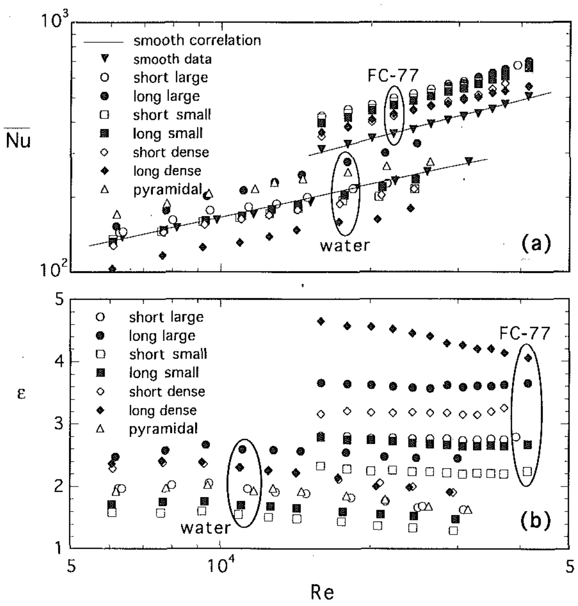

Fig. 3 Variation of the average Nusselt number, $\overline{Nu}$, and overall system effectiveness, ϵ, with Reynolds number for all surfaces investigated and both fluids

Results and Discussion

Measurements were made for the modified surface configurations described in the foregoing paragraphs in the approximate Reynolds number range $6000 \leq Re \leq 40{,}000$ at a nozzle-to-base surface spacing of five diameters for two different fluids, water and FC-77, a dielectric liquid proposed for use in immersion cooling of electronic equipment manufactured by the 3M Company.

Figure 3 illustrates the variation of the average Nusselt number and overall system effectiveness with Reynolds number for all modified surfaces investigated and for the two working fluids. The water ($Pr \approx 9$) and FC-77 ($Pr \approx 28$) data for the smooth reference surface collected as part of this study follow the functional relationship

$$\overline{Nu}/Pr^{1/3} = 1.126Re^{0.46} \qquad (5)$$

with an average and maximum error of 1.7 and 4.5 percent, respectively. Thermophysical properties are based on the liquid temperature at the jet exit. This correlation is shown separately with the experimental smooth surface data for both fluids in Fig. 3(*a*). The experimentally determined average Nusselt number data of this study were found to be within 10 percent of the empirical correlation developed in a previous independent investigation (Stevens and Webb, 1991).

Recall that the average Nusselt number illustrates the dependence of the average heat transfer coefficient on the modified surface configuration, rather than the total heat transfer. Comparison of the $\overline{Nu}$ data for the modified surfaces with that of the smooth surface reveals the extent to which the surface roughness elements influence the heat transfer coefficient. Those data lying above the smooth surface correlation indicate surface modifications that enhance the heat transfer coefficient, while surfaces for which $\overline{Nu}$ lies below suggest a degradation in the transport mechanism. It should be noted, however, that the total heat transfer dissipated is a complex combination of the average heat transfer coefficient and total surface area. Figure 3(*a*) and Eq. (5) reveal that the average Nusselt number is roughly dependent on $Re^{1/2}$ for both smooth and modified surfaces. Such is the functional dependence of $\overline{Nu}$ on Re for smooth surface jet impingement (Martin, 1977). The addition of surface roughness elements does not appreciably change the functional dependence of $\overline{Nu}$ on Re. Since the heat transfer coefficient in turbulent, parallel flow applications is roughly proportional to $Re^{0.8}$, this suggests that the heat transfer coefficient is impingement-dominated, either normally on the fin tips and surface base or on the lateral faces of the fins as the fluid exits radially through the fin array.

Figure 3(*b*) illustrates that all modified surfaces exhibit enhanced heat transfer coefficient (relative to the smooth surface) for the FC-77 fluid. By contrast, only the modified surfaces with effectively large interfin spacing (short large, long large, and pyramidal fins) feature average heat transfer coefficient higher than the smooth surface for water. Apparently the fins disrupt the relatively thick momentum boundary layer for the higher Prandtl number dielectric fluid, resulting in enhanced heat transfer coefficient for all surfaces. The smooth-surface transport is so effective for the water that, in some cases, the addition of surface modifications results in reduction of the average Nusselt number. For both fluids, the average Nusselt number is highest for the large, sparsely populated fins, and lowest for the densely packed fins. The fluid penetration plays a significant role in the transport in these systems. The interfin spacing for the dense fins is so small that fluid is unable to penetrate the heat transfer surfaces effectively. By contrast, the large fins reveal large lateral surface area and interfin spacing, resulting in effective impingement-type cooling over much of the heater convective surface area. Whereas the results of this study on varying fin size suggest relatively large fins with large interfin spacing are optimum, the results of Sullivan et al. (1992) for sawcut surfaces of much smaller, more closely packed fins of higher thermal conductivity reveal augmentation also for small, densely packed fins. The results of these two studies suggest that the heat transfer enhancement is a complex function of fin geometry, fin material, and impingement fluid.

For the most part, overall system effectiveness is not a strong function of Reynolds number. There is, however, a generally decreasing trend of ϵ with Re. The modified surfaces' ability to enhance the overall heat transfer reduces with increasing jet Reynolds number. The slight but noticeable local maximum in the ϵ versus Re data for water at $Re \approx 10^4$ was explained previously (Priedeman et al., 1993).

Recall that the effectiveness reflects the increase in total heat transfer due to the addition of fins for the same base area. The surface modifications influence both the average heat transfer coefficient and the total convective surface area. For the fins studied, the ratio of total surface area to the reference surface area ranges from 1.55 for the pyramidal fin configuration to 4.84 for the long dense fins. Figure 3(*a*) revealed that the presence of the fins can result in both positive and negative changes in $\bar{h}$. The changes in average heat transfer coefficient and total surface area combine to effect a change in the overall heat transfer relative to the smooth surface. Comparing the area ratios of Table 1 with the overall system effectiveness of Fig. 3(*b*) reveals that, with the exception of the long dense fins, the FC-77 experiences heat transfer enhancement relative to the smooth surface by a factor greater than the increase in total heater surface area. This is a consequence of the increase in $\bar{h}$ for these modified surfaces seen in the $\overline{Nu}$ data for FC-77 in Fig. 3(*a*). By contrast, the increase in total heat transfer for the water jet is generally lower than the increase in convective surface area due to the addition of the fins. Recall that for the water jet, the addition of surface modifications resulted in either an increase or decrease in $\overline{Nu}$, depending on fin type. It should be finally noted from Fig. 3(*b*) that significant increases in total heat transfer can be achieved for the same heater base area and jet Reynolds number for both water and FC-77. Heat transfer rates can be increased nearly threefold for the water jet, and nearly fivefold for the FC-77. These enhancements are important in light of the already high transport characteristics of liquid impinging jets.

In conclusion, the average Nusselt number for the water experiments was seen to increase above the smooth reference value for some surface modifications, and decrease for others.

Increases in $\overline{\mathrm{Nu}}$ were observed for all modified surface configurations for the dielectric liquid. Enhancement of the total heat transfer, as compared to the smooth surface, was demonstrated by a factor ranging from 1.3 to nearly 3 for the water, and 2.2 to nearly 5 for the FC-77.

Acknowledgments

This work was sponsored by the U.S. National Science Foundation under Grant No. CBT-8552493.

References

Ali Khan, M. M., Kasagi, N., Hirata, M., and Nishiwaki, N., 1982, "Heat Transfer Augmentation in an Axisymmetric Impinging Jet," *Proceedings of the 7th International Heat Transfer Conference*, Paper FC6.3, pp. 363-368.

Downs, S. T., and James, E. H., 1987, "Jet Impingement Heat Transfer—A Literature Survey," ASME Paper No. 87-HT-35.

Fleishman, R. V., and Yuen, W. W., 1988, "Mesh Enhanced Force Convection Heat Transfer for High Heat Flux Applications," *Proceedings of 1988 National Heat Transfer Conference*, Vol. 1, H. R. Jacobs, ed., ASME, New York, pp. 653-660.

Hansen, L. G., and Webb, B. W., 1993, "Air Jet Impingement Heat Transfer From Modified Surfaces," *International Journal of Heat and Mass Transfer*, Vol. 36, pp. 889-998.

Heindel, T. J., Ramadhyani, S., Incropera, F. P., and Campo, A., 1993, "Surface Enhancement of a Heat Source Exposed to a Circular Liquid Jet With Annular Collection of the Spent Fluid," in: *Topics in Heat Transfer*, M. Toner et al., eds., ASME, New York, pp. 111-118.

Hrycak, P., 1981, "Heat Transfer From Impinging Jets—A Literature Review," AFWAL-TR-81-3504, Flight Dynamics Laboratory, Wright-Patterson AFB, OH.

Hrycak, P., 1984, "Heat Transfer From Impinging Jets to a Flat Plate With Conical and Ring Protuberances," *International Journal of Heat and Mass Transfer*, Vol. 27, pp. 2145-2154.

Livingood, J. N. B., and Hrycak, P., 1973, "Impingement Heat Transfer From Turbulent Air Jets to Flat Plates—A Literature Survey," NASA TM X-2778.

Kline, S. J., and McClintock, F. A., 1953, "Describing Uncertainties in Single-Sample Experiments," *Mechanical Engineering*, Jan., pp. 3-12.

Martin, H., 1977, "Heat and Mass Transfer Between Impinging Gas Jets and Solid Surfaces," *Advances in Heat Transfer*, Vol. 13, Academic Press, New York, pp. 1-60.

Obot, N. T., and Trabold, T. A., 1987, "Impingement Heat Transfer Within Arrays of Circular Jets: Part II—Effects of Crossflow in the Presence of Roughness Elements," ASME *Journal of Turbomachinery*, Vol. 109, pp. 594-601.

Priedeman, D., Callahan, V., and Webb, B. W., 1993, "Enhanced Surface Liquid Jet Impingement Heat Transfer," in: *Enhanced Cooling Techniques for Electronics Applications*, S. V. Garimella et al., eds., ASME, New York, pp. 43-48.

Stevens, J., and Webb, B. W., 1991, "Local Heat Transfer Coefficients Under an Axisymmetric, Single-Phase Liquid Jet," ASME JOURNAL OF HEAT TRANSFER, Vol. 113, pp. 71-78.

Sullivan, P. F., Ramadhyani, S., and Incropera, F. P., 1992, "Use of Smooth and Roughened Spreader Plates to Enhance Impingement Cooling of Small Heat Sources With Single Circular Liquid Jets," in: *Topics in Heat Transfer*, M. Toner et al., eds., ASME, New York, pp. 103-110.

Heat Transfer Correlation for Reactor Riser in Mixed Convection Air Flow

G. Fu,[1] N. E. Todreas,[2] P. Hejzlar,[2] and M. J. Driscoll[2]

Introduction

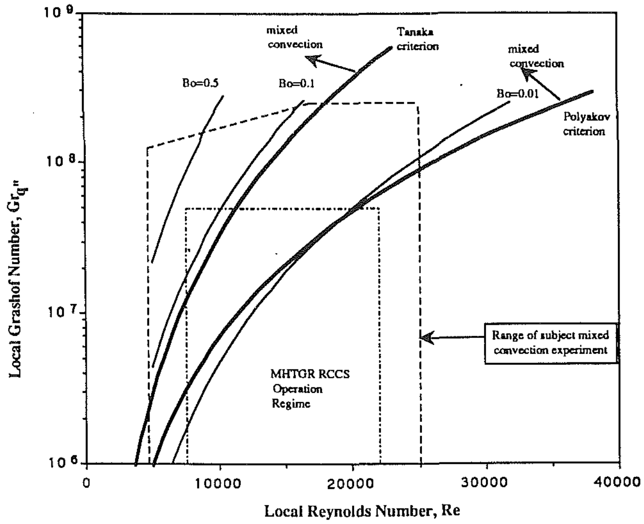

Fig. 1 Experiment range compared to MHTGR operating regime

The Modular High-Temperature Gas-Cooled Reactor (MHTGR) is one of the next generation power reactors currently being developed in the United States under Department of Energy sponsorship. A major emphasis in the development of this concept is improvement of safety margins by use of passive safety systems. An important feature of the MHTGR design is the use of an array of riser tubes in the reactor cavity to provide a passive decay heat removal path from the core to ambient air. The design of this Reactor Cavity Cooling System (RCCS) requires attention, since the system may operate under mixed convection conditions—a regime not yet well understood. Accordingly, the objective of the present work was to determine the heat transfer coefficient inside the riser under its projected operating conditions, and provide the designers with an effective design correlation for the range of interest based on mixed convection characteristics. We used calculated plant conditions at about 100 hours after occurrence of a loss of coolant accident (LOCA) as the reference case. At this time in the transient it was estimated that an average 800 W/m^2 heat flux would be imposed on the riser wall, and a nearly 200 °C air temperature increase would happen inside the riser. The operating regime of the RCCS system is illustrated in Fig. 1. It should be noted that the RCCS operates not at a point on the figure; rather, it always operates along a trajectory. This is due to the air temperature rise and, therefore, property changes, along the heated flow direction.

Figure 1 also illustrates criteria commonly used to determine the operating regime of the RCCS system. Although the principle upon which to establish a criterion for onset of mixed convection is clear, i.e., when buoyancy effects have a measurable influence on the flow field, where the boundaries should be drawn is far less clear. Different investigators have their own criterion based on how they define the importance of the buoyancy effect on the flow field. The Petukhov and Polyakov (1988) criterion represents a conservative estimate. It is based on the deviation of Nu from its forced convection value by more than 1 percent, i.e.,

$$\mathrm{Gr}_{q''} > \frac{1.3\times 10^{-4}\mathrm{Re}^{2.75}\mathrm{Pr}[\mathrm{Re}^{0.125}+2.4(\mathrm{Pr}^{0.667}-1)]}{\log_{10}\mathrm{Re}+1.15\log_{10}(5\mathrm{Pr}+1)+0.5\mathrm{Pr}-1.8} \quad \text{for } \mathrm{Pr}\geq 0.5 \qquad (1)$$

Tanaka's criterion (Tanaka et al., 1987), on the other hand, is based on the Nusselt number reaching 80 percent of the forced convection Nusselt number. Jackson and his co-workers (Cotton and Jackson, 1978) utilized a dimensionless buoyancy number, Bo, to measure the degree of mixed convection:

$$\mathrm{Bo} = \frac{8\times 10^4 \mathrm{Gr}_{q''}}{\mathrm{Re}^{3.425}\mathrm{Pr}^{0.8}} \qquad (2)$$

---

[1] S3 Technologies, Columbia, MD 21045.

[2] Department of Nuclear Engineering, Massachusetts Institute of Technology, Cambridge, MA 02139.

Contributed by the Heat Transfer Division and presented at the National Heat Transfer Conference, Minneapolis, Minnesota, July 28-31, 1991. Manuscript received by the Heat Transfer Division June 1992; revision received August 1993. Keywords: Mixed Convection. Associate Technical Editor: J. H. Kim.

Increases in $\overline{Nu}$ were observed for all modified surface configurations for the dielectric liquid. Enhancement of the total heat transfer, as compared to the smooth surface, was demonstrated by a factor ranging from 1.3 to nearly 3 for the water, and 2.2 to nearly 5 for the FC-77.

Acknowledgments

This work was sponsored by the U.S. National Science Foundation under Grant No. CBT-8552493.

References

Ali Khan, M. M., Kasagi, N., Hirata, M., and Nishiwaki, N., 1982, "Heat Transfer Augmentation in an Axisymmetric Impinging Jet," *Proceedings of the 7th International Heat Transfer Conference*, Paper FC6.3, pp. 363–368.

Downs, S. T., and James, E. H., 1987, "Jet Impingement Heat Transfer—A Literature Survey," ASME Paper No. 87-HT-35.

Fleishman, R. V., and Yuen, W. W., 1988, "Mesh Enhanced Force Convection Heat Transfer for High Heat Flux Applications," *Proceedings of 1988 National Heat Transfer Conference*, Vol. 1, H. R. Jacobs, ed., ASME, New York, pp. 653–660.

Hansen, L. G., and Webb, B. W., 1993, "Air Jet Impingement Heat Transfer From Modified Surfaces," *International Journal of Heat and Mass Transfer*, Vol. 36, pp. 889–998.

Heindel, T. J., Ramadhyani, S., Incropera, F. P., and Campo, A., 1993, "Surface Enhancement of a Heat Source Exposed to a Circular Liquid Jet With Annular Collection of the Spent Fluid," in: *Topics in Heat Transfer*, M. Toner et al., eds., ASME, New York, pp. 111–118.

Hrycak, P., 1981, "Heat Transfer From Impinging Jets—A Literature Review," AFWAL-TR-81-3504, Flight Dynamics Laboratory, Wright-Patterson AFB, OH.

Hrycak, P., 1984, "Heat Transfer From Impinging Jets to a Flat Plate With Conical and Ring Protuberances," *International Journal of Heat and Mass Transfer*, Vol. 27, pp. 2145–2154.

Livingood, J. N. B., and Hrycak, P., 1973, "Impingement Heat Transfer From Turbulent Air Jets to Flat Plates—A Literature Survey," NASA TM X-2778.

Kline, S. J., and McClintock, F. A., 1953, "Describing Uncertainties in Single-Sample Experiments," *Mechanical Engineering*, Jan., pp. 3–12.

Martin, H., 1977, "Heat and Mass Transfer Between Impinging Gas Jets and Solid Surfaces," *Advances in Heat Transfer*, Vol. 13, Academic Press, New York, pp. 1–60.

Obot, N. T., and Trabold, T. A., 1987, "Impingement Heat Transfer Within Arrays of Circular Jets: Part II—Effects of Crossflow in the Presence of Roughness Elements," ASME *Journal of Turbomachinery*, Vol. 109, pp. 594–601.

Priedeman, D., Callahan, V., and Webb, B. W., 1993, "Enhanced Surface Liquid Jet Impingement Heat Transfer," in: *Enhanced Cooling Techniques for Electronics Applications*, S. V. Garimella et al., eds., ASME, New York, pp. 43–48.

Stevens, J., and Webb, B. W., 1991, "Local Heat Transfer Coefficients Under an Axisymmetric, Single-Phase Liquid Jet," ASME JOURNAL OF HEAT TRANSFER, Vol. 113, pp. 71–78.

Sullivan, P. F., Ramadhyani, S., and Incropera, F. P., 1992, "Use of Smooth and Roughened Spreader Plates to Enhance Impingement Cooling of Small Heat Sources With Single Circular Liquid Jets," in: *Topics in Heat Transfer*, M. Toner et al., eds., ASME, New York, pp. 103–110.

Heat Transfer Correlation for Reactor Riser in Mixed Convection Air Flow

G. Fu,[1] N. E. Todreas,[2] P. Hejzlar,[2] and M. J. Driscoll[2]

Introduction

The Modular High-Temperature Gas-Cooled Reactor (MHTGR) is one of the next generation power reactors currently being developed in the United States under Department of Energy sponsorship. A major emphasis in the development of this concept is improvement of safety margins by use of passive safety systems. An important feature of the MHTGR design is the use of an array of riser tubes in the reactor cavity to provide a passive decay heat removal path from the core to ambient air. The design of this Reactor Cavity Cooling System (RCCS) requires attention, since the system may operate under mixed convection conditions—a regime not yet well understood. Accordingly, the objective of the present work was to determine the heat transfer coefficient inside the riser under its projected operating conditions, and provide the designers with an effective design correlation for the range of interest based on mixed convection characteristics. We used calculated plant conditions at about 100 hours after occurrence of a loss of coolant accident (LOCA) as the reference case. At this time in the transient it was estimated that an average 800 W/m^2 heat flux would be imposed on the riser wall, and a nearly 200 °C air temperature increase would happen inside the riser. The operating regime of the RCCS system is illustrated in Fig. 1. It should be noted that the RCCS operates not at a point on the figure; rather, it always operates along a trajectory. This is due to the air temperature rise and, therefore, property changes, along the heated flow direction.

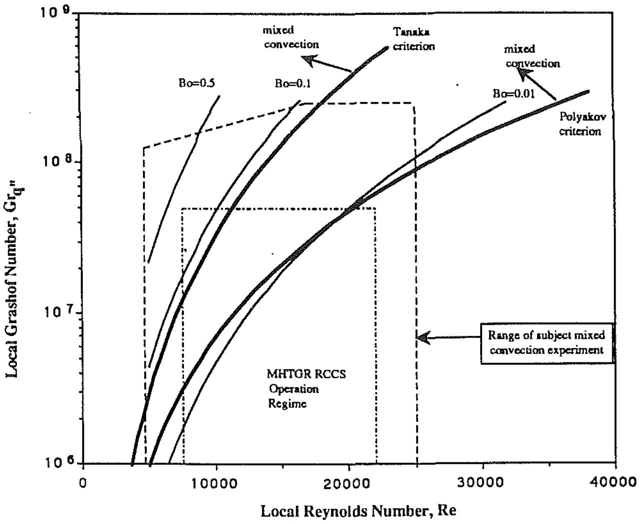

Fig. 1 Experiment range compared to MHTGR operating regime

Figure 1 also illustrates criteria commonly used to determine the operating regime of the RCCS system. Although the principle upon which to establish a criterion for onset of mixed convection is clear, i.e., when buoyancy effects have a measurable influence on the flow field, where the boundaries should be drawn is far less clear. Different investigators have their own criterion based on how they define the importance of the buoyancy effect on the flow field. The Petukhov and Polyakov (1988) criterion represents a conservative estimate. It is based on the deviation of Nu from its forced convection value by more than 1 percent, i.e.,

$$\mathrm{Gr}_{q''} > \frac{1.3\times10^{-4}\mathrm{Re}^{2.75}\mathrm{Pr}[\mathrm{Re}^{0.125}+2.4(\mathrm{Pr}^{0.667}-1)]}{\log_{10}\mathrm{Re}+1.15\log_{10}(5\mathrm{Pr}+1)+0.5\mathrm{Pr}-1.8} \quad \text{for } \mathrm{Pr}\geq 0.5 \qquad (1)$$

Tanaka's criterion (Tanaka et al., 1987), on the other hand, is based on the Nusselt number reaching 80 percent of the forced convection Nusselt number. Jackson and his co-workers (Cotton and Jackson, 1978) utilized a dimensionless buoyancy number, Bo, to measure the degree of mixed convection:

$$\mathrm{Bo} = \frac{8\times10^{4}\mathrm{Gr}_{q''}}{\mathrm{Re}^{3.425}\mathrm{Pr}^{0.8}} \qquad (2)$$

---

[1] S3 Technologies, Columbia, MD 21045.

[2] Department of Nuclear Engineering, Massachusetts Institute of Technology, Cambridge, MA 02139.

Contributed by the Heat Transfer Division and presented at the National Heat Transfer Conference, Minneapolis, Minnesota, July 28–31, 1991. Manuscript received by the Heat Transfer Division June 1992; revision received August 1993. Keywords: Mixed Convection. Associate Technical Editor: J. H. Kim.

They established that the onset of mixed convection occurs at a Bo value between 0.01 and 0.1. Therefore, according to the above criteria, a portion of the MHTGR riser operating regime is in mixed convection. This is of design significance, since heat transfer coefficients can vary significantly from forced convection values under mixed convection conditions.

Carr et al. (1973) measured the velocity profile of air flow in the mixed convection regime; however, most of the measurement points were in a narrow range. The measurements made by Steiner (1971) have a wide range of Re and Gr, but no detailed temperature data were given. In addition, the heated length of his experiment is much shorter than the RCCS riser length. Based on the theory that buoyancy force causes turbulent shear stress reduction, Jackson et al. (1989) derived a semi-empirical correlation for turbulent mixed convection:

$$\frac{\mathrm{Nu}}{\mathrm{Nu}_{fc}}=\left(\left|1-\frac{\mathrm{Bo}}{\left(\frac{\mathrm{Nu}}{\mathrm{Nu}_{fc}}\right)^{2}}\right|\right)^{0.46} \tag{3}$$

where the subscript *fc* is for forced convection. Equation (3) does not take into account fluid property changes between the bulk and film temperatures, which are not negligible in the RCCS riser case. On the other hand, considerable work has been performed on heat transfer with variable fluid properties (e.g., Petukhov, 1970; McEligot, 1986). In particular, McEligot proposed an accurate and easy to use correlation for turbulent flow:

$$\mathrm{Nu}_{fc}=0.021\mathrm{Re}^{0.8}\mathrm{Pr}^{0.4}(T_w/T_b)^{-0.5} \tag{4}$$

where T_w and T_b are wall and bulk temperatures, respectively, and Re and Pr are evaluated at the local air bulk temperature. No mixed convection effect is incorporated in this correlation.

Experimental Results

Due to the lack of existing data and the desire to provide a design correlation focused on MHTGR needs, an experiment was designed to bracket the expected operating regime of the RCCS. It consists of a vertical pipe, 8.6 m long and 63.5 mm inside diameter, provided with atmospheric air by a blower. A detailed description of the experiment apparatus can be found from Fu et al. (1991a). The experiment was designed to have a constant heat flux condition, although nonuniform heat loss along the pipe was measured. The Nusselt number variation with buoyancy and property change effects is the major result sought. The changes of the dimensionless numbers, Re, Gr, and Bo, along the channel flow direction are also of interest, since this behavior is related to the local Nusselt number behavior. Table 1 summarizes the experimental conditions.

The use of air as the flow medium in the experiments leads to significant temperature changes over the test length. Since gas properties are much more sensitive to temperature change than are those of liquids, the property change of the flowing air must be considered in interpreting the experimental results. For example, the air density will decrease about 40 percent when the temperature increases from the ambient temperature, 20 °C, to 200 °C, a temperature that a number of runs reached. These property changes will affect the dimensionless numbers. Table 1 shows the inlet and outlet Re, Gr, and Bo numbers for each run. For a typical run, the Re decreases at an almost constant rate; $\mathrm{Gr}_{q''}$ exhibits a rapid decrease in the first half of the channel, then decreases at a much slower rate; and the rate of decrease of the Bo number is intermediate.

Table 1 Experimental conditions for heated test runs

Run	Bo (Inlet/Exit)	T_{air}(°C) (Inlet/Exit)	T_w(°C) (Inlet/Exit)	Re (Inlet/Exit)	$\mathrm{Gr}_{q''}$ x 10^7 (Inlet/Exit)
1	0.0092/0.0051	18.2/68.7	53.8/93.6	21800/19600	6.22/2.41
2	0.031/0.014	17.3/88.3	60.2/115.1	15600/13500	67.1/1.84
3	0.037/0.008	14.2/195.5	136.6/270.9	21800/15500	24.9/1.64
4	0.020/0.007	16.8/120.5	91.5/174.4	21900/17800	13.7/2.46
5	0.060/0.017	16.0/148.1	98.5/196.5	15700/12100	13.2/1.52
6	0.10/0.017	21.5/258.1	169.9/332.3	15400/10100	21.4/0.79
7	0.15/0.042	25.8/153.3	107.0/204.8	10200/8000	7.80/0.91
8	0.23/0.045	26.6/212.4	151.5/286.5	10200/7300	11.5/0.69
9	0.29/0.045	22.6/249.7	173.8/336.6	10400/6900	15.4/0.58
10	0.50/0.13	17.4/133.1	111.4/242.3	7000/5600	7.03/0.79
11	0.87/0.13	12.9/216.8	167.9/254.8	7200/4900	13.0/0.52

* Inlet at 0.6m downstream from start of heating and exit at 0.6m upstream of end of heating

Local Nusselt number results are given as functions of axial location and the inlet Bo number in Fig. 2. The data span the inlet Bo number range investigated and represent different Nusselt number variation trends. The McEligot correlation prediction based on the local parameters is also shown for each case. The inlet Bo number of Run 3 is close to 0.037 and hence the data are considered to be in the forced convection regime. The measured Nusselt number is very close to the values calculated from the McEligot correlation for large *z/D*. For Bo increased to 0.29 as in Run 9, the effect of the buoyancy force is reflected by a gradual decrease in Nusselt number for data from the inlet until the midlength of the channel and then a gradual recovery. At the channel exit, the Nusselt number of the data recovers to the forced convection value. For further increase of Bo number, the Nusselt numbers stop recovering from their minimum value, as shown by Run 10 (Bo = 0.50). The Nusselt results for the data of Run 10 are clustered at about 30 percent to 50 percent of the forced convection Nusselt number values.

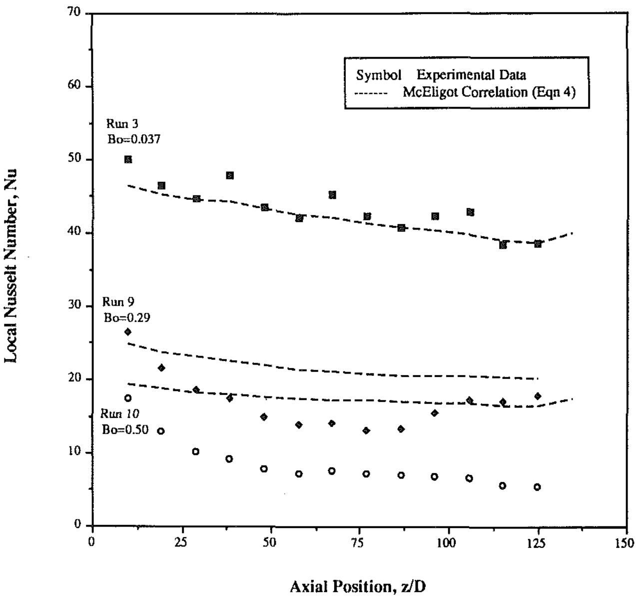

Fig. 2 Heat transfer behavior for the range of Bo number tested

Assessment of Predictive Correlations

As evident in Fig. 2, although the McEligot correlation accounts for the property change effect (Run 3), it fails when buoyancy effects are present and will overpredict the Nusselt number results under mixed convection conditions (Runs 9 and 10). The Jackson correlation, on the other hand, does better than the McEligot correlation in predicting the mixed convection effect, although it does not include large property change

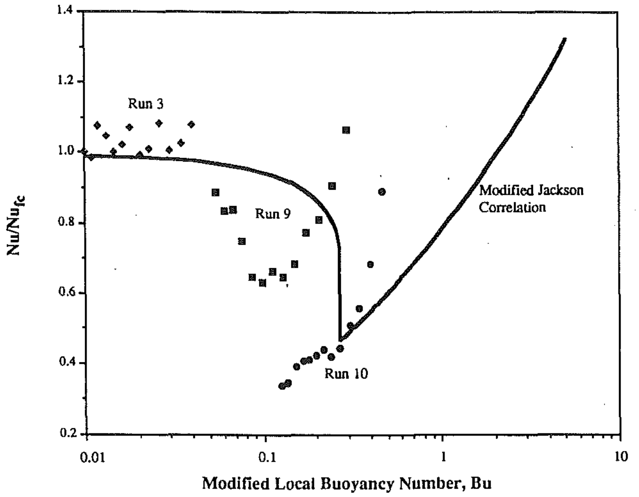

Fig. 3 Evaluation of modified Jackson Nu number correlation against test results

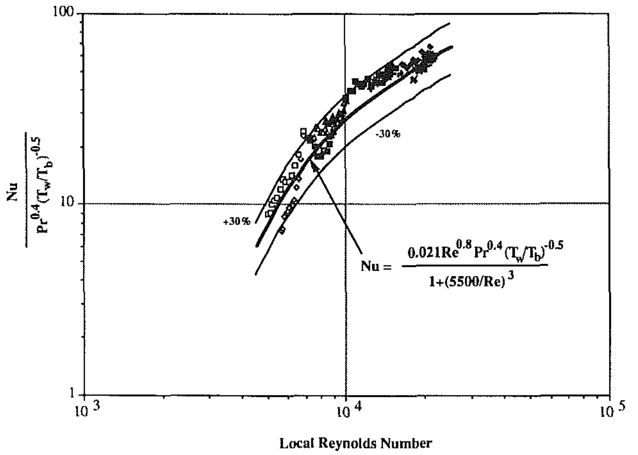

Fig. 4 Comparison of the proposed design correlation with experimental data

effects. The Jackson equation, however, can be modified to incorporate local property effects by using a local-fluid-property-dependent forced convection correlation, say the McEligot correlation (Fu, 1991b), which gives:

$$\frac{\mathrm{Nu}}{\mathrm{Nu}_{fc}}=\left(\left|1-\frac{\mathrm{Bu}}{\left(\dfrac{\mathrm{Nu}}{\mathrm{Nu}_{fc}}\right)^{2}}\right|\right)^{0.46} \tag{5}$$

where the modified buoyancy number $\mathrm{Bu} = \mathrm{Bo}(T_w/T_b)$. Comparing this modified Jackson correlation with the experiment results, Fig. 3, we observe three characteristics:

1 The trend of the average Nu number is represented reasonably well by the correlation.

2 The Nusselt number appears to recover after a precipitous decrease in the moderate mixed convection region (Run 9; recall that Bo decreases with distance along the channel).

3 The local Bu value for recovery (0.15) is lower than that predicted (0.25) by the modified Jackson correlation.

Since the design needs are typically for low Bo values, the modified Jackson correlation is reasonably satisfactory in terms of its accuracy. However, it poses some difficulty in design applications due to its iterative nature in calculating the mixed convection Nusselt numbers. Therefore, for a limited design application range, developing a simple, noniterative correlation from the correlation of Eq. (5) is preferable.

Only a few percent error will be introduced if a power of 0.5 instead of 0.46 is used in Eq. (5) and if the ratio T_w/T_b is taken as 1 (for most data the ratio is below 1.3). This permits analytical solution of Eq. (3), for heated upflow as:

$$\frac{\mathrm{Nu}}{\mathrm{Nu}_{fc}}=\begin{cases}\sqrt{\dfrac{1+\sqrt{1-4\mathrm{Bo}}}{2}} & \text{for Bo} \leq 0.25\\[2ex] \sqrt{\dfrac{-1+\sqrt{1+4\mathrm{Bo}}}{2}} & \text{for Bo} > 0.25\end{cases} \tag{6}$$

The above equation is to first order for small Bo:

$$\frac{\mathrm{Nu}}{\mathrm{Nu}_{fc}}\approx\frac{1}{1+0.5\mathrm{Bo}} \tag{7}$$

Substituting $\mathrm{Gr}_{q''}$ into the Bo definition, Eq. (2), and employing energy balance and pressure balance conditions, it can be shown that (Fu et al., 1991b)

$$\mathrm{Bo}=\frac{C\mathrm{Pr}^{0.2}}{\mathrm{Re}^{0.675}} \tag{8}$$

where C is a riser geometry dependent constant. Using this relation in Eq. (7), neglecting the weak dependence on the Prandtl number we obtain

$$\frac{\mathrm{Nu}}{\mathrm{Nu}_{fc}}=\frac{1}{1+(C'/\mathrm{Re}^{k})} \tag{9}$$

Note, however, that the transition from Eqs. (6) to (7) is valid only for very small Bo number. To obtain Nusselt numbers close to those measured by the experiment, the exponent k of Eq. (9) must be correspondingly increased to accommodate the high Bo number and variable temperature effects. For the range of design interest: $\mathrm{Re} > 5000$; $1 \times 10^7 < \mathrm{Gr}_{q''} < 2.5 \times 10^8$, the set of constants $C' = 1.66 \times 10^{11}$ and $k = 3$ are found to give a good representation of the experimental results, Fig. 4,

$$\frac{\mathrm{Nu}}{\mathrm{Nu}_{fc}}=\frac{1}{1+\left(\dfrac{5500}{\mathrm{Re}}\right)^{3}} \tag{10}$$

where Nu_{fc} is given by Eq. (4) and fluid properties are evaluated at local bulk temperature. Observe that all the data effectively lie within about 30 percent of this proposed correlation.

Conclusions

The present mixed convection air experiments provide an opportunity to examine the local Nusselt number behavior along the flow direction under mixed convection in the presence of substantial property changes. The Jackson correlation is in good agreement with the experimental results regarding the extent of the heat transfer impairment. However, the correlation does not replicate well the variation of Nusselt number with Bo number. Therefore, for design applications in a limited range, the data are presented using a simple equation, which is based on a synthesis of the McEligot and Jackson correlations, as shown on Fig. 4.

Acknowledgments

This study was sponsored by the DOE and conducted under the technical direction of Bechtel National, Inc. The authors are grateful for the technical assistance provided during the course of this work by Dr. S. Ghose of Bechtel and others at GA Technologies, Inc. and Oak Ridge National Laboratory. An earlier version of this work was published in AIChE Symposium Series 283, Vol. 87, 1991.

References

Carr, A. D., Connor, M. A., and Buhr, H. O., Jr., 1973, "Velocity, Temperature, and Turbulence Measurements in Air for Pipe Flow With Combined Free and Forced Convection," ASME Journal of Heat Transfer, Vol. 95, pp. 445–452.

Cotton, M. A., and Jackson, J. D., 1987, "Comparison Between Theory and Experiment for Turbulent Flow of Air in a Vertical Tube With Interaction Between Free and Forced Convection," ASME HTD-Vol. 84, pp. 43–50.

Fu, G., Driscoll, M. J., Todreas, N. E., and Yesilyurt, S., 1991a, "Heat Transfer and Friction Factor Behavior in the Mixed Convection Regime for Air Up-Flow in a Heated Vertical Pipe," *AIChE Heat Transfer Conf.*, Minneapolis, MN, Symp. Series 382, Vol. 87, pp. 326–335.

Fu, G., Gavrilas, M., Hejzlar, P., Driscoll, M. J., and Todreas, N. E., 1991b, "Experimental and Analytic Evaluation of Gas-Cooled Reactor Cavity Cooling System Performance," MIT Report MITNPI-TR-038, Rev. 1.

Jackson, J. D., Cotton, M. A., and Axcell, B. P., 1989, "Studies of Mixed Convection in Vertical Tubes," *International Journal of Heat and Fluid Flow*, Vol. 10, No. 1, pp. 2–15.

McEligot, D. M., 1986, "Basic Thermofluidynamic Problems in High Temperature Heat Exchangers," in: *High Temperature Heat Exchangers*, Y. Hori, A. E. Sheindlin, and N. Afgan, eds., Hemisphere, New York.

Petukhov, B. S., 1970, "Heat Transfer and Friction in Turbulent Pipe Flow With Variable Physical Properties," *Advances in Heat Transfer*, Vol. 6, pp. 503–565.

Petukhov, B. S., and Polyakov, A. F., 1988, *Heat Transfer in Turbulent Mixed Convection*, Hemisphere Publishing Corp., New York.

Steiner, A., 1971, "On Reverse Transition of a Turbulent Flow Under the Action of Buoyancy Forces," *Journal of Fluid Mechanics*, Vol. 47, Part 3, pp. 503–512.

Tanaka, H., Maruyama, S., and Hatano, S., 1987, "Combined Forced and Natural Convection Heat Transfer for Upflow in a Uniformly Heated Vertical Pipe," *Int. J. Heat Mass Transfer*, Vol. 30, pp. 165–174.

Investigation of Double-Diffusive Convection in a Trapezoidal Enclosure

Z. F. Dong[1] **and M. A. Ebadian**[1, 2]

1 Introduction

Double-diffusive convection is important to various fields, such as oceanography, astrophysics, geology, biology, chemical processes, the material solidification process, crystal growth, etc. Studies of double-diffusive convection were first conducted in the oceanographic sciences, and emphasis was placed on the development of the linear stability theory for a simple salt-stratified fluid heat from below (cf. Turner, 1979). Double-diffusive convection by lateral heating in a stable salt-stratified flow has been studied since the 1970s, a conspicuous feature of which is the layered flow structure. Several reviews on double-diffusive convection have been found in the literature by Turner (1974, 1985) and Viskanta et al. (1985). Inspection of the literature reveals that most of the research emphasizes double-diffusive convection in a rectangular enclosure or square cavity. Lee and Hyun (1990, 1991a, 1991b) conducted research on double-diffusive convection in a rectangular enclosure with an aspect ratio equal to 2. The transient process of natural convection due to thermal and solutal gradients has been investigated experimentally or numerically by Lee et al. (1988), Hyun and Lee (1990), and Lee and Hyun (1990). They included assisting flow as well as opposing flow in their investigation. A layered flow structure has been confirmed under appropriate conditions in the case of lateral heating. Han and Kuehn (1991a, 1991b) have studied double-diffusive natural convection experimentally and numerically in a vertical rectangular enclosure with an aspect ratio reaching up to 4. The layered multicell flow structure in the enclosure for both assisting and opposing flow has been visualized by the schlieren method and simulated by the numerical method. Beghein et al. (1992) investigated the double-diffusive phenomena in a square cavity. Based on the authors' knowledge, double-diffusive convection in irregular geometries has scarcely been investigated experimentally or numerically. Basic understanding of double-diffusive convection in irregular geometry, such as in a trapezoidal cavity, is absent from the open literature. Therefore, the study of double-diffusive convection in a trapezoidal enclosure with the lateral thermal and solutal gradients imposed on the sidewalls is investigated in this technical note. Depending on the directions of the buoyancy forces due to temperature gradient and concentration gradient, flow can be either assisting or opposing flow. Both assisting flow and opposing flow are considered in the analysis.

2 Mathematical Formulation

Consideration is given to the two-dimensional trapezoidal enclosure having a width, b, at the bottom wall, height, h, and sidewall angle, ψ ($\psi = 75$ deg). The aspect ratio is defined as h/b. The flow in the enclosure is considered to be two-dimensional steady laminar flow of Newtonian fluid with negligible viscous dissipation. The thermal properties of the fluid are treated as constants, except the density in the buoyancy forces term, which is approximated by Boussinesq assumption. By employing the assumptions above, the conservation equations of mass, momentum, energy, and heavier species are obtained as follows:

$$\frac{\partial U}{\partial X}+\frac{\partial V}{\partial Y}=0 \tag{1}$$

$$U\frac{\partial U}{\partial X}+V\frac{\partial U}{\partial Y}=-\frac{\partial P}{\partial X}+\mathrm{Pr}\left(\frac{\partial^2 U}{\partial X^2}+\frac{\partial^2 U}{\partial Y^2}\right) \tag{2}$$

$$U\frac{\partial V}{\partial X}+V\frac{\partial V}{\partial Y}=-\frac{\partial P}{\partial Y}+\mathrm{Pr}\left(\frac{\partial^2 V}{\partial X^2}+\frac{\partial^2 V}{\partial Y^2}\right)+\mathrm{Pr}\,\mathrm{Ra}_t\,(\theta-SN) \tag{3}$$

$$U\frac{\partial \theta}{\partial X}+V\frac{\partial \theta}{\partial Y}=\frac{\partial^2 \theta}{\partial X^2}+\frac{\partial^2 U}{\partial Y^2} \tag{4}$$

$$U\frac{\partial S}{\partial X}+V\frac{\partial S}{\partial Y}=\frac{1}{\mathrm{Le}}\left(\frac{\partial^2 S}{\partial X^2}+\frac{\partial^2 S}{\partial Y^2}\right). \tag{5}$$

The equations above have been dimensionalized by using the following parameters:

$$U=[u/(\alpha_T/D_h)],\quad V=[v/(\alpha_T/D_h)],\quad X=x/D_h,$$
$$Y=y/D_b,\quad P=p/(\rho\alpha_T^2/D_h^2)],\quad \Delta T=T_h-T_t,$$
$$\Delta C=C_h-C_t,\quad \theta=(T-T_t)/\Delta T,\quad S=(C-C_t)/\Delta C,$$
$$\mathrm{Pr}=\nu/\alpha_T,\quad \mathrm{Le}=\alpha_T/D,\quad \mathrm{Ra}_t=g\beta_T\Delta T D_h^3/\alpha_T\nu,$$
$$\mathrm{Ra}_s=g\beta_s\Delta C D_a^3/\alpha_T\nu,\quad N=(\beta_s\Delta C)/(\beta_t\,\Delta T)=\mathrm{Ra}_s/\mathrm{Ra}_t, \tag{6}$$

where u and v are the velocities in the x and y directions, respectively; and T, C, and P are the temperature, concentration, and pressure of the fluid, respectively. In addition, the relevant fluid properties are kinematic viscosity, ν; thermal diffusivity, α_T; solutal diffusivity, D; and the coefficients of volumetric expansion with temperature and solute, β_T and β_s, respectively. The hydraulic diameter, D_h, is used simply as a scale for length. The Prandtl number, Pr, the Lewis number, Le, the thermal Rayleigh number, Ra_t, and the solutal Rayleigh number, Ra_s are all included in the governing equations.

The associated boundary conditions for temperature and concentration are:

---

[1] Department of Mechanical Engineering, Florida International University, Miami, FL 33199.

[2] Fellow ASME; corresponding author.

Contributed by the Heat Transfer Division of The American Society of Mechanical Engineers. Manuscript received by the Heat Transfer Division May 1993; revision received October 1993. Keywords: Double Diffusion Systems, Natural Convection, Numerical Methods. Associate Technical Editor: R. Viskanta.

References

Carr, A. D., Connor, M. A., and Buhr, H. O., Jr., 1973, "Velocity, Temperature, and Turbulence Measurements in Air for Pipe Flow With Combined Free and Forced Convection," ASME Journal of Heat Transfer, Vol. 95, pp. 445–452.

Cotton, M. A., and Jackson, J. D., 1987, "Comparison Between Theory and Experiment for Turbulent Flow of Air in a Vertical Tube With Interaction Between Free and Forced Convection," ASME HTD-Vol. 84, pp. 43–50.

Fu, G., Driscoll, M. J., Todreas, N. E., and Yesilyurt, S., 1991a, "Heat Transfer and Friction Factor Behavior in the Mixed Convection Regime for Air Up-Flow in a Heated Vertical Pipe," *AIChE Heat Transfer Conf.*, Minneapolis, MN, Symp. Series 382, Vol. 87, pp. 326–335.

Fu, G., Gavrilas, M., Hejzlar, P., Driscoll, M. J., and Todreas, N. E., 1991b, "Experimental and Analytic Evaluation of Gas-Cooled Reactor Cavity Cooling System Performance," MIT Report MITNPI-TR-038, Rev. 1.

Jackson, J. D., Cotton, M. A., and Axcell, B. P., 1989, "Studies of Mixed Convection in Vertical Tubes," *International Journal of Heat and Fluid Flow*, Vol. 10, No. 1, pp. 2–15.

McEligot, D. M., 1986, "Basic Thermofluidynamic Problems in High Temperature Heat Exchangers," in: *High Temperature Heat Exchangers*, Y. Hori, A. E. Sheindlin, and N. Afgan, eds., Hemisphere, New York.

Petukhov, B. S., 1970, "Heat Transfer and Friction in Turbulent Pipe Flow With Variable Physical Properties," *Advances in Heat Transfer*, Vol. 6, pp. 503–565.

Petukhov, B. S., and Polyakov, A. F., 1988, *Heat Transfer in Turbulent Mixed Convection*, Hemisphere Publishing Corp., New York.

Steiner, A., 1971, "On Reverse Transition of a Turbulent Flow Under the Action of Buoyancy Forces," *Journal of Fluid Mechanics*, Vol. 47, Part 3, pp. 503–512.

Tanaka, H., Maruyama, S., and Hatano, S., 1987, "Combined Forced and Natural Convection Heat Transfer for Upflow in a Uniformly Heated Vertical Pipe," *Int. J. Heat Mass Transfer*, Vol. 30, pp. 165–174.

Investigation of Double-Diffusive Convection in a Trapezoidal Enclosure

Z. F. Dong[1] and M. A. Ebadian[1, 2]

1 Introduction

Double-diffusive convection is important to various fields, such as oceanography, astrophysics, geology, biology, chemical processes, the material solidification process, crystal growth, etc. Studies of double-diffusive convection were first conducted in the oceanographic sciences, and emphasis was placed on the development of the linear stability theory for a simple salt-stratified fluid heat from below (cf. Turner, 1979). Double-diffusive convection by lateral heating in a stable salt-stratified flow has been studied since the 1970s, a conspicuous feature of which is the layered flow structure. Several reviews on double-diffusive convection have been found in the literature by Turner (1974, 1985) and Viskanta et al. (1985). Inspection of the literature reveals that most of the research emphasizes double-diffusive convection in a rectangular enclosure or square cavity. Lee and Hyun (1990, 1991a, 1991b) conducted research on double-diffusive convection in a rectangular enclosure with an aspect ratio equal to 2. The transient process of natural convection due to thermal and solutal gradients has been investigated experimentally or numerically by Lee et al. (1988), Hyun and Lee (1990), and Lee and Hyun (1990). They included assisting flow as well as opposing flow in their investigation. A layered flow structure has been confirmed under appropriate conditions in the case of lateral heating. Han and Kuehn (1991a, 1991b) have studied double-diffusive natural convection experimentally and numerically in a vertical rectangular enclosure with an aspect ratio reaching up to 4. The layered multicell flow structure in the enclosure for both assisting and opposing flow has been visualized by the schlieren method and simulated by the numerical method. Beghein et al. (1992) investigated the double-diffusive phenomena in a square cavity. Based on the authors' knowledge, double-diffusive convection in irregular geometries has scarcely been investigated experimentally or numerically. Basic understanding of double-diffusive convection in irregular geometry, such as in a trapezoidal cavity, is absent from the open literature. Therefore, the study of double-diffusive convection in a trapezoidal enclosure with the lateral thermal and solutal gradients imposed on the sidewalls is investigated in this technical note. Depending on the directions of the buoyancy forces due to temperature gradient and concentration gradient, flow can be either assisting or opposing flow. Both assisting flow and opposing flow are considered in the analysis.

2 Mathematical Formulation

Consideration is given to the two-dimensional trapezoidal enclosure having a width, b, at the bottom wall, height, h, and sidewall angle, ψ ($\psi = 75$ deg). The aspect ratio is defined as h/b. The flow in the enclosure is considered to be two-dimensional steady laminar flow of Newtonian fluid with negligible viscous dissipation. The thermal properties of the fluid are treated as constants, except the density in the buoyancy forces term, which is approximated by Boussinesq assumption. By employing the assumptions above, the conservation equations of mass, momentum, energy, and heavier species are obtained as follows:

$$\frac{\partial U}{\partial X} + \frac{\partial V}{\partial Y} = 0 \tag{1}$$

$$U\frac{\partial U}{\partial X} + V\frac{\partial U}{\partial Y} = -\frac{\partial P}{\partial X} + \Pr\left(\frac{\partial^2 U}{\partial X^2} + \frac{\partial^2 U}{\partial Y^2}\right) \tag{2}$$

$$U\frac{\partial V}{\partial X} + V\frac{\partial V}{\partial Y} = -\frac{\partial P}{\partial Y} + \Pr\left(\frac{\partial^2 V}{\partial X^2} + \frac{\partial^2 V}{\partial Y^2}\right) + \Pr\,\mathrm{Ra}_t\,(\theta - SN) \tag{3}$$

$$U\frac{\partial \theta}{\partial X} + V\frac{\partial \theta}{\partial Y} = \frac{\partial^2 \theta}{\partial X^2} + \frac{\partial^2 U}{\partial Y^2} \tag{4}$$

$$U\frac{\partial S}{\partial X} + V\frac{\partial S}{\partial Y} = \frac{1}{\mathrm{Le}}\left(\frac{\partial^2 S}{\partial X^2} + \frac{\partial^2 S}{\partial Y^2}\right). \tag{5}$$

The equations above have been dimensionalized by using the following parameters:

$$\begin{gathered} U = [u/(\alpha_T/D_h)], \quad V = [v/(\alpha_T/D_h)], \quad X = x/D_h, \\ Y = y/D_b, \quad P = p/(\rho\alpha_T^2/D_h^2)], \quad \Delta T = T_h - T_t, \\ \Delta C = C_h - C_t, \quad \theta = (T - T_t)/\Delta T, \quad S = (C - C_t)/\Delta C, \\ \Pr = \nu/\alpha_T, \quad \mathrm{Le} = \alpha_T/D, \quad \mathrm{Ra}_t = g\beta_T \Delta T D_h^3/\alpha_T \nu, \\ \mathrm{Ra}_s = g\beta_s \Delta C D_a^3/\alpha_T \nu, \quad N = (\beta_s \Delta C)/(\beta_t\,\Delta T) = \mathrm{Ra}_s/\mathrm{Ra}_t, \end{gathered} \tag{6}$$

where u and v are the velocities in the x and y directions, respectively; and T, C, and P are the temperature, concentration, and pressure of the fluid, respectively. In addition, the relevant fluid properties are kinematic viscosity, ν; thermal diffusivity, α_T; solutal diffusivity, D; and the coefficients of volumetric expansion with temperature and solute, β_T and β_s, respectively. The hydraulic diameter, D_h, is used simply as a scale for length. The Prandtl number, Pr, the Lewis number, Le, the thermal Rayleigh number, Ra_t, and the solutal Rayleigh number, Ra_s are all included in the governing equations.

The associated boundary conditions for temperature and concentration are:

---

[1] Department of Mechanical Engineering, Florida International University, Miami, FL 33199.

[2] Fellow ASME; corresponding author.

Contributed by the Heat Transfer Division of The American Society of Mechanical Engineers. Manuscript received by the Heat Transfer Division May 1993; revision received October 1993. Keywords: Double Diffusion Systems, Natural Convection, Numerical Methods. Associate Technical Editor: R. Viskanta.

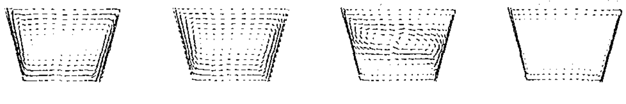

(a) vectors

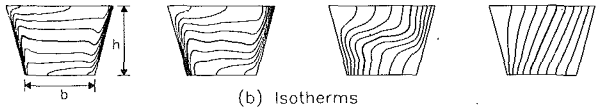

(b) Isotherms

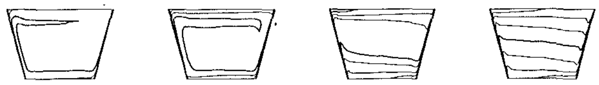

(c) Iso-concentration lines

(1) N = 0.5 (2) N = 5 (3) N = 15 (4) N = 20

Fig. 1 Assisting flow for $Ar = 1$

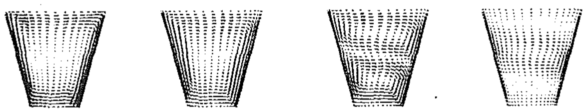

(a) vectors

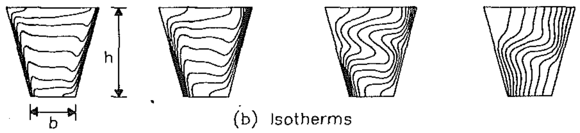

(b) Isotherms

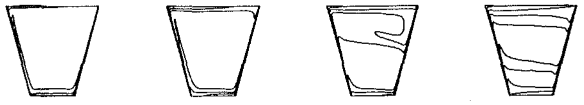

(c) Iso-concentration lines

(1) N = 0.5 (2) N = 5 (3) N = 10 (4) N = 20

Fig. 2 Assisting flow for $Ar = 2$

on the left sidewall

$\theta = 1$, $S = 0$ (for assisting flow)

$$\text{or } S = 1 \text{ (for opposing flow)} \quad (7)$$

on the right sidewall

$\theta = 0$, $S = 0$ (for assisting flow)

$$\text{or } S = 0 \text{ (for opposing flow)} \quad (8)$$

on the bottom and top walls

$$\partial\theta/\partial Y = 0, \ \partial S/\partial Y = 0. \quad (9)$$

A nonslip boundary condition has been applied on all of the walls, which is:

$$U = V = 0. \quad (10)$$

Results and Discussion

The governing equations, Eqs. (1)-(5), have been transformed into those in the boundary fitted coordinate system and are approximated with finite difference equations by the control volume method. The nonuniform grid, characterized by more grids close to the wall, is applied. The SIMPLE algorithm (Patankar, 1980) is adopted to handle the nonlinearity of the equations. Fully converged solutions are reached when the maximum values of residuals, U, V, S, and θ, are less than 10^{-5}.

Grid-independent experiments have been performed and it is shown that nonuniform grids of 41×31 and 41×61 can be used for the trapezoidal enclosures with the aspect ratio ($Ar = h/b$) equal to 1 and 2, respectively. Validation of the present numerical code has also been performed by comparing the results obtained from the present method for double-diffusive convection in a square enclosure with those from Beghein et al. (1992). In the case of assisting flow for parameters of $\mathrm{Le} = 1$, $\mathrm{Pr} = 0.7$, $\mathrm{Ra}_t = \mathrm{Ra}_s = 10^4$, the deviation of the local Nusselt number and Sherwood number along the left wall of the square cavity is found to be less than 2 percent.

In this technical note, emphasis is placed on the effects of the buoyancy forces ratio ($N = \mathrm{Ra}_s/\mathrm{Ra}_t$) and the aspect ratio ($Ar = h/b$). The Prandtl number, 7, and Lewis number, 100, are employed to simulate the aqueous solution, and Ra_s is set to 10^6 in the computation. The results are presented in terms of vectors, isotherms, and isoconcentration lines for both $Ar = 1$ and $Ar = 2$ for the different buoyancy forces ratios. The intervals of isothermal and isoconcentration lines are 0.1 in the corresponding figures.

In Fig. 1, the typical feature of assisting double-diffusive flow is plotted for $Ar = 1$. It is seen from Fig. 1(a) that the fluid in the enclosure flows clockwise when $N = 0.5$. The fluid near the left wall of the hot and low concentration flows to the top, and the fluid near the right wall of cold and high concentration moves toward the bottom, leading to a unicellular flow structure in the enclosure. The center region of the cell is located in the middle level of the enclosure. When the buoyancy forces ratio increases, the flow gradually changes. Two small cells may be formed in the center region at $N = 5$. However, those two small cells can be detected at $N = 15$. Furthermore, in the case of $N = 15$, the flow in the boundary layer region, as well as the cell flow, is much stronger. However, the flow occurs only in the boundary layer region of concentration when the buoyancy forces ratio equals 20. Stagnant fluid occupies a greater portion of the enclosure. Figure 1(b) shows the temperature distribution in the enclosure. At $N = 0.5$, more isotherms appear near the left and right side walls, and a deformation of the isotherms is seen near the boundary, with the temperature stratification in the center region. When the buoyancy forces ratio increases to 5, the deformation of isotherms is extended from the boundary layer region to the entire cross section and the temperature gradient on the left and right side walls is decreased. At $N = 15$, a deformation of isotherms occurs in the center region of the cross section, which indicates stronger flow there. The temperature distribution is similar to that of conduction when $N = 20$. These temperature distribution variations reflect the predomination of flow from thermal convection to solutal convection. From the distribution of concentration, Fig. 1(c), it is apparent that solutal convection is gradually enhanced as the buoyancy forces ratio increases. Because of the larger Lewis number, the boundary layer of concentration is much thinner than that of temperature. The concentration is changed mainly in the boundary layer at $N = 0.5$. Only in the case of a greater value of N do the stratified isoconcentration lines take up the whole cross section. The flow induced by solutal buoyancy forces makes the isocentration lines deform only in the boundary layer when $N = 20$.

The characteristics of assisting flow in the trapezoidal enclosure, when $Ar = 2$, are shown in Fig. 2(a). Thermal convection is dominant when $N = 0.5$ and a unicellular flow structure can be seen there. When the buoyancy forces ratio increases, the unicell separates into two small cells in the center region when $N = 5$, and a two-layered cell flow structure appears when $N = 10$; one strong flow cell can be detected in the middle level of the enclosure when $N = 20$. Figure 2(b) displays the temperature distribution variation with the buoyancy forces ratio. When $N < 5$, the isotherm shape deforms in the boundary layer region, and the temperature of the fluid in the core region is more stratified. A greater variation takes place when the buoyancy forces ratio is large, and as a result, it generates a two-layered cell flow structure and a zig-zag like shape of isotherms appears. When solutal convection dominates the

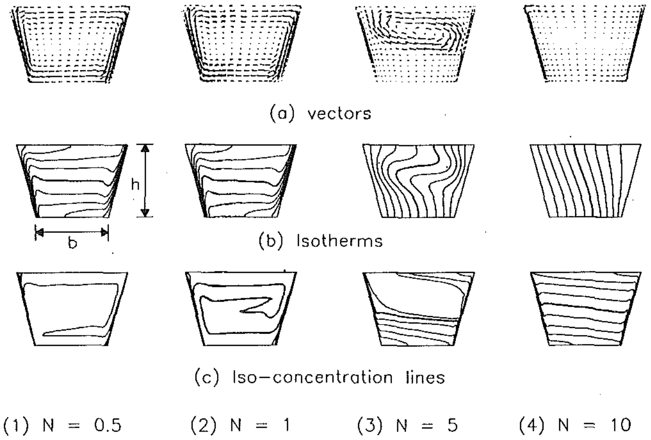

Fig. 3 Opposing flow for $Ar=1$

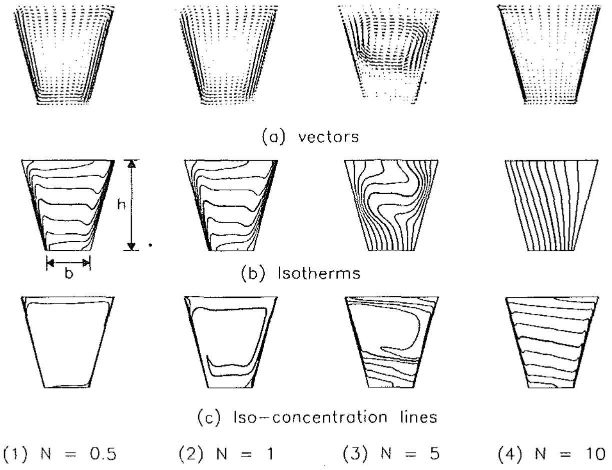

Fig. 4 Opposing flow for $Ar=2$

flow, the temperature distribution is one of conduction, where heat transfer is dominated mainly by conduction. The isoconcentration lines are given in Fig. 2(*c*). It is seen that when solutal convection is not strong ($N=0.5$ and $N=5$), the concentration varies only in its thin boundary layer. However, when the two-layered cell flow structure forms, the concentration distributions are more or less stratified horizontally ($N=10$). Finally, the stratified concentration distribution will be seen in the whole cross section ($N=20$).

The opposing flow in the trapezoidal enclosures, with aspect ratio equal to 1, is displayed in Fig. 3. In opposing flow, the direction of flow induced by thermal buoyancy is opposite to that induced by solutal buoyancy. In the present study, the left side wall has a higher temperature and higher concentration than the right side wall. The direction of the thermal flow is clockwise, whereas the direction of the solutal flow is counterclockwise. At a smaller buoyancy forces ratio, the flow is dominated by thermal convection. The resulting combined flow direction is clockwise and the unicell flow structure is formed in the whole cross section when $N=0.5$ and $N=1$. When solutal convection is stronger ($N=5$), two different flow directions can be observed in this figure. The flow induced by solutal buoyancy is centered on the concentration boundary layer, and a three-layered flow appears in the cross section, with the middle layer flow being much stronger than the other two. When the solutal buoyancy increases further, the thermal convection becomes weak and the resulting flow is totally dominated by solutal convection, which is mainly counterclockwise flow in the boundary layer, and a larger portion of the core region is stagnant. Temperature and concentration distributions are similar to those for assisting flow in the trapezoidal enclosure with the aspect ratio equal to 1, except for the opposite orientation of the isothermal and isoconcentration lines.

By comparing Fig. 4(*a*) with Fig. 3(*a*), it can be seen that the opposing flow in the enclosure with aspect ratio equal to 2 behaves the same as the one in the enclosure with aspect ratio equal to 1. For $N=5$, the three-layered flow structure is observed. The dominant thermal convection leads to a unicell flow stucture at a small value of N ($N=0.5$ and 1). The opposite direction of unicell flow is induced by the dominant solutal convection ($N=10$). The isotherms in Fig. 4(*b*) are similar to those in Fig. 3(*b*). The isoconcentration lines in Fig. 4(*c*) are also similar to those in Fig. 3(*c*) for the case of $N=1.0$ and $N=10$. For a smaller buoyancy forces ratio, the concentration of fluid in the core region is the same ($N=0.5$). For the case of the three-layered flow structure ($N=5$), the concentration distribution appears to be stratified, and the stratified concentration distribution is formed when the buoyancy forces ratio reaches 10.

The mean Nusselt and Sherwood numbers are given in Table 1. It is noted that for assisting flow, both the mean Nusselt and Sherwood numbers decrease as the buoyancy forces ratio increases. For opposing flow, there are minimum mean Nusselt and Sherwood numbers at certain buoyancy forces ratios. Both the Nusselt and Sherwood numbers decrease to their minimum values and then increase slowly again as the buoyancy forces ratio increases.

Table 1 Mean Nusselt and Sherwood numbers

N	Assisting Flow				Opposing Flow			
	$\overline{Nu}$		$\overline{Sh}$		$\overline{Nu}$		$\overline{Sh}$	
	Ar=1	Ar=2	Ar=1	Ar=2	Ar=1	Ar=2	Ar=1	Ar=2
0.5	16.868	16.539	79.765	78.481	16.563	16.258	77.106	76.713
1	13.896	13.732	69.829	68.070	13.359	13.209	63.242	62.114
5	8.421	8.450	53.544	52.691	2.234	3.369	38.573	37.049
10	5.210	5.217	50.025	49.846	1.431	1.854	44.647	42.760
20	1.536	2.749	49.634	47.994	1.453	1.877	46.235	44.256
30	1.521	1.946	49.255	47.331	1.463	1.887	46.727	44.722
40	1.513	1.937	49.054	47.132	1.468	1.892	46.966	44.948
50	1.502	1.931	48.930	47.009	1.471	1.895	47.106	45.081

Concluding Remarks

Double-diffusive convection in trapezoidal enclosure has been numerically investigated. Both assisting and opposing flows are taken into consideration. It is found that in spite of assisting flow or opposing flow, there exists a unicellular flow structure in the cross section of the trapezoidal enclosure at both high and low buoyancy forces ratio values. For assisting flow, the unicellular flow structure is dominant in the trapezoidal enclosure with aspect ratio equal to 1 at all buoyancy forces ratios. However, a two-layered cell flow structure is seen in the enclosure with the aspect ratio equal to 2 when the buoyancy forces ratio is around 10. On the other hand, when $N=5$, a three-layered cell flow structure appears for opposing flow in the cross section of the trapezoidal enclosures with aspects ratios equal to 1 and 2. Furthermore, the flow in the middle cell is stronger than the others. In addition, the mean Nusselt and Sherwood numbers decrease as the buoyancy forces ratio increases for the case of assisting flow in a trapezoidal enclosure. For opposing flow in a trapezoidal enclosure, the mean Nusselt and Sherwood numbers decrease to their minimum values and then increase as the buoyancy forces ratio increases.

There are similarities between the double-diffusive flow in a trapezoidal enclosure and a rectangular cavity. In the two geometries, the multilayered flow structure has been depicted in both assisting and opposing flow under certain conditions of buoyancy forces ratios, which are dependent on the geometry. In the high or low buoyancy forces ratio, the unicell flow is also clearly discerned. The variation of the mean Nusselt number and Sherwood number with the buoyancy forces ratio has the same tendency between the rectangular and trapezoidal enclosures. However, the multilayered flow was not detected for assisting flow in a trapezoidal enclosure with the aspect ratio equal to 1 in the present considered range of buoyancy forces ratio. On the other hand, the slanted wall of the trapezoidal enclosure makes the distributions of temperature and concentration different from those of the rectangular enclosure.

Acknowledgments

The results presented in this paper were obtained in the course of research sponsored by the National Science Foundation under Grant No. HRD-9250087.

References

Beghein, C., Haghighat, F., and Allard, F., 1992, "Numerical Study of Double Diffusive Natural Convection in a Square Cavity," *Int. J. Heat Mass Transfer*, Vol. 35, pp. 833–846.

Han, H., and Kuehn, T. H., 1991a, "Double Diffusive Natural Convection in a Vertical Rectangular Enclosure—I. Experimental Study," *Int. J. Heat Mass Transfer*, Vol. 34, pp. 449–459.

Han, H., and Kuehn, T. H., 1991b, "Double Diffusive Natural Convection in a Vertical Rectangular Enclosure—II. Numerical Study," *Int. J. Heat Mass Tranfer*, Vol. 34, pp. 461–471.

Hyun, J. M., and Lee, J. W., 1990, "Double Diffusive Convection in a Rectangle With Cooperating Horizontal Gradients of Temperature and the Concentration Gradients," *Int. J. Heat Mass Transfer*, Vol. 33, pp. 1605–1716.

Lee, J. W., Hyun, J. M., and Kim, K. W., 1988, "Natural Convection in Confined Fluids With Combined Horizontal Temperature and Concentration Gradients," *Int. J. Heat Mass Transfer*, Vol. 31, pp. 1969–1977.

Lee, J. W., and Hyun, J. M., 1990, "Double Diffusive Convection in a Rectangle With Opposing Horizontal Temperature and the Concentration Gradients," *Int. J. Heat Mass Transfer*, Vol. 33, pp. 1619–1622.

Lee, J. W., and Hyun, J. M., 1991a, "Time Dependent Double Diffusion in a Stable Stratified Fluid Under Lateral Heating," *Int. J. Heat Mass Transfer*, Vol. 34, No. 9, pp.2409–2421.

Lee, J. W., and Hyun, J. M., 1991b, "Double Diffusive Convection in a Cavity Under a Vertical Solutal Gradient and a Horizontal Temperature Gradient," *Int. J. Heat Mass Transfer*, Vol. 34, No. 9, pp. 2403–2427.

Patankar, S. V., 1980, *Numerical Heat Transfer and Fluid Flow*, Hemisphere, Washington, DC.

Turner, J. S., 1974, "Double Diffusion Phenomena," in: *Ann. Rev. Fluid Mech.*, Vol. 6, pp. 37–56. M. Van Dyke, W. G. Vincent, and J. V. Wehausen, eds., Annual Reviews Inc., Palo Alto, CA.

Turner, J.S., 1979, *Buoyancy Effects in Fluids*, Cambridge University Press, London, United Kingdom.

Turner, J. S., 1985, "Multicomponent Convection," in: *Ann. Rev. Fluid Mech.*, Vol. 17, pp. 11–44.

Viskanta, R., Bergman, T. L., and Incropera, F. P., 1985, "Double Diffusive Natural Convection," in: *Natural Convection, Fundamental and Applications*, S. Kakac, W. Aung, and R. Viskanta, eds., Hemisphere Publishing Corporation, Washington, DC, pp. 1075–1099.

An In Situ Technique for Measuring Heat Transfer From a Power Transistor to a Boiling Liquid

C. L. Struble[1, 3] and L. C. Witte[2, 3]

Introduction

Management of the waste heat from microelectronics has become a critical part of the design of high-speed computers. Closer packing of components in VLSI and multichip packages will result in heat fluxes of 100 W/cm^2 or greater in future generations of high-speed electronic devices. Such levels are beyond the capabilities of most indirect cooling systems, and will require direct immersion cooling with dielectric liquids.

The large temperature excursion at boiling incipience, and the relatively low burnout heat flux of dielectric liquids, has limited this application. Both incipience excursion and burnout can be partially alleviated by the use of forced convection. Monde and Katto (1978) studied downward-impinging jets of water and R-113 in air, and found that fully developed nucleate jet boiling is unaffected by jet diameter, velocity, or subcooling, and could be treated as an extension of pool boiling to higher flux. This was confirmed by Ma and Bergles (1983, 1986) in studies of horizontal submerged jets in R-113. They found, however, that the incipience temperature and heat flux are strong functions of the surface cavity radius and that smooth surfaces such as silicon chips will have different incipience characteristics than a machined surface with a wide range of cavity sizes. Depending on the jet velocity, liquid subcooling, and surface characteristics, incipience excursion may be reduced or eliminated.

This suggests further study of boiling on heaters with surfaces and electrical properties similar to computer chips. Few such studies have been done because of the difficulty of measuring heat flux and temperature accurately. Hwang and Moran (1981), Park and Bergles (1986), and Hijikata et al. (1988) have used the forward voltage of a diode intrinsic to a silicon "thermal chip" as a temperature-sensitive parameter in boiling experiments. However, in none of these studies could heat flux be measured with certainty because of heat losses to chip substrates, bonding wires, etc.

A similar technique has been used to measure temperature of power transistors in enclosed packages. Blackburn (1975), Oettinger et al. (1976), and Zommer et al. (1976) used a switching circuit allowing alternate heating and measurements of the transistor emitter-base voltage as a temperature sensitive parameter. In this technique, the cooling curve is traced back to power cutoff to obtain the temperature. The cooling curve can also be used to measure heat flux with reasonable accuracy.

As simulated chips for boiling experiments, power transistors have several advantages. They can generate heat levels of up to 200 W on a small (~5 mm) chip, and can sustain temperatures up to 200°C, enabling study of transition to burnout. They are inexpensive, widely available, and have similar surface characteristics to IC chips. They are also compatible with dielectric liquids.

Temperature Measurement

The emitter-base voltage V_{eb} of a transistor is a decreasing, nearly linear function of temperature. This property has been used for commercial temperature sensors; see Timko (1976) and Ohte et al. (1982); and precision reference voltage sources; see Kujik (1973) and Brokaw (1974). The expression for V_{eb} is, from Widlar (1971):

$$V_{eb} = V_{g0}\,(1-\gamma) + V_{ebr}\,\gamma + \frac{k_B\,T_j}{q}\ln\left[\left(\frac{1}{\gamma}\right)^n\left(\frac{I_c}{I_{cr}}\right)\right], \qquad (1)$$

where V_{g0} is the extrapolated bandgap voltage at 0 K, γ is the ratio of the junction temperature T_j to a reference temperature T_r, k_B is Boltzmann's constant, q is the electronic charge, and n is a constant dependent on the transistor manufacture. V_{ebr} and I_{cr} are emitter-base voltage V_{eb} and collector current I_c at T_r. Early studies assumed that V_{g0} and n were constants, at 1.205 V and 1.5, respectively, and were the same for all transistors. But Kujik (1973) found somewhat different values, while Ohte et al. (1982) found that n varies with transistor type, and that V_{g0} varies with n and T_r. They proposed an empirical relation,

---

[1] Research Assistant.

[2] Professor and Chairman; Fellow ASME.

[3] Department of Mechanical Engineering, University of Houston, Houston, TX 77204-4792.

Contributed by the Heat Transfer Division of THE AMERICAN SOCIETY OF MECHANICAL ENGINEERS. Manuscript received by the Heat Transfer Division May 1993; revision received September 1993. Keywords: Boiling, Electronic Equipment, Measurement Techniques. Associate Technical Editor: R. Viskanta.

ometry. In the high or low buoyancy forces ratio, the unicell flow is also clearly discerned. The variation of the mean Nusselt number and Sherwood number with the buoyancy forces ratio has the same tendency between the rectangular and trapezoidal enclosures. However, the multilayered flow was not detected for assisting flow in a trapezoidal enclosure with the aspect ratio equal to 1 in the present considered range of buoyancy forces ratio. On the other hand, the slanted wall of the trapezoidal enclosure makes the distributions of temperature and concentration different from those of the rectangular enclosure.

Acknowledgments

The results presented in this paper were obtained in the course of research sponsored by the National Science Foundation under Grant No. HRD-9250087.

References

Beghein, C., Haghighat, F., and Allard, F., 1992, "Numerical Study of Double Diffusive Natural Convection in a Square Cavity," *Int. J. Heat Mass Transfer*, Vol. 35, pp. 833–846.

Han, H., and Kuehn, T. H., 1991a, "Double Diffusive Natural Convection in a Vertical Rectangular Enclosure—I. Experimental Study," *Int. J. Heat Mass Transfer*, Vol. 34, pp. 449–459.

Han, H., and Kuehn, T. H., 1991b, "Double Diffusive Natural Convection in a Vertical Rectangular Enclosure—II. Numerical Study," *Int. J. Heat Mass Tranfer*, Vol. 34, pp. 461–471.

Hyun, J. M., and Lee, J. W., 1990, "Double Diffusive Convection in a Rectangle With Cooperating Horizontal Gradients of Temperature and the Concentration Gradients," *Int. J. Heat Mass Transfer*, Vol. 33, pp. 1605–1716.

Lee, J. W., Hyun, J. M., and Kim, K. W., 1988, "Natural Convection in Confined Fluids With Combined Horizontal Temperature and Concentration Gradients," *Int. J. Heat Mass Transfer*, Vol. 31, pp. 1969–1977.

Lee, J. W., and Hyun, J. M., 1990, "Double Diffusive Convection in a Rectangle With Opposing Horizontal Temperature and the Concentration Gradients," *Int. J. Heat Mass Transfer*, Vol. 33, pp. 1619–1622.

Lee, J. W., and Hyun, J. M., 1991a, "Time Dependent Double Diffusion in a Stable Stratified Fluid Under Lateral Heating," *Int. J. Heat Mass Transfer*, Vol. 34, No. 9, pp.2409–2421.

Lee, J. W., and Hyun, J. M., 1991b, "Double Diffusive Convection in a Cavity Under a Vertical Solutal Gradient and a Horizontal Temperature Gradient," *Int. J. Heat Mass Transfer*, Vol. 34, No. 9, pp. 2403–2427.

Patankar, S. V., 1980, *Numerical Heat Transfer and Fluid Flow*, Hemisphere, Washington, DC.

Turner, J. S., 1974, "Double Diffusion Phenomena," in: *Ann. Rev. Fluid Mech.*, Vol. 6, pp. 37–56. M. Van Dyke, W. G. Vincent, and J. V. Wehausen, eds., Annual Reviews Inc., Palo Alto, CA.

Turner, J.S., 1979, *Buoyancy Effects in Fluids*, Cambridge University Press, London, United Kingdom.

Turner, J. S., 1985, "Multicomponent Convection," in: *Ann. Rev. Fluid Mech.*, Vol. 17, pp. 11–44.

Viskanta, R., Bergman, T. L., and Incropera, F. P., 1985, "Double Diffusive Natural Convection," in: *Natural Convection, Fundamental and Applications*, S. Kakac, W. Aung, and R. Viskanta, eds., Hemisphere Publishing Corporation, Washington, DC, pp. 1075–1099.

An In Situ Technique for Measuring Heat Transfer From a Power Transistor to a Boiling Liquid

C. L. Struble[1, 3] and L. C. Witte[2, 3]

Introduction

Management of the waste heat from microelectronics has become a critical part of the design of high-speed computers. Closer packing of components in VLSI and multichip packages will result in heat fluxes of 100 W/cm^2 or greater in future generations of high-speed electronic devices. Such levels are beyond the capabilities of most indirect cooling systems, and will require direct immersion cooling with dielectric liquids.

The large temperature excursion at boiling incipience, and the relatively low burnout heat flux of dielectric liquids, has limited this application. Both incipience excursion and burnout can be partially alleviated by the use of forced convection. Monde and Katto (1978) studied downward-impinging jets of water and R-113 in air, and found that fully developed nucleate jet boiling is unaffected by jet diameter, velocity, or subcooling, and could be treated as an extension of pool boiling to higher flux. This was confirmed by Ma and Bergles (1983, 1986) in studies of horizontal submerged jets in R-113. They found, however, that the incipience temperature and heat flux are strong functions of the surface cavity radius and that smooth surfaces such as silicon chips will have different incipience characteristics than a machined surface with a wide range of cavity sizes. Depending on the jet velocity, liquid subcooling, and surface characteristics, incipience excursion may be reduced or eliminated.

This suggests further study of boiling on heaters with surfaces and electrical properties similar to computer chips. Few such studies have been done because of the difficulty of measuring heat flux and temperature accurately. Hwang and Moran (1981), Park and Bergles (1986), and Hijikata et al. (1988) have used the forward voltage of a diode intrinsic to a silicon "thermal chip" as a temperature-sensitive parameter in boiling experiments. However, in none of these studies could heat flux be measured with certainty because of heat losses to chip substrates, bonding wires, etc.

A similar technique has been used to measure temperature of power transistors in enclosed packages. Blackburn (1975), Oettinger et al. (1976), and Zommer et al. (1976) used a switching circuit allowing alternate heating and measurements of the transistor emitter-base voltage as a temperature sensitive parameter. In this technique, the cooling curve is traced back to power cutoff to obtain the temperature. The cooling curve can also be used to measure heat flux with reasonable accuracy.

As simulated chips for boiling experiments, power transistors have several advantages. They can generate heat levels of up to 200 W on a small (~5 mm) chip, and can sustain temperatures up to 200°C, enabling study of transition to burnout. They are inexpensive, widely available, and have similar surface characteristics to IC chips. They are also compatible with dielectric liquids.

Temperature Measurement

The emitter-base voltage V_{eb} of a transistor is a decreasing, nearly linear function of temperature. This property has been used for commercial temperature sensors; see Timko (1976) and Ohte et al. (1982); and precision reference voltage sources; see Kujik (1973) and Brokaw (1974). The expression for V_{eb} is, from Widlar (1971):

$$V_{eb} = V_{g0}\,(1-\gamma) + V_{ebr}\,\gamma + \frac{k_B\,T_j}{q}\,\ln\left[\left(\frac{1}{\gamma}\right)^n\left(\frac{I_c}{I_{cr}}\right)\right], \qquad (1)$$

where V_{g0} is the extrapolated bandgap voltage at 0 K, γ is the ratio of the junction temperature T_j to a reference temperature T_r, k_B is Boltzmann's constant, q is the electronic charge, and n is a constant dependent on the transistor manufacture. V_{ebr} and I_{cr} are emitter-base voltage V_{eb} and collector current I_c at T_r. Early studies assumed that V_{g0} and n were constants, at 1.205 V and 1.5, respectively, and were the same for all transistors. But Kujik (1973) found somewhat different values, while Ohte et al. (1982) found that n varies with transistor type, and that V_{g0} varies with n and T_r. They proposed an empirical relation,

---

[1] Research Assistant.

[2] Professor and Chairman; Fellow ASME.

[3] Department of Mechanical Engineering, University of Houston, Houston, TX 77204-4792.

Contributed by the Heat Transfer Division of THE AMERICAN SOCIETY OF MECHANICAL ENGINEERS. Manuscript received by the Heat Transfer Division May 1993; revision received September 1993. Keywords: Boiling, Electronic Equipment, Measurement Techniques. Associate Technical Editor: R. Viskanta.

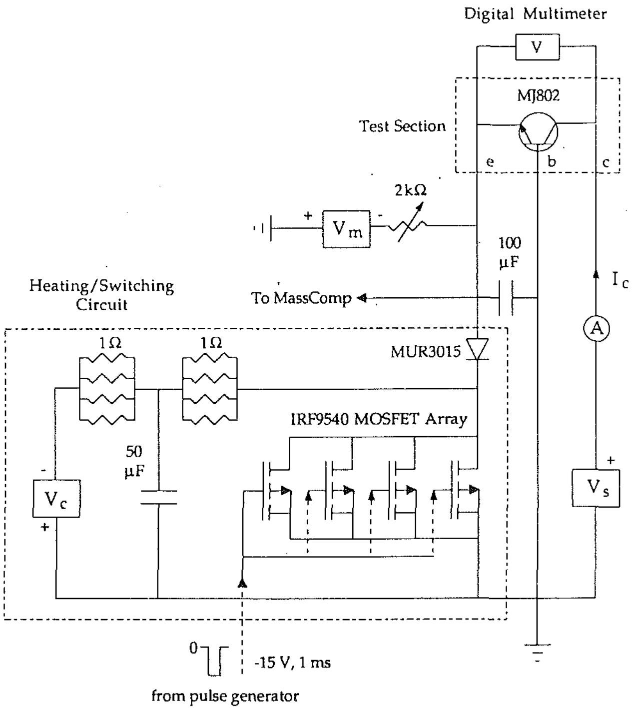

Fig. 1 Emitter-base voltage heating and measurement circuit

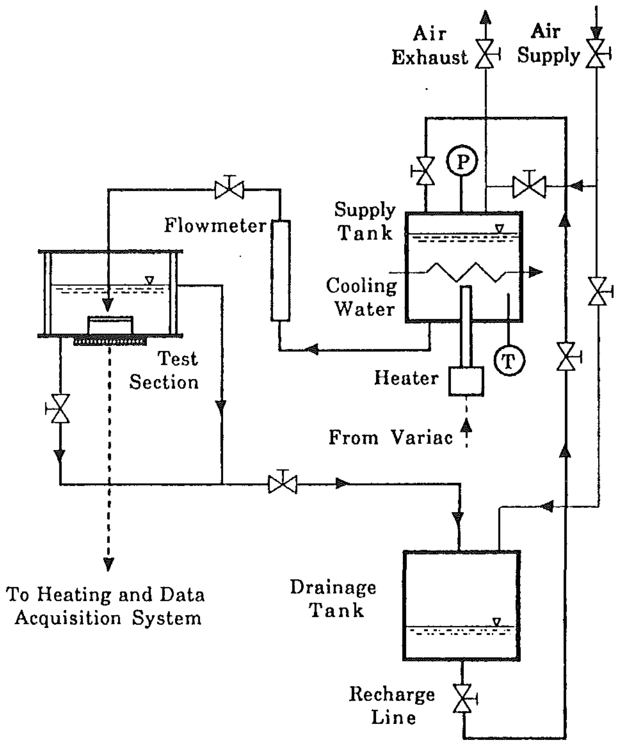

Fig. 2 Diagram of the jet/spray cooling test facility

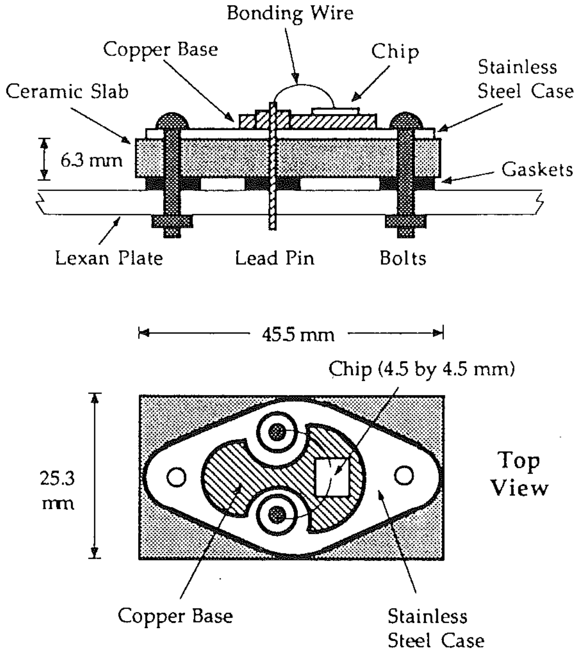

Fig. 3 Detailed view of transistor mounting assembly

$$V_{g0}=1.264-\frac{k_B T_r}{q}n \qquad (2)$$

for discrete and IC transistors, and for a value of n from 3.0 to 5.0. For typical power transistors, Zommer et al. (1976) found that the T_j-V_{eb} relation is linear, meaning $n=0$.

Calibration curves for several power transistors were obtained in this study; see Struble and Witte (1991) for details. In this study an MJ802 high current transistor was used. The cover of the transistor package was removed, and a thermocouple bead attached to the copper base close to the chip. Its V_{eb}-T_j relation is linear, with sensitivities of about $2.5+/-0.1$ mV/°C, and V_{g0} of from 1.264 to 1.268 V, agreeing very closely with that predicted by Eq. (2) for $n=0$. Given this close agreement, we can then assume $n=0$, so that Eq. (1) becomes,

$$V_{eb}=V_{g0}(1-\gamma)+V_{ebr}\gamma-\frac{k_B T_j}{q}\ln\left[\frac{I_c}{I_{cr}}\right], \qquad (3)$$

The use of a power transistor as both heater and sensor requires that the heating current be removed for a brief "window" during which V_{eb} is measured. This is done with a heating/switching circuit shown in Fig. 1. It is based on similar circuits used by Blackburn (1975) and others. Every 2-3 seconds a 1 ms pulse biases a switching transistor, cutting out the current heating supply V_c, and leaving only the measurement circuit encompassed by supplies V_s and V_m. V_{eb} is then measured and traced back to power cut-off to find the steady-state temperature. Data acquisition is performed with a MassComp 5400 workstation using Laboratory Workbench software, at a sampling rate of 20 kHz.

Jet Boiling Apparatus

Experiments were performed in a test facility shown in Fig. 2. A pressurized tank supplies liquid R-113 to a jet nozzle above the transistor chip. Liquid level is controlled by exit valves to allow free or submerged jet experiments if desired. Temperature of the liquid bulk (for submerged jet boiling) is maintained by continual introduction of liquid from the supply tank, which contains a cooling coil and an immersion heater for temperature control. Pre-boiling of the liquid in the supply tank, followed by venting, removes noncondensable gas. A tube through the top plate is attached to a single-stream jet nozzle with a diameter of 1.04 mm, impinging 6.35 mm above the chip center.

A detailed view of the mounting assembly is shown in Fig. 3. The transistor is mounted to a copper base on a conventional stainless steel (TO-3) case. The cover is removed to expose the chip, and the case is sanded to minimize stray boiling. Lead wires exit the bottom of the case through a ceramic slab, which provides thermal insulation to confine boiling to the upper

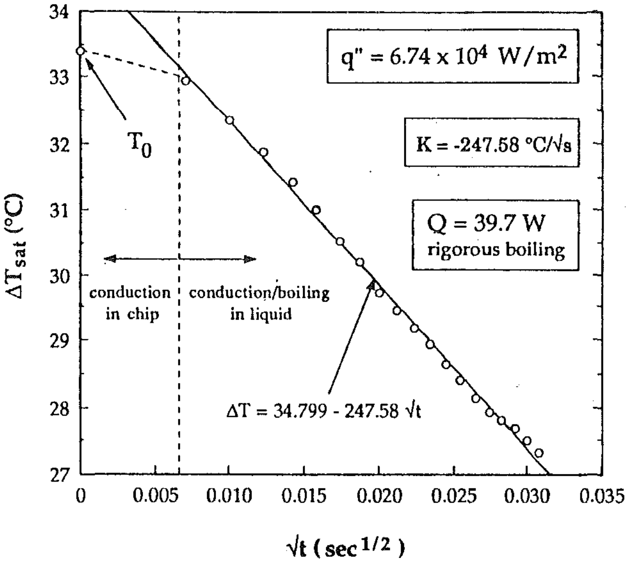

Fig. 4 Typical trace, showing development of liquid cooling curve

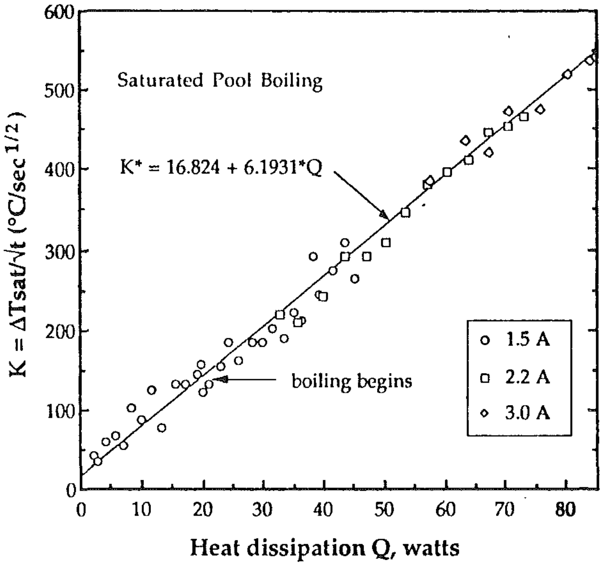

Fig. 5 Dependence of cooling rate *K* on heat dissipation *Q*

surface of the chip and the case. The entire mounting assembly can be quickly removed for replacement of the transistors.

Most of the heat flow in this configuration will not be directly from the chip to the liquid, but to the copper base. This makes it impossible to determine boiling heat flux by steady-state analysis.

Heat Flux Measurement

The heat flux can be determined by measuring the slope K of the cooling curve after power is removed, given by

$$T_0 - T = K(t - t_s)^{0.5} + \text{const}, \tag{4}$$

where $t > t_s$ where t_s is the time required for cooling at the chip surface to reach the junction. This will occur when the "penetration depth" of transient conduction through the chip is equal to the distance h between the junction and the surface. This is assumed to be about half the chip thickness, or 0.18 mm since the exact internal configuration of the transistor is unknown. Using properties for the thermal conductivity of silicon in Blackburn (1975) and Johnsen 1988), t_s is found to be from 24 to 40 μs, depending on the chip temperature. In Fig. 4, we see a linear relationship between T and $t^{0.5}$.

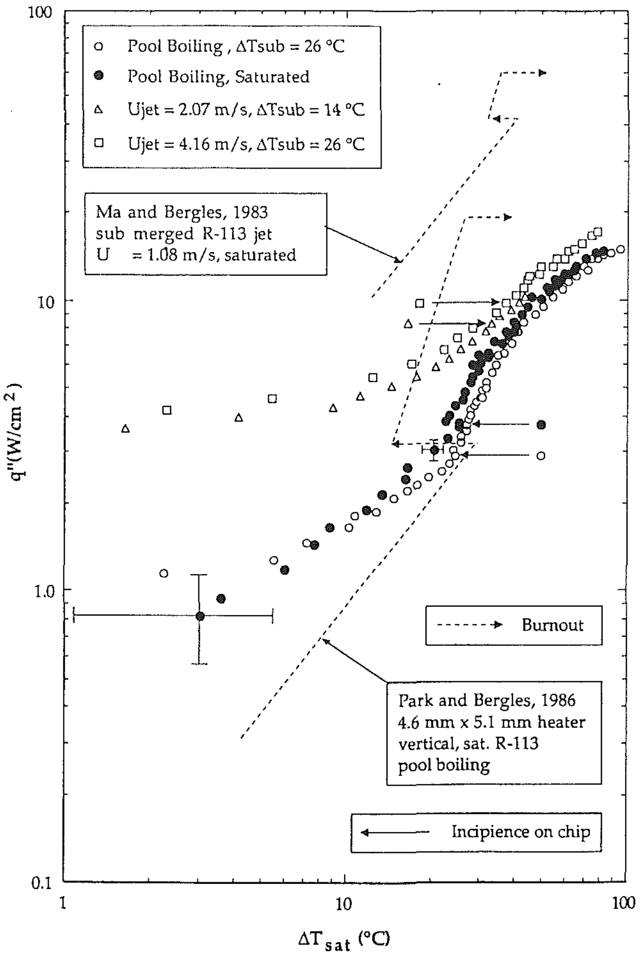

Fig. 6 Pseudo-boiling curve for MJ802 transistor chip

The heat flux q'' can be determined by using Eq. (2.10.10) of Carslaw and Jaeger (1959) for a constant flux heater after heat is removed:

$$T_0 - T = \frac{2q''\sqrt{\alpha t}}{k} \operatorname{erfc} \frac{x}{2\sqrt{\alpha t}} \tag{5}$$

which, at the surface ($x=0$), can be written

$$q'' = \frac{K}{2}\sqrt{\pi k \rho c} \tag{6}$$

where k, ρ, and c are the properties of R-113. So the heat flux through the chip junction out to the surface can be found from the junction cooling rate.

Figure 5 plots the cooling curve K versus the heat dissipation Q just prior to power removal over a wide range. The relationship is virtually linear. This suggests that the fraction of heat flowing through the top of the chip is nearly constant. The fraction of heat that goes to the copper base cannot be calculated unless the coppper base is instrumented to determine its thermal behavior along with the junction temperature.

Experimental Results

The method outlined above was used to measure the boiling curve of an MJ802 chip for pool boiling and for a submerged impinging jet. At each Q, four V_{eb} data sets were obtained and averaged to minimize electrical noise. Struble and Witte (1991) give the details of the temperature correction; they are omitted here for brevity.

Figure 6 shows typical results based on this approach. T_{sat} was determined from the pressure in the chamber. Because the temperature is not fully controlled by the boiling heat flux, but also by the heat flow into the copper base, we refer to this as a psuedo-boiling curve. These results are compared to natural convection and boiling data of Park and Bergles (1986) and Ma and Bergles (1983) for simulated chips in R-113. Error bars based on conventional uncertainty analysis (Struble, 1990) are shown on the low and intermediate values of the temperature difference. Temperature uncertainty was due primarily to uncertainties in measured V_{ce} and I_c, while the heat flux uncertainty depended upon how accurately K could be determined. At high ΔT_{sat}, the uncertainty is less than 1 percent in Q and ΔT; thus the error bars are hidden by the size of the symbols for the data. Uncertainty due to heat loss to the copper base is not included in these estimates.

For pool boiling, bubbles were observed at isolated spots on the edges of the copper base and from the gap between the case and the ceramic long before incipience on the chip surface. At incipience, the center of the chip near the emitter bonding wire began to produce bubbles. At a slightly higher flux, the entire chip surface became blanketed in bubbles. Incipience was accompanied by a temperature drop of 3°C. In the case of subcooled pool boiling the temperature drop was 0.5°C. These temperature drops are much smaller than these obtained by Park and Bergles (1986), possibly because the temperature is stabilized by the thermal mass of the metal package.

For submerged jet boiling, no boiling was observed on the case prior to incipience. Incipience was characterized by the appearance of very small ($\ll$ 1 mm) microbubbles emanating from the chip. At high flux, the bubbles became large slugs, which actually broke up the stagnation flow of the jet and filled the gap between the chip and the jet nozzle.

It was not possible to obtain saturated jet boiling data in this experiment because of premature flashing of the saturated liquid prior to its reaching the nozzle exit. Therefore, we cannot easily separate the subcooling and velocity effects. However, from Fig. 6 we observe a slight increase in heat flux for increased velocity and subcooling for the impinging jet. It is also observed that the jet boiling curves approach the pool boiling curve at high flux, which is typical of the data of Ma and Bergles for submerged jets.

Concluding Remarks

A technique for in situ measurement of temperature and heat flux in boiling heat transfer from electronic chips is developed in this paper. The method was used to obtain accurate partial boiling curves for jet impingment and pool boiling in R-113. While the characteristics of the heat transfer behavior agree with previous data, the data in general lie below data obtained with specialized test chips.

Acknowledgments

The primary source of support for this research was the Texas Advanced Technology Program Grant ATP-2040. Auxiliary support was provided by NASA in the form of a NASA Graduate Student grant to Mr. Struble.

References

Blackburn, D. L., 1975, "An Electrical Technique for Measurement of the Peak Junction Temperature of Power Transistors," *13th Annual Proc. on Reliability Physics*, pp. 142–145.

Brokaw, A. P., 1974, "A Simple Three-Terminal IC Bandgap Reference," *IEEE Journal of Solid State Circuits*, Vol. SC-9, No. 6, pp. 388–393.

Carslaw, H. S., and Jaeger, J. C., 1959, *Conduction of Heat in Solids*, Oxford University Press, London, United Kingdom, p. 76.

Hijikata, K., Nagasaki, T., and Kurata, N., 1988, "A Study on Boiling Heat Transfer From Diode Elements in an Integrated Circuit Chip," *Proc. 1st ASME-JSME Thermal and Fluids Conference*, Vol. 1, pp. 67–72.

Hwang, U. P., and Moran, K. P., 1981, "Boiling Heat Transfer of Silicon Integrated Circuit Chips Mounted on a Substrate," ASME HTD-Vol. 20, pp. 53–59.

Johnsen, R. J., 1988, "Thermal Rating of RF Power Transistors," Applications Note AN-790, Motorola Semiconductor Products, Phoenix, AZ.

Kujik, K. E., 1973, "A Precision Reference Voltage Source," *IEEE Journal of Solid State Circuits*, Vol. SC-8, No. 3, pp. 222–226.

Ma, C. F., and Bergles, A., 1983, "Boiling Jet Impingement Cooling of Simulated Microelectronic Chips," *Heat Transfer in Electronic Equipment*, ASME, New York, pp. 5–12.

Ma, C. F., and Bergles, A., 1986, "Jet Impingement Nucleate Boiling," *Int. J. Heat Mass Transfer*, Vol. 29, No. 8, pp. 1095–1101.

Monde, M., and Katto, Y., 1978, "Burnout in a High Heat Flux System With an Impinging Jet," *Int. J. Heat Mass Transfer*, Vol. 21, pp. 295–305.

Oettinger, F. F., Blackburn, D., and Rubin, S., 1976, "Thermal Characteristics of Power Transistors," *IEEE Transactions on Electron Devices*, Vol. ED-23, No. 8, pp. 831–838.

Ohte, A., Yamagata, M., and Akiyama, K., 1982, "Precision Silicon Transistor Thermometer," *Temperature*, Vol. 5, Am. Institute of Physics, pp. 1197–1203.

Park, K. A., and Bergles, A. E., 1986, "Boiling Heat Transfer Characteristics of Simulated Microelectronic Chips With Flourinert Electronic Liquids," Technical Report HTL-40, Department of Mech. Engineering, Iowa State University.

Struble, C., 1990, "An Electrical Method for Measurement of Jet Nucleate Boiling Heat Transfer on Power Transistors in Dielectric Liquids," MS Thesis, Dept. of Mech. Engineering, University of Houston, Houston, TX.

Struble, C., and Witte, L. C., 1991, "Jet Nucleate Boiling on Power Transistors in Dielectric Liquids Using Emitter-Base Voltage Measurement Technique," *Proc. of JSME/ASME Joint Thermal Engineering Conference*, Vol. 2, pp. 405–412.

Timko, M. P., 1976, "A Two-Terminal IC Temperature Transducer," *IEEE Journal of Solid State Circuits*, Vol. SC-11, No. 6, pp. 748–758.

Widlar, R. J., 1971, "New Developments in IC Voltage Regulators," *IEEE Joural of Solid State Circuits*, Vol. SC-6, pp. 2–7.

Zommer, N. D., Feucht, D. L., and Heckel, R. W., 1976, "Reliability and Thermal Impedance Studies in Soft-Soldered Power Transistors," *IEEE Transactions on Electron Devices*, Vol. ED-23, No. 8, pp. 843–850.

Analytical Prediction of the Axial Dryout Point for Evaporating Liquids in Triangular Microgrooves

J. M. Ha[1,3] and G. P. Peterson[2,3]

Nomenclature

A, B = constants
Bo = Bond number
c, C = constants in Eqs. (4) and (19)
Ca = Capillary number
D = dimensionless shape parameter in Eq. (23)
F_v = viscous term defined in Eq. (1)
g = gravitational acceleration
h = central height of liquid film in the groove
h_{fg} = latent heat of vaporization
K = parameter in Eq. (3)
$\dot{m}$ = mass flow rate in the x direction at a given axial location
P = pressure
q'' = local heat flux normal to the bottom of the plate
Q_b'' = constant heat flux normal to the bottom of the plate
$r(x)$ = radius of the meniscus at location x
w = half of the top groove width

---

[1] Graduate Research Assistant.

[2] Tenneco Professor and Head; Fellow ASME.

[3] Department of Mechanical Engineering, Texas A&M University, College Station, TX 77843.

Contributed by the Heat Transfer Division and presented at the 29th National Heat Transfer Conference, Atlanta, Georgia, August 8–11, 1993. Manuscript received by the Heat Transfer Division March 1993; revision received September 1993. Keywords: Modeling and Scaling, Moving Boundaries, Phase-Change Phenomena. Associate Technical Editor: A. Faghri.

temperature is not fully controlled by the boiling heat flux, but also by the heat flow into the copper base, we refer to this as a psuedo-boiling curve. These results are compared to natural convection and boiling data of Park and Bergles (1986) and Ma and Bergles (1983) for simulated chips in R-113. Error bars based on conventional uncertainty analysis (Struble, 1990) are shown on the low and intermediate values of the temperature difference. Temperature uncertainty was due primarily to uncertainties in measured V_{ce} and I_c, while the heat flux uncertainty depended upon how accurately K could be determined. At high ΔT_{sat}, the uncertainty is less than 1 percent in Q and ΔT; thus the error bars are hidden by the size of the symbols for the data. Uncertainty due to heat loss to the copper base is not included in these estimates.

For pool boiling, bubbles were observed at isolated spots on the edges of the copper base and from the gap between the case and the ceramic long before incipience on the chip surface. At incipience, the center of the chip near the emitter bonding wire began to produce bubbles. At a slightly higher flux, the entire chip surface became blanketed in bubbles. Incipience was accompanied by a temperature drop of 3°C. In the case of subcooled pool boiling the temperature drop was 0.5°C. These temperature drops are much smaller than these obtained by Park and Bergles (1986), possibly because the temperature is stabilized by the thermal mass of the metal package.

For submerged jet boiling, no boiling was observed on the case prior to incipience. Incipience was characterized by the appearance of very small ($\ll$ 1 mm) microbubbles emanating from the chip. At high flux, the bubbles became large slugs, which actually broke up the stagnation flow of the jet and filled the gap between the chip and the jet nozzle.

It was not possible to obtain saturated jet boiling data in this experiment because of premature flashing of the saturated liquid prior to its reaching the nozzle exit. Therefore, we cannot easily separate the subcooling and velocity effects. However, from Fig. 6 we observe a slight increase in heat flux for increased velocity and subcooling for the impinging jet. It is also observed that the jet boiling curves approach the pool boiling curve at high flux, which is typical of the data of Ma and Bergles for submerged jets.

Concluding Remarks

A technique for in situ measurement of temperature and heat flux in boiling heat transfer from electronic chips is developed in this paper. The method was used to obtain accurate partial boiling curves for jet impingment and pool boiling in R-113. While the characteristics of the heat transfer behavior agree with previous data, the data in general lie below data obtained with specialized test chips.

Acknowledgments

The primary source of support for this research was the Texas Advanced Technology Program Grant ATP-2040. Auxiliary support was provided by NASA in the form of a NASA Graduate Student grant to Mr. Struble.

References

Blackburn, D. L., 1975, "An Electrical Technique for Measurement of the Peak Junction Temperature of Power Transistors," *13th Annual Proc. on Reliability Physics*, pp. 142–145.

Brokaw, A. P., 1974, "A Simple Three-Terminal IC Bandgap Reference," *IEEE Journal of Solid State Circuits*, Vol. SC-9, No. 6, pp. 388–393.

Carslaw, H. S., and Jaeger, J. C., 1959, *Conduction of Heat in Solids*, Oxford University Press, London, United Kingdom, p. 76.

Hijikata, K., Nagasaki, T., and Kurata, N., 1988, "A Study on Boiling Heat Transfer From Diode Elements in an Integrated Circuit Chip," *Proc. 1st ASME-JSME Thermal and Fluids Conference*, Vol. 1, pp. 67–72.

Hwang, U. P., and Moran, K. P., 1981, "Boiling Heat Transfer of Silicon Integrated Circuit Chips Mounted on a Substrate," ASME HTD-Vol. 20, pp. 53–59.

Johnsen, R. J., 1988, "Thermal Rating of RF Power Transistors," Applications Note AN-790, Motorola Semiconductor Products, Phoenix, AZ.

Kujik, K. E., 1973, "A Precision Reference Voltage Source," *IEEE Journal of Solid State Circuits*, Vol. SC-8, No. 3, pp. 222–226.

Ma, C. F., and Bergles, A., 1983, "Boiling Jet Impingement Cooling of Simulated Microelectronic Chips," *Heat Transfer in Electronic Equipment*, ASME, New York, pp. 5–12.

Ma, C. F., and Bergles, A., 1986, "Jet Impingement Nucleate Boiling," *Int. J. Heat Mass Transfer*, Vol. 29, No. 8, pp. 1095–1101.

Monde, M., and Katto, Y., 1978, "Burnout in a High Heat Flux System With an Impinging Jet," *Int. J. Heat Mass Transfer*, Vol. 21, pp. 295–305.

Oettinger, F. F., Blackburn, D., and Rubin, S., 1976, "Thermal Characteristics of Power Transistors," *IEEE Transactions on Electron Devices*, Vol. ED-23, No. 8, pp. 831–838.

Ohte, A., Yamagata, M., and Akiyama, K., 1982, "Precision Silicon Transistor Thermometer," *Temperature*, Vol. 5, Am. Institute of Physics, pp. 1197–1203.

Park, K. A., and Bergles, A. E., 1986, "Boiling Heat Transfer Characteristics of Simulated Microelectronic Chips With Flourinert Electronic Liquids," Technical Report HTL-40, Department of Mech. Engineering, Iowa State University.

Struble, C., 1990, "An Electrical Method for Measurement of Jet Nucleate Boiling Heat Transfer on Power Transistors in Dielectric Liquids," MS Thesis, Dept. of Mech. Engineering, University of Houston, Houston, TX.

Struble, C., and Witte, L. C., 1991, "Jet Nucleate Boiling on Power Transistors in Dielectric Liquids Using Emitter-Base Voltage Measurement Technique," *Proc. of JSME/ASME Joint Thermal Engineering Conference*, Vol. 2, pp. 405–412.

Timko, M. P., 1976, "A Two-Terminal IC Temperature Transducer," *IEEE Journal of Solid State Circuits*, Vol. SC-11, No. 6, pp. 748–758.

Widlar, R. J., 1971, "New Developments in IC Voltage Regulators," *IEEE Joural of Solid State Circuits*, Vol. SC-6, pp. 2–7.

Zommer, N. D., Feucht, D. L., and Heckel, R. W., 1976, "Reliability and Thermal Impedance Studies in Soft-Soldered Power Transistors," *IEEE Transactions on Electron Devices*, Vol. ED-23, No. 8, pp. 843–850.

Analytical Prediction of the Axial Dryout Point for Evaporating Liquids in Triangular Microgrooves

J. M. Ha[1,3] and G. P. Peterson[2,3]

Nomenclature

A, B = constants
Bo = Bond number
c, C = constants in Eqs. (4) and (19)
Ca = Capillary number
D = dimensionless shape parameter in Eq. (23)
F_v = viscous term defined in Eq. (1)
g = gravitational acceleration
h = central height of liquid film in the groove
h_{fg} = latent heat of vaporization
K = parameter in Eq. (3)
$\dot{m}$ = mass flow rate in the x direction at a given axial location
P = pressure
q'' = local heat flux normal to the bottom of the plate
Q_b'' = constant heat flux normal to the bottom of the plate
$r(x)$ = radius of the meniscus at location x
w = half of the top groove width

---

[1] Graduate Research Assistant.

[2] Tenneco Professor and Head; Fellow ASME.

[3] Department of Mechanical Engineering, Texas A&M University, College Station, TX 77843.

Contributed by the Heat Transfer Division and presented at the 29th National Heat Transfer Conference, Atlanta, Georgia, August 8–11, 1993. Manuscript received by the Heat Transfer Division March 1993; revision received September 1993. Keywords: Modeling and Scaling, Moving Boundaries, Phase-Change Phenomena. Associate Technical Editor: A. Faghri.

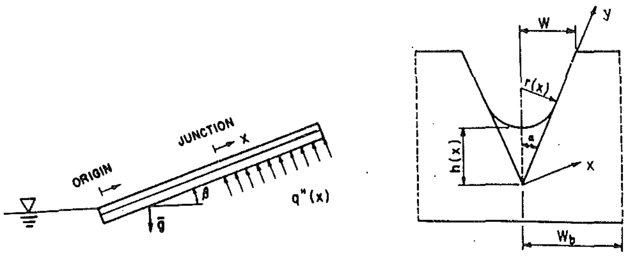

Fig. 1 (*a*) Schematic of the modeled region; (*b*) groove geometry

w_b = half of the bottom groove width
x, x' = coordinate along the groove channel
y = coordinate along the groove wall
α = half the vertex angle of the groove
β = slope of the plate with respect to gravity
$\eta_{\max}$ = dimensionless wetted length
ν = kinematic viscosity
ξ_j = dimensionless radius at the junction
ρ = density
σ = surface tension

Subscripts

b = bottom of plate
j = junction of the adiabatic and evaporator regions
l = density
max = dryout region
o = origin where the plate is immersed in the liquid pool
ν = density

Analysis

Analytical studies of the surface wetting and fluid flow in small capillary grooves have been conducted by Ayyaswamy et al. (1974), Renk et al. (1978), Renk and Wayner (1979), and Swanson and Peterson (1994). These have been followed more recently by the experimental studies of Peng and Peterson (1992), Stroes et al. (1992), and Xu and Carey (1990). While these investigations have been helpful in understanding the behavior of the meniscus and how it affects the heat transfer, little information has been obtained about the axial or cross-sectional flow fields occurring in these grooves. For this reason, an analytical investigation was undertaken to develop a method for predicting the axial dryout location in a closed form for triangular grooves containing an evaporating liquid.

The current investigation is restricted to thin liquid films flowing in **V**-shaped microgrooves, of the type illustrated in Fig. 1. One end of the grooved plate is immersed in a pool of liquid and held stationary at an inclination angle β. For small grooves and small inclination angles, the liquid will wick up the groove against the gravitational body force and for the case of evaporating liquids, against the frictional pressure gradients caused by continuous flow. The wicking action or capillary pumping is the result of a decrease in the radius of curvature caused by the intrinsic meniscus receding into the groove. As the liquid recedes toward the apex of the groove, the liquid film thins, approaching a film thickness of nearly zero. In the current model, an axial adiabatic region was included between the origin point where the plate emerges from the liquid pool and the junction point from which a uniform heat flux was applied.

In a very small groove, the capillary radius of the intrinsic meniscus is nearly constant and the axial flow is confined to the intrinsic meniscus region due to the large resistance to flow in the evaporating thin film and adsorbed layer regions. For grooves relying primarily on capillary pumping, the axial flow of liquid occurs entirely in the groove (i.e., no flow occurs over the flat ridge portion between the grooves). To determine the end of the wetted axial length or the location of the dryout point, several assumptions have been made:

(*i*) The axial flow along the groove in the x direction occurs primarily in the intrinsic meniscus region.
(*ii*) Meanwhile, at any x, the intrinsic meniscus shape is circular (i.e., the radius of curvature is constant), and the radius of curvature decreases in the x direction. The capillary pressure gradient due to this variation drives the liquid flow in the x direction.
(*iii*) The curvature effect is neglected in the extended thin film region, and in this region the disjoining pressure gradient along the y direction due to the variation of the film thickness drives the film flow up the **V**-groove wall.
(*iv*) The vapor pressure is constant.

The flow in the x direction can be described by a force-momentum balance:

$$\frac{dP_l}{dx} + \rho_l g \sin\beta + F_\nu = 0 \tag{1}$$

Since the vapor pressure was assumed to be constant, the liquid pressure gradient can be related to the radius of curvature as

$$\frac{dP_l}{dx} = -\frac{d}{dx}(P_\nu - P_l) = -\frac{d}{dx}\left(\frac{\sigma}{r(x)}\right) \tag{2}$$

For the viscous term, F_ν, using a procedure similar to that originally proposed by Xu and Carey (1990), Eq. (1) can be rewritten as

$$\frac{d}{dx}\left(\frac{\sigma}{r(x)}\right) = \frac{2K\nu_l}{cr(x)^4}\dot{m} + \rho_l g \sin\beta \tag{3}$$

where

$$c = 4\tan^2\alpha\left(\frac{1}{\tan\alpha} + \alpha - \frac{\pi}{2}\right)^3 \tag{4}$$

In the above expression, the parameter K, originally determined by Ayyaswamy et al. (1974) is a function of the groove half-angle and the contact angle.

Evaporating Region. If the liquid in the evaporating region is saturated and the heat flux is uniform, the mass flow rate at x can be expressed as

$$\dot{m} = \int_0^{\dot{m}} d\dot{m} = \frac{1}{h_{fg}}\int_{x_{\max}}^{x} \dot{q}''\, 2w_b(-dx) = \frac{2}{h_{fg}} Q_b'' w_b (x_{\max} - x) \tag{5}$$

where $x_{\max}$ is the dryout point measured from the junction point, at which the mass flow rate is zero. Combining the governing Eq. (3), with Eq. (5) yields

$$\frac{dr(x)}{dx} r(x)^2 = -A(x_{\max} - x) - Br(x)^4 \tag{6}$$

where

$$A = \frac{4K\nu_l Q_b'' w_b}{c\sigma h_{fg}} \quad \text{and} \quad B = \frac{\rho_l g \sin\beta}{\sigma} \tag{7}$$

Equation (6) is a nonlinear first-order ordinary differential equation with respect to x and must be solved numerically. However, to obtain a better physical insight into the flow behavior in these types of situations, an approximate closed-form solution for $x_{\max}$ can be obtained assuming that the axial profile of $h(x)$ is of a general polynomial form. This requires that $h(x)$ satisfy the following three boundary conditions:

$$\begin{aligned} &\text{at } x = 0 && h = h_j \\ &\text{at } x = x_{\max} && h \sim 0 = 0 \\ &\text{at } x = x_{\max} && dh/dx = 0 \end{aligned} \tag{8}$$

where h_j is h at the junction. The third boundary condition results from the assumption that the axial variation of h near the dryout point is negligible due to the effect of the axial dispersion forces. Solution of the assumed polynomial expression for h, with only three boundary conditions, yields a quadratic expression of the form

$$h(x)=\frac{h_j}{x_{\max}^2}(x-x_{\max})^2=\left(\frac{1}{\sin\alpha}-1\right)r(x) \tag{9}$$

Relating h and r by geometry suggests the following form for dr/dx:

$$\frac{d}{dx}r(x)=\frac{2r_j}{x_{\max}^2}(x-x_{\max}) \tag{10}$$

where r_j corresponds to h_j at the junction and equals r. Using this as a first approximation, Eq. (6) can be changed into the following algebraic expression:

$$2r_j r(x)^2\left(\frac{x-x_{\max}}{x_{\max}^2}\right)=-A(x_{\max}-x)-Br(x)^4 \tag{11}$$

Applying the boundary conditions at $x=0$ yields the following expression for $x_{\max}$, in terms of r_j, A, and B:

$$x_{\max}=\frac{r_j}{2A}\left(-Br_j^3+\sqrt{B^2r_j^6+8Ar_j}\right) \tag{12}$$

Because $x_{\max}$ is dependent upon A and B, it is helpful to understand the physical meaning of these terms along with the effect of r_j, the value of which can be found by analyzing the liquid film behavior in the adiabatic region.

Adiabatic Region. In the adiabatic region, the axial mass flow rate at any position is constant and equal to the total mass flow rate evaporated over the entire length of the evaporating region. This can be expressed as a function of $x_{\max}$ as follows:

$$\dot{m}_f=\dot{m}_o=\frac{2Q_b''w_b}{h_{fg}}x_{\max} \tag{13}$$

Substituting this expression into Eq. (3) and rearranging yields

$$\frac{dr(x')}{dx'}=-\frac{Ax_{\max}}{r(x')^2}-Br(x')^2 \tag{14}$$

which can be solved numerically. Since the meniscus completely fills the groove at the origin, the applicable boundary condition is

$$\text{at}\quad x'=0\quad r(x')=r_o=\frac{w}{\cos\alpha} \tag{15}$$

With Eq. (14) and this boundary condition, r_j can be found and related to $x_{\max}$ by Eq. (12). It is worth noting that r_j is numerically calculated in the adiabatic region.

Isothermal Case. For the isothermal case with no applied heat flux, the mass flow rate is nearly zero, causing the entire viscous term in Eq. (1) to disappear. This yields an expression of the form

$$\frac{dr(x)}{dx}=-Br(x)^2 \tag{16}$$

Using an approach similar to that outlined previously results in a similar expression for dr/dx, i.e., Eq. (10), but with r_o instead of r_j. With the boundary condition at $x=0$, of $r(x)=r_o$, the above equation yields an expression for $x_{\max}$, for the isothermal case of

$$x_{\max}=\frac{2}{Br_o}\quad\text{where}\quad r_o=\frac{w}{\cos\alpha} \tag{17}$$

Nonuniform Heat Flux Case. If an adiabatic region is not included and the heat flux distribution is represented by $q''(x)=ax^2+bx$. The mass flow rate at a given position x can be expressed as

$$\dot{m}=\frac{2w_b}{h_{fg}}\left[\frac{a}{3}(x_{\max}^3-x^3)+\frac{b}{2}(x_{\max}^2-x^2)\right] \tag{18}$$

Combining Eq. (3) with Eq. (18) and using an approach similar to that described previously yields

$$2r^2r_o\left(\frac{x-x_{\max}}{x_{\max}^2}\right)=-C\left[\frac{a}{3}(x_{\max}^3-x^3)+\frac{b}{2}(x_{\max}^2-x^2)\right]-Br^4 \tag{19}$$

where $C=A/Q_b''$. Comparing Eqs. (11) and (19) indicates that the first term on the right-hand side is considerably more complicated due to the nonuniform heat flux distribution.

Using the boundary condition at $x=0$, $r=r_o$ yields the following expression for $x_{\max}$

$$Cx_{\max}^3\left(\frac{a}{3}x_{\max}+\frac{b}{2}\right)+Br_o^4x_{\max}-2r_o^3=0 \tag{20}$$

The equation for $x_{\max}$ without an adiabatic region is expressed implicitly in terms of constants a, b, B, C, and r_o for the nonuniform heat flux case. If the average integrated nonuniform heat flux is used, and $Cx_{\max}(ax_{\max}/3+b/2)$ is set equal to the parameter A in Eq. (7), the expression above reduces to Eq. (12).

Results and Discussion

In order to determine the validity of the technique developed here, the model was used to predict the location of the dryout point for several cases investigated experimentally. For the uniform heat flux case, the predicted values were compared to the experimental data of Stroes et al. (1992). As shown in the inset in Fig. 2, the actual grooves used in these experiments were not triangular, which will cause a somewhat larger value than predicted for $x_{\max}$. As shown in Fig. 2, the predicted values for the isothermal case are quite close to the experimental data, particularly for tilt angles greater than 7 deg.

Equation (17) can be nondimensionalized in terms of the Bond number, Bo, as

$$\eta_{\max}=\frac{2}{\mathrm{Bo}\sin\beta}\quad\text{where}\quad\eta_{\max}=\frac{x_{\max}}{r_o},\ \mathrm{Bo}=\frac{\rho_l g r_o^2}{\sigma} \tag{21}$$

Here r_o, which characterizes the groove width and depth, is the reference length for the Bond number, and $\eta_{\max}$ is dependent on two parameters Bo and β. Thus, if two fluids have the same or similar Bo with a fixed β, the predicted values of $\eta_{\max}$ will be similar. For ethanol and methanol, the ratio of the Bond numbers is 1.068 and hence, these two liquids should yield nearly the same values for the wetted length. This expectation is confirmed by the experimental data illustrated in Fig. 2. As β approaches zero, $1/(\sin\beta)$ goes to infinity very rapidly, indicating that the prediction is reliable even in the range of very small tilt angles.

Figures 2 and 3 present a comparison for the nonisothermal case (for ethanol with $Q_b''=0.75$ W/cm^2, and for methanol with $Q_b''=0.75$ and 2.1 W/cm^2). The predicted trends show some features that agree well with the experimental observation, and examining Eq. (12) provides considerable insight into the location of the dryout point.

The magnitude of $x_{\max}$ is approximately proportional to the inverse of the square root of A. This fact can explain the effect of the fluid properties and the heat flux. For a given fluid, increasing the heat flux causes $x_{\max}$ to decrease. The rate of this decrease will be approximately proportional to the inverse of the square root of the applied heat flux. This trend is illustrated by the experimental data shown in Fig. 3. The effect of different fluid properties on $x_{\max}$ can also be found in this manner. For the same geometry and heat flux, the properties

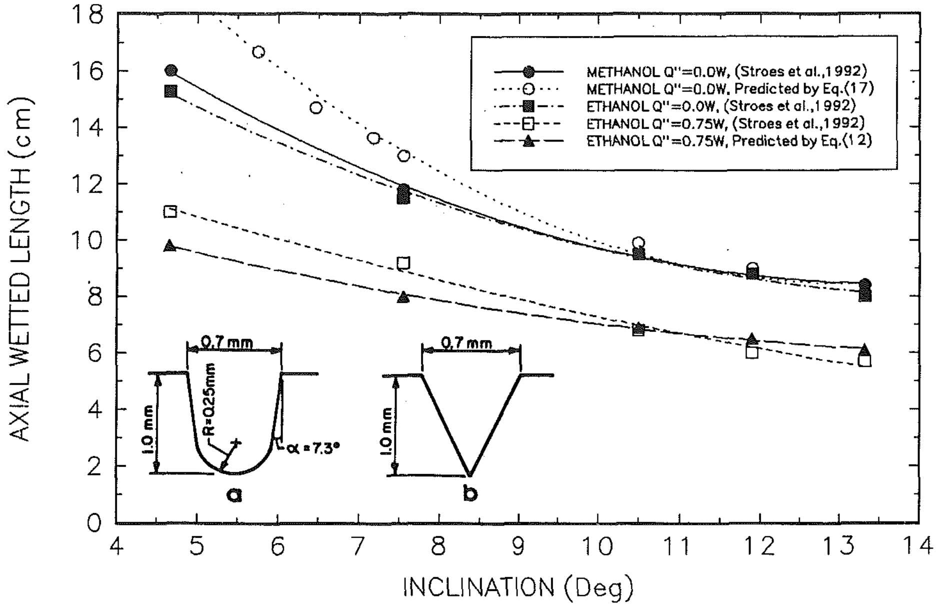

Fig. 2 Actual (*a*) and modeled (*b*) groove dimensions and comparison of the modeling predictions and the experimental data of Stroes et al. (1992) for an isothermal plate and for a uniformly heated plate with ethanol

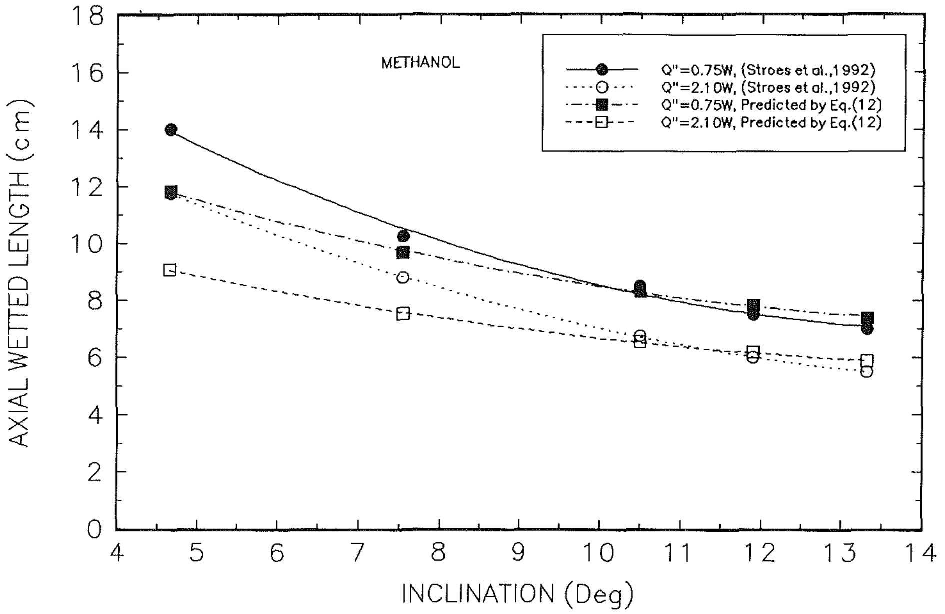

Fig. 3 Comparison of the modeling predictions and the experimental data of Stroes et al. (1992) for a uniformly heated plate with methanol

of ethanol yield a slightly larger value of A than for methanol, resulting in a smaller value for $x_{\max}$. Thus, the wetted length of ethanol should be less than that of methanol, which as shown in Figs. 2 and 3 is what occurs.

As seen so far, Eq. (12) clearly illustrates the parametric relationship that exists between the geometry, the fluid properties, and the heat flux, and describes the effect of variations in each of these. Nondimensionalizing Eq. (12) gives a more physically meaningful explanation of the effect of variations in the Bond number, Bo, and the Capillary number, Ca, i.e.,

$$\eta_{\max}=\frac{-\mathrm{Bo}\sin\beta\xi_j^4}{D\mathrm{Ca}}+\sqrt{\left(\frac{\mathrm{Bo}\sin\beta\,\xi_j^4}{D\mathrm{Ca}}\right)^2+\frac{4\xi_j^3}{D\mathrm{Ca}}} \qquad (22)$$

where

$$\eta_{\max}=\frac{x_{\max}}{r_o},\quad \xi_j=\frac{r_j}{r_o},\quad \mathrm{Bo}=\frac{\rho_l g r_o^2}{\sigma},$$

$$\mathrm{Ca}=\frac{\nu_l Q_b'' w_b}{\sigma h_{fg} w},\quad D=\frac{8K\cos\alpha}{c_3} \qquad (8)$$

In this expression, $\eta_{\max}$ is described in a closed form by five dimensionless variables, ξ_j, β, Bo, Ca, and D. The first of these, ξ_j, accounts for the length of the adiabatic region, β for the inclination angle, Bo for some of the fluid properties, Ca for the combined effect of the remaining fluid properties and the heat flux, and D for the groove shape.

For the case of nonuniform heat fluxes, the model was also used to predict $x_{\max}$ and compared with the experimental results obtained by Xu and Carey (1990). To obtain a better comparison, additional data were provided by Carey (1993) and are presented in Tables 1 and 2. For this case, the shape of the groove utilized in the experiment was triangular with dimensions of $w=32$ μm, $w_b=45.45$ μm, $\alpha=9.35$ deg, making these data more suitable for comparison; however, no adiabatic region was included. The capillary performances of acetone and methanol were tested for varying tilt angles and heat fluxes. As explained in the original reference, heat fluxes were calculated from two temperatures measured on the inner surface of the plate, at $x=3.23$ mm and at $x=7.47$ mm.

The procedure for obtaining $x_{\max}$ was as follows: Because the heat flux could only be determined for two locations on the plate, a quadratic form of $q''(x)=ax^2+bx$ was assumed (Carey, 1990). After determining the constants a and b in $q''(x)$ from the two known values of the heat flux, Eq. (20) was solved numerically for $x_{\max}$. The results, shown in Tables 1 and 2, are quite close to the reported experimental data, especially for acetone, and are almost all within the reported experimental uncertainty.

Table 1 Experimental results for acetone (Carey, 1993)

Case	β		x (mm)		$x_{\max}$ (mm) Experiment	$x_{\max}$ (mm) Predicted
			3.23	7.47		
A1	10°	$q''(x)$	2.51	8.69	9.6 ± 1.5	12.16
A2	20°	$q''(x)$	4.97	11.31	9.6 ± 1.5	11.285
A3	20°	$q''(x)$	6.32	12.14	9.6 ± 1.5	10.999
A4	30°	$q''(x)$	9.48	13.25	9.6 ± 1.5	10.390
A5	30°	$q''(x)$	9.09	14.67	9.6 ± 1.5	10.066

Table 2 Experimental results for methanol (Carey, 1993)

Case	β		x (mm)		$x_{\max}$ (mm) Experiment	$x_{\max}$ (mm) Predicted
			3.23	7.47		
M1	10°	$q''(x)$	2.51	8.69	9.6 ± 1.5	13.849
M2	10°	$q''(x)$	3.30	9.47	9.6 ± 1.5	13.710
M3	20°	$q''(x)$	4.97	11.31	9.6 ± 1.5	13.205
M4	20°	$q''(x)$	6.32	12.14	9.6 ± 1.5	13.156
M5	30°	$q''(x)$	9.09	14.67	9.6 ± 1.5	12.384

In the experimental data, all cases show identical values for the wetted length, 9.6 mm, regardless of the heat flux or the type of fluid. However, for a given fluid at the same tilt angles, larger heat flux values should yield shorter wetted lengths. This expectation is confirmed by the results predicted by the analytical model, as shown in Tables 1 and 2. This is also apparent in Fig. 4, where for each test case, various $q''(x)$ values were integrated to obtain the corresponding values of $x_{\max}$. As shown, for acetone and methanol, the larger β and the larger $q''(x)$ values yield smaller $x_{\max}$ terms (e.g., cases $A1$, $A2$, and $A4$). For acetone and methanol at the same β, the larger heat flux, $q''(x)$, yields a smaller $x_{\max}$ (e.g., cases $A2$ and $A3$). At the same β and $q''(x)$, the $x_{\max}$ for acetone is smaller than that for methanol (e.g., cases $A2$ and $M3$). This appears to be reasonable, since the latent heat of acetone is smaller than for methanol. Through these results, it is apparent that the model is capable of predicting subtle differences, which may be hard to detect experimentally.

Conclusions

An analytical investigation of the vaporization process occurring in thin liquid films flowing in **V**-shaped microgrooves has been conducted with the objective of predicting the axial dryout location in a closed form as a function of the input heat flux, thermophysical properties of the system, and geometric parameters of the grooves. The governing equation represented by a nonlinear differential equation was changed to an algebraic form by approximation. The predicted values agreed well with the experimental data and help to validate the assumptions made. The resulting expression provides additional insight into this type of flow phenomena.

For the isothermal case, the nondimensionalized wetted length was found to be twice the inverse of the Bond number multiplied by $\sin\beta$. For the evaporating, nonisothermal case with uniform heat flux, the nondimensionalized wetted length can be described by five variables. If the physical geometry is fixed, the Bond number and Capillary number are the most important of these, and the length of the evaporating liquid film is approximately proportional to the inverse of the square root of the applied heat flux. For the nonuniform heat flux case, even the subtle differences that are difficult to detect experimentally are apparent.

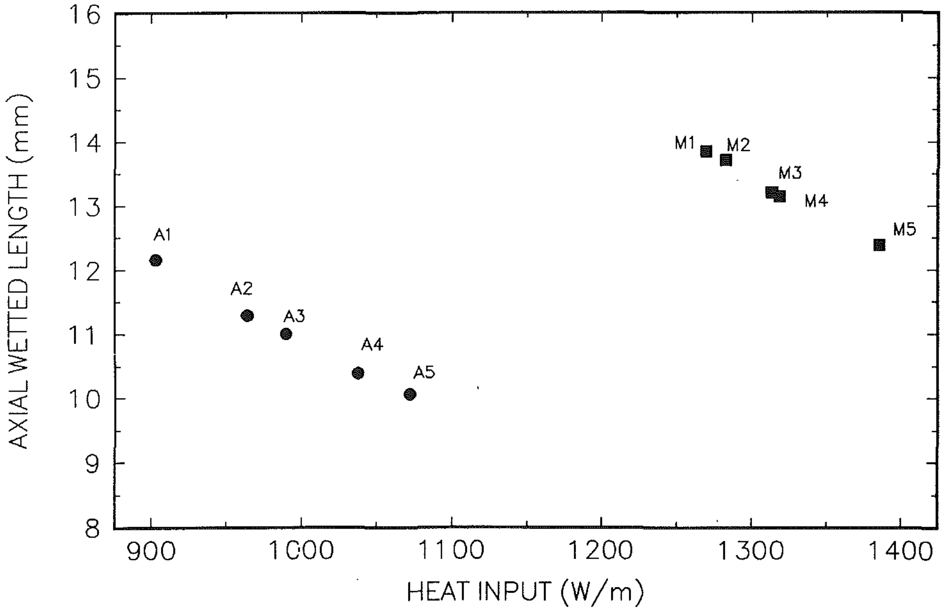

Fig. 4 Predicted wetted length for various tilt angles and heat inputs

Acknowledgments

The authors would like to acknowledge the support of the National Aeronautics and Space Administration (NASA) provided under Contract No. NAG9-511 and the TAMU Center for Space Power. In addition, they would like to thank Professor V. P. Carey for providing access to the additional experimental data shown in Tables 1 and 2.

References

Ayyaswamy, P. S., Catton, I., and Edwards, D. K., 1974, "Capillary Flow in Triangular Grooves," ASME *Journal of Applied Mechanics*, Vol. 41, pp. 332–336.

Carey, V. P., 1993, personal communication to G. P. Peterson.

Peng, X. F., and Peterson, G. P., 1992, "Analytical Investigation of the Rewetting of Grooved Surfaces," *AIAA J. of Thermophysics and Heat Transfer*, Vol. 6, No. 3, pp. 563–565.

Renk, F. J., Wayner, P. C., Jr., and Homsy, G. M., 1978, "On the Transition Between a Wetting Film and a Capillary Meniscus," *J. Colloid Science*, Vol. 67, No. 3, pp. 408–414.

Renk, F. J., and Wayner, P. C., Jr., 1979, "An Evaporating Ethanol Meniscus, Part II: Analytical Studies," ASME JOURNAL OF HEAT TRANSFER, Vol. 101, No. 1, pp. 59–62.

Stroes, G., Rohlloff, T., and Catton, I., 1992, "An Experimental Study of the Capillary Forces in Rectangular Channels Versus Triangular Channels," *1992 ASME National Heat Transfer Conference*, ASME HTD-Vol. 200, pp. 1–8.

Swanson, L., and Peterson, G. P., 1994, "The Evaporating Extended Meniscus in a V-Shaped Channel," *AIAA J. Thermophysics and Heat Transfer*, Vol. 8, No. 1, pp. 172–181 (also as ASME HTD-Vol. 200, pp. 9–22).

Xu, X., and Carey, V. P., 1990, "Film Evaporation From a Micro-grooved Surface—An Approximate Heat Transfer Model and Its Comparison With Experimental Data," *AIAA J. of Thermophysics and Heat Transfer*, Vol. 4, No. 4, pp. 512–520.

Modeling Thermally Governed Transient Flows in Multitube Evaporating Flow Systems With Thermal and Flow Distribution Asymmetry

G. L. Wedekind[1] **and C. J. Kobus**[2]

Introduction

The objective of this paper is to present the results of an investigation into the transient response characteristics of multiple-tube evaporating flow systems where complete vaporization takes place. This type of problem is important since most industrial applications utilize multitube evaporators, where parallel tubes are connected at both ends with common headers. The background for this investigation originated from the success of past research concerned with evaporating flow transients (Wedekind and Beck, 1981) and from the more recent success in the modeling of multitube condensing flow transients (Wedekind and Bhatt, 1989). Therefore, there was a natural motivation to extend the ideas of the latter research to include evaporating flow systems as well.

The major focus here is the investigation of the primary mechanisms for, and the magnitudes of, the influence of thermal and flow distribution asymmetry on outlet flow transients, not system stability. Therefore, heat fluxes will be considered to be sufficiently low to preclude film boiling, and initiated inlet flow changes small enough so that flow regime transition does not take place during the ensuing transient. Under these conditions, the thermal and flow distribution parameters, which describe the asymmetry, can be considered independent of each other and constant.

The approach taken here will be first to summarize the development of the governing equations for a two-tube evaporating flow system; then, the results of an investigation into the influence of thermal and flow distribution asymmetries on the characteristics of thermally governed flow transients will be presented. Finally, utilizing the similarity to multitube condensing flow systems (Wedekind and Bhatt, 1989), an equivalent single-tube model for an *n*-tube system will be suggested, and its predictive accuracy will be verified by comparison with the analytical results obtained from the developed two-tube model.

Development of Two-Tube Model

The analysis is similar to that done by Wedekind and Bhatt (1989) for condensing flow, so the details will not be presented here. Referring to Fig. 1, the conservation of mass principle is applied to each of the two tubes for both the superheated vapor and two-phase regions, under the assumption of a time invariant system mean void fraction.[3] The transient term in each of the equations will have a first-order derivative of the point of complete vaporization, $\eta(t)$. The differential equation governing the motion of the effective point of complete vaporization for each tube can be determined by utilizing the *unified system mean void fraction model* (Wedekind et al., 1984). Referring to the inlet and outlet headers depicted in Fig. 1, the total inlet and outlet mass flowrates can be expressed as the sum of the individual mass flowrates at the inlet and outlet of both tubes, respectively. Also, assuming the inlet flow quality of both tubes to be the same, the combined conservation equation expressing the outlet vapor flow rate of the system becomes

$$m_{t,o}(t) = \{1 - [1-(\rho'/\rho)](1-x_i)\} m_{t,i}(t) + \frac{[1-(\rho'/\rho)]}{(h'-h)} \{\bar{f}_{q,1} P_1 \eta_1(t) + \bar{f}_{q,2} P_2 \eta_2(t)\} \qquad (1)$$

Introducing a flow distribution parameter, γ, defined as the ratio of the mass flowrate entering tube #1 to the total mass flowrate, the inlet flowrates for each tube are related with the following equations:

$$m_{t,1}(z,\, t)_{z=0} = \gamma m_{t,i}(t), \qquad (2)$$

$$m_{t,2}(z,\, t)_{z=0} = (1-\gamma) m_{t,i}(t) \qquad (3)$$

Consider the special case where the time varying inlet flowrate is approximated as an exponential function (which is probably quite realistic), thus

$$m_{t,i}(t) = m_{t,f} + (m_{t,i} - m_{t,f}) e^{-t/\tau_m} \qquad (4)$$

where $m_{t,i}$ and $m_{t,f}$ are the initial and final total inlet mass flowrates, respectively, and τ_m is the time constant for the inlet flowrate variation.

Substituting Eq. (4) into Eqs. (2) and (3) and then Eqs. (2) and (3) into the respective differential equations governing the

---

[1] Professor of Engineering, Oakland University, Rochester, MI 48309; Mem. ASME.

[2] Graduate Assistant, Oakland University, Rochester, MI 48309; Mem. ASME.

Contributed by the Heat Transfer Division of THE AMERICAN SOCIETY OF MECHANICAL ENGINEERS. Manuscript received by the Heat Transfer Division February 1993, revision received July 1993. Keywords: Modeling and Scaling, Phase-Change Phenomena, Transient and Unsteady Heat Transfer. Associate Technical Editor: R. Nelson, Jr.

[3] A detailed discussion of the time invariance of the system mean void fraction is given by Wedekind et al. (1978). In short, time invariance requires that a specific redistribution of liquid and vapor within the two-phase region takes place at a rate faster than that of the particular flow transient under consideration, so that a similarity relationship exists. Consequently, only the steady-state form of the momentum equation is required to compute the system mean void fraction.

Acknowledgments

The authors would like to acknowledge the support of the National Aeronautics and Space Administration (NASA) provided under Contract No. NAG9-511 and the TAMU Center for Space Power. In addition, they would like to thank Professor V. P. Carey for providing access to the additional experimental data shown in Tables 1 and 2.

References

Ayyaswamy, P. S., Catton, I., and Edwards, D. K., 1974, "Capillary Flow in Triangular Grooves," ASME *Journal of Applied Mechanics*, Vol. 41, pp. 332–336.

Carey, V. P., 1993, personal communication to G. P. Peterson.

Peng, X. F., and Peterson, G. P., 1992, "Analytical Investigation of the Rewetting of Grooved Surfaces," *AIAA J. of Thermophysics and Heat Transfer*, Vol. 6, No. 3, pp. 563–565.

Renk, F. J., Wayner, P. C., Jr., and Homsy, G. M., 1978, "On the Transition Between a Wetting Film and a Capillary Meniscus," *J. Colloid Science*, Vol. 67, No. 3, pp. 408–414.

Renk, F. J., and Wayner, P. C., Jr., 1979, "An Evaporating Ethanol Meniscus, Part II: Analytical Studies," ASME JOURNAL OF HEAT TRANSFER, Vol. 101, No. 1, pp. 59–62.

Stroes, G., Rohlloff, T., and Catton, I., 1992, "An Experimental Study of the Capillary Forces in Rectangular Channels Versus Triangular Channels," *1992 ASME National Heat Transfer Conference*, ASME HTD-Vol. 200, pp. 1–8.

Swanson, L., and Peterson, G. P., 1994, "The Evaporating Extended Meniscus in a V-Shaped Channel," *AIAA J. Thermophysics and Heat Transfer*, Vol. 8, No. 1, pp. 172–181 (also as ASME HTD-Vol. 200, pp. 9–22).

Xu, X., and Carey, V. P., 1990, "Film Evaporation From a Micro-grooved Surface—An Approximate Heat Transfer Model and Its Comparison With Experimental Data," *AIAA J. of Thermophysics and Heat Transfer*, Vol. 4, No. 4, pp. 512–520.

Modeling Thermally Governed Transient Flows in Multitube Evaporating Flow Systems With Thermal and Flow Distribution Asymmetry

G. L. Wedekind[1] **and C. J. Kobus**[2]

Introduction

The objective of this paper is to present the results of an investigation into the transient response characteristics of multiple-tube evaporating flow systems where complete vaporization takes place. This type of problem is important since most industrial applications utilize multitube evaporators, where parallel tubes are connected at both ends with common headers. The background for this investigation originated from the success of past research concerned with evaporating flow transients (Wedekind and Beck, 1981) and from the more recent success in the modeling of multitube condensing flow transients (Wedekind and Bhatt, 1989). Therefore, there was a natural motivation to extend the ideas of the latter research to include evaporating flow systems as well.

The major focus here is the investigation of the primary mechanisms for, and the magnitudes of, the influence of thermal and flow distribution asymmetry on outlet flow transients, not system stability. Therefore, heat fluxes will be considered to be sufficiently low to preclude film boiling, and initiated inlet flow changes small enough so that flow regime transition does not take place during the ensuing transient. Under these conditions, the thermal and flow distribution parameters, which describe the asymmetry, can be considered independent of each other and constant.

The approach taken here will be first to summarize the development of the governing equations for a two-tube evaporating flow system; then, the results of an investigation into the influence of thermal and flow distribution asymmetries on the characteristics of thermally governed flow transients will be presented. Finally, utilizing the similarity to multitube condensing flow systems (Wedekind and Bhatt, 1989), an equivalent single-tube model for an n-tube system will be suggested, and its predictive accuracy will be verified by comparison with the analytical results obtained from the developed two-tube model.

Development of Two-Tube Model

The analysis is similar to that done by Wedekind and Bhatt (1989) for condensing flow, so the details will not be presented here. Referring to Fig. 1, the conservation of mass principle is applied to each of the two tubes for both the superheated vapor and two-phase regions, under the assumption of a time invariant system mean void fraction.[3] The transient term in each of the equations will have a first-order derivative of the point of complete vaporization, $\eta(t)$. The differential equation governing the motion of the effective point of complete vaporization for each tube can be determined by utilizing the *unified system mean void fraction model* (Wedekind et al., 1984). Referring to the inlet and outlet headers depicted in Fig. 1, the total inlet and outlet mass flowrates can be expressed as the sum of the individual mass flowrates at the inlet and outlet of both tubes, respectively. Also, assuming the inlet flow quality of both tubes to be the same, the combined conservation equation expressing the outlet vapor flow rate of the system becomes

$$m_{t,o}(t) = \{1 - [1 - (\rho'/\rho)](1 - x_i)\} m_{t,i}(t) + \frac{[1 - (\rho'/\rho)]}{(h' - h)} \{\bar{f}_{q,1} P_1 \eta_1(t) + \bar{f}_{q,2} P_2 \eta_2(t)\} \tag{1}$$

Introducing a flow distribution parameter, γ, defined as the ratio of the mass flowrate entering tube #1 to the total mass flowrate, the inlet flowrates for each tube are related with the following equations:

$$m_{t,1}(z, t)_{z=0} = \gamma m_{t,i}(t), \tag{2}$$

$$m_{t,2}(z, t)_{z=0} = (1 - \gamma) m_{t,i}(t) \tag{3}$$

Consider the special case where the time varying inlet flowrate is approximated as an exponential function (which is probably quite realistic), thus

$$m_{t,i}(t) = m_{t,f} + (m_{t,i} - m_{t,f}) e^{-t/\tau_m} \tag{4}$$

where $m_{t,i}$ and $m_{t,f}$ are the initial and final total inlet mass flowrates, respectively, and τ_m is the time constant for the inlet flowrate variation.

Substituting Eq. (4) into Eqs. (2) and (3) and then Eqs. (2) and (3) into the respective differential equations governing the

---

[1] Professor of Engineering, Oakland University, Rochester, MI 48309; Mem. ASME.

[2] Graduate Assistant, Oakland University, Rochester, MI 48309; Mem. ASME.

Contributed by the Heat Transfer Division of THE AMERICAN SOCIETY OF MECHANICAL ENGINEERS. Manuscript received by the Heat Transfer Division February 1993, revision received July 1993. Keywords: Modeling and Scaling, Phase-Change Phenomena, Transient and Unsteady Heat Transfer. Associate Technical Editor: R. Nelson, Jr.

[3] A detailed discussion of the time invariance of the system mean void fraction is given by Wedekind et al. (1978). In short, time invariance requires that a specific redistribution of liquid and vapor within the two-phase region takes place at a rate faster than that of the particular flow transient under consideration, so that a similarity relationship exists. Consequently, only the steady-state form of the momentum equation is required to compute the system mean void fraction.

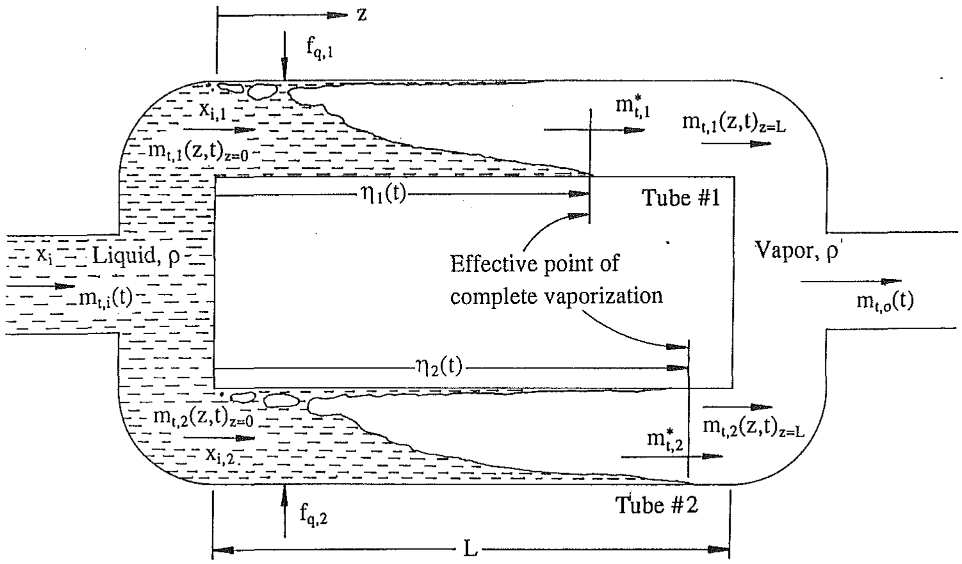

Fig. 1 Schematic of two-tube horizontal evaporating system with complete vaporization

effective point of complete vaporization for each individual tube, these equations can be solved subject to their respective initial conditions. When these solutions are substituted back into Eq. (1), after considerable algebraic rearrangement, the result can be expressed as

$$\frac{m_{t,o}(t)-m_{t,f}}{m_{t,i}-m_{t,f}}=e^{-t/\tau_m}+\gamma\,\frac{(\tau_1/\tau_m)[1-(\rho'/\rho)]}{[(\tau_1/\tau_m)-1]}\times(1-x_i)\{e^{-t/\tau_1}-e^{-t/\tau_m}\}$$
$$+(1-\gamma)\,\frac{\beta(\tau_1/\tau_m)[1-(\rho'/\rho)]}{[\beta(\tau_1/\tau_m)-1]}\,(1-x_i)\{e^{-t/\beta\tau_1}-e^{-t/\tau_m}\} \quad (5)$$

where

$$\beta=\frac{\tau_2}{\tau_1}=\frac{\bar{f}_{q,1}}{\bar{f}_{q,2}},\quad \tau_1=\frac{\rho(1-\bar{\alpha}_1)A_{t,1}}{\bar{f}_{q,1}P_1}\,(h'-h),$$
$$\tau_2=\frac{\rho(1-\bar{\alpha}_2)A_{t,2}}{\bar{f}_{q,2}P_2}\,(h'-h) \quad (6)$$

The system mean void fraction,[4] $\bar{\alpha}$, is defined as

$$\bar{\alpha}=\frac{1}{\eta(t)}\int_{z=0}^{\eta(t)}\alpha(z,\,t)dz=\frac{1}{(x_o-x_i)}\int_{x=x_i}^{x_o}\alpha(x)dx=\frac{1}{(1-a)}$$
$$+\frac{a}{(1-a)^2(x_o-x_i)}\,Ln\left|\frac{a+(1-a)x_i}{a+(1-a)x_o}\right| \quad (7)$$

where

$$a=(\rho'/\rho)^{2/3},\ x_o=1.0;\ \text{complete vaporization}$$

The relationship above predicts the transient response of the outlet vapor flowrate for a two-tube evaporating flow system, where the parameters β and γ describe the thermal and flow distribution asymmetries, respectively, for the common geometry of circular tubes of equal diameters.[5] In general, $\beta \geq 0$ and $0 \leq \gamma \leq 1$; however, the case of $\gamma = 0.5$ and $\beta = 1$ represents flow distribution and thermal symmetry, respectively.

It is interesting to note that Eq. (5) is the exact same form as that for a two-tube condensing flow system (Wedekind and Bhatt, 1989). The only difference[6] is that the term $[1 - (\rho'/\rho)]$ becomes $[(\rho/\rho') - 1]$, $(1 - x_i)$ becomes x_i, and in the expression for the system mean void fraction, given by Eq. (7), $x_o = 1$ becomes $x_o = 0$.

Parametric Study of Two-Tube Model

As mentioned earlier, the objective here is to investigate the influence of thermal and flow distribution asymmetry on the transient response of the outlet vapor flowrate. The theoretical model, as expressed by Eq. (5), will be used for the parametric study. The effects of various β and γ combinations on the transient response of the outlet vapor flowrate are shown in Fig. 2, for an exponential decrease in the inlet flowrate. Practical ranges of both parameters are illustrated. It is clear from the illustration that both thermal and flow distribution asymmetry can have a substantial influence on the system's transient response characteristics. For instance, $\beta = 2$ and $\gamma = 0.25$ illustrates the case where tube #2 has half the heat flux of tube #1, but 75 percent of the total flow. In this case, the system response time is greater than that of the balanced case ($\beta = 1$, $\gamma = 0.5$). Also, $\beta = 0.5$ and $\gamma = 0.25$ corresponds to the case where tube #2 has twice the heat flux of tube #1, and again 75 percent of the total flow. It can be seen that in this case, the system response time is less than the balanced case ($\beta = 1$, $\gamma = 0.5$). It is also of interest that in the case of thermal symmetry, $\beta = 1$, flow distribution asymmetry has no relative effect on the transient response characteristics.

Equivalent Single-Tube Model

Wedekind et al. (1989) demonstrated a method of approximating an n-tube condensing flow system with an equivalent single-tube model (ESTM). The same approach will be utilized here for evaporating flows. The concept of the ESTM is to obtain an equivalent single-tube system time constant, which,

---

[4] The particular void fraction model used in this paper is that proposed by Zivi (1964), and was chosen for reasons of simplicity and proven accuracy for the particular flow situation under investigation. However, any void fraction relationship that is valid over the full range of flow quality would yield similar results.

[5] It is noted that in practical applications of multitube evaporating flow systems, it is rare to encounter geometric asymmetry. For this reason, geometric asymmetry will not be fully investigated in this paper. However, the model will easily handle geometric asymmetries as well.

[6] Although the form of the equations is similar, the differences indicated cause the response characteristics for condensing flows to be significantly different from those of evaporating flows.

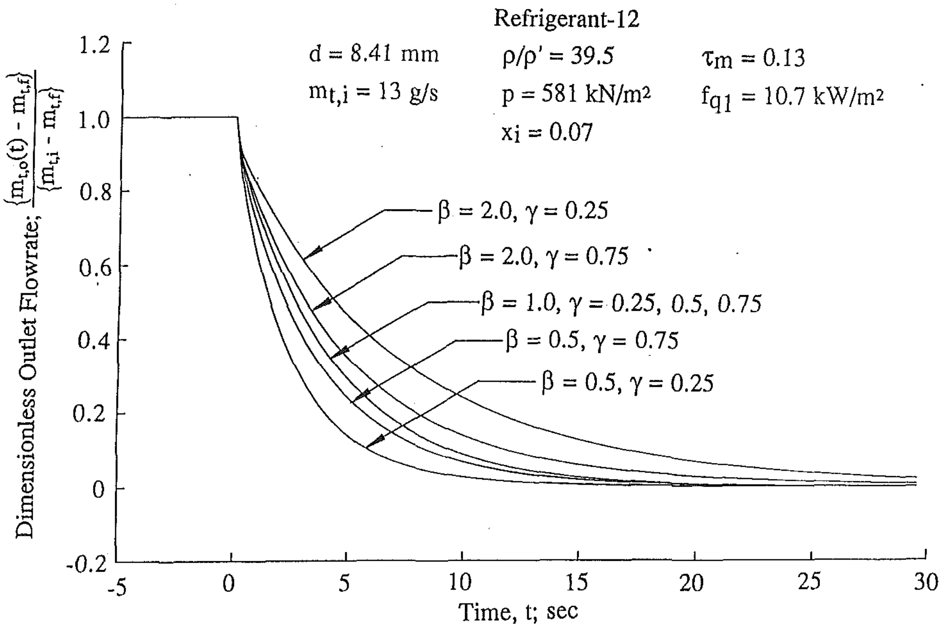

Fig. 2 Influence of thermal and flow distribution asymmetry for a two-tube model on the transient response characteristics of outlet vapor flow rate after a decrease in inlet flow rate

in its generalized form for an n-tube system, is simply a weighted average of the time constants for each of the individual tubes. The weighting factors are the corresponding flow distribution asymmetry parameters. Utilizing this concept, the ESTM can be used to approximate the transient response characteristics of a multitube evaporating system. For the case of a two-tube system, the equivalent single-tube time constant, $\tau_{s,2}$, becomes

$$\tau_{s,2} = \gamma\tau_1 + (1-\gamma)\tau_2 \tag{8}$$

Therefore, the transient response characteristics of the outlet vapor flowrate for this two-tube evaporating flow system can be approximated by the following ESTM:

$$\frac{m_{t,o}(t) - m_{t,f}}{m_{t,i} - m_{t,f}} = e^{-t/\tau_m} + (1-x_i)$$
$$\times [1-(\rho'/\rho)] \frac{(\tau_{s,2}/\tau_m)}{[(\tau_{s,2}/\tau_m) - 1]} \{e^{-t/\tau_{s,2}} - e^{-t/\tau_m}\} \tag{9}$$

A graph of the predictions of the ESTM, for various combinations of thermal and flow distribution asymmetry parameters, would plot almost on top of the curves depicted in Fig. 2, indicating that the ESTM is very accurate for the range of thermal and flow distribution parameters presented. Although no experimental verification has been presented in this paper, the predictive capability of the system mean void fraction model has been substantially verified with experimental measurements in previous papers, such as those listed in the references. Good agreement has always been found to exist, especially when consideration is given to the complexity of the physical mechanisms involved, and the relative simplicity of the model.

References

Wedekind, G. L., Bhatt, B. L., and Beck, B. T., 1978, "A System Mean Void Fraction Model for Predicting Various Transient Phenomena Associated With Two-Phase Evaporating and Condensing Flows," *International Journal of Multiphase Flow*, Vol. 4, pp. 97-114.

Wedekind, G. L., and Beck, B. T., 1981, "A Generalization of the System Mean Void Fraction Model for Transient Two-Phase Evaporating Flows," ASME Journal of Heat Transfer, Vol. 103, pp. 81-85.

Wedekind, G. L., Beck, B. T., Bhatt, B. L., and Roslund, G. L., 1984, "A Unified System Mean Void Fraction Model for Predicting Transient Characteristics of Flow Quality, Void Fraction, Flowrate and Pressure Drop in Evaporating and Condensing Flows," *Two-Phase Flow and Heat Transfer; China-U.S. Progress*, Xue-jun Chen and T. N. Veziroglu, eds., Hemisphere Publishing Co., Washington, DC, pp. 633-646.

Wedekind, G. L., and Bhatt, B. L., 1989, "Modeling the Thermally Governed Transient Flow Surges in Multitube Condensing Flow Systems With Thermal and Flow Distribution Asymmetry," ASME Journal of Heat Transfer, Vol. 111, pp. 786-791.

Zivi, S. M., 1964, "Estimation of Steady-State Stream Void Fraction by Means of the Principle of Minimum Entropy Production," ASME Journal of Heat Transfer, Vol. 86, p. 247.

A Note on Free Convection Along a Vertical Wavy Surface in a Porous Medium

D. A. S. Rees[1] **and I. Pop**[2]

Nomenclature

a = amplitude of the wavy surface
f = reduced streamfunction
g = acceleration due to gravity
k = thermal conductivity of the porous medium
K = permeability of the porous medium
l = wavelength of the surface undulations
Nu_x = $-\ (\bar{x}/T_w - T_\infty)\ (\partial T/\partial \bar{y})_{y=a \sin x/l}$ = the local Nusselt number
Q = integrated rate of heat transfer

---

[1] School of Mechanical Engineering, University of Bath, Claverton Down, Bath, BA2 7AY, United Kingdom.

[2] Faculty of Mathematics, University of Cluj, R-3400, Cluj, CP 253, Romania.

Contributed by the Heat Transfer Division of The American Society of Mechanical Engineers. Manuscript received by the Heat Transfer Division August 1992; revision received August 1993. Keywords: Flow Nonuniformity, Natural Convection, Porous Media. Associate Technical Editor: C. E. Hickox, Jr.

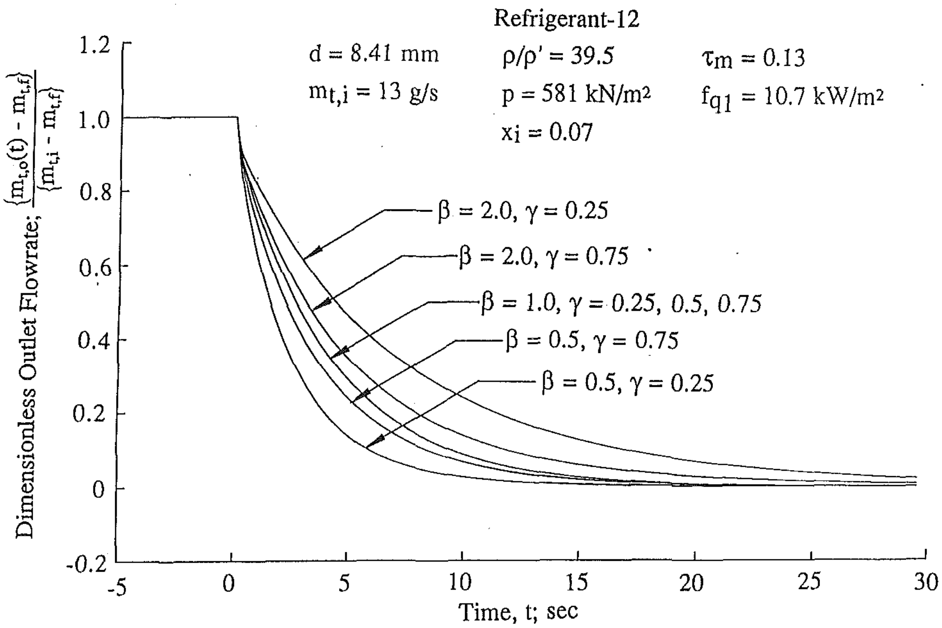

Fig. 2 Influence of thermal and flow distribution asymmetry for a two-tube model on the transient response characteristics of outlet vapor flow rate after a decrease in inlet flow rate

in its generalized form for an n-tube system, is simply a weighted average of the time constants for each of the individual tubes. The weighting factors are the corresponding flow distribution asymmetry parameters. Utilizing this concept, the ESTM can be used to approximate the transient response characteristics of a multitube evaporating system. For the case of a two-tube system, the equivalent single-tube time constant, $\tau_{s,2}$, becomes

$$\tau_{s,2} = \gamma\tau_1 + (1-\gamma)\tau_2 \tag{8}$$

Therefore, the transient response characteristics of the outlet vapor flowrate for this two-tube evaporating flow system can be approximated by the following ESTM:

$$\frac{m_{t,o}(t)-m_{t,f}}{m_{t,i}-m_{t,f}} = e^{-t/\tau_m} + (1-x_i) \times [1-(\rho'/\rho)] \frac{(\tau_{s,2}/\tau_m)}{[(\tau_{s,2}/\tau_m)-1]} \{e^{-t/\tau_{s,2}} - e^{-t/\tau_m}\} \tag{9}$$

A graph of the predictions of the ESTM, for various combinations of thermal and flow distribution asymmetry parameters, would plot almost on top of the curves depicted in Fig. 2, indicating that the ESTM is very accurate for the range of thermal and flow distribution parameters presented. Although no experimental verification has been presented in this paper, the predictive capability of the system mean void fraction model has been substantially verified with experimental measurements in previous papers, such as those listed in the references. Good agreement has always been found to exist, especially when consideration is given to the complexity of the physical mechanisms involved, and the relative simplicity of the model.

References

Wedekind, G. L., Bhatt, B. L., and Beck, B. T., 1978, "A System Mean Void Fraction Model for Predicting Various Transient Phenomena Associated With Two-Phase Evaporating and Condensing Flows," *International Journal of Multiphase Flow*, Vol. 4, pp. 97-114.

Wedekind, G. L., and Beck, B. T., 1981, "A Generalization of the System Mean Void Fraction Model for Transient Two-Phase Evaporating Flows," ASME JOURNAL OF HEAT TRANSFER, Vol. 103, pp. 81-85.

Wedekind, G. L., Beck, B. T., Bhatt, B. L., and Roslund, G. L., 1984, "A Unified System Mean Void Fraction Model for Predicting Transient Characteristics of Flow Quality, Void Fraction, Flowrate and Pressure Drop in Evaporating and Condensing Flows," *Two-Phase Flow and Heat Transfer; China-U.S. Progress*, Xue-jun Chen and T. N. Veziroglu, eds., Hemisphere Publishing Co., Washington, DC, pp. 633-646.

Wedekind, G. L., and Bhatt, B. L., 1989, "Modeling the Thermally Governed Transient Flow Surges in Multitube Condensing Flow Systems With Thermal and Flow Distribution Asymmetry," ASME JOURNAL OF HEAT TRANSFER, Vol. 111, pp. 786-791.

Zivi, S. M., 1964, "Estimation of Steady-State Stream Void Fraction by Means of the Principle of Minimum Entropy Production," ASME JOURNAL OF HEAT TRANSFER, Vol. 86, p. 247.

A Note on Free Convection Along a Vertical Wavy Surface in a Porous Medium

D. A. S. Rees[1] **and I. Pop**[2]

Nomenclature

a = amplitude of the wavy surface
f = reduced streamfunction
g = acceleration due to gravity
k = thermal conductivity of the porous medium
K = permeability of the porous medium
l = wavelength of the surface undulations
Nu_x = $-(\bar{x}/T_w - T_\infty)\,(\partial T/\partial\bar{y})_{y=a\sin x/l}$ = the local Nusselt number
Q = integrated rate of heat transfer

---

[1] School of Mechanical Engineering, University of Bath, Claverton Down, Bath, BA2 7AY, United Kingdom.

[2] Faculty of Mathematics, University of Cluj, R-3400, Cluj, CP 253, Romania.

Contributed by the Heat Transfer Division of THE AMERICAN SOCIETY OF MECHANICAL ENGINEERS. Manuscript received by the Heat Transfer Division August 1992; revision received August 1993. Keywords: Flow Nonuniformity, Natural Convection, Porous Media. Associate Technical Editor: C. E. Hickox, Jr.

Ra = $g\beta K(T_w - T_\infty)l/\alpha\nu$ = the Darcy–Rayleigh number based on l
Ra_x = $g\beta K(T_w - T_\infty)\bar{x}/\alpha\nu$ = the local Darcy–Rayleigh number based on $\bar{x}$
s = arc length of the surface
T = temperature
x, y = streamwise and cross-streamwise coordinates
X = representative distance from the leading edge
α = thermal diffusivity of the saturated medium
β = coefficient of thermal expansion
θ = dimensionless temperature
ν = kinematic viscosity
ξ, η = transformed variables
ψ = streamfunction

Superscripts

$\underline{\quad}'$ = differentiation with respect to η
= dimensional variables
$\hat{}$ = boundary layer variables

Subscripts

w = condition at the wall
∞ = condition at infinity

Introduction

The use of Darcy's law and the energy equation has met with considerable success in the modeling of flow and heat transfer within fluid-saturated porous media. This is reflected in the particularly large number of papers concerned with convection in porous media that have now been published. An excellent review of this topic to date can be found in the monograph by Nield and Bejan (1992).

Heat transfer by natural convection from vertical, horizontal, and inclined surfaces embedded in a porous medium are of fundamental importance for many practical applications. In general, it is not easy to determine the flow field and the associated heat transfer characteristics either in porous media flows, or, indeed, for flows of Newtonian fluids because of the complexity of practical geometries. The present note studies, for the first time, the free convection along a vertically oriented, isothermally heated, wavy surface placed within a porous medium. The configuration is analogous to that considered by Yao (1983) and Moulic and Yao (1989a, b) for a Newtonian fluid. Such surfaces can be considered as approximations to many practical geometries for which free convective heat transfer is of interest. It is shown that, with a generalized similarity transformation, the governing boundary layer equations and associated boundary conditions reduce to those of a vertical smooth isothermal surface first studied by Cheng and Minkowycz (1977).

Basic Equations and Analysis

Consider a vertical sinusoidally wavy surface embedded in a porous medium with constant ambient temperature, T_∞, as shown in FIg. 1. The wavy surface is held at a constant temperature, T_w, where $T_w > T_\infty$, and the characteristic length scale associated with the sinusoidal waves is l.

The dimensional governing equations are Darcy's law and the energy equation framed in two-dimensional Cartesian coordinates, $(\bar{x}, \bar{y})$. The dimensionless form of these equations, subject to the Boussinesq approximation, are

$$\frac{\partial^2\psi}{\partial x^2}+\frac{\partial^2\psi}{\partial y^2}=\mathrm{Ra}\,\frac{\partial\theta}{\partial y}, \tag{1}$$

$$\frac{\partial^2\theta}{\partial x^2}+\frac{\partial^2\theta}{\partial y^2}=\frac{\partial\psi}{\partial y}\frac{\partial\theta}{\partial x}-\frac{\partial\psi}{\partial x}\frac{\partial\theta}{\partial y}, \tag{2}$$

with the boundary conditions

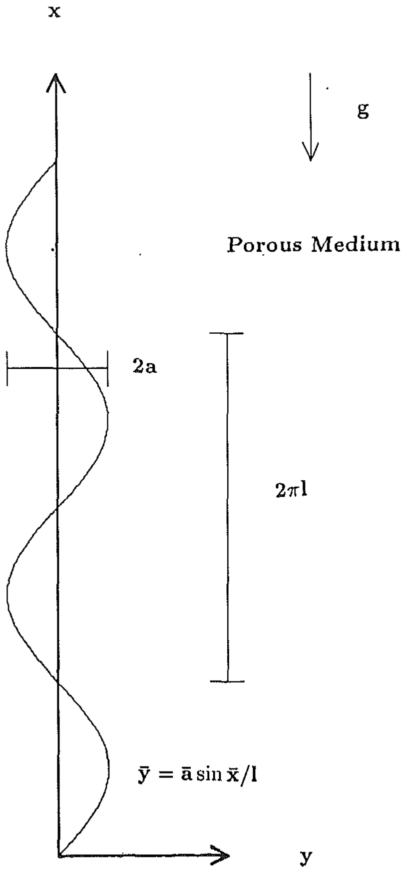

Fig. 1 Physical model and coordinate system

$$\psi=0,\ \theta=1 \text{ on } y=a\sin x, \tag{3a}$$

$$\psi_y\to 0,\ \theta\to 0 \text{ as } y\to\infty. \tag{3b}$$

The dimensionless variables are defined as

$$x=\bar{x}/l,\quad y=\bar{y}/l,\quad \psi=\bar{\psi}/\alpha, \tag{4a}$$

$$\theta=(T-T_\infty)/(T_w-T_\infty),\quad a=\bar{a}/l. \tag{4b}$$

Here $\bar{\psi}$ is the dimensional streamfunction, which is defined in the usual way, and $\bar{a}$ is the amplitude of the wavy surface. In this fundamental study of the effect of surface undulations on free convection in porous media, we assume that boundary and inertia effects are negligible.

We now assume that the Darcy–Rayleigh number is large so that free convection takes place within a boundary layer whose cross-stream width is substantially smaller than the ($O(1)$) amplitude of the surface waves. Accordingly we define new variables by subtracting out the effect of the surface waves and then introducing the usual boundary layer variables. Thus we transform according to

$$x=\xi,\ y=\xi^{1/2}\mathrm{Ra}^{-1/2}\eta+a\sin x, \tag{5a}$$

$$\psi=\mathrm{Ra}^{1/2}\hat{\psi}, \tag{5b}$$

where Ra = $g\beta K(T_w - T_\infty)l/\alpha\nu$ is the Darcy–Rayleigh number. Equations (1) and (2) become

$$\nabla_1^2\hat{\psi}=\xi^{1/2}\frac{\partial\theta}{\partial\eta}, \tag{6}$$

$$\nabla_1^2\theta=\xi^{1/2}\left(\frac{\partial\hat{\psi}}{\partial\eta}\frac{\partial\theta}{\partial\xi}-\frac{\partial\hat{\psi}}{\partial\xi}\frac{\partial\theta}{\partial\eta}\right), \tag{7}$$

and the boundary conditions are now

$$\hat{\psi}=0,\ \theta=1 \text{ on } \eta=0, \tag{8a}$$

$$\hat{\psi}_\eta \to 0,\ \theta \to 0 \text{ as } \eta \to \infty. \tag{8b}$$

Equations (6) and (7) are the full equations of motion and the operator, ∇_1^2, is defined to be

$$\nabla_1^2 = (1+a^2\cos^2\xi)\frac{\partial^2}{\partial\eta^2} + a\xi^{1/2}\mathrm{Ra}^{-1/2}\sin\xi\frac{\partial}{\partial\eta} - 2a\xi^{1/2}\mathrm{Ra}^{-1/2}\cos\xi\left(\frac{\partial^2}{\partial\xi\partial\eta} - \frac{\eta}{2\xi}\frac{\partial^2}{\partial\eta^2} - \frac{1}{2\xi}\frac{\partial}{\partial\eta}\right) + \mathrm{Ra}^{-1}\left(\xi\frac{\partial^2}{\partial\xi^2} - \eta\frac{\partial^2}{\partial\xi\partial\eta} + \frac{\eta^2}{4\xi}\frac{\partial^2}{\partial\eta^2} + \frac{3\eta}{4\xi}\frac{\partial}{\partial\eta}\right). \tag{9}$$

If we formally let Ra → ∞, then the leading order terms in Eqs. (6) and (7) become

$$(1+a^2\cos^2\xi)\frac{\partial^2\hat{\psi}}{\partial\eta^2} = \xi^{1/2}\frac{\partial\theta}{\partial\eta}, \tag{10}$$

$$(1+a^2\cos^2\xi)\frac{\partial^2\theta}{\partial\eta^2} = \xi^{1/2}\left(\frac{\partial\hat{\psi}}{\partial\eta}\frac{\partial\theta}{\partial\xi} - \frac{\partial\hat{\psi}}{\partial\xi}\frac{\partial\theta}{\partial\eta}\right); \tag{11}$$

these equations are to be solved subject to the boundary conditions (8).

A similarity solution of Eqs. (10) and (11) is possible, and the streamfunction and temperature take the form

$$\hat{\psi} = \xi^{1/2}f(\hat{\eta}),\ \theta = \theta(\hat{\eta}), \tag{12a}$$

where the similarity variable, $\hat{\eta}$, is defined as

$$\hat{\eta} = \frac{\eta}{1+a^2\cos^2\xi}. \tag{12b}$$

Using Eq. (12), Eqs. (10) and (11) reduce to

$$f''' + \frac{1}{2}ff'' = 0 \tag{13a}$$

and the boundary conditions are

$$f(0)=0,\ f'(0)=1, \text{ and } f'(\hat{\eta})\to 0 \text{ as } \hat{\eta}\to\infty, \tag{13b}$$

where primes denote differentiation with respect to $\hat{\eta}$. It should be noted that the temperature field is given by $\theta = f'(\hat{\eta})$. Equation (13) for f is precisely that obtained by Cheng and Minkowycz (1977) in their study of thermal boundary layer flow induced by an isothermally heated plane vertical surface embedded in a porous medium.

The local Nusselt number, defined in terms of the temperature drop, $T_w - T_\infty$, the thermal conductivity of the saturated medium, k, and the local Rayleigh number based on the downstream distance, $\bar{x}$, Ra_x, can be expressed as

$$\mathrm{Nu}_x = \frac{-\theta'(0)\mathrm{Ra}_x^{1/2}}{(1+a^2\cos^2 x)^{1/2}} \simeq \frac{0.44375\ \mathrm{Ra}_x^{1/2}}{(1+a^2\cos^2 x)^{1/2}}, \tag{14}$$

where the numerical value for $-\theta'(0)$ has been taken from Rees and Bassom (1991). The variation of Nu_x with x for various values of the dimensionless wave amplitude is shown in Fig. 2. In this figure it may be seen that the *local* Nusselt number is less than or equal to that corresponding to a plane heated surface; this may be explained as follows. When the heated surface is not vertical the component of the buoyancy force along the surface is reduced from its maximum value when the surface is vertical—this is true for both upward and downward facing surfaces. Consequently, the boundary layer thickness is locally thicker, and hence local rates of heat transfer at the surface are reduced.

A quantity of greater physical significance than the local Nusselt number is the integrated rate of heat transfer:

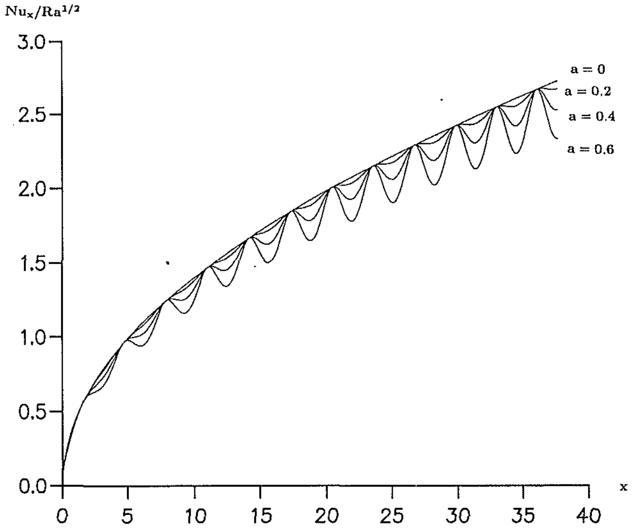

Fig. 2 Variation of the local Nusselt number, Nu_x, as a function of x for dimensionless wave amplitudes: $a = 0$, $a = 0.2$, $a = 0.4$, $a = 0.6$

$$Q = \int_0^X -k(\underline{n}\cdot\nabla T)_{y=a\sin(x/l)}\frac{d\bar{s}}{d\bar{x}}\,d\bar{x}, \tag{15}$$

where $\bar{X}$ is the dimensional distance from the leading edge and $\bar{s}$ is the dimensional arc length along the wavy surface. Equation (15) may be shown to reduce to

$$Q = 0.88750\ k(T_w - T_\infty)\mathrm{Ra}^{1/2}X^{1/2}/l \tag{16}$$

at leading order. Hence the total heat transfer between $x = 0$ and $x = X$ is independent of the amplitude and phase of the wavy surface (and even the shape of the surface providing that it is sufficiently smooth that boundary layer theory remains valid), and is, by implication, equal to that of a plane surface. Therefore we conclude that the presence of sufficiently smooth boundary deformations does not serve to change the rate of heat transfer into a porous medium at leading order.

Discussion

We have shown that the boundary layer flow induced by an isothermally heated surface exhibiting sinusoidal undulations is described by the solution of an ordinary differential equation identical to that which applies when no undulations are present. Therefore, the flow depends only on the local slope of the surface wave. This is in contrast to the identical configuration in a Newtonian fluid, which was considered by Yao (1983). There, the boundary layer equations formed a set of parabolic partial differential equations whose solution has to be obtained numerically and hence the flow also depends on conditions upstream. For the present problem we have seen that the total heat transfer rate in the medium is unchanged by the presence of surface waves, although the local heat transfer rate is less than or equal to that for a plane surface.

Our analysis is not confined to cases where the heated surface exhibits sinusoidal undulations but can be extended very easily to other shapes such as a plane surface with a (1 − cos) hump. More generally, a surface that has $O(1)$ variations and $O(1)$ gradients as Ra → ∞ can also be incorporated into the analysis. Thus, if the boundary conditions (3a) are imposed at $y = F(x)$, and the transformation defined by Eq. (5a) has $a\sin x$ replaced by $F(x)$, where $F(x)$ and its first two derivatives are continuous, then the final solution, Eq. (12a), applies but with $\hat{\eta}$ defined according to

$$\hat{\eta} = \frac{\eta}{1+(F'(x))^2}. \tag{17}$$

Even for this more general form of surface nonuniformity the total rate of heat transferred into the porous medium is unchanged to leading order.

Finally, it is necessary to point out that the solution presented here is valid for $O(1)$ distances from the leading edge; the corresponding boundary layer thickness is $O(\mathrm{Ra}^{-1/2})$. An examination of definition (9) shows that when $x = O(\mathrm{Ra})$, streamwise diffusion terms can no longer be neglected. This situation corresponds to an $O(1)$ boundary layer thickness, which is the same order of magnitude as the amplitude of the undulations. For such large distances from the leading edge it may therefore be necessary to solve a set of elliptic partial differential equations.

Acknowledgments

The first-named author would like to thank the SERC for providing a travel grant to enable this research to be undertaken, and the University of Cluj for their hospitality and generosity.

References

Cheng, P., and Minkowycz, W. J., 1977, "Free Convection About a Vertical Flat Plate Embedded in a Porous Medium With Application to Heat Transfer From a Dike," *J. Geophys. Res.*, Vol. 82, pp. 2040–2044.

Moulic, S. G., and Yao, L. S., 1989a, "Mixed Convection Along a Wavy Surface," ASME JOURNAL OF HEAT TRANSFER, Vol. 111, pp. 974–979.

Moulic, S. G., and Yao, L. S., 1989b, "Natural Convection Along a Vertical Wavy Surface With Uniform Heat Flux," ASME JOURNAL OF HEAT TRANSFER, Vol. 111, pp. 1106–1108.

Nield, D. A., and Bejan, A., 1992, *Convection in Porous Media*, Springer-Verlag, Berlin.

Rees, D. A. S., and Bassom, A. P., 1991, "Some Exact Solutions for Free Convective Flows Over Heated Semi-infinite Surfaces in Porous Media," *Int. J. Heat Mass Transf.*, Vol. 34, pp. 1564–1567.

Yao, L. S., 1983, "Natural Convection Along a Vertical Wavy Surface," ASME JOURNAL OF HEAT TRANSFER, Vol. 105, pp. 465–468.

A Unified Theory for Non-Darcy Free, Forced, and Mixed Convection Problems Associated With a Horizontal Line Heat Source in a Porous Medium

A. Nakayama[1]

Nomenclature

C = Forchheimer constant

C_p = specific heat of fluid at constant pressure

g = acceleration due to gravity

Gr_{Kc} = microscale Grashof number based on ΔT_c

Gr_{Kq} = microscale Grashof number based on q^*

k = equivalent thermal conductivity of the fluid-saturated porous medium

K = permeability of the fluid-saturated porous media

m_t = $d \ln \Delta T_c / d \ln x$

Pe_x = local Peclet number based on u_e

Pe_{xc} = modified local Peclet number based on u_c

q^* = strength of line heat source

Ra_{xq} = local Rayleigh number based on q^*

Ra^*_{xq} = modified local Rayleigh number for Forchheimer free convection

T = local temperature

ΔT_c = $T_c - T_e$ = centerline-ambient temperature difference

ΔT^*_c = $\Delta T_c/(q^*/k\, \mathrm{Pe}_x^{1/2})$ = dimensionless temperature difference

u, v = Darcian or superficial velocity components

x, y = boundary layer coordinates

x^*_D = $(\mathrm{Pe}_x/\mathrm{Ra}_{xq})^3$ = dimensionless coordinate for Darcy mixed convection

x^*_F = $\mathrm{Pe}_x^5/\mathrm{Ra}_{xq}^{*\,5/2}$ = dimensionless coordinate for Forchheimer mixed convection

α = equivalent thermal diffusivity of the fluid-saturated porous medium

β = expansion coefficient of the fluid

δ = plume width

η = similarity variable

μ = fluid viscosity

ρ = fluid density

Subscripts

c = plume centerline

e = ambient

Introduction

Due to a wide range of practical applications in geophysics and energy-related problems such as geophysical flows, cooling of underground electric cables, and environmental impact of buried heat generating waste, numerous investigations have been carried out for the convection problems associated with concentrated heat sources in fluid-saturated porous media (Wooding, 1963; Yih, 1965; Hickox and Watts, 1980; Hickox, 1981; Nield and White, 1982; Cheng, 1978; Masuoka et al., 1986; Ingham, 1988; Lai, 1991a). All these previous investigations, however, are restricted to the case of pure free convection. Despite its importance in practical applications, the study of mixed convection in the plume in a porous medium (Cheng and Zheng, 1986; Lai, 1991b) is very much limited.

In this study, we propose a unified integral treatment for the non-Darcy mixed convection in the plume rising from a line heat source, along the lines of Nakayama and Pop (1991). From the proposed flow regime map, one can readily find out which convection mode is realized for given conditions, and then select the appropriate set of solutions to describe the corresponding velocity and temperature fields.

Governing Equations and Flow Regime Map

Consider the mixed convective flow in the thermal plume above a horizontal line heat source, as illustrated in Fig. 1. Under the boundary layer approximations, the governing equations are given as follows:

$$\frac{\partial u}{\partial x} + \frac{\partial v}{\partial y} = 0 \tag{1}$$

$$\frac{\mu}{K} u + \frac{\rho C}{K^{1/2}} u^2 = \rho g \beta (T - T_e) + \frac{\mu}{K} u_e + \frac{\rho C}{K^{1/2}} u_e^2 \tag{2}$$

and

$$u \frac{\partial T}{\partial x} + v \frac{\partial T}{\partial y} = \alpha \frac{\partial^2 T}{\partial y^2} \tag{3}$$

where the Boussinesq approximation is evoked for the buoy-

---

[1] Department of Energy and Mechanical Engineering, Shizuoka University, 3-5-1 Johoku, Hamamatsu, 432 Japan.

Contributed by the Heat Transfer Division of THE AMERICAN SOCIETY OF MECHANICAL ENGINEERS. Manuscript received by the Heat Transfer Division October 1992; revision received August 1993. Keywords: Mixed Convection, Natural Convection, Porous Media. Associate Technical Editor: C. E. Hickox, Jr.

Even for this more general form of surface nonuniformity the total rate of heat transferred into the porous medium is unchanged to leading order.

Finally, it is necessary to point out that the solution presented here is valid for $O(1)$ distances from the leading edge; the corresponding boundary layer thickness is $O(\mathrm{Ra}^{-1/2})$. An examination of definition (9) shows that when $x = O(\mathrm{Ra})$, streamwise diffusion terms can no longer be neglected. This situation corresponds to an $O(1)$ boundary layer thickness, which is the same order of magnitude as the amplitude of the undulations. For such large distances from the leading edge it may therefore be necessary to solve a set of elliptic partial differential equations.

Acknowledgments

The first-named author would like to thank the SERC for providing a travel grant to enable this research to be undertaken, and the University of Cluj for their hospitality and generosity.

References

Cheng, P., and Minkowycz, W. J., 1977, "Free Convection About a Vertical Flat Plate Embedded in a Porous Medium With Application to Heat Transfer From a Dike," *J. Geophys. Res.*, Vol. 82, pp. 2040–2044.

Moulic, S. G., and Yao, L. S., 1989a, "Mixed Convection Along a Wavy Surface," ASME JOURNAL OF HEAT TRANSFER, Vol. 111, pp. 974–979.

Moulic, S. G., and Yao, L. S., 1989b, "Natural Convection Along a Vertical Wavy Surface With Uniform Heat Flux," ASME JOURNAL OF HEAT TRANSFER, Vol. 111, pp. 1106–1108.

Nield, D. A., and Bejan, A., 1992, *Convection in Porous Media*, Springer-Verlag, Berlin.

Rees, D. A. S., and Bassom, A. P., 1991, "Some Exact Solutions for Free Convective Flows Over Heated Semi-infinite Surfaces in Porous Media," *Int. J. Heat Mass Transf.*, Vol. 34, pp. 1564–1567.

Yao, L. S., 1983, "Natural Convection Along a Vertical Wavy Surface," ASME JOURNAL OF HEAT TRANSFER, Vol. 105, pp. 465–468.

A Unified Theory for Non-Darcy Free, Forced, and Mixed Convection Problems Associated With a Horizontal Line Heat Source in a Porous Medium

A. Nakayama[1]

Nomenclature

C = Forchheimer constant
C_p = specific heat of fluid at constant pressure
g = acceleration due to gravity
Gr_{Kc} = microscale Grashof number based on ΔT_c
Gr_{Kq} = microscale Grashof number based on q^*
k = equivalent thermal conductivity of the fluid-saturated porous medium
K = permeability of the fluid-saturated porous media
m_t = $d \ln \Delta T_c / d \ln x$
Pe_x = local Peclet number based on u_e
Pe_{xc} = modified local Peclet number based on u_c
q^* = strength of line heat source
Ra_{xq} = local Rayleigh number based on q^*
Ra^*_{xq} = modified local Rayleigh number for Forchheimer free convection
T = local temperature
ΔT_c = $T_c - T_e$ = centerline-ambient temperature difference
ΔT^*_c = $\Delta T_c / (q^*/k\, \mathrm{Pe}_x^{1/2})$ = dimensionless temperature difference
u, v = Darcian or superficial velocity components
x, y = boundary layer coordinates
x^*_D = $(\mathrm{Pe}_x/\mathrm{Ra}_{xq})^3$ = dimensionless coordinate for Darcy mixed convection
x^*_F = $\mathrm{Pe}_x^5/\mathrm{Ra}_{xq}^{*5/2}$ = dimensionless coordinate for Forchheimer mixed convection
α = equivalent thermal diffusivity of the fluid-saturated porous medium
β = expansion coefficient of the fluid
δ = plume width
η = similarity variable
μ = fluid viscosity
ρ = fluid density

Subscripts

c = plume centerline
e = ambient

Introduction

Due to a wide range of practical applications in geophysics and energy-related problems such as geophysical flows, cooling of underground electric cables, and environmental impact of buried heat generating waste, numerous investigations have been carried out for the convection problems associated with concentrated heat sources in fluid-saturated porous media (Wooding, 1963; Yih, 1965; Hickox and Watts, 1980; Hickox, 1981; Nield and White, 1982; Cheng, 1978; Masuoka et al., 1986; Ingham, 1988; Lai, 1991a). All these previous investigations, however, are restricted to the case of pure free convection. Despite its importance in practical applications, the study of mixed convection in the plume in a porous medium (Cheng and Zheng, 1986; Lai, 1991b) is very much limited.

In this study, we propose a unified integral treatment for the non-Darcy mixed convection in the plume rising from a line heat source, along the lines of Nakayama and Pop (1991). From the proposed flow regime map, one can readily find out which convection mode is realized for given conditions, and then select the appropriate set of solutions to describe the corresponding velocity and temperature fields.

Governing Equations and Flow Regime Map

Consider the mixed convective flow in the thermal plume above a horizontal line heat source, as illustrated in Fig. 1. Under the boundary layer approximations, the governing equations are given as follows:

$$\frac{\partial u}{\partial x} + \frac{\partial v}{\partial y} = 0 \tag{1}$$

$$\frac{\mu}{K} u + \frac{\rho C}{K^{1/2}} u^2 = \rho g \beta (T - T_e) + \frac{\mu}{K} u_e + \frac{\rho C}{K^{1/2}} u_e^2 \tag{2}$$

and

$$u \frac{\partial T}{\partial x} + v \frac{\partial T}{\partial y} = \alpha \frac{\partial^2 T}{\partial y^2} \tag{3}$$

where the Boussinesq approximation is evoked for the buoy-

---

[1] Department of Energy and Mechanical Engineering, Shizuoka University, 3-5-1 Johoku, Hamamatsu, 432 Japan.

Contributed by the Heat Transfer Division of THE AMERICAN SOCIETY OF MECHANICAL ENGINEERS. Manuscript received by the Heat Transfer Division October 1992; revision received August 1993. Keywords: Mixed Convection, Natural Convection, Porous Media. Associate Technical Editor: C. E. Hickox, Jr.

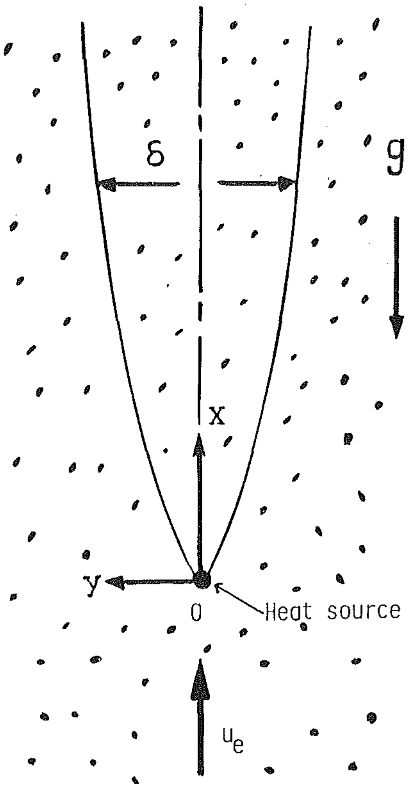

Fig. 1 Physical model and its boundary layer coordinates

ancy force. The energy equation must satisfy the boundary condition:

$$y=\infty: \quad T=T_e \tag{4}$$

and the enthalpy conservation constraint:

$$\rho C_p \int_{-\infty}^{\infty} u(T-T_e)dy=q^* \tag{5}$$

The modified Peclet number Pe_{xc} based on the unknown centerline velocity u_c may be defined as

$$\mathrm{Pe}_{xc}=\frac{u_c x}{\alpha}=\mathrm{Pe}_x \frac{[(1+2\,\mathrm{Re}_K)^2+4\mathrm{Gr}_{Kc}]^{1/2}-1}{2\,\mathrm{Re}_K} \tag{6a}$$

$$=\mathrm{Ra}_{xq} \frac{[(1+2\,\mathrm{Re}_K)^2+4\mathrm{Gr}_{Kc}]^{1/2}-1}{2\,\mathrm{Gr}_{Kq}} \tag{6b}$$

where

$$\mathrm{Pe}_x=u_e x/\alpha \quad \text{and} \quad \mathrm{Ra}_{xq}=\left(\frac{Kg\beta q^* x}{\alpha \nu k}\right)^{2/3} \tag{7a, b}$$

are the Peclet number (relevant for the case of pure forced convection), and the Rayleigh number (based on the heat source q^*, relevant for the case of pure free convection), respectively. Furthermore,

$$\mathrm{Re}_k=\frac{C\,K^{1/2}u_e}{\nu}$$

$$\text{and} \quad \mathrm{Gr}_{Kq}=\frac{C\,K^{7/6}}{\nu}\left(\frac{g\beta q^*}{\nu k}\right)^{2/3}\left(\frac{\alpha}{x}\right)^{1/3} \tag{8a, b}$$

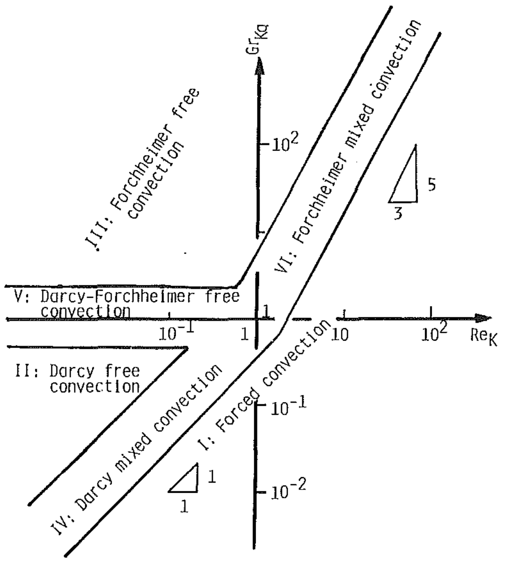

Fig. 2 Convective flow regime map

are what we may call the "microscale" Reynolds and Grashof numbers, respectively, in which the reference length scale is chosen to be the length scale of the microstructure, namely, the square root of the permeability of the porous medium. The other microscale Grashof number Gr_{Kc} defined as

$$\mathrm{Gr}_{Kc}=\frac{C\,K^{3/2}\,g\beta\Delta T_c}{\nu^2} \tag{9}$$

is unknown, since the centerline-ambient temperature difference $\Delta T_c\,(=T_c-T_e)$ is one of the quantities we shall determine. The unknown microscale Grashof number Gr_{Kc}, however, may be estimated from an order of magnitude analysis as follows:

$$\mathrm{Gr}_{Kc}\sim\frac{C\,K^{3/2}g\beta q^*}{\nu^2 k\,\mathrm{Pe}_{xc}^{1/2}}\sim \begin{array}{lll} \mathrm{Gr}_{Kq}^{3/2}/\mathrm{Re}_K^{1/2} & \text{: Forced convection} & (10a) \\ \mathrm{Gr}_{Kq} & \text{: Darcy free convection} & (10b) \\ \mathrm{Gr}_{Kq}^{6/5} & \text{: Forchheimer free convection} & (10c) \end{array}$$

Nakayama and Pop (1991) argued that it is the modified Peclet number Pe_{xc} (rather than Pe_x or Ra_{xq}) that virtually controls the temperature field and heat transfer characteristics of the thermal plume as influenced by both forced flow and buoyancy force. Using these estimates, it can be shown that the modified Peclet number Pe_{xc} transforms itself as follows:

For Regime I : Forced convection regime:

$$\mathrm{Pe}_{xc}=\mathrm{Pe}_x \quad \text{for} \quad \mathrm{Re}_K^{3/2}+\mathrm{Re}_K^{5/2}\gg \mathrm{Gr}_{Kq}^{3/2} \tag{11a}$$

For Regime II : Darcy free convection regime:

$$\mathrm{Pe}_{xc}\sim\mathrm{Ra}_{xq} \quad \text{for} \quad \mathrm{Re}_K \ll \mathrm{Gr}_{Kq} \ll 1 \tag{11b}$$

For Regime III : Forchheimer free convection regime:

$$\mathrm{Pe}_{xc}\sim\mathrm{Ra}_{xq}^{*\,1/2}$$

$$\text{for} \quad \mathrm{Re}_K+\mathrm{Re}_K^2 \ll \mathrm{Gr}_{Kq}^{6/5} \quad \text{and} \quad \mathrm{Gr}_{Kq}\gg 1 \tag{11c}$$

where

$$\mathrm{Ra}_{xq}^*=\left(\frac{K^{1/2}g\beta\,q^*x^2}{C\,\alpha^2 k}\right)^{4/5} \tag{12}$$

These three distinct flow regimes are illustrated in Fig. 2 along with the corresponding intermediate regimes (connecting the three regimes), namely, the Darcy mixed convection regime (IV), the Darcy-Forchheimer free convection regime (V), and the Forchheimer mixed convection regime (VI). Consulting with this flow regime map, one can easily see which convection mode will be realized for a given set of the microscale dimensionless numbers, Re_K and Gr_{Kq}. It should be noted that among Pe_x, Ra_{xq}, Ra_{xq}^*, Re_K, and Gr_{Kq}, only three out of the five dimensionless numbers are independent, since

$$\mathrm{Gr}_{Kq}/\mathrm{Re}_K=\mathrm{Ra}_{xq}/\mathrm{Pe}_x \quad \text{and} \quad \mathrm{Gr}_{Kq}^{4/5}=\mathrm{Ra}_{xq}^2/\mathrm{Ra}_{xq}^* \qquad (13a,\ b)$$

Darcy–Forchheimer Free Convection Regime (Regime V)

The enthalpy conservation constraint (5) is considered together with the energy balance relation along the centerline, namely,

$$B\rho C_p u_c \Delta T_c \delta = q^* \qquad (14)$$

and

$$m_t \frac{u_c}{x} = D\frac{\alpha}{\delta^2} \qquad (15)$$

where

$$m_t=\frac{d\ln \Delta T_c}{d\ln x},\quad B=\int_{-\infty}^{\infty}\left(\frac{u}{u_c}\right)\left(\frac{T-T_e}{\Delta T_c}\right)d\eta \qquad (16a,\ b)$$

$$D=\frac{\partial^2}{\partial\eta^2}\left(\frac{T-T_e}{\Delta T_c}\right)\Bigg|_{\eta=0} \quad \text{and} \quad \eta=y/\delta \qquad (16c,\ d)$$

Equation (9) together with Eqs. (14) and (15) yields

$$\mathrm{Gr}_{Kc}=\frac{1}{B}\left(\frac{m_t}{D}\right)^{1/2}\frac{CK^{3/2}g\beta q^*}{\nu^2 k}\left(\frac{\alpha}{u_c x}\right)^{1/2} \qquad (17)$$

Since

$$\frac{T-T_e}{\Delta T_c}=\frac{(1+4\ \mathrm{Gr}_{Kc})^{1/2}-1}{4\ \mathrm{Gr}_{Kc}} \times\left[2\left(\frac{u}{u_c}\right)+\{(1+4\ \mathrm{Gr}_{Kc})^{1/2}-1\}\left(\frac{u_2}{u_c}\right)^2\right] \qquad (18)$$

for this Darcy–Forchheimer free convection regime, the shape factors B and D may readily be evaluated assuming an exponential velocity profile as

$$u/u_c=\exp(-\eta^2) \qquad (19)$$

Furthermore, differentiating Eq. (14) with respect to x under the local similarity assumption, we find m_t as

$$m_t=\frac{2(1+4\ \mathrm{Gr}_{Kc})^{1/2}}{1+5(1+4\ \mathrm{Gr}_{Kc})^{1/2}} \qquad (20)$$

Thus, Eq. (17) reduces to

$$\mathrm{Gr}_{Kc}^3\{1+5(1+4\ \mathrm{Gr}_{Kc})^{1/2}\}\left\{1+\frac{(1+4\ \mathrm{Gr}_{Kc})^{1/2}-1}{6^{1/2}}\right\}^2 \times\left\{\frac{(1+4\ \mathrm{Gr}_{Kc})^{1/2}-1}{2\ \mathrm{Gr}_{Kc}}\right\}^4=\frac{2}{\pi}\mathrm{Gr}_{Kq}^3 \qquad (21)$$

which can readily be solved to find the unknown Gr_{Kc}. Once Gr_{Kc} is known, the temperature and velocity fields of our interest are given by

$$\frac{T-T_e}{(q^*/k\ \mathrm{Ra}_{xq}^{1/2})}=\left(\frac{\mathrm{Gr}_{Kc}}{\mathrm{Gr}_{Kq}}\right)\left(\frac{T-T_e}{\Delta T_c}\right) =\frac{(1+4\ \mathrm{Gr}_{Kc})^{1/2}-1}{4\ \mathrm{Gr}_{Kq}}[2+\{(1+4\ \mathrm{Gr}_{Kc})^{1/2}-1\} \times\exp(-\eta^2)]\exp(-\eta^2) \qquad (22a)$$

and

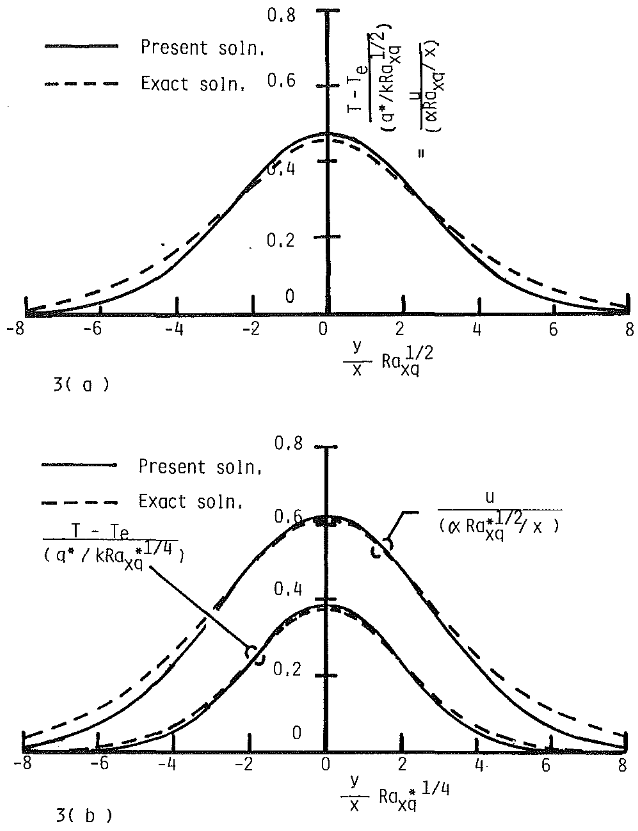

Fig. 3 Velocity and temperature profiles for pure free convection: (*a*) Darcy free convection; (*b*) Forchheimer free convection

$$\frac{u}{(\alpha\mathrm{Ra}_{xq}/x)}=\left(\frac{\mathrm{Pe}_{xc}}{\mathrm{Ra}_{xq}}\right)\left(\frac{u}{u_c}\right) =\frac{(1+4\ \mathrm{Gr}_{Kc})^{1/2}-1}{2\ \mathrm{Gr}_{Kq}}\exp(-\eta^2) \qquad (22b)$$

where

$$\eta=\left\{\frac{\mathrm{Gr}_{Kc}/\mathrm{Gr}_{Kq}}{1+5(1+4\ \mathrm{Gr}_{kc})^{1/2}}\right\}^{1/2}\frac{y}{x}\mathrm{Ra}_{xq}^{1/2} \qquad (23)$$

The resulting temperature and velocity profiles are plotted in Figs. 3(*a*) and 3(*b*) for the two asymptotic cases of Darcy and Forchheimer free convection against those from the exact solutions given by Wooding (1963) and Nakayama (1992), respectively. The present approximate profiles agree fairly well with those generated from the exact solutions. For the intermediate Forchheimer-Darcy free convection regime, a standard shooting scheme was applied to find Gr_{Kc} as a function of Gr_{Kq} from the characteristic Eq. (21). It has been found that the numerical results can be closely approximated by matching the foregoing asymptotic results, using the well-known procedure proposed by Churchill and Usagi (1972), as follows:

$$\frac{k(T_c-T_e)}{q^*}=\frac{Gr_{Kc}}{Gr_{Kq}Ra_{xq}^{1/2}}=\frac{(1+0.4645\ \mathrm{Gr}_{Kq}^{4/5})^{1/4}}{(3\pi)^{1/3}\ \mathrm{Ra}_{xq}^{1/2}} \qquad (24)$$

The error using this approximate formula stays within 2 percent at any value of Gr_{Kq}. The development of temperature and velocity profiles is illustrated in Fig. 4 where the dimensionless coordinates $x/L_{DF}=\mathrm{Gr}_{Kq}^{-3}$ and $(y\mathrm{Ra}_{xq}^{1/2}/x)_{x=L_{DF}}$ are used along with a reference length L_{DF} chosen such that $(\mathrm{Gr}_{Kq})_{x=L_{DF}=1}$. Thus, the transition from one convection mode to another takes place around $x = L_{DF}$. The figure shows that the convection mode changes from the Forchheimer free convection

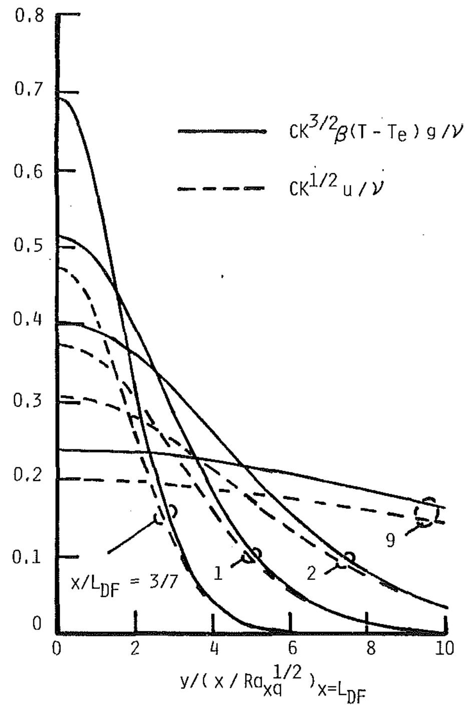

Fig. 4 Development of velocity and temperature profiles for Forchheimer-Darcy free convection

mode (Regime III), through the Darcy-Forchheimer free convection mode (Regime V), and to the Darcy free convection mode (Regime II), as the buoyant fluid departs from the origin of heat source, and develops downstream. The boundary layer theory breaks down in close proximity of the source. Nevertheless, the results obtained at small x/L_{DF} are relevant since the local Rayleigh number can be quite high even there. The effects of porous inertia on the profiles are less pronounced along the edge than the centerline, since the velocity is low and more or less Darcian near the edge.

Darcy Mixed Convection Regime (Regime IV)

A similar integral treatment can be made for the case of Darcy mixed convection, assuming an exponential temperature profile, to obtain the following characteristic equation in terms of the unknown centerline-ambient temperature difference:

$$\Delta T_c^* = \frac{1+\dfrac{\Delta T_c^*}{x_D^{*\,1/2}}}{2\pi^{1/2}\left(1+\dfrac{\Delta T_c^*}{(2x_{D^*})^{1/2}}\right)\left(1+\dfrac{3}{2}\,\dfrac{\Delta T_c^*}{x_D^{*\,1/2}}\right)^{1/2}} \tag{25}$$

where

$$\Delta T_c^* = \Delta T_c/(q^*/k\ \mathrm{Pe}_x^{1/2}) \tag{26a}$$

and

$$x_D^* = \left(\frac{\mathrm{Pe}_x}{\mathrm{Ra}_{xq}}\right)^3 = \left(\frac{\mathrm{Re}_K}{\mathrm{Gr}_{Kq}}\right)^3 = \frac{u_e^3}{\alpha}\left(\frac{\nu k}{Kg\beta q^*}\right)^2 x \tag{26b}$$

Since ΔT_c^* can be determined from the foregoing equation for given x_D^*, the temperature and velocity fields of our interest are given as

$$\frac{T-T_e}{(q^*/k\ \mathrm{Pe}_x^{1/2})} = \Delta T_c^*\left(\frac{T-T_e}{\Delta T_c}\right) = \Delta T_c^*\exp(-\eta^2) \tag{27a}$$

and

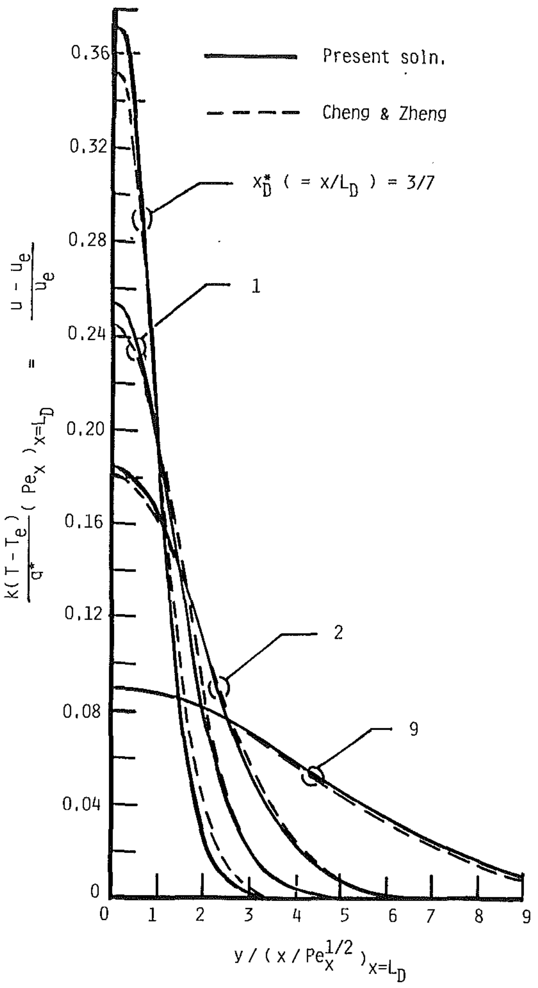

Fig. 5 Development of velocity and temperature profiles for Darcy mixed convection

$$u/u_e = 1+(\Delta T_c^*/x_D^{*\,1/2})\exp(-\eta^2) \tag{27b}$$

where

$$\eta = \frac{1+\dfrac{\Delta T_c^*}{x_D^{*\,1/2}}}{2\left(1+\dfrac{3}{2}\,\dfrac{\Delta T_c^*}{x_D^{*\,1/2}}\right)^{1/2}}\,\frac{y}{x}\,\mathrm{Pe}_x^{1/2} \tag{28}$$

For the case of Darcy free convection, the temperature and velocity profiles given by Eqs. (27a) and (27b) naturally reduce to those for the Darcy free convection of Wooding, while for the other asymptotic case of pure forced convection, namely, $x_D^* \gg 1$, we have the exact solution reported by Bejan (1984).

For the intermediate Darcy mixed convection regime, a shooting scheme must be used to find ΔT_c^* as a function of x_D^*. As in the case of the Darcy-Forchheimer free convection, the matching procedure was applied to the foregoing asymptotic results to generate the following approximate formula valid for any value of x_D^*:

$$\frac{k(T_c-T_e)}{q^*} = \frac{\Delta T_c^*}{\mathrm{Pe}_x^{1/2}} = \frac{1}{2\pi^{1/2}(1+0.2741\,x_D^{*\,-5/12})^{2/5}\,\mathrm{Pe}_x^{1/2}} \tag{29}$$

The error using this approximate formula falls within 3 percent at any value of x_D^*. The temperature profiles at several locations are presented in Fig. 5, which also includes the profiles obtained by Cheng and Zheng (1986) using the local similarity approximation. The dimensionless coordinates $x_D^* = x/L_D$ and $(y\mathrm{Pe}_x^{1/2}/x)_{x=L_D}$ are used.

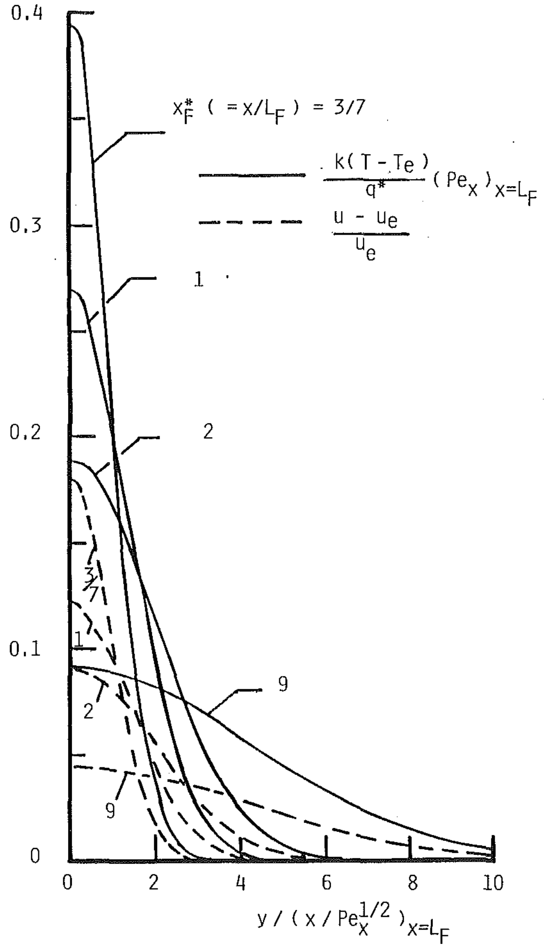

Fig. 6 Development of velocity and temperature profiles for Forchheimer mixed convection

Forchheimer Mixed Convection Regime (Regime VI)

For the case of Forchheimer mixed convection, the following characteristic equation can be obtained, assuming $(u-u_e)/(u_c-u_e)=\exp(-\eta^2)$:

$$\Delta T_c^* = \frac{\left\{\left(1+\frac{\Delta T_c^*}{x_F^{*\,1/2}}\right)^{1/2}+1\right\}^{3/2}\left(1+\frac{\Delta T_c^*}{x_F^{*\,1/2}}\right)^{1/2}}{(32\pi)^{1/2}\left(1+\frac{5}{4}\frac{\Delta T_c^*}{x_F^{*\,1/2}}\right)^{1/2}\left[1+\frac{3\sqrt{2}}{4}\left\{\left(1+\frac{\Delta T_c^*}{x_F^{*\,1/2}}\right)^{1/2}-1\right\}+\frac{\sqrt{3}}{6}\left\{\left(1+\frac{\Delta T_c^*}{x_F^{*\,1/2}}\right)^{1/2}-1\right\}^2\right]} \qquad (30)$$

where

$$x_F^* = \frac{\mathrm{Pe}_x^5}{\mathrm{Ra}_{xq}^{*\,5/2}} = \frac{\mathrm{Re}_k^5}{\mathrm{Gr}_{Kq}^3} = \frac{u_e^5}{\alpha K}\left(\frac{Ck}{g\beta q^*}\right)^2 x \qquad (31)$$

Then, the temperature and velocity profiles for given x_F^* are given by

$$\frac{T-T_e}{(q^*/k\,\mathrm{Pe}_x^{1/2})} = \Delta T_c^* \times \frac{\left[2+\left\{\left(1+\frac{\Delta T_c^*}{x_F^{*\,1/2}}\right)^2-1\right\}\exp(-\eta^2)\right]\exp(-\eta^2)}{1+\left(1+\frac{\Delta T_c^*}{x_F^{*\,1/2}}\right)^{1/2}} \qquad (32a)$$

and

$$\frac{u}{u_e} = 1+\left\{\left(1+\frac{\Delta T_c^*}{x_F^{*\,1/2}}\right)^{1/2}-1\right\}\exp(-\eta^2) \qquad (32b)$$

where

$$\eta = \frac{\left\{\left(1+\frac{\Delta T_c^*}{x_F^{*\,1/2}}\right)^{1/2}+1\right\}^{1/2}\left(1+\frac{\Delta T_c^*}{x_F^{*\,1/2}}\right)^{1/2}}{2\sqrt{2}\left(1+\frac{5}{4}\frac{\Delta T_c^*}{x_F^{*\,1/2}}\right)^{1/2}}\frac{y}{x}\mathrm{Pe}_x^{1/2} \qquad (33)$$

For the asymptotic case of Forchheimer free convection, namely, $x_{F^*} \ll 1$, the temperature and velocity profiles given by Eqs. (32*a*) and (32*b*), for this case, become identical to those given by Eqs. (22) under $\mathrm{Gr}_{Kq} \gg 1$. Naturally, for the case of pure forced convection, namely, $x_{F^*} \gg 1$, the foregoing results reduce to those as we extracted from the Darcy-mixed convection formulas. Thus, the following approximate formula was obtained by matching the asymptotic results:

$$\frac{k(T_c-T_e)}{q^*} = \frac{\Delta T_c^*}{\mathrm{Pe}_x^{1/2}} = \frac{1}{2\pi^{1/2}(1+0.2714\,x_F^{*\,-2/5})^{1/4}\mathrm{Pe}_x^{1/2}} \qquad (34)$$

The approximate expressions can be used for any value of x_P^*. The maximum error using this approximate formula turns out to be less than 3 percent of the exact value. Finally, the developing profiles of the dimensionless temperature and velocity, namely, $(T-T_e)/\{q^*/k(u_eL_F/\alpha)^{1/2}\}$ and $(u-u_e)/u_e$, are presented together in Fig. 6 where the dimensionless coordinates $x_F^* = x/L_F$ and $(y\mathrm{Pe}_x^{1/2}/x)_{x=L_F}$ are used. Drastic changes in the profiles take place as the flow goes away from the origin of heat source, adjusting itself first to the Forchheimer free convection mode (Regime III), and then to the Forchheimer mixed convection mode (Regime VI), and finally to the pure forced convection regime (Regime I).

References

Bejan, A., 1984, *Convection Heat Transfer*, Wiley, New York.

Cheng, P., 1978, "Heat Transfer in Geothermal Systems," *Adv. Heat Transfer*, Vol. 14, pp. 59–60.

Cheng, P., and Zheng, T. M., 1986, "Mixed Convection in the Thermal Plume Above a Horizontal Line Source of Heat in a Porous Medium of Infinite Extent," *Proc. 8th Int. Heat Transfer Conference*, San Francisco, Vol. 5, pp. 2671–2675.

Churchill, S. W., and Usagi, R., 1972, "A General Expression for the Correlation of Rates of Heat Transfer and Other Phenomena," *AIChE J.*, Vol. 18, pp. 1121–1128.

Hickox, C. E., and Watts, H. A., 1980, "Steady Thermal Convection From a Concentrated Source in a Porous Medium," ASME JOURNAL OF HEAT TRANSFER, Vol. 102, pp. 248–253.

Hickox, C. E., 1981, "Thermal Convection at Low Rayleigh Number From Concentrated Sources in Porous Media," ASME JOURNAL OF HEAT TRANSFER, Vol. 103, pp. 232–236.

Ingham, D. B., 1988, "An Exact Solution for Non-Darcy Free Convection From a Horizontal Line Source of Heat," *Wärme- und Stoffübertragung*, Vol. 22, pp. 125–127.

Lai, F. C., 1991a, "Non-Darcy Natural Convection From a Line Source of Heat in a Saturated Porous Medium," *Int. Comm. Heat Mass Transfer*, Vol. 18, pp. 445–457.

Lai, F. C., 1991b, "Non-Darcy Mixed Convection From a Line Source of Heat in Saturated Porous Medium," *Int. Comm. Heat Mass Transfer*, Vol. 18, pp. 875–887.

Masuoka, T., Tohda, Y., Tsuruta, T., and Yasuda, Y., 1986, "Buoyant Plume

Above Concentrated Heat Source in Stratified Porous Media," *Trans. JSME*, Ser. B, pp. 2656–2662.

Nakayama, A., and Pop, I., 1991, "A Unified Similarity Transformation for Free, Forced and Mixed Convection in Darcy and Non-Darcy Porous Media," *Int. J. Heat Mass Transfer*, Vol. 34, pp. 357–367.

Nakayama, A., 1992, "Free Convection From a Horizontal Line Heat Source in a Power-Law Fluid-Saturated Porous Medium," to appear in *Int. J. Heat Fluid Flow*.

Nield, D. A., and White, S. P., 1982, "Natural Convection in an Infinite Porous Medium Produced by a Line Heat Source," *Mathematical Models in Engineering Science*, A. McNabb, R. A. Wooding, and M. Rosser, eds., Dept. Sci. and Indust. Res., Wellington, New Zealand.

Wooding, R. A., 1963, "Convection in a Saturated Porous Medium at Large Rayleigh or Peclet Number," *J. Fluid Mech.*, Vol. 15, pp. 527–544.

Yih, C. S., 1965, *Dynamics of Nonhomogeneous Fluids*, Macmillan, New York, p. 234.

A Re-evaluation of Non-Darcian Forced and Mixed Convection in Cylindrical Packed Tubes

F. C. Chou,[1,3] **J. H. Su,**[2,3] **and S. S. Lien**[2,3]

Introduction

Recently, several theoretical models of non-Darcian forced convection had been reported, but there are great discrepancies in the values of Nusselt number obtained. It can be seen in Fig. 1 that the values of Nusselt number for the fully developed region of cylindrical packed tubes with $D/d = 17$ obtained by using the models of Cheng and Zhu (1987) and Hunt and Tien (1988) are 100 percent higher when $\mathrm{Pe}_p = 10$ and 800–1000 percent higher when $\mathrm{Pe}_p = 100$ than that of Poulikakos and Renken (1987). The Peclet number, Pe_p, is based upon the diameter of the packed sphere, d, and D is the tube diameter. Therefore, there is a great necessity for a re-evaluation of the non-Darcian forced convection in cylindrical packed tubes. Experimental data from the existing literature and the present measurement for the cylindrical packed-spheres tubes are reexamined and further compared with the results from theoretical models.

Experimental Apparatus and Procedures

The experimental apparatus is shown in Fig. 2. The heated test section is preceded by a constant head tank with an overflow bypass for water head control. An 8-cm-long tube for flow development is placed before entering the test section. The heated sections were made of stainless steel circular tubes with diameters, D, 5.25 and 8.3 cm, and lengths, L, 126 and 102 cm, respectively. The tubes are packed with 5-mm-dia, d, glass spheres. The measured global porosity, ϵ, for the whole packed-sphere tubes are 0.386 and 0.35 for the tubes with $D = 5.25$ and 8.3 cm, respectively. Details of experimental procedures, for example, how to pack the beads, prepare the heaters, and measure the local heat flux as well as temperature, have been described by Chou et al. (1992a, b).

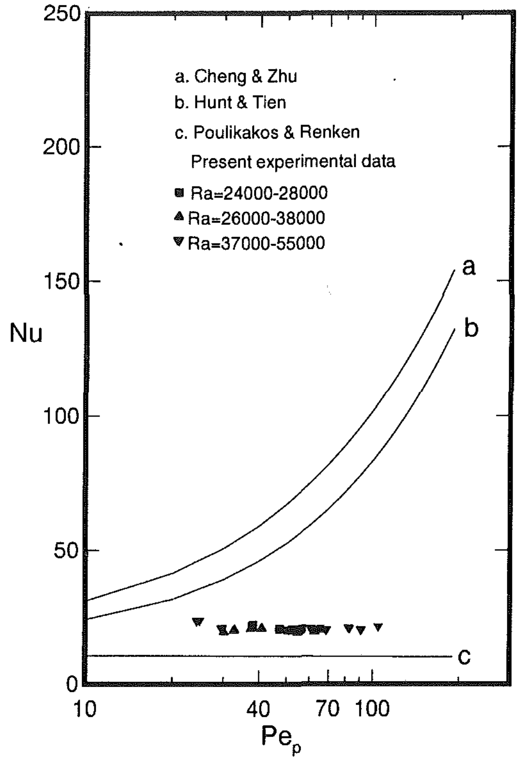

Fig. 1 Comparison of the theoretical predictions of Nu by the existing models with the present experimental data for $D/d = 17$

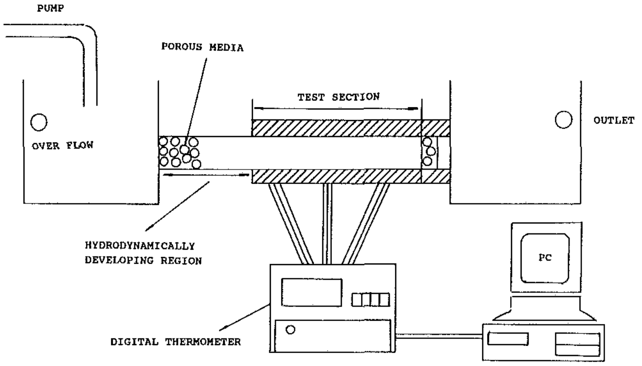

Fig. 2 Experimental apparatus

The averaged wall temperature was calculated by averaging the readings of the eight thermocouples, which were placed at axial positions located at 126 and 98 cm away from the entrance of heated section for the tubes of $D = 5.25$ and 8.3 cm, respectively. The local averaged heat transfer coefficient $\bar{h}$ was calculated by the local heat flux, averaged wall temperature, and the local bulk mean fluid temperature. The evaluation of Nusselt number is based on the diameter D of the tube and the fluid conductivity k_f as follows:

$$\mathrm{Nu} = \bar{h}D/k_f = q_w D/[k_f(T_w - \langle T_b \rangle)] \tag{1}$$

where q_w is the heat flux imposed at the outer surface of tube wall, and T_w and $\langle T_b \rangle$ are the averaged wall temperature and bulk mean fluid temperature. The experimental uncertainties in Nusselt number mainly due to experimental errors in heat balance and temperature measurements are estimated to be in the range of 11 to 16 percent.

Numerical Simulation

In order to consider the buoyancy effect existing in the present experiment, numerical simulation of fully developed non-Darcian mixed convection is proposed. The physical configuration is shown in Fig. 3. Some numerical simulations have been made to ensure the validity of the fully developed as-

---

[1] Professor; Mem. ASME.

[2] Graduate student.

[3] Department of Mechanical Engineering, National Central University, Chung-Li 320, Taiwan.

Contributed by the Heat Transfer Division and presented at the National Heat Transfer Conference, San Diego, California, August 9–12, 1992. Manuscript received by the Heat Transfer Division June 1992; revision received August 1993. Keywords: Conjugate Heat Transfer, Forced Convection, Mixed Convection. Associate Technical Editor: G. E. Hickox, Jr.

Above Concentrated Heat Source in Stratified Porous Media," *Trans. JSME*, Ser. B, pp. 2656–2662.

Nakayama, A., and Pop, I., 1991, "A Unified Similarity Transformation for Free, Forced and Mixed Convection in Darcy and Non-Darcy Porous Media," *Int. J. Heat Mass Transfer*, Vol. 34, pp. 357–367.

Nakayama, A., 1992, "Free Convection From a Horizontal Line Heat Source in a Power-Law Fluid-Saturated Porous Medium," to appear in *Int. J. Heat Fluid Flow*.

Nield, D. A., and White, S. P., 1982, "Natural Convection in an Infinite Porous Medium Produced by a Line Heat Source," *Mathematical Models in Engineering Science*, A. McNabb, R. A. Wooding, and M. Rosser, eds., Dept. Sci. and Indust. Res., Wellington, New Zealand.

Wooding, R. A., 1963, "Convection in a Saturated Porous Medium at Large Rayleigh or Peclet Number," *J. Fluid Mech.*, Vol. 15, pp. 527–544.

Yih, C. S., 1965, *Dynamics of Nonhomogeneous Fluids*, Macmillan, New York, p. 234.

A Re-evaluation of Non-Darcian Forced and Mixed Convection in Cylindrical Packed Tubes

F. C. Chou,[1,3] J. H. Su,[2,3] and S. S. Lien[2,3]

Introduction

Recently, several theoretical models of non-Darcian forced convection had been reported, but there are great discrepancies in the values of Nusselt number obtained. It can be seen in Fig. 1 that the values of Nusselt number for the fully developed region of cylindrical packed tubes with $D/d = 17$ obtained by using the models of Cheng and Zhu (1987) and Hunt and Tien (1988) are 100 percent higher when $\mathrm{Pe}_p = 10$ and 800–1000 percent higher when $\mathrm{Pe}_p = 100$ than that of Poulikakos and Renken (1987). The Peclet number, Pe_p, is based upon the diameter of the packed sphere, d, and D is the tube diameter. Therefore, there is a great necessity for a re-evaluation of the non-Darcian forced convection in cylindrical packed tubes. Experimental data from the existing literature and the present measurement for the cylindrical packed-spheres tubes are re-examined and further compared with the results from theoretical models.

Experimental Apparatus and Procedures

The experimental apparatus is shown in Fig. 2. The heated test section is preceded by a constant head tank with an overflow bypass for water head control. An 8-cm-long tube for flow development is placed before entering the test section. The heated sections were made of stainless steel circular tubes with diameters, D, 5.25 and 8.3 cm, and lengths, L, 126 and 102 cm, respectively. The tubes are packed with 5-mm-dia, d, glass spheres. The measured global porosity, ϵ, for the whole packed-sphere tubes are 0.386 and 0.35 for the tubes with $D = 5.25$ and 8.3 cm, respectively. Details of experimental procedures, for example, how to pack the beads, prepare the heaters, and measure the local heat flux as well as temperature, have been described by Chou et al. (1992a, b).

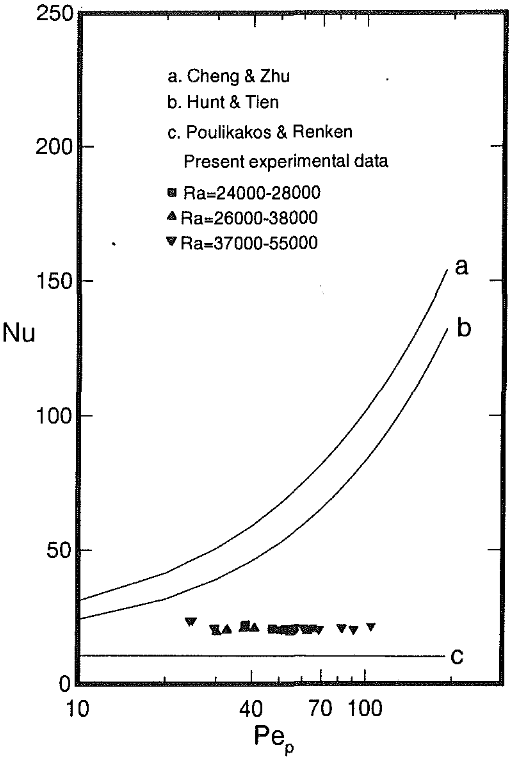

Fig. 1 Comparison of the theoretical predictions of Nu by the existing models with the present experimental data for $D/d = 17$

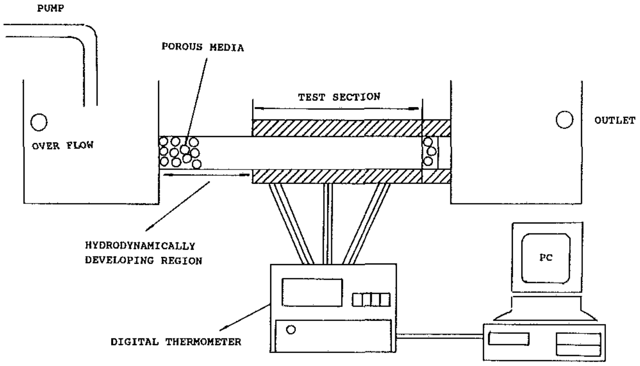

Fig. 2 Experimental apparatus

The averaged wall temperature was calculated by averaging the readings of the eight thermocouples, which were placed at axial positions located at 126 and 98 cm away from the entrance of heated section for the tubes of $D = 5.25$ and 8.3 cm, respectively. The local averaged heat transfer coefficient $\bar{h}$ was calculated by the local heat flux, averaged wall temperature, and the local bulk mean fluid temperature. The evaluation of Nusselt number is based on the diameter D of the tube and the fluid conductivity k_f as follows:

$$\mathrm{Nu} = \bar{h}D/k_f = q_w D/[k_f(T_w - \langle T_b \rangle)] \tag{1}$$

where q_w is the heat flux imposed at the outer surface of tube wall, and T_w and $\langle T_b \rangle$ are the averaged wall temperature and bulk mean fluid temperature. The experimental uncertainties in Nusselt number mainly due to experimental errors in heat balance and temperature measurements are estimated to be in the range of 11 to 16 percent.

Numerical Simulation

In order to consider the buoyancy effect existing in the present experiment, numerical simulation of fully developed non-Darcian mixed convection is proposed. The physical configuration is shown in Fig. 3. Some numerical simulations have been made to ensure the validity of the fully developed as-

---

[1] Professor; Mem. ASME.

[2] Graduate student.

[3] Department of Mechanical Engineering, National Central University, Chung-Li 320, Taiwan.

Contributed by the Heat Transfer Division and presented at the National Heat Transfer Conference, San Diego, California, August 9–12, 1992. Manuscript received by the Heat Transfer Division June 1992; revision received August 1993. Keywords: Conjugate Heat Transfer, Forced Convection, Mixed Convection. Associate Technical Editor: G. E. Hickox, Jr.

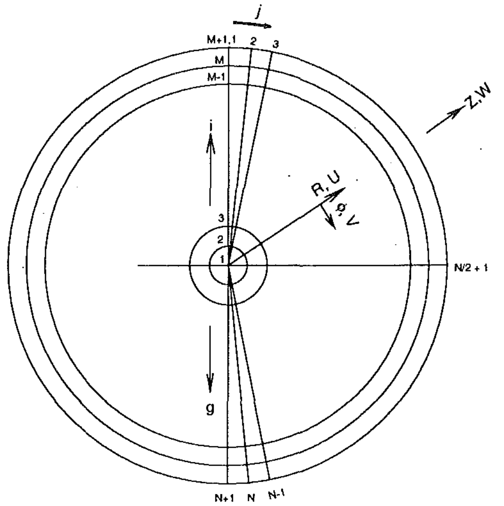

Fig. 3 Schematic for the numerical solution and the coordinate system

sumption. The Boussinesq approximation is used to characterize the buoyancy effect. Viscous dissipation and the compressibility effect in the energy equation are neglected. Referring to the coordinate system r, ϕ, and z shown in Fig. 3, the following dimensionless variables and parameters are introduced:

$$R=r/d, \quad U=\langle u\rangle/(\alpha_f/d), \quad V=\langle v\rangle/(\alpha_f/d),$$
$$W=\langle w\rangle/\langle\overline{w}\rangle, \quad \theta=(\langle T\rangle-T_w)/\theta_c,$$
$$\theta_c=q_w d/k_f, \quad \mathrm{Da}=K_\infty/d^2$$
$$\mathrm{Ra}=g\beta q_w d^4/(\nu_f\alpha_f k_f), \quad \mathrm{Re}_p=\langle\overline{w}\rangle d/\nu_f,$$
$$\mathrm{Pr}=\nu_f/\alpha_f, \quad \mathrm{Pe}_p=\mathrm{Pr}\mathrm{Re}_p \quad (2)$$

where d is the diameter of a packed sphere, $\langle\ \rangle$ represents a volume-averaged quantity, $\langle u\rangle$, $\langle v\rangle$, and $\langle w\rangle$ are the local velocity components in the radial, circumferential, and axial directions. Da is Darcy number. Ra, Re_p and Pe_p are the Rayleigh number, Reynolds number, and Peclet numbers based on particle diameter. α_f and ν_f are the thermal diffusivity and viscosity of fluid. K is the permeability, and the subscript ∞ represents a quantity in the core region.

By introducing the stream function, ψ, and vorticity, ξ, the governing equations are as follows:

$$U=(\partial\psi)/(\partial\phi)/R, \quad V=-(\partial\psi)/(\partial R) \quad (3)$$

$$\xi=\nabla^2\psi \quad (4)$$

$$\begin{aligned}&[U\partial\xi/\partial R+V(\partial\xi/\partial Y)/R]/(\epsilon\mathrm{Pr})+\{U[(\partial V/\partial R)(\partial\epsilon/\partial R)\\&-(\partial U/\partial R)(\partial\epsilon/\partial\phi)/R]+V[(\partial V/\partial\phi)(\partial\epsilon/\partial R)\\&-(\partial U/\partial\phi)(\partial\epsilon/\partial\phi)]/R\}/(\epsilon^2\mathrm{Pr})+(V^2/R^2)(\partial\epsilon/\partial R)\\&+UV(\partial\epsilon/\partial R)=-(\epsilon d^2)/K)\xi+\nabla^2\xi\\&+300(1-\epsilon)(U\partial\epsilon/\partial\phi/R-V\partial\epsilon/\partial R)/\epsilon^2\\&-2\epsilon Cd(U\partial U/\partial/\phi R-V\partial V/\partial R)/\mathrm{Pr}\\&+1.75(2-\epsilon)(U^2\partial\epsilon/\partial\phi/R-V^2\partial\epsilon/\partial R)/(\epsilon^3\mathrm{Pr})\\&+\epsilon\mathrm{Ra}[(\sin\phi)(\partial\theta/\partial R)+(\cos\phi)(\partial\theta/\partial\phi)/R)]\\&+\mathrm{Ra}\theta[(\sin\phi)(\partial\epsilon/\partial R)+(\cos\phi)(\partial\epsilon/\partial\phi)/R] \quad (5)\end{aligned}$$

$$\begin{aligned}&(U\partial W/\partial R+V\partial W/\partial\phi/R)/(\epsilon\mathrm{Pr})\\&=\epsilon[-K_\infty(dp/dz)/(\mu\langle\overline{w}\rangle)]/\mathrm{Da}-(\epsilon d^2/K)W\\&-\epsilon Cd\mathrm{Re}W^2+\nabla^2W \quad (6)\end{aligned}$$

$$\begin{aligned}&U\partial\theta/\partial R+V\partial\theta/\partial\phi/R-4Wd/D\\&=(\partial/\partial R)[(k_e/k_f)R(\partial\theta/\partial R)]/R\\&+(\partial/\partial\phi)[(k_e/k_f)(\partial\theta/\partial\phi)]R^2 \quad (7)\end{aligned}$$

where $\nabla^2=(\partial^2/\partial R^2+\partial/\partial R/R+\partial^2/\partial\phi^2/R^2)$, and C is the inertial coefficient. The value of the dimensionless axial pressure gradient term in Eq. (6) is determined by the constraint $\overline{W}=1$.

From the experimental results of Benenati and Brosilow (1962), the functional dependence of the porosity ϵ on the distance from the tube wall can be represented approximately by an exponential function as used in Chandrasekhara and Vortmeyer (1979)

$$\epsilon=\epsilon_\infty[1+a_1\exp(-a_2n/d)] \quad (8)$$

where ϵ_∞ is the porosity at the core region, n is the normal distance from the wall, and a_1 and a_2 are empirical constants. The permeability, K, and empirical inertia coefficient, C, are given by the approximation developed by Ergun (1952) for flow in a packed bed:

$$K=d^2\epsilon^3/[150(1-\epsilon)^2] \quad (9)$$

$$C=1.75(1-\epsilon)/(d\epsilon^3) \quad (10)$$

The effective conductivity k_e is composed of a sum of the stagnant and dispersion conductivities, $k_e=k_o+k_d$. The value of stagnant conductivity, k_o, depends on the porosity variation and the conductivities of the fluid and solid. The variation of stagnant conductivity near the wall can be written as:

$$k_o=k_\infty[1+(k_f/k_\infty-1)\exp(-a_3n/d)] \quad (11)$$

where a_3 is an empirical constant and k_∞ is the stagnant conductivity in the core region, which can be obtained from the semitheoretical model by Zehner and Schlunder (1970)

$$\begin{aligned}&k_\infty=k_f\{1-(1-\epsilon_\infty)^{0.5}+2\Lambda(1-\epsilon_\infty)^{0.5}\\&\times[B_o\Lambda(\Lambda-1)\ln(\Lambda/B_o)/(\Lambda-B_o)^2\\&-(B_o+1)/2-\Lambda(B_o-1)/(\Lambda-B_o)]/(\Lambda-B_o)\} \quad (12)\end{aligned}$$

where $B_o=1.25[(1-\epsilon_\infty)/\epsilon_\infty]^{10/9}$ and $\Lambda=k_s/k_f$.

From Eqs. (11) and (12) one can see that the effect of stagnant conductivity is characterized by the conductivity ratio of solid-sphere to fluid, $\Lambda=k_s/k_f$. The values of $\mathrm{Pr}=7.02$ and $\Lambda=1.3$ are used to simulate the water flow through glass packed spheres, and $\mathrm{Pr}=0.7$ and $\Lambda=38.8$ are used for air flow through glass spheres. The effective conductivity also includes thermal transport due to the effect of thermal dispersion. Thermal dispersion results from the velocity gradients within the pore and existence of the solid matrix, which forces the flow to undergo a tortuous path around the solid particles. The value of the thermal dispersion conductivity was proposed to be proportional to a product of the local velocity and mixing length function, also called the damping function, $l(n)$, by Cheng and Zhu (1987) and Hunt and Tien (1988)

$$k_d/k_f=\gamma_\infty\mathrm{Pe}_p^\lambda[(U^2+V^2)/\mathrm{Pe}_p^2+W^2]^{0.5\lambda}l(n)/d \quad (13)$$

where γ_∞ is the value of the thermal dispersion coefficient at the core region.

Because of symmetry, it suffices to solve the problem in half the circular tube. The boundary conditions are:

$$U=V=W=\theta=0 \qquad \text{at tube wall } (R=1)$$
$$\partial U/\partial\phi=V=\partial W/\partial\phi=\partial\theta/\partial\phi=0 \qquad \text{at symmetry plane} \quad (14)$$

The local Nusselt number Nu can be calculated on the basis of overall energy balance:

$$\mathrm{Nu}=\overline{h}D/k_f=(D/d)/(1-\theta_b) \quad (15)$$

Results and Discussion

To track accurately the dispersion damping near the wall, a nonuniform grid system in the radial direction ($\Delta R_j=1.05\times\Delta R_{j-1}$) is used. A numerical experiment similar to that of Chou et al. (1991) was made to ensure that the numerical results should be grid independent.

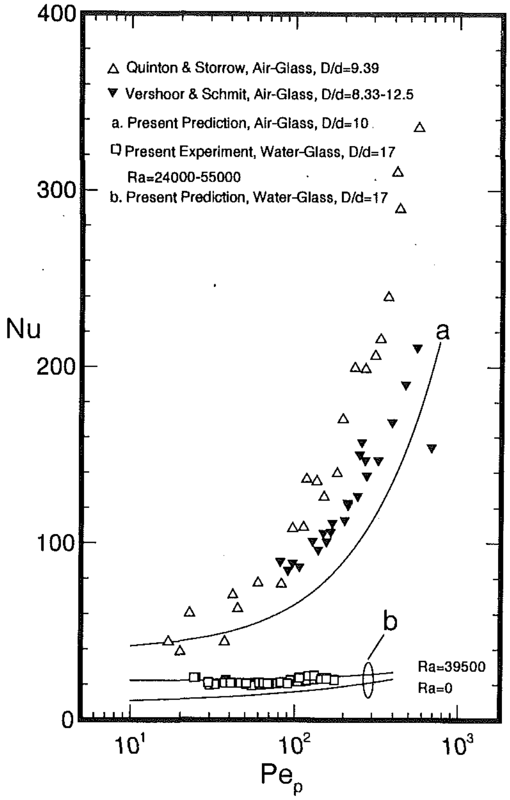

Fig. 4 Comparison of present predictions of Nu with the data of Quinton and Storrow (1956) and Vershoor and Schuit (1952) for air-glass medium and the present data for water-glass medium with *D/d* = 17

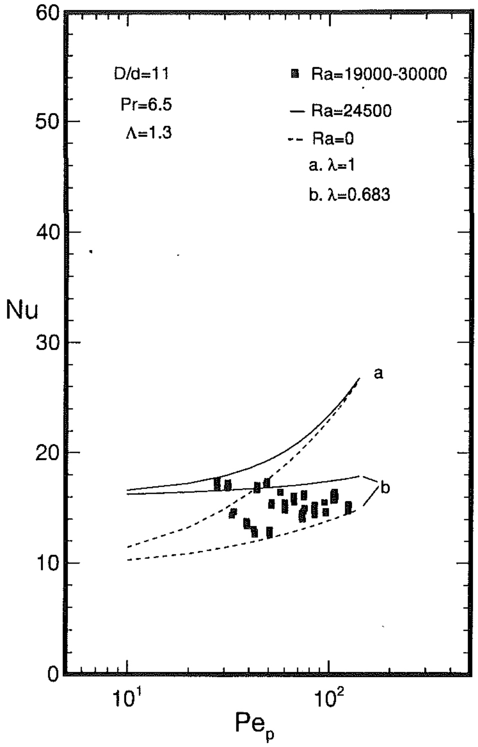

Fig. 5 Comparison of present predictions of Nu with the present experimental data for *D/d* = 11

A detailed inspection of the existing models cited in Fig. 1 shows that the discrepancies among the existing models are mainly due to the modelings of channeling and thermal dispersion effects for the cases of low and high Peclet number, respectively. In the present work, we use the empirical constants $a_1 = 0.43$ and $a_2 = 3$ as suggested by Chandrasekhara and Vortmeyer (1979) and Poulikakos and Renken (1987). It is shown in Fig. 4 that the predictions of Nu become the lower bound of the data of Quinton and Storrow (1956) for $Pe_p < 60$. It was found by Chandrasekhara and Vortmeyer (1979) that if $a_1 = 1$ and $a_2 = 3$ were used, which was suggested by Benenati and Brosilow (1962), the velocity profile exhibited a sharp peak at the wall with 3 to 4 times higher magnitude than the maximum experimental value. It is also noteworthy that Szekely and Poveromo (1975) in their study had limited the porosity value adjacent to the wall to a maximum of 0.49.

From a brief review of the existing models of thermal dispersion effect, it is found that the thermal dispersive conductivity, k_d, is proposed to be linearly proportional to Peclet number for air flow, that is $\lambda = 1$, by all the existing models. But nonlinear dependence of k_d and Pe, say $\lambda = 0.683$, is proposed for water flow by Levec and Carbonell (1985). It is noteworthy that none pointed out that the models of thermal dispersion effect for air and water flows should be different. In the present work we propose a model of non-Darcian forced convection for water flow through glass sphere beds by using $Pr = 7.02$, $a_1 = 0.43$, $a_2 = 3$, $a_3 = 1$, $\Lambda = 1.3$, $\gamma_\infty = 0.07$, $l(n)/d = 1 - \exp[(n/d)^2/a_4]$, $a_4 = 1$, and $\lambda = 0.683$. A comparison of calculated values of Nu and the experimental data are shown in Fig. 4 for the tube of $D/d = 17$. It is seen that the curve of calculated Nu for Ra = 0 falls below the present experimental data of Ra = 24,000–55,000, but the curves of calculation for Ra = 39,500 are in good agreement with the present experimental data. For the air flow through glass sphere bed, we assign $Pr = 0.7$, $\Lambda = 38.8$, $l(n)/d = 1 - \exp[(n/d)/a_4]$, $a_4 = 0.5$ and $\lambda = 1$, and let all other coefficients a_1, a_2, a_3 and constant γ_∞ be the same with the foregoing model for water flow. It is promising to see that the present calculations of Nu for air flow are in good agreement with the experimental data of Quinton and Storrow (1956) and Vershoor and Schuit (1952).

In order to study whether the present model can predict Nusselt number in another different size packed tube, a comparison of calculated Nu with the experimental data for $D/d = 11$ is shown in Fig. 5. It is seen that the calculated Nu for $\lambda = 0.683$ and Ra = 0 fall below the data, but the curve for $\lambda = 0.683$ and Ra = 24,500 shows better agreement with the data. It is also seen that if $\lambda = 1$ is used, the curves for Ra = 0 and 24,500 are all about 100 percent higher than the experimental data at Pe = 100. It was found by Chou et al. (1992a, b) that if $\lambda = 1$ was used for water flow, the calculated Nu could agree well with the experimental data for $D_e/d = 10$ by a certain damping function for dispersion effect, then the calculated Nu would be higher than the experimental data for $D_e/d = 19$ at high Peclet number. Now in the light of the present work, we may say that the worse agreement at high Peclet number in the cases of $D_e/d = 19$ shown by Chou et al. (1992a, b) is caused by the overestimation of thermal dispersion effect by using $\lambda = 1$.

Concluding Remarks

1 The discrepancies among the existing models are mainly due to the modelings of channeling and thermal dispersion effects for the cases of low and high Peclet number, respectively. We use the flow model reported by Chandrasekhara and Vortmeyer (1979), which was also used by Poulikakos and Renken (1987); the predicted values of Nusselt number are found to agree well with the data of Quinton and Storrow (1956) for air flow and also agree well with the present data for water flow for the cases of low Peclet number.

2 The re-evaluation shows that the modeling of thermal dispersion effect for air and water flows should be different.

A linear dependence of dispersive conductivity, k_d, with Peclet number is used for air flow as reported by many investigators. But a nonlinear dependence of k_d and Pe, say $k_d \propto \mathrm{Pe}_p^{0.683}$, is used in the present work for water flow. Then the present predictions of Nu can be in good agreement with the existing and present experimental data for both air and water flows.

Acknowledgments

Financial support for this research provided by the National Science Council of Republic of China through Grant NSC 80-0401-E008-09 is greatly appreciated.

References

Benenati, R. F., and Brosilow, C. B., 1962, "Void Fraction Distribution in Packed Beds," *AIChE J.*, Vol. 8, pp. 359–361.

Chandrasekhara, B. C., and Vortmeyer, D., 1979, "Flow Model for Velocity Distribution in Fixed Porous Beds Under Isothermal Conditions," *Wärme- und Stoffübertragung*, Vol. 12, pp. 105–111.

Cheng, P., and Zhu, H., 1987, "Effects of Radial Thermal Dispersion on Fully-Developed Forced Convective Flow in Cylindrical Packed Tubes," *Int. J. Heat Mass Transfer*, Vol. 30, pp. 2373–2383.

Chou, F. C., Chung, P. Y., and Cheng, C. J., 1991, "Dual Solutions of Fully-Developed Non-Darcian Mixed Convection in Horizontal Square Channels," *Mixed Convection Heat Transfer, Proc. 1991 National Heat Transfer Conf.*, ASME HTD-Vol. 163, pp. 85–95.

Chou, F. C., Lien, W. Y., and Lin, S. H., 1992a, "Analysis and Experiment of Non-Darcian Convection in Horizontal Square Packed-Square Channels—Part 1: Forced Convection," *Int. J. Heat Mass Transfer*, Vol. 35, pp. 195–205.

Chou, F. C., Cheng, C. J., and Lien, W. Y., 1992b, "Analysis and Experiment of Non-Darcian Convection in Horizontal Square Packed-Square Channels—Part 2: Mixed Convection," *Int. J. Heat Mass Transfer*, Vol. 35, pp. 1197–1207.

Ergun, S., 1952, "Fluid Flow Through Packed Columns," *Chem. Eng. Prog.*, Vol. 48, pp. 89–94.

Hunt, M. L., and Tien, C. L., 1988, "Non-Darcian Convection in Cylindrical Packed Beds," ASME JOURNAL OF HEAT TRANSFER, Vol. 110, pp. 378–384.

Levec, J., and Carbonell, R. G., 1985, "Longitudinal and Lateral Thermal Dispersion in Packed Beds, Part 2: Comparison Between Theory and Experiment," *AIChE J.*, Vol. 31, pp. 591–602.

Poulikakos, D., and Renken, K. J., 1987, "Forced Convection in a Channel Filled With Porous Medium, Including the Effects of Flow Inertia, Variable Porosity, and Brinkman Friction," ASME JOURNAL OF HEAT TRANSFER, Vol. 109, pp. 880–888.

Quinton, J. H., and Storrow, J. A., 1956, "Heat Transfer to Air Flowing Through Packed Tubes," *Chem. Eng. Sci.*, Vol. 5, pp. 245–257.

Szekely, J., and Poveromo, J. J., 1975, "Flow Maldistribution in Packed Beds. A Comparison of Measurements With Predictions," *AIChE J.*, Vol. 21, pp. 769–775.

Vershoor, H., and Schuit, G. C. A., 1952, "Heat Transfer to Fluids Flowing Through a Bed of Granular Solids," *Appl. Scient. Res.*, Vol. A2, pp. 97–119.

Zehner, P., and Schlunder, E. U., 1970, "Thermal Conductivity of Packed Beds at Moderate Temperatures," *Chem. Eng. Sci.* [in German], Vol. 42, pp. 933–940.

A Similarity Solution for Combined Hydrodynamic and Heat Transfer Controlled Bubble Growth in a Porous Medium

M. Epstein[1]

Nomenclature

A = dimensionless flow resistance parameter $= \mu_f k_m T_{bp}(1-\rho_g/\rho_f)/(\kappa \rho_g^2 h_{fg}^2)$
c_p = specific heat
d = length scale of porous medium solid (particle diameter)
h_{fg} = latent heat of evaporation
H_o = reference mean curvature of menisci that make up liquid–vapor interface
Ja = Jacob number $= \rho_m c_m \Delta T/(\epsilon \rho_g h_{fg})$
k = thermal conductivity
P = pressure
r = radial coordinate measured from center of bubble
R = bubble radius
s = transformed coordinate, Eq. (6)
t = time
T = temperature
α = thermal diffusivity
β = dimensionless heat capacity parameter $= \rho_f c_{p,f} \epsilon (1-\rho_g/\rho_f)/(\rho_m c_m)$
ΔT = liquid superheat $= T_\infty - T_{bp}$
ϵ = porosity
θ = dimensionless temperature, Eq. (6)
κ = permeability
λ = bubble growth constant, Eq. (6)
μ = viscosity
ρ = density
σ = liquid surface tension
Σ = capillary parameter, Eq. (16)

Subscripts

bp = boiling point of liquid at ambient pressure P_∞
f = refers to liquid properties
g = refers to bubble (vapor) properties
m = refers to porous medium/liquid "mixture" properties
s = refers to porous medium solid material
∞ = refers to ambient conditions (far from bubble)

Introduction

The pioneering studies of bubble growth in pure liquids by Plesset and Zwick (1953), Forster and Zuber (1954), Scriven (1959), and others have all shown that the asymptotic phase of this growth is well described by the so-called "parabolic" growth law ($R \sim t^{1/2}$). Recently there has been an interest in bubble growth in porous media because of the importance of this problem to geothermal systems and nuclear waste disposal (Satik and Yortsos, 1991). In connection with an ongoing study of the stability of radioactive waste sludge composed of combustible solid precipitate particles in an aqueous solution, it is desirable to have mathematical expressions for vapor cavity growth in a porous medium model of the sludge in which the precipitate particles are assumed stationary and the sludge is locally superheated relative to the boiling point of the interstitial liquid. In the present note it is shown that a potentially useful similarity (parabolic-law) solution can be obtained that incorporates the effects of simultaneous hydrodynamic (Darcy law) and heat-conduction limitations to bubble growth in porous media. We conclude with a brief discussion of the assumptions underlying this asymptotic result.

Model of Bubble Growth

Let us consider the spherically symmetric growth of an isolated sphere (bubble) of pure vapor in a porous medium saturated with liquid. We may be using a sphere to represent what is in reality an irregular vapor region. Our justification for this approach is that the spherically symmetric viewpoint and description has been conceptually valuable in dealing quantitatively with other moving boundary problems for which the spherical form is unlikely (crystal growth, solid particle dissolution, flame growth from a point source igniter, etc.). Moreover, when capillary effects in pores are not important, which is the situation of interest here (see below), it is possible that

---

[1] Fauske & Associates, Inc., 16W070 West 83rd Street, Burr Ridge, IL 60521.

Contributed by the Heat Transfer Division of THE AMERICAN SOCIETY OF MECHANICAL ENGINEERS. Manuscript received by the Heat Transfer Division April 1993; revision received September 1993. Keywords: Boiling, Moving Boundaries, Porous Media. Associate Technical Editor: V. K. Dhir.

A linear dependence of dispersive conductivity, k_d, with Peclet number is used for air flow as reported by many investigators. But a nonlinear dependence of k_d and Pe, say $k_d \propto \mathrm{Pe}_p^{0.683}$, is used in the present work for water flow. Then the present predictions of Nu can be in good agreement with the existing and present experimental data for both air and water flows.

Acknowledgments

Financial support for this research provided by the National Science Council of Republic of China through Grant NSC 80-0401-E008-09 is greatly appreciated.

References

Benenati, R. F., and Brosilow, C. B., 1962, "Void Fraction Distribution in Packed Beds," *AIChE J.*, Vol. 8, pp. 359–361.

Chandrasekhara, B. C., and Vortmeyer, D., 1979, "Flow Model for Velocity Distribution in Fixed Porous Beds Under Isothermal Conditions," *Wärme- und Stoffübertragung*, Vol. 12, pp. 105–111.

Cheng, P., and Zhu, H., 1987, "Effects of Radial Thermal Dispersion on Fully-Developed Forced Convective Flow in Cylindrical Packed Tubes," *Int. J. Heat Mass Transfer*, Vol. 30, pp. 2373–2383.

Chou, F. C., Chung, P. Y., and Cheng, C. J., 1991, "Dual Solutions of Fully-Developed Non-Darcian Mixed Convection in Horizontal Square Channels," *Mixed Convection Heat Transfer, Proc. 1991 National Heat Transfer Conf.*, ASME HTD-Vol. 163, pp. 85–95.

Chou, F. C., Lien, W. Y., and Lin, S. H., 1992a, "Analysis and Experiment of Non-Darcian Convection in Horizontal Square Packed-Square Channels—Part 1: Forced Convection," *Int. J. Heat Mass Transfer*, Vol. 35, pp. 195–205.

Chou, F. C., Cheng, C. J., and Lien, W. Y., 1992b, "Analysis and Experiment of Non-Darcian Convection in Horizontal Square Packed-Square Channels—Part 2: Mixed Convection," *Int. J. Heat Mass Transfer*, Vol. 35, pp. 1197–1207.

Ergun, S., 1952, "Fluid Flow Through Packed Columns," *Chem. Eng. Prog.*, Vol. 48, pp. 89–94.

Hunt, M. L., and Tien, C. L., 1988, "Non-Darcian Convection in Cylindrical Packed Beds," ASME JOURNAL OF HEAT TRANSFER, Vol. 110, pp. 378–384.

Levec, J., and Carbonell, R. G., 1985, "Longitudinal and Lateral Thermal Dispersion in Packed Beds, Part 2: Comparison Between Theory and Experiment," *AIChE J.*, Vol. 31, pp. 591–602.

Poulikakos, D., and Renken, K. J., 1987, "Forced Convection in a Channel Filled With Porous Medium, Including the Effects of Flow Inertia, Variable Porosity, and Brinkman Friction," ASME JOURNAL OF HEAT TRANSFER, Vol. 109, pp. 880–888.

Quinton, J. H., and Storrow, J. A., 1956, "Heat Transfer to Air Flowing Through Packed Tubes," *Chem. Eng. Sci.*, Vol. 5, pp. 245–257.

Szekely, J., and Poveromo, J. J., 1975, "Flow Maldistribution in Packed Beds. A Comparison of Measurements With Predictions," *AIChE J.*, Vol. 21, pp. 769–775.

Vershoor, H., and Schuit, G. C. A., 1952, "Heat Transfer to Fluids Flowing Through a Bed of Granular Solids," *Appl. Scient. Res.*, Vol. A2, pp. 97–119.

Zehner, P., and Schlunder, E. U., 1970, "Thermal Conductivity of Packed Beds at Moderate Temperatures," *Chem. Eng. Sci.* [in German], Vol. 42, pp. 933–940.

A Similarity Solution for Combined Hydrodynamic and Heat Transfer Controlled Bubble Growth in a Porous Medium

M. Epstein[1]

Nomenclature

A = dimensionless flow resistance parameter $= \mu_f k_m T_{bp}(1-\rho_g/\rho_f)/(\kappa \rho_g^2 h_{fg}^2)$
c_p = specific heat
d = length scale of porous medium solid (particle diameter)
h_{fg} = latent heat of evaporation
H_o = reference mean curvature of menisci that make up liquid–vapor interface
Ja = Jacob number $= \rho_m c_m \Delta T/(\epsilon \rho_g h_{fg})$
k = thermal conductivity
P = pressure
r = radial coordinate measured from center of bubble
R = bubble radius
s = transformed coordinate, Eq. (6)
t = time
T = temperature
α = thermal diffusivity
β = dimensionless heat capacity parameter $= \rho_f c_{p,f} \epsilon (1-\rho_g/\rho_f)/(\rho_m c_m)$
ΔT = liquid superheat $= T_\infty - T_{bp}$
ϵ = porosity
θ = dimensionless temperature, Eq. (6)
κ = permeability
λ = bubble growth constant, Eq. (6)
μ = viscosity
ρ = density
σ = liquid surface tension
Σ = capillary parameter, Eq. (16)

Subscripts

bp = boiling point of liquid at ambient pressure P_∞
f = refers to liquid properties
g = refers to bubble (vapor) properties
m = refers to porous medium/liquid "mixture" properties
s = refers to porous medium solid material
∞ = refers to ambient conditions (far from bubble)

Introduction

The pioneering studies of bubble growth in pure liquids by Plesset and Zwick (1953), Forster and Zuber (1954), Scriven (1959), and others have all shown that the asymptotic phase of this growth is well described by the so-called "parabolic" growth law ($R \sim t^{1/2}$). Recently there has been an interest in bubble growth in porous media because of the importance of this problem to geothermal systems and nuclear waste disposal (Satik and Yortsos, 1991). In connection with an ongoing study of the stability of radioactive waste sludge composed of combustible solid precipitate particles in an aqueous solution, it is desirable to have mathematical expressions for vapor cavity growth in a porous medium model of the sludge in which the precipitate particles are assumed stationary and the sludge is locally superheated relative to the boiling point of the interstitial liquid. In the present note it is shown that a potentially useful similarity (parabolic-law) solution can be obtained that incorporates the effects of simultaneous hydrodynamic (Darcy law) and heat-conduction limitations to bubble growth in porous media. We conclude with a brief discussion of the assumptions underlying this asymptotic result.

Model of Bubble Growth

Let us consider the spherically symmetric growth of an isolated sphere (bubble) of pure vapor in a porous medium saturated with liquid. We may be using a sphere to represent what is in reality an irregular vapor region. Our justification for this approach is that the spherically symmetric viewpoint and description has been conceptually valuable in dealing quantitatively with other moving boundary problems for which the spherical form is unlikely (crystal growth, solid particle dissolution, flame growth from a point source igniter, etc.). Moreover, when capillary effects in pores are not important, which is the situation of interest here (see below), it is possible that

---

[1] Fauske & Associates, Inc., 16W070 West 83rd Street, Burr Ridge, IL 60521.

Contributed by the Heat Transfer Division of THE AMERICAN SOCIETY OF MECHANICAL ENGINEERS. Manuscript received by the Heat Transfer Division April 1993; revision received September 1993. Keywords: Boiling, Moving Boundaries, Porous Media. Associate Technical Editor: V. K. Dhir.

the vapor space may be nearly spherical, at least during the early phase of its growth period. Indeed, Popov and Cherepanov (1986) have treated the dynamics of gas bubbles in porous media by using a spherical coordinate system. In keeping with our objectives, we introduce the following additional simplifying assumptions:

1 The equation of motion of the surrounding liquid may be replaced by Darcy's law. Thus the Newtonian viscosity term and inertia term in the momentum equation, which are important during the very early stages of growth, are ignored.
2 The liquid flow is slow enough so that the temperature of the stationary solid and the adjacent moving liquid are equal.
3 Meaningful, constant (average) physical properties of the porous medium (liquid plus stationary solid) may be defined.
4 The vapor phase within the bubble is at uniform temperature T_g and at uniform pressure P_g, which are, respectively, larger than the ambient pressure P_∞ and ambient temperature T_∞.
5 The capillary pressure difference due to surface tension effects across the liquid-vapor interface is assumed small compared to $P_g - P_\infty$ so that P_g is, approximately, equal to the pressure in the liquid at the liquid-vapor interface.
6 The pressure P_g is equal to the saturation pressure at T_g as given by the linearized form of the Clausius-Clapeyron equation.

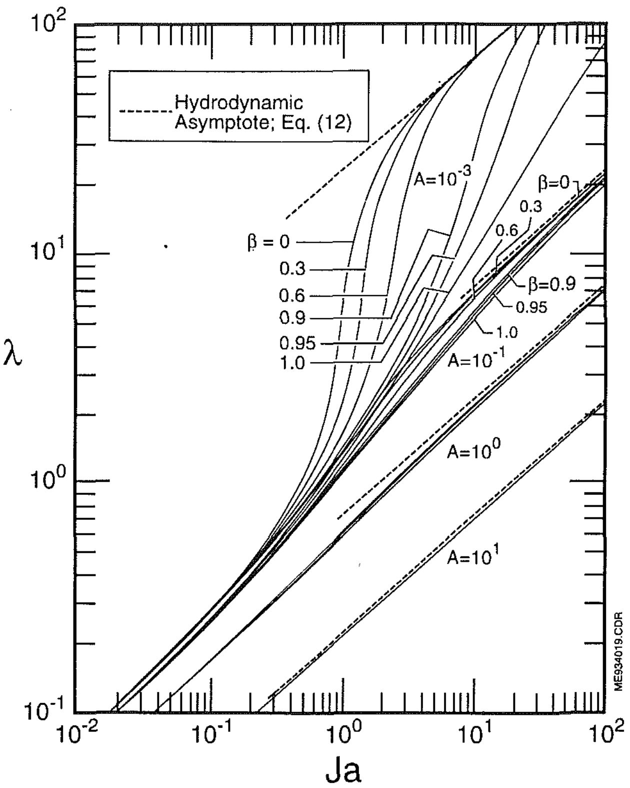

Fig. 1 Bubble growth constant versus Jacob number; β and A as parameters

Analysis

The temperature of the liquid must satisfy the local energy conservation relation

$$\rho_m c_{p,m} \frac{\partial T}{\partial t} + \rho_f c_{p,f} \epsilon \frac{R^2}{r^2} \frac{dR}{dt} \left(1 - \frac{\rho_g}{\rho_f}\right) \frac{\partial T}{\partial r} = \frac{k_m}{r^2} \frac{\partial}{\partial r} \left(r^2 \frac{\partial T}{\partial r}\right) \quad (1)$$

together with the obvious boundary conditions

$$T(R, t) = T_g; \quad T(\infty, t) = T_\infty; \quad T(r, 0) = T_\infty \quad (2)$$

The instantaneous bubble growth rate dR/dt is related to the instantaneous value of $(\partial T/\partial r)_{r=R}$ through an energy balance at the interface; namely

$$\rho_g h_{fg} \epsilon \frac{dR}{dt} = k_m \left(\frac{\partial T}{\partial r}\right)_{r=R} \quad (3)$$

Darcy's law written for spherically symmetric liquid flow gives the following relation between the pressure difference $P_g - P_\infty$ and the bubble growth rate:

$$\frac{\kappa}{\mu_f} (P_g - P_\infty) = \epsilon \left(1 - \frac{\rho_g}{\rho_f}\right) R \frac{dR}{dt} \quad (4)$$

Finally, from the "linearized" condition of thermodynamic equilibrium at the bubble surface, we have

$$P_g - P_\infty = \frac{\rho_g h_{fg}}{T_{bp}} (T_g - T_\infty + \Delta T) \quad (5)$$

In Eq. (5) ρ_g and h_{fg} are evaluated at the boiling point T_{bp} of the liquid. Within the accuracy of this linear approximation it is permissible also to evaluate ρ_g in Eqs. (1), (3), and (4) at T_{bp}.

We now assume the dimensionless similarity variables

$$s = \frac{r}{2(\alpha_m t)^{1/2}}, \quad R = 2\lambda(\alpha_m t)^{1/2}, \quad \theta(s) = \frac{T(r, t) - T_\infty}{T_g - T_\infty} \quad (6)$$

which are essentially the same as those assumed by Scriven (1959) in his study of heat transfer limited bubble growth in a pure liquid, except that in the present problem of combined hydrodynamic and heat transfer controlled bubble growth in porous media T_g in the last equation of Eq. (6) is not equal to T_{bp} but, instead, takes on some constant and as yet unknown value between T_{bp} and T_∞. The parameter λ in the second equation of Eq. (6) is the bubble growth rate constant and is the quantity we desire to determine. The variables given by Eq. (6) transform the equation of energy, Eq. (1), into the ordinary differential equation

$$\frac{d^2\theta}{ds^2} + 2\left(s + \frac{1}{s} - \beta \frac{\lambda^3}{s^2}\right) \frac{d\theta}{ds} = 0 \quad (7)$$

subject to the boundary conditions (see Eqs. (2) and (3))

$$\theta(\lambda) = 1; \quad \theta(\infty) = 0; \quad \text{Ja} \left(\frac{d\theta}{ds}\right)_{s=\lambda} = -\frac{2\lambda \Delta T}{T_\infty - T_g} \quad (8)$$

The definitions of the dimensionless parameters β, Ja, A (see below) are given in the nomenclature.

Using Eq. (5) and the second part of Eq. (6) to eliminate $P_g - P_\infty$ and R, respectively, from Darcy's law, Eq. (4), yields an expression for the normalized bubble temperature in terms of λ:

$$\frac{T_\infty - T_g}{\Delta T} = 1 - \frac{2A\lambda^2}{\text{Ja}} \quad (9)$$

Now integrating Eq. (7) twice and using the boundary conditions in Eqs. (8) to evaluate the constants of integration and $d\theta/ds$ at $s = \lambda$ results in another expression for the normalized bubble temperature in terms of λ:

$$\text{Ja}\left(\frac{T_\infty - T_g}{\Delta T}\right) = 2\lambda^3 \exp(\lambda^2 + 2\beta\lambda^2) \int_\lambda^\infty \times \exp\left(-s^2 - \frac{2\beta\lambda^3}{s}\right) \frac{ds}{s^2} \quad (10)$$

To obtain the dimensionless bubble growth constant λ we eliminate $(T_\infty - T_g)/\Delta T$ between Eqs. (9) and (10) to get

$$\mathrm{Ja}=2A\lambda^2+2\lambda^3\exp(\lambda^2+2\beta\lambda^2)\int_{\lambda}^{\infty}\exp\left(-s^2-\frac{2\beta\lambda^3}{s}\right)\frac{ds}{s^2} \tag{11}$$

If $\epsilon=1.0$, or equivalently $A=0$ (since $\kappa\rightarrow\infty$), Eq. (11) reduces to the heat transfer controlled case for bubble growth in a pure liquid (Scriven, 1959).

The results of solving Eq. (11) for λ are presented in Fig. 1 for several values of A and for the range of parameter values β and Ja of practical interest. It is evident from an examination of Eq. (11) that the growth rate constant for purely hydrodynamic-limited growth is .

$$\lambda=\left(\frac{\mathrm{Ja}}{2A}\right)^{1/2} \tag{12}$$

This limiting case is represented by the dashed lines in Fig. 1. If Ja (or liquid superheat) is large, all the curves for a fixed value of A converge to the hydrodynamic asymptote given by Eq. (12). If Ja is small and, therefore, bubble growth is slow, growth is still hydrodynamically controlled as long as the flow resistance parameter A is sufficiently large. In fact, if $A\gtrsim 1.0$ the growth constant may be estimated without serious error (<20 percent) by Eq. (12), regardless of the value of Ja. The heat transfer controlled limit is not so readily apparent in Fig. 1. How small A has to be to be considered negligible depends very much on the values of both β and Ja. One can at least say that heat transfer is controlling along the segments of the curves for $A\lesssim 0.1$ that lie well below their hydrodynamic asymptote.

Validity of the Model

While most of the approximations exploited herein have been discussed by Satik and Yortsos (1991) it is prudent to reconsider them briefly to avoid applying the principal result (Eq. (11)) in unreasonable situations.

The Darcy law approximation of the liquid momentum equation breaks down when the bubble is small, as this is when the inertia term $\rho_f(dR/dt)^2$ and the viscosity term $4\mu(dR/dt)/R$ are not small compared with the Darcy term $\epsilon\mu R(dR/dt)/\kappa$. Consideration of these terms reveals that a sufficient condition for the neglect of liquid viscosity is

$$R\gg\left(\frac{\kappa}{\epsilon}\right)^{1/2} \tag{13}$$

while a sufficient condition for the neglect of liquid inertia is

$$R\gg\left(\frac{\rho_f\kappa\lambda^2\alpha_m}{\epsilon\mu_f}\right)^{1/2} \tag{14}$$

These conditions are usually adequately satisfied after the initial expansion of the bubble nucleus. For example, for steam-bubble growth in a water-saturated porous medium characterized by $\mu_f=2.8\times10^{-4}$ kg m^{-1} s^{-1}, $\alpha_m=2.0\times10^{-7}$ m^2 s^{-1}, $\kappa=10^{-12}$ m^2, $\epsilon=0.4$, $\Delta T=1.0$°C, and, from Eq. (11), $\lambda=8.3$, the right-hand sides of Eqs. (13) and (14) are about 1.6 μm and 11.0 μm, respectively.

Thermal equilibrium between the stationary solid and the liquid flow is a valid approximation providing that the thermal "time constant" based on the length scale d of the solid (particle diameter), namely $t\approx d^2/(8\alpha_s)$, is less than the time for the bubble surface (at $r=R$) to traverse the distance d. This leads to yet another condition on the bubble radius R:

$$R\gtrsim\frac{\lambda^2 d\,\alpha_m}{4\,\alpha_s} \tag{15}$$

From the preceding example $\lambda\approx8.3$, and if $\alpha_m\approx\alpha_s$, thermal equilibrium is established when the bubble radius is about 17 times the length scale of the solid.

The assumption that the pressure is continuous across the liquid-vapor interface implies that the bubble has grown to a size that well exceeds its nucleus size and that the capillary pressure difference $2\sigma H_o$ (Satik and Yortsos, 1991) across the vapor-liquid interface (bubble surface) within the porous medium is small compared with P_g-P_∞. The latter condition is the one of concern and from Eq. (5) takes the form

$$\Sigma=\frac{2\sigma H_o T_{bp}}{\rho_g h_{fg}\Delta T}\ll 1 \tag{16}$$

Referring to our previous example, H_o^{-1} would have to be larger than about 100 μm in order to satisfy Eq. (16). In closing it should be noted that for an idealized porous structure with a spatially uniform curvature H_o of the menisci the pressure discontinuity at the liquid-vapor interface is readily included in the similarity solution by simply replacing Ja by Ja$(1-\Sigma)$ on the left-hand side of Eq. (11).

References

Forster, H. K., and Zuber, N., 1954, "Growth of a Vapor Bubble in a Superheated Liquid," *J. Appl. Phys.*, Vol. 25, pp. 474-478.

Plesset, M. S., and Zwick, S. A., 1954, "The Growth of Bubbles in Superheated Liquids," *J. Appl. Phys.*, Vol. 25, pp. 493-500.

Popov, V. N., and Cherepanov, A. N., 1986, "Dynamics of the Behavior of a Gas-Bubble Nucleus in a Heterophase Medium," translated in: *J. Applied Mech. & Tech. Physics*, Vol. 27, pp. 538-546.

Satik, C., and Yortsos, Y. C., 1991, "Percolation Models for Boiling and Bubble Growth in Porous Media at Low Superheats," *Multiphase Transport in Porous Media*, ASME FED-Vol. 122/HTD-Vol. 186, pp. 61-72.

Scriven, L. A., 1959, "On the Dynamics of Phase Growth," *Chem. Eng. Sci.*, Vol. 10, pp. 1-13.

Journal of Heat Transfer Discussion

Natural Convection From L-Shaped Corners With Adiabatic and Cold Isothermal Horizontal Walls[1]

A. Bejan.[2] In this note I would like to show a way in which the two main conclusions of Angirasa and Mahajan could be anticipated qualitatively. The following argument is based on an earlier paper, which was apparently overlooked.

The second configuration studied by Angirasa and Mahajan, namely the cold horizontal wall joined with a hot vertical wall, was investigated earlier by Kimura dn Bejan (1985a). The corresponding natural convection flow in a corner filled with fluid saturated porous medium was documented in this very journal (Kimura and Bejan, 1985b).

Kimura and Bejan's (1985a) study contained a scaling theory of the high Rayleigh number regime, finite difference simulations that validated the theory, isothermal versus constant flux walls, and an asymptotic series analysis of the flow and heat transfer in the limit Ra→0. The corner region model is reproduced here in Fig. 1. The scaling theory predicted that in $\mathrm{Pr} \geq 1$ fluids the total heat transfer rate q' [W/m] from the vertical wall to the horizontal wall is of the order of

$$\mathrm{Nu} \sim \left(\frac{L}{H}\right)^{3/7} \mathrm{Ra}_H^{1/7} \tag{1}$$

where $\mathrm{Nu} = q'/k(T_H - T_C)$ and $\mathrm{Ra}_H = g\beta(T_H - T_C)H^3/\alpha\nu$. The finite-difference calculations showed that Eq. (1) is correct (as expected, within a factor of order 1, see Fig. 7 of Kimura and Bejan, 1985a).

One high Ra_H implication of Eq. (1) is that in the corner of Fig. 1 the heat transfer rate is *negligible* when compared with the heat transfer rate that occurs when the same wall (H, T_H) is immersed in a cold fluid reservoir maintained at T_c. The heat transfer rate in this second case can be estimated based on scale analysis (e.g., Bejan, 1984),

$$\mathrm{Nu} \sim \mathrm{Ra}_H^{1/4} \tag{2}$$

For example, when $\mathrm{Ra}_H \sim 10^8$ and $L/H \sim 1$, Eq. (1) yields $\mathrm{Nu} \sim 10$ and Eq. (2) yields $\mathrm{Nu} \sim 10^2$. The gap between the two Nu estimates widens as Ra_H increases. In conclusion, the natural convection thermal resistance between a vertical wall and a cold reservoir is much smaller than the resistance between the same wall and a cold horizontal wall attached as in Fig. 1.

Equations (1) and (2) are relevant as a review of the existing work, and because they can be used to anticipate Angirasa and Mahajan's conclusion regarding the vertical wall perpendicular to a cold isothermal wall. Their numerical results for $10^5 < \mathrm{Ra}_H < 10^9$ and $0.7 < \mathrm{Pr} < 7$ were correlated by the power law

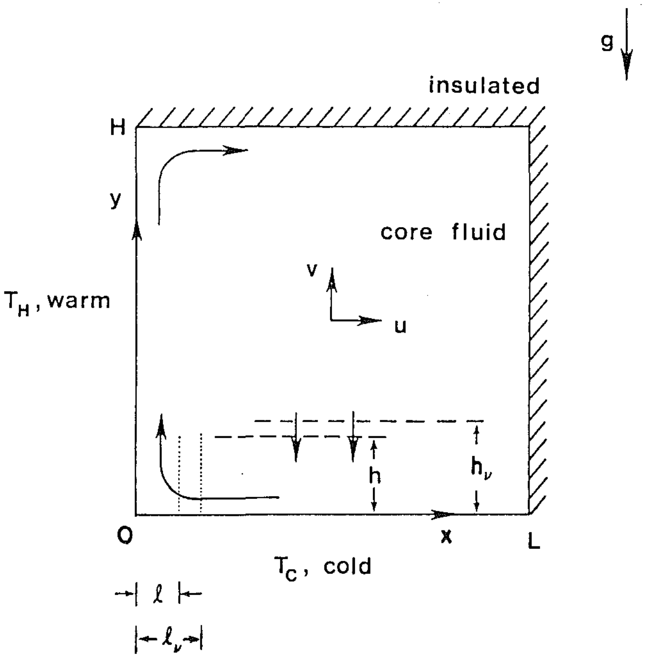

Fig. 1 Natural convection and boundary layer structure in the corner region bounded by a hot vertical wall and a cold horizontal wall (Kimura and Bejan, 1985a)

$$\mathrm{Nu} = 0.833\ \mathrm{Ra}_H^{0.221} \tag{3}$$

which, numerically, turns out to be very close to the classical result for the vertical wall immersed in a cold isothermal reservoir, $\mathrm{Nu} = 0.671\ \mathrm{Ra}_H^{1/4}$ if $\mathrm{Pr} > 1$ (e.g., Bejan, 1984, p. 129).

Why then does Eq. (3) look a lot like Eq. (2), and not like Eq. (1)? The answer is that in Angirasa and Majahan's numerical work the horizontal wall was set isothermal and cold *in addition* to specifying that the fluid pool is isothermal and cold. In other words, the authors' heat transfer rate could sink simultaneously into two heat sinks, the cold reservoir and the cold horizontal wall. The shape of Eq. (3) shows that the heat transfer prefers to sink into the cold reservoir, which must mean that the path of least resistance is from the vertical wall to the cold reservoir. As pointed out above, this finding should be expected based on a comparison of Eqs. (1) and (2), coupled with the observation that Ra_H is high.

All this can be summarized by saying that when the vertical wall is bathed (with high Ra_H) by a reservoir that is maintained cold, the presence of an isothermal cold wall at $y = 0$ has a negligible effect on the total heat released by the vertical wall. If this effect is negligible when the horizontal wall is thermally active (cold), then it must certainly be negligible when the horizontal attachment is inactive (adiabatic). In this way we

---

[1] By D. Angirasa and R. L. Mahajan, published in the February 1993 issue of the ASME JOURNAL OF HEAT TRANSFER, Vol. 115, pp. 149–157.

[2] J. A. Jones Professor of Mechanical Engineering, Duke University, Durham, NC 27708; Fellow ASME.

recover Angirasa and Mahajan's conclusion to their first problem, in which the vertical wall was attached to an adiabatic wall.

References

Bejan, A., 1984, *Convection Heat Transfer*, Wiley, New York, p. 116.

Kimura, S., and Bejan, A., 1985a, "Natural Convection in a Differentially Heated Corner Region," *The Physics of Fluids*, Vol. 28, pp. 2980–2989.

Kimura, S., and Bejan, A., 1985b, "Natural Convection in a Stably Heated Corner Filled With Porous Medium," ASME Journal of Heat Transfer, Vol. 107, pp. 293–298.

Authors' Closure

We thank Professor Bejan for his thoughtful comments on our work. We agree with him that it is possible to obtain qualitative understanding of the effects studied from scaling theory. The objective of our paper was to provide quantitative results for an important configuration and describe the physics underlying these observed effects. His comment on heat transfer following the path of least resistance in a corner is, in general, valid for all heat transfer processes in different configurations as well.

recover Angirasa and Mahajan's conclusion to their first problem, in which the vertical wall was attached to an adiabatic wall.

References

Bejan, A., 1984, *Convection Heat Transfer*, Wiley, New York, p. 116.

Kimura, S., and Bejan, A., 1985a, "Natural Convection in a Differentially Heated Corner Region," *The Physics of Fluids*, Vol. 28, pp. 2980–2989.

Kimura, S., and Bejan, A., 1985b, "Natural Convection in a Stably Heated Corner Filled With Porous Medium," ASME JOURNAL OF HEAT TRANSFER, Vol. 107, pp. 293–298.

Authors' Closure

We thank Professor Bejan for his thoughtful comments on our work. We agree with him that it is possible to obtain qualitative understanding of the effects studied from scaling theory. The objective of our paper was to provide quantitative results for an important configuration and describe the physics underlying these observed effects. His comment on heat transfer following the path of least resistance in a corner is, in general, valid for all heat transfer processes in different configurations as well.